MPM
SCIENTIFIC
JOURNAL

MATERIALS PHYSICS AND MECHANICS

MATERIALS PHYSICS AND MECHANICS

МЕХАНИКА И ФИЗИКА МАТЕРИАЛОВ

Materials Physics and Mechanics

Том 47, номер 2, 2021 год

Тел.: +7(812)552 77 78, доб. 224 **E-mail:** mpmjournal@spbstu.ru **Web-site:** http://www.mpm.spbstu.ru

Тематика журнала

Международный научный журнал "Materials Physics and Mechanics" издается Санкт-Петербургским политехническим университетом Петра Великого в сотрудничестве с Институтом проблем машиноведения Российской Академии Наук в печатном виде и электронной форме. Журнал публикует обзорные и оригинальные научные статьи на английском языке по следующим тематикам:

• Механика композиционных и наноструктурированных материалов.
• Физика прочности и пластичности композиционных и наноструктурированных материалов.
• Механика процессов деформации и разрушения в традиционных материалах (твердых телах).
• Физика прочности и пластичности традиционных материалов (твердых тел).
• Физика и механика дефектов в композиционных, наноструктурированных и традиционных материалах.
• Механика и физика материалов в связанных полях.

Редколлегия принимает статьи, которые нигде ранее не опубликованы и не направлены для опубликования в другие научные издания. Все представляемые в редакцию журнала "Механика и физика материалов" статьи рецензируются. Статьи могут отправляться авторам на доработку. Не принятые к опубликованию статьи авторам не возвращаются.

Журнал "Механика и физика материалов" ("Materials Physics and Mechanics") включен в систему цитирования Web of Science Emerging Sources Citation Index (ESCI), SCOPUS и РИНЦ.

Содержание

Contents

BALLISTIC RESISTANCE OF CERAMIC METALLIC TARGET FOR VARYING LAYER THICKNESSES

M.K. Khan[1], M.A. Iqbal[1*], V. Bratov[2], N.F. Morozov[2,3], N.K. Gupta[4]

[1]Department of Civil Engineering, Indian Institute of Technology Roorkee, Roorkee-247667, India

[2]Institute for Problems in Mechanical Engineering, Russian Academy of Sciences, Saint Petersburg, Russia

[3]Department of Theory of Elasticity, Saint Petersburg State University, Saint Petersburg, Russia

[4]Department of Applied Mechanics, Indian Institute of Technology Delhi, New Delhi-110016, India

*e-mail: iqbal_ashraf@rediffmail.com

Abstract. The ballistic behaviour of a bi-layer ceramic-metal target against steel projectile with varying layer thicknesses has been investigated using a three-dimensional finite element model. The bi-layer target was made of alumina 99.5 % ceramic front layer and aluminium 2024-T3 metallic back layer with an areal dimension of 100×100 mm and the thickness of both layers were varied, with the total thickness of the composite being kept as 10 mm and 20 mm. A steel 4340 cylindrical blunt-nosed projectile was used with 30 grams mass and 10.9 mm diameter. The Johnson-Holmquist 2 (JH-2) constitutive model was used for reproducing the high strain behavior of alumina and Johnson-Cook (JC) model was used for aluminium alloy and steel. The impact velocity of the projectile was varied in the range 200-700 m/s for 10 mm total thickness and 500-800 m/s in the case of 20 mm total thickness for studying the effects of thickness ratios on ballistic resistance of the bi-layer target. The residual velocities were compared and the ratio of front to back layer providing the highest ballistic limit velocity was found for both cases.
Keywords: Ballistic resistance, Ceramic-metallic target, ballistic limit velocity

1. Introduction
The behaviour of ceramic under large deformation and high strain rate loading has been extensively studied for its application in protective structures. The ceramic is widely used in composite armours due to its higher compressive strength, higher hardness, and lower density. In case of a ballistic impact, the ceramic layer shatters and erodes the high-velocity incoming projectile leading to distortion of the nose and drop in the momentum of the projectile. The ceramic based composite armour has its primary application as protective layers in mobile structures like vehicles, aircraft, and body armour, where lightweight is a prime requirement [1].

When the projectile impacts the ceramic layer of the composite target, the ceramic is broken instantly. The functional utility of the metallic layer in composite armour is to support the ceramic fragments and absorbing the remaining kinetic energy of the projectile while undergoing plastic deformation. The alloys of aluminium have lesser weight density and are commonly used as backing material having sufficient tensile strength to support ceramic layer during a ballistic impact. The ballistic resistance capacity of alumina based bi-layer composite target with different aluminium alloys as the backing layer was varied significantly at lower velocities when impacted by steel 4340 blunt cylindrical projectile. The performance of

alumina backed by four different aluminium alloys; namely 1100-H12, 6061, 2024-T3 and 7075 was being compared. The bi-layer target with aluminium alloys 7075 backing layer shows the best ballistic resistance. The ballistic resistance of bi-layer target was found to be lower in the case of aluminium alloy 6061 backing layer in comparison of alloy 2024 and 1100 backing layer although 6061 alloy has higher yield strength than alloy 2024 and 1100. The performance of the bi-layer target was found to be not showing dependence only on the yield strength of the backing material [2]. The tensile strength and hardness of aluminium 2024 were reported to be increased with heat treatment leading to superior ballistic performance of alumina-aluminium composite target against 7.62 mm AP projectiles. The addition of cover plate by reducing the thickness of other components to maintain a constant thickness reduces the ballistic efficiency of a composite target. The alumina-aluminum bi-layer target was found to be having higher ballistic resistance for the ratio of front layer alumina to back layer aluminium lying in the range of 1-3 [3]. The depth of penetration in an aluminium block of 100 mm cube with alumina layer protection and without alumina layer protection was compared against high velocity impact of steel spheres of 6.35 mm diameter. The alumina layer of 4 mm thickness backed by 2 mm aluminium layer was provided with a gap of 30 mm in front of aluminum cube. The depth of penetration was always found to be lesser for alumina layer protected block. The weight saving for the same level of protection with alumina layer protection was higher for impact velocities under 1800 m/s. The diameter of the damage zone in the aluminium block was measured and found to be higher in the case of alumina protection due to the shattering of the projectile after interaction with the ceramic layer. The brittle nature of the projectile leads to lesser depth of penetration for incidence velocities higher than 1800 m/s for aluminium block without alumina protection [4]. The ballistic behaviour of 100 mm square alumina (Al_2O_3) target of 5 mm thickness without any back layer was investigated against the impact of steel 4340 ogival projectile of 10.9 mm shank diameter. The velocity of the impacting projectile was achieved in a range of 52-275 m/s. The damage area in ceramic was found to be increasing and ceramic fragment size was found to be decreasing with the increase in incidence velocity of the projectile. The damage in the projectile and ceramic target was found to be increased in the case of oblique impact of 15° and 30° obliquity [5]. The diameter to length ratio (D/L) of a steel 4340 projectile was varied while maintaining constant mass to study the effects of D/L ratio on the ballistic behaviour of a bi-layer alumina-aluminium target. The bi-layer target attained higher ballistic limit velocity against projectiles having higher D/L ratios [6]. The properties of metallic backing layer as mentioned like tensile strength, hardness, and nature of impacting projectile and ratio of the front layer to back layer effects the performance of a bi-layer target. The thickness ratios of the front layer to the back layer is found to be of paramount importance for design optimization in terms of weight, for providing desired level of protection at minimum possible weight. The optimization of thickness of layers in terms of constant total thickness involves the determination of the ratio providing maximum ballistic limit velocity for a given total thickness of a composite target.

In the present study, a finite element three-dimensional model has been developed to compare the ballistic behaviour of alumina 99.5% and aluminium 2024-T3 composite target of varying layer thickness ratios. The optimum ratio of front to back layer thickness for a constant total thickness has been achieved. Two cases of 10 mm total thickness and 20 mm total thickness of the target have been considered. The residual velocities for three different ratios have been compared for both cases.

2. Constitutive Models

The Johnson-Holmquist-2 (JH-2) model has been used for brittle ceramic and Johnson-Cook (JC) model has been applied for metallic projectile and back layer for reproducing their behaviour under ballistic load.

Johnson-Holmquist-2 (JH-2). The JH-2 [7] model proposed by Johnson and Holmquist has been widely used for modelling the behaviour of ceramic under loading conditions resulting in high strain rate, large deformation, and high pressure and high stress [6,8-9]. The model gives the equivalent strength related to pressure and damage, see Fig. 1. The normalized equivalent stress for strength:

$$\sigma^* = \sigma_i^* - D\left(\sigma_i^* - \sigma_f^*\right) \tag{1}$$

Where, σ_i^* and σ_f^* are normalized intact and fracture strength, D is the damage varying between 0 for intact material and 1 for fully fractured material. The equivalent stresses are normalized by dividing the value by the equivalent stress value at Hugoniot elastic limit (HEL). The HEL is the net compressive stress corresponding to the uniaxial strain (shock wave) exceeding the elastic limit of the material. The HEL contains both the pressure and deviator stress components [10].

Strength

$$\sigma_i^* = A(P^* + T^*)^N(1 + C\ln\dot{\varepsilon}^*)$$

Intact (D=0)

Damaged (0<D<1.0)

$$\sigma^* = \sigma_i^* - D(\sigma_i^* - \sigma_f^*)$$

$\sigma_{f_{max}}^*$

Fractured (D=1.0)

$$\sigma_f^* = B(P^*)^M(1 + C\ln\dot{\varepsilon}^*)$$

Normalized Equivalent Stress, $\sigma^* = \sigma/\sigma_{HEL}$

HEL

T^*

Normalized Pressure, $P^* = P/P_{HEL}$

Damage

$$D = \sum\frac{\Delta\varepsilon_p}{\varepsilon_p^f}$$

$$\varepsilon_p^f = D_1(P^* + T^*)^{D_2}$$

Equivalent Plastic Fracture Strain, ε_p^f

T^*

$$P^* = P/P_{HEL}$$

Pressure

$$P = K_1\mu + K_2\mu^2 + K_3\mu^3 + \Delta P$$

0<D<1

D=1.0

ΔP

D=0

Pressure, P

$T(1-D)$

$$\mu = \frac{\rho}{\rho_o} - 1$$
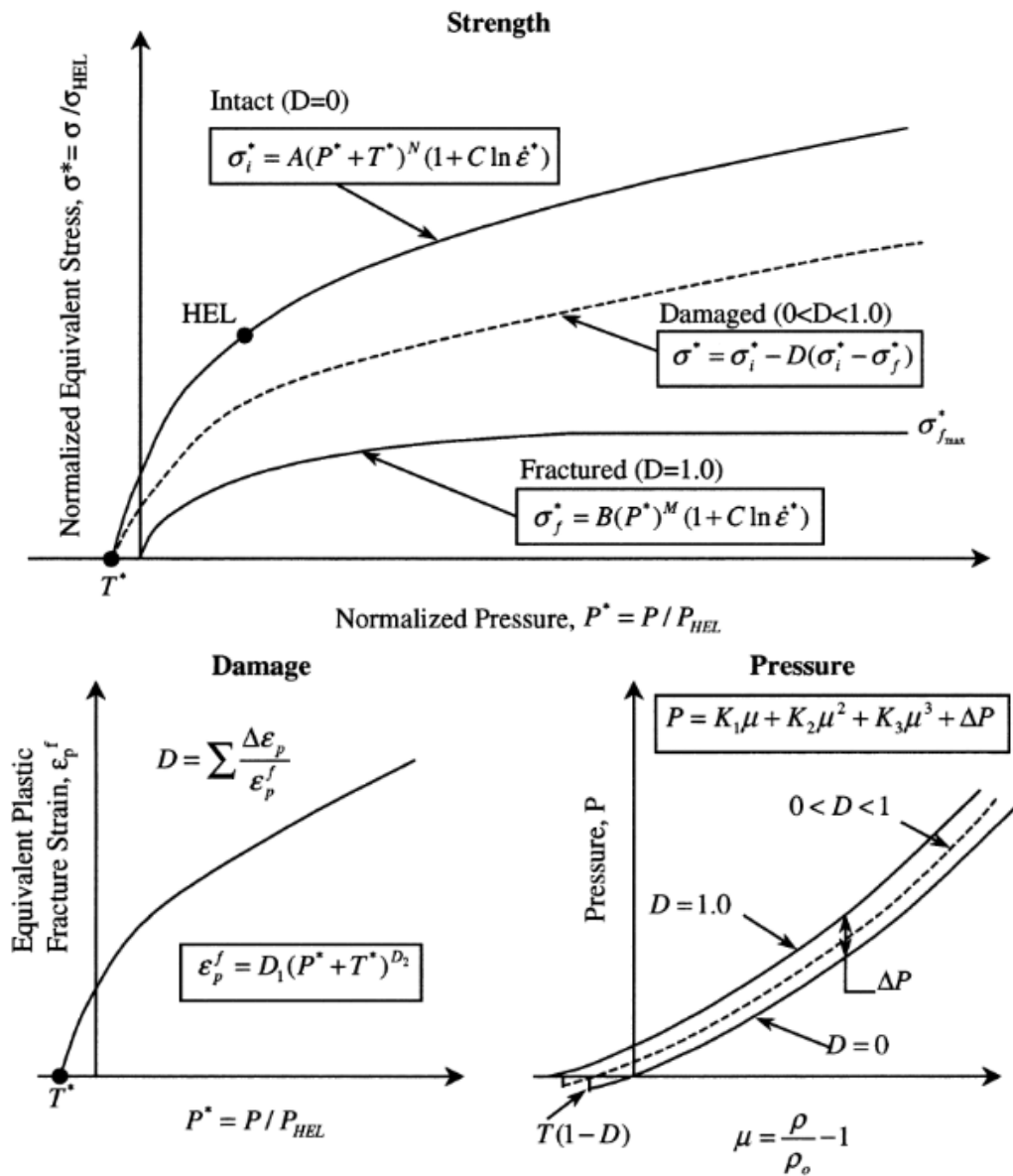
Fig. 1. The JH-2 Model [10]

The intact and fracture strength are:

$$\sigma_i^* = A(P^* + T^*)^N(1 + C \ln \dot{\varepsilon}^*) \tag{2}$$
$$\sigma_f^* = B(P^*)^M(1 + C \ln \dot{\varepsilon}^*) \tag{3}$$

Where, $A, B, C, M,$ and N are the material constants. The normalized pressure P^* is the actual pressure divided by pressure at HEL; whereas normalized maximum tensile hydrostatic pressure T^* is the maximum tensile hydrostatic pressure the material can withstand divided by pressure at HEL. The dimensionless strain rate $\dot{\varepsilon}^*$ is the actual equivalent strain rate divided by reference strain rate. The damage for fracture accumulated in the JH-2 model as:

$$D = \sum \frac{\Delta \varepsilon_p}{\varepsilon_p^f}, \tag{4}$$

where $\Delta \varepsilon_p$ is the equivalent plastic strain during a cycle of integration and is ε_p^f the plastic strain to fracture, calculated as:

$$\varepsilon_p^f = D_1(P^* + T^*)^{D_2}, \tag{5}$$

where D_1 and D_2 are the damage constants. The pressure is related to volumetric strain (μ) before and after damage accumulations are:

$$P = K_1\mu + K_2\mu^2 + K_3\mu^3, \tag{6}$$
$$P = K_1\mu + K_2\mu^2 + K_3\mu^3 + \Delta P, \tag{7}$$

where K_1, K_2 and K_3 are pressure constants, and K_1 is the bulk modulus of the material. The material parameters have been taken from [5], see Table 1. The parameters determination of a material needs extensive work consisted of experiments at high strain rate and high pressure and exhaustive numerical study [10].

Table 1. JH-2 constitutive model parameters for alumina 99.5% [5]

Material parameters	Numerical values
Density (kg/m³)	3700
EOS	**Polynomial**
Bulk modulus, K₁ (GPa)	130.95
Pressure constant, K₂ (GPa)	0
Pressure constant, K₃ (GPa)	0
Strength model	**JH-2**
Shear modulus, G (GPa)	90.16
Hugoniot elastic limit (HEL) (GPa)	19
Intact strength constant, A	0.93
Intact strength exponent, N	0.6
Strain rate constant, C	0
Fracture strength constant, B	0.31
Fracture strength exponent, M	0.6
Normalized maximum fractured strength	1
Pressure at HEL (GPa)	1.46
Failure model	**JH-2**
Damage constant, d₁	0.005
Damage exponent, d₂	1
Bulking factor, β	1

Johnson-Cook (JC). The behaviour of aluminium backing layer and steel 4340 projectile under the impact load have been modelled using the Johnson-Cook (JC) elasto-viscoplastic material model [11-12]. The JC model has been used for aluminium [13-14] and steel [15-16] under large deformations at high strain rate loading in the available literature.

The JC model is used for modelling the flow and fracture behaviour of metals incorporating the effects of material yielding, plastic flow, isotropic strain hardening, strain rate hardening, and thermal softening. The equivalent von Mises stress $\bar{\sigma}$ represented as:

$$\bar{\sigma} = \{A + B(\bar{\varepsilon}^{pl})^n\}\left\{1 + C\ln\left(\frac{\dot{\bar{\varepsilon}}^{pl}}{\dot{\varepsilon}_0}\right)\right\}\{1 - \hat{T}^m\}, \tag{8}$$

where A, B, n, C and m are the material parameters. $\bar{\varepsilon}^{pl}, \dot{\bar{\varepsilon}}^{pl}\ \dot{\varepsilon}_0$ are equivalent plastic strain and the equivalent plastic strain rate and a reference strain rate. $\hat{T}$ is the non-dimensional temperature:

$$\hat{T} = \begin{cases} 0 & \text{for T} < \text{T}_0 \\ \frac{(\text{T}-\text{T}_0)}{(\text{T}_{melt}-\text{T}_0)} & \text{for T}_0 \leq \text{T} \leq \text{T}_{melt} \\ 1 & \text{for T} > \text{T}_{melt} \end{cases} \tag{9}$$

where T_0 is the transition temperature and T_{melt} is the melting point temperature. The damage is accumulated in a similar manner as discussed in JH-2 model, see Eqn. (4). The equivalent plastic strain at failure represented as a function of stress-triaxiality, strain rate, and adiabatic effects:

$$\bar{\varepsilon}_f^{pl} = \left[D_1 + D_2 exp\left(D_3\frac{\sigma_m}{\bar{\sigma}}\right)\right]\left[1 + D_4 ln\left(\frac{\dot{\bar{\varepsilon}}^{pl}}{\dot{\varepsilon}_0}\right)\right][1 + D_5\hat{T}], \tag{10}$$

where $D_1 - D_5$ are the material damage parameters. The determination of all the parameters of JC model has been discussed in detail in Iqbal et al. [16]. The JC model parameters for aluminium 2024-T3 and steel 4340 are given in Table 2 [6].

Table 2. The parameters of JC Model [6]

Constants with units	Al 2024-T3	Steel 4340
Density (Kg/m^3)	2785	7770
EOS	Shock	Linear
Strength Model	JC	JC
Shear Modulus, G (GPa)	26.92	77
Static Yield Strength, A (GPa)	0.167	0.950
Strain Hardening Constant, B (GPa)	0.596	0.725
Strain Hardening Exponent, n	0.551	0.375
Strain Rate Constant, C	0.001	0.015
Thermal Softening Exponent, m	0.859	0.625
Melting Temperature, K	893	1793
Reference Strain Rate	1	1
Failure Model	JC	JC
Damage Constant, D_1	0.112	-0.8
Damage Constant, D_2	0.123	2.1
Damage Constant, D_3	1.5	-0.5
Damage Constant, D_4	0.007	0.002
Damage Constant, D_5	0	0.61

3. Validation

The experimental data of a previous study was used for the validation of the numerical model developed in the present study [5]. The alumina 99.5% ceramic with 95×95 mm areal clear

span and 5 mm thickness was impacted on by steel 4340 ogival nosed projectiles of 10.9 mm shank diameter and 30 grams mass. The residual velocity was reported to be 153 m/s corresponding to an incidence velocity of 215 m/s. The numerical simulation model developed in the present study gave the residual velocity of 151 m/s with a minor error of only 1%. The mode of failure of ceramic was also closely matched. Henceforth, the model developed was found to be giving rational predictions.

4. Numerical Model

The finite element simulations have been performed on ABAQUS/Explicit finite element code employing validated JH-2 and JC model for the target and the projectile material. The alumina 99.5% with a planar dimension of 95 × 95 mm has been used with varied thickness. The alumina is backed by aluminium 2420-T3 layer of 95×95 mm planar dimension. The interaction between both the layers has been provided as general contact with the kinematic contact algorithm having a coefficient of friction 0.5. The projectile has been taken as a 10.9 mm diameter cylinder with length 46 mm, weighing equivalent to 30 grams. The interaction between the projectile and centre zone of the target was modelled using the surface to surface contact with kinematic contact algorithm assuming negligible friction due to high velocity of the projectile and small thickness of the target.

The target was restrained with respect to translation and rotation at the peripheral edges. A typical model of the target with and without meshing is shown in Fig. 2, showing the meshing style and boundary conditions. The central portion of the target of size 50 mm × 50 mm is provided with linear C3D8R elements of size 0.6 mm × 0.6 mm × 0.6 mm, while the remaining portion of the plate was modelled using 1 mm × 1 mm × 1 mm sized linear C3D8R elements. The linear C3D8R elements of size 0.6 mm × 0.6 mm × 0.6 mm were used for the meshing of the projectile.
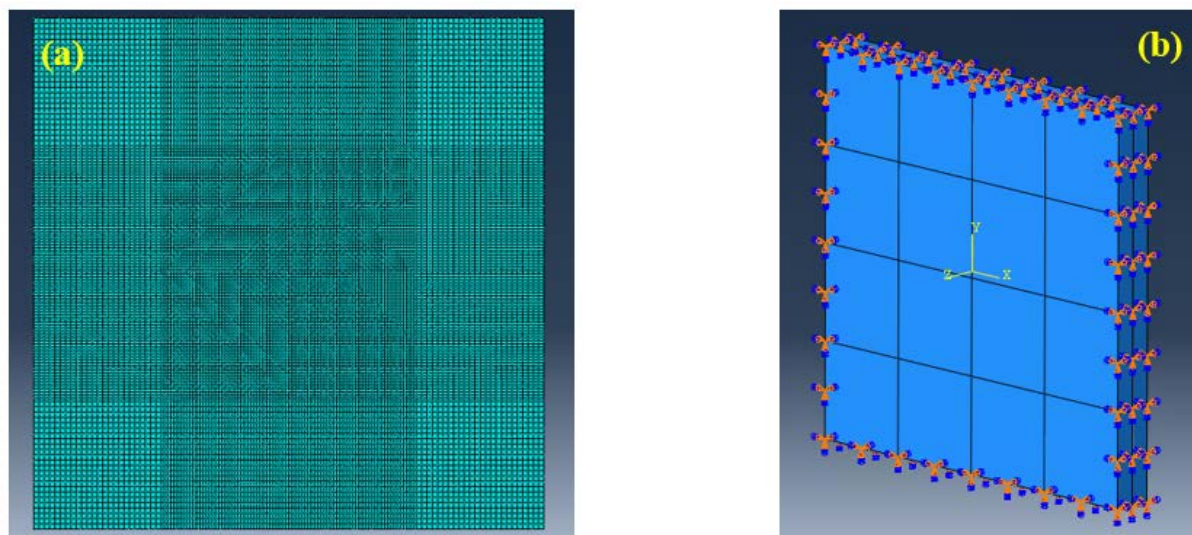
Fig. 2. The typical target (a) Meshing of the target (b) restrained against all degrees of freedom at the edges

Six cases of different thickness of the layers have been investigated in the present study, see Table 3. The total thickness of bi-layer composite target has been taken as 10 mm and 20 mm. Three ratios of front layer to back layer thickness (1, 1.5 and 2.3) were considered for both 10 mm and 20 mm thickness. The least thickness ratio of front layer to back layer has

been taken equivalent to unity as the ballistic resistance of a bilayer target reduced significantly for the ratio of front layer to back layer thickness less than unity [17].

Table 3. The different configuration based on ratio of front layer to back layer thickness

S. No.	Cases	Front layer thickness (mm)	Back layer thickness (mm)	Ratio of front layer to back layer
1	10R1	5	5	1
2	10R2	6	4	1.5
3	10R3	7	3	2.3
4	20R1	10	10	1
5	20R2	12	8	1.5
6	20R3	14	6	2.3

5. Results and discussions

The bi-layer alumina-aluminium target has been impacted by 10.9 mm diameter cylindrical blunt projectile with incidence velocity ranging, 200-700 m/s for 10 mm total thickness and 500-800 m/s for 20 mm total thickness. When the projectile impacts the ceramic front layer, the ceramic gets comminuted in front of the projectile, and cracks are initiated and propagates in the ceramic. The fracture conoid is formed in the ceramic layer by the interaction of radial and circumferential cracks. The load is transferred to the backing layer through this fracture conoid. The remaining energy of the projectile is dissipated by plastic deformation of the backing layer. As the stresses in the backing layer reaches to failure stress of the metallic backing layer, the plugging occurs, see Fig. 3.
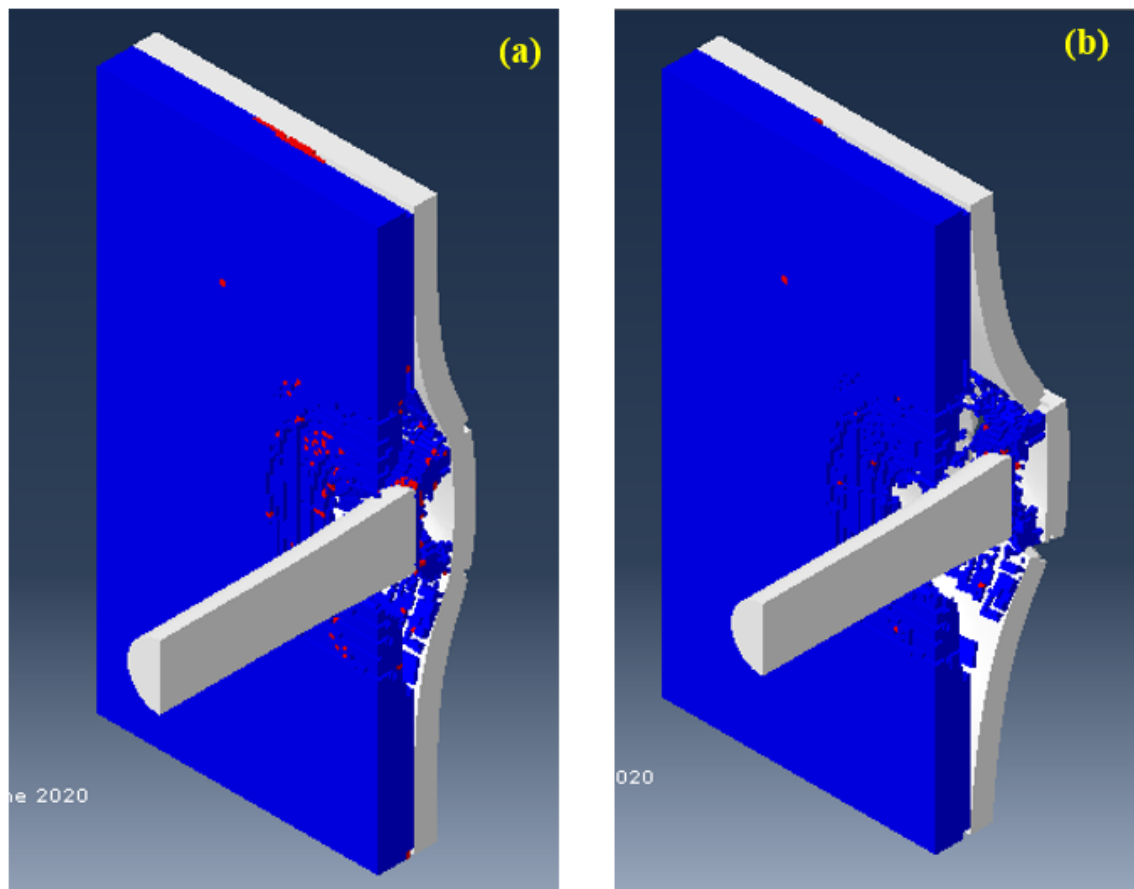
Fig. 3. The failure mechanics of 10R1 configuration (a) 40 µs (b) 80 µs when impacted with an 300 m/s incidence velocity

The residual velocities have been compared for three cases of the different front layer to back layer thickness ratios, see Table 4. At the incidence velocity of 200 m/s the 10R1 ratio gave the best performance with the lowest residual velocity among the three cases. In the variation of incidence velocities from 300 to 700 m/s with an interval of 100 m/s, the 10R2 configuration seems to perform better with lesser residual velocities among the three cases. Although, the difference in the residual velocities is of very small order but overall best ballistic performance was found for the 10R2 configuration in terms of residual velocities.

Table 4. The residual velocities of the projectile at different incidence velocities for three cases of varying front to back layer thickness ratio

S. No.	Incidence Velocity (m/s)	Residual Velocity (m/s)		
		10R1	10R2	10R3
1	200	27	46	45
2	300	170	168	163
3	400	259	253	255
4	500	342	335	342
5	600	439	426	444
6	700	532	518	521

The variation in the ballistic limit velocity is also found to be very small. The ballistic limit velocity is worked out as the average of lowest incidence velocity with complete perforation and the highest incidence velocity with no perforation. The ballistic limit velocities are presented in Table 5. The best performance in terms of ballistic limit velocity is found to be for 10R1 configuration; the ratio of front layer to back layer thickness is equivalent to unity.

Table 5. The values ballistic limit velocities for 10 mm composite bi-layer target

S. No.	Configuration	Ballistic limit velocity (m/s)
1	10R1	185
2	10R2	175
3	10R3	165

The failure of both the layer in the bi-layer target of 20 mm total thickness is shown in Fig. 4. The failure of the ceramic layer with formation of fracture conoid is evident at 20 µs and plugging of the back layer aluminium is occurred at 80 µs. The mushrooming of the projectile has also occurred in the initial phase of the interaction of the projectile with the ceramic layer.
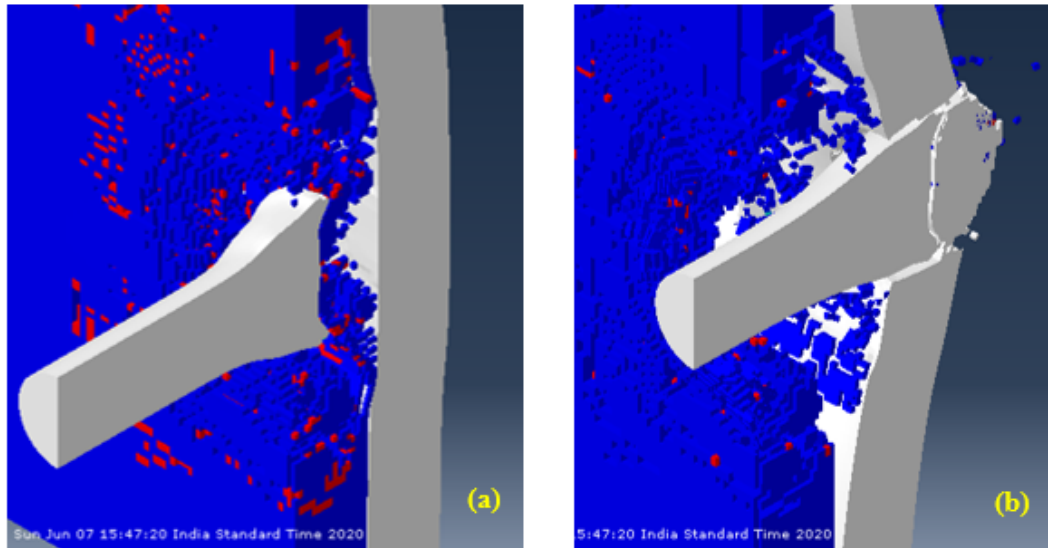
Fig. 4. The failure mechanics of 20R1 configuration (a) 20 µs (b) 80 µs when impacted with an 700 m/s incidence velocity

The residual velocities for 20 mm total thickness have been compared in Table 6. The incidence velocities has been taken in the range, 500-800 m/s, with an interval of 100 m/s. The 20R2 case was found to be having minimum residual velocities among the three ratios. The residual velocities are much higher for both the case 20R1 and 20R2 than 20R2 at relatively lower incidence velocities.

Table 6. The residual velocities of the projectile at different incidence velocities for three cases of varying front to back layer thickness ratio

S. No.	Incidence Velocity (m/s)	Residual Velocity (m/s)		
		20R1	20R2	20R3
1	500	109	0	244
2	600	236	133	298
3	700	295	235	353
4	800	336	321	427

The ballistic limit velocities are given in Table 7. The highest ballistic limit velocity has been achieved in the case of 20R2; the ratio of front layer thickness to back layer thickness was 1.5. The ballistic limit velocity is very close for 20R1 and 20R2, although 20R2 is also found to be giving lesser values of residual velocities for corresponding incidence velocities which means higher level of dissipation of the kinetic energy of the incoming projectile.

Table 7. The values ballistic limit velocities for 10 mm composite bi-layer target

S. No.	Configuration	Ballistic limit velocity (m/s)
1	20R1	490
2	20R2	505
3	20R3	415

The ratio of front layer to back layer thickness giving the highest ballistic limit velocity was found to be 1 and 1.5 for 10 mm and 20 mm total thickness respectively among the three cases considered for both the thicknesses.

6. Conclusion

The variation of ballistic performance of alumina 99.5% ceramic backed by aluminium 2024-T3 with varying thickness of the layers was studied. The thickness of front layer and back layer of the composite target was varied with the total thickness being kept constant at 10 and 20 mm.

Three ratios of front layer to back layer thickness 1, 1.5, and 2.3 were considered. The composite bi-layer target was impacted by blunt-nosed cylindrical steel 4340 projectile.

The residual velocities for three ratios were compared for 10 mm composite target under incidence velocities in the range, 200-700 m/s. The variation in the residual velocities was not very high, although overall 1.5 ratio was giving lesser residual velocities for most of the incidence velocities.

The ballistic limit velocity was found to be highest when the ratio of front layer to back layer thickness was equivalent to unity for 10 mm composite target. Although, the performance of the three cases was not significantly varying in the range of ratios considered.

The 20 mm composite target was impacted with incidence velocities lying in the range, 500-800 m/s. The residual velocities were found to be significantly lesser for 1.5 ratio and also the ballistic limit was highest for this ratio.

The ratio of front layer to back layer thickness giving the highest ballistic limit velocity was found to be varying with the variation in total thickness of the composite target.

References

[1] Bresciani LM, Manes A, Giglio M. An analytical model for ballistic impacts against ceramic tiles. *Ceramics International.* 2018;44(17): 21249-21261.

[2] Venkatesan J, Iqbal MA, Gupta NK, Bratov V, Kazarinov N, Morozov F. Ballistic characteristics of bi-layered armour with various aluminium backing against ogive nose projectile. *Procedia Structural Integrity.* 2017;6: 40-47.

[3] Übeyli M, Yıldırım RO, Ögel B. Investigation on the ballistic behavior of Al2O3/Al2024 laminated composites. *Journal of Materials Processing Technology.* 2008;196(1-3): 356-364.

[4] Hazell PJ, Fellows NA, Hetherington JG. A note on the behind armour effects from perforated alumina/aluminium targets. *International Journal of Impact Engineering.* 19981;21(7): 589-595.

[5] Khan MK, Iqbal MA, Bratov V, Morozov NF, Gupta NK. An investigation of the ballistic performance of independent ceramic target. *Thin-Walled Structures.* 2020;154: 106784.

[6] Khan MK, Iqbal MA, Bratov V, Gupta NK, Morozov NF. A numerical study of ballistic behaviour of ceramic metallic bi-layer armor under impact load. *Materials Physics and Mechanics.* 2019;42(6): 699-710.

[7] Johnson GR, Holmquist TJ. An improved computational constitutive model for brittle materials. *AIP Conference Proceedings* 1994;309(1): 981-984.

[8] Venkatesan J, Iqbal MA, Madhu V. Experimental and numerical study of the dynamic response of B4C ceramic under uniaxial compression. *Thin-Walled Structures.* 2020;154: 106785.

[9] Serjouei A, Gour G, Zhang X, Idapalapati S, Tan GE. On improving ballistic limit of bi-layer ceramic–metal armor. *International Journal of Impact Engineering.* 2017;105: 54-67.

[10] Holmquist TJ, Templeton DW, Bishnoi KD. Constitutive modeling of aluminum nitride for large strain, high-strain rate, and high-pressure applications. *International Journal of Impact Engineering.* 2001;25(3): 211-231.

[11] Johnson GR, Cook WH. Fracture characteristics of three metals subjected to various strains, strain rates, temperatures and pressures. *Engineering Fracture Mechanics.* 1985;21(1): 31-48.

[12] Johnson GR, Cook WH. A constitutive model and data for metals subjected to large strains, high strain rates and high temperatures. In: *Proceedings of the 7th International Symposium on Ballistics.* 1983. p.541-547.

[13] Gupta PK, Iqbal MA, Mohammad Z. Energy dissipation in plastic deformation of thin aluminum targets subjected to projectile impact. *International Journal of Impact Engineering.* 2017;110: 85-96.

[14] Iqbal MA, Tiwari G, Gupta PK, Bhargava P. Ballistic performance and energy absorption characteristics of thin aluminium plates. *International Journal of Impact Engineering.* 2015;77: 1-5.

[15] Senthil K, Iqbal MA. Prediction of superior target layer configuration of armour steel, mild steel and aluminium 7075-T651 alloy against 7.62 AP projectile. In: *Structures.* Elsevier; 2020.

[16] Iqbal MA, Senthil K, Bhargava P, Gupta NK. The characterization and ballistic evaluation of mild steel. *International Journal of Impact Engineering.* 2015;78: 98-113.

[17] Hetherington JG. The optimization of two component composite armours. *International journal of Impact Engineering.* 1992;12(3): 409-414.

THERMOELECTRIC VISCOELASTIC SPHERICAL CAVITY WITH MEMORY-DEPENDENT DERIVATIVE

Mohamed H. Hendy[1,2], **Sayed I. El-Attar**[1], **Magdy A. Ezzat**[3*]

[1]Department of Mathematics, Faculty of Science, Northern Border University, Arar,

Saudi Arabia

[2]Department of Mathematics, Faculty of Science, Al Arish University, Al Arish, Egypt

[3]Department of Mathematics, College of Science and Arts, Qassim University, Al Bukairiyah, Saudi Arabia

*e-mail: maezzat2000@yahoo.com

Abstract. We apply the memory-dependent derivative theory of thermoelasticity to the one-dimensional problem for a viscoelastic spherical cavity subjected to thermal loading. The predictions of the theory are discussed and compared with those for the coupled theory of thermoelasticity.
Keywords: thermo-viscoelasticity, thermoelectric properties, memory-dependent derivative, spherical cavity, Laplace transforms, numerical results

1. Introduction
Biot [1] formulated the theory of coupled thermoelasticity to eliminate the paradox inherent in the classical uncoupled theory that elastic changes have no effect on temperature. Lord and Shulman [2] introduced the theory of generalized thermoelasticity in one relaxation time by using the Maxwell-Cattaneo law of heat conduction instead of the conventional Fourier's law. The heat equation associated with this theory is hyperbolic and hence eliminates the paradox of infinite speeds of propagation inherent in both the uncoupled and the coupled theories of thermoelasticity.

The uniqueness of solution for thermoelasticity theory was proved under different conditions by Ignaczak [3], Sherief [4], Chandrasekharaiah [5], and thermo-viscoelasticity theory by Ezzat and El-Karamany [6,7]. Ezzat and Awad [8,9] extended this theory to deal with micropolar materials.

An immediate change amongst electricity and heat by utilizing thermoelectric materials has pulled in much consideration as a result of their potential applications in Peltier coolers also, thermoelectric power generators [10]. Among the commitments in continuum mechanics of thermoelectric materials are crafted by Shercliff [11] and Ezzat and Youssef [12,13] in MHD.

Differential equations of fractional order have been the focal point of numerous examinations because of their continuous appearance in different applications in liquid mechanics, viscoelasticity, science, material science, and building. Povstenko [14] investigated new thermoelasticity models that use fractional derivatives. The fractional-order theory of thermoelasticity was derived by Sherief et al. [15]. As of late, Ezzat [16-19] and Ezzat, El-Karamany [20,21] and Ezzat et al. [22,23] set up another model of partial heat conduction equation utilizing the Taylor-Riemann series extension of time-fractional order.

Wang and Li [24] proposed the memory-dependent derivative (MDD) to characterize the memory effect of systems and materials. Yu et al. [25] introduced the first-order MDD model to describe the rate of heat flux in the Lord and Shulman generalized thermoelasticity. In this model, the heat transfer equation has been modified, which may be better than fractional equations. It may be mentioned that the definition of MDD is more intuitive in the perception of physical importance, and therefore, the resultant differential equations based on memory-dependent are more efficient in real-world applications [25]. Recently, memory-dependent heat transfer has been applied to solve many related thermoelastic and thermo-viscoelastic problems [26–28].

Ezzat et al. [29] proposed the generalized Ohm and Fourier laws for elasto-thermoelectric materials subjected to MDD heat transfer when the medium is permeated by an external magnetic field, as

$$J = \sigma_o \left(E + \frac{\partial u}{\partial t} \wedge \mu_o H - k_o \nabla T \right),$$ (1)

$$q + \omega D_\omega q = -k \nabla T + \pi_o J,$$ (2)

where q is the heat flux vector and ω is the time delay.

Among the few works devoted to MDD applications of heat transfer equation for thermoelectric materials, we can refer to the survey of Ezzat and El-Bary [30], Ezzat et al. [31], Hendy et al. [32] and Ezzat [33].

In light of the advantage in describing the memory effect of thermoelectric materials, we solve a 1D thermal shock problem for a viscoelastic spherical cavity by using the memory-dependent derivative theory. The solution is obtained for different values of the parameters of the MDD model. Some comparisons are made and shown in figures to estimate the effects of the time-delay parameter for different forms of kernel function on all studied fields.

2. Physical problem

Let (r, ψ, φ) denote spherical polar coordinates. We shall consider a homogeneous, isotropic, thermoelectric viscoelastic medium occupying the region $a \leq r < \infty$, where a is the radius of the spherical cavity. The surface of the cavity is taken to be traction-free and subjected to a thermal shock that is a function of time. A constant magnetic field of intensity H with components $(0, H_o, 0)$ permeates the medium in the absence of an external electric field E. Since no external electric field is applied, and the effect of polarization of the ionized medium can be neglected, it follows that the total electric field E vanishes identically inside the medium [34].

Because of spherical symmetry, the displacement vector u will have the components

$$u_r = u(r,t), \quad u_\psi = 0, \quad u_\varphi = 0.$$ (3)

The components of the electric current density vector J are [17]

$$J_r = -\sigma_o k_o \frac{\partial T}{\partial r}, \quad u_\psi = 0, \quad u_\varphi = \mu_o H_o \frac{\partial u}{\partial t}.$$ (4)

The components of the electromagnetic induction vector are given by [18]

$$B_\psi = \mu_o H_o = B_o = \text{constant}, \quad B_r = B_\varphi = 0.$$ (5)

The Lorentz force components are given by [19]

$$F_r = -\sigma_o \mu_o^2 H_o^2 \frac{\partial u}{\partial t}, \quad F_\psi = 0, \quad F_\varphi = 0.$$ (6)

The components of strain tensor are given by [37]:

$$e_{rr} = \frac{\partial u}{\partial r}, \quad e_{\psi\psi} = e_{\varphi\varphi} = \frac{u}{r}, \quad e_{r\psi} = e_{r\varphi} = e_{\psi\varphi} = 0.$$ (7)

The figure-of-merit ZT_o at some reference temperature T_o [35]:

$$ZT_o = \frac{\sigma_o k_o^2}{k} T_o.$$ (8)

The first Thomson relation at T_o [36]:

$$\pi_o = k_o T_o,$$ (9)

where π_o is the Peltier coefficient at T_o.

The components of the stress tensor are given by [38, 39]

$$\sigma_{rr} = K_o e + \left(\frac{2}{3}\widehat{R} + K_o\right)\left(\frac{\partial u}{\partial r}\right) - \gamma (T - T_o),$$ (10)

$$\sigma_{\psi\psi} = \sigma_{\varphi\varphi} = K_o e + \left(\frac{2}{3}\widehat{R} + K_o\right)\left(\frac{u}{r}\right) - \gamma (T - T_o),$$ (11)

$$\sigma_{r\psi} = \sigma_{r\varphi} = \sigma_{\psi\varphi} = 0,$$ (12)

where e is the cubical dilatation given by

$$e = e_{rr} + e_{\psi\psi} + e_{\varphi\varphi} = \frac{\partial u}{\partial r} + \frac{2u}{r} = \frac{1}{r^2}\frac{\partial}{\partial r}(r^2 u),$$ (13)

and $\widehat{R}(t)$ is relaxation function given by

$$\widehat{R}(t) = 2\mu\left[1 - A^* \int_0^t e^{-\beta^* t} t^{\alpha^*-1} dt\right],$$ (14)

where α^*, β^*, and A^* are non-dimensional empirical constants and $\Gamma(\alpha^*)$ is the Gamma function, $0 < \alpha^* < 1$, $\beta^* > 0$, $0 \leq A^* < \dfrac{\beta^*}{\Gamma(\alpha^*)}$, $\widehat{R}(t) > 0$, $\dfrac{d}{dt}\widehat{R}(t) < 0$ [40].

The equation of motion is given by [41]:

$$\rho\frac{\partial^2 u}{\partial t^2} = \left(\frac{2}{3}\widehat{R} + K_o\right)\frac{\partial e}{\partial r} - \sigma_o B_o^2 \frac{\partial u}{\partial t} - \gamma\frac{\partial T}{\partial r}.$$ (15)

The MDD energy equation [28]:

$$k\left(1 + ZT_o\right)\nabla^2 T = \left(1 + \omega D_\omega\right)\left(\rho C_E \frac{\partial T}{\partial t} + \gamma T_o \frac{\partial e}{\partial t}\right),$$ (16)

where ∇^2 is the one-dimensional Laplace's operator in spherical polar coordinates, given by

$$\nabla^2 = \frac{\partial^2}{\partial r^2} + \frac{2}{r}\frac{\partial}{\partial r} = \frac{1}{r^2}\frac{\partial}{\partial r}\left(r^2\frac{\partial}{\partial r}\right)$$

and in the memory-dependent derivative theory, the first order of function f which is essentially characterized in a vital type of a typical subordinate with a part work on a slipping interim [24]:

$$D_\omega f(t) = \frac{1}{\omega}\int_{t-\omega}^t K(t-\xi)f'(\xi)\,d\xi,$$

where ω is the time delay and $K(t-\omega)$ is the kernel function in which they can be chosen freely.

Let us introduce the following non-dimensional variables:

$$r' = c_o \zeta_o r, \quad u' = c_o \zeta_o u, \quad t' = c_o^2 \zeta_o t, \quad \sigma' = \frac{\sigma}{K_o}, \quad \theta^* = \frac{\gamma(T - T_o)}{K_o}, \quad q^* = \frac{\gamma}{k \rho c_o^3 \zeta_o} q,$$

$$\zeta_o = \rho C_E / k, \quad c_o^2 = \frac{K_o}{\rho}, \quad \varepsilon = \frac{\gamma}{\rho C_E}, \quad M = \frac{\sigma_o \mu_o^2 H_o^2}{K_o \eta_o}, \quad T_o = \frac{K}{\gamma}, \quad \hat{R}' = \frac{2}{3K_o} \hat{R}.$$

The Equations (15), (16), (10) and (11) in non-dimensional form become

$$\frac{\partial^2 u}{\partial t^2} = \left(1 + \hat{R}\right)\frac{\partial e}{\partial r} - M \frac{\partial u}{\partial t} - \frac{\partial \theta}{\partial r}, \tag{17}$$

$$(1 + ZT_o)\nabla^2 \theta = \left(1 + \omega D_\omega\right)\left(\frac{\partial \theta}{\partial t} + \varepsilon \frac{\partial e}{\partial t}\right), \tag{18}$$

$$\sigma_{rr} = e + \left(\hat{R} + 1\right)\left(\frac{\partial u}{\partial r}\right) - \theta, \tag{19}$$

$$\sigma_{\psi\psi} = \sigma_{\varphi\varphi} = e + \left(\hat{R} + 1\right)\left(\frac{u}{r}\right) - \theta. \tag{20}$$

The boundary conditions are taken as follows:

(i) The warm limit condition is that the outside of the cavity exposed to a warm stun that is a component of time

$$\theta(r, t) = f(t), \quad r = a. \tag{21}$$

(ii) The outside of the cavity are without footing (zero stress) i.e.

$$\sigma_{rr}(r, t) = 0, \quad r = a. \tag{22}$$

Condition (21) means that the surface of the cavity is traction-free, that is, there are no mechanical loads on the surface while Condition (22) means that the surface of the cavity is kept at a known temperature that is a function of time.

The initial conditions are taken to be homogeneous, that is, we take

$$u(r, t)\big|_{t=0} = 0, \quad \frac{\partial u(r, t)}{\partial t}\bigg|_{t=0} = 0, \tag{23a}$$

$$\theta(r, t)\big|_{t=0} = 0, \quad \frac{\partial \theta(r, t)}{\partial t}\bigg|_{t=0} = 0, \tag{23b}$$

$$\sigma_{rr}(r, t)\big|_{t=0} = 0, \quad \frac{\partial \sigma_{rr}(r, t)}{\partial t}\bigg|_{t=0} = 0, \tag{23c}$$

$$\sigma_{\psi\psi}(r, t)\big|_{t=0} = 0, \quad \frac{\partial \sigma_{\psi\psi}(r, t)}{\partial t}\bigg|_{t=0} = 0, \tag{23d}$$

$$\sigma_{\varphi\varphi}(r, t)\big|_{t=0} = 0, \quad \frac{\partial \sigma_{\varphi\varphi}(r, t)}{\partial t}\bigg|_{t=0} = 0. \tag{23e}$$

3. The analytical solutions in the Laplace-transform domain

Playing out the Laplace transform characterized by the connection

$$\bar{g}(x, s) = L\{g(x, t)\} = \int_0^\infty e^{-st} g(x, t) \, dt$$

of both sides Eqs. (17)-(22), and using the initial Conditions (23), we obtain

$$s(s + M)\bar{u} = \beta^2 \frac{\partial \bar{e}}{\partial r} - \frac{\partial \bar{\theta}}{\partial r}, \tag{24}$$

$$\left(\nabla^2 - \varpi\right)\bar{\theta} = \varpi\,\varepsilon\bar{e}\,, \tag{25}$$

$$\bar{\sigma}_{rr} = \bar{e} + \beta^2\left(\frac{\partial\bar{u}}{\partial r}\right) - \bar{\theta}\,, \tag{26}$$

$$\bar{\sigma}_{\psi\psi} = \bar{\sigma}_{\varphi\varphi} = \bar{e} + \beta^2\left(\frac{\bar{u}}{r}\right) - \bar{\theta}\,, \tag{27}$$

$$\bar{R}(s) = \frac{4\mu}{3\,sK_o}\left[1 - \frac{A*\Gamma(\alpha*)}{(s+\beta*)^{\alpha*}}\right], \tag{28}$$

where

$$G(s) = (1-e^{-s\omega})(1 - \frac{2n}{\omega s} + \frac{2m^2}{\omega^2 s^2}) - (m^2 - 2n + \frac{2m^2}{\omega s})e^{-s\omega}\,, \tag{29}$$

and $L\left\{\hat{R}\,\dfrac{\partial^2 u}{\partial x^2}\right\} = s\bar{R}(s)\dfrac{\partial^2\bar{u}}{\partial x^2}$, $\beta^2 = 1 + s\bar{R}$, $\varpi = s\left(\dfrac{1+G(s)}{1+ZT_o}\right)$.

Applying the divergence operator on both sides of Equation (24) we obtain the equation of motion in the form

$$\left[\beta^2\nabla^2 - s(s+M)\right]\bar{e} = \nabla^2\bar{\theta}\,. \tag{30}$$

Removing $\bar{\theta}$ between Eqs. (25) and (30), we are getting

$$\left\{\beta^2\nabla^4 - \left[s(s+M) + \varpi(\beta^2+\varepsilon)\right]\nabla^2 + \varpi s(s+M)\right\}\bar{e} = 0\,. \tag{31}$$

The above equation can be made as a factor

$$\left(\nabla^2 - \xi_1^2\right)\left(\nabla^2 - \xi_2^2\right)\bar{e} = 0\,, \tag{32}$$

where ξ_1, ξ_2 are the roots with positive real parts of the characteristic equation

$$\beta^2\xi^4 - \left[s(s+M) + \varpi(\beta^2+\varepsilon)\right]\xi^2 + \varpi s(s+M) = 0\,. \tag{33}$$

The roots of the characteristic equation are given by

$$\xi_{1,2}^2 = \frac{1}{2\beta^2}\left[s(s+M) + \varpi(\beta^2+\varepsilon) \pm \sqrt{\left[\varpi(\beta^2+\varepsilon) - s(s+M)\right]^2 + 4s(s+M)\varpi\varepsilon}\right].$$

Because of linearity, Eq. (32) solution can be written as

$$\bar{e} = \bar{e}_1 + \bar{e}_2\,, \tag{34}$$

where

$$\left(\nabla^2 - \xi_1^2\right)\bar{e}_1 = 0,\quad \left(\nabla^2 - \xi_2^2\right)\bar{e}_2 = 0\,. \tag{35}$$

We consider the equation

$$\left(\nabla^2 - \xi^2\right)f = 0\,,$$

this can be written as

$$\frac{\partial^2 f}{\partial r^2} + \frac{2}{r}\frac{\partial f}{\partial r} - \xi^2 f = 0.$$

Taking the replacement

$$f = \frac{h}{\sqrt{r}}\,,$$

the equation above is reduced to

$$r^2\frac{d^2 h}{dr^2} + r\frac{dh}{dr} - \left(r^2\xi^2 + \frac{1}{4}\right)h = 0.$$

The solution of this equation bounded at infinity has the form

$h = K_{1/2}(\xi r)$,

where $K_{1/2}(\cdot)$ is the modified Bessel function of the second kind of the order of 1/2.

The solution of Eq. (32) can be written on the basis of the above outcomes as

$$\bar{e} = \frac{1}{\sqrt{r}}\left[A\,\xi_1^2 K_{1/2}(\xi_1 r) + B\,\xi_2^2 K_{1/2}(\xi_2 r)\right], \tag{36}$$

where A and B are parameters depending on s.

Eliminating $\bar{e}$ between Equations (25) and (30), we obtain

$$\left(\nabla^2 - \xi_1^2\right)\left(\nabla^2 - \xi_2^2\right)\bar{\theta} = 0. \tag{37}$$

The solution of Eq. (32) that is compatible with Eqs. (25) and (36) is given by

$$\bar{\theta} = \frac{1}{\sqrt{r}}\left[A\left(\beta^2\,\xi_1^2 - s\,(s+M)\right)K_{1/2}(\xi_1 r) + B\left(\beta^2\,\xi_2^2 - s\,(s+M)\right)K_{1/2}(\xi_2 r)\right]. \tag{38}$$

Differentiating Eqs. (36) and (38) with respect to r and substituting the results into Eq. (24) gives

$$\bar{u} = -\frac{1}{\sqrt{r}}\left[A\,\xi_1 K_{3/2}(\xi_1 r) + B\,\xi_2 K_{3/2}(\xi_2 r)\right]. \tag{39}$$

Substituting from Equations (36), (38) and (39) into Equations (26), (27), we obtain

$$\bar{\sigma}_{rr} = \frac{1}{\sqrt{r}}\left[A\left([\xi_1^2 + s(s+M)]K_{1/2}(\xi_1 r) + \frac{2\beta^2}{r}\xi_1 K_{3/2}(\xi_1 r)\right)\right.$$
$$\left. + B\left([\xi_2^2 + s(s+M)]K_{1/2}(\xi_2 r) + \frac{2\beta^2}{r}\xi_2 K_{3/2}(\xi_2 r)\right)\right] \tag{40}$$

$$\bar{\sigma}_{\psi\psi} = \bar{\sigma}_{\varphi\varphi} = \frac{1}{\sqrt{r}}\left[A\left([(1-\beta^2)\xi_1^2 + s(s+M)]K_{1/2}(\xi_1 r) - \frac{\beta^2}{r}\xi_1 K_{3/2}(\xi_1 r)\right)\right.$$
$$\left. + B\left([(1-\beta^2)\xi_2^2 + s(s+M)]K_{1/2}(\xi_2 r) - \frac{\beta^2}{r}\xi_2 K_{3/2}(\xi_2 r)\right)\right]. \tag{41}$$

The boundary conditions (21) and (22) can be written in the Laplace transform domain as

$$\bar{\theta}(r,s) = \bar{f}(s), \quad r = a, \tag{42}$$
$$\bar{\sigma}_{rr}(r,s) = 0, \quad r = a. \tag{43}$$

Using the boundary conditions (42) and (43) into Eqs. (38) and (40), we get

$$A\left(\beta^2\,\xi_1^2 - s(s+M)\right)K_{1/2}(\xi_1 a) + B\left(\beta^2\,\xi_2^2 - s(s+M)\right)K_{1/2}(\xi_2 a) = \sqrt{a}\,\bar{f}(s), \tag{44}$$

$$A\left([(1-\beta^2)\xi_1^2 + s(s+M)]K_{1/2}(\xi_1 a) - \frac{\beta^2}{a}\xi_1 K_{3/2}(\xi_1 a)\right)$$
$$+ B\left([(1-\beta^2)\xi_2^2 + s(s+M)]K_{1/2}(\xi_2 a) - \frac{\beta^2}{a}\xi_2 K_{3/2}(\xi_2 a)\right) = 0 \tag{45}$$

From now on, we shall utilize the exponential type of the modified Bessel functions of the second kind, in particular

$$K_{1/2}(z) = \sqrt{\frac{\pi}{2z}}\,e^{-z}, \quad K_{3/2}(z) = \sqrt{\frac{\pi}{2z}}\left(1 + \frac{1}{z}\right)e^{-z}. \tag{46}$$

By solving the system of two Equations (43) and (45) and using Eq. (46), we get the values of the two parameters A and B as

$$A = \frac{a}{\gamma_1}\sqrt{\frac{2}{\pi}}\left(\sqrt{\xi_1}\left[a^2[(1-\beta^2)\xi_1^2 + s(s+M)] + \beta^2(a\xi_2+1)\right]e^{\xi_1 a}\right)\overline{f}(s), \tag{47a}$$

$$B = -\frac{a}{\delta}\sqrt{\frac{2}{\pi}}\left(\sqrt{\xi_2}\left[a^2[(1-\beta^2)\xi_2^2 + s(s+M)] + \beta^2(a\xi_2+1)\right]e^{\xi_2 a}\right)\overline{f}(s), \tag{47b}$$

where $\delta = (\xi_1 - \xi_2)\left(a^2[(1-\beta^2)\xi_1^2 - s(s+M)] + \beta^2[\xi_1 + \xi_2 + as(s+M) + a\xi_1\xi_2]\right).$

This completes the solution in the Laplace transform domain.

4. Inversion of Laplace transforms

We shall now outline the method used to invert the Laplace transforms in the above equations. Let $\overline{f}(s)$ be the Laplace transform of a function $f(t)$. The inversion formula for Laplace transforms can be written as described in Honig and Hirdes [42]:

$$f(t) = \frac{e^{dt}}{2\pi}\int_{-\infty}^{\infty} e^{ity}\,\overline{f}(d+iy)\,\mathrm{d}y,$$

where d is an arbitrary real number greater than all the real parts of the singularities of $\overline{f}(s)$.

Expanding the function $h(t) = \exp(-dt)f(t)$ in a Fourier series in the interval [0, 2L], we obtain the approximate formula [42]

$$f(t) \approx f_N(t) = \frac{1}{2}c_0 + \sum_{k=1}^{N} c_k, \text{ for } 0 \le t \le 2\ell, \tag{48}$$

where

$$c_k = \frac{e^{dt}}{\ell}\mathrm{Re}\left[e^{ik\pi t/\ell}\,\overline{f}\left(d + ik\pi/\ell\right)\right]. \tag{49}$$

Two methods are used to reduce the total error. First, the "Korrektur" method is used to reduce the discretization error. Next, the ε-algorithm is used to reduce the truncation error and therefore to accelerate convergence.

The "Korrektur" method uses the following formula to evaluate the function $f(t)$

$$f(t) = f_{NK}(t) = f_N(t) - e^{-2d\ell}f_{N'}(2\ell+t). \tag{50}$$

We shall now describe the ε-algorithm that is used to accelerate the convergence of the series in (48). Let N be an odd natural number and let $s_m = \sum_{k=1}^{m} c_k$ be the sequence of partial sums of (48). We define the ε-sequence by

$$\varepsilon_{0,m} = 0, \varepsilon_{1,m} = s_m, \quad m = 1, 2, 3, \ldots$$

and $\varepsilon_{n+1,m} = \varepsilon_{n-1,m+1} + 1/\left(\varepsilon_{n,m+1} - \varepsilon_{n,m}\right), \quad n, m = 1, 2, 3, \ldots$

It can be shown that the sequence $\varepsilon_{1,1}, \varepsilon_{3,1}, \ldots, \varepsilon_{N,1}, \ldots$ converges to $f(t) - c_0/2$ faster than the sequence of partial sums.

5. Numerical results and discussion

In this area, we intend to outline numerical consequences of the scientific articulations got in the past segment and explain the impact of time-delay ω and figure-of-merit ZT on the conduct of the field amounts for different forms of the kernel function. So as to translate the numerical calculations, we consider the material properties of Polymethyl Methacrylate (Plexiglas) which has wide applications in industry and prescription. Following the values of physical constants are shown in Table 1 [26]:

Table 1. Value of the constants

$\rho = 1.2 \times 10^3 \, kg \, / \, m^3$	$k = 0.55 \, J \, / \, m.sec.K$	$T_o = 293 \, K$
$C_E = 1.4x10^3 \, J \, / \, kg.K$	$\lambda = 453.7 \times 10^7 \, N \, / \, m^2$	$\mu = 194 \times 10^7 \, N \, / \, m^2$
$\gamma = 210 \times 10^4 \, N \, / \, m^2 K$	$\eta_0 = 3.36 \times 10^6 \, sec/ \, m^2$	$c_o = 2200 \, m \, / \, sec$
$\alpha_T = 13 \times 10^{-5}$	$4\mu / 3K_o = 0.8$	$\varepsilon = 0.12$
$\beta* = 0.005$	$A* = 0.106$	$\alpha* = 0.5$
$\mu_o H_o = 1 \, Tesla$	$a = 1$	

The calculations were carried out for the function $f(t)$, which represents a time-dependent thermal shock:

$$f(t) = t \, H(t) \qquad \text{or} \qquad \bar{f}(s) = \frac{1}{s^2}.$$

Thinking about the above physical information, we have assessed the numerical estimations of the field amounts with the assistance of a PC program created by utilizing the Fortran 90 programming language on a personal computer with a 17 processor. The amount of calculation (and hence the execution time) depends on several parameters within the program. First, there is a parameter "nsig" which is the number of significant digits defining the relative error as $(10)^{-nsig}$. We usually take nsig = 5. Near points of discontinuity of the function, the program might fail to converge, and we have to decrease nsig. Another parameter is the maximum number of terms in the Fourier series to be added within one saw-tooth of the ε-algorithm. This is taken as 10000. The last parameter is the number of saw-teeth of the ε-algorithm to be considered. This is taken as 50. All in all, the program evaluates the value of θ at 50 points in less than 2 minutes [43].

The calculations were completed for certain parameters, where an estimation of time, namely, $t = 0$. The investigation of the effects of the time delay and the figure-of-merit for different forms of kernel function as well as the magnetic number on thermoelectric material within the sight of a consistently attractive field was done in the former areas. Run-of-the-mill numerical outcomes have appeared in Figs. 1-8.

Figure 1 speaks to the dimensionless estimation of heat flux for a wide scope of outspread separation r $(0 \leq r \leq 1)$ and for different forms of the kernel function. In these figures, strong lines speak to the arrangement got in the casing of Biot theory $(\omega = 0)$ and broken lines represent the solution corresponding to using generalized electro-thermoelasticity $(\omega > 0)$ with MDD when the kernel function is taken as the form $[1 - (t - \xi) / \omega]^2$, while dotted lines when the kernel function is $1 - (t - \xi)$. We noticed that the maximum value of heat fluxes when $K = [1 - (t - \xi) / \omega]^2$ and $K = 1 - (t - \xi)$ are 2.02 and 1.8 and cut r-axis at $r = 1.0$. So, we learned from these figures that vital wonder saw in these assumes that the arrangement of any of the considered capacity in the new model is confined in a limited locale. Past this area, the varieties of these appropriations try not to occur. This implies to the arrangements concurring the new generalized hypothesis show the conduct of limited rates of wave spread.

Figure 2 indicates the variation of heat flux against the figure-of-merit for Biot theory $(\omega = 0)$ and for the generalized electro-thermoelasticity theory with MDD $(\omega > 0)$ when the kernel function has two forms, namely, $[1 - (t - \xi) / \omega]^2$ and $1 - (t - \xi)$. We noticed from this figure that the efficiency of a thermoelectric material figure-of-merit is proportional to the

temperature of the solid particles and the choice of the kernel function forms has a significant effect on the heat flux field.
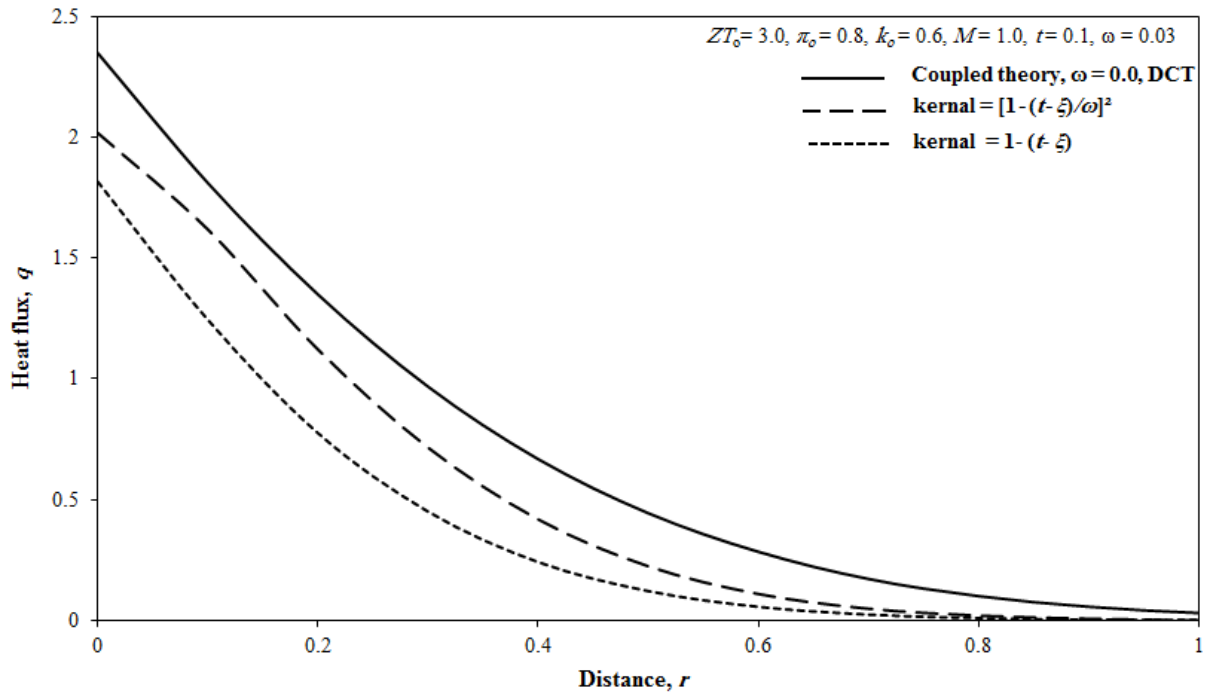
Fig. 1. The variation of heat flux vs. distance for different forms of kernal function $K(t, \xi)$
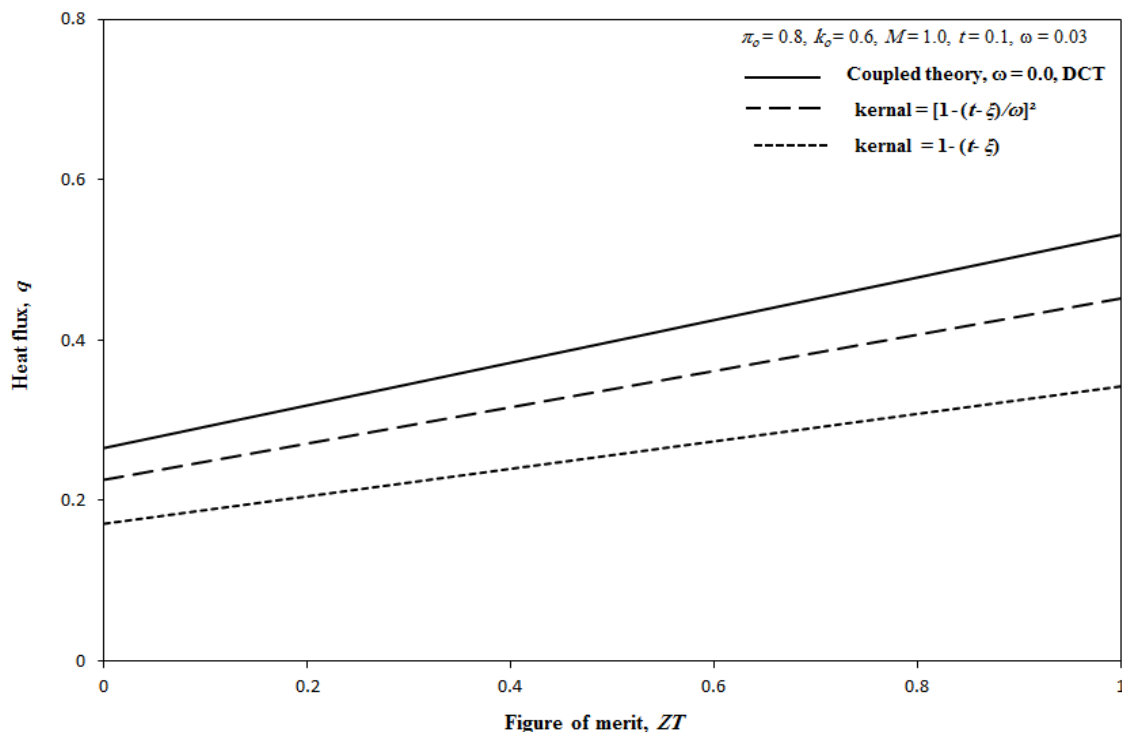
Fig. 2. The variation of heat flux q versus figure of merit ZT for different forms of kernal function $K(t, \xi)$

Figure 3 exhibits the space variation of the temperature distribution. In this figure, the solid line represents the solution obtained in the frame of dynamic coupled theory (Biot theory, $\omega = 0$ [1]) and the other lines represent the solutions obtained in the case $\omega > 0$. We

observed that the temperature fields have been influenced when delay ω, where the expanding of the estimation of the parameter causes diminishing in temperature fields. The warm waves are consistent capacities, smooth, and reach to unfaltering state contingent upon the estimation of time-delay ω, which implies that the particles transport the warmth to different particles effectively and this makes the diminishing rate of the temperature more noteworthy than different ones. Additionally, the warm waves cut the x-hub all the more quickly when increments.
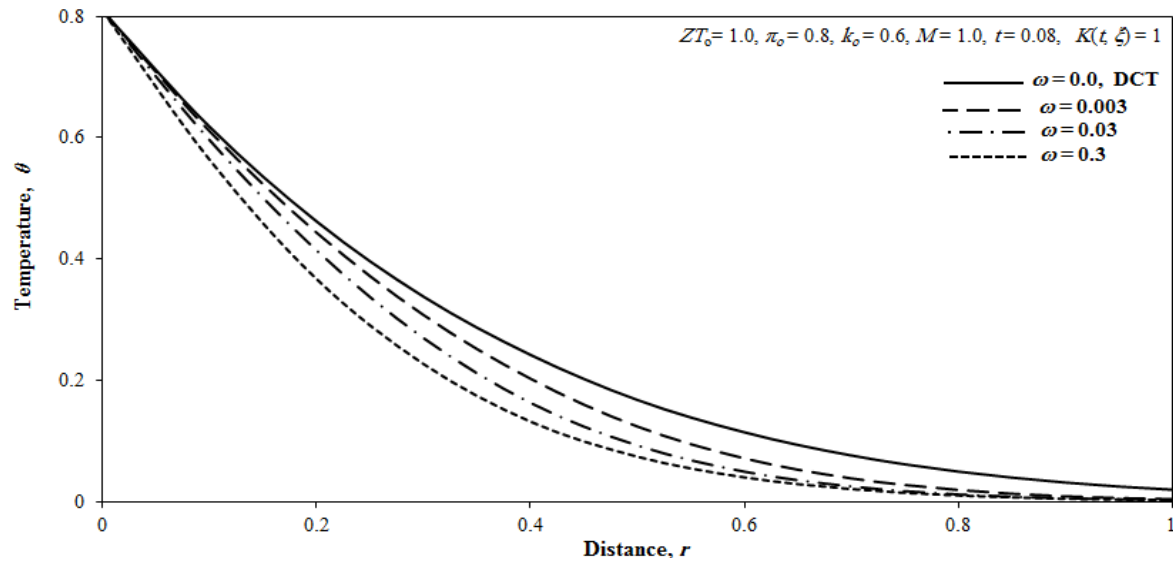
Fig. 3. The variation of temperature vs. distance for different values of time-delay ω

Figures 4, 5, and 6 show the variety of temperature, displacement, and stress circulations in thermoelectric circular depression with spiral separation r for three values of figure-of-merit at room temperature ZT_o, namely, $ZT_o = 1$, 3 and 5. We noticed that the stress and displacement field has been affected by the figure-of-merit values, where the expanding of the estimation of figure-of-merit causes decreasing in the magnitude of the stress and displacement field while causes increasing in the temperature.
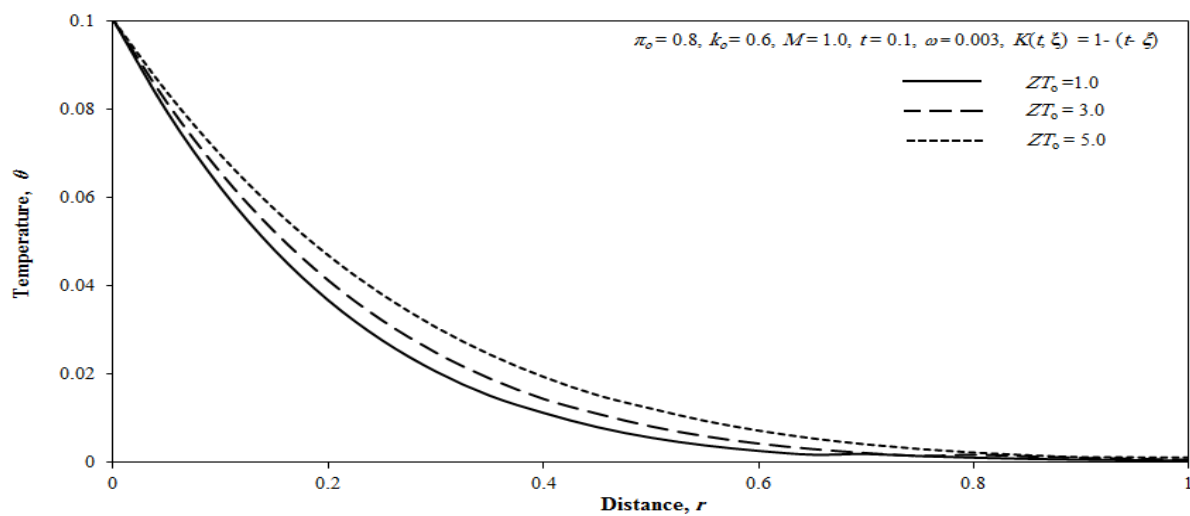
Fig. 4. The variation of temperature vs. distance for different values of figure-of-merit at room temperature ZT_o
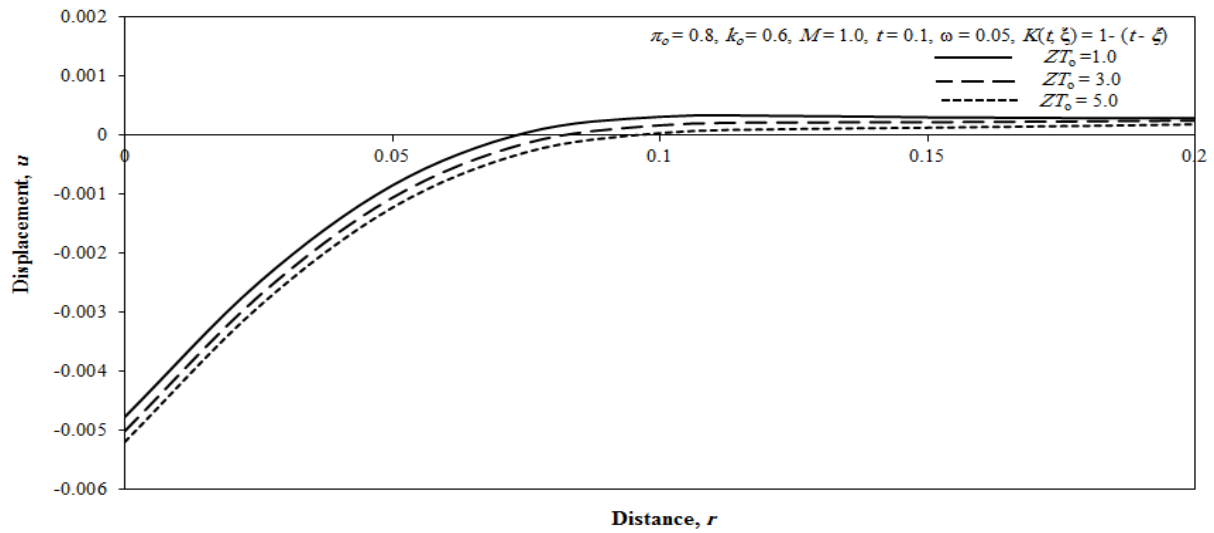
Fig. 5. The variation of displacement vs. distance for different values of figur-of-miret at room temperature ZT_o
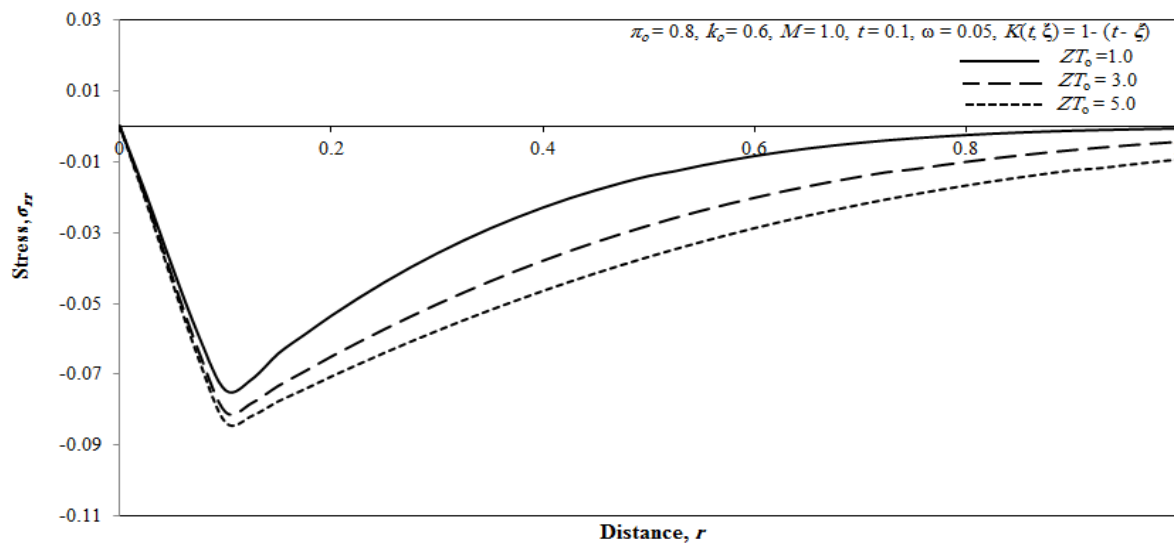
Fig. 6. The variation of stress vs. distance for different values of figur-of-miret at room temperature ZT_o

Figures 7 and 8 display the displacement and stress distributions with distance for two different theories; Biot theory, $\omega = 0$ and MDD theory, $\omega > 0$ when the magnetic number has two values M ($M = 0$, absent of the magnetic field and $M > 0$ in the presence of the magnetic field). We find that the attractive field acts to diminish the displacement and stress fields. This is generally known as attractive damping. It is possible to compare the results with those for the generalized thermoelasticity theory [44,45] and generalized thermo-viscoelasticity theory [46]. It was found that thermoelectric viscoelasticity's memory-dependent theory predicts a value for less than the generalized theory predicts. On the other hand, the stress value in the memory-dependent theory is greater.
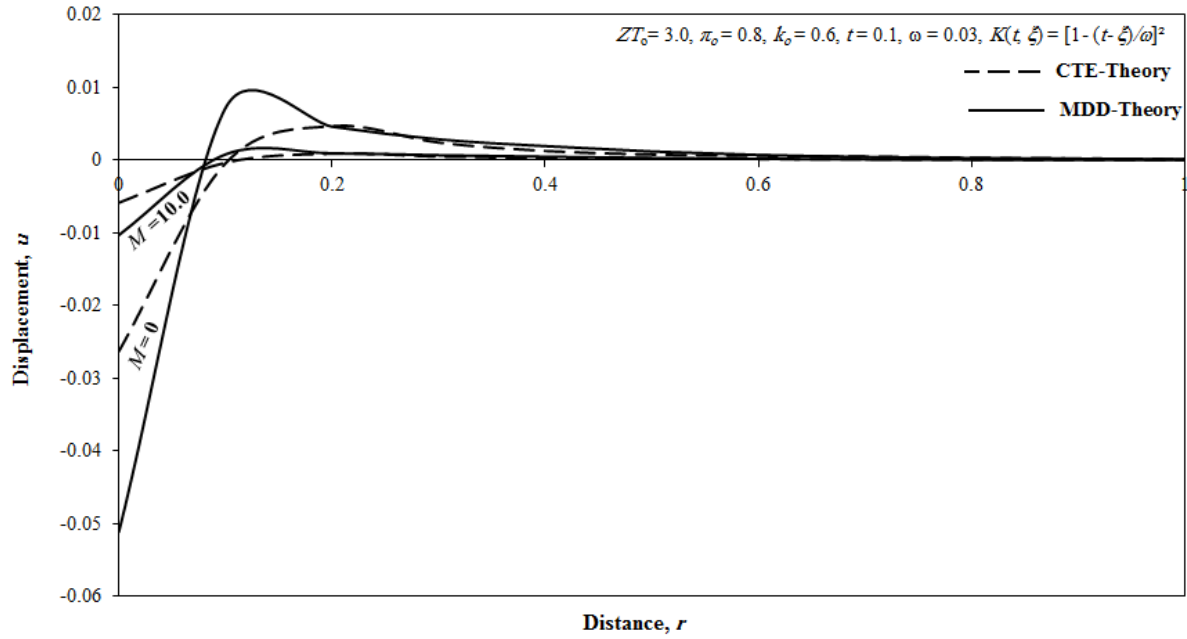
Fig. 7. The variation of displacement vs. distance for different values of magnetic number M
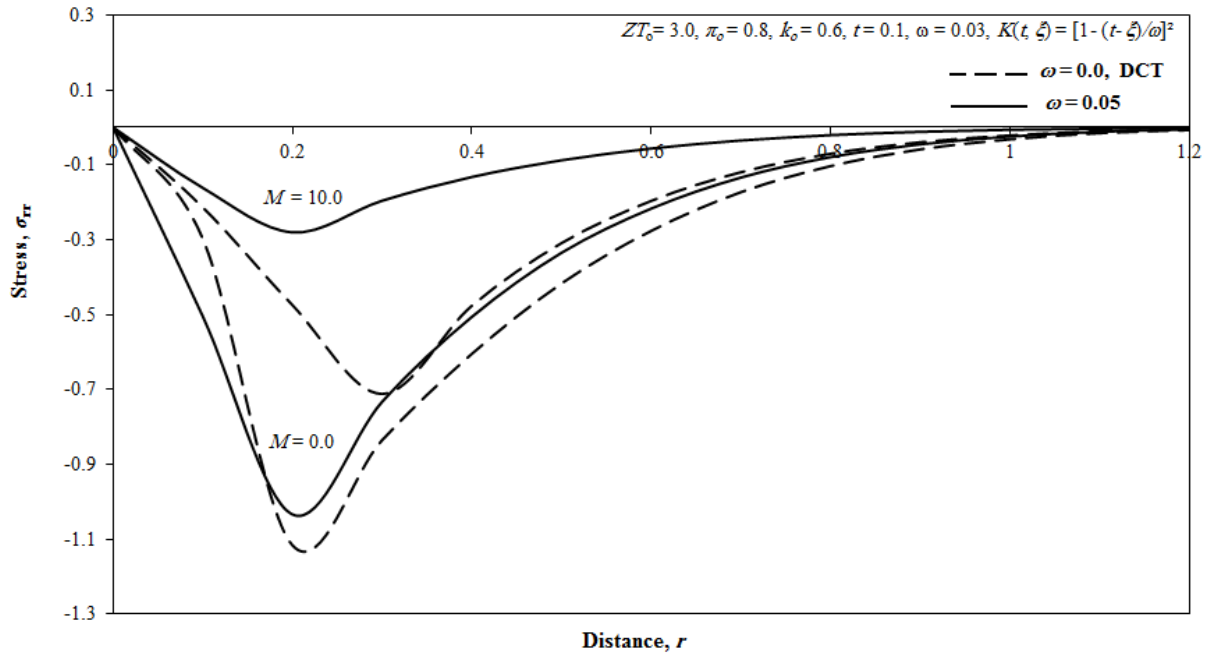
Fig. 8. The variation of stress component vs. distance for different values of magnetic number M

6. Conclusions

- The main goal of this work is to introduce a new mathematical model for the Fourier law of heat conduction with memory-dependent derivative and include the thermoelectric figure-of-merit. According to this new theory, we have to construct a new classification for materials according to a time-delay and kernel function where these variables become the new indicator of its ability to conduct heat in conducting medium. The certain issues of warm excitations in the hypothesis of coupled fields have a place with the electro-thermo-viscoelasticity. The expanding wide use in detecting and activation has pulled in much consideration towards hypotheses about materials displaying couplings between versatile, electric, attractive, and thermal fields. This model is more intuitionistic for understanding the physical significance and the comparing memory-dependent derivative condition is progressively expressive. The conditions of wave hypothesis of electro-thermo-viscoelasticity exposed to MDD based on the change of the Fourier law was built rough phenomenological conditions of thermo-electromagnetic versatility described by a limited speed of engendering of electromagnetic and flexible excitations. From the considered model we can set up some fundamental hypotheses on the straight coupled and generalized speculations of electro-thermo-viscoelasticity; for example, the coupled hypothesis $(\omega = 0)$ and the generalized case hypothesis $(\omega > 0)$. As per the after-effects of the work, we can see the nearness of MDD's parameters in Fourier law of warmth conduction can assume a crucial job in expanding or diminishing the speed of the wave proliferation of all fields through the thermoelectric medium. This model is more intuitionistic for understanding the physical significance and the comparing memory-dependent derivative condition is progressively expressive.

- This model enables us to improve the efficiency of a thermoelectric material figure-of-merit ZT. For a material to be a good thermoelectric cooler, it must have a high thermoelectric figure of merit, ZT. The result provides a motivation to investigate conducting thermoelectric materials as a new class of applicable thermoelectric materials [47]. The efficiency of a thermoelectric figure-of-merit is proportional to the temperature of the material particles.

- Owing to the complicated nature of the governing equations for the generalized thermo-viscoelasticity, few attempts have made to solve different problems in this field. These attempts utilized an approximate method valid for only a specific range of some parameters [48]. In this work, a simple method is introduced in the field of generalized thermoelectric viscoelasticity with memory-dependent derivative heat transfer and applied to the one-dimensional problem for a viscoelastic spherical cavity. This method gives exact solutions in the Laplace transform domain without any assumed restrictions on either the temperature or the displacement distributions. A numerical method based on a Fourier-series expansion has been used for the inversion process.

- Representative results for all functions for generalized theory are distinctly different from those obtained for the coupled theory. This due to the fact that thermal waves in the coupled theory travel with an infinite speed of propagation as opposed to finite speed in the generalized case. It is clear that for small values of time the solution is localized in a finite region. This region grows with increasing time and its edge is the location of the wavefront. This region is determined by the values of time t and time-delay. The predictions of the new theory are discussed and compared with dynamic classical coupled theory.

- The advantage of the considered a new model consists in:
  i) The discontinuities in temperature distribution disappeared.
  ii) The negative values of temperature that usually appear in the generalized theories of thermoelasticity vanished.

iii) The Kernel functions and time-delay of memory-dependent derivative can be arbitrarily chosen freely according to the necessity of applications [25].

Compliance with ethical standards. *Conflict of interest On behalf of all authors, the corresponding author states that there is no conflict of interest.*

References
[1] Biot M. Thermoelasticity and irreversible thermodynamics. *J. Appl. Phys.* 1956;27(3): 240-253.
[2] Lord H, Shulman Y. A generalized dynamical theory of thermo-elasticity. *J. Mech. Phys. Solids.* 1967;15(5): 299-309.
[3] Ignaczak J. Uniqueness in generalized thermoelasticity. *J. Therm. Stress.* 1979;2(2): 171-179.
[4] Sherief HH. On uniqueness and stability in generalized thermoelasticity. *Q. Appl. Math.* 1987;45: 773-778.
[5] Chandrasekharaiah DS. Hyperbolic thermoelasticity: a review of recent literature. *Appl. Mech. Rev.* 1998;51(12): 705-729.
[6] Ezzat MA, El-Karamany AS. The uniqueness and reciprocity theorems for generalized thermoviscoelasticity for anisotropic media. *J. Therm. Stress.* 2002;25(6): 507-522.
[7] Ezzat MA, El-Karamany AS. On uniqueness and reciprocity theorems for generalized thermoviscoelasticity with thermal relaxation. *Can. J. Phys.* 2003;81(6): 823-833.
[8] Ezzat MA, Awad ES. Constitutive relations, uniqueness of solution, and thermal shock application in the linear theory of micropolar generalized thermoelasticity involving two temperatures. *J. Therm. Stress.* 2010;33(3): 226-250.
[9] Ezzat MA, Awad ES. Analytical aspects in the theory of thermoelastic bodies with microstructure and two temperatures. *J. Therm. Stress.* 2010;33(7): 674-693.
[10] Rowe DM. *Handbook of Thermoelectrics.* CRC Press; 1995.
[11] Shercliff JA. Thermoelectric magnetohydrodynamics. *J. Fluid Mech.* 1979;91(2): 231-251.
[12] Ezzat MA, Youssef, HM. Stokes' first problem for an electro-conducting micropolar fluid with thermoelectric properties. *Can. J. Phys.* 2010;88(1): 35-48.
[13] Ezzat MA, Youssef, HM. Thermoelectric figure-of-merit effects on fluid flow. *Materials Physics and Mechanics.* 2014;19(1): 39-50.
[14] Povstenko YZ. Thermoelasticity that uses fractional heat conduction equation. *J. Math. Sci.* 2009;162: 296-305.
[15] Sherief H, El-Sayed, AM Abd El-Latief AM. Fractional order theory of thermoelasticity. *Int. J. Solids Struct.* 2010;47(2): 269-275.
[16] Ezzat MA. Thermoelectric MHD non-Newtonian fluid with fractional derivative heat transfer. *Phys. B.* 2010;405(19): 4188-4194.
[17] Ezzat MA. Theory of fractional order in generalized thermoelectric MHD. *Appl. Math. Modell.* 2011;35(10): 4965-4978.
[18] Ezzat MA. Thermoelectric MHD with modified Fourier's law. *Int. J. Therm. Sci.* 2011;50(4): 449-455.
[19] Ezzat MA. Magneto-thermoelasticity with thermoelectric properties and fractional derivative heat transfer. *Phys. B.* 2011;406(1): 30-35.

[20] Ezzat MA, El-Karamany AS. Fractional thermoelectric viscoelastic materials. *J. Appl. Poly. Sci.* 2012;124(3): 2187-2199.

[21] Ezzat MA, El-Karamany AS. Fractional order heat conduction law in magneto-thermoelasticity involving two temperatures. *ZAMP.* 2011;62: 937-952.

[22] Ezzat MA, El-Karamany AS, El-BaryAA, Fayik MA. On fractional ultra-laser two-step thermoelasticity. *Materials Physics and Mechanics.* 2013;18(2): 108-123.

[23] Ezzat MA, El-Karamany AS, El-Bary AA, Fayik MA. Fractional calculus in one-dimensional isotropic thermo-viscoelasticity. *CR Mecanique* 2013;341(7): 553-566.

[24] Wang JL, Li HF. Surpassing the fractional derivative: concept of the memory-dependent derivative. *Comput. Math. Appl.* 2011;62(3): 1562-1567.

[25] Yu YJ, Hu W, Tian XG. A novel generalized thermoelasticity model based on memory-dependentderivative. *Int. J. Eng. Sci.* 2014;81: 123-134.

[26] Zhang P, He T. A generalized thermoelastic problem with nonlocal effect and memory-dependent derivative when subjected to a moving heat source. *Waves Ran. Complex Med.* 2018;30(1): 142-156.

[27] El-Karamany AS, Ezzat MA. Thermoelastic diffusion with memory-dependent derivative. *J. Therm. Stress.* 2016;39(9): 1035-1050.

[28] Ezzat MA, El-Karamany AS, El-Bary AA. Generalized thermo-viscoelasticity with memory-dependent derivatives. *Int. J. Mech. Sci.* 2014;89: 470-475.

[29] Ezzat, MA, El-Karamany, AS, El-Bary, A. Electro-thermoelasticity theory with memory-dependent derivative heat transfer. *Int. J. Eng. Sci.* 2016;99: 22-38.

[30] Ezzat MA, El-Bary AA. Magneto-thermoelectric viscoelastic materials with memory-dependent derivative involving two-temperature. *Int. J. Appli. Electromag.Mech.* 2016;50: 549-567.

[31] Ezzat MA, El-Karamany AS, El-Bary A. Thermoelectric viscoelastic materials with memory-dependent derivative. *Smart Struct. Sys.* 2017;19: 539-551.

[32] Hendy MH, El-Attar SI, Ezzat MA. On thermoelectric materials with memory-dependent derivative and subjected to a moving heat source. *Microsys.Techn.* 2020;26: 595-608.

[33] Ezzat MA. Modeling of gn type III with MDD for a thermoelectric solid subjected to a moving heat source. *Geomech. Eng.* 2020;23(4): 393-403.

[34] Kaliski S, Petykiewicz, J. Equation of motion coupled with the field of temperature in a magnetic field involving mechanical and electrical relaxation for anisotropic bodies, *Proc. Vibr. Probl.* 1959;4: 3-11.

[35] Tritt TM. *Semiconductors and semimetals, recent trends in thermoelectric materials research.* San Diego: Academic Press; 2000.

[36] Hiroshige Y, Makoto O, Toshima N. Thermoelectric figure-of-merit of iodine-doped copolymer of phenylenevinylene with dialkoxyphenylenevinylene. *Synthetic Metals.* 2007;157(10-12): 467- 474.

[37] Sherief H, Abd El-Latief AM. A one-dimensional fractional order thermoelastic problem for a spherical cavity. *Math. Mech. Solids.* 2015;20(5): 512-521.

[38] Ezzat MA, El-Bary AA. Thermoelectric spherical shell with fractional order heat transfer. *Micrsys. Tech.* 2018;24: 891-899.

[39] Ezzat MA, Othman MI, El-Karamany AS. State space approach to generalized thermo-viscoelasticity with two relaxation times. *Int. J. Eng. Sci.* 2002;40(3): 283-302.

[40] Fung YC. *Foundation of Solid Mechanics.* NJ: Prentice-Hall; 1965.

[41] Ezzat MA. The relaxation effects of the volume properties of electrically conducting viscoelastic material. *Mater. Sci. Eng, B.* 2006;130(1-3): 11-23.

[42] Honig G, Hirdes U. A method for the numerical inversion of the Laplace transform. *J. Comp. Appl. Math.* 1984;10(1): 113-132.

[43] Sherief HH, Hussein EM. Contour integration solution for a thermoelastic problem of a spherical cavity. *Appl. Math. Compu.* 2018;320: 557-571.

[44] Ezzat, MA: Fundamental solution in generalized magneto-thermoelasticity with two relaxation times for perfect conductor cylindrical region. *Int. J. Eng. Sci.* 2004;42(13-14): 1503-1519.

[45] Ezzat MA, Attef, HM: Influence of thermoelectricity properties on magneto- viscoelastic material. *J. Poly. Eng.* 2010;30(1): 1-28.

[46] Ezzat MA, Othman MI, Samaa, AA: State space approach to two-dimensional electromagneto-thermoelastic problem with two relaxation times. *Int. J. Eng. Sci.* 2001;39(12): 1383-1404.

[47] Mahan G, Sales B, Sharp J. Thermoelectric materials: New approaches to an old problem. *Phys. Today.* 1997;50(3): 42-47.

[48] Tschoegl N. Time dependence in material properties: An overview. *Mech. Time-Depend. Mat.* 1997;1: 3-31.

Nomenclature

λ, μ	Lame' constants
ρ	mass density
t	time
T	absolute temperature
θ	$= T - T_0$, such that $\left| \theta / T_0 \right| << 1$
ε_{ij}	components of strain tensor
e	$= \varepsilon_{ii}$, dilatation
e_{ij}	components of strain deviator tensor
σ_{ij}	components of stress tensor
k_o	Seebeck coefficient
π_o	Peltier coefficient
k	thermal conductivity
C_E	specific heat at constant strains
K_o	$= \lambda + (2/3)\mu$, bulk modulus
c_o^2	$= \dfrac{K}{\rho}$, longitudinal wave speed
α_T	coefficient of linear thermal expansion
γ	$= 3K \alpha_T$
T_o	reference temperature
c_o	$= \left[(\lambda + 2\mu)/\rho \right]^{1/2}$, speed of propagation of isothermal elastic waves
η_o	$= \rho C_E / \kappa$
ε	$= \dfrac{\gamma^2 T_o}{k \eta_o \rho c_o^2}$, Thermal coupling parameter
Z	thermoelectric figure-of-merit
$\Gamma(.)$	Gamma function
A^*, β^*, α^*	empirical constants

ON THE ISSUE OF ANALYTICAL DERIVATION OF STRESS STATE IN A CYLINDRICAL SHELL WITH A CIRCULAR HOLE UNDER AXIAL TENSION

S.V. Kashtanova[1*], A.V. Rzhonsnitskiy[2], A.A. Gruzdkov[2]

[1]Institute for Problems in Mechanical Engineering of the Russian Academy of Sciences,

199178, V.O., Bolshoj pr., 61, St.-Petersburg, Russia

[2]Saint-Petersburg State Institute of Technology, 190013, Moskovsky prospect, 26, St.-Petersburg, Russia

*e-mail: kastasya@yandex.ru

Abstract. The stress field in the cylindrical shell with the circular hole is considered. Thoroughly analyzing previous works we concluded that up to the present there are no explicit formulae useful for applications despite numerous works on this subject. Moreover, the classical analytical approach lacks a rigorous mathematical foundation. Its applicability is limited to cases that slightly differ from the plane Kirsch problem. The numerical results of various researches show a significant discrepancy. This paper proposes a new analytical approach based on a different form of representation for the fundamental system of solutions of governing equations. Since, in contrast to previous works, cutting of series is not required the boundary conditions are satisfied with a very high degree of accuracy. Our model works in all ranges that mechanics allows and there are no mathematical restrictions. Some numerical results are presented.
Keywords: cylindrical shell, cutouts, stress state, circular hole, elasticity theory

1. Introduction
Motivation. The purpose of this article is to develop a new approach to the analytical derivation of the stress state in a cylindrical shell with a circular hole under axial tension. The buckling problem, nonlocal fracture mechanics, and some other problems require a full stress field, but not just the values of stresses at the boundary.

The problems of determining the stress field in cylindrical shells with a hole for various loading conditions are considered in a number of recent works in connection with numerous engineering applications [1,2,11].

Analysis of numerous papers of 1940-70 as Lurie, Guz, Savin, Lekkerkerker, Eringen, and Naghdi, Murthy, Van Dyke [3-10] revealed that there are no explicit formulas that can be used for further investigations or for engineering applications. The problem was formulated by Lurie [3]. His followers Guz, Savin, Naghdi, Murthy [4,5,7,9], and some others tried to get an analytical solution but without proper mathematical justification. Besides that their approach is applicable in a very narrow range of parameters that will be discussed below in more detail. Some other researchers as Eringen, Lekkerkerker, and Van Dyke [8,6,10] used numerical procedures based on the collocation method. There were significant discrepancies in the results obtained in different papers and we estimate the results of Van Dyke [10] as more realistic since they are in good agreement with the results obtained in this paper.

Therefore we assume that it is time to reconsider some approaches with more high accuracy in ideas and calculations.

2. Formulation of the Problem

Government equation. The cylindrical shell with a circular hole under axial tension (in x-coordinate) is considered. A dimensionless parameter that takes into account the curvature of the circular cylinder is $\boldsymbol{\beta^2} = \dfrac{r_0^2\sqrt{3\,(1-v^2)}}{4Rh}$ [3]. The limit case $\boldsymbol{\beta \to 0}$ corresponds to the plane Kirsch problem. In classical works, in the frame of analytical approach, the ratio between the size of the hole and dimensions of the shell is considered to be $\boldsymbol{\beta \ll 1}$ while numerical approach allows us to consider $\boldsymbol{\beta > 1}$. E.g., in the paper of Van Dyke parameter $\boldsymbol{\beta}$ varies up to 4 [10].

The solution of this problem is represented as a composition of two solutions – perturbated and unperturbated. The first one is responsible for the problem with a hole and the second one – for axial tension applied along x-coordinate at the edge of the infinite cylinder that can be expressed through shell forces as

$$T_x = p, \quad T_{xy} = 0, \quad T_y = 0. \tag{1}$$

The system of equilibrium equations of the membrane shell for the search of the perturbated problem solution can be reduced to the equation [3,12]

$$\Delta\Delta\Phi + 8i\beta^2 \frac{\partial^2 \Phi}{\partial x^2} = 0, \tag{2}$$

where $\Phi = \dfrac{Eh}{8\beta^2 R} w - iU$, w – displacement normal to the middle surface, U – stress function. The connection between shell forces in Cartesian coordinates and stress function is given by

$$\begin{pmatrix} T_x & T_{xy} \\ T_{xy} & T_y \end{pmatrix} = \begin{pmatrix} \dfrac{\partial^2 U}{\partial y^2} & -\dfrac{\partial^2 U}{\partial y \partial x} \\ -\dfrac{\partial^2 U}{\partial y \partial x} & \dfrac{\partial^2 U}{\partial x^2} \end{pmatrix}. \tag{3}$$

In order to split an operator into conjugate let us introduce substitution

$$\alpha = (1+i)\beta \quad => \quad \alpha^2 = 2i\beta^2 \quad => \quad 8i\beta^2 = -(2i\alpha)^2 \tag{4}$$

that follow us to the next equation:

$$\left(\Delta\Delta - (2i\alpha)^2 \frac{\partial^2}{\partial x^2}\right)\Phi = 0.$$

Since Δ and $\dfrac{\partial}{\partial x}$ commute, we get

$$\left(\Delta - 2i\alpha\frac{\partial}{\partial x}\right)\left(\Delta + 2i\alpha\frac{\partial}{\partial x}\right)\Phi = 0. \tag{5}$$

It should be noted that operators $L_1 = \left(\Delta - 2i\alpha\frac{\partial}{\partial x}\right)$ and $L_2 = \left(\Delta + 2i\alpha\frac{\partial}{\partial x}\right)$ are commutative:

$$L_1 L_2 = L_2 L_1, \quad \mathrm{Ker}L_1 + \mathrm{Ker}L_2 \subseteq \mathrm{Ker}L_1 L_2 .$$

In this problem $\mathrm{Ker}L_1 + \mathrm{Ker}L_2$ are being found which means that some solutions of equation (5) can be missed. However, obtained solutions are enough to satisfy boundary conditions.

Function Φ can be introduced in form $\Phi = e^{i\alpha x} \cdot \Psi$. Since the symmetry of equation (5) relative to transform $\alpha \leftrightarrow (-\alpha)$ the function $\Phi = e^{-i\alpha x} \cdot \Psi$ is also the solution. Hence equation (5) can be rewritten in the following form

$$e^{i\alpha x} \cdot (\Delta\Psi - (i\alpha)^2\Psi) = 0 \quad => \quad \Delta\Psi + \alpha^2\,\Psi = 0. \tag{6}$$

Polarizing and separating variables in (6) $\Psi(x,y) = \Psi(r,\vartheta) = z(r) \cdot f(\vartheta)$ we obtain

$$\frac{r^2\left[z''(r)+\frac{1}{r}\cdot z'(r)+\alpha^2\cdot z(r)\right]}{z(r)} = -\frac{f''(\vartheta)}{f(\vartheta)} = C = +n^2. \tag{7}$$

Due to 2π-periodicity of the solution regarding ϑ we get the condition $C = +n^2$ that brings us integers n:

$$f'' + Cf = 0, \qquad C = n^2, \qquad f_1 = \cos\sqrt{C}\vartheta, \qquad f_2 = \sin\sqrt{C}\vartheta.$$

Considering the left part of the equation (7) regarding r we got Bessel equation

$$r^2\cdot z''(r) + r\cdot z'(r) + (\alpha^2 r^2 - n^2)\cdot z(r) = 0, \tag{8}$$

that after substitutes $z(r) = \tilde{z}(\alpha r)$ and $t = \alpha r$ appears in its classical form:

$$\tilde{z}''(t) + \frac{1}{t}\cdot\tilde{z}'(t) + \left(1 - \frac{n^2}{t^2}\right)\cdot\tilde{z}(t) = 0. \tag{9}$$

The fundamental system of solutions for the equation (9) is expressed through Hankel's functions that are linear combinations of Bessel and Neiman functions:

$$H_n^{(1)}(t) = J_n(t) + iY_n(t), \ H_n^{(2)}(t) = J_n(t) - iY_n(t). \tag{10}$$

The choice of Hankel functions here is due to the fact that they are the only functions from Bessel functions class that tends to zero with an unlimited increase of their complex argument modulus

$$\lim_{r\to+\infty} H_n^{(1)}\left(r\,e^{i\vartheta}\right) = \lim_{r\to+\infty} H_n^{(2)}\left(r\,e^{-i\vartheta}\right) = 0, \quad \vartheta \in [\varepsilon; \pi - \varepsilon]. \tag{11}$$

Since $\alpha = (1 + i)\beta$ corresponds to the value $\vartheta = \frac{\pi}{4} \in [0; \pi]$ we should use only $H_n^{(1)}(t)$ function.

Thus similar to the paper [4] the solution of equation (5) can be written as

$$\Phi = \Phi_1 + \Phi_2 \tag{12}$$

$$\Phi_1 = e^{i\alpha x}\cdot\Psi = e^{i\alpha x}\sum_{n=-\infty}^{+\infty} C_n\cdot e^{in\vartheta}\cdot H_n^{(1)}(\alpha r) = \left[C_n = i^{-n}a_n^{(1)}\right] =$$

$$= e^{i\alpha x}\sum_{n=-\infty}^{+\infty} i^{-n}\cdot e^{in\vartheta}\cdot H_n^{(1)}(\alpha r)\cdot a_n^{(1)},$$

$$\Phi_2 = e^{-i\alpha x}\cdot\Psi = e^{-i\alpha x}\sum_{n=-\infty}^{+\infty} i^{n}\cdot e^{in\vartheta}\cdot H_n^{(1)}(\alpha r)\cdot a_n^{(2)}.$$

Due to the symmetry of the problem, it is convenient to change the basis of linear independent solutions

$$\begin{pmatrix} e^{i\alpha x}\cdot H_n^{(1)}(\alpha r)\cdot\cos(n\vartheta) \\ e^{i\alpha x}\cdot H_n^{(1)}(\alpha r)\cdot\sin(n\vartheta) \\ e^{-i\alpha x}\cdot H_n^{(1)}(\alpha r)\cdot\cos(n\vartheta) \\ e^{-i\alpha x}\cdot H_n^{(1)}(\alpha r)\cdot\sin(n\vartheta) \end{pmatrix} = \begin{pmatrix} 1 & 0 & i & 0 \\ 0 & 1 & 0 & i \\ 1 & 0 & -i & 0 \\ 0 & 1 & 0 & -i \end{pmatrix} \begin{pmatrix} \cos(\alpha x)\cdot H_n^{(1)}(\alpha r)\cdot\cos(n\vartheta) \\ \cos(\alpha x)\cdot H_n^{(1)}(\alpha r)\cdot\sin(n\vartheta) \\ \sin(\alpha x)\cdot H_n^{(1)}(\alpha r)\cdot\cos(n\vartheta) \\ \sin(\alpha x)\cdot H_n^{(1)}(\alpha r)\cdot\sin(n\vartheta) \end{pmatrix}$$

where only $\cos(\alpha x)\cdot H_n^{(1)}(\alpha r)\cdot\cos(n\vartheta)$ with even n и $\sin(\alpha x)\cdot H_n^{(1)}(\alpha r)\cdot\cos(n\vartheta)$ with odd n are remained. Thus the form of solution for Φ is obtained in the following form

$$\Phi = -i\frac{py^2}{2} + \sum_{n=0}^{\infty}(A_n + iB_n)\cdot\begin{bmatrix} \cos(\alpha x)\cdot H_n^{(1)}(\alpha r)\cdot\cos(n\vartheta) \\ \sin(\alpha x)\cdot H_n^{(1)}(\alpha r)\cdot\cos(n\vartheta) \end{bmatrix}, \tag{13}$$

$$\alpha x = (1 + i)\beta\cdot r\cos\vartheta,$$

term $-i\frac{py^2}{2}$ added from unperturbated solution and satisfies the boundary condition

$$T_x = -\frac{\partial^2 U}{\partial y^2} = p.$$

Lurie and his followers [3,4,7,9] used the expansion of basic functions $\cos(\alpha x) \cdot H_n^{(1)}(\alpha r) \cdot \cos(n\vartheta)$ and $\sin(\alpha x) \cdot H_n^{(1)}(\alpha r) \cdot \cos(n\vartheta)$ into power series in βr. The attempts to determine coefficients A_n and B_n were based on the expansions

$$A_n = \sum_{k=0}^{\infty} a_n^k \beta^{2k}, \quad B_n = \sum_{k=0}^{\infty} b_n^k \beta^{2k} \tag{14}$$

using stress-free boundary conditions

$$\begin{cases} T_{rr}|_{r=r_0} = 0 \\ T_{r\vartheta}|_{r=r_0} = 0 \\ M_r|_{r=r_0} = 0 \\ Q_r|_{r=r_0} = 0. \end{cases} \tag{15}$$

It should be mentioned that a reasonable algorithm had not been proposed. Eringen and Naghdi [7] continued this approach with correct boundary conditions; the work of Murthy is an extension of Lurie's ideas for an elliptic case [9].

The other approach to the determination of coefficients in formulae (13-14) used the collocation procedure. Lekkerkerker, Eringen and Naghdi, Van Dyke [6,8,10] got some numerical results.

Classical approaches discussion. The idea of the expansion by small parameter $\boldsymbol{\beta}$ leads to the representation of the solution through a linear combination of Kirsch's solution and terms depending on $\boldsymbol{\beta}$:

$$\sigma = \sigma_0 + \beta^2 \sigma_2 + \beta^4 \sigma_4 + \cdots \tag{16}$$

where σ_0 – Kirsch stresses. The authors of this paper have repeated this way and have got the explicit second term σ_2 in polar coordinates as final formulae for stress field are not yet prescribed anywhere:

$$\sigma_{2rr} = \frac{p\pi}{8}\left(1 - \frac{4}{r^2} + \frac{3}{r^4}\right)\cos(2\vartheta),$$

$$\sigma_{2r\vartheta} = -\frac{p\pi}{8}\left(1 + \frac{2}{r^2} - \frac{3}{r^4}\right)\sin(2\vartheta), \tag{17}$$

$$\sigma_{2\vartheta\vartheta} = -\frac{p\pi}{8}\left(1 + \frac{3}{r^4}\right)\cos(2\vartheta).$$

The term $\beta^4 \sigma_4$ and following terms contain Poison's coefficient and are very heavy for prescribing however for small β they do not improve the solution as it was previously expected (see Fig. 1).

For small β just a very small difference with the solution of the Kirsch problem is observed. For bigger β the analytical theory based on expansion in a small parameter is not valid hence some other methods like the collocation procedure should be used. In the works of Lekkerkerker, Eringen, Naghdi, Van Dyke [6,8,10] numerical solutions were presented in form of tables. However, there were contradictions between the results presented in different papers of the same authors.

The general feature of this approach is an expansion of expressions that contain the Hankel function in parameter β. Since the argument of Hankel functions also contains parameter β it leads to a significant loss of accuracy. So it is more reasonable to calculate values of these functions at certain points.
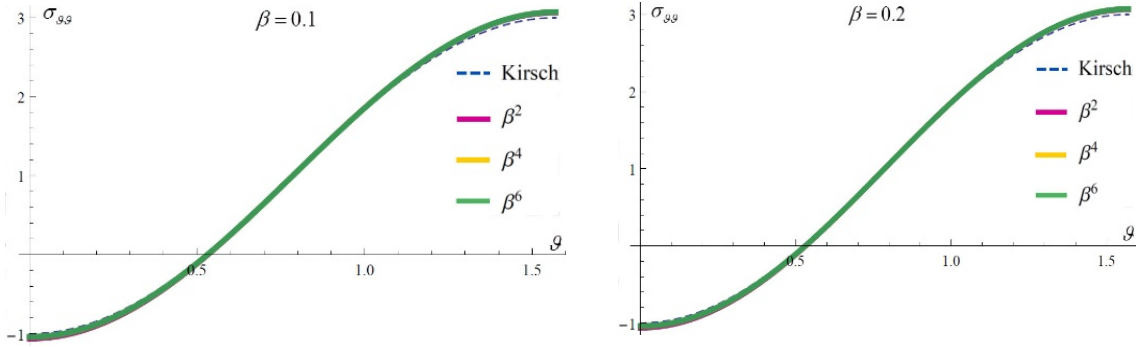
Fig. 1. Membrane stress $\sigma_{\vartheta\vartheta}$ depending on ϑ on the boarder up to $\beta = 0.1$ (a) and $\beta = 0.2$ (b)

It is also worth mentioning that normal displacement which is given by the formula

$$w = \left(\frac{Eh}{8\beta^2 R}\right)^{-1} \text{Re } \Phi$$

in papers [3,9] does not vanish with $\beta \to 0$ as one would expect for the plane problem. This contradiction is eliminated by adding some constant to the solution [3,9].

3. Our Approach

We propose to consider the fundamental system of solutions of equation (2) in the following form

$$\begin{bmatrix} \cos(\alpha x) \cdot H_n^{(1)}(\alpha r) \cdot \cos(n\vartheta) \\ \sin(\alpha x) \cdot H_n^{(1)}(\alpha r) \cdot \cos(n\vartheta) \end{bmatrix} =$$

$$= (-1)^{\left[\frac{n}{2}\right]} \cdot \frac{H_n^{(1)}((1+i)\beta r)}{H_n^{(1)}((1+i)\beta)} \cdot \Big[J_n\big((1+i)\beta r\big) +$$

$$+ \sum_{l=1}^{\infty}(-1)^l \cdot \Big(J_{n+2l}\big((1+i)\beta r\big) + J_{n-2l}\big((1+i)\beta r\big)\Big) \cdot \cos 2l\vartheta \Big]. \tag{18}$$

The full derivation of this formula demands special attention and is published in a separate paper [13].

Thus the general solution is presented as

$$\Phi = -i\frac{py^2}{2} + \sum_{n=0}^{\infty}(a_n + ib_n) \cdot f_n, \tag{19}$$

where f_n is a right-hand side of the equation (18), a_n, b_n – unknown coefficients that should be found by using boundary conditions. There is no need to expand these coefficients into series.

The advantage of this representation is in the separation of variables. It should be noted that in this case there are no functions that depend on both ϑ and β. It is easy to see that Bessel and Hankel's functions depend only on βr while cosine depends only on ϑ. The validity of the equality (18) is proved in a separate paper. The combination of Bessel functions with different indexes in this expansion has a deep mechanical sense since the frequency and amplitude of perturbed solution are observable.

One more advantage of this approach is the more convenient representation of boundary conditions. Since no cutting of series is needed we get high accuracy for the satisfaction of boundary conditions and a wide range of parameter β can be considered.

Let us introduce

$$g_{n,l} = (-1)^{\left[\frac{n}{2}\right]+l} \cdot \frac{H_n^{(1)}\big((1+i)\beta r\big)}{H_n^{(1)}\big((1+i)\beta\big)} \cdot \Big(J_{n+2l}\big((1+i)\beta r\big) + J_{n-2l}\big((1+i)\beta r\big)\Big)$$

which are trigonometric coefficients of Fourier in (18).

Expansion into Fourier series in ϑ of four boundary conditions gives us the next algebraic system.

Table 1. First boundary condition $T_{rr}|_{r=r_0} = 0$

$\cos 0$	$\dfrac{p}{2} - \text{Im} \sum\limits_{n=0}^{\infty} (a_n + ib_n) \cdot \dfrac{g'(n,0)}{2}$
$\cos 2\vartheta$	$\dfrac{p}{2} + \text{Im} \sum\limits_{n=0}^{\infty} (a_n + ib_n) \cdot \left(4g(n,1) - g'(n,1)\right)$
$\cos 4\vartheta$	$\text{Im} \sum\limits_{n=0}^{\infty} (a_n + ib_n) \cdot \left(16g(n,2) - g'(n,2)\right)$
$\cos 6\vartheta$	$\text{Im} \sum\limits_{n=0}^{\infty} (a_n + ib_n) \cdot \left(36g(n,3) - g'(n,3)\right)$
...	...
$\cos 2l\vartheta$	$\text{Im} \sum\limits_{n=0}^{\infty} (a_n + ib_n) \cdot \left(4l^2 g(n,l) - g'(n,l)\right)$

Table 2. Second boundary condition $T_{r\vartheta}|_{r=r_0} = 0$

$\sin 2\vartheta$	$-\dfrac{p}{2} - \text{Im} \sum\limits_{n=0}^{\infty} 2(a_n + ib_n) \cdot \left(g'(n,1) - g(n,1)\right)$
$\sin 4\vartheta$	$-\text{Im} \sum\limits_{n=0}^{\infty} 4(a_n + ib_n) \cdot \left(g'(n,2) - g(n,2)\right)$
$sin\,6\vartheta$	$-\text{Im} \sum\limits_{n=0}^{\infty} 6(a_n + ib_n) \cdot \left(g'(n,3) - g(n,3)\right)$
...	...
$\sin 2l\vartheta$	$-\text{Im} \sum\limits_{n=0}^{\infty} 2l(a_n + ib_n) \cdot \left(g'(n,l) - g(n,l)\right)$

Table 3. Third boundary condition $M_r|_{r=r_0} = 0$

$\cos 0$	$\text{Re} \sum\limits_{n=0}^{\infty} (a_n + ib_n) \cdot \left(\dfrac{vg'(n,0) + g''(n,0)}{2}\right)$
$\cos 2\vartheta$	$\text{Re} \sum\limits_{n=0}^{\infty} (a_n + ib_n) \cdot \left(-4vg(n,1) + vg'(n,1) + g''(n,1)\right)$
$\cos 4\vartheta$	$\text{Re} \sum\limits_{n=0}^{\infty} (a_n + ib_n) \cdot \left(-16vg(n,2) + vg'(n,2) + g''(n,2)\right)$
$\cos 6\vartheta$	$\text{Re} \sum\limits_{n=0}^{\infty} (a_n + ib_n) \cdot \left(-36vg(n,3) + vg'(n,3) + g''(n,3)\right)$
...	...

$\cos 2l\vartheta$	$\mathrm{Re} \sum\limits_{n=0}^{\infty} (a_n + ib_n) \cdot \left(-4l^2 v g(n,l) + v g'(n,l) + g''(n,l)\right)$

Table 4. Forth boundary condition $Q_r|_{r=r_0} = 0$

$\cos 0$	$\mathrm{Re} \sum\limits_{n=0}^{\infty} (a_n + ib_n) \cdot \left(\dfrac{-g'(n,0) + g''(n,0) + g'''(n,0)}{2}\right)$
$\cos 2\vartheta$	$\mathrm{Re} \sum\limits_{n=0}^{\infty} (a_n + ib_n)$ $\cdot (4(3-v)g(n,1) - (9-4v)g'(n,1) + g''(n,1) + g'''(n,1))$
$\cos 4\vartheta$	$\mathrm{Re} \sum\limits_{n=0}^{\infty} (a_n + ib_n)$ $\cdot (16(3-v)g(n,2) - (33-16v)g'(n,2) + g''(n,2) + g'''(n,2))$
$\cos 6\vartheta$	$\mathrm{Re} \sum\limits_{n=0}^{\infty} (a_n + ib_n)$ $\cdot (36(3-v)g(n,3) - (73-36v)g'(n,3) + g''(n,3) + g'''(n,3))$
...	...
$\cos 2l\vartheta$	$\mathrm{Re} \sum\limits_{n=0}^{\infty} (a_n + ib_n)$ $\cdot \left(4l^2(3-v) \cdot g(n,l) - \left(1 + 4l^2(2-v)\right)g'(n,l) + g''(n,l) + g'''(n,l)\right)$

For convenience in this paper, we take $r_0 = 1$. Thus we got a system that has a block structure and all elements can be found easily. A more detailed analysis of this system and technique of founding coefficients is written in a separate paper [13].

4. Results and Discussion

Stresses can be found using formulae (3) and (19) with coefficients a_n, b_n that are determined as a solution of the linear system presented in Tables 1-4. According to [4] from the point of view of mechanics, such model works for small and middle cutouts for $0 \leq \beta \leq 3,5 - 4,5$. This paper shows the first analytical approach that allows getting results for all acceptable range of parameter β. Membrane circumferential stresses obtained for various curvature parameters are presented below. The reason to choose the value of parameter $\beta = 0.3/\sqrt{2}$ (Fig. 1) is determined by comparison with the results obtained in the work of Eringen and Naghdi [8]. Their data have a significant difference from those of Van Dyke [10] with whom we have almost 100 % agreements in the results (Fig. 5).
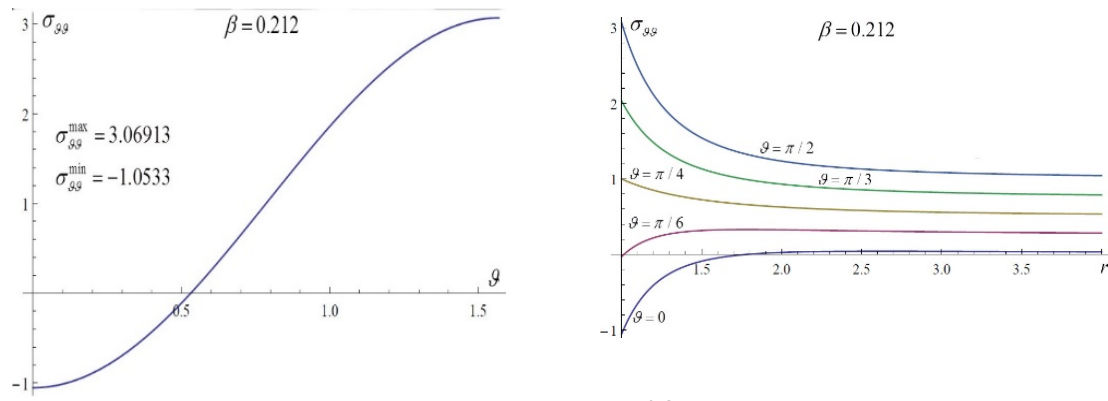
Fig. 2. Membrane stress $\sigma_{\vartheta\vartheta}$ for $\beta = \frac{0.3}{\sqrt{2}} \approx 0.212$ and $\nu = 0.3$
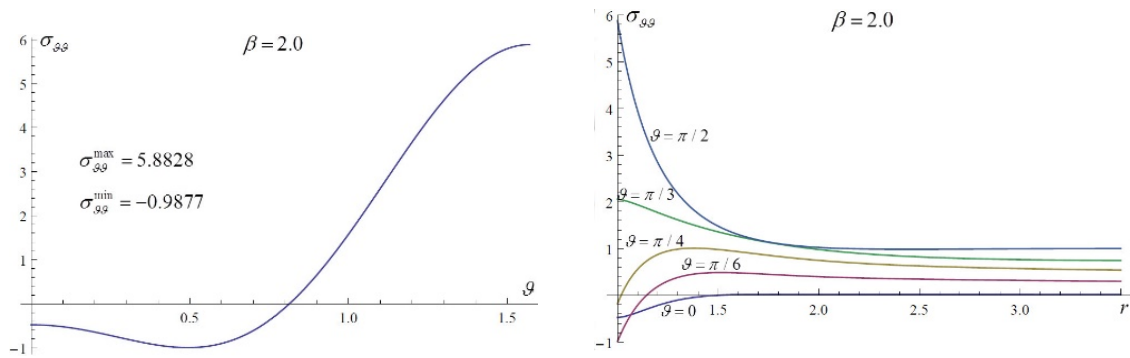
Fig. 3. Membrane stress $\sigma_{\vartheta\vartheta}$ for $\beta = 2.0$ and $\nu = 0.3$
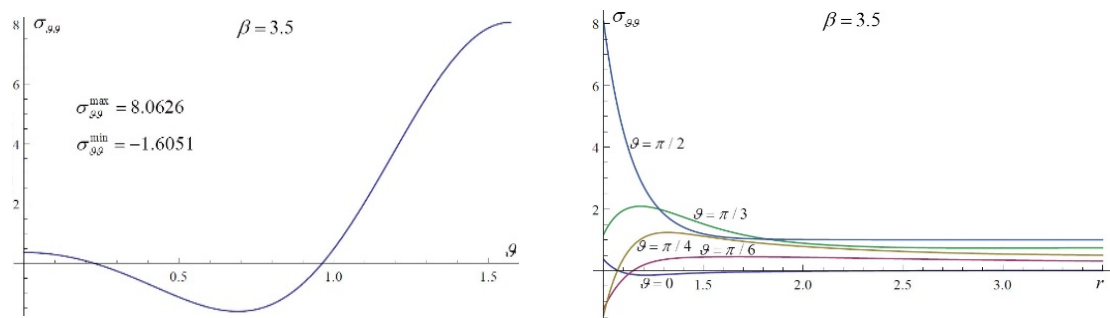
Fig. 4. Membrane stress $\sigma_{\vartheta\vartheta}$ for $\beta = 3.5$ and $\nu = 0.3$
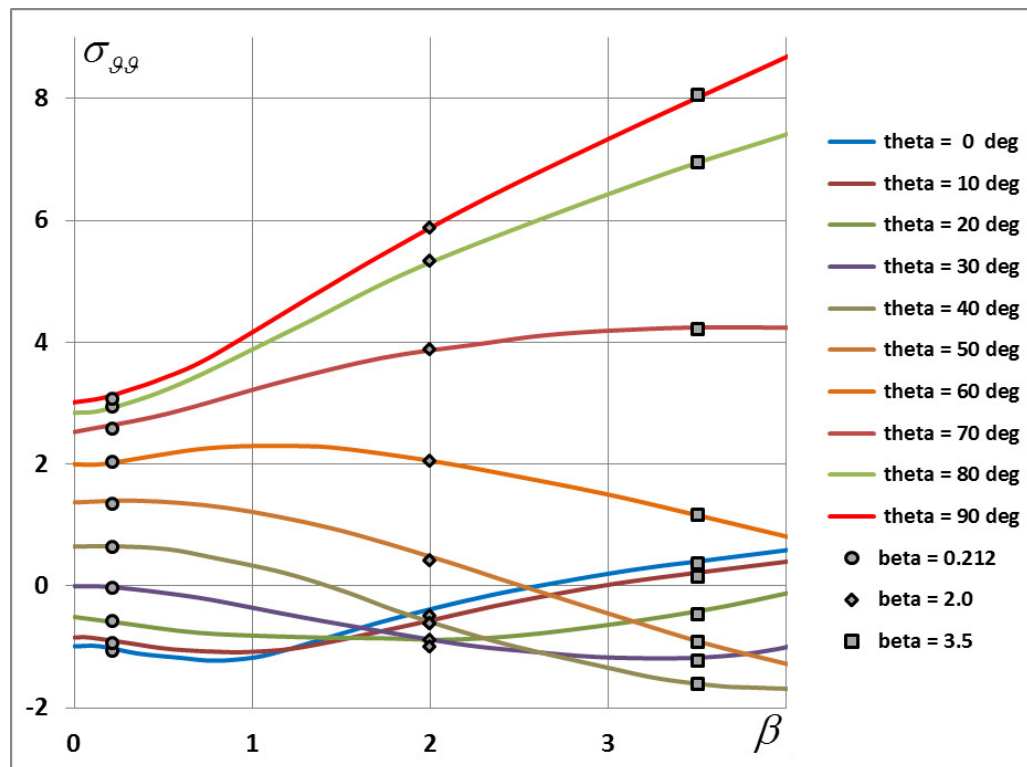
Fig. 5. Comparison with data of paper [10]: lines correspond to results of P.Van Dyke, dots for $\beta = 0.212;\ 2.0;\ 3.5$ are results of current paper

Considering researches of recent years it is observed the prevalence of approaches based on Finite Elements Method (FEM) [2,11]. However, results obtained by FEM need to be compared with analytical results and exact solutions. This explains the importance and value of the development of theoretical approaches.

References
[1] Storozhuk EA, Chernyshenko IS, Yatsura AV. Stress–Strain State near a Hole in a Shear-Compliant Composite Cylindrical Shell with Elliptical Cross-Section. *International Applied Mechanics*. 2018;54: 559-567.
[2] Labans E, Bisagni C, Celebi M, Tatting B, Gürdal Z, Blom-Schieber A, Rassaian M and Wanthal S. Bending of Composite Cylindrical Shells with Circular Cutouts: Experimental Validation. In: *58th AIAA/ASCE/AHS/ASC Structures, Structural Dynamics, and Materials Conference.* 2017.
[3] Lurie AI. Concentration of stresses in the Vicinity of an Aperture in the Surface of a Circular Cylinder. *Prikladnaya Matematica I Mekhanica*. 1946;10: 397. (In Russian)
[4] Guz AN. *Cylindrical Shells with cutout.* Kiev: Naukova Dumka; 1974. (In Russian)
[5] Savin GN. *Stress concentration around holes.* Kiev: Naukova Dumka; 1968. (In Russian)
[6] Lekkerkerker JG. On the stress distribution in cylindrical shells weakened by a circular hole. *Delft: Uitgeverij Waltman*; 1965.
[7] Naghdi AK, Eringen AC. Stress Distribution in a Circular Cylindrical Shell with a Circular Cutout. *Archive of Applied Mechanics*. 1965;34(3): 161-172.
[8] Eringen AC, Naghdi AK, Thiel CC. State of Stress in a Circular Cylindrical Shell With a Circular Hole. *Welding Research Council Bulletin*. 1965;102.

[9] Murthy VVM. Stresses Around an Elliptic Hole in a Cylindrical Shell. *J. of App. Mech.* 1969;36: 39-46.

[10] Van Dyke P. Stresses about a Circular Hole in a Cylindrical Shell. *AIAA Journal.* 1965;3(9): 1733-1742.

[11] Celebi M, Gürdal Z, Tatting BF, Blom-Schieber A, Rassaian M, Wanthal SP. Effects of Size and Location of a Circular Cutout on Buckling and Failure of a Cylindrical Shell in Bending. In: *AIAA 2017-0433*. 2017.

[12] Green AE, Zerna W. *Theoretical Elasticity*. Oxford; 1960.

[13] Kashtanova SV, Rzhonsnitskiy AV. Analytical approach to the conclusion of the stress field of a cylindrical shell with a circular hole in tension. *PNRPU Mechanics Bulletin*. 2021. (In Russian)

Appendix A
Nomenclature

R, h – radius and thickness of the cylindrical shell

r_0 – radius of the hole

$r_0 = 1$ in the present paper

ν – Poisson's ratio

E – Young's modulus

$\beta^2 = \dfrac{r_0^2 \sqrt{3\,(1-\nu^2)}}{4Rh}$ – curvature parameter

w – displacement normal to the shape

U – stress function

T_x, T_{xy}, T_y – forces of the shell in Cartesian coordinates

$T_{rr}, T_{r\vartheta}, T_{\vartheta\vartheta}$ – forces of the shell in polar coordinates

$\sigma = T/h$ – middle surface stresses

p – axial tension applied at the edge of an infinite cylinder along x-coordinate

$\alpha = (1+i)\beta$

$t = \alpha r$

$H_n^{(1)}, H_n^{(2)}$ – Hankel function

J_n – Bessel function

Y_n – Neiman function

M_r – bending moment

Q_r – Kirchhoff shear

SOME THEOREMS AND WAVE PROPAGATION IN A PIEZOTHERMOELASTIC MEDIUM WITH TWO-TEMPERATURE AND FRACTIONAL ORDER DERIVATIVE

Rajneesh Kumar, Poonam Sharma[*]

Department of Mathematics, Kurukshetra University, Kurukshetra 136119, Haryana, India

*e-mail: poonamattri189@gmail.com

Abstract. Wave propagation and some basic theorems like variational principle, uniqueness theorem, and theorem of reciprocity are studied for an anisotropic piezothermoelastic solid with two-temperature and fractional order derivative. The basic governing equations are used to study the interesting problem. Also, we characterize an alternative formulation of the mixed initial boundary value problem. These theorems are also summarised for a special case of orthotropic piezothermoelastic solid with the consideration of two-temperature theory and fractional order derivative. The non-trivial solution of the system is insured by a quartic equation whose roots represent the complex velocities of four attenuating waves in the medium. The different characteristics of the waves like phase velocity and attenuation quality factor are plotted three-dimensionally with the change in direction for two different models. Some special cases are also deduced from the present investigation.

Keywords: piezothermoelastic, orthotropic, variational principle, uniqueness, plane waves, phase velocity

1. Introduction

The two-temperature theory of thermoelasticity with two distinct temperatures (conductive temperature φ and the thermodynamic temperature T) was introduced by Chen and Gurtin [1], and Chen et al. [2,3]. Said et al. [4] investigated a problem of rotating-micropolar thermoelastic medium with two-temperature under influence of the magnetic field. Kumar et al. [5] studied the propagation of plane waves in an anisotropic thermoelastic medium with void and two-temperature in the context of three phase lag theory of thermoelasticity.

The theory of thermopiezoelectric material was first proposed by Mindlin [6] and derived governing equations of a thermopiezoelectric plate. The physical laws for the thermopiezoelectric material have been explored by Nowacki [7,8]. Sharma [9] investigated the piezoelectric effect on the velocities of waves in an anisotropic piezo-poroelastic medium. Vashishth and Sukhija [10] studied the inhomogeneous waves at the boundary of an anisotropic piezothermoelastic solid. Kumar and Sharma [11] established basic theorems and discussed wave propagation in a piezothermoelastic medium with the consideration of dual phase lag.

Fractional Calculus is a field of mathematic study that grows out of the traditional definitions of the calculus integral and derivative operators in much the same way, fractional exponents is an outgrowth of exponents with an integer value. Meral and Royston [12] investigated the response of the fractional order on viscoelastic half-space to surface and subsurface sources. Bassiouny and Sabry [13] discussed the two-temperature thermo-elastic behaviour of piezoelectric materials with fractional order derivative. Kumar and Sharma [14]

discussed the effect of fractional order derivative on energy ratios at the boundary surface of the elastic-piezothermoelastic medium. Lata [15] discussed the fractional order thermoelastic thick circular plate with two temperatures in the frequency domain.

Youssef and Bassiouny [16] proposed the generalised two-temperature theory of thermoelasticity to solve the boundary value problems of one dimensional piezothermoelastic half-space with heating its boundary with different types of heating. Ezzat et al. [17] formulated the theory of two-temperature theory of thermoelasticity for piezoelectric/piezomagnetic materials. Bassiouny and Sabry [18] investigated the propagation of a thermal wave through a semi-infinite slab subjected to thermal loading of the fractional order of exponential type applied for a finite period of time.

Comprehensive work has been done on uniqueness, reciprocity theorems and variational principle by different authors in different media notable among them are Nickell and Sackman [19], Iesan [20], Karamany and Ezzat [21], Othman [22], Ezzat, Kumar et al. [23], Kuang [24], Vashishth and Gupta [25], and Kumar and Sharma [26,27].

In the present investigation, the variational principle, reciprocity theorem, and the uniqueness theorem have been proved. The mixed initial boundary value problem and its alternative approach are also discussed. Further, wave propagation in an orthotropic piezothermoelastic medium with the effect of the two-temperature and fractional order parameter is studied and characteristics like phase velocity and attenuation quality factor of waves are demonstrated graphically depicting the effect of fractional order and two-temperature parameter. The established results will be helpful for further investigation of the various problems.

2. Basic Equations

Following Kumar et al. [5] and Kumar and Sharma [11], the governing equations in a homogeneous, anisotropic piezothermoelastic medium with two-temperature and fractional order derivative in the absence of thermal sources and independent of free charge density are:

Constitutive equations:

$$\sigma_{ij} = c_{ijkl}\,\varepsilon_{kl} - e_{ijk}E_k - \alpha_{ij}T\,, \tag{1}$$

$$-q_{i,i} = \rho T_0 \dot{S}\,, \tag{2}$$

$$\rho S = \alpha_{ij}\varepsilon_{ij} + \tau_i E_i + rT\,, \tag{3}$$

$$D_i = \xi_{ij}E_j + e_{ijk}\varepsilon_{jk} + \tau_i T\,, \tag{4}$$

$$E_i = -\Phi_{,i}\,, \ (i,j,k,l = 1,2,3). \tag{5}$$

Equations of motion:

$$\sigma_{ij,j} + \rho(F_i - \ddot{u}_i) = 0. \tag{6}$$

Equation of heat conduction:

$$-K_{ij}\,\varphi_{,j} = \left(1 + \tau_q \frac{\partial^\alpha}{\partial t^\alpha}\right)q_i\,, \tag{7}$$

such that $\varphi - T = a_{ij}\varphi_{,ij}$.

Gauss equation:

$$D_{i,i} = 0. \tag{8}$$

In the equations (1)-(8), the Cartesian reference frame system is used and repeated subscripts imply summation. The subscripts preceded by comma notations are used to represent the partial derivatives with respect to the space variables and the superposed dots denote the order of time differentiation.

$c_{ijkl}\ (= c_{klij} = c_{jikl} = c_{ijlk})$ – Elastic constants,

ρ – Mass density,

q_i – Components of heat flux vector $\mathbf{q}$,

F_i – Components of the external forces per unit mass,

u_i – Components of the displacement vector $\mathbf{u}$,

σ_{ij} – Stress tensor,

ε_{ij} – Strain tensor,

K_{ij} – Thermal conductivity tensor,

S – Entropy per unit mass,

E_i – Electric field intensity,

D_i – Electric displacement,

Φ – Electric potential,

T, φ – Absolute and conductive temperature of the medium,

$a_{ij}(>0)$ – Two-Temperature parameters,

T_0 – Reference temperature of the body,

$\alpha_{ij}, \tau_i, \xi_{ij}, e_{ijk}, r$ – Piezothermal moduli, respectively,

τ_q – Thermal relaxation time,

α – Fractional order derivative such that $0 \le \alpha < 1$.

3. Variational Principle

The principle of virtual work with a variation of displacements for the elastic deformable body of volume V and surface A is written as

$$\int_V \rho(F_i - \ddot{u}_i)\delta u_i \, dV + \int_A h_i \delta u_i \, dA + \int_A c_0 \delta\Phi \, dA = \int_A (\sigma_{ij} n_j)\delta u_i \, dA + \int_A (D_i n_i)\delta\Phi \, dA, \tag{9}$$

where $h_i = \sigma_{ij} n_j$ and $c_0 = D_i n_i$.

On the left hand side, we have the virtual work of body forces F_i, inertial forces $\rho \ddot{u}_i$, surface forces h_i, whereas, on the right hand side, we have the virtual work of internal forces and n_i denotes the outward normal of ∂V, c_0 is the electric charge density. Using divergence theorem and the symmetry of the stress tensor, equation (9) can be written in the alternative form as

$$\int_V \rho(F_i - \ddot{u}_i)\delta u_i \, dV + \int_A h_i \delta u_i \, dA + \int_A c_0 \delta\Phi \, dA = \int_V (\sigma_{ij}\delta u_{i,j}) \, dV + \int_V (D_i \delta\Phi_{,i}) \, dV. \tag{10}$$

Substituting the value of σ_{ij} from the relation (1) in the equation (10), we obtain

$$\int_V \rho(F_i - \ddot{u}_i)\delta u_i \, dV + \int_A h_i \delta u_i \, dA + \int_A c_0 \delta\Phi \, dA = \int_V (c_{ijkl} \varepsilon_{kl} - e_{ijk} E_k - \alpha_{ij} T)\delta\varepsilon_{ij} \, dV - \int_V D_i \delta E_i dV$$

$$= \delta W - \int_V e_{ijk} E_k \delta\varepsilon_{ij} dV - \int_V \alpha_{ij}\left(\varphi - a_{ij}\varphi_{,ij}\right)\delta\varepsilon_{ij} dV - \int_V D_i \delta E_i dV, \tag{11}$$

where $W = \dfrac{1}{2}\displaystyle\int_V c_{ijkl} \varepsilon_{kl}\varepsilon_{ij} \, dV$, $\delta u_{i,j} = \delta\varepsilon_{ij}$, $\delta\Phi_{,i} = -\delta E_i$, $T = \varphi - a_{ij}\varphi_{,ij}$.

The equation (11) formulated the uncoupled problem of anisotropic piezothermoelastic with two temperature and fractional order derivative where φ and Φ are known functions. In this case, when we take into account the coupling of the deformation field with the temperature, there arises the necessity of considering an additional relation characterizing the

phenomenon of the thermal conductivity. Following Biot [28] we define a vector $\boldsymbol{J}$ connected with the entropy through the relation

$$\rho S = -J_{i,i}. \tag{12}$$

Equations (2) and (12) implies

$$q_i = \dot{J}_i T_0.$$

Combination of equations (2), (3), (7), and (12) yield

$$T_0 L_{ij} \left(\frac{\partial}{\partial t} + \tau_q \frac{\partial^{\alpha+1}}{\partial t^{\alpha+1}} \right) J_i + \varphi_{,j} = 0, \tag{13}$$

$$-J_{i,i} = \alpha_{ij} \varepsilon_{ij} + \tau_i E_i + rT, \tag{14}$$

where L_{ij} the resistivity matrix, is the inverse of the thermal conductivity K_{ij}. Multiplying both sides of the equation (13) by δJ_j and integrating over the region of the body, gives

$$\int_V \left[\varphi_{,j} + T_0 L_{ij} \left(\frac{\partial J_i}{\partial t} + \tau_q \frac{\partial^{\alpha+1} J_i}{\partial t^{\alpha+1}} \right) \right] \delta J_j \, dV = 0. \tag{15}$$

Also, we have,

$$\int_V \varphi_{,j} \delta J_j dV = \int_V \left(\varphi \delta J_j \right)_{,j} dV - \int_V \varphi \delta J_{j,j} dV. \tag{16}$$

Applying the divergence theorem defined by

$$\int_V \left(\varphi \delta J_j \right)_{,j} dV = \int_A \left(\varphi \delta J_j \right) n_j dA, \tag{17}$$

in the equation (16), yield

$$\int_V \varphi_{,j} \delta J_j dV = \int_A \left(\varphi \delta J_j \right) n_j dA - \int_V \varphi \delta J_{j,j} dV. \tag{18}$$

Substituting equation (18) in equation (15), we obtain

$$\int_A \left(\varphi \delta J_j \right) n_j dA - \int_V \varphi \delta J_{j,j} dV + T_0 \int_V L_{ij} \left(\frac{\partial J_i}{\partial t} + \tau_q \frac{\partial^{\alpha+1} J_i}{\partial t^{\alpha+1}} \right) \delta J_j dV = 0. \tag{19}$$

Making use of equation (14) in equation (19), yield the second variational equation

$$\int_A \left(\varphi \delta J_j \right) n_j dA + \int_V \varphi \alpha_{ij} \delta \varepsilon_{ij} dV + \int_V \varphi \tau_j \delta E_j dV - r \int_V a_{ij} \varphi_{,ij} \varphi dV + \delta(M + H) = 0, \tag{20}$$

where δM is defined by

$$\delta M = r \int_V \varphi \delta \varphi dV, \tag{21}$$

and δH is

$$\delta H = T_0 \int_V L_{ij} \left(\frac{\partial J_i}{\partial t} + \tau_q \frac{\partial^{\alpha+1} J_i}{\partial t^{\alpha+1}} \right) \delta J_j dV. \tag{22}$$

Thus, we obtain the variational principle in the following form

$$\delta(W + M + H) = \int_V \rho(F_i - \ddot{u}_i) \delta u_i \, dV + \int_A h_i \delta u_i \, dA + \int_A c_0 \delta \Phi \, dA + \int_V D_i \delta E_i dV + \int_V e_{ijk} E_k \delta \varepsilon_{ij} dV$$
$$- \int_A \left(\varphi \delta J_j \right) n_j dA - \int_V \varphi \tau_j \delta E_j dV - \int_V a_{ij} \alpha_{ij} \varphi_{,ij} \delta \varepsilon_{ij} dV + r \int_V a_{ij} \varphi \delta \varphi_{,ij} dV. \tag{23}$$

On the right-hand side of equation (23), we find all the causes, the mass forces, inertial forces, the surface forces, the heating, the electric potential on the surface A bounding the body.

Mixed initial boundary value problem. For the mixed initial boundary value problem we assume, that $\bar{V}$ denotes the closure of an open, bounded, and connected set characterizing anisotropic piezothermoelastic solid with two-temperature such that the constitutive and field equations are defined on $\bar{V} = V \times [0, \infty)$. Let ∂V denotes the boundary of $\bar{V}$. Let ∂V_i $(i = 1, 2, 3, 4, 5, 6)$ denotes the subsets of ∂V such that $\partial V = \partial V_1 \bigcup \partial V_2 = \partial V_3 \bigcup \partial V_4 = \partial V_5 \bigcup \partial V_6$ and $\partial V_1 \bigcap \partial V_2 = \partial V_3 \bigcap \partial V_4 = \partial V_5 \bigcap \partial V_6 = \emptyset$ with initial conditions on the surface at $t = 0$,

$$u_i = u_i^{\,0}, \dot{u}_i = \dot{u}_i^{\,0}, \varphi = \varphi^0, \Phi = \Phi^0, q_i = q_i^{\,0}, \dot{q}_i = \dot{q}_i^{\,0} \text{ on } V, \tag{24}$$

and boundary conditions on the surface are

$$u_i = u_{i1} \text{ on } \partial V_1 \times [0, \infty), h_i = \sigma_{ij} n_j = h_{i1} \text{ on } \partial V_2 \times [0, \infty), q = q_i n_i = q_{i1} \text{ on } \partial V_3 \times [0, \infty),$$

$$\varphi = \varphi_1 \text{ on } \partial V_4 \times [0, \infty), c_0 = D_i n_i = c_{01} \text{ on } \partial V_5 \times [0, \infty), \Phi = \Phi_1 \text{ on } \partial V_6 \times [0, \infty). \tag{25}$$

where $u_i^{\,0}, \dot{u}_i^{\,0}, \varphi^0, \Phi^0, q_i^{\,0}, \dot{q}_i^{\,0}$ are the known initial displacements, temperature, electric potential, heat flux, and heat flux rate, respectively and $u_{i1}, h_{i1}, \varphi_1, q_{i1}, c_{01}, \Phi_1$ denotes the surface displacement, tractions, temperature, heat flux, electric charge density, and electric potential. In order to meet the smoothness requirements and the other regularity assumptions these functions are introduced as the hypothesis on the data

  (i) $u_i^{\,0}, \varphi^0, \Phi^0, q_i^{\,0}$ are continuous on $\bar{V} = V \times [0, \infty)$.

  (ii) $\dot{u}_i^{\,0}, \dot{q}_i^{\,0}$ are continuously differentiable on $\bar{V} = V \times [0, \infty)$.

  (iii) $u_{i1}, \varphi_1, \Phi_1$ are continuous on $\partial V_1 \times [0, \infty), \partial V_4 \times [0, \infty), \partial V_6 \times [0, \infty)$, respectively.

  (iv) h_{i1}, q_{i1}, c_{01} are piecewise continuous on $\partial V_2 \times [0, \infty), \partial V_3 \times [0, \infty), \partial V_5 \times [0, \infty)$, respectively.

Further, we assume that the material constants satisfy the following inequalities

$$C_e > 0, T_0 > 0, \tau_q > 0, \rho > 0, \tag{26a}$$

and $c_{ijkl}, \alpha_{ij}, L_{ij}$ are smooth on V such that

$$C_{ijkl} \varepsilon_{ij} \varepsilon_{kl} > 0 \text{ for all tensors } \varepsilon_{ij} \text{ and } L_{ij} \vartheta_i \vartheta_j > 0 \text{ for any real } \vartheta_i \text{ defined on } V. \tag{26b}$$

A solution of the mixed initial boundary value problem is defined as an admissible state $R = [u_i, \varepsilon_{ij}, \sigma_{ij}, T, q_i, \Phi, D_i, E_i, S]$, an ordered array of functions with properties $u_i \in C^{2,2}$, $\sigma_{ij} \in C^{1,0}, \varphi \in C^{2,2}, q_i \in C^{1,2}, D_i \in C^{1,0}, \Phi \in C^{1,0}, S \in C^{0,1}$ on $V \times [0, \infty)$. The set of all admissible states is a linear space as it satisfies the addition of admissible states and scalar multiplication of an admissible state. R satisfies the equations (1)-(8), initial conditions (24), and boundary conditions (25). Now, we assume that the virtual displacements δu_i, the virtual increment of the temperature $\delta \varphi$, etc. correspond to the increments occurring in the body. Then

$$\delta u_i = \frac{\partial u_i}{\partial t} dt = \dot{u}_i \, dt \quad, \delta \varphi = \frac{\partial \varphi}{\partial t} dt = \dot{\varphi} dt, \text{ etc.} \tag{27}$$

and equation (23) reduces to the following relation

$$\frac{d}{dt}(W + M + H) = \int_V \rho F_i \, \dot{u}_i \, dV - \int_V \rho \ddot{u}_i \, \dot{u}_i \, dV + \int_A h_i \, \dot{u}_i \, dA + \int_A c_0 \dot{\Phi} \, dA + \int_V D_i \dot{E}_i dV$$

$$+ \int_V e_{ijk} E_k \dot{\varepsilon}_{ij} dV - \int_A (\varphi \dot{J}_j) n_j dA - \int_V \varphi \tau_j \dot{E}_j dV - \int_V a_{ij} \alpha_{ij} \varphi_{,ij} \dot{\varepsilon}_{ij} dV \tag{28}$$

$$+ r \int_V a_{ij} \varphi \dot{\varphi}_{,ij} dV.$$

Now,

$$\int_V \rho \, \ddot{u}_i \, \dot{u}_i \, dV = \frac{\partial K}{\partial t},\tag{29}$$

where $K = \dfrac{1}{2}\int_V \rho \, \dot{u}_i \, \dot{u}_i \, dV$, is the kinetic energy of the body enclosed by the volume V.

Using equation (29) in the equation (28), we obtain

$$\frac{d}{dt}\left(W + H + K + \frac{1}{2}\int_V r\varphi^2 \, dV\right) = \int_V \rho F_i \, \dot{u}_i \, dV + \int_A h_i \, \dot{u}_i \, dA + \int_A c_0 \dot{\Phi} \, dA + \int_V e_{ijk} \, E_k \dot{\varepsilon}_{ij} dV$$
$$+ \int_V D_i \dot{E}_i dV - \int_A \left(\varphi \dot{J}_j\right) n_j dA - \int_V \varphi \tau_j \dot{E}_j dV - \int_V a_{ij}\alpha_{ij} \, \varphi_{,ij}\dot{\varepsilon}_{ij} dV + r\int_V a_{ij}\varphi\dot{\varphi}_{,ij} dV.\tag{30}$$

The above equation is the basis for the proof of the following uniqueness theorem.

Theorem1: The mixed initial boundary value problem with two-temperature theory has only one solution of the equations (6)-(8), subject to the initial conditions (24) and boundary conditions (25).

Proof: Let $u_i^{(1)}$, $\varphi^{(1)}, \Phi^{(1)}$ and $u_i^{(2)}$, $\varphi^{(2)}, \Phi^{(2)}$ be two solutions sets of equations (1)-(8). Let us take

$$u_i = u_i^{(1)} - u_i^{(2)}, \quad \varphi = \varphi^{(1)} - \varphi^{(2)}, \quad \Phi = \Phi^{(1)} - \Phi^{(2)}.\tag{31}$$

The functions u_i, φ and Φ satisfy the governing equations with zero body forces and homogeneous initial and boundary conditions. Thus, these functions satisfy an equation similar to the equation (30) with zero right hand side, that is,

$$\frac{d}{dt}\left(W + H + K + \frac{1}{2}\int_V r\varphi^2 dV\right) = 0.\tag{32}$$

Since we have

$$L_{ij} = L_{ji},$$

therefore, from equation (22) and with the aid of the definition of fractional order derivative given by Riemann Liouville i.e.

$$_a D_t^\alpha(f(t)) = \frac{1}{\Gamma(n-\alpha)}\left(\frac{d}{dt}\right)^n \int_a^t \frac{f(\tau)}{(t-\tau)^{\alpha-n+1}} d\tau, \ (n-1) \le \alpha < n, \text{ where } n \text{ is an integer and } \alpha \text{ is}$$

a real number, we obtain

$$\frac{dH}{dt} = T_0 \int_V L_{ij}\dot{J}_i\dot{J}_j dV + \frac{T_0\tau_q}{\Gamma(1-\alpha)}\frac{d}{dt}\left[\int_V L_{ij}\left(\int_0^t \frac{\dot{J}_i(\tau)}{(t-\tau)^\alpha} d\tau\right)\dot{J}_j dV\right].\tag{33}$$

Substitution of equation (33) in the equation (32), yields

$$\frac{d}{dt}\left(W + K + \frac{1}{2}\int_V r\varphi^2 \, dV + \frac{T_0\tau_q}{\Gamma(1-\alpha)}\left[\int_V L_{ij}\left(\int_0^t \frac{\dot{J}_i(\tau)}{(t-\tau)^\alpha} d\tau\right)\dot{J}_j dV\right]\right) + T_0\int_V L_{ij}\dot{J}_i\dot{J}_j dV = 0.\tag{34}$$

Integrating equation (34) twice with respect to time variable over the interval $(0,t)$ and using homogeneous initial conditions we thus, see that

$$\int_0^t\left(W + K + \frac{1}{2}\int_V r\varphi^2 dV + \frac{T_0\tau_q}{\Gamma(1-\alpha)}\left[\int_V L_{ij}\left(\int_0^t \frac{\dot{J}_i(\tau)}{(t-\tau)^\alpha} d\tau\right)\dot{J}_j dV\right]\right)d\zeta +$$
$$+ T_0\int_0^t\int_0^t\int_V L_{ij}\dot{J}_i\dot{J}_j dV d\zeta d\zeta = 0.\tag{35}$$

We also note that the expression $\int_V r\varphi^2 dV$ occurring in the equation (35) is always

positive, since by the laws of thermodynamics Nowacki [7], $0 < a^2 < rT$. Following Kothari and Mukhopadhyay [29], the inequalities (26) implies,

$$\int_0^t \left(W + K + \frac{1}{2}\int_V r\varphi^2 dV + \frac{T_0\tau_q}{\Gamma(1-\alpha)}\left[\int_V L_{ij}\left(\int_0^t \frac{j_i(\tau)}{(t-\tau)^\alpha} d\tau \right) j_j dV \right] \right) d\zeta + T_0 \int_0^t \int_0^t \int_V L_{ij} j_i j_j dV d\zeta d\zeta. \quad (36)$$

The component in each integrand of expression (36) is non-negative. Thus, we conclude that each term in the expression (36) must be zero, which implies that $u_i = \Phi = \varphi = \varepsilon_{ij} = \sigma_{ij} = 0$ on $V \times [0,\infty)$. This proves the uniqueness of the solution to the complete system of field equations subjected to the displacement- electric potential-temperature, initial and boundary conditions.

Alternative formulation: Following Nickel and Sackman [19] and Iesan [20], an alternative approach to solving the mixed initial boundary problem is formulated by incorporating the initial conditions explicitly into the field equations. Let χ, ψ be the two functions defined on $\overline{V} = V \times [0,\infty)$, and their convolution is defined as

$$[\chi * \psi] = \int_0^t \chi(x, t-s)\psi(x,s)\,ds, \quad (x,t) \in V \times [0,\infty), \quad (37)$$

and satisfy the following properties
(i) $\chi * \psi = \psi * \chi$.
(ii) $\chi * (\psi + \tau) = (\chi * \psi) + (\chi * \tau)$.
(iii) $\chi * (\psi * \tau) = (\chi * \psi) * \tau$.
(iv) $\chi * \psi = 0 \Rightarrow \chi = 0$ or $\psi = 0$.

Consider Laplace transform of equations (2), (6). Using initial conditions (24), we obtain

$$\overline{q}_{i,i} - \rho C_e \left(\varphi^0 - a_{ij}\varphi^0_{,ij} \right) - T_0\alpha_{ij}\,u^0_{i,j} + T_0\tau_i\Phi^0_{,i} + \rho T_0\overline{S} = 0, \quad (38a)$$

$$\overline{\sigma}_{ij,j} + \overline{F}_i + \rho s\,u^0_i + \rho\dot{u}^0_i = \rho s^2\,\overline{u}_i, \quad (38b)$$

$$\overline{D}_{i,i} + \xi_{i,j}\overline{\Phi}_{,ji} - e_{ijk}\,\overline{u}_{j,ki} - \tau_i\overline{T}_{,i} = 0, \quad (38c)$$

where "s" is the transformation parameter and a superimposed bar indicates the transformed function. Applying the inverse transformation, yields

$$\rho T_0 S = h - g'* q_{i,i}, \quad (39a)$$

$$\rho\,u_i = g * \sigma_{ij,j} + f_i, \quad (39b)$$

$$D_{i,i} + \xi_{i,j}\Phi_{,ji} - e_{ijk}\,u_{j,ki} - \tau_i T_{,i} = 0, \quad (39c)$$

where g, g', f_i and h are

$$g(t) = t, \; g'(t) = 1, \quad t \in [0,\infty), \quad (40a)$$

$$f_i(x,t) = g * F_i(x,t) + \rho t\,u^0_i(x) + \rho\dot{u}^0_i(x), \quad (40b)$$

$$h(x) = \rho C_e \left(\varphi^0 - a_{ij}\varphi^0_{,ij} \right)(x) + \alpha_{ij}T_0 u^0_{i,j}(x) - \tau_i T_0\Phi^0_{,i}(x), \quad (40c)$$

with the aid of equations (38)-(40), alternative formulations of the problem can be made.

Theorem 2: Let $u_i \in C^{0,2}$, $\sigma_{ij} \in C^{0,1}$, and suppose $\sigma_{ij} = \sigma_{ji}$. Then, u_i, σ_{ji} satisfy the equations of motion (6) as well as the initial conditions (24) on u_i iff

$$g * \sigma_{ij,j} + f_i = \rho\,u_i, \text{ on } V \times [0,\infty). \quad (41)$$

Following Gurtin [30], the proof of this theorem is trivial.

Theorem 3: Let $S \in C^{0,2}$, $q_i \in C^{0,1}$, suppose the equation (3) holds for $t = 0$. Then, S, q_i satisfy the energy equation (2) as well as the initial conditions (24) iff

$$h - g' * q_{i,i} = \rho T_0 S \quad \text{on} \quad V \times [0, \infty).$$ (42)

Proof: Suppose equations (2), (3) and initial conditions (24) hold for $t = 0$. Then, equations (2) and (40a) implies

$$-g' * q_{i,i} = \rho T_0 \int_0^t \dot{S}(x, \zeta) d\zeta = \rho T_0 S(x,t) - \rho T_0 S(x,0).$$

Since at $t = 0$, $S(x,0) = \rho C_e \left(\varphi^0 - a_{ij} \varphi_{,ij}^0 \right)(x) - \alpha_{ij} T_0 u_{i,j}^0(x) + \tau_i T_0 \Phi_{,i}^0(x)$. Therefore,

$$-g' * q_{i,i} = \rho T_0 S(x,t) - \rho C_e \left(\varphi^0 - a_{ij} \varphi_{,ij}^0 \right)(x) - \alpha_{ij} T_0 u_{i,j}^0(x) + \tau_i T_0 \Phi_{,i}^0(x).$$ (43)

Then, by equation (40c), $h - g' * q_{i,i} = \rho T_0 S(x,t)$.

Hence, equation (42) is proved on $V \times [0, \infty)$. Conversely, suppose equation (42) holds. Then, by reversing the argument, and utilizing the equations (40), it is directly verified that S, q_i meet energy equation (2). Since equations (3), (40a), (40b), (40c), (42) imply initial conditions (24) on φ, and therefore the proof of the theorem is complete.

Theorem 4: Let $R = [u_i, \varepsilon_{ij}, \sigma_{ij}, \varphi, q_i, S, D_i, E_i, \Phi]$ be an admissible state. Then R is a solution to the mixed initial boundary value problem of piezothermoelasticity with two-temperature iff it meets the equations (1), (2), (4), (39a), (39b), (39c) and the boundary conditions (25).

The result of this theorem is the trivial consequence of Theorem 2 and Theorem 3.

This provides an alternative formulation of the solution of the mixed initial boundary value problem by incorporating initial conditions explicitly into field equations.

4. Reciprocity Theorem

We shall consider a homogeneous anisotropic piezothermoelastic body with two-temperature occupying the region V and bounded by the surface A. We assume that the stresses σ_{ij} and the strains ε_{ij} are continuous together with their first derivatives whereas the displacements u_i, temperature φ and the electrical potential Φ are continuous and have continuous derivatives up to second order, for $x \in V + A$, $t > 0$. The components of surface traction, the normal component of the heat flux, the normal component of the electric displacement at regular points of ∂V, are given by

$$h_i = \sigma_{ij} n_j, \quad q = q_i n_i, \quad c_0 = D_i n_i, \quad i = 1, 2, 3,$$ (44)

respectively. To the system of field equations, we must adjoin boundary conditions and initial conditions. We consider the following boundary conditions:

$$u_i(x,t) = u_{i1}(x,t), \quad \varphi(x,t) = \varphi_1(x,t), \quad \Phi(x,t) = \Phi_1(x,t),$$ (45)

for all $x \in A$, $t > 0$ and the homogeneous initial conditions

$$\left. \begin{array}{l} u_i(x,0) = \dot{u}_i(x,0) = 0, \quad \varphi(x,0) = \dot{\varphi}(x,0) = 0, \\ \text{and} \ \Phi(x,0) = \dot{\Phi}(x,0) = 0, \ \text{for all} \ x \in V, t = 0. \end{array} \right\}$$ (46)

We derive the dynamic reciprocity relationship for a generalised piezothermoelastic bounded body V with two- temperature, which satisfies equations (1)-(8), the boundary conditions (45) and the homogeneous initial conditions (46), and are subjected to the action of body forces $F_i(x,t)$, surface traction $h_i(x,t)$, the heat flux $q(x,t)$, and the surface charge density $c_0(x,t)$. We define the Laplace transform as

$$\overline{f}(x,s) = L(f(x,t)) = \int_0^\infty f(x,t)e^{-st}\,dt. \tag{47}$$

Applying the Laplace transform defined by the equation (47) on the equations (1)-(8) and omitting the bars for simplicity, we obtain

$$\sigma_{ij} = c_{ijkl}\,\varepsilon_{kl} - e_{ijk}E_k - \alpha_{ij}T, \tag{48}$$

$$-q_{i,i} = \rho T_0 sS, \tag{49}$$

$$\rho S = \alpha_{ij}\varepsilon_{ij} + \tau_i E_i + rT, \tag{50}$$

$$\sigma_{ij,j} + \rho F_i = \rho s^2 u_i, \tag{51}$$

$$-K_{ij}\,\varphi_{,j} = (1 + \tau_q s^\alpha)\,q_i, \tag{52}$$

$$D_{i,i} = 0, \tag{53}$$

$$D_i = \xi_{ij}E_j + e_{ijk}\varepsilon_{jk} + \tau_i T, \tag{54}$$

$$E_i = -\Phi_{,i}, (i,j,k,l = 1,2,3). \tag{55}$$

We now consider two problems where applied body forces, surface temperature, and the electric potential are specified differently. Let the variables involved in these two problems be distinguished by superscripts in parentheses. Thus, we have $u_i^{(1)}, \varepsilon_{ij}^{(1)}, \sigma_{ij}^{(1)}, \varphi^{(1)}, \Phi^{(1)}$ for the first problem and $u_i^{(2)}, \varepsilon_{ij}^{(2)}, \sigma_{ij}^{(2)}, \varphi^{(2)}, \Phi^{(2)}$ for the second problem. Each set of variables satisfies the equations (48) - (55). Using the assumption $\sigma_{ij} = \sigma_{ji}$, we obtain

$$\int_V \sigma_{ij}^{(1)}\varepsilon_{ij}^{(2)}\,dV = \int_V \sigma_{ij}^{(1)}u_{i,j}^{(2)}\,dV = \int_V \left(\sigma_{ij}^{(1)}u_i^{(2)}\right)_{,j}\,dV - \int_V \sigma_{ij,j}^{(1)}u_i^{(2)}\,dV. \tag{56}$$

Using the divergence theorem in the first term of the right hand side of equation (56) yields

$$\int_V \sigma_{ij}^{(1)}\varepsilon_{ij}^{(2)}\,dV = \int_A \sigma_{ij}^{(1)}u_i^{(2)}n_j\,dA - \int_V \sigma_{ij,j}^{(1)}u_i^{(2)}\,dV. \tag{57}$$

Equation (57) with the aid of equations (44) and (51) gives

$$\int_V \sigma_{ij}^{(1)}\varepsilon_{ij}^{(2)}\,dV = \int_A h_i^{(1)}u_i^{(2)}\,dA - \rho\int_V s^2 u_i^{(1)}u_i^{(2)}\,dV + \rho\int_V F_i^{(1)}u_i^{(2)}\,dV. \tag{58}$$

A similar expression is obtained for the integral $\int_V \sigma_{ij}^{(2)}\varepsilon_{ij}^{(1)}\,dV$, from which together with the equation (58), it follows that

$$\int_V (\sigma_{ij}^{(1)}\varepsilon_{ij}^{(2)} - \sigma_{ij}^{(2)}\varepsilon_{ij}^{(1)})\,dV = \int_A (h_i^{(1)}u_i^{(2)} - h_i^{(2)}u_i^{(1)})\,dA + \rho\int_V (F_i^{(1)}u_i^{(2)} - F_i^{(2)}u_i^{(1)})\,dV. \tag{59}$$

Now multiplying equation (48) by $\varepsilon_{ij}^{(2)}$ and $\varepsilon_{ij}^{(1)}$ for the first and second problems respectively, subtracting and integrating over the region V, we obtain

$$\int_V (\sigma_{ij}^{(1)}\varepsilon_{ij}^{(2)} - \sigma_{ij}^{(2)}\varepsilon_{ij}^{(1)})\,dV = \int_V c_{ijkl}(\varepsilon_{kl}^{(1)}\varepsilon_{ij}^{(2)} - \varepsilon_{kl}^{(2)}\varepsilon_{ij}^{(1)})\,dV - \int_V e_{ijk}(\Phi_{,k}^{(2)}\varepsilon_{ij}^{(1)} - \Phi_{,k}^{(1)}\varepsilon_{ij}^{(2)})\,dV$$

$$- \int_V \alpha_{ij}(\varphi^{(1)}\varepsilon_{ij}^{(2)} - \varphi^{(2)}\varepsilon_{ij}^{(1)})\,dV + \int_V a_{ij}\alpha_{ij}(\varphi_{,ij}^{(1)}\varepsilon_{ij}^{(2)} - \varphi_{,ij}^{(2)}\varepsilon_{ij}^{(1)})\,dV.$$

Using the symmetry properties of c_{ijkl}, we obtain

$$\int_V (\sigma_{ij}^{(1)}\varepsilon_{ij}^{(2)} - \sigma_{ij}^{(2)}\varepsilon_{ij}^{(1)})\,dV = -\int_V e_{ijk}(\Phi_{,k}^{(2)}\varepsilon_{ij}^{(1)} - \Phi_{,k}^{(1)}\varepsilon_{ij}^{(2)})\,dV - \int_V \alpha_{ij}(\varphi^{(1)}\varepsilon_{ij}^{(2)} - \varphi^{(2)}\varepsilon_{ij}^{(1)})\,dV$$

$$+ \int_V a_{ij}\alpha_{ij}(\varphi_{,ij}^{(1)}\varepsilon_{ij}^{(2)} - \varphi_{,ij}^{(2)}\varepsilon_{ij}^{(1)})\,dV. \tag{60}$$

Equating equations (59) and (60), we get the first part of the reciprocity theorem

$$\int_A (h_i^{(1)} u_i^{(2)} - h_i^{(2)} u_i^{(1)}) dA + \rho \int_V (F_i^{(1)} u_i^{(2)} - F_i^{(2)} u_i^{(1)}) dV = -\int_V e_{ijk} (\Phi_{,k}^{(2)} \varepsilon_{ij}^{(1)} - \Phi_{,k}^{(1)} \varepsilon_{ij}^{(2)}) dV$$

$$-\int_V \alpha_{ij} (\varphi^{(1)} \varepsilon_{ij}^{(2)} - \varphi^{(2)} \varepsilon_{ij}^{(1)}) dV + \int_V a_{ij} \alpha_{ij} (\varphi_{,ij}^{(1)} \varepsilon_{ij}^{(2)} - \varphi_{,ij}^{(2)} \varepsilon_{ij}^{(1)}) dV. \tag{61}$$

This contains the mechanical causes of motion F_i and h_i.

Now, taking the divergence of both sides of equation (52) and using equations (49), (50), we arrive at the equation of heat conduction, namely

$$\frac{\partial}{\partial x_i} (K_{ij} \varphi_{,j}) = (s + \tau_q s^{\alpha+1}) T_0 (\alpha_{ij} \varepsilon_{ij} + \tau_i E_i + rT). \tag{62}$$

To derive the second part, multiplying equation (62) by $\varphi^{(2)}$ and $\varphi^{(1)}$ for the first and the second problems respectively, subtracting and integrating over V, we get

$$\int_V \left((K_{ij} \varphi_{,j}^{(1)})_{,i} \varphi^{(2)} - (K_{ij} \varphi_{,j}^{(2)})_{,i} \varphi^{(1)} \right) dV = \Omega_1 T_0 \int_V \alpha_{ij} \left(\varepsilon_{ij}^{(1)} \varphi^{(2)} - \varepsilon_{ij}^{(2)} \varphi^{(1)} \right) dV$$

$$-\Omega_1 T_0 \int_V \alpha_{ij} a_{ij} \left(\varepsilon_{ij}^{(1)} \varphi_{,ij}^{(2)} - \varepsilon_{ij}^{(2)} \varphi_{,ij}^{(1)} \right) dV + \Omega_1 T_0 \int_V \tau_i \left(E_i^{(1)} \varphi^{(2)} - E_i^{(2)} \varphi^{(1)} \right) dV$$

$$-\Omega_1 T_0 \int_V ra_{ij} \left(E_i^{(1)} \varphi_{,ij}^{(2)} - E_i^{(2)} \varphi_{,ij}^{(1)} \right) dV, \tag{63}$$

where, $\Omega_1 = s + \tau_q s^{\alpha+1}$. Now,

$$(K_{ij} \varphi_{,j}^{(1)})_{,i} \varphi^{(2)} = (K_{ij} \varphi_{,j}^{(1)} \varphi^{(2)})_{,i} - K_{ij} \varphi_{,j}^{(1)} \varphi_{,i}^{(2)} \text{ and}$$

$$(K_{ij} \varphi_{,j}^{(2)})_{,i} \varphi^{(1)} = (K_{ij} \varphi_{,j}^{(2)} \varphi^{(1)})_{,i} - K_{ij} \varphi_{,j}^{(2)} \varphi_{,i}^{(1)}. \tag{64}$$

Equation (63) with the help of equations (44), (45), (64) and the divergence theorem can be written as

$$\int_A \Omega_1 \left(q^{(1)} \varphi^{(2)} - q^{(2)} \varphi^{(1)} \right) dA = -\Omega_1 T_0 \int_V \alpha_{ij} \left(\varepsilon_{ij}^{(1)} \varphi^{(2)} - \varepsilon_{ij}^{(2)} \varphi^{(1)} \right) dV$$

$$+\Omega_1 T_0 \int_V \alpha_{ij} a_{ij} \left(\varepsilon_{ij}^{(1)} \varphi_{,ij}^{(2)} - \varepsilon_{ij}^{(2)} \varphi_{,ij}^{(1)} \right) dV + \Omega_1 T_0 \int_V \tau_i \left(\Phi_{,i}^{(1)} \varphi^{(2)} - \Phi_{,i}^{(2)} \varphi^{(1)} \right) dV$$

$$-\Omega_1 T_0 \int_V ra_{ij} \left(\Phi_{,i}^{(1)} \varphi_{,ij}^{(2)} - \Phi_{,i}^{(2)} \varphi_{,ij}^{(1)} \right) dV. \tag{65}$$

This constitutes the second part of the reciprocity theorem which contains the thermal causes of motion φ_1 and q. To derive the third part, multiplying equation (54) by $E_i^{(2)}$ and $E_i^{(1)}$ for the first and the second problems respectively, subtracting and integrating over V, we get

$$\int_V \left(D_i^{(1)} E_i^{(2)} - D_i^{(2)} E_i^{(1)} \right) dV = \int_V \xi_{ij} (E_j^{(1)} E_i^{(2)} - E_j^{(2)} E_i^{(1)}) dV + \int_V e_{ijk} (\varepsilon_{jk}^{(1)} E_i^{(2)} - \varepsilon_{jk}^{(2)} E_i^{(1)}) dV +$$

$$\int_V \tau_i (\varphi^{(1)} E_i^{(2)} - \varphi^{(2)} E_i^{(1)}) dV - \int_V \tau_i a_{ij} (\varphi_{,ij}^{(1)} E_i^{(2)} - \varphi_{,ij}^{(2)} E_i^{(1)}) dV.$$

Since $\xi_{ij} = \xi_{ji}$, therefore, we have

$$\int_V \left(D_i^{(1)} E_i^{(2)} - D_i^{(2)} E_i^{(1)} \right) dV = \int_V e_{ijk} (\varepsilon_{jk}^{(1)} E_i^{(2)} - \varepsilon_{jk}^{(2)} E_i^{(1)}) dV + \int_V \tau_i (\varphi^{(1)} E_i^{(2)} - \varphi^{(2)} E_i^{(1)}) dV$$

$$-\int_V \tau_i a_{ij} (\varphi_{,ij}^{(1)} E_i^{(2)} - \varphi_{,ij}^{(2)} E_i^{(1)}) dV. \tag{66}$$

Equation (66) with the aid of equation (55) yields

$$\int_V \left(D_i^{(1)} E_i^{(2)} - D_i^{(2)} E_i^{(1)} \right) dV = -\int_V e_{ijk} (\varepsilon_{jk}^{(1)} \Phi_{,i}^{(2)} - \varepsilon_{jk}^{(2)} \Phi_{,i}^{(1)}) dV - \int_V \tau_i (\varphi^{(1)} \Phi_{,i}^{(2)} - \varphi^{(2)} \Phi_{,i}^{(1)}) dV$$

$$+ \int_V \tau_i a_{ij} (\varphi_{,ij}^{(1)} \Phi_{,i}^{(2)} - \varphi_{,ij}^{(2)} \Phi_{,i}^{(1)}) dV. \tag{67}$$

Also, using (55) with equation (67), we have

$$\int_V \left(D_i^{(1)} E_i^{(2)} - D_i^{(2)} E_i^{(1)} \right) dV = \int_V \left(D_i^{(2)} \Phi_{,i}^{(1)} - D_i^{(1)} \Phi_{,i}^{(2)} \right) dV. \tag{68}$$

Now,

$$\left. \begin{aligned} D_i^{(2)} \Phi_{,i}^{(1)} &= \left(D_i^{(2)} \Phi^{(1)} \right)_{,i} - D_{i,i}^{(2)} \Phi^{(1)}, \\ D_i^{(1)} \Phi_{,i}^{(2)} &= \left(D_i^{(1)} \Phi^{(2)} \right)_{,i} - D_{i,i}^{(1)} \Phi^{(2)}. \end{aligned} \right\} \tag{69}$$

Using equation (69), (54) and divergence theorem in equation (68), we obtain

$$\int_V \left(D_i^{(1)} E_i^{(2)} - D_i^{(2)} E_i^{(1)} \right) dV = \int_V \left(\left(D_i^{(2)} \Phi^{(1)} \right)_{,i} - \left(D_i^{(1)} \Phi^{(2)} \right)_{,i} \right) dV + \int_V \left(D_{i,i}^{(1)} \Phi^{(2)} - D_{i,i}^{(2)} \Phi^{(1)} \right) dV$$

$$= \int_A \left(\left(D_i^{(2)} \Phi^{(1)} n_i \right) - \left(D_i^{(1)} \Phi^{(2)} n_i \right) \right) dA. \tag{70}$$

With the aid of equation (44), we obtain

$$\int_V \left(D_i^{(1)} E_i^{(2)} - D_i^{(2)} E_i^{(1)} \right) dV = \int_A \left(\left(c_0^{(2)} \Phi^{(1)} \right) - \left(c_0^{(1)} \Phi^{(2)} \right) \right) dA. \tag{71}$$

From equations (67) and (71), we have

$$\int_A \left(\left(c_0^{(1)} \Phi^{(2)} \right) - \left(c_0^{(2)} \Phi^{(1)} \right) \right) dA = \int_V e_{ijk} (\varepsilon_{jk}^{(1)} \Phi_{,i}^{(2)} - \varepsilon_{jk}^{(2)} \Phi_{,i}^{(1)}) dV + \int_V \tau_i (\varphi^{(1)} \Phi_{,i}^{(2)} - \varphi^{(2)} \Phi_{,i}^{(1)}) dV$$

$$- \int_V \tau_i a_{ij} (\varphi_{,ij}^{(1)} \Phi_{,i}^{(2)} - \varphi_{,ij}^{(2)} \Phi_{,i}^{(1)}) dV. \tag{72}$$

This constitutes the third part of the reciprocity theorem which contains the electric potential Φ and surface charge density c_0. Combining equations (61), (65), and (72) we obtain

$$\Omega_1 T_0 \left[\int_A (h_i^{(1)} u_i^{(2)} - h_i^{(2)} u_i^{(1)}) dA + \rho \int_V (F_i^{(1)} u_i^{(2)} - F_i^{(2)} u_i^{(1)}) dV + \int_A \left(c_0^{(1)} \Phi^{(2)} - c_0^{(2)} \Phi^{(1)} \right) dA \right.$$

$$\left. + \int_V (\tau_i - r) a_{ij} (\varphi_{,ij}^{(1)} \Phi_{,i}^{(2)} - \varphi_{,ij}^{(1)} \Phi_{,i}^{(2)}) dV \right] + \int_A \Omega_1 \left(q^{(1)} \varphi_1^{(2)} - q^{(2)} \varphi_1^{(1)} \right) dA = 0. \tag{73}$$

This is the general reciprocity theorem in the Laplace transform domain. For applying inverse Laplace transform on the equations (61), (65), (72), and (73), we shall use the convolution theorem

$$L^{-1}(F(s)G(s)) = \int_0^t f(t - \zeta) g(\zeta) d\zeta = \int_0^t g(t - \zeta) f(\zeta) d\zeta, \tag{74}$$

and the symbolic notation

$$\wedge(f) = 1 + \tau_q \frac{\partial^\alpha f(x, \zeta)}{\partial \zeta^\alpha}. \tag{75}$$

Equations (61), (65), (72) and (73) with the aid of equation (75) yield the first, second, third, and fourth parts of the reciprocity theorem in the final form

$$\int_A \int_0^t (h_i^{(1)}(x,t-\zeta)\mathrm{u}_i^{(2)}(x,\zeta)d\zeta\,dA + \rho\int_V \int_0^t (F_i^{(1)}(x,t-\zeta)\mathrm{u}_i^{(2)}(x,\zeta)d\zeta\,dV$$

$$-\int_V \int_0^t e_{ijk}(\Phi_{,k}^{(1)}(x,t-\zeta)\varepsilon_{ij}^{(2)}(x,\zeta))d\zeta\,dV - \int_V \alpha_{ij}\varphi^{(1)}(x,t-\zeta)\varepsilon_{ij}^{(2)}(x,\zeta)dV$$

$$+\int_V a_{ij}\alpha_{ij}\varphi_{,ij}^{(1)}(x,t-\zeta)\varepsilon_{ij}^{(2)}(x,\zeta)dV = S_{21}^{12}, \tag{76}$$

$$\int_A \int_0^t \left(q^{(1)}(x,t-\zeta)\frac{\partial \wedge \varphi^{(2)}(x,\zeta)}{\partial\zeta} \right)d\zeta\,dA + T_0\int_V \int_0^t \alpha_{ij}\left(\varepsilon_{ij}^{(1)}(x,t-\zeta)\frac{\partial \wedge (\varphi^{(2)}(x,\zeta))}{\partial\zeta} \right)d\zeta\,dV$$

$$-T_0\int_V \int_0^t \alpha_{ij}a_{ij}\left(\varepsilon_{ij}^{(1)}(x,t-\zeta)\frac{\partial \wedge (\varphi_{,ij}^{(2)}(x,\zeta))}{\partial\zeta} \right)d\zeta\,dV - T_0\int_V \int_0^t \tau_i\left(\Phi_{,i}^{(1)}(x,t-\zeta)\frac{\partial \wedge (\varphi^{(2)}(x,\zeta))}{\partial\zeta} \right)d\zeta\,dV$$

$$+T_0\int_V \int_0^t \tau_i a_{ij}\left(\Phi_{,i}^{(1)}(x,t-\zeta)\frac{\partial \wedge (\varphi_{,ij}^{(2)}(x,\zeta))}{\partial\zeta} \right)d\zeta\,dV = S_{21}^{12}, \tag{77}$$

and,

$$\int_A \int_0^t c_0^{(1)}(x,t-\zeta)\Phi^{(2)}(x,\zeta)\,d\zeta\,dA + \int_V \int_0^t e_{ijk}\Phi_{,i}^{(1)}(x,t-\zeta)\varepsilon_{jk}^{(2)}(x,\zeta)d\zeta\,dV$$

$$+\int_V \int_0^t \tau_i \Phi_{,i}^{(1)}(x,t-\zeta)\varphi^{(2)}(x,\zeta)d\zeta\,dV + \int_V \int_0^t \tau_i a_{ij}\Phi_{,i}^{(1)}(x,t-\zeta)\varphi_{,ij}^{(2)}(x,\zeta)d\zeta\,dV = S_{21}^{12}. \tag{78}$$

Here, S_{21}^{12} indicates the same expression as on the left-hand side except that the superscripts (1) and (2) are interchanged. Finally, equation (73) with the aid of equation (74) gives the general reciprocity theorem in the final form

$$\int_A \int_0^t h_i^{(1)}(x,t-\zeta)\frac{\partial \wedge (\mathrm{u}_i^{(2)}(x,\zeta))}{\partial\zeta}d\zeta\,dA + \rho\int_V \int_0^t F_i^{(1)}(x,t-\zeta)\frac{\partial \wedge (\mathrm{u}_i^{(2)}(x,\zeta))}{\partial\zeta}d\zeta\,dV$$

$$+\int_A \int_0^t c_0^{(1)}(x,t-\zeta)\frac{\partial \wedge (\Phi^{(2)}(x,\zeta))}{\partial\zeta}d\zeta\,dA + \int_V \int_0^t (\tau_i - r)a_{ij}\varphi_{,ij}^{(1)}(x,t-\zeta)\frac{\partial \wedge (\Phi_{,i}^{(2)}(x,\zeta))}{\partial\zeta}d\zeta\,dV$$

$$+\frac{1}{T_0}\int_A \int_0^t \left(q^{(1)}(x,t-\zeta)\frac{\partial \wedge \varphi^{(2)}(x,\zeta)}{\partial\zeta} \right)d\zeta\,dA = S_{21}^{12}. \tag{79}$$

Special Cases. If we restrict our work to the following sub-cases with two-temperature, the constitutive relations change according to the following independent constants. The variational principle, uniqueness, and reciprocity theorems can be established by following similar steps.

Case 1: Monoclinic medium

$$\sigma_{11} = c_{11}u_{1,1} + c_{12}u_{2,2} + c_{13}u_{3,3} + c_{14}(u_{2,3} + u_{3,2}) + e_{11}\Phi_{,1} - \alpha_{11}T,$$

$$\sigma_{22} = c_{12}u_{1,1} + c_{22}u_{2,2} + c_{23}u_{3,3} + c_{24}(u_{2,3} + u_{3,2}) + e_{12}\Phi_{,1} - \alpha_{22}T,$$

$$\sigma_{33} = c_{13}u_{1,1} + c_{23}u_{2,2} + c_{33}u_{3,3} + c_{34}(u_{2,3} + u_{3,2}) + e_{13}\Phi_{,1} - \alpha_{33}T,$$

$$\sigma_{23} = c_{41}u_{1,1} + c_{42}u_{2,2} + c_{43}u_{3,3} + c_{44}(u_{2,3} + u_{3,2}) + e_{14}\Phi_{,1},$$

$$\sigma_{13} = c_{55}(u_{1,3} + u_{3,1}) + e_{25}\Phi_{,2} + e_{35}\Phi_{,3},$$

$$\sigma_{12} = c_{66}(u_{1,2} + u_{2,1}) + e_{26}\Phi_{,2} + e_{36}\Phi_{,3},$$

$$D_1 = e_{11}u_{1,1} + e_{12}u_{2,2} + e_{13}u_{3,3} + e_{14}(u_{2,3} + u_{3,2}) - \xi_{11}\Phi_{,1} + \tau_1 T, \qquad (80)$$

$$D_2 = e_{25}(u_{1,3} + u_{3,1}) + e_{26}(u_{1,2} + u_{2,1}) - \xi_{22}\Phi_{,2} - \xi_{23}\Phi_{,3} + \tau_2 T,$$

$$D_3 = e_{35}(u_{1,3} + u_{3,1}) + e_{36}(u_{1,2} + u_{2,1}) - \xi_{23}\Phi_{,2} - \xi_{33}\Phi_{,3} + \tau_3 T,$$

Case 2: Orthotropic medium

$$\sigma_{11} = c_{11}u_{1,1} + c_{12}u_{2,2} + c_{13}u_{3,3} + e_{31}\Phi_{,3} - \alpha_{11}T,$$

$$\sigma_{22} = c_{12}u_{1,1} + c_{22}u_{2,2} + c_{23}u_{3,3} + e_{32}\Phi_{,3} - \alpha_{22}T,$$

$$\sigma_{33} = c_{13}u_{1,1} + c_{23}u_{2,2} + c_{33}u_{3,3} + e_{33}\Phi_{,3} - \alpha_{33}T,$$

$$\sigma_{23} = c_{44}(u_{2,3} + u_{3,2}) + e_{24}\Phi_{,2},$$

$$\sigma_{13} = c_{55}(u_{1,3} + u_{3,1}) + e_{15}\Phi_{,1}, \qquad (81)$$

$$\sigma_{12} = c_{66}(u_{1,2} + u_{2,1}),$$

$$D_1 = -\xi_{11}\Phi_{,1} + e_{15}(u_{1,3} + u_{3,1}),$$

$$D_2 = -\xi_{22}\Phi_{,2} + e_{24}(u_{2,3} + u_{3,2}),$$

$$D_3 = -\xi_{33}\Phi_{,3} + e_{31}u_{1,1} + e_{32}u_{2,2} + e_{33}u_{3,3} + \tau_3 T,$$

Case 3: Transversely Isotropic medium

$$\sigma_{11} = c_{11}u_{1,1} + c_{12}u_{2,2} + c_{13}u_{3,3} + e_{13}\Phi_{,3} - \alpha_{11}T,$$

$$\sigma_{22} = c_{12}u_{1,1} + c_{11}u_{2,2} + c_{13}u_{3,3} + e_{13}\Phi_{,3} - \alpha_{11}T,$$

$$\sigma_{33} = c_{13}u_{1,1} + c_{13}u_{2,2} + c_{33}u_{3,3} + e_{33}\Phi_{,3} - \alpha_{33}T,$$

$$\sigma_{23} = c_{44}(u_{2,3} + u_{3,2}) + e_{15}\Phi_{,2},$$

$$\sigma_{13} = c_{44}(u_{1,3} + u_{3,1}) + e_{15}\Phi_{,1}, \qquad (82)$$

$$\sigma_{12} = c_{66}(u_{1,2} + u_{2,1}),$$

$$D_1 = e_{15}(u_{1,3} + u_{3,1}) - \xi_{11}\Phi_{,1},$$

$$D_2 = e_{15}(u_{1,2} + u_{2,1}) - \xi_{11}\Phi_{,2},$$

$$D_3 = e_{13}u_{1,1} + e_{13}u_{2,2} + e_{33}u_{3,3} - \xi_{33}\Phi_{,3} + \tau_3 T,$$

5. Plane wave propagation

Formulation and solution of the problem. Substituting the constitutive relations (81) (Following Tzou and Bao [31]) into the field equations (6)-(8) without body forces, heat sources, yield

$$c_{11}u_{1,11} + c_{12}u_{2,21} + c_{13}u_{3,13} + e_{31}\Phi_{,31} + c_{66}(u_{1,22} + u_{2,12}) + c_{55}(u_{1,33} + u_{3,13}) - \alpha_{11}(\varphi - a_{11}\varphi_{,11} - a_{22}\varphi_{,22} - a_{33}\varphi_{,33})_{,1}$$

$$+ e_{15}\Phi_{,13} - \rho\ddot{u}_1 = 0, \qquad (83a)$$

$$c_{66}(u_{1,21} + u_{2,11}) + c_{12}u_{1,12} + c_{22}u_{2,22} + c_{23}u_{3,32} + e_{32}\Phi_{,32} - \alpha_{22}(\varphi - a_{11}\varphi_{,11} - a_{22}\varphi_{,22} - a_{33}\varphi_{,33})_{,2} + c_{44}(u_{2,33} + u_{3,23})$$

$$+e_{24}\Phi_{,23}-\rho\,\ddot{u}_2=0,\tag{83b}$$

$$c_{55}(u_{1,31}+u_{3,11})+c_{44}(u_{2,32}+u_{3,22})+c_{13}\,u_{1,13}+c_{23}\,u_{2,23}+c_{33}\,u_{3,33}-\alpha_{33}(\varphi-a_{11}\varphi_{,11}-a_{22}\varphi_{,22}-a_{33}\varphi_{,33})_{,3}$$

$$+e_{15}\Phi_{,11}+e_{24}\Phi_{,22}+e_{33}\Phi_{,33}-\rho\,\ddot{u}_3=0,\tag{83c}$$

$$-\xi_{11}\Phi_{,11}+e_{15}(u_{1,31}+u_{3,11})-\xi_{22}\Phi_{,22}+e_{24}(u_{2,32}+u_{3,22})-\xi_{33}\Phi_{,33}+e_{31}\,u_{1,31}+e_{32}\,u_{2,23}+e_{33}\,u_{3,33}$$

$$+\tau_3(\varphi-a_{11}\varphi_{,11}-a_{22}\varphi_{,22}-a_{33}\varphi_{,33})_{,3}=0,\tag{83d}$$

$$(K_{11}\varphi_{,11}+K_{22}\varphi_{,22}+K_{33}\varphi_{,33})-\left(1+\tau_q\frac{\partial^\alpha}{\partial t^\alpha}\right)T_0(\alpha_{11}\,\dot{u}_{1,1}+\alpha_{22}\,\dot{u}_{2,2}+\alpha_{33}\,\dot{u}_{3,3}-\tau_3\dot{\Phi}_{,3}+r(\dot{\varphi}-a_{11}\dot{\varphi}_{,11}-a_{22}\dot{\varphi}_{,22}$$

$$-a_{33}\dot{\varphi}_{,33}))=0.\tag{83e}$$

To facilitate a solution, we introduce the following dimensionless quantities

$$\left(x_i{}',u_i{}'\right)=\frac{\omega_1}{c_1}\left(x_i,u_i\right),\ \left(t',\tau_q{}'\right)=\omega_1\left(t,\tau_q\right),\ (T',\varphi')=\frac{\alpha_{11}}{\rho c_1^2}(T,\varphi),\ \ \Phi'=\frac{\omega_1 e_{31}\Phi}{c_1\alpha_{11}T_0},\ a_{ij}{}'=\frac{\omega_1^2}{c_1^2}a_{ij},$$

where $c_1=\sqrt{\dfrac{c_{11}}{\rho}}$ and $\omega_1=\dfrac{\rho c_e c_1^2}{K_{11}}$, $i=1,2,3$.

Incorporating these dimensionless quantities, the system of equations (83), after removal of prime (') , reduces to the following form

$$c_{11}\,u_{1,11}+(c_{12}+c_{66})u_{2,12}+(c_{13}+c_{55})u_{3,13}+c_{66}\,u_{1,22}+c_{55}\,u_{1,33}+\frac{\alpha_{11}T_0}{e_{31}}(e_{31}+e_{15})\Phi_{,13}-\rho c_1^2(\varphi-a_{11}\varphi_{,11}$$

$$-a_{22}\varphi_{,22}-a_{33}\varphi_{,33})_{,1}-\rho c_1^2\,\ddot{u}_1=0,\tag{84a}$$

$$(c_{66}+c_{12})u_{1,12}+c_{66}\,u_{2,11}+c_{22}\,u_{2,22}+(c_{23}+c_{44})u_{3,23}+c_{44}\,u_{2,33}+\frac{\alpha_{11}T_0}{e_{31}}(e_{32}+e_{24})\Phi_{,32}-\rho c_1^2\frac{\alpha_{22}}{\alpha_{11}}(\varphi-a_{11}\varphi_{,11}$$

$$-a_{22}\varphi_{,22}-a_{33}\varphi_{,33})_{,2}-\rho c_1^2\,\ddot{u}_2=0,\tag{84b}$$

$$(c_{55}+c_{13})u_{1,31}+c_{55}\,u_{3,11}+(c_{44}+c_{23})u_{2,23}+c_{44}\,u_{3,22}+c_{33}\,u_{3,33}-\rho c_1^2\frac{\alpha_{33}}{\alpha_{11}}(\varphi-a_{11}\varphi_{,11}-a_{22}\varphi_{,22}-a_{33}\varphi_{,33})_{,3}$$

$$+\frac{\alpha_{11}T_0}{e_{31}}(e_{15}\Phi_{,11}+e_{24}\Phi_{,22}+e_{33}\Phi_{,33})-\rho c_1^2\,\ddot{u}_3=0,\tag{84c}$$

$$-\frac{\alpha_{11}T_0}{e_{31}}(\xi_{11}\Phi_{,11}+\xi_{22}\Phi_{,22}+\xi_{33}\Phi_{,33})+e_{15}(u_{1,31}+u_{3,11})+e_{24}(u_{2,32}+u_{3,22})+e_{31}\,u_{1,31}+e_{32}\,u_{2,23}+e_{33}\,u_{3,33}$$

$$+\tau_3\frac{\rho c_1^2}{\alpha_{11}}(\varphi-a_{11}\varphi_{,11}-a_{22}\varphi_{,22}-a_{33}\varphi_{,33})_{,3}=0,\tag{84d}$$

$$\frac{\rho\omega_1}{\alpha_{11}}(K_{11}\varphi_{,11}+K_{22}\varphi_{,22}+K_{33}\varphi_{,33})-\left(1+\tau_q\frac{\partial^\alpha}{\partial t^\alpha}\right)T_0(\alpha_{11}\,\dot{u}_{1,1}+\alpha_{22}\,\dot{u}_{2,2}+\alpha_{33}\,\dot{u}_{3,3}-\tau_3\dot{\Phi}_{,3}+r(\dot{\varphi}-a_{11}\dot{\varphi}_{,11}$$

$$-a_{22}\dot{\varphi}_{,22}-a_{33}\dot{\varphi}_{,33})))=0.\tag{84e}$$

For plane harmonic waves, we assume

$$\left(u_k,\Phi,\varphi\right)=\left(\bar{u}_k,\bar{\Phi},\bar{\varphi}\right)\exp\left[i\omega\left(\frac{n_k x_k}{v}-t\right)\right],k=1,2,3,\tag{85}$$

where, ω – circular frequency, v – phase velocity of the wave propagating along the direction vector n, $\bar{u}_1,\bar{u}_2,\bar{u}_3,\bar{\Phi}$ and $\bar{\varphi}$ – the undetermined amplitude vectors.

Upon using equation (85) in the set of equations (84), we obtain a system $PX=0$, where

$$P = \begin{bmatrix} t_{11}v^2 + x_{11} & x_{12} & x_{13} & x_{14} & t_{12}v^2 + m_{11} \\ x_{15} & t_{11}v^2 + x_{16} & x_{17} & x_{18} & t_{14}v^2 + m_{12} \\ x_{19} & x_{20} & t_{11}v^2 + x_{21} & x_{22} & t_{15}v^2 + m_{13} \\ x_{23} & x_{24} & x_{25} & x_{26} & t_{16}v^2 + m_{14} \\ x_{27}v & x_{28}v & x_{29}v & x_{30}v & t_{17}v^2 + m_{15} \end{bmatrix}$$

and $X = \begin{bmatrix} \bar{u}_1 & \bar{u}_2 & \bar{u}_3 & \bar{\Phi} & \bar{\varphi} \end{bmatrix}^{tr}$, "$tr$" represents the transpose of the matrix. The symbols used in the matrix P are mentioned in Appendix A. For this system to possess a non-trivial solution, the determinant of the matrix P vanishes which yields a characteristic equation in v^2. On Solving this characteristic equation, we obtain four roots of v^2, in which we are interested in those roots whose imaginary parts are positive. The complex phase velocities of the quasi-waves, given by $v_i, i = 1, 2, 3, 4$ will be varying with the direction of phase propagation. Corresponding to these roots, there exist four waves corresponding to descending order of their velocities, namely quasi longitudinal wave (qP), two quasi transverse waves (qS$_1$) and (qS$_2$), and quasi thermal wave (qT). The complex velocity of the quasi-waves, i.e. $v = v_R + iv_I$, defines the phase propagation velocity $V_i = \left(\dfrac{v_R^2 + v_I^2}{v_R} \right)_i$ and

attenuation quality factor $Q_i^{-1} = \dfrac{\text{Img}(1/v_i^2)}{\text{Re}(1/v_i^2)}$, $i = 1, 2, 3, 4$, for the corresponding waves.

Therefore, the four waves in such a medium are attenuating.

Special cases.
(a) For propagation of wave along the x$_1$ axis, $n = (1, 0, 0)$ Then,

$$t_{11} = -\omega \rho c_1^2, t_{12} = i\rho c_1^2, \ t_s = \frac{\alpha_{11}T_0\omega}{e_{31}}, t_{13} = \omega^2 a_{11}, t_{14} = 0, t_{15} = 0, t_{16} = 0, \tau_H = T_0(1 + (-i\omega)^\alpha \tau_q),$$

$$t_{17} = ir\tau_H \rho c_1^2, x_{11} = \omega c_{11}, x_{12} = x_{13} = x_{14} = x_{15} = 0, x_{16} = \omega c_{66}, x_{17} = x_{18} = x_{19} = x_{20} = 0,$$

$$x_{21} = \omega c_{55}, x_{22} = t_s e_{15}, x_{23} = x_{24} = 0, x_{25} = -\omega e_{15}, x_{26} = t_s \xi_{11}, x_{27} = -\tau_H \omega \alpha_{11}, x_{28} = x_{29} = x_{30} = 0,$$

$$x_{31} = -\frac{\rho \omega_1}{\alpha_{11}} \omega K_{11}, m_{11} = t_{12} t_{13}, m_{12} = 0, m_{13} = 0, m_{14} = 0, m_{15} = x_{31} + t_{17} t_{13}.$$

Substituting these expressions, we can solve the determinant i.e. det $(P) = 0$, and further, the obtained characteristic equation can be solved to find the characteristics of the waves. Similarly, if we consider wave propagating in x$_2$ axis then its direction is given by $n = (0, 1, 0)$ and for a wave propagating along x$_3$ axis then its direction is given by $n = (0, 0, 1)$. Further, we can solve the det $(P) = 0$ in order to find the characteristic equation and the characteristics of the waves. In these cases, the generated waves will not be known as quasi since the waves propagate along with the principal directions.

(b) Let's consider the plane wave propagation in x$_1$-x$_2$ plane i.e. $n = (\sin\theta, \cos\theta, 0)$ such that $n_1^2 + n_2^2 = 1$ and,

$$t_{11} = -\omega \rho c_1^2, t_{12} = i \sin\theta \rho c_1^2, \ t_s = \frac{\alpha_{11} T_0 \omega}{e_{31}}, t_{13} = \omega^2 (a_{11} \sin^2\theta + a_{22} \cos^2\theta), t_{14} = i \cos\theta \rho c_1^2 \frac{\alpha_{22}}{\alpha_{11}},$$

$$t_{15} = 0, t_{16} = 0, \tau_H = T_0 (1 + (-i\omega)^\alpha \tau_q), t_{17} = ir\tau_H \rho c_1^2, x_{11} = \omega(c_{11} \sin^2\theta + c_{66} \cos^2\theta),$$

$$x_{12} = \omega(c_{12} + c_{66})\sin\theta\cos\theta, x_{13} = 0, x_{14} = 0, x_{15} = x_{12}, x_{16} = \omega(c_{66} \sin^2\theta + c_{22} \cos^2\theta),$$

$$x_{17} = x_{18} = x_{19} = x_{20} = 0, x_{21} = \omega(c_{55} \sin^2\theta + c_{44} \cos^2\theta), x_{22} = t_s(e_{15} \sin^2\theta + e_{24} \cos^2\theta),$$

$$x_{23} = x_{24} = 0, x_{25} = -\omega(e_{15} \sin^2\theta + e_{24} \cos^2\theta), x_{26} = t_s(\xi_{11} \sin^2\theta + \xi_{22} \cos^2\theta),$$

$$x_{27} = -\tau_H \omega \alpha_{11} \sin\theta, x_{28} = -\tau_H \omega \alpha_{22} \cos\theta, x_{29} = x_{30} = 0, x_{31} = -\frac{\rho\omega_1}{\alpha_{11}} \omega(K_{11} \sin^2\theta +$$

$$K_{22} \cos^2\theta), m_{11} = t_{12} t_{13}, m_{12} = t_{14} t_{13}, m_{13} = 0, m_{14} = 0, m_{15} = x_{31} + t_{17} t_{13}.$$

Substituting these expressions in the matrix P and solving the det $(P) = 0$, we obtain the characteristic equation and further, the characteristics of the waves. Similarly, if we consider wave propagating in x_2- x_3 plane then its direction is given by $n = (0, \sin\theta, \cos\theta)$ and for a wave propagating in x_1- x_3 plane then its direction is given by $n = (\sin\theta, 0, \cos\theta)$. Further, we can solve the det $(P) = 0$ in order to find the characteristic equation and different characteristics of the waves like phase velocity, attenuation quality factor, specific heat loss, and penetration depth.

Numerical results and discussion. The characteristics of the plane wave propagating in the orthotropic piezothermoelastic medium with the consideration of two- temperature and fractional order derivative can be explained through numerical examples. Matlab 9.0 software is used to solve the different characteristics like phase velocity, attenuation quality factor, specific heat loss, and penetration depth. Also, the effect of two-temperature parameter on phase velocity and attenuation quality factor with respect to thermal relaxation time is computed. The numerical values of cadmium selenide (CdSe) have been taken. Elastic constants (in units of GPa) are $c_{11} = 74.1$, $c_{12} = 45.2$, $c_{13} = 39.3$, $c_{22} = 79.4$, $c_{23} = 42.6$, $c_{33} = 83.6$, $c_{44} = 13.2$, $c_{55} = 15.1$, $c_{66} = 14.7$. Thermoelastic coupling constants (in units of $10^5 NK^{-1}m^{-2}$) are given by $\alpha_{11} = 6.21$, $\alpha_{22} = 5.93$, $\alpha_{33} = 5.51$, electric permittivity constants $(10^{-11} C^2 N^{-1}m^{-2})$ are $\xi_{11} = 8.26, \xi_{22} = 8.71$, $\xi_{33} = 9.03$, thermal conductivity constants $(Wm^{-1}K^{-1})$ are $K_{11} = 9$, $K_{22} = 7$, $K_{33} = 8$. The pyroelectric constant is $\tau_3 = -2.6 \times 10^{-6} Cm^{-2}K^{-1}$, piezoelectric constants $(10^{-3} Cm^{-2})$ are $e_{15} = 3$, $e_{24} = 2$, $e_{31} = 35$, $e_{32} = 32$, $e_{33} = 34$, thermal constants are given by $a_{11} = 5 \times 10^{-5}$, $a_{22} = 3 \times 10^{-5}$, $a_{33} = 7 \times 10^{-5}$. Numerical values for the remaining constants are $\rho = 5500 Kgm^{-3}, T_0 = 300K$, $\tau_T = 10^{-8} s, C_e = 260 JKg^{-1}K^{-1}$, $\tau_q = 2 \times 10^{-8} s$, $\omega = 2\pi \times 10^{-6} Hz$. A unit vector $n = (\cos\phi_n \sin\theta_n, \sin\phi_n \sin\theta_n, \cos\theta_n)$, where θ denotes the polar angle with x_3-axis and ϕ is the azimuthal angle between x_1-axis and x_2-axis.represents the direction of propagation of the waves such that θ_n is varying from 0 to 200°. Using the above numerical values the variations of phase velocity and attenuation quality factor of four waves are displayed for the fixed different values of $\phi = 30°, 78°, 156°$, respectively but with the variation in the angle of incidence and fractional order parameter. These characteristics are compared for TT (Two-Temperature i.e. $a_{ij} \neq 0$) model and for WTT (Without Two-Temperature i.e. $a_{ij} = 0$) model.

The comparison of corresponding plots in these figures signifies the effectiveness of two-temperature and fractional order parameters with the change in direction as exhibited in graphs as follows.

(a)
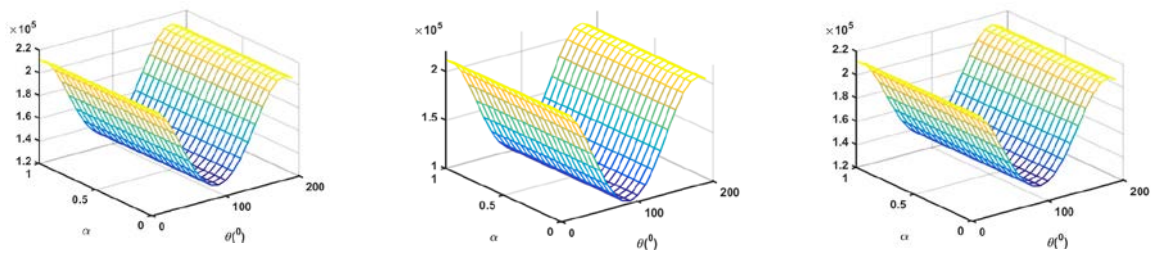
(b)
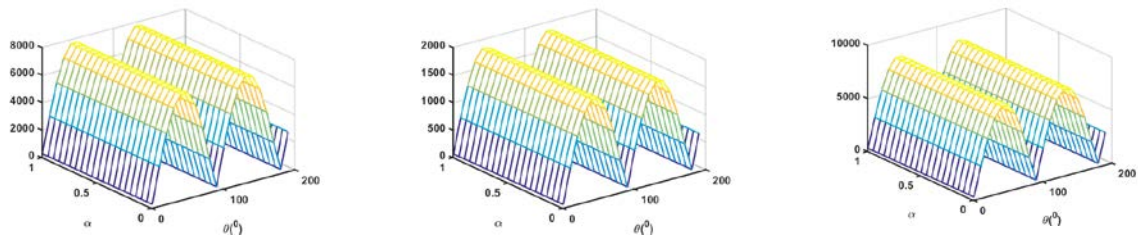
(c)
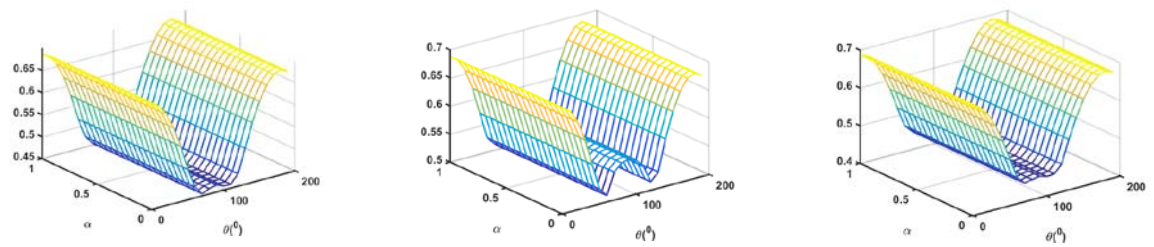
(d)
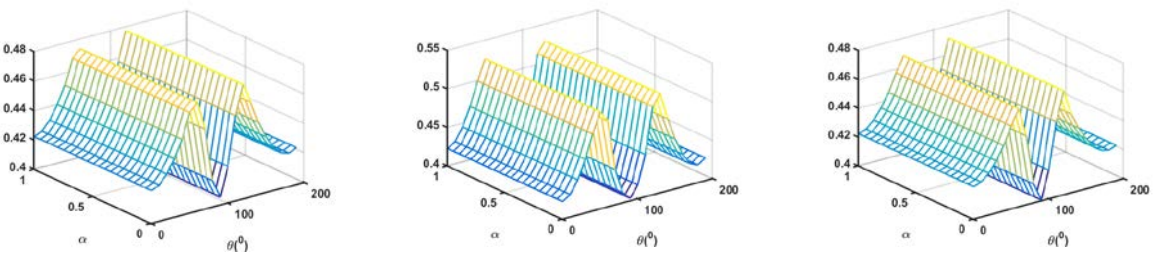
Fig. 1. Profile of (a) V_1 (b) V_2 (c) V_3 (d) V_4 w.r.t. α and θ for $\phi = 30^\circ, 78^\circ, 156^\circ$, respectively for TT model

(a)

(b)

(c)

(d)
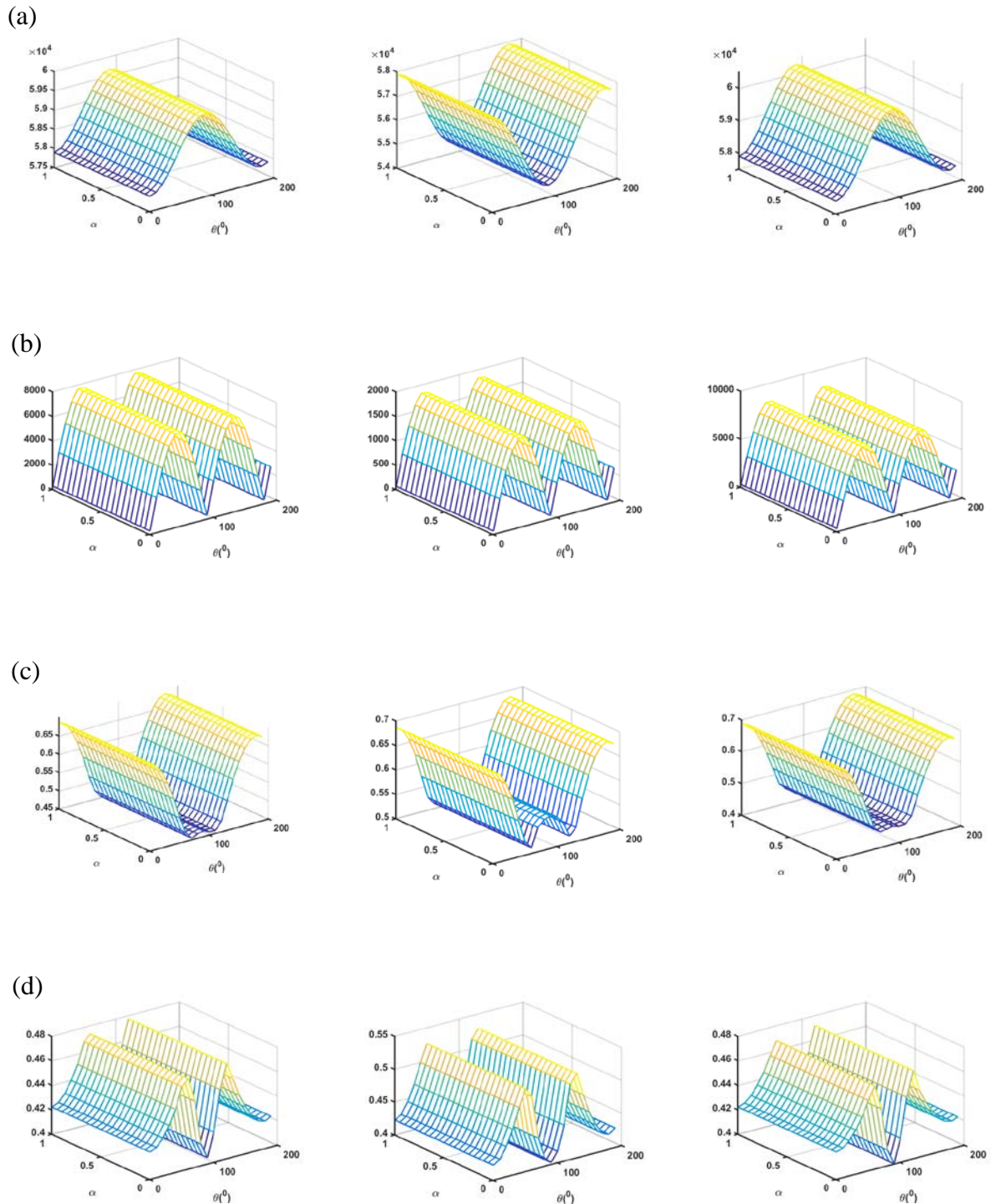
Fig. 2. Profile of (a) V_1 (b) V_2 (c) V_3 (d) V_4 w.r.t. α and θ for $\phi = 30º, 78º, 156º$, respectively for WTT model

Comparing Figures 1 and 2, it is clear that for the different values of ϕ, the phase velocity of qP wave (V_1) depict the significant impact of factional order parameter and two-temperature parameters as the angle of incidence varies. It possesses the highest value which is near to 2.2×10^5 for $\phi = 78°$ and at $\theta = 0, 200°$. For $\phi = 30°, 156°$ and for WTT, V_1 increases when $\theta \leq 100°$ and decreases as θ exceeds $100°$. For the different values of α, the

phase velocities $V_i (i = 2,3,4)$ of other waves depict the similar behaviour for both models with a slight difference in numerical values as ϕ and θ vary. It is noticed that the phase velocities of the waves for both TT and WTT models exhibit an abrupt change in trend at $\theta = 100°$. The variations of phase velocity of the respective waves clearly signify the impact of ϕ, θ, α and a_{ij}.

(a)

(b)

(c)

(d)
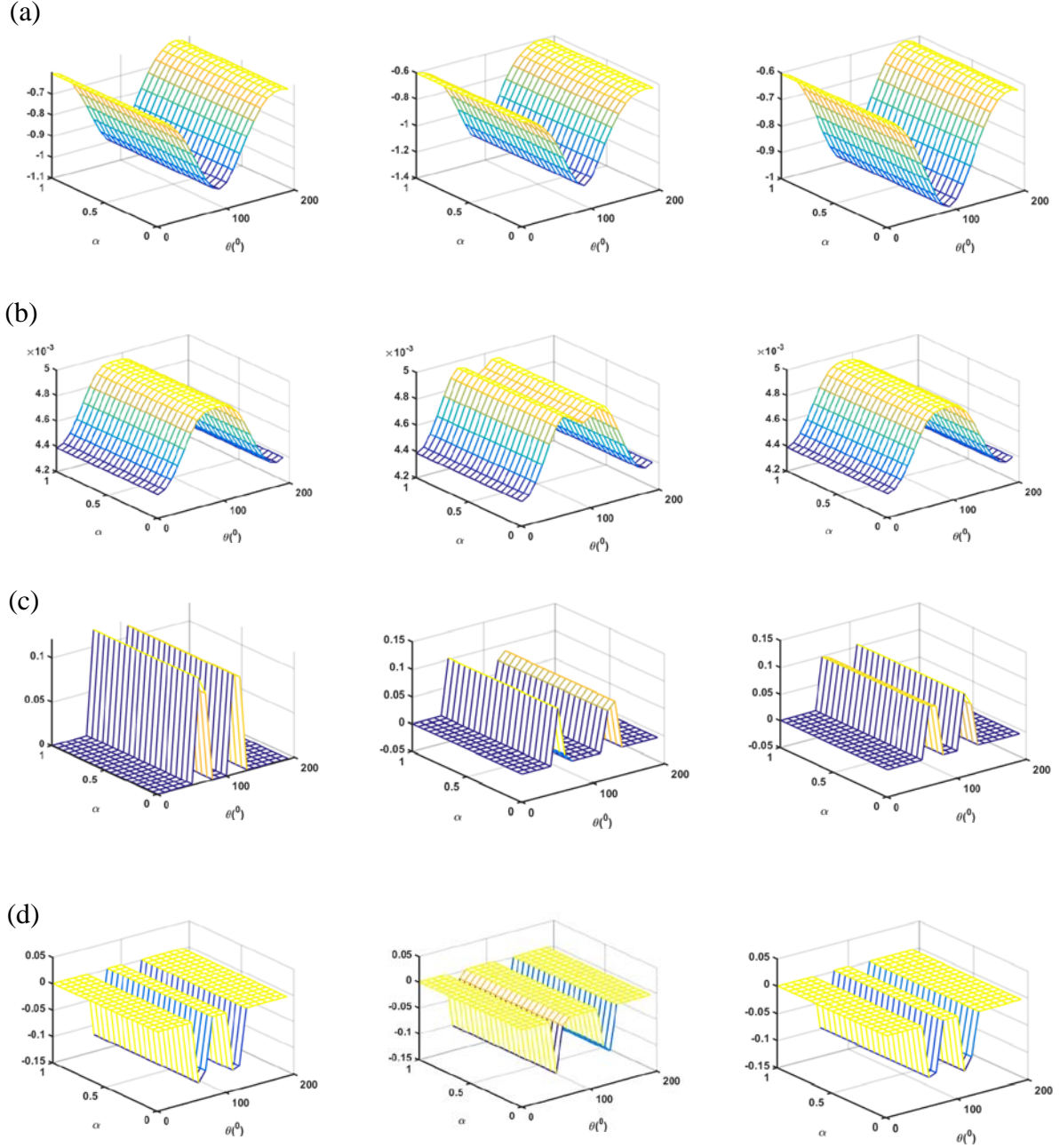
Fig. 3. Profile of (a) Q_1^{-1} (b) Q_2^{-1} (c) Q_3^{-1} (d) Q_4^{-1} w.r.t. α and θ for $\phi = 30°, 78°, 156°$, respectively for TT model

(a)

(b)

(c)

(d)
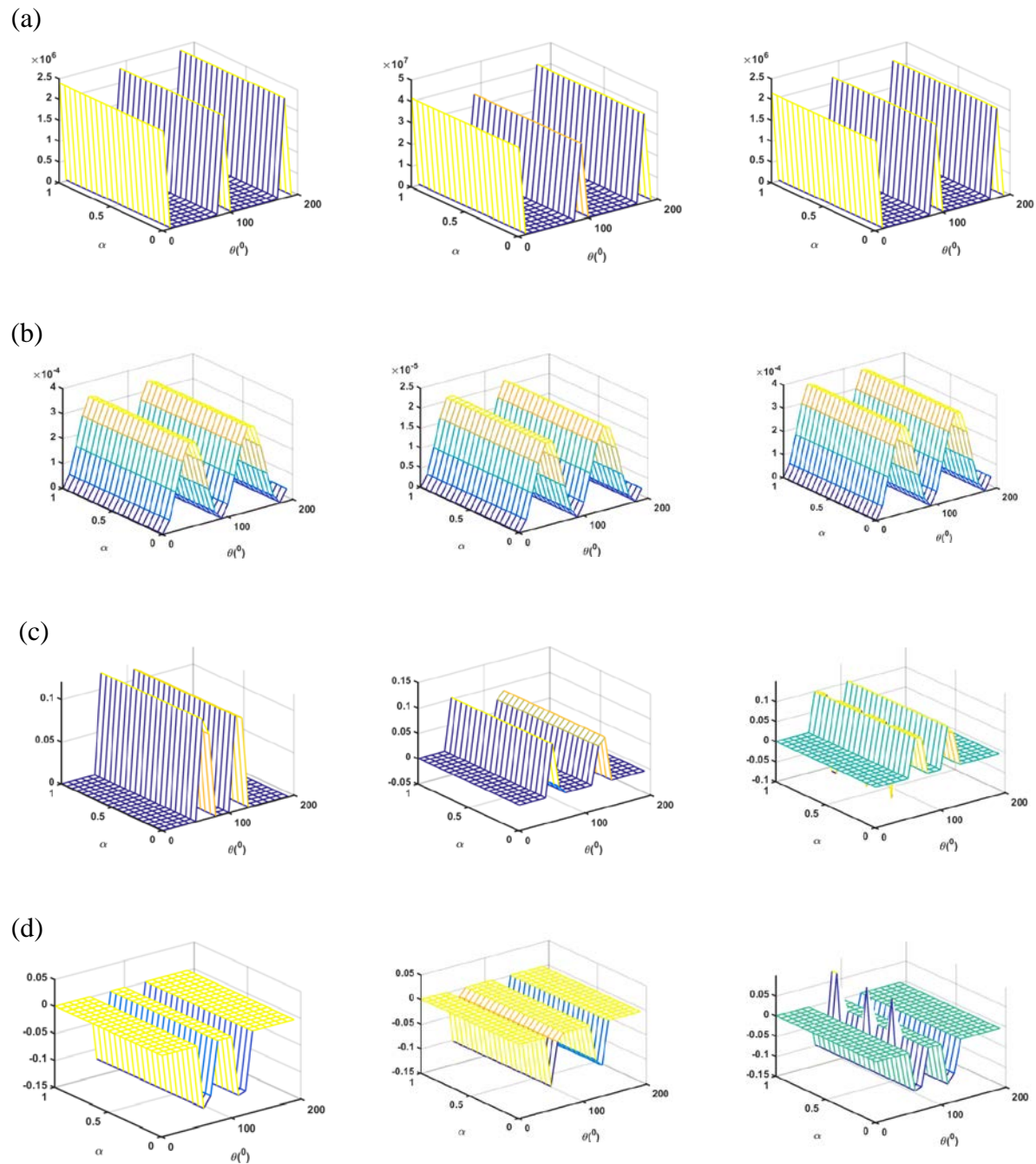
Fig. 4. Profile of (a) Q_1^{-1} (b) Q_2^{-1} (c) Q_3^{-1} (d) Q_4^{-1} w.r.t. α and θ for $\phi = 30°, 78°, 156°$, respectively for WTT model

It is clear from Fig. 3(a) that for TT model the attenuation quality factor of qP wave initially tends to decrease then increases as θ exceeds 100° for the different values of ϕ while in the case of WTT, Q_1^{-1} demonstrates an oscillatory behaviour as shown in Fig. 4(a). Evidently, two-temperature parameters and α have a substantial effect. Figure 3(b) depicts that for $\phi = 78°$ and $\theta = 100°$, the attenuation quality factor of qS$_1$ wave (Q_2^{-1}) is less than the value obtained for $\phi = 30°, 156°$ and $\theta = 100°$. It gradually decreases for the same value of α as the angle of incidence increases whereas, for WTT, it displays oscillatory behaviour

with variations in numerical values for different values of ϕ and θ. The attenuation quality factor of qS$_2$ wave (Q_3^{-1}) is similar for WTT and TT models as shown in Figs. 3(c) and 4(c). Q_3^{-1} and Q_4^{-1} of qS$_2$ and qT waves are noticed as unaffected for both mediums attaining smaller values with some variations and may not be of that much significance. Both exhibit constant behaviour as θ increases for different values of ϕ, α.

6. Conclusions

A mathematical model of an anisotropic piezothermoelastic medium with two-temperature and fractional order derivative is presented. Also, the mathematical formulation for orthotropic piezothermoelastic medium with two-temperature and fractional order derivative is presented. Significant theorems like variational principle, uniqueness theorem for the mixed initial boundary value problem, and theorem of reciprocity are established. Some special cases of interest are also given.

Appreciable effects of two-temperature parameters and fractional order parameters are observed on the various characteristics of the waves for the considered model.

Phase velocity and attenuation quality factor are presented graphically for two different models (TT, WTT) to depict the response of the considered model.

It is observed that the qP wave propagates with the highest phase velocity with the change in direction in comparison to the other plots. Phase velocities of qS$_1$ qS$_2$ and qT waves are also affected by both parameters as shown by variations in numerical values.

Due to the effects of fractional order and two-temperature parameters, the attenuation quality factor of qP wave increases for different values of ϕ and $\theta \geq 100°$. Attenuation quality factor of qS$_1$ wave also show the impact of both parameters. It attains the highest value for the intermediate values of θ.

Attenuation quality factor of qS$_2$ and qT waves are also affected by α, ϕ and θ.

There is no independent wave mode in the electric field, whereas the electric potential wave still can propagate with the elastic wave modes via constitutive relations.

The established results will be helpful for the investigators working on piezothermoelastic models.

References

[1] Chen PJ, Gurtin ME. On a theory of heat conduction involving two temperatures. *Z. Angew. Math. Phys.* 1968;19: 614-627.
[2] Chen PJ, Williams WO. A note on non-simple heat conduction. *Z. Angew. Math. Phys.* 1968;19: 969-970.
[3] Chen PJ, Gurtin ME, Williams WO. On the thermodynamics of non-simple elastic materials with two temperatures. *Z. Angew. Math. Phys.* 1969;20(1): 107-112.
[4] Said SM, Elmaklizi YD, Othman MIA. A two-temperature rotating-micropolar thermoelastic medium under influence of magnetic field. *Chaos, Solitons & Fractals.* 2017;97: 75-83.
[5] Kumar R, Vashishth AK, Ghangas S. Waves in anisotropic thermoelastic medium with phase lag, two-temperature and void. *Mater. Phys. Mech.* 2018;35(1): 126-138.
[6] Mindlin RD. Equation of high frequency of thermopiezoelectric crystals plates. *Int. J. Solid Struc.* 1974;10(6): 625-637.
[7] Nowacki W. Some general theorems of thermo-piezoelectricity. *J. Thermal Stresses.* 1978;1(2): 171-182.

[8] Nowacki W. Foundation of linear piezoelectricity. In: Parkus H. (Ed.) *Interactions in Elastic Solids. Springer.* Wein; 1979.

[9] Sharma MD. Piezoelectric effect on the velocities of waves in an anisotropic piezo-poroelastic medium. *Proc. R. Soc. A.* 2010;466(2119): 1977-1992.

[10] Vashishth AK, Sukhija H. Inhomogeneous waves at the boundary of an anisotropic piezo-thermoelastic medium. *Acta Mech.* 2014;225: 3325-3338.

[11] Kumar R, Sharma P. Basic theorems and wave propagation in a piezothermoelastic medium with dual phase lag. *Indian J. Phys.* 2020;94: 1975-1992.

[12] Meral FC, Royston TJ. Surface response of a fractional order viscoelastic half space to surface and subsurface sources. *J. Acoust. Soc. Am.* 2009;126(6): 3278-3285.

[13] Bassiouny E, Sabry R. Fractional order two temperature thermo-elastic behaviour of piezoelectric materials. *J. Appl. Math. Phys.* 2013;1(5): 110-120.

[14] Kumar R, Sharma P. Effect of fractional order on energy ratios at the boundary surface of elastic-piezothermoelastic media. *Coupled System Mech.* 2017;6(2): 157-174.

[15] Lata P. Fractional order thermoelastic thick circular plate with two temperatures in frequency domain. *Appl. Appl. Math.* 2018;13(2): 1216-1229.

[16] Bassiouny E, Youssef HM. Two-temperature generalised thermopiezoelasticity of finite rod subjected to different types of thermal loadings. *J. Thermal Stresses.* 2008;31(1): 233-245.

[17] Ezzat MA, El-Karamany AS, Awad, ES. On the coupled theory of thermo-piezoelectric/piezomagnetic materials with two temperature. *Canadian J. Phys.* 2010;88(5): 307-315.

[18] Nickell R, Sackman J. Variational principles for linear coupled thermoelasticity. *Quart. Appl. Math.* 1968;26: 11–26.

[19] Iesan D. On some reciprocity theorems and variational theorems in linear dynamic theories of continuum mechanics. *Memorie dell'Accad. Sci. Torino. Cl. Sci. Fis. Mat. Nat. Ser.* 1974;4(17): 1-20.

[20] Ezzat MA, El Karamany AS. The uniqueness and reciprocity theorems for generalised thermoviscoelasticity for anisotropic media. *J. Thermal Stresses.* 2002;25(6): 507-522.

[21] Othman MIA. The uniqueness and reciprocity theorems for generalised thermoviscoelasticity with thermal relaxation times. *Mech. and Mech. Eng.* 2004;7(2): 77-87.

[22] Kumar R, Prasad R, Mukhopadhyay S. Variational and reciprocal principles in two-temperature generalized thermoelasticity. *J. Thermal Stresses.* 2010;33: 161-171.

[23] Kuang ZB. Variational principles for generalised thermodiffusion theory in pyroelectricity. *Acta Mech.* 2010;214: 275-289.

[24] Vashishth AK, Gupta V. Uniqueness theorem, theorem of reciprocity and eigenvalue problems in linear theory of porous piezoelectricity. *Appl. Math.-Engl. Ed.* 2011;32(4): 479-494.

[25] Kumar R, Sharma P. Variational principle, uniqueness and reciprocity theorems in porous magneto-piezothermoelastic medium. *Cogent Mathematics.* 2016;3: 1231947.

[27] Kumar R, Sharma P. Variational principle, uniqueness and reciprocity theorems in porous piezothermoelastic with mass diffusion. *J. Solid Mech.* 2016;8(2): 446-465.

[28] Biot MA. Thermoelasticity and irreversible thermodynamics. *J. Appl. Phys.* 1956;27: 240-253.

[29] Kothari S, Mukhopadhyay S. Some theorems in linear thermoelasticity with dual phase-lags for an anisotropic medium. *J. Thermal Stresses.* 2013;36(10): 985-1000.

[30] Gurtin ME. Variational principles for linear initial-value problems. *Q. Appl. Math.* 1964;22(3): 252-256.

[31] Tzou HS, Bao Y. A theory on anisotropic piezothermoelastic shell laminates with sensor/actuator applications. *J. Sound Vib.* 1995;184(3): 453-473.

Appendix A

$$t_{11} = -\omega\rho c_1^2, \qquad t_{12} = in_1\rho c_1^2, \qquad t_s = \frac{\alpha_{11}T_0\omega}{e_{31}}, \qquad t_{13} = \omega^2(a_{11}n_1^2 + a_{22}n_2^2 + a_{33}n_3^2),$$

$$t_{14} = in_2\rho c_1^2\frac{\alpha_{22}}{\alpha_{11}}, \qquad t_{15} = in_3\rho c_1^2\frac{\alpha_{33}}{\alpha_{11}}, \qquad t_{16} = in_3\rho c_1^2\frac{\tau_3}{\alpha_{11}}, \qquad \tau_H = T_0(1 + (-i\omega)^\alpha \tau_q),$$

$$t_{17} = ir\tau_H\rho c_1^2.$$

$$x_{11} = \omega(c_{11}n_1^2 + c_{66}n_2^2 + c_{55}n_3^2), \qquad x_{12} = \omega(c_{12} + c_{66})n_1n_2, \qquad x_{13} = \omega(c_{13} + c_{55})n_1n_3,$$

$$x_{14} = t_s(e_{31} + e_{15})n_1n_3, \qquad x_{15} = x_{12}, \qquad x_{16} = \omega(c_{66}n_1^2 + c_{22}n_2^2 + c_{44}n_3^2),$$

$$x_{17} = \omega(c_{23} + c_{44})n_2n_3, \qquad x_{18} = t_s(e_{32} + e_{24})n_2n_3, \qquad x_{19} = x_{13}, x_{20} = x_{17},$$

$$x_{21} = \omega(c_{55}n_1^2 + c_{44}n_2^2 + c_{33}n_3^2), \qquad x_{22} = t_s(e_{15}n_1^2 + e_{24}n_2^2 + e_{33}n_3^2), \qquad x_{23} = -\omega(e_{31} + e_{15})n_1n_3,$$

$$x_{24} = -\omega(e_{32} + e_{24})n_2n_3, \qquad x_{25} = -\omega(e_{15}n_1^2 + e_{24}n_2^2 + e_{33}n_3^2), \qquad x_{26} = t_s(\xi_{11}n_1^2 + \xi_{22}n_2^2 + \xi_{33}n_3^2),$$

$$x_{27} = -\tau_H\omega\alpha_{11}n_1, \qquad x_{28} = -\tau_H\omega\alpha_{22}n_2, \qquad x_{29} = -\tau_H\omega\alpha_{33}n_3,$$

$$x_{30} = \tau_H\omega\alpha_{11}T_0 n_3\frac{\tau_3}{e_{31}}, \qquad x_{31} = -\frac{\rho\omega_1}{\alpha_{11}}\omega(K_{11}n_1^2 + K_{22}n_2^2 + K_{33}n_3^2).$$

$$m_{11} = t_{12}\,t_{13}, \qquad m_{12} = t_{14}\,t_{13}, \qquad m_{13} = t_{15}\,t_{13}, \qquad m_{14} = t_{16}\,t_{13}, \qquad m_{15} = x_{31} + t_{17}\,t_{13}.$$

MODIFIED DUGDALE MODEL FOR MULTIPLE CIRCULAR ARC-CRACKS WITH UNIFIED PLASTIC ZONES: A COMPLEX VARIABLE APPROACH

Naved Akhtar[*], **S. Hasan**

Department of Mathematics, Jamia Millia Islamia, New Delhi-110 025, India.

*e-mail: naved.a86@gmail.com

Abstract. A crack arrest model is presented in this paper for multiple circular arc-cracks with coalesced yield zones. The geometry of cracks discussed in the article assumes as a prelude to the case of two equal circular arc-cracks. Further, the influence of variable stress distribution on the rims of the cracks is studied. Analytical expressions for stress intensity factors and applied load ratios are obtained using the complex variable method. Numerical results are obtained for applied load ratio, yield zone length, and reported graphically.
Keywords: circular-arc cracks, Dugdale strip-yield model, yield zone length, stress intensity factor

1. Introduction

Due to considerable mathematical difficulties, the journey of determining the precise residual strength of engineering materials is always a hard nut to crack. Particularly, when the material is damaged due to the development/ presence of multiple cracks or crack-like defects. In the case of multiple cracks, two or more closely located small cracks when interacting with each other form a big crack, which may cause a severe problem to the integrity of the structure. Before the formation of a big crack, the yield zones developed at each internal tip of the cracks get coalesced due to an increase in applied stress at the infinite boundary of the plate.

The residual strength of the structure containing cracks is inversely proportional to the crack size. Therefore, it is imperative to evaluate the residual strength of the structure as a function of crack size. In this connection, Dugdale [1] formulated the relationship between the residual strength of the structure and the crack size, which is now known as the Dugdale strip yield model. However, the model was used largely to study the size of the yield zone in the case of straight cracks. Moreover, the geometry of the crack also makes an impression on the residual strength of the structure. Therefore, large of work has been done in past to study the problem of multiple circular-arc cracks which includes the work of Smith [2], Chen [3], [4], Bhargava et al. [5], [6], Jagannadham [7], Zhang [8], etc. The problem of circular arc cracks may be considered as a generalization to the Dugdale model due to the complexity of the crack geometries.

Furthermore, the problem of circular-arc cracks, using different mathematical approaches, was discussed by several researchers e.g., Shiah [9] used a complex variable approach to solve a circular arc crack under partial loading conditions and Zhong et al. [10] used it to analyze the problem of a circular arc-crack in piezoelectric materials under antiplane shear and in-plane

electric field. Gao et al. [11] used Green's function approach for the treatment of a circular arc-crack at the interface between a circular piezoelectric material and an infinite matrix. Semi inverse method used to solve the problem of arc crack by Shen et al. [12]. The boundary collocation method was applied by Cheung et al. [13] to calculate the stress intensity factor at the crack tip of a circular-arc crack in an infinite plate. Bhargava et al. [14] using the complex variable approach obtained the analytical expressions of the residual strength of an infinite isotropic plate containing a single circular arc crack. Gdoutos et al. [15] discussed the problem of two asymmetric circular arc cracks in an infinite isotropic plate and also the case of two equal and symmetrically positioned cracks. Bhargava et al. [16] addressed the issue of coalescence of yield zones between two adjacent circular-arc cracks. The theoretical and experimental study is carried for various arrangements of arc cracks by Pourseifi [17]. Stress intensity factors for circular-arc cracks in finite plates were calculated using finite element analysis by Shim et al. [18].

In the present study, an effort has been made to obtain a closed-form expression for the residual strength of a damaged plate in the presence of four circular-arc cracks with unified yield zones. Thomson's [19] and Muskhelishvili's [20] complex variable approach is used to obtain analytical expressions for stress intensity factor, yield zone ratio at each crack tip. The Crack-arrest model under general yielding condition was discussed recently [21] for similar cracks configuration.

2. Circular-arc-crack problem

A schematic diagram of the problem of four circular-arc cracks with coalesced yield zones is depicted in two Fig. 1 and Fig. 2. The cracks, $L_i (i = 1,2,3,4)$, occupy the intervals $[b_1 = Re^{-i\beta}, d_1 = Re^{-i\gamma}]$, $[c_1 = Re^{i\gamma}, a_1 = Re^{i\beta}]$, $[-b_1 = -Re^{-i\beta}, -d_1 = -Re^{-i\gamma}]$, and $[-c_1 = -Re^{i\gamma}, -a_1 = -Re^{i\beta}]$, respectively on the circumference of a circle $|z| = R$ in an infinite elastic perfectly-plastic plate occupy the entire complex-plane.
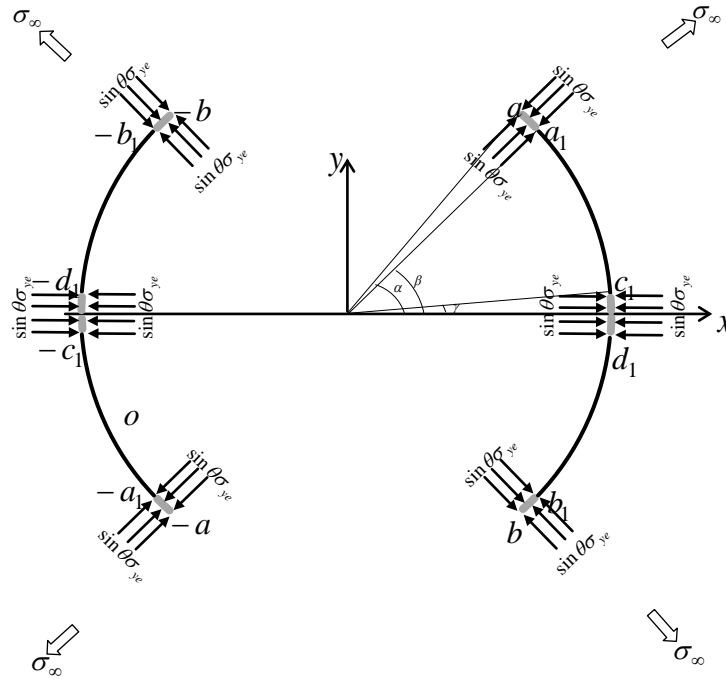
Fig. 1. Configuration of the problem when loading condition $\sin \theta \, \sigma_{ye}$
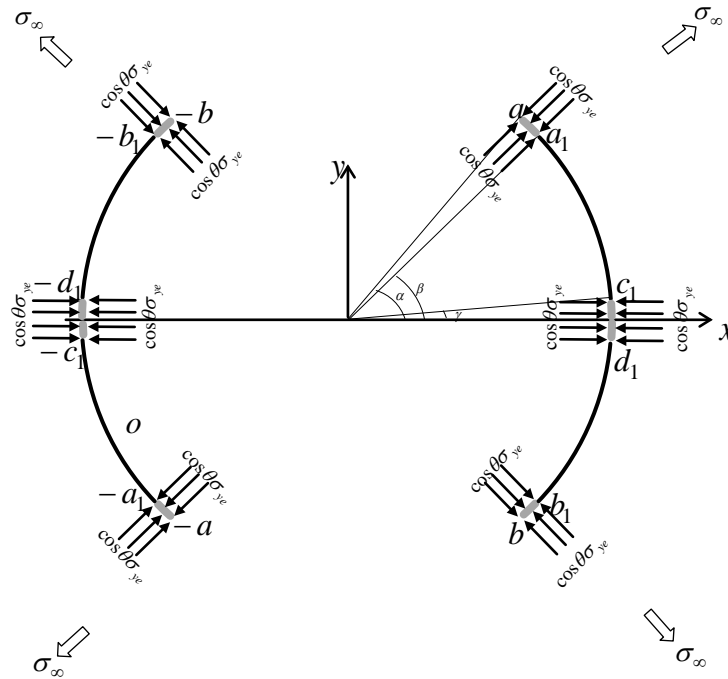
Fig. 2. Configuration of the problem when loading condition $\cos\theta\,\sigma_{ye}$

Rims of the cracks open in mode-I type deformation as the infinite boundary of the plate are subjected to stress distribution σ_∞. As a result, the formation of yield zones takes place at each crack tip. Stresses applied at the infinite boundary of the plate increases to such a limit that the yield zones developed at the inner crack tips d_1, c_1 and $-d_1$, $-c_1$ get coalesced.

The yield zones together with the coalesced yield zones are denoted by $\Gamma_j (j = 1,2,3,4,5,6)$ and occupy the intervals $(b = Re^{-i\alpha}, b_1 = Re^{-i\beta})$, $(d_1 = Re^{-i\gamma}, c_1 = Re^{i\gamma})$, $(a_1 = Re^{i\beta}, a = Re^{i\alpha})$, $(-b = -Re^{-i\alpha}, -b_1 = -Re^{-i\beta})$, $(-d_1 = -Re^{-i\gamma}, -c_1 = -Re^{i\gamma})$, $(-a_1 = -Re^{i\beta}, -a = -Re^{i\alpha})$, respectively on one and the same circle $|Z| = R$.

According to Gdoutos [22], materials may fail at stresses that are well below the yield stress of the material. Therefore, to study the behavior of yield zone length under the influence of variable yield stress distribution. Two different types of stress distributions have to be distinguished. First $\sigma_{rr} = \sin\theta\sigma_{ye}$ as shown in Fig. 1 and second $\sigma_{rr} = \cos\theta\sigma_{ye}$ presented in Fig. 2., where σ_{ye} is the yield stress of the material and $t = Re^{i\theta}$ is any point on the rims of the yield zones. Moreover, the article discussed two different cases of remotely applied stress. Firstly, when the infinite boundary is subjected to a uniform stress distribution as shown in Fig. 3 and second when remote stress reduces to tension p making an angle ξ with positive x −axis, shown in Fig. 4.

3. Solution of the circular-arc-crack problem
The solution of the problem discussed in section 2 for multiple interacting circular-arc cracks is obtained by dividing the problem into two different sub-problems, namely, opening case and closing case and denoted by subproblem-A and subproblem-B respectively. These subproblems are solved separately, and the solution of the main problem is then obtained by superposing the

solutions of them.

Subproblem-A and its solution. The problem discussed in this section is related to the case of opening of circular-arc cracks due to remotely applied stresses at the infinite boundary of the plate. These cracks are assumed to be open in mode-I type deformation. Two different types of stress profiles were used to analyze the opening of the cracks theoretically. These cases of two different stress profiles, as shown in Fig. 3 and Fig. 4, are discussed here.
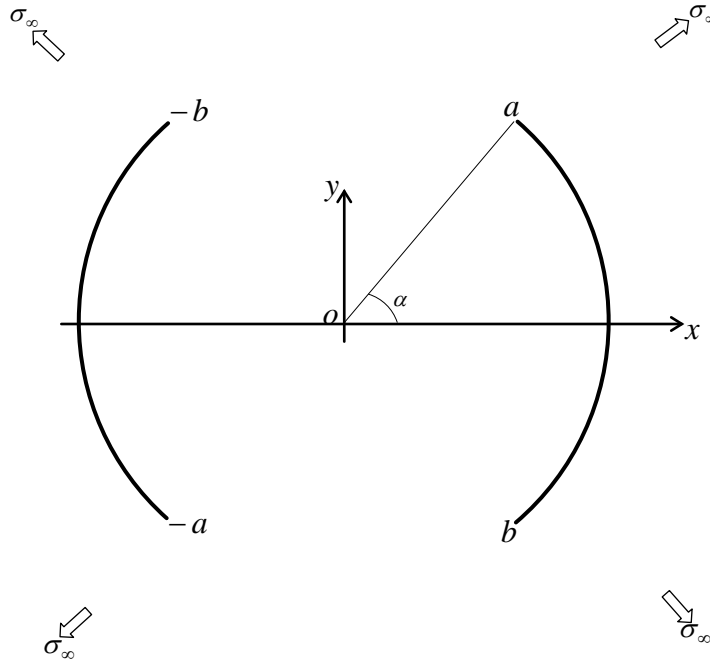
Fig. 3. Configuration of the Sub-problem A: uniform stress distribution σ_∞

Case-I: uniform tensile stress distribution. Consider the boundary of the plate is subjected to uniform remotely applied stress distribution, as shown in Fig. 3. Four circular arc cracks, weaken the plate, open in mode-I type deformation. In this case, the boundary conditions are:
1. Remote stresses are distributed equally in all directions ($\sigma_{rr}^\pm = \sigma_\infty$).
2. Rotation vanishes at the infinite boundary of the plate.
3. Body forces are absent.
4. Displacement components are single-valued throughout the plate.

Using the above boundary conditions and the mathematical formulation given in Appendix-A the complex potential function for the opening case of the problem is,

$$\Phi_A^m(z) = \frac{\sigma_\infty}{2(2 - H^2)}\left\{1 - H^2 + \frac{z^2 + R^2(1 - 2H^2)}{X(z)}\right\},\tag{1}$$

where $H^2 = E(k)/F(k)$ and $F(k)$, $E(k)$ are complete elliptical integral of first and second kind respectively as defined by Byrd [23], $k = \sin\alpha$. The superscript m indicates that the function refers to the stress profile shown in Fig. 3.

Stress intensity factor at the crack tip $a = Re^{i\alpha}$ for opening mode may be calculated by substituting $\Phi_A^m(z)$ from equation (1) into (41),

$$(K_A^m)_I = \frac{\sigma_\infty\sqrt{R\pi}}{2 - H^2}\left(H^2\sqrt{\tan\alpha} - i(1 - H^2)\sqrt{\cot\alpha}\right),\tag{2}$$

here subscript I refer to the mode-I (opening mode) type of deformation.
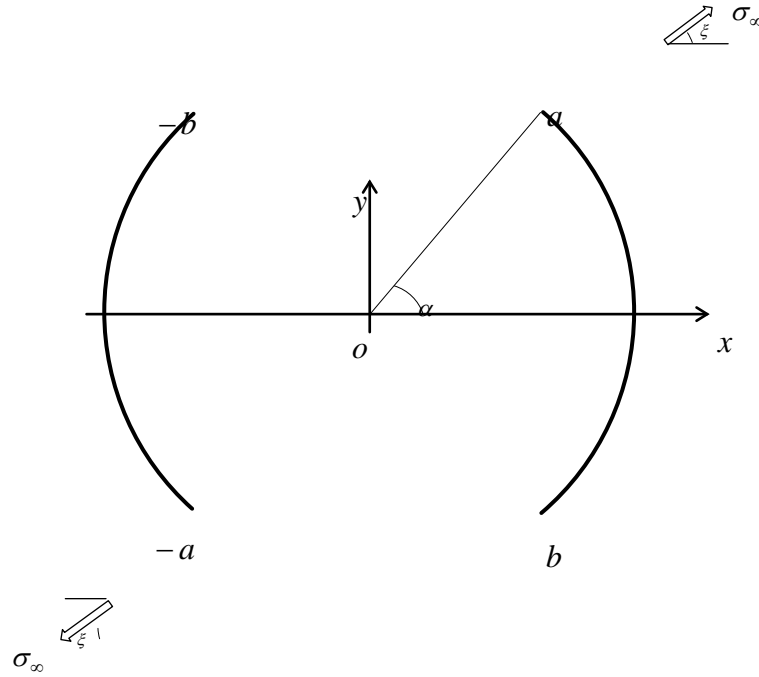
Fig. 4. Configuration of the Sub-problem A: stresses acting at an angle ξ to the ox-axis

Case-II: tensile stress distribution at a point. In this section, the case when applied remote stress reduces to a tension $\boldsymbol{p}$ acting in the direction, making an angle $\boldsymbol{\xi}$ with $\boldsymbol{ox}$-axis as depicted in Fig. 4 will be discussed. In view of that, the boundary conditions of the problem are as follows,

1. Remote stresses $\sigma_{rr}^{\pm} = \sigma_{\infty}$, $\sigma_{r\theta}^{\pm} = 0$ are applied in a direction making an angle ξ with ox-axis.
2. The rims of the cracks are stress-free.
3. Body forces are absent.
4. Displacement components are single-valued throughout the plate.

The complex potential function is then obtained under the boundary conditions and mathematical formulation given in Appendix-A yields the following

$$\Phi_A^n(z) = \frac{\sigma_{\infty}}{8}\left[\left(\frac{z^2 + R^2(1 - 2H^2)}{X(z)} - 1\right)Q_2 - \frac{2R^2 e^{2i\xi}}{z^2}\left(\frac{R^2}{X(z)} + 1\right)\right] \tag{3}$$

where

$$Q_2 = \frac{2 + \cos2\xi\cos2\alpha}{2 - H^2} - i\frac{\sin2\xi\cos2\alpha}{H^2},$$

superscript n refers to the stress profile shown in Fig. 4.

The state of stresses in the crack tip $z = Re^{i\alpha}$ may be obtained using equations (3) and (41) as

$$(K_A^n)_I = K_1 - iK_2 \tag{4}$$

where,

$$K_1 = \frac{\sigma_\infty}{2}\sqrt{R\pi \tan\alpha}\left\{\frac{H^2}{2-H^2} + \cos2\xi\left(2 + \cos^2\alpha - \frac{2(1+\sin^2\alpha)}{2-H^2}\right)\right.$$

$$\left. + \sin2\xi\cot\alpha\left(1 + \sin^2\alpha - \frac{\cos^2\alpha}{H^2}\right)\right\},$$

$$K_2 = \frac{\sigma_\infty}{2}\sqrt{R\pi\cot\alpha}\left\{\frac{1-H^2}{2-H^2} - \cos2\xi\left(\cos^2\alpha - \frac{1+\sin^2\alpha}{2-H^2}\right) - \sin2\xi\sin\alpha\cos\alpha\right\}.$$

Subproblem-B and its solution. The study of variable pressure arresting of arc cracks, in an infinite isotropic plate, is the main objective of subproblem-B. Presence of these cracks $L_i(i = 1, 2, 3, 4)$ with unified yield zones $(\Gamma_j, j = 1, 2, ..., 6)$ influence the strength of the plate. Variable stress distribution applied over the rims of the developed yield zones seized the opening of cracks. Two different stress profiles of closing stresses are discussed in this section.

1. Yield stresses are distributed in the form of $\sigma_{rr} = \sin\theta\sigma_{ye}$, as shown in Fig. 5.
2. Yield stresses are distributed in the form of $\sigma_{rr} = \cos\theta\sigma_{ye}$, as shown in Fig. 6.

Case of $\sigma_{rr} = sin\theta\sigma_{ye}$. The yield zones, developed at each crack tip of four circular arc cracks with unified yield zones, are subjected to a variable stress distribution $\sigma_{rr} = \sin\theta\sigma_{ye}$ as shown in Fig. 5. To arrest the further opening of these cracks. Therefore, the boundary conditions for this case are as follows:

1. Rims of yield zones are subjected to $\sigma_{rr} = \sin\theta\sigma_{ye}$.
2. Boundary of the plate is stress-free.
3. Body forces are absent.
4. Displacement components are single-valued throughout the plate.

Using methodology is given in Appendix-A and above boundary conditions, the complex potential function for this case is

$$\Phi_{B_1}(z) = \frac{\sigma_{ye}}{2\pi i X(z)}\int_\Gamma \frac{X(t)\sin\theta}{t-z}dt + \frac{1}{2X(z)}\{C_0 z^2 + C_2\} + \frac{D_0}{2}, \tag{5}$$

where C_0, C_2 and D_0 are the constants to be determined using the boundary conditions, and $X(z) = \sqrt{z^2 - R^2 e^{2i\alpha}}\sqrt{z^2 - R^2 e^{-2i\alpha}}$, $\left(\Gamma = \bigcup_{j=1}^6 \Gamma_j\right)$, Γ_j denotes the yield zones.

Integral on the right-hand side of the equation (5) is solved by substituting $\sin\theta = \frac{t-\bar{t}}{2i}$ and $t\bar{t} = R^2$. Thus,

$$\int_\Gamma \frac{X(t)\sin\theta}{t-z}dt \tag{6}$$

$$= -\frac{1}{a}\left[S_1 + (z^2 - R^2(1 + 2\cos2\alpha))S_2 + (z^4 - R^2(z^2 - R^2)(1 + 2\cos2\alpha))S_3\right.$$

$$\left. - (z^2 - b^2)(z^2 - R^2)S_4\right].$$

where,

$$S_1 = \frac{a^4}{3}\left((k^2-1)S_3 - 2(k^2-2)\frac{S_2}{a^2} + k^2 S_5\right),$$

$$S_2 = a^2(E(\theta_1, k) - E(\theta_2, k) + E(k) - E(\theta_3, k) + E(\theta_4, k)),$$

$$S_3 = F(\theta_1, k) - F(\theta_2, k) + F(k) - F(\theta_3, k) + F(\theta_4, k),$$

$$S_4 = \Pi(\theta_1, \alpha^2, k) - \Pi(\theta_2, \alpha^2, k) + \Pi\left(\frac{\pi}{2}, \alpha^2, k\right) - \Pi(\theta_3, \alpha^2, k) + \Pi(\theta_4, \alpha^2, k)),$$

$$S_5 = \sin\theta_1\cos\theta_1\sqrt{1 - k^2\sin^2\theta_1} - \sin\theta_2\cos\theta_2\sqrt{1 - k^2\sin^2\theta_2} - \sin\theta_3\cos\theta_3\sqrt{1 - k^2\sin^2\theta_3}$$
$$+ \sin\theta_4\cos\theta_4\sqrt{1 - k^2\sin^2\theta_4},$$

$$\theta_1 = \sqrt{\frac{e^{2i\alpha} - e^{2i\beta}}{e^{2i\alpha} - e^{-2i\alpha}}}, \theta_2 = \sqrt{\frac{e^{2i\alpha} - e^{-2i\beta}}{e^{2i\alpha} - e^{-2i\alpha}}}, \theta_3 = \sqrt{\frac{e^{2i\alpha} - e^{2i\gamma}}{e^{2i\alpha} - e^{-2i\alpha}}}, \theta_4 = \sqrt{\frac{e^{2i\alpha} - e^{-2i\gamma}}{e^{2i\alpha} - e^{-2i\alpha}}},$$

$$\alpha^2(z) = \frac{a^2 - b^2}{a^2 - z^2}, k^2 = 1 - e^{-4i\alpha}.$$
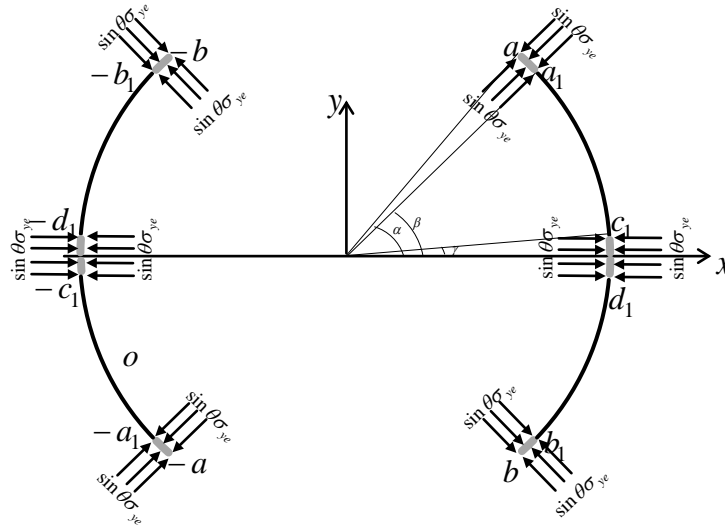
Fig. 5. Configuration of the closing case for $\sin\theta\sigma_{ye}$ loading

Constants given in equation (5) are obtained using the condition of single valuedness of displacement and loading conditions of the problem

$$C_0 = \frac{\sigma_{ye}}{ia\pi(3 - \cos2\alpha)}\left(\frac{S_1}{R^2} - 2\cos2\alpha S_2 + R^2\cos2\alpha S_3 - b^2(S_4 - \overline{S_4}) + 2R^2\sin^2\alpha\overline{S_4}\right.$$
$$\left. + 2G_1 - G_3 - G_4 S_4 + G_2(S_4 + \overline{S_4})\right) = \frac{\sigma_{ye}}{ia\pi}C_{00}, \tag{7}$$

$$C_2 = \frac{R^2\sigma_{ye}}{ia\pi}(G_3 + G_4 S_4) - C_0 R^2\cos2\alpha = \frac{R^2\sigma_{ye}}{ia\pi}C_{22}, \tag{8}$$

$$D_0 = \frac{\sigma_{ye}}{ia\pi}(G_1 + G_2 S_4) - C_0, \tag{9}$$

$$G_1 = S_2 - 2R^2\cos^2\alpha S_3, \tag{10}$$

$$G_2 = 2R^2\sin^2\alpha + b^2, \tag{11}$$

$$G_3 = \frac{S_1}{R^2} - 2\cos^2\alpha S_2 + \frac{R^2}{4}(1 + 4\cos2\alpha - \cos4\alpha)S_3, \tag{12}$$

$$G_4 = \frac{R^2}{2}(3\sin^2 2\alpha - 4\sin^2\alpha(1 + e^{-2i\alpha})). \tag{13}$$

Hence, substituting equations (6 – 13) into the equation (5), one gets the closed-form of the complex potential function for this case,

$$\Phi_{B_1}(z) = -\frac{\sigma_{ye}}{2ia\pi X(z)}[S_1 + (z^2 - R^2(1 + 2\cos2\alpha))S_2 + (z^4 - R^2(z^2 - R^2)(1 \tag{14}$$

$$+ 2\cos2\alpha))S_3 - (z^4 - z^2R^2 - b^2(z^2 - R^2))S_4] + \frac{C_0z^2 + C_2}{2X(z)} + \frac{D_0}{2}.$$

The stress intensity factor is obtained by putting the value of $\Phi_{B_1}(z)$ from equation (14) into the equation (41) and can be written as,

$$K_{B_1}^I = \frac{\sigma_{ye}\sqrt{R}}{ae^{i\alpha}\sqrt{2\pi\sin2\alpha}}\left[\frac{S_1}{R^2} - (1 + e^{-2i\alpha})S_2 + R^2e^{-2i\alpha}S_3 - R^2(e^{4i\alpha} - 1 - 2i\sin2\alpha)S_4\right.$$

$$\left. - C_{00}e^{2i\alpha} - C_{22}\right]. \tag{15}$$

Case of $\sigma_{rr} = cos\theta\sigma_{ye}$. In this case, rims of the yield zone are subjected to stress distribution $\sigma_{rr} = \cos\theta\sigma_{ye}$ and $\sigma_{r\theta}=0$. Pictorial representation for this case is given in Fig. 6.

The complex potential functions for the case, when variable stress $\cos\theta\sigma_{ye}$ is distributed over the rims of yield zones, may be written as

$$\Phi_{B_2}(z) = \frac{\sigma_{ye}}{2\pi iX(z)}\int_\Gamma \frac{\cos\theta X(t)}{t - z}dt + \frac{1}{2X(z)}\{C_0z^2 + C_2\} + \frac{D_0}{2}, \tag{16}$$

where C_0, C_2 and D_0 are the constants and subscript B_2 refers to the case of compressing stress profile $\cos\theta\sigma_{ye}$.

Using well-known relation $2\cos\theta = t + \bar{t}$. The integral given in equation (16) may be written as,

$$\int_\Gamma \frac{X(t)\cos\theta}{t - z}dt$$

$$= -\frac{i}{a}[S_1 + (z^2 + R^2(1 - 2\cos2\alpha))S_2 + (z^4 + R^2(z^2 + R^2)(1 - 2\cos2\alpha))S_3 - (z^2$$

$$- b^2)(z^2 + R^2)S_4]. \tag{17}$$

Constants C_0, C_2 and D_0 given in equation (16) are obtained using the above boundary conditions,

$$D_0 = \frac{\sigma_{ye}}{a\pi}(H_1 + H_2S_4) - C_0, \tag{18}$$

$$C_2 = \frac{R^2\sigma_{ye}}{a\pi}(H_3 + H_4S_4) - C_0R^2\cos2\alpha = \frac{R^2\sigma_{ye}}{ia\pi}C_{33}, \tag{19}$$

$$C_0 = \frac{\sigma_{ye}}{a\pi(3 - \cos2\alpha)}\left(\frac{S_1}{R^2} + 4\sin^2\alpha S_2 + R^2(2 - 3\cos2\alpha)S_3 + b^2(S_4 + \overline{S_4})\right.$$

$$\left. - 2R^2\cos^2\alpha\overline{S_4} + 2H_1 - H_3 - H_4S_4 + H_2(S_4 + \overline{S_4})\right) = \frac{\sigma_{ye}}{ia\pi}C_{44}, \tag{20}$$

$$H_1 = S_2 + 2R^2\sin^2\alpha S_3, \tag{21}$$

$$H_2 = -2R^2\cos^2\alpha + b^2, \tag{22}$$

$$H_3 = \frac{S_1}{R^2} + 2\sin^2\alpha S_2 - \frac{R^2}{2}(2\cos2\alpha - \sin^22\alpha)S_3, \tag{23}$$

$$H_4 = \frac{R^2}{2}\left(3\sin^2 2\alpha - 4\cos^2\alpha\left(1 - e^{-2i\alpha}\right)\right). \tag{24}$$
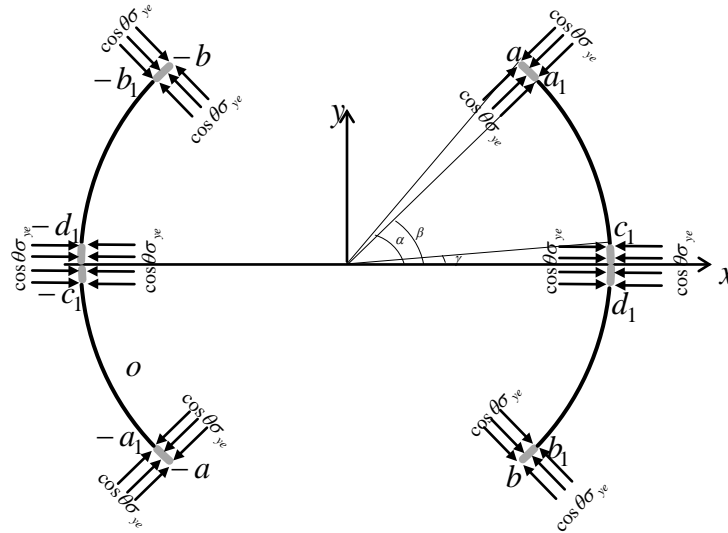
Fig. 6. Configuration of the closing case for $\cos\theta\sigma_{ye}$ loading

Thus, the final expression of the complex potential function for this case is then obtained by putting equations (17 – 24) in equation (16),

$$\Phi_{B_2}(z) = -\frac{\sigma_{ye}}{2a\pi X(z)}[S_1 + (z^2 + R^2(1 - 2\cos2\alpha))S_2 + (z^4 + R^2(z^2 + R^2)(1$$

$$- 2\cos2\alpha))S_3 - (z^4 + z^2 R^2 - b^2(z^2 + R^2))S_4] + \frac{C_0 z^2 + C_2}{2X(z)} + \frac{D_0}{2}. \tag{25}$$

The state of stress in the crack tip $a = Re^{i\alpha}$ for the present case may be obtained on inserting the value of $\Phi_B(z)$ from equation (25) in equation (41) as,

$$K_{B_2}^I = \frac{\sigma_{ye}\sqrt{R}}{aie^{i\alpha}\sqrt{2\pi\sin2\alpha}}\left[\frac{S_1}{R^2} + (1 - e^{-2i\alpha})S_2 - R^2 e^{-2i\alpha}S_3 - R^2\left(e^{4i\alpha} - 1 + 2i\sin2\alpha\right)S_4\right.$$

$$\left. - C_{44}e^{2i\alpha} - C_{33}\right]. \tag{26}$$

4. Numerical Study

A numerical study is carried out in this section to study the efficiency and accuracy of the analytical results obtained in the previous sections for various stress profiles. Analytical and numerical results for yield zone length have been acquired by superposing the solutions of two sub-problems, Subproblem-A (opening case) and Subproblem-B (closing case).

Case of $\sin\theta\sigma_{ye}$. The length of yield zones at the crack tip, a, due to the stress distribution $\sin\theta\sigma_{ye}$ is obtained by ensuring the Dugdale hypothesis that the stresses remain finite in the vicinity of the crack. Which is governed by the equation, $(K_A^m)_I = K_{B_1}^I$ and $(K_A^n)_I = K_{B_1}^I$. Thus, using equations (2), (4) and (15) one can obtain two non-linear equations corresponding to two different stress profiles discussed in section 3.1 as,

$$\left(1 - 2H^2 + e^{2i\alpha}\right)\left(\frac{\sigma_\infty}{\sigma_{ye}}\right)_m$$

$$= -\frac{2 - H^2}{a\pi}\left[\frac{S_1}{R^2} - \left(1 + e^{-2i\alpha}\right)S_2 + R^2 S_3 e^{-2i\alpha} - R^2\left(e^{4i\alpha} - 1 - 2i\sin 2\alpha\right)S_4 - C_{00}e^{2i\alpha}\right.$$

$$\left. - C_{22}\right],\tag{27}$$

$$\left(\left(1 + e^{2i\alpha} - 2H^2\right)\left(\frac{2 + \cos 2\xi\cos 2\alpha}{2 - H^2} - i\frac{\sin 2\xi\cos 2\alpha}{H^2}\right) - \frac{2e^{2i\xi}}{e^{2i\alpha}}\right)\left(\frac{\sigma_\infty}{\sigma_{ye}}\right)_n$$

$$= -\frac{4(2 - H^2)}{a\pi}\left[\frac{S_1}{R^2} - \left(1 + e^{-2i\alpha}\right)S_2 + R^2 e^{-2i\alpha}S_3 - R^2(e^{4i\alpha} - 1 - 2i\sin 2\alpha)S_4\right.$$

$$\left. - C_{00}e^{2i\alpha} - C_{22}\right].\tag{28}$$

It is almost impossible to solve the non-linear equations (27) and (28) in terms of yield zone length. However, normalized yield zone length at each crack tip is evaluated numerically against the applied load ratio $\frac{\sigma_\infty}{\sigma_{ye}}$ for each stress profile and reported graphically.
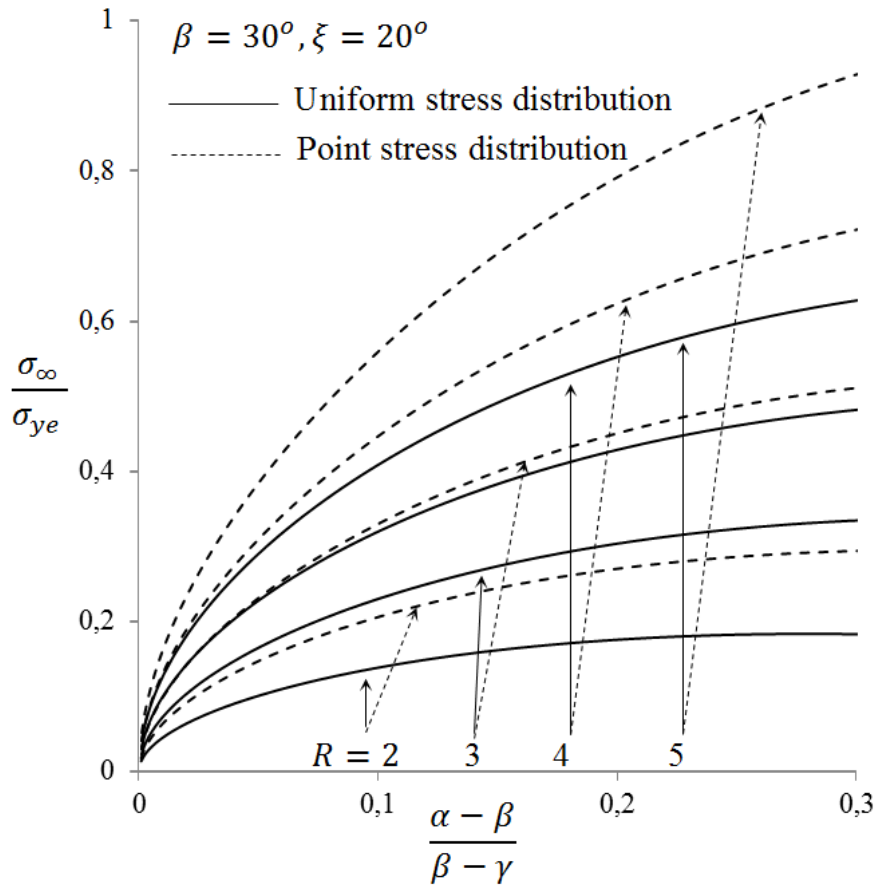
Fig. 7. $\frac{\sigma_\infty}{\sigma_{ye}}$ versus $\frac{\alpha - \beta}{\beta - \gamma}$ for the case of $\sin\theta\sigma_{ye}$ at different crack radius
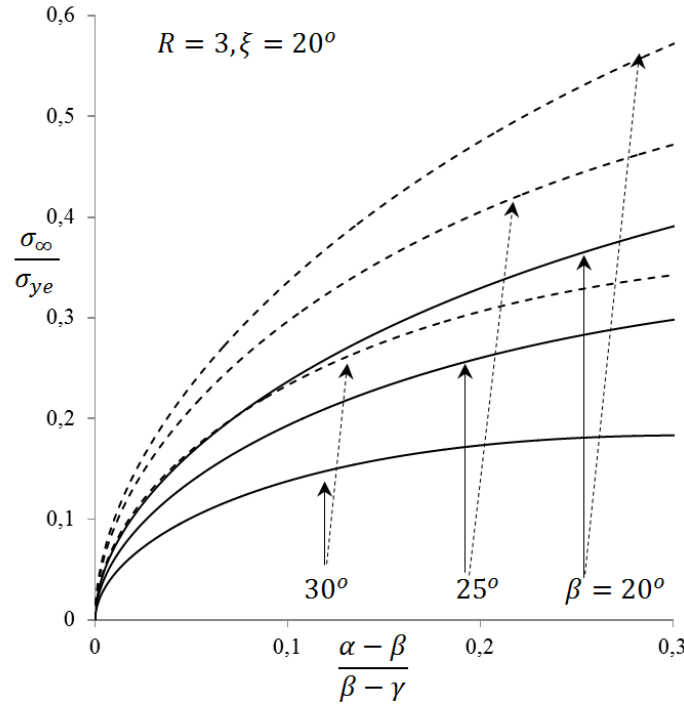
Fig. 8. $\frac{\sigma_\infty}{\sigma_{ye}}$ versus $\frac{\alpha-\beta}{\beta-\gamma}$ for the case of $\sin\theta\,\sigma_{ye}$ at different crack length

Figure 7 shows the behavior of normalized yield zone length, $\frac{R(\alpha-\beta)}{R(\beta-\gamma)}$, with respect to change in applied load ratio on the increasing radius of the circle (on which cracks lie). Increasing radius means an increase in inter crack distance. In the case of $R = 2$ (angle γ is very small) plate shows a low bearing capacity vis a vis $R = 5$ (γ is much larger) and much more significant in case of stress distribution act at an angle ξ. Further, it may be noted that the load applied at the boundary of the plate is significantly different in both the stress profiles. Hence, the plate under stress distribution act at an angle ξ be considered in a much safer position in the presence of the cracks as compared to the case of uniform stress distribution.

The same variation has been plotted in Fig. 8. for different crack length $R(\beta - \gamma)$, means increasing crack length. It has been observed that as the crack length increases, the load-bearing capacity of the plate decreases, which means that bigger cracks are more dangerous for the safe operation of the structures. In other words, the figure shows that the length of the plastically deformed region is more at each tip of bigger cracks as compared to the smaller ones for the fixed load required ratio $\left(\frac{\sigma_\infty}{\sigma_{ye}} = 0.1, say\right)$.

The effect of increasing angle of point stress applied at the boundary of the plate, in the case of four circular-arc cracks, is given in Fig. 9. It is found that as the angle ξ of stress distribution is increased, the residual strength of the plate also increases.
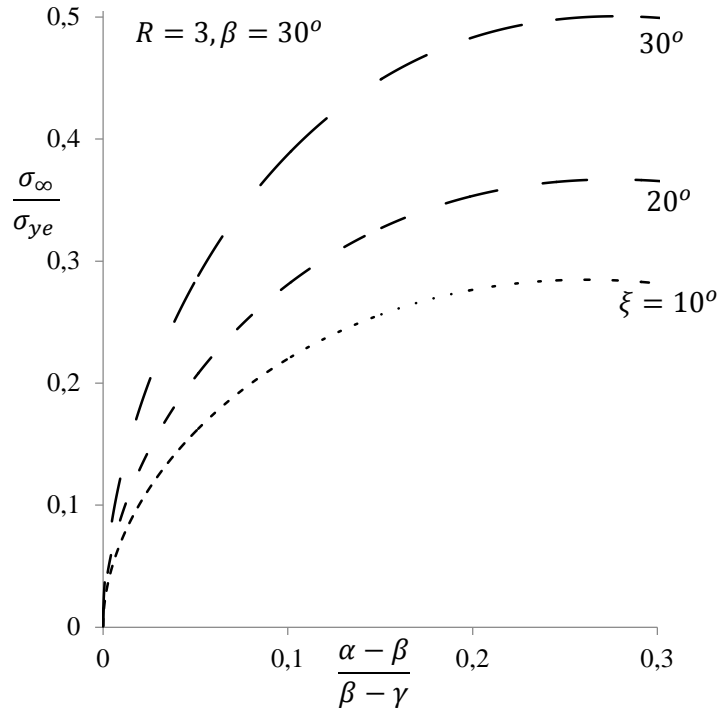
Fig. 9. $\frac{\sigma_\infty}{\sigma_{ye}}$ versus $\frac{\alpha-\beta}{\beta-\gamma}$ for $\sin\theta\,\sigma_{ye}$ at different angles ξ

Case of $\cos\theta\sigma_{ye}$. The length of developed yield enclaves for the case when yield stress distribution acting on the yield zones is varying as $\cos\theta\sigma_{ye}$ obtained in this section using the Dugdale hypothesis. Therefore, using equations (2), (4), and (26), one can get two non-linear equations corresponding to two different types of remote stress profiles in terms of applied and yield stress. These equations are

$$
\left(1 - 2H^2 + e^{2i\alpha}\right)\left(\frac{\sigma_\infty}{\sigma_{ye}}\right)_m
$$

$$
= -\frac{2 - H^2}{i\alpha\pi}\left[\frac{S_1}{R^2} + \left(1 - e^{-2i\alpha}\right)S_2 - R^2 e^{-2i\alpha}S_3 - R^2\left(e^{4i\alpha} - 1 + 2i\sin2\alpha\right)S_4 - C_{44}e^{2i\alpha}\right.
$$

$$
\left. - C_{33}\right],
$$
(29)

$$
\left(1 + e^{2i\alpha} - 2H^2\right)\left(\frac{2 + \cos2\xi\cos2\alpha}{2 - H^2} - i\frac{\sin2\xi\cos2\alpha}{H^2}\right) - \frac{2e^{2i\xi}}{e^{2i\alpha}}\left(\frac{\sigma_\infty}{\sigma_{ye}}\right)_n
$$

$$
= -\frac{4(2 - H^2)}{i\alpha\pi}\left[\frac{S_1}{R^2} + (1 - e^{-2i\alpha})S_2 - R^2 e^{-2i\alpha}S_3 - R^2(e^{4i\alpha} - 1 + 2i\sin2\alpha)S_4\right.
$$

$$
\left. - C_{44}e^{2i\alpha} - C_{33}\right].
$$
(30)

Yield zone length developed at the crack tip, a, may be calculated from equations (29) and (30) corresponding to two different stress profiles of remotely applied stresses. Yield zone length at crack tip a is normalized with the corresponding crack length. In the following figures, normalised yield zone lengths are presented graphically with respect to the increasing values of the applied load ratio.
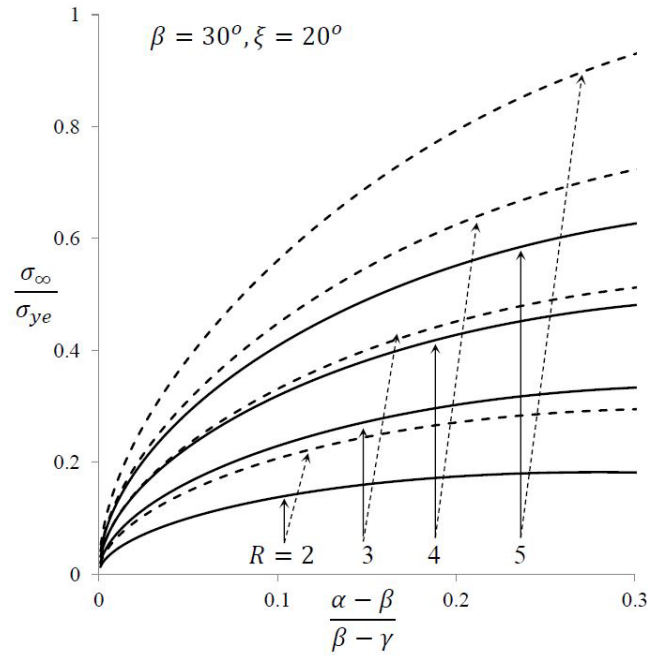
Fig. 10. $\frac{\sigma_\infty}{\sigma_{ye}}$ versus $\frac{\alpha-\beta}{\beta-\gamma}$ for stress profile $\cos\theta\ \sigma_{ye}$
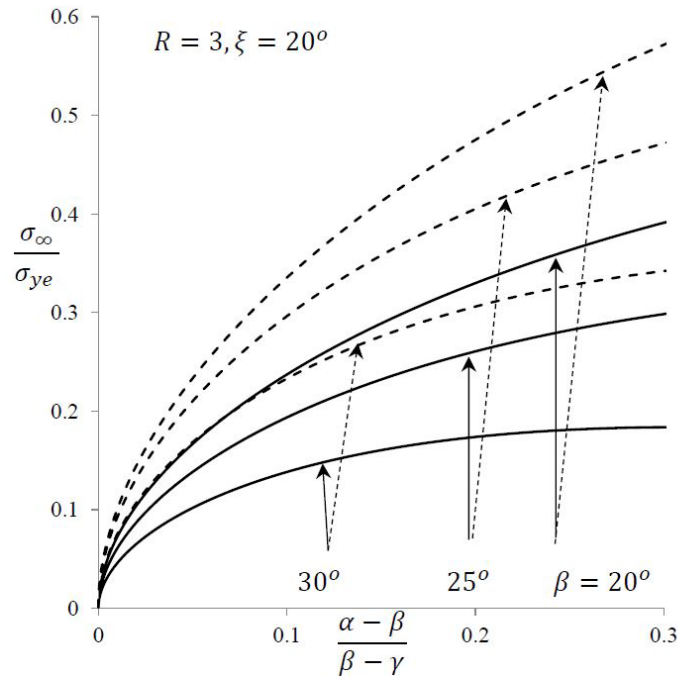
Fig. 11. $\frac{\sigma_\infty}{\sigma_{ye}}$ versus $\frac{\alpha-\beta}{\beta-\gamma}$ for stress profile $\cos\theta\ \sigma_{ye}$

Figure 10 shows the variation of sizes of normalized yield zone length with increasing values of applied stresses at crack tip $a = Re^{i\alpha}$ for different crack radius. Solid lines show the case of uniform stress distribution, while dashed lines show the evidence of stress distribution act at an angle ξ. It has been observed from the figure that the length of the yield zone increases as the stress applied at the infinite boundary of the plate is increased. Therefore, the load-carrying

capacity of the plate is more in case of stress distribution act at an angle ξ in comparison to the case of uniform remote stress distribution.

Figure 11 shows the variation between applied load ratio with normalized yield zone length for increasing crack angles β. The load-carrying capacity of the plate becomes larger in case of the small cracks ($\beta = 20°$) as compared to the big cracks ($\beta = 30°$). Moreover, the less load-bearing capacity of the plate is seen in the case of uniform stress distribution in comparison to the case of stress distribution act at an angle ξ.
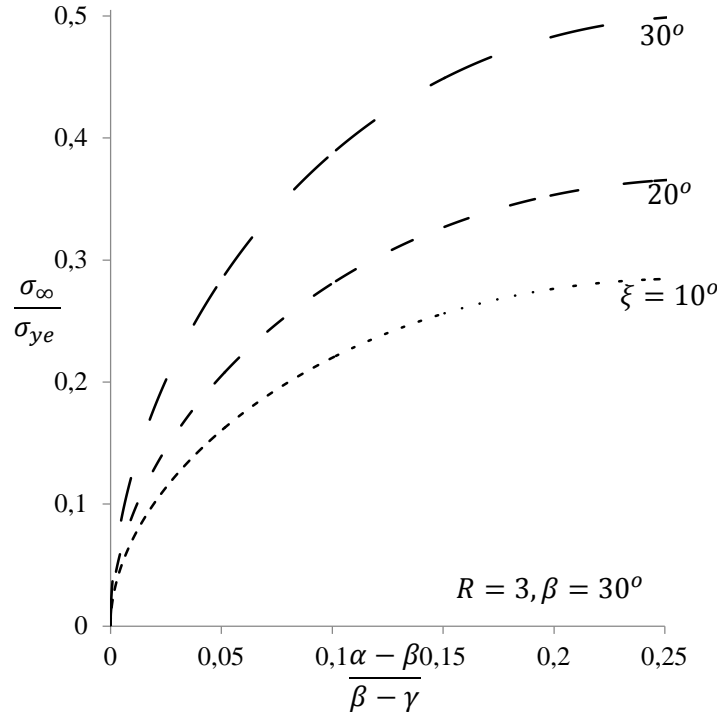
Fig. 12. $\dfrac{\sigma_\infty}{\sigma_{ye}}$ versus $\dfrac{\alpha-\beta}{\beta-\gamma}$ for different angles ξ

Finally, variation has been plotted in Fig. 12 between yield zone length and applied load ratio at different angles ξ. It is observed that as the angle ξ increases the load-bearing capacity of the plate will increases.

5. Conclusions

We considered the problem of multiple circular arc-cracks with coalesced yield zones. Analytical expressions for complex potential functions and stress intensity factors, for multiple circular-arc crack problems, were obtained for different types of mechanical loading conditions at the infinite boundary of the plate and variable yield stress distribution on the rims of yield zones. The analytical expressions for the opening-mode stress intensity factors given in equations (2), (4) are validated with the results provided by Tada [24]. The numerical study is carried out in the previous section to investigate the behaviour of yield zone length under variable loading conditions. It is seen that the yield zone length in the case of uniform stress distribution is larger as compared to point stress distribution. It is observed that as the angle of point stress distribution increases yield zone length decreases.

References

[1] Dugdale DS. Yielding of steel sheets containing slits. *J. Mech. Phys. of Solids*. 1960;8(2): 100-104.

[2] Smith E. The extension of circular-arc cracks in anti-plane strain deformation. *Int. J. Engg. Sci.* 1969;7(9): 973-991.

[3] Chen YZ. New singular integral equations for circular arc crack and rigid line problem. *Eng. Frac. Mech.* 1994;47(1): 139-145.

[4] Chen YZ, Hasebe N. Fredholm integral equation for the multiple circular arc crack problem in plane elasticity. *Archieve of Applied Mechanics*. 1997;67: 433-446.

[5] Bhargava RR, Kumar R. Two equal symmetric circular arc cracks in an elastic medium - the Dugdale approach. *J. of Eng. Math*. 1998;34: 359-368.

[6] Bhargava RD, Narayan R. Circular inhomogeneity and two cocentric symmetric circular arc cracks problem in an infinite isotropic elastic plate under tension. *Int. J. Fract*. 1975;11: 509-520.

[7] Jagannadham K. Two cocentric circular arc cracks in anti-plane strain. *Eng. Fract. Mech.* 1977;9: 211-215.

[8] Zhang XS. The new general solutions of an infinite plate weakend by a circular-arc crack of mode I, II, and III. *Eng. Fract. Mech.* 1989;34(2): 275-282.

[9] Shish YC, Lin YJ. An infinitely large plate weakened by a circular-arc crack subjected to partially distributed loads. *J. of Engineering Mathematics*. 2004;49: 1-18.

[10] Zhong Z, Meguid SA. Analysis of a circular arc-crack in piezoelectric materials. *International Journal of Fracture*. 1997;84: 143-158.

[11] Gao CF, Kessler H, Balke H. Green's functions for anti-plane deformations of a circular arc-crack at the interface of piezoelectric materials. *Archive of Applied Mechanics*. 2003;73: 467-480.

[12] Shen D, Fan T. Semi inverse method for solving circular arc crack problems. *Eng. Fract. Mech*. 2004;71(12): 1705-1724.

[13] Cheung YK, Woos CW, Wang YH. Stress intensity factor for a circular-arc crack by Boundary collocation method. *Eng. Frac. Mech.* 1989;34(4): 841-849.

[14] Bhargava RR, Kumar R. Dugdale model solution for an infinite plate with a circular arc crack. *Eng. Fract. Mech.* 1993;46(2): 256-273.

[15] Gdoutos EE, Kattis MA, Argyokosta VK, Koutsougeras TJ, Papanelopoulou MC. Two circular arc-cracks in an infinite elastic plate. *Eng. Fract. Mech.* 19991;39(4): 671-681.

[16] Bhargava RR, Hasan S. Arrest of opening of two circular-arc cracks with coalesced plastic zones. *Mechanics of Composite Materials*. 2001;37: 201-206.

[17] Pourseifi M, Rahimi AS. Ductile failure analysis of epoxy resin plates containing multiple circular arc cracks by means of the equivalent material concept. *International Journal of Mechanical and Materials Engineering*. 2021;16(1): 1-13.

[18] Shim DJ, Tang S, Kim TJ, Huh NS. Stress intensity factors for circular arc cracks in plates. In: *Proceedings of ASME, Pressure Vessels and Piping Conference PVP*. 2018.

[19] Milne-Thomson LM. *Plane Elastic System*. Springer; 1960.

[20] Muskhelishvili NI. *Some basic problems of mathematical theory of elasticity*. Leiden: P. Noordhoff; 1963.

[21] Akhtar N, Hasan S. Four circular-arc cracks with coalesced yield zones in an infinite plate: A theoretical approach. *Strength, Fracture and Complexity*. 2018;11(4): 279-294.

[22] Gdoutos EE. *Fracture Mechanics: An Introduction*. Springer; 2005.

[23] Byrd PF, Friedman MD. *Handbook of elliptical integrals for engineers and scientist*, Springer; 1971.

[24] Tada H, Paris PC, Erwin GR. *The stress analysis of cracks handbook*. 3rd ed. NY: ASME Press; 2000.

Appendix. A. Mathematical formulation for circular arc cracks

This appendix is given to discuss the theory and methodology for solving the circular-arc crack problem as given by Muskhelishvili [20], Thomson [19] without any change. Here, the hypothetical thing is that n circular-arc cracks L_i $(i = 1,2,3, \dots, n)$ are appeared in an infinite isotropic elastic-perfectly plastic plate along with one and the same circle $|z| = R$.

In the two-dimensional theory of elasticity for isotropic plates, stresses $(\sigma_{rr}, \sigma_{\theta\theta}, \sigma_{r\theta})$ are expressed in terms of two Muskhelishvili's complex potentials $\Phi(z), \Psi(z)$ as:

$$\sigma_{rr} + \sigma_{\theta\theta} = 2[\Phi(z) + \overline{\Phi(z)}], \tag{31}$$

$$\sigma_{rr} + i\sigma_{r\theta} = \Phi(z) + \overline{\Phi(z)} - \overline{z}\overline{\Phi'(z)} - \frac{\overline{z}}{z}\overline{\Psi(z)}. \tag{32}$$

Prime and bar over a function denote its first-order derivative and complex conjugate respectively.

For the solution of circular-arc crack problems, instead of potential function $\Psi(z)$ a new complex potential function $\Omega(z)$, related to $\Phi(z)$ and $\Psi(z)$, may be introduced as,

$$\Omega(z) = \overline{\Phi}\left(\frac{R^2}{z}\right) - \frac{R^2}{z}\overline{\Phi'}\left(\frac{R^2}{z}\right) - \frac{R^2}{z^2}\overline{\Psi}\left(\frac{R^2}{z}\right). \tag{33}$$

Equation (32) is then re-written using equation (33) as

$$\sigma_{rr} + i\sigma_{r\theta} = \Phi(z) + \Omega\left(\frac{R^2}{\overline{z}}\right) + \overline{z}\left(\frac{\overline{z}}{R^2} - \frac{1}{z}\right)\overline{\Psi(z)}. \tag{34}$$

Under the assumption

$$\lim_{r \to R}\left\{e^{-i\theta}\left(\frac{r}{R^2} - \frac{1}{r}\right)\Psi(z)\right\} = 0,$$

equation (34) may be converted into two subproblems of linear relationship, (since $z\overline{z} = r^2$)

$$\Phi^+(t) + \Omega^-(t) = \sigma_{rr}^+ + i\sigma_{r\theta}^+, \quad \Phi^-(t) + \Omega^+(t) = \sigma_{rr}^- + i\sigma_{r\theta}^-, \tag{35}$$

where $t = Re^{i\theta}$ be any point on $L = \cup_{i=1}^{n} L_i$, $\sigma_{rr}^{\pm} + i\sigma_{r\theta}^{\pm}$ represent stress components acting over the rims of the crack L and superscript (+) and (-) refers to the value of t from the inside $(r < R)$ and from outside $(r > R)$ of the circle on which cracks exist.

Adding and subtracting the equations in Eq.(35), one gets

$$[\Phi(t) + \Omega(t)]^+ = 2p(t), \quad [\Phi(t) + \Omega(t)]^- = 2q(t), \tag{36}$$

where

$$2p(t) = (\sigma_{rr}^+ + \sigma_{rr}^-) + i(\sigma_{r\theta}^+ + \sigma_{r\theta}^-), \quad 2q(t) = (\sigma_{rr}^+ - \sigma_{rr}^-) + i(\sigma_{r\theta}^+ - \sigma_{r\theta}^-). \tag{37}$$

In the absence of the body forces, the general solution of the boundary value problems expressed in Eq. (36) may be written directly from [20], as

$$\Phi(z) = \Phi_0(z) + \frac{1}{2X(z)}\left\{P_n(z) + \frac{D_1}{z} + \frac{D_2}{z^2}\right\} + \frac{D_0}{2} + \frac{\overline{\Gamma'}}{2z^2}, \tag{38}$$

$$\Omega(z) = \Omega_0(z) + \frac{1}{2X(z)}\left\{P_n(z) + \frac{D_1}{z} + \frac{D_2}{z^2}\right\} - \frac{D_0}{2} - \frac{\overline{\Gamma'}}{2z^2}, \tag{39}$$

where

$$\Phi_0(z) = \frac{1}{2\pi i X(z)}\int_L \frac{X(t)p(t)dt}{t-z} + \frac{1}{2\pi i}\int_L \frac{q(t)dt}{t-z},$$

$$\Omega_0(z) = \frac{1}{2\pi i X(z)}\int_L \frac{X(t)p(t)dt}{t-z} - \frac{1}{2\pi i}\int_L \frac{q(t)dt}{t-z},$$

$$X(z) = \prod_{k=1}^n \sqrt{z-a_k}\sqrt{z-b_k},$$

$$P_n(z) = C_0 z^n + C_1 z^{n-1} + C_2 z^{n-2} + \cdots,$$

a_k, b_k denotes the endpoints of kth crack.

Constants $D_i (i = 0,1,2)$ and polynomial $P_n(z)$ are determined from the boundary conditions of the considered problem and the condition of single valuedness of displacement around the rims of the cracks or cuts,

$$2(\kappa + 1)\int_{L_i} \frac{P_n(z)}{X(z)}dz + \kappa \int_{L_i}[\Phi_0^+(z) - \Phi_0^-(z)]dz + \int_{L_i}[\Omega_0^+(z) - \Omega_0^-(z)]dz = 0. \tag{40}$$

Stress intensity factor for mode-I type deformation at each crack tip $z = a$ and $z = b$ may be calculated from the formulae given in [4],

$$K = K_1 - iK_2 = -2\sqrt{2\pi}\lim_{z\to a}\sqrt{(z-a)e^{-i\left(\frac{\pi}{2}+\alpha\right)}}\Phi(z), \tag{41}$$

$$K = K_1 - iK_2 = 2\sqrt{2\pi}\lim_{z\to b}\sqrt{(z-b)e^{-i\left(\frac{3\pi}{2}-\alpha\right)}}\Phi(z). \tag{42}$$

Mathematical formulations given in this appendix are taken from [19], [20], and [4] to make the paper easily understandable and self-sufficient.

Appendix B. List of constants

$D_i(i = 0,1,2), C_i(i = 0,1,2)$	constants of the problem.
E	Young's modulus.
$F(\theta,k), E(\theta,k), \Pi(\theta,\alpha^2,k)$	incomplete elliptic integral of first, second and third kind, respectively.
$F(k), E(k)$	complete elliptic integral of first, second kind, respectively.
$L_i(i = 1,2,3,4)$	circular-arc cracks.
$P_n(z)$	polynomial of degree n.
$p(t), q(t)$	applied stresses on the yield zones.
$z = re^{i\theta}$	complex variable.
Γ'	$-\frac{1}{2}(N_1 - N_2)e^{-2i\alpha}, N_1$ and N_2 are the values of principal stresses at infinity, α be the angle between N_1 and the ox-axis.

$\Gamma_i (i = 1,2,\ldots,6)$	developed plastic/ yield zones.
$\Omega(z) = \omega'(z), \Phi(z) = \phi'(z)$	complex stress functions.
γ	Poisson's ratio.
μ	shear modulus.
κ	$= \frac{3-\gamma}{1+\gamma}$ for the plane-stress,
	$= 3 - 4\gamma$ for the plane-strain.
$\sigma_{rr}, \sigma_{\theta\theta}, \sigma_{r\theta}$	components of stress in polar coordinates.
σ_∞	remotely applied stress at infinite boundary of the plate.
σ_{ye}	yield stress of the plate.

MOLECULAR DYNAMICS STUDY OF STRESS-STRAIN CURVES FOR γ-Fe AND HADFIELD STEEL IDEAL CRYSTALS AT SHEAR ALONG THE <111> DIRECTION

G.M. Poletaev[1], R.Y. Rakitin[2]

[1]Altai State Technical University, Lenin Str. 46, 656038 Barnaul, Russia

[2]Altai State University, Lenin Str. 61, 656049 Barnaul, Russia

*e-mail: gmpoletaev@mail.ru

Abstract. The molecular dynamics method was used to simulate the shear along the <111> direction in Hadfield steel and a pure fcc Fe crystal. The stress-strain curves are obtained depending on the shear rate, the size of the computational cell, and temperature. It is shown that the shear rate in the range of 10–100 m/s has little effect on the theoretical strength at a constant temperature. With increasing temperature, the slope of the stress-strain dependences in the elastic region decreased, which is due to the temperature dependence of the elastic moduli. In addition, the temperature significantly influenced the theoretical strength – with an increase in temperature, plastic deformation began in ideal crystals at lower deformation values. Moreover, this dependence was more pronounced for a pure fcc Fe crystal than for Hadfield steel, which initially had structural imperfections caused by the presence of impurities that facilitate the initiation of plastic shears in a pure crystal. In this regard, at medium and low temperatures, the theoretical strength of pure iron was higher than that of steel. But at high temperatures (above 1200 K), its values for both materials became almost the same.

Keywords: molecular dynamics, theoretical strength, stress-strain curve, Hadfield steel

1. Introduction

Hadfield steel, due to its excellent ability to work hardening [1,2], has great practical importance and a long history of research into its unique properties. At the same time, today there are very few works devoted to modeling its atomic structure and the processes occurring in it under conditions of deformation at the atomic level, which is due, in particular, to the complexity of modeling such multicomponent systems. Currently, there are a number of issues related to the mechanisms of plastic deformation at the atomic level in steels and which can be solved mainly by computer simulation methods. Such questions include, for example, the features of the formation and propagation of dislocations depending on various factors, the mechanisms of interaction with each other, grain boundaries, twins, and other defects.

The presence of impurity atoms in the metal lattice, as is the case in steel, complicates the process of dislocation motion. Impurity atoms of light elements (in this case, it is mainly carbon), even at low concentrations, strongly affect the mechanical properties of metals and alloys. Interacting with dislocations and preventing their movement, impurities lead to an increase in the strength, hardness, and frictional properties of metals, together, as a rule, with brittleness [3-5]. The energy of their bonding with dislocations is positive, as a result of which they tend to be fixed on dislocations and form the so-called Cottrell atmosphere [6-8]. In

addition to the Cottrell mechanism, impurities, like most other defects, are effective stoppers for moving dislocations, which was confirmed not only by experimental studies but also by computer simulations [9,10]. In [9], for example, using molecular dynamics, it was found that the critical stress at which a dislocation begins to slip in α-Fe increases with an increase in the concentration of carbon atoms. In [10], also carried out using the method of molecular dynamics, it was shown that with an increase in the carbon concentration, the slip rate of dislocations in iron decreases. In metals with an fcc lattice, in addition to the aforementioned mechanisms of deceleration of dislocations by impurities, the Suzuki mechanism is also connected – the pinning of impurity atoms at a stacking fault between partial dislocations [3,4].

This work is devoted to the study of stress-strain curves depending on various factors for γ-Fe and Hadfield steel ideal crystals at shear along the <111> direction. Separate consideration of the behavior of an ideal crystal of fcc iron is associated with the desire to highlight the role of impurities in Hadfield steel – manganese and carbon. It is known that in crystals with an fcc lattice, the {111}<110> slip system is predominant [11,12]. The choice of the <111> direction of shear is due to two reasons. First, in this case, two slip systems are involved, and it is of interest to study the joint operation and interaction of dislocations of two different systems. Second, this model is supposed to be used to further study the plastic deformation of samples containing a system of parallel twins oriented perpendicular to the shear direction.

2. Description of the model

Hadfield steel, as is known, is a multi-component system and, in addition to classical iron, manganese, and carbon, may contain some other alloying elements [1,2]. In this study, we limited to a system that included three elements: γ-Fe as a matrix, Mn, and C.

To describe the Fe-Fe interactions in austenite matrix, it was used Lau EAM potential [13], which reproduces well the structural, energy, and elastic characteristics of austenite. These are classic EAM potentials, where the energy of the i-th atom is calculated as the sum of the pair and multiparticle components:

$$E_{\alpha,i} = -A_\alpha \sqrt{\sum_{j \neq i} \rho_{\beta\alpha}(r_{ij})} + \frac{1}{2}\sum_{j \neq i} \phi_{\beta\alpha}(r_{ij}),$$

$$\rho_{\beta\alpha}(r_{ij}) = t_1(r - r_{c,\rho})^2 + t_2(r - r_{c,\rho})^3, \qquad r \leq r_{c,\rho}, \qquad (1)$$

$$\phi_{\beta\alpha}(r_{ij}) = (r - r_{c,\phi})^2(k_1 + k_2 r + k_3 r^2), \qquad r \leq r_{c,\phi}.$$

We drew attention to this potential primarily because it was tested in detail in [14] when describing the structural, energy, and elastic characteristics of austenite.

For all other five interactions, Morse potentials are proposed, the parameters of which were found from various experimental characteristics, in particular, the energy of dissolution and the energy of migration of an impurity in fcc iron crystal, the radius of atoms, their electronegativity, mutual binding energy, etc. The Morse potential is pair, but it is often used in molecular dynamics calculations, including the description of interatomic interactions in metals. Pair potentials are relatively often used by various researchers to describe interatomic interactions in metal-impurity systems [15-21]. The Morse potential determines the interaction energy of a pair of atoms located at a distance r from each other:

$$\varphi(r) = D\beta e^{-\alpha r}(\beta e^{-\alpha r} - 2), \qquad (2)$$

where α, β, D are the potential parameters.

All Morse potentials were found for a cutoff radius of 4.7 Å, i.e. taking into account the three coordination spheres in fcc Fe. Considering a larger number, for example, of five spheres, as we did, for example, in [20-22], leads to a significant slowdown in the counting

speed compared to taking into account three spheres, but at the same time, to a relatively small increase in accuracy, not exceeding a few percent.

Table 3. Parameters of Morse potentials for the considered interactions

Bond	α (A$^{\circ-1}$)	β	D eV)
Fe-C	1.82	41	0.41
C-C	1.97	50	0.65
Mn-Mn	1.321	39.792	0.373
Mn-Fe	1.306	38.030	0.413
Mn-C	1.87	43	0.777

The standard ratio of components was used: Mn – 13 wt.% and C – 1.2 wt.% (12.63 at.% и 5.33 at.%, respectively) [1,2]. Mn atoms were introduced into fcc iron lattice randomly by replacing Fe atoms. The sizes of Fe and Mn atoms are very close, therefore, Mn atoms create small distortions in the iron lattice. But at the same time, Mn atoms have a much stronger bond with carbon atoms. The binding energy of Mn and C atoms in austenite lattice is very high – 0.35 eV, according to [23], which is approximately the same as, for example, the binding energy of carbon atoms with vacancies (0.37-0.41 eV [24]). Both of them are a kind of effective "traps" for impurity carbon atoms, not allowing them, in particular, to form clusters on dislocations and grain boundaries. This has a positive effect on the mechanical properties of steel, since these accumulations of carbon atoms, as a rule, lead to the development of negative phenomena such as embrittlement and aging [6].

In fcc, hcp, and bcc lattices of metals, impurity atoms of light elements (such as C, N, O, etc.), according to numerous studies, occupy octahedral voids, in which, as is known, the largest amount of free volume of the crystal lattice is concentrated [3,4]. In this connection, carbon atoms were introduced into the octahedral voids closest to Mn atoms. The number of carbon atoms corresponded to a given concentration. The choice of Mn atoms near which C atoms were introduced, as well as the selection of one of the neighboring octahedral voids, were made randomly.

In pure fcc iron, which was considered in this work for comparison with Hadfield steel, the type of the crystal lattice remained constant over the entire temperature range; the polymorphic transformation was not taken into account in this work. As mentioned above, pure austenite was considered to determine the contribution of Mn and C impurities in the processes under study.

The computational cell of fcc Fe contained 122760 atoms (of Hadfield steel – 130173 atoms) and had a length of 27.2 nm, a height of 20.3 nm, and a thickness of 2.5 nm. Along the X and Y axes (Fig. 1), an endless repetition of the structure was simulated, i.e. periodic boundary conditions were imposed. The shear in the model was initiated by the displacement of atoms in the upper and lower regions highlighted by light gray in Fig. 1 in opposite directions along and against the Y-axis (the [111] direction). The areas in the upper and lower parts of the cell in the course of the computer experiment moved as a whole. The movement of the remaining atoms in the computational cell was not limited; it was described by the classical equations of motion of Newton.

The strain rate usually varies from 10^{-5} to 10^{5} s^{-1} [25]. At rates above 10^{3} s^{-1}, deformation is usually considered high-rate, which is characterized by a significant increase in strength and, as a rule, a brittle nature of fracture [25]. Due to the peculiarities of the molecular dynamics method, the deformation rate in the model can be set in the range 10^{8}-10^{11} s^{-1}. However, this does not mean that the imaginary "clamps" on the sample move at a tremendous speed, their speed is quite ordinary: 10^{0}-10^{3} m/s. Such a high rate of

deformation is caused to the very small size of the sample (as a rule, only a few tens of nm), due to which the rate of change in the relative deformation is relatively high.
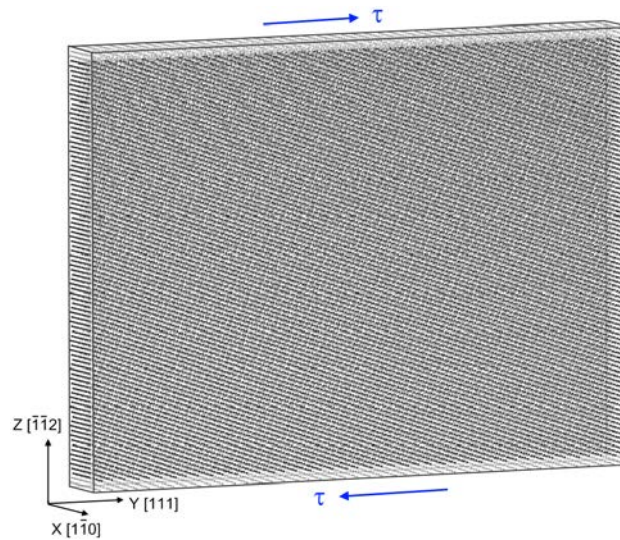

Fig. 1. Computational cell for modeling shear along the [111] direction (Y axis)

The time integration step in the molecular dynamics method was 2 fs. The temperature in the model was set through the initial velocities of the atoms according to the Maxwell-Boltzmann distribution, taking into account the change in the lattice parameter due to thermal expansion. To keep the temperature constant during the simulation, a Nose-Hoover thermostat was used.

3. Results and discussion

In the present work, we investigated the effect of strain rate, computational cell size, and temperature on stress-strain curves. Figure 2a shows stress-strain plots obtained at shear rates (displacements relative to each other of the upper and lower regions of the computational cell) of 10, 20, 50, and 100 m/s.

The theoretical shear strength of metal crystals is known to be very high and can reach more than ten GPa [26]. The introduction of just one dislocation into a pure crystal in the molecular dynamics model reduces the strength to several hundred MPa [27]. As seen from Fig. 2, plastic deformation in a pure fcc iron crystal at a temperature of 300 K began only when shear deformation along the [111] direction was more than 12% and shear stress of 9 GPa. It should also be emphasized that the crystal was initially not only ideal but also did not contain any sources of dislocation formation, even a free surface. In this regard, the intervals of elastic deformation on the graphs were relatively large.

The slope of the stress-strain dependence, as can be seen, does not change with increasing strain rate. The slope is essentially the shear modulus in Hooke's equation, i.e. the resistance of the crystal to elastic deformation does not change with an increase in the rate of this deformation. However, at the same time, as seen in Fig. 2a, the value of deformation changes slightly at which irreversible plastic shears begin in the computational cell. The crystal response is, as it were, lagged at very high shear rates. Because of this "lag" connected with the finite speed of propagation of elastic waves, the stepped nature of the stress-strain dependence at high strain rates is associated. Moreover, the higher the deformation rate, the greater these steps (in Fig. 2a, for example, steps for speeds of 50 and 100 m/s are clearly visible).

The results obtained at rates of 10 and 20 m/s were almost the same. However, it was decided to use a shear rate of 10 m/s for further research. In units of relative deformation, this is $4.9 \cdot 10^8$ s^{-1}.

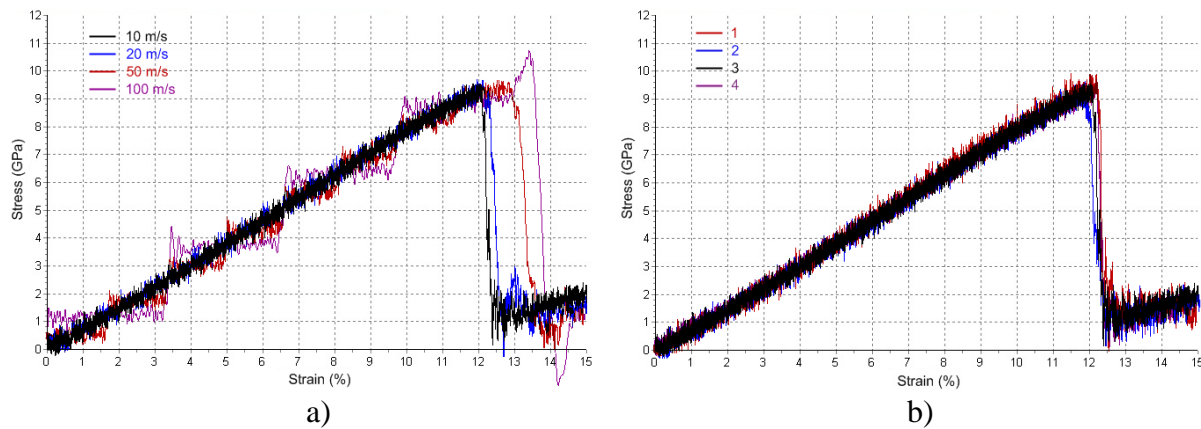<div align="center">a)   b)</div>

Fig. 2. Stress-strain curves for a pure fcc iron crystal at a temperature of 300 K: a) at different shear rates along the Y axis of 10, 20, 50, and 100 m/s; b) for four sizes of the computational cell at a shear rate of 10 m/s: 1 – 12.4×9.2 nm, 2 – 17.3×12.9 nm, 3 – 22.3×16.8 nm, 4 – 27.2×20.3 nm

The second step was to study the effect of the size of the computational cell on the stress-strain curves. For this, we considered four cells of different sizes along the Y and Z axes: 12.4×9.2 nm, 17.3×12.9 nm, 22.3×16.8 nm, 27.2×20.3 nm. The thickness in all cases was the same – 2.5 nm. According to the results obtained (Fig. 2b), all the considered sizes of the computational cells give identical stress-strain dependences. The differences are completely insignificant and relate mainly to the plastic mode of deformation. In the rest of the computer experiments, we used cells No. 4 – 27.2×20.3 nm.

Figure 3 shows the dependences τ(ε) for an ideal crystal of fcc iron (a) and Hadfield steel (b) at different temperatures. It is known that elastic moduli in a wide temperature range decrease almost linearly with increasing temperature, which is usually associated with thermal expansion [28]. In addition, it can be seen that the temperature significantly affects the probability of dislocation formation and the onset of the plastic phase – with increasing temperature, plastic deformation begins earlier. Moreover, this dependence is quite strong – at a temperature of 100 K, plastic shears in fcc Fe began at a deformation of about 14.5%, and at a temperature of 1200 K – already at 8%. This is most likely explained by the fact that the formation of dislocation is an activation process (i.e. certain finite activation energy is required for the formation of a dislocation), which obeys the classical Arrhenius law, i.e. the probability of dislocation formation is proportional to *exp(-E/kT)*, where *E* is the activation energy of plastic shear formation in the considered computational cell, *k* is the Boltzmann constant, and *T* is the temperature.

The shift of the point of the beginning of the plastic phase with increasing temperature occurs faster in iron than in steel, and at a temperature of 1200 K they almost coincide. At medium and low temperatures, the curves for steel and pure austenite differ greatly – in steel the plastic phase occurs at much lower deformation values than in pure iron. For example, at a temperature of 300 K, dislocations are formed in steel already at a shear of 9%, whereas in fcc iron at 12% (black graphs in Fig. 3). This is explained by the presence of imperfections in the steel, distortions of the crystal lattice, caused by the presence of impurities, which facilitates the initiation of plastic shears, i.e. the formation of dislocations in a pure crystal.

Another noticeable difference between the graphs for iron and steel is that in steel, after the onset of the plastic phase, the stresses remain approximately two times higher than in iron.

As for the similarity, it is the same slope of the dependencies in the elastic region for steel and iron at the same temperatures. This is due to the fact that, despite significant differences in the strength of iron and steel, their elastic characteristics, as a rule, are very close [29].

<div align="center">a)   b)</div>
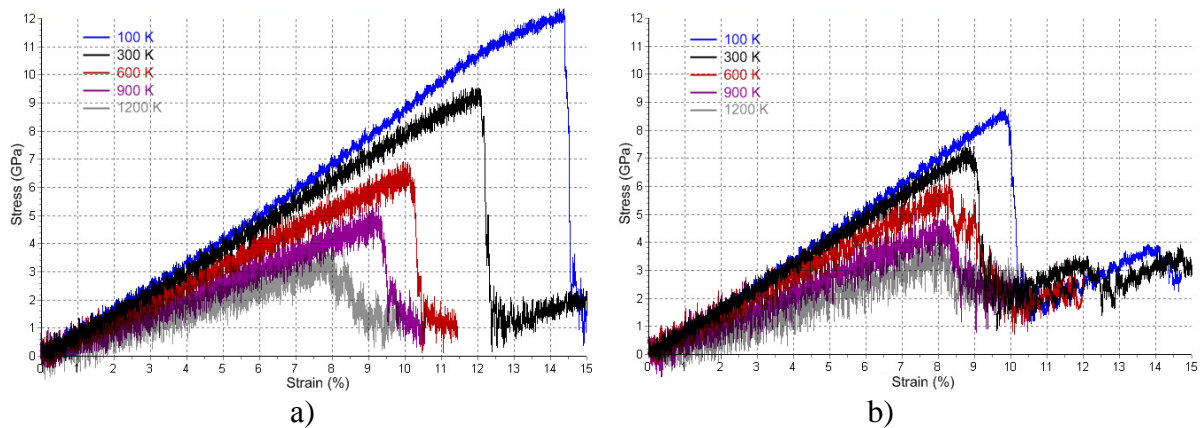
Fig. 3. The dependences $\tau(\varepsilon)$ for an ideal crystal of fcc iron (a) and Hadfield steel (b) at different temperatures

Figure 4 shows examples of plastic shears in the computational cells of fcc iron and Hadfield steel deformed by 15%. For this type of loading, shears appear in two planes of the (111) type. The effect of impurities in steel is clearly seen: despite the fact that plastic shears are initiated earlier in steel than in pure iron dislocations propagate and develop much weaker, slip bands are smaller and their number is fewer (Fig. 4b). In pure iron, the process of formation of deformation twins was also more intense – wide vertical dark bands in Fig. 4a.

<div align="center">a)   b)</div>
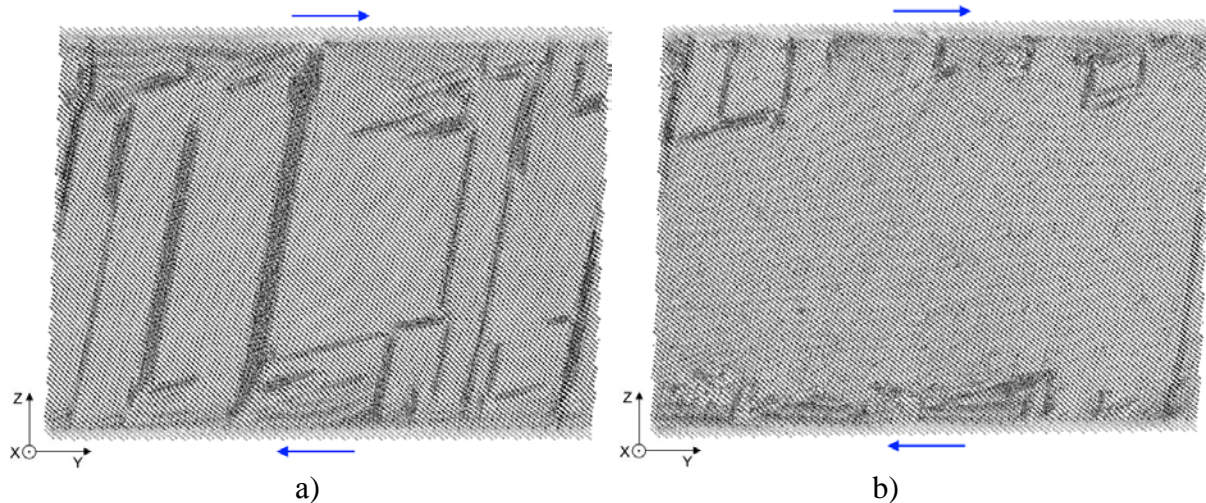
Fig. 4. Dislocations in pure fcc Fe (a) and Hadfield steel (b) formed as a result of shear along the Y axis [111] by 15%. The computational cell is rotated so that the slip bands are better visible

4. Conclusion

The molecular dynamics method was used to simulate the shear along the <111> direction in Hadfield steel and a pure fcc Fe crystal. The stress-strain curves are obtained depending on the shear rate, the size of the computational cell, and temperature. It is shown that the shear rate in the considered range of 10–100 m/s has little effect on the theoretical strength at a constant temperature. One should, of course, expect a change in the theoretical strength at high strain rates, close in order to the speed of sound in the metal.

With increasing temperature, the slope of the stress-strain dependences in the elastic region decreased, which is due to the temperature dependence of the elastic moduli. In addition, the temperature significantly influenced the theoretical strength – with an increase in temperature, plastic deformation began in ideal crystals at lower deformation values. Moreover, this dependence was more pronounced for a pure fcc Fe crystal than for Hadfield steel, which initially had structural imperfections caused by the presence of impurities that facilitate the initiation of plastic shears in a pure crystal. In this regard, at medium and low temperatures, the theoretical strength of pure iron was higher than that of steel. But at high temperatures (above 1200 K), its values for both materials became almost the same.

For the considered type of loading, shear along the <111> direction, dislocations arose in two slip systems. Moreover, in steel, due to the action of impurities, plastic shears occurred at lower deformation values than in pure iron, but the dislocations propagated and developed much weaker, slip bands were noticeably smaller, and their number was also smaller.

References
[1] Zhang FC, Lv B, Wang TS, Zheng CL, Zhang M, Luo HH, Liu H, Xu AY. Explosion hardening of Hadfield steel crossing. *Materials Science and Technology*. 2010;26(2): 223-229.
[2] Chen C, Lv B, Ma H, Sun D, Zhang F. Wear behavior and the corresponding work hardening characteristics of Hadfield steel. *Tribology International.* 2018;121: 389-399.
[3] Goldschmidt HJ. *Interstitial Alloys*. London: Butterworths; 1967.
[4] Toth LE. *Transition metal carbides and nitrides.* New York: Academic Press; 1971.
[5] Poletaev GM, Zorya IV. Effect of light element impurities on the edge dislocation glide in nickel and silver: molecular dynamics simulation. *Journal of Experimental and Theoretical Physics.* 2020;131(3): 432-436.
[6] Clouet E, Garruchet S, Nguyen H, Perez M, Becquart CS. Dislocation interaction with C in α-Fe: A comparison between atomic simulations and elasticity theory. *Acta Materialia.* 2008;56: 3450-3460.
[7] Veiga RGA, Goldenstein H, Perez M, Becquart CS. Monte Carlo and molecular dynamics simulations of screw dislocation locking by Cottrell atmospheres in low carbon Fe–C alloys. *Scripta Materialia.* 2015;108: 19-22.
[8] Poletaev GM, Zorya IV, Rakitin RY, Glubokova LG. The binding energy of impurity atoms C, N, O with edge dislocations and the energy of their migration along dislocation core in Ni, Ag, Al. *Materials Physics and Mechanics.* 2020;44(3): 404-410.
[9] Granberg F, Terentyev D, Nordlund K. Interaction of dislocations with carbides in BCC Fe studied by molecular dynamics. *Journal of Nuclear Materials.* 2015;460: 23-29.
[10] Njoroge KD, Rading GO, Kihiu JM, Witcomb MJ, Cornish LA. The impact of interstitial carbon on dislocation motion in the alpha-Fe lattice. *International Journal of Computational Engineering Research.* 2014;4: 5-9.
[11] Friedel J. *Dislocations*. Oxford: Pergamon press; 1964.
[12] Hirth JP, Lothe J. *Theory of Dislocations.* 2nd ed. NY: Wiley; 1982.
[13] Lau TT, Forst CJ, Lin X, Gale JD, Yip S, Van Vliet KJ. Many-body potential for point defect clusters in Fe-C alloys. *Physical Review Letters.* 2007;98: 215501.
[14] Oila A, Bull SJ. Atomistic simulation of Fe–C austenite. *Computational Materials Science.* 2009;45(2): 235-239.
[15] Xie JY, Chen NX, Shen J, Teng L, Seetharaman S. Atomistic study on the structure and thermodynamic properties of Cr_7C_3, Mn_7C_3, Fe_7C_3. *Acta Materialia.* 2005;53(9): 2727-2732.

[16] Ruda M, Farkas D, Abriata J. Interatomic potentials for carbon interstitials in metals and intermetallics. *Scripta Materialia.* 2002;46: 349-355.

[17] Vashishta P, Kalia RK, Nakano A, Rino JP. Interaction potentials for alumina and molecular dynamics simulations of amorphous and liquid alumina. *Journal of Applied Physics.* 2008;103(8): 083504.

[18] Liu SJ, Shi SQ, Huang H, Woo CH. Interatomic potentials and atomistic calculations of some metal hydride systems. *Journal of Alloys and Compounds.* 2002;330-332: 64-69.

[19] San Miguel MA, Sanz JF. Molecular-dynamics simulations of liquid aluminum oxide. *Physical Review B.* 1998;58(5): 2369-2371.

[20] Poletaev GM, Zorya IV, Rakitin RY, Iliina MA. Interatomic potentials for describing impurity atoms of light elements in fcc metals. *Materials Physics and Mechanics*. 2019;42(4): 380-388.

[21] Poletaev GM, Zorya IV. Influence of light impurities on the crystal-melt interface velocity in Ni and Ag. Molecular dynamics simulation. *Technical Physics Letters.* 2020;46: 575-578.

[22] Poletaev GM, Novoselova DV, Zorya IV, Starostenkov MD. Formation of the excess free volume in triple junctions during nickel crystallization. *Physics of the Solid State.* 2018;60: 847-851.

[23] Massardier V, Le Patezour E, Soler M, Merlin J. Mn-C interaction in Fe-C-Mn steels: study by thermoelectric power and internal friction. *Metallurgical and Materials Transactions A.* 2005;36A: 1745-1755.

[24] Slane JA, Wolverton C, Gibala R. Carbon-vacancy interactions in austenitic alloys. *Materials Science and Engineering A.* 2004;370(1-2): 67-72.

[25] Evstifeev AD, Gruzdkov AA, Petrov YV. Dependence of the type of fracture on temperature and strain rate. *Technical Physics. The Russian Journal of Applied Physics.* 2013;58(7): 989-993.

[26] Bukreeva KA, Iskandarov AM, Dmitriev SV, Mulyukov RR, Umeno Y. Theoretical shear strength of fcc and hcp metals. *Physics of the Solid State.* 2014;56: 423-428.

[27] Krasnikov VS, Kuksin AY, Mayer AE, Yanilkin AV. Plastic deformation under high-rate loading: the multiscale approach. *Physics of the Solid State.* 2010;52: 1386-1396.

[28] Shtremel MA. *Strength of alloys. P.1. Lattice defects.* Moscow: Metallurgiya; 1982. (In Russian)

[29] Lide DR. (Ed.) *CRC Handbook of Chemistry and Physics* Boca Raton: CRC Press; 2005.

INVESTIGATION OF WEAR BEHAVIOUR OF DUPLEX STAINLESS STEELS (DSS) USING DESIGN OF EXPERIMENTS

C. Rajkumar, J. Udaya Prakash, Sachin Salunkhe[*], S. Jayavelu

Department of Mechanical Engineering, Vel Tech Rangarajan Dr. Sagunthala, R&D Institute of Science and Technology, Avadi, Chennai – 600 062, India

*e-mail: drsalunkhesachin@veltech.edu.in

Abstract. Duplex Stainless Steels (DSS) fabricated from powder metallurgy method finds many applications in offshore, paper, and petrochemical industries. DSS consists of austenite and ferrite in equal volume in microstructure, used in various industries due to combined mechanical and corrosion properties. The need of DSS is increasing every year in the automobile industries. In this paper, two-phase structure steels manufactured through the powder metallurgy route are presented. DSS (A and B) are the two compositions made by pre-alloyed powders (310L & 430L) adding with elemental powders such as chromium, molybdenum, and nickel. The powders were mixed in a pot mill for 12 hours. Sintering of powder preforms was carried out at 1350°C in partial vacuum and hydrogen atmospheres respectively. Sintered compacts subjected to forging operation at 1150ºC and quenched in water. DSS (A and B) steels have exhibited the coefficient of friction of 0.52 to 0.602.
Keywords: wear, duplex stainless steels, design of experiments, powder metallurgy

1. Introduction

Duplex Stainless Steels (DSS) consists of approximately equal volume fraction of austenite (fcc) structure and ferrite (bcc) structure. Austenite has a fcc lattice and ferrite has a bcc lattice [1]. This combined microstructure provides DSS with good resistance to stress corrosion better than Austenitic Stainless Steels (ASS) [2]. The microstructure plays a crucial role in the wear behaviour of metals [3]. The applications of DSS are in chemical plants, paper industries, and modern nuclear power plants. But these DSS have the drawback of forming embrittlement at a higher temperature of more than 250ºC [4]. The formation of embrittlement is due to the formation of sigma and chi phases in the temperature range of 700-900ºC [5]. The embrittlement formed below 500ºC is popularly called 475ºC embrittlement, various mechanical properties have changed in the sigma and chi phases [6]. DSS can be produced by various manufacturing methods such as casting, powder metallurgy, etc. Generally, Powder metallurgy provides different methods of fabricating DSS. In that, the first method is obtaining stainless steel with the required duplex composition using pre-alloyed powders [7]. The second method is mixing powders such as chromium, nickel, powders with pre-alloyed powders to achieve duplex structure [8-9]. Sintering is an essential step in powder metallurgy which affects phase balance and corrosion properties of sintered steels. By optimising sintering processing parameters, mechanical and corrosion features can be achieved [10]. The wear characteristics of powder metallurgy DSS are increased by adding aluminum oxide and yttria to the stainless steel [11-12]. The wear characteristics of Nitrogen sintered DSS were better than argon sintered DSS, owing to the presence of more lamellar constituents with ferrite matrix [13]. The wear behaviour of DSS is mainly influenced by

chromium content in DSS [14]. The wear characteristics of aluminum metal matrix composite influenced by sliding distance and are the main factor driving the wear features of composite [15]. Design of Experiments (DOE) employs the statistical technique to influence the variable used to find the outcome of the required process [16]. Very few works of literature are available in the specific wear rate and coefficient of friction for DSS analysed by DOE. In this paper the fabrication of DSS by using powder metallurgy route and the wear behaviour such as specific wear rate and coefficient of friction by Design of Experiments are present.

2. Experimental procedure

Two atomized powders are as 310L and 430L are combined with chromium, nickel, molybdenum, and manganese mixed for 12 hours in a pot mill (INSMART Systems).In Universal Testing Machine (FIE Model) at 550 MPa, the powders were compacted to the appropriate shape and size. The green compacts were sintered in a hot press (BIRSON, 100 T) at a temperature of 1350°C. At 1150°C Sintered compacts were forged and followed by quenching. The chemical constituents of pre-alloyed powders and DSS are given in Tables 1 and 2 respectively.

Table 1. Chemical constituents of stainless steels powders [17]

Powder Grade	Elements (%wt)						
	Ni	Cr	C	Si	Mn	Mo	Fe
310L	10	24	0.02	0.30	2.00	0.3	Balance
430L	-	16.6	0.02	1.20	0.10	-	Balance

Table 2. Chemical constituents of DSS [17]

Composition	Elemental Concentration (%wt)									
	Ni	Cr	C	Si	Mn	Mo	Fe	Ni_{eq}	Cr_{eq}	PREN
DSS A	5	20.3	0.02	0.75	1.05	0.15	Bal.	6.1	21.57	20.53
DSS B	8.5	23.27	0.018	0.67	0.945	1.13	Bal.	9.51	25.41	27.01
DSS A : 50 % 310L + 50 % 430L										
DSS B : 45 % 310L + 45 % 430L +4% Ni+ 5 %Cr + 1 % Mo										

Wear test – pin on disc machine. A Pin-on-disctype machine is deployed to find the wear properties of the stainless steel PM duplex preforms. Sliding velocity, sliding distance, load, and temperature conditions are the main variables which influence friction and wear. The wear testing unit consists of a rotating spindle attached by M6 counter bolt to the disc. A pivoting hanging arm has the provision to insert the pin and the holder to get them to have access to the diameter of the track. With the help of a screw, the pin was firmly fixed in the holder. The lever's arm rested on that disk after confirming the diameter of the track. The sample of the pin is shown in Fig. 1.

The pin size is 6 mm in diameter and 34 mm in length respectively. DSS were used as the pin material, counter disc with 65 mm diameter and 10 mm thickness was fabricated using high carbon high chromium steel (die steel). The constituents of high carbon high chromium steel are chromium 11%, manganese, silicon 0.60%, cobalt 1.0%, carbon 1%, and remaining iron. The hardness of the counter disc is 62 HRC whereas the hardness for the pin is 70 HRA. The disc and the pin were washed with acetone to confirm that the wear tests were carried out in the dry sliding condition. The weight-loss calculation was used to determine the wear rate. At 20 N and 30 N, the tests were performed. The wear test is performed at ambient temperature. The duration of the test is 6 minutes.

Fig. 1. Sample of pin

Taguchi method. The systematic application of design and analysis of experiments for the purpose of designing and improving product quality is the Taguchi method. Taguchi's approach to parametric design provides the design engineer with an efficient and systematic method for determining near optimum design parameters. The Taguchi method uses orthogonal arrays (OA) from DoE theory to study a large number of variables with a small number of experiments. To design an experiment is to select the most suitable OA and to assign the parameters and interactions of interest to the appropriate columns.

Taguchi method uses a statistical measure of performance called signal-to-noise (S/N) ratio which is maximized to obtain optimal parametric combination. Usually, there are three types of signal-to-noise ratios such as lower-the-better (LTB), higher-the-better (HTB), and nominal-the-best (NTB)

The type of S/N ratios used in this research is smaller the better for SWR and COF.

Smaller the better: Here, the quality characteristic is continuous and non-negative. It can take any value between 0-∞. The desired value (the target) is zero. These problems are characterized by the absence of scaling factors (ex: surface roughness, specific wear rate, coefficient of friction, etc.). The S/N ratio (η) is given by

$\eta = -10 \log \left[\frac{1}{n} \sum_{i=1}^{n} Y_i^2 \right],$

where n is the number of replications and Y is the responses.

The process parameters and their levels are tabulated in Table 3.

Table 3. Process parameters and their levels

Level	Load (N)	Material	Condition	Atmosphere
1	20	DSS A	Sintered	Partial Vacuum
2	30	DSS B	Forged	Hydrogen

3. Results and discussions

Specific wear rate (SWR). Table 4 reveals the experimental results of specific wear rate and COF for DSS under sintered and forged conditions.

Table 4. Experimental results of SWR for DSS

Exp No.	Load (N)	Material	Condition	Atmosphere	SWR (mm^3/Nm)	COF
1	20	DSS-A	Sintered	Hydrogen	0.0022	0.522
2	20	DSS-A	Sintered	Partial-Vacuum	0.0026	0.602
3	20	DSS-A	Forged	Hydrogen	0.0033	0.565
4	20	DSS-A	Forged	Partial-Vacuum	0.0008	0.598
5	20	DSS-B	Sintered	Hydrogen	0.0018	0.548
6	20	DSS-B	Sintered	Partial-Vacuum	0.0021	0.62
7	20	DSS-B	Forged	Hydrogen	0.0020	0.525
8	20	DSS-B	Forged	Partial-Vacuum	0.0007	0.53
9	30	DSS-A	Sintered	Hydrogen	0.0017	0.56
10	30	DSS-A	Sintered	Partial-Vacuum	0.0020	0.633
11	30	DSS-A	Forged	Hydrogen	0.0025	0.59
12	30	DSS-A	Forged	Partial-Vacuum	0.0014	0.636
13	30	DSS-B	Sintered	Hydrogen	0.0014	0.575
14	30	DSS-B	Sintered	Partial-Vacuum	0.0016	0.669
15	30	DSS-B	Forged	Hydrogen	0.0005	0.562
16	30	DSS-B	Forged	Partial-Vacuum	0.0010	0.568

DSS A and DSS B steels displayed a specific wear rate of 0.0007 mm^3 / Nm to 0.0033 mm^3 / Nm. In a partial vacuum atmosphere, the lowest average wear rate of 0.0007 mm^3 / Nm was shown for forged DSS B.

Specific wear rate of DSS – design of experiments. Figures 2 and 3 display the response graph for the specific wear rate of DSS and show the interaction plot for specific wear rate. The interaction plot shows that negligible interaction between the parameters material, condition, and atmosphere affecting the specific wear rate of DSS.

Table 5 shows the response table for the specific wear rate of DSS. The response table reveals the mean of individual features for the individual level of the factor. The response table gives rank depends upon delta statistics, which measure the relative magnitude of effects.
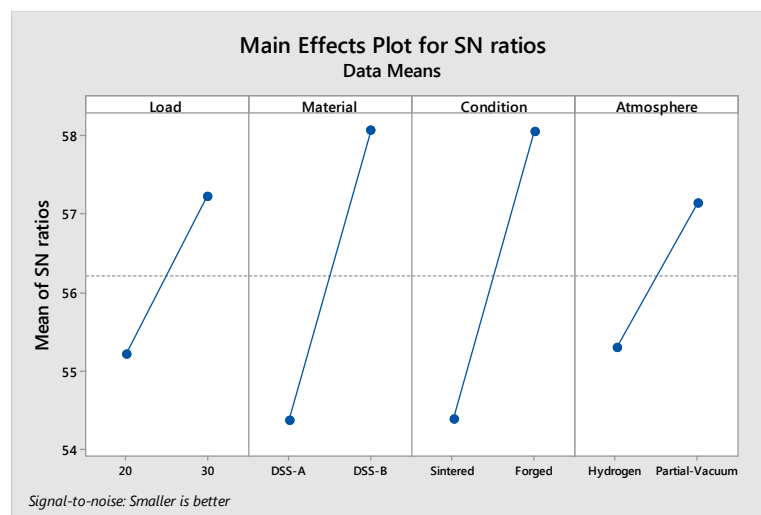

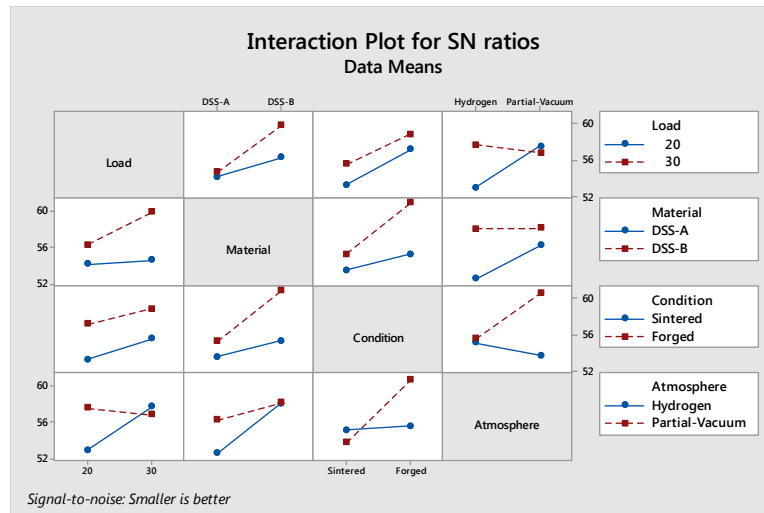**Fig. 2.** Response graphs for specific wear rate

Fig. 3. Interaction plots for specific wear rate

Table 5. Response table for specific wear rate

Level	Load	Material	Condition	Atmosphere
1	55.21	54.36	54.38	55.29
2	57.21	58.06	58.04	57.13
Delta	2.01	3.7	3.66	1.84
Rank	3	1	2	4

The delta measurement is the difference of largest to least average for each factor. Ranks are allotted based on values of delta; rank 1 indicates the highest value, rank 2 to the next higher value, and so on. The rank reveals the significance of each factor to the individual response. The rank shows the material is the main factor influencing the specific wear rate of duplex stainless steels. In order to evaluate the influence of the process variables on the Specific wear rate, ANOVA was performed. ANOVA of the S/N data for specific wear rate value is given in Table 6. ANOVA table reveals that material has influenced 17.66% towards specific wear rate compared to other factors such as condition and atmosphere.

Table 6. ANOVA table for specific wear rate

Source	Degrees of Freedom	Seq SS	Adj MS	F	P	Contribution %
Load	1	16.093	16.0927	1.28	0.31	5.2
Material	1	54.677	54.6771	4.34	0.092	17.6
Condition	1	53.588	53.5877	4.25	0.094	17.2
Atmosphere	1	13.561	13.5608	1.08	0.347	4.4
Load*Material	1	9.35	9.3497	0.74	0.429	3.0
Load*Condition	1	0.366	0.3663	0.03	0.871	0.1
Load*Atmosphere	1	30.865	30.8648	2.45	0.179	9.9
Material*Condition	1	15.027	15.0271	1.19	0.325	4.8
Material*Atmosphere	1	12.628	12.6278	1	0.363	4.1
Condition*Atmosphere	1	41.682	41.6822	3.3	0.129	13.4
Residual Error	5	63.062	12.6123			20.3
Total	15	310.898				100.0

Confirmation experiment for specific wear rate. The optimum process parameters for specific wear rates and their predicted and experimental values are given in Table 7. The

optimum predicted value is 0.0006 mm^3/mm, for 30 N whereas the experimental value is 0.0010 mm^3/Nm. The error is 5%, so the optimization technique adopted for validating Specific Wear Rate is satisfied.

Table 7. Optimum process parameters for specific wear rate

Load (N)	Material	Condition	Atmosphere	Predicted Values (mm/Nm)	Experimental Values (mm/Nm)
30	DSS-B	Forged	Partial Vacuum	0.00095	0.0010

Coefficient of friction for DSS. Two DSS A and B steels have exhibited the coefficient of friction of 0.52 to 0.602. The lowest coefficient of friction exhibited for DSS B under the forged condition in hydrogen sintering atmosphere is observed.

Coefficient of friction (COF) for DSS-design of experiments. Figures 4 and 5 show the response graph for the Coefficient of Friction of DSS and show the interaction plot for Coefficient of Friction. The interaction plot reveals that negligible interaction among the parameters material, condition, and atmosphere influencing the Coefficient of Friction of DSS.
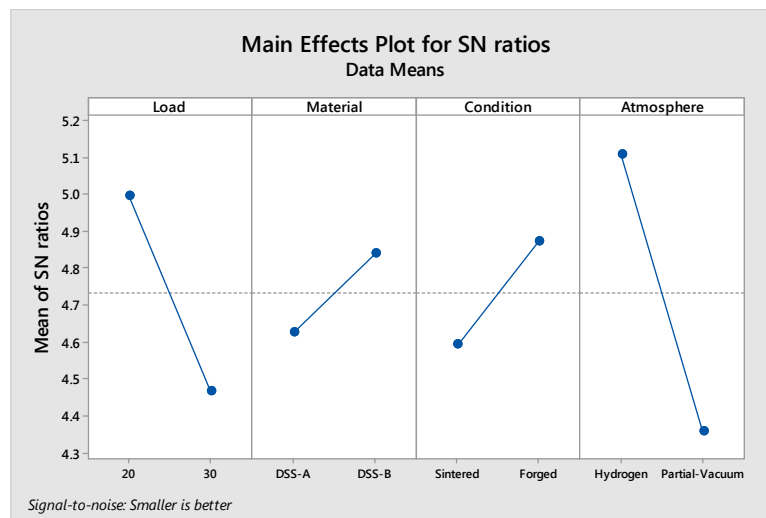

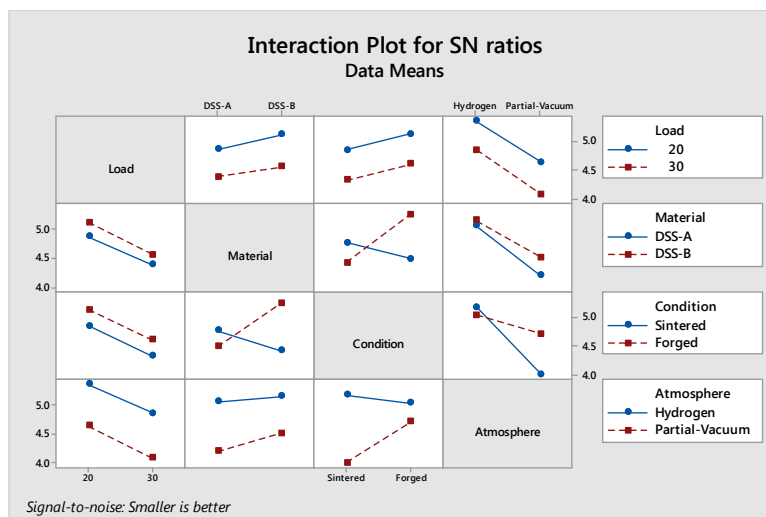**Fig. 4.** Response graphs for COF

Fig. 5. Interaction plots for COF

Table 8 shows the response table for the coefficient of friction for DSS. The response table reveals the mean of individual features for the individual level of the factor. The response table gives rank depends upon delta statistics, which measure the relative magnitude of effects.

Table 8. Response table for COF

Level	Load	Material	Condition	Atmosphere
1	4.996	4.625	4.592	5.107
2	4.467	4.838	4.871	4.356
Delta	0.529	0.213	0.279	0.751
Rank	2	4	3	1

Table 9. ANOVA table for COF

Source	DF	Seq SS	Adj MS	F	P	Contribution %
Load	1	1.11783	1.11783	56.66	0.001	18.7
Material	1	0.18118	0.18118	9.18	0.029	3.0
Condition	1	0.31106	0.31106	15.77	0.011	5.2
Atmosphere	1	2.25747	2.25747	114.42	0	37.7
Load*Material	1	0.00615	0.00615	0.31	0.601	0.1
Load*Condition	1	0.00003	0.00003	0	0.972	0.0
Load*Atmosphere	1	0.00353	0.00353	0.18	0.69	0.1
Material*Condition	1	1.2538	1.2538	63.55	0.001	20.9
Material*Atmosphere	1	0.04907	0.04907	2.49	0.176	0.8
Condition*Atmosphere	1	0.71001	0.71001	35.99	0.002	11.9
Residual Error	5	0.09864	0.01973			1.6
Total	15	5.98879				100.0

The delta measurement is the difference of largest to least average for each factor. Ranks are allotted based on delta values rank 1 indicates the highest value, rank 2 to the next higher value, and so on. The rank reveals the significance of each factor to the individual response. The rank shows the atmosphere is the main factor influencing the coefficient of friction for duplex stainless steels. The interaction plot reveals that negligible interaction among the parameters material, condition, and atmosphere influencing the COF. To evaluate the influence of the process parameters towards coefficient of friction for DSS ANOVA was carried out. ANOVA of the S/N data for the coefficient of friction value is given in Table 9. ANOVA table reveals that atmosphere has influenced 37.7% towards coefficient of friction compared to other factors such as condition and material.

Confirmation experiment for coefficient of friction. The optimum process parameters for COF and their predicted and experimental values are given in Table 10. The optimum predicted value is 0.522 for 20 N whereas the experimental value is 0.525. The error is 0.57%, so the optimization technique adopted for validating the Coefficient of Friction is satisfied.

Table 10. Optimum process parameters for COF

Load	Material	Condition	Atmosphere	Predicted Values	Experimental Values
20	DSS-B	Forged	Hydrogen	0.522	0.525

4. Conclusions

The DSS A and B wear experiments were conducted with the aid of the design of experiments. From the results of DSS A and B, the following primary observations were made:

1. DSS B in forged condition subjected to 30 N loading conditions under hydrogen atmosphere exhibited SWR of 0.0010 mm/Nm. This is also proved by DOE, and the error is 5% only.
2. The statistical findings of the experiments were well aligned with the surface plots achieved. The model of wear intensity is statistically verified with ANOVA with a strong multi-coefficient correlation.
3. DSS B in forged condition subjected to 20 N loading conditions under hydrogen atmosphere exhibited COF of 0.525. This is also proved by DOE, and the error is 0.57% only.
4. The model established is more suitable for automotive and offshore industries and for inexperienced consumers to reach the lowest wear rate without realistic experiments.

References

[1] Kurgan N. Effects of sintering atmosphere on microstructure and mechanical property of sintered powder metallurgy 316L stainless steel. *Materials & Design (1980-2015).* 2013;52: 995-998.

[2] Alvarez-Armas I, Degallaix-Moreuil S. (Eds.) *Duplex stainless steels.* John Wiley & Sons; 2013.

[3] Marques F, Da Silva WM, Pardal JM, Tavares SS, Scandian C. Influence of heat treatments on the micro-abrasion wear resistance of a superduplex stainless steel. *Wear.* 2011;271(9-10): 1288-1294.

[4] Nilsson JO. Super duplex stainless steels. *Materials Science and Technology.* 1992;8(8): 685-700.

[5] Chen TH, Weng KL, Yang JR. The effect of high-temperature exposure on the microstructural stability and toughness property in a 2205 duplex stainless steel. *Materials Science and Engineering: A.* 2002;338(1-2): 259-270.

[6] Sahu JK, Krupp U, Ghosh RN, Christ HJ. Effect of 475 C embrittlement on the mechanical properties of duplex stainless steel. *Materials Science and Engineering: A.* 2009;508(1-2): 1-4.

[7] Munez CJ, Utrilla MV, Urena A. Effect of temperature on sintered austeno-ferritic stainless steel microstructure. *Journal of Alloys and Compounds.* 2008;463(1-2): 552-558.

[8] Iacoviello F, Iacoviello D, Cavallini M. Analysis of stress ratio effects on fatigue propagation in a sintered duplex steel by experimentation and artificial neural network approaches. *International Journal of Fatigue.* 2004;26(8): 819-828.

[9] Kazior J, Nykiel M, Pieczonka T, Puscas TM, Molinari A. Activated sintering of P/M duplex stainless steel powders. *Journal of Materials Processing Technology.* 2004;157: 712-717.

[10] Li SL, Huang BY, Li DX, Li Y, Liang S, Zhou H. Influences of sintering atmospheres on densification process of injection moulded gas atomised 316L stainless steel. *Powder Metallurgy.* 2003;46(3): 241-245.

[11] Lal S, Upadhyaya GS. Effect of phosphorus and silicon addition on the sintered properties of 316L austenitic stainless steel and its composites containing 4 vol% yttria. *Journal of Materials Science.* 198;24(9): 3069-3075.

[12] Velasco F, Antón N, Torralba JM, Vardavoulias M, Bienvenu Y. Sinterability of Y_2O_3-Al_2O_3 particulate stainless steel matrix composites. *Applied Composite Materials.* 1996;3(1): 15-27.

[13] Mariappan R, Kumar PK, Jayavelu S, Dharmalingam G, Prasad MA, Stalin A. Wear properties of P/M duplex stainless steels developed from 316L and 430L powders. *International Journal of ChemTech Research.* 2015;8(10): 109-115.

[14] Chinnaraj R, Ramajayam M. Studies on Mechanical Properties of Hot-Forged Duplex Stainless Steels Sintered in Hydrogen Atmosphere. *Journal of The Institution of Engineers (India): Series D.* 2019;100(2): 283-290.

[15] Prakash JU, Ananth S, Sivakumar G, Moorthy TV. Multi-objective optimization of wear parameters for aluminium matrix composites (413/B4C) using grey relational analysis. *Materials Today: Proceedings.* 2018;5(2): 7207-7216

[16] Sorrentino L, Simeoli G, Iannace S, Russo P. Mechanical performance optimization through interface strength gradation in PP/glass fibre reinforced composites. *Composites Part B: Engineering.* 2015;76: 201-208.

[17] Rajkumar C, Mariappan R, Prakash JU. Microstructure and Corrosion Behavior of Hot-Forged Duplex Stainless Steels Sintered in Partial Vacuum and Hydrogen Atmospheres. *Metallography, Microstructure, and Analysis.* 2020;9(1): 6-15.

THE SYNTHESIS OF COMPOSITES WITH REINFORCING
PARTICLES ON A THIN SUBSTRATE

A.G. Knyazeva[*], O.N. Kryukova

Institute of Strength Physics and Materials Science of Siberian Branch of Russian Academy of Sciences,

2/4, pr. Akademicheskii, Tomsk, Russia

*e-mail: anna-knyazeva@mail.ru

Abstract. The article proposes the model for synthesizing a composite coating "intermetallic matrix-reinforcing oxide inclusions" on a substrate under controlled heating by an external moving heat source. The problem is solved in dimensionless variables. The study reveals the main criteria determining the composition of the fabricated composite. It is discovered that, depending on the treatment conditions, the matrix composition may include the main total product or residual unspent reagents and intermediate products, which testifies the nonequilibrium composition of the composite.
Keywords: electron beam treatment, chemical reaction, numerical modeling

1. Introduction
High-temperature technologies for synthesizing novel materials are based on the application of chemical energy sources and accompanied by various physicochemical processes while having a lot in common with the processes that are studied in the combustion theory. In particular, this is valid for electron-beam treatment of materials and coating synthesis on a substrate. The electron-beam coating cladding technologies are also fairly diverse. Some include the application of a powder layer on the material surface (using one of the methods available) with subsequent thermal treatment of the coated material using the energy of an electron or laser beam [1-7]. Others form the coating immediately during the thermal treatment due to the interaction of the particles (coming into the melt) with the substrate material [8]. Depending on the chemical composition of the treated material and powder modifying the properties, as well as on the technological parameters, the phase and chemical structure of the forming coatings are different, as are the physicochemical processes limiting the formation of the properties and the physicomathematical model interpreting and describing the observed regularities. The known models of technological synthesis and treatment are limited by the accounting of solely thermal processes (heating, melting, crystallization) [9-13] or the analysis of the hydrodynamic flow in the molten pool [14,15]. There are many works that involve PhFM for modeling the formation of the phase structure [16]. However, the majority of works deal with "modelled" situations that hardly take into account the technological conditions. More preferable is the approach based on the description of the composition evolution using thermokinetic models [17], which does not exclude the consideration of various phenomena and processes at different scale levels.

The capabilities of the model taking into account the transformation stages, as well as the coupling effects of different physical processes, are exemplified in [18-21]. Work [22] unveils the critical conditions distinguishing various cladding modes and leading to the formation of the virtually homogeneous or composite coating. It is shown that in the case of

exothermic dissolution, the electron-beam treatment process has much in common with the processes of the thermal theory of ignition and combustion. It would be impossible to detect such an effect without a detailed parametric investigation. A chapter of monograph [17] and publications [18,19,21,23-26] show the capabilities of the models with "detailed" chemistry.
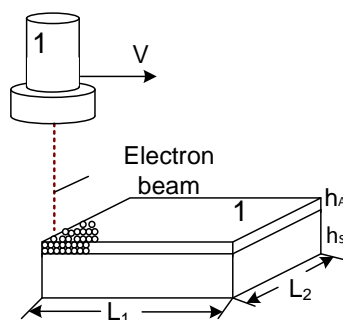

Fig. 1. Illustration of the model formulation

The present work proposes the model for synthesizing a composite coating "intermetallic matrix-reinforcing oxide inclusions" on a substrate under controlled heating by an external moving heat source (Fig. 1). The study is aimed at establishing the criteria that allow assessing possible modes of coating synthesis on a substrate.

2. Mathematical model

Let us consider the problem in the following statement. Along the plate with a thickness h with a powder layer on it, moves a source with its energy distributed as per a given law. The source can be coupled with an electron or laser beam having various natures of movement along the surface. In the present work, let us confine ourselves by the following source:

$$W_e = \begin{cases} 0 & , |y| > y_0 / 2; \\ q_0 \exp\left(-(x - \mathrm{V}t)^2 / a_t^2\right) & , |y| \le y_0 / 2, \end{cases} \tag{1}$$

which corresponds to the scanning high-frequency electron beam unwrapped into a line [27,28]. Here, q_0 is the maximum flow capacity density, a_t is the effective source radius, y_0 is proportional to the scanning rate of the electron beam, V is the electron beam movement velocity along axis x.

The temperature field follows from the solution of the thermal conductivity set of equations (with effective thermophysical properties) and chemical kinetics.

In the laboratory system of coordinates, the thermal conductivity equation has the following form:

$$c_{eff} \rho_{eff} \frac{dT}{dt} = -\nabla \cdot \mathbf{J}_q + W_{ch} + \frac{W_e}{h} - \sigma_0 \varepsilon_0 \left(T^4 - T_w^4\right) - \alpha_{eff} (T - T_0), \tag{2}$$

where T is the temperature; c_{eff} is the thermal capacity, ρ_{eff} is the density; the heat flux $\mathbf{J}_q$ is assumed to satisfy the Fourier law; the second summand to the right $W_{ch} = Q_1 w_1 + Q_2 w_2$ corresponds to heat release or absorption due to chemical reactions and is determined by a given reaction scheme; Q_k are heat effects for reactions, $k = 1, 2$, w_k are the reaction rates; the fourth summand to the right describes the heat emission from the surface of the plate under treatment as per the Stefan-Boltzmann law, where σ_0 is Stephan-Boltzmann constant, ε_0 is blackness level, T_w is the temperature of vacuum chamber; the fifth summand corresponds to the heat losses into the substrate, where α_{eff} – effective heat loss coefficient in

Newton's law (this term takes into account possible heat losses deep into a massive sample); T_0 – is environment temperature. The heat flow obeys Fourier's law. The thermophysical characteristics, in the general case, depend on the temperature and composition, which is accounted during the describing of the process of electron-beam cladding of specific systems [29]. However, to study the qualitative effects, let us confine ourselves by certain averaged effective properties.

The melting of the reacting mixture and/or mixture of reagents and reaction products is accounted via thermal capacity [30]. Let us assume that the main material, determining the matrix composition, is melting. The thermal capacity sharply rises in the vicinity of the substrate melting temperature T_{ph}, which is reflected by the equation

$$c_{eff}\rho_{eff} = \rho_s L_{ph}\delta(T - T_{ph}) + \begin{cases} (c\rho)_s , & T < T_{ph} \\ (c\rho)_L , & T \geq T_{ph} \end{cases},$$
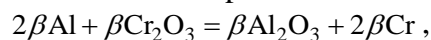
where δ is the Dirac delta function, L_{ph} is the latent heat of melting; index "s" corresponds to the solid phase and "L" relates to the liquid phase.

We assume that the composite material on the substrate is synthesized using metallothermic transformations. The reinforcing particles (oxide inclusions) and matrix composition are formed in a system of exothermic reactions. Such systems include, for instance, powder mixtures of Al+Cr2O3+Ti and Al+Fe2O3+Ni. In each of the systems Al+Cr_2O_3+Ti and Al+Fe_2O_3+Ni, according to the enthalpies of the oxides, only one reaction of metal reduction from oxides by aluminium is anticipated. In both the systems, of three initial components, aluminium is spent for forming both the particles and the matrix.
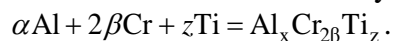
In the first case, we have an initial mixture of the form

$(\alpha + 2\beta)\text{Al} + \beta\text{Cr}_2\text{O}_3 + z\text{Ti}$.
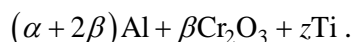
One of the products of the reaction

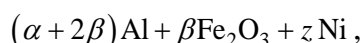$2\beta\text{Al} + \beta\text{Cr}_2\text{O}_3 = \beta\text{Al}_2\text{O}_3 + 2\beta\text{Cr}$,

that leads to the formation of oxide reinforcing particles, spends to matrix formation in accordance with the summary reaction

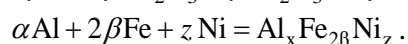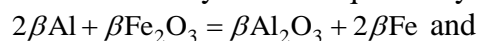$\alpha\text{Al} + 2\beta\text{Cr} + z\text{Ti} = \text{Al}_x\text{Cr}_{2\beta}\text{Ti}_z$.

Hence, here we have to summary sequentially-parallel stages.

The second mixture is similar to the first. Of the three initial mixture components

$(\alpha + 2\beta)\text{Al} + \beta\text{Fe}_2\text{O}_3 + z\,\text{Ni}$,

aluminum is spent on both particle formation and matrix formation. Consequently, we again have a summary of two sequentially-parallel stages:

$2\beta\text{Al} + \beta\text{Fe}_2\text{O}_3 = \beta\text{Al}_2\text{O}_3 + 2\beta\text{Fe}$ and

$\alpha\text{Al} + 2\beta\text{Fe} + z\,\text{Ni} = \text{Al}_x\text{Fe}_{2\beta}\text{Ni}_z$.

Depending on the concentration of the initial substances, the composition of the matrix can be different, can include intermetallides, triple compounds, and solid solutions.

So, the two-stage total reaction scheme for these systems can be represented as

2X+Y → P1+2P2,   (I)

X+2P2+Z → P.   (II)

By formally applying the law of mass action to the set of reactions (I)–(II), we can write for the reaction rates:

$w_1 = \Phi_1(T)X^2Y$; $w_2 = \Phi_2(T)P_2^2 XZ$,

where X=1-P_1-P_2-P is the total concentration of reagents; $\Phi_1(T)$ and $\Phi_2(T)$ are the reaction rates (that in the general case can depend both on the temperature, the concentration of the reaction solid-phase products, which is connected with real kinetic obstructions, and

mechanical stresses. It should be born in mind that the law of mass action is applicable to individual stages, while one can apply it to total reactions only formally.

From this scheme, component Y can be explicitly excluded with the assumption that the concentration of this reagent alters the rate of the first reaction Φ_1 and the concentration of the formed reinforcing particles. The concentrations of nickel and titanium can also be neglected; it only affects the rate of the second reaction, i.e. Φ_2 and the matrix composition. Therefore,

$$w_1 = \Phi_1(T)X^2; \; w_2 = \Phi_2(T)P_2^2 X .$$

Let us assume, that chemical reaction rates depend on the temperature as per the Arrhenius equation.

$$\Phi_1 = k_{01} \exp\left(-\frac{E_{a1}}{RT}\right); \; \Phi_2 = k_{02} \exp\left(-\frac{E_{a2}}{RT}\right),$$

where k_{0i}, $E_{a,i}$ are pre-exponential factors and activation energies for reactions (I) and (II).

Hence, the set of kinetic equations can be expressed as

$$\frac{dP_1}{dt} = \Phi_1(T),$$

$$\frac{dP_2}{dt} = 2\left[\Phi_1(T) - \Phi_2(T)\right], \tag{3}$$

$$\frac{dP}{dt} = \Phi_2(T).$$

The boundary condition $y = 0$ is as follows: $\partial T/\partial y = 0$ is the condition on the symmetry axis; conditions $x = 0, \infty$: $\partial T/\partial x = 0$ and $y \to \infty$, $\partial T/\partial y = 0$ mean the absence of the heat sources and sinks at infinite distance from the heated-up region and at the free end of the plate.

Assuming at the initial moment of time

$t = 0$: $\quad T = T_0, \; X = 1, \; P = P_1 = P_2 = 0$.

The initial mixture composition in this model actually reflects the relation of the pre-exponential factors of the two reactions.

3. Statement of the problem in dimensionless variables

Let us turn to the problem in dimensionless variables

$$\tau = \frac{t}{t_*}, \; \xi = \frac{x}{x_*}, \; \eta = \frac{y}{x_*}, \; \theta = \frac{T - T_*}{T_* - T_0},$$

where $T_* = \dfrac{Q_1}{c_s \rho_s} + T_0$ is the temperature characteristic for the problem (the temperature of the product if only the metallothermic reaction would proceed in the system); $t_* = \dfrac{c_s \rho_s RT_*^2}{k_{01}E_{a1}Q_1} \exp\left(\dfrac{E_{a1}}{RT_*}\right)$ is the period of the adiabatic induction for this reaction at the temperature T_*; $x_* = \sqrt{\dfrac{\lambda t_*}{c_{eff} \rho_{eff}}}$ is the thickness of the thermal boundary layer that is formed over the time t*.

Then, the equations, initial and boundary conditions will be as follows:

$$f_C(\theta)\frac{d\theta}{d\tau} = \left[\frac{\partial^2\theta}{\partial\xi^2} + \frac{\partial^2\theta}{\partial\eta^2}\right] + \bar{\Phi}_1 + \bar{\Phi}_2 + f_1 - S_b\left(\left(\theta + \sigma^{-1}\right)^4 - \left(\sigma^{-1} - \theta_w\right)^4\right) - Bi(\theta + 1). \tag{4}$$

$$\frac{dP_1}{d\tau} = \gamma\varphi_1 \exp\left(\frac{\theta\sigma}{\theta_0\sigma(1+\theta\sigma)}\right) = \gamma\varphi_1 \exp\left(\frac{\theta}{\theta_0(1+\theta\sigma)}\right),$$

$$\frac{dP_2}{d\tau} = 2\gamma\left[\varphi_1 \exp\left(\frac{\theta\sigma}{\theta_0\sigma(1+\theta\sigma)}\right) - \varphi_2 k_{ch} \exp\left(\frac{\theta\sigma + e_k}{\theta_0\sigma(1+\theta\sigma)}\right)\right], \qquad (5)$$

$$\frac{dP}{d\tau} = \gamma k_{ch} \exp\left(\frac{\theta\sigma + e_k}{\theta_0\sigma(1+\theta\sigma)}\right)\varphi_2.$$

$$\xi \to 0, \infty: \quad \frac{\partial\theta}{\partial\xi} = 0; \quad \eta \to 0, \infty: \quad \frac{\partial\theta}{\partial\eta} = 0. \qquad (6)$$

$$\tau = 0 \quad \theta = -1 \quad X = 0 \quad P_1 = 0 \quad P_2 = 0, \qquad (7)$$

where

$$\varphi_1 = X^2, \ \varphi_2 = P_2^2 X \ ; \ f_C = S_{ph}\delta(\theta - \theta_{ph}) + \begin{bmatrix} 1, & \theta < \theta_{ph} \\ K_C, & \theta \geq \theta_{ph} \end{bmatrix},$$

$$\overline{\Phi}_1 = \frac{1}{\theta_0}\exp\left(\frac{\theta\sigma}{\beta(1+\theta\sigma)}\right)\varphi_1, \quad \overline{\Phi}_2 = S_{ch}z_{ch}\frac{1}{\theta_0}\exp\left(\frac{\theta\sigma + e_k}{\beta(1+\theta\sigma)}\right)\varphi_2,$$

$$f_1 = \begin{cases} 0 & , |\eta| > \eta_0 \\ S_e \exp\left(-\frac{(\xi - \overline{V}\tau)^2}{\delta_t^2}\right) & , |\eta| \leq \eta_0 \end{cases} \qquad (8)$$

As a result, the problem contains the following parameters:

$$\gamma = \frac{(c\rho)_S RT_*^2}{E_{a1}Q_1}, \ \sigma = \frac{T_* - T_0}{T_*}, \ \beta = \frac{E_{a1}}{RT_*}, \ \theta_0 = \frac{\beta}{\sigma}, \ S_{ch} = \frac{Q_2}{Q_1}, \ z_{ch} = \frac{k_2}{k_1}, \ e_k = 1 - \frac{E_{a2}}{E_{a1}},$$

$$S_{ph} = \frac{L_{ph}}{c_S(T_* - T_0)}, \ \theta_{ph} = \frac{T_{ph} - T_*}{T_* - T_0}, \ K_C = \frac{(c\rho)_L}{(c\rho)_S}, \ S_e = \frac{q_0}{h}\frac{t_*}{(T_* - T_0)c_s\rho_s}, \ \delta_t = a_t / x_*, \ \overline{V} = Vt_* / x_*,$$

$$S_b = \frac{t_*\sigma_0\varepsilon_0(T_* - T_0)^3}{c_s\rho_s}, \ \theta_w = \frac{T_* - T_w}{T_* - T_0}, \ Bi = \alpha_{eff}\frac{t_*}{c_s\rho_s}.$$

For instance, $\delta_t > 1$ means that the effective beam radius is more than the thickness of the thermal boundary layer; in the case of $\delta_t < 1$, the situation is opposite. If $e_k = \frac{E_{a1} - E_{a2}}{E_{a1}} > 0$, then the second reaction, in the presence of product P_2 in the initial mixture, activates faster than the first one. Therefore, when the first reaction initiates, the second reaction starts following it. In the case of $e_k = \frac{E_{a1} - E_{a2}}{E_{a1}} < 0$, the second reaction may initiate with some delay. Obviously, the reaction rates will depend on both the temperature and the relation of the pre-exponential factors.

Let us define the domains of the change of the dimensionless parameters using literature sources on different substances (Ti, Al, Cr, Fe, O) and varying the parameters of the heat sources and formally kinetic parameters (q_0, V, E_{ai}, Q_i, k_{0i}) [31-34].

$$S_{ch} = 0.1 \div 1, \quad z_{ch} = 10^{-6} \div 10^6, \quad S_e = 10^{-8} \div 10^3, \quad \theta_w = 0.4 \div 0.9, \quad e_k = 0 \div 0.7, \quad \theta_{ph} = 0 \div 5,$$

$$S_{ph} = 0.1 \div 1, \quad \overline{V} = 10^{-8} \div 10^3, \quad \delta_t = 0.03 \div 10^5, \quad \sigma = 0.3 \div 0.9, \quad \gamma = 0.009 \div 0.1, \quad Bi = 0 \div 4,$$

$$K_C = 0.1 \div 10.$$

For the numerical solution of the problem (4)–(8), the implicit absolutely stable difference scheme and the sweep method were used. In the calculations, we varied the dimensionless parameters that characterize the kinetics of the chemical reactions: S_{ch}, z_{ch}, S_e, e_k. The rest of the parameters were fixed: $\theta_{ph} = 0.5$, $S_{ph} = 0.5$, $\bar{V} = 0.25$, $\sigma = 0.5$, $\beta = 0.025$, $\gamma = 0.035$, $Bi = 0$, $\mathrm{K}_C = 1$, $\delta_t = 2$, $S_b = 0.0015$, $\theta_w = 0.5$, $\eta_0 = 0.5$. In real calculations, the Dirac delta function is replaced by the delta-like function that satisfies the normalization requirement $\int\limits_{-\infty}^{+\infty} \Phi(x)\,dx = 1$. This requirement is met, for instance, by the function from [35].

$$\Phi = \frac{1}{\sigma_0\sqrt{\pi}}\exp\left[-\left(\frac{T-T_{ph}}{\sigma_0}\right)^2\right].$$

4. Analysis of the result of numerical study

Let us demonstrate some of the results of the numerical investigation of the electron-beam cladding within the presented model. Figure 2 shows the spatial distribution of the temperature along axis ξ at consecutive moments of time depending on the parameter S_e. Over some time, starting from the source movement initiation, the mode stabilizes in a quasi-stationary mode, i.e. the maximum temperature θ_{max} seizes to change. At $S_e = 2.5$, the temperature exceeds the temperature of the phase transition ($\theta_{ph} = 0.5$); at $S_e = 1$, the temperature is close to θ_{ph}. Figure 3 depicts thermal cycles in different points along the axis of heat source movement $\xi = 0, 5, 10, 15, 20$ for two sets of parameters: I) $S_{ch} = 0.5$, $z_{ch} = 100$, $S_e = 1$, $e_k = 0.1$; II) $S_{ch} = 0.5$, $z_{ch} = 100$, $S_e = 2.5$, $e_k = 0.1$ The shape of the thermal cycles depends on the beam movement velocity, flux density, and the dimensions of the part under treatment. The curves $\theta(\tau)$ built in different locations of the specimen, there is a plateau that corresponds to the melting temperature. The increased parameter S_e up to $S_e = 2.5$ (Fig. 3) may lead to a considerable overheating connected as with the heat accumulation during heating by the electron beam, as with the chemical heat liberation.
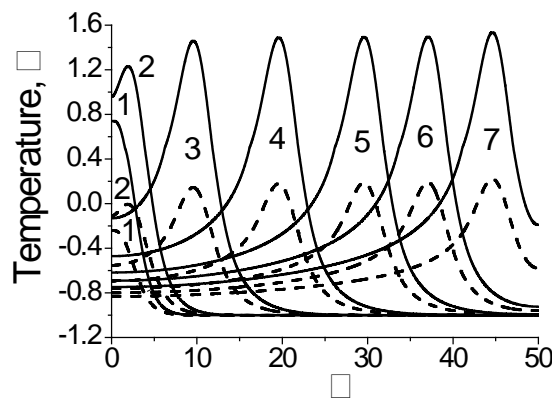

Fig. 2. Temperature distribution along the source movement axis at different moments of time $\tau = 4$ (*1*); 10 (*2*); 40 (*3*); 80 (*4*); 120 (*5*); 150 (*6*); 180 (*7*).

$z_{ch} = 100$, $e_k = 0.1$, $\theta_{ph} = 0.5$, $S_{ph} = 0.5$, $V = 0.25$; $\sigma = 0.5$; $\beta = 0.025$, $\gamma = 0.035$, $Bi = 0$,

$$S_{ch} = 0.5,\ \mathrm{K}_C = 1.$$

The solid curves correspond to $S_e = 2.5$, the dashed curves correspond to $S_e = 1$
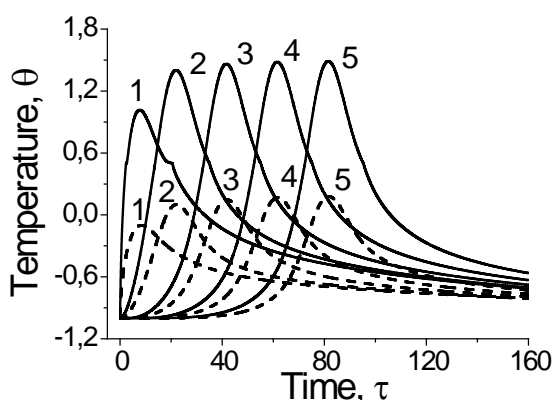

Fig. 3. Thermal cycles in different points along the heat source movement axis.
$\xi = 0$ (*1*); 5 (*2*); 10 (*3*); 15 (*4*); 20 (*5*).
The solid curves correspond to $S_e = 2.5$, the dashed curves correspond to $S_e = 1$

The impact of the parameters determining the chemical transformations e_k and z_{ch} is shown in Figs. 4–5. Figure 4 illustrates the spatial distributions of all concentrations of the products and reagents that are formed in the chemical transformations. The fraction of the particles in the composite and the fraction of the matrix depend on the practically complete set of the model parameters. The composition of the synthesized composite matrix can include both reagents unspent under certain conditions and the residual intermediate product. Practically important is the composition depending on the input parameter of the model: the fraction of particles and the composition of the matrix that influence the proportion of the synthesized material or coating.

Figure 5 demonstrates the non-stationary development of the synthesis. The variation of S_e shows that at $S_e = 1$ only the region adjacent to the beam affected area is heated to the temperature sufficient for melting and acceleration of the chemical reactions. The shape of the molten pool and heat affected zone cannot stabilize, which does not allow using stationary models – widely implemented for modeling welding and modern three-dimensional laser- and electron-beam-based technologies – for alike processes of thermal treatment and synthesis of composite coatings.

Nonuniform heating correspondingly leads to nonuniform phase composition (Fig. 6). Different dynamics of phase accumulation corresponds to different treatment conditions (different values of S_e) and different conditions of reaction initiation (alteration of parameters z_{ch} and e_k). For instance, at $z_{ch} = 100$, $S_e = 2.5$, $e_k = -0.2$ and $z_{ch} = 0.1$, $S_e = 2.5$, $e_k = -0.2$, the reactions start to accelerate from $\tau \sim 1.5$ (Fig. 6a) and then all the reactions rapidly complete, while at $z_{ch} = 100$, $S_e = 1$, $e_k = 0.1$, the reactions accelerate at $\tau \sim 10$ (not shown in the figures). The resulting phase composition by the end of the treatment (which can be assessed by both integral curves and the concentration in the region where the sources have been removed from) turns out to be different as well.
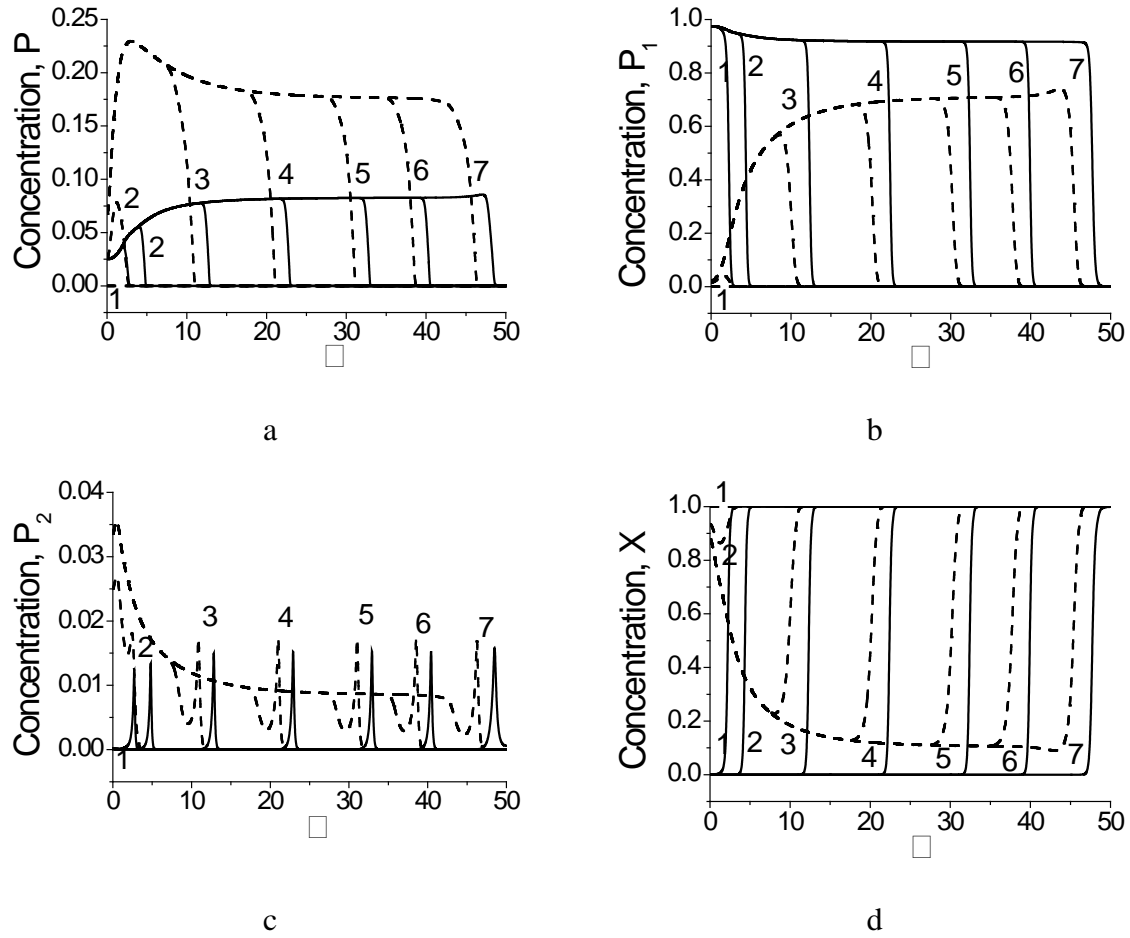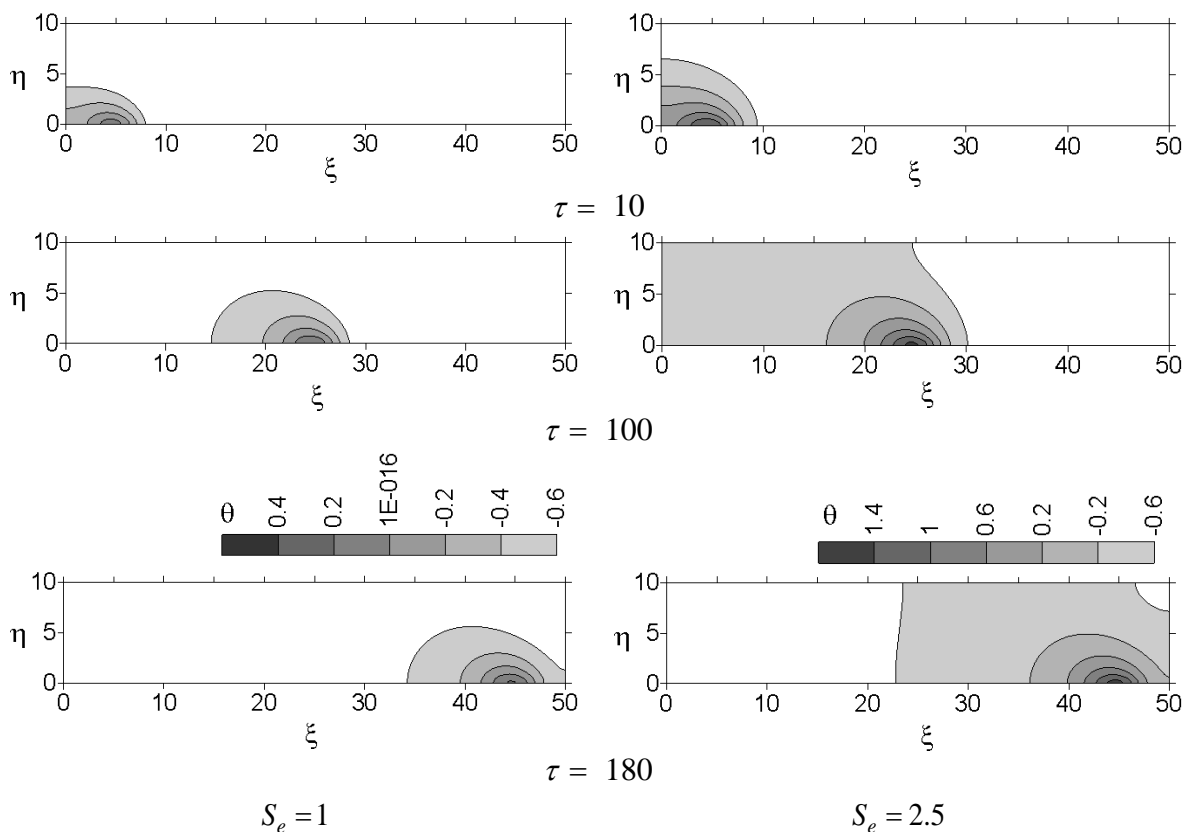
a   b

c   d

Fig. 4. Spatial concentration distributions for the products and reagent along the source
movement axis at different moments of time

$\tau = $ 4 (*1*); 10 (*2*); 40 (*3*); 80 (*4*); 120 (*5*); 150 (*6*); 180 (*7*).

$z_{ch} = 100$, $e_k = 0.1$, $\theta_{ph} = 0.5$, $S_{ph} = 0.5$, $V = 0.25$; $\sigma = 0.5$;

$\beta = 0.025$, $\gamma = 0.035$, $Bi = 0$, $S_{ch} = 0.5$, $K_C = 1$.

The solid curves correspond to $S_e = 2.5$, the dashed curves correspond to $S_e = 1$

Fig. 5 Nonuniform temperature field during electron-beam melting for different values of S_e. $S_{ch} = 0.5$, $z_{ch} = 100$, $e_k = 0.1$

The parameter z_{ch} (the relation of the reaction pre-exponential factors) has an appreciable effect on the change to the phase composition. In the case of $z_{ch} = 0.1$ (Fig. 6a), the product P does not form, only products P_1 and P_2 are formed; the increase in z_{ch} up to 100 (Fig. 6b) alters the phase composition in other proportions. In this case, product P starts to accrue, product P_1 also grows, while product P_2 considerably diminishes.

a   b
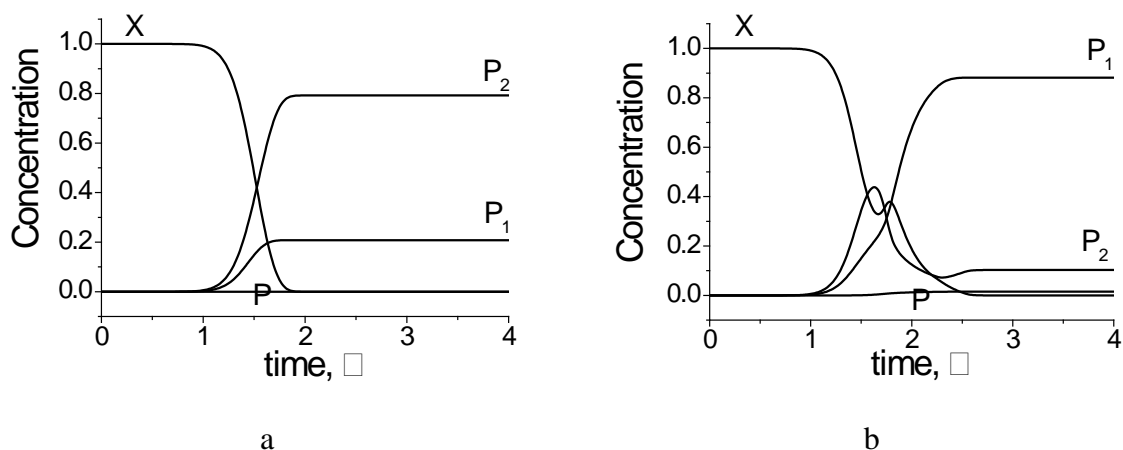
Fig. 6. Dependence of the concentrations of the products and reagents on time at different parameters of the problem.
a) $z_{ch} = 0.1$; b) $z_{ch} = 100$. $S_{ch} = 0.5$, $S_e = 2.5$, $e_k = -0.2$

The changes to the parameter e_k, together with the alteration of the relation of the pre-exponential factors is of great interest. At $e_k = 0.1$ and fixed $S_{ch} = 0.5$ and $z_{ch} = 100$ the product P_1 primarily forms; the rest of the products remain in negligible amounts (not shown in the figures). This means that the matrix includes a mixture of initial reagents not involved in the metallothermic reactions and small amounts of the products P_2 and P.

5. Conclusions

The work proposes the model for synthesizing a composite coating "intermetallic matrix-reinforcing oxide inclusions" on a substrate under controlled heating by an external moving heat source. The process of synthesis was investigated in dimensionless variables, which allowed unveiling the main criteria determining the composition of the synthesized composite. It was shown that the process cannot be considered quasi-stationary, despite the established maximum temperature in the beam-affected region. It was discovered that, depending on the conditions, the matrix composition may include the main total product or residual unspent reagents and intermediate products, which testifies the nonequilibrium composite composition that can alter during operation of the treated part.

References
[1] Negi S, Nambolan AA, Kapil S, Joshi PS, Manivannan R, Karunakaran KP, Bhargava P. Review on electron beam based additive manufacturing. *Rapid Prototyping Journal.* 2019;26(3): 485-498.
[2] Galati M, Iuliano L. A literature review of powder-based electron beam melting focusing on numerical simulations Author links open overlay panel. *Additive Manufacturing.* 2018;19: 1-20.
[3] Murr LE, Johnson WL. 3D metal droplet printing development and advanced materials additive manufacturing. *Journal of Materials Research and Technology.* 2017;6(1): 77-89.
[4] Körner C. Additive manufacturing of metallic components by selective electron beam melting – a review. *International Materials Reviews.* 2016;61(5): 361-377
[5] Olakanmi EO, Cochrane RF, Dalgarno KW. A review on selective laser sintering/melting (SLS/SLM) of aluminium alloy powders: Processing, microstructure, and properties. *Progress in Materials Science.* 2015;74: 401-477.
[6] Abe N, Morimoto J, Tomie M, Doi Ch. Formation of WC-Co layers by an electron beam cladding method and evaluation of the layer properties. *Vacuum.* 2000;59: 373-380.
[7] Kruth JP, Froyen L, Van Vaerenbergh J, Mercelis P, Rombouts M, Lauwers B. Selective laser melting of iron-based powder. *Journal of Materials Processing Technology.* 2004;149(1-3): 616-622.
[8] Panin VE, Belyuk SI, Durakov VG, Pribytkov GA, Rempe NG. Electron beam vacuum surfacing: Equipment, technology and properties of coatings. *Welding International.* 2000;14(7): 580-584.
[9] Hailang L, Zhengwei Q, Bo W, Guopei Zh, Xiaoyu W, Dezhi W. Numerical simulation of temperature field during electron beam cladding for NbSi2 on the surface of Inconel617. *Material Research Express.* 2018;5: 036528.
[10] Hong Z, Zhengxing M, Jiukai L, Yongjie L, Qingyuan W. Numerical Simulation of the Electron Beam Welding and Post Welding Heat Treatment Coupling Process. *High Temperature Materials and Processes.* 2018;37(9-10): 793-800.
[11] Chen L, Mi G, Zhang X, Wang C. Numerical and experimental investigation on microstructure and residual stress of multi-pass hybrid laser-arc welded 316L steel. *Materials and Design.* 2019;168: 107653.

[12] Körner C, Attar E, Heinl H. Mesoscopic simulation of selective beam melting processes. *Journal of Materials Processing Technology*. 2011;211: 978-987.

[13] Xina L, Boutaousa M, Xin S, Siginer DA. Numerical modeling of the heating phase of the selective laser sintering process. *International Journal of Thermal Sciences*. 2017;120: 50-62.

[14] Ai Y, Liu X, Huang Y, Yu L. Numerical analysis of the influence of molten pool instability on the weld formation during the high speed fiber laser welding. *International Journal of Heat and Mass Transfer*. 2020;160: 120103.

[15] Yang Z, Fang Y, He J. Numerical simulation of heat transfer and fluid flow during vacuum electron beam welding of 2219 aluminium girth joints. *Vacuum*. 2020;175: 109256.

[16] Requena G, Bugelnig K, Sket F, Milenkovic S, R¨odler G, Weisheit A, Gussone J, Haubrich J, Barriobero-Vila P, Pusztai T, Gr´an´asy L, Theofilatos A, da Silva JC, Hecht U, Ultrafine Fe-Fe$_2$Ti eutectics by directed energy deposition: insights into microstructure formation based on experimental techniques and phase field modelling. *Additive Manufacturing*. 2020;33: 101133.

[17] Knyazeva A, Kryukova O, Sorokova S, Shanin S. Coupling Models of New Material Synthesis in Modern Technologies. In: Hsueh CH. (ed.) *Handbook of Mechanics of Materials*. Singapore: Springer; 2018.

[18] Sorokova SN, Knyazeva AG. A coupled model of sintering of Ti-TiAl3 powders. *Bulletin of TPU*. 2009;314(2): 96-101. (In Russian)

[19] Sorokova SN, Knyazeva AG. Simulation of intermetallide synthesis on a cylindrical substrate. *Physical Mesomechanics*. 2009;12(5): 77-90.

[20] Sorokova SN, Knyazeva AG. Numerical study of the influence of the technological parameters on the composition and stressed-deformed state of a coating synthesized under electron-beam heating. *Theoretical Foundations of Chemical Engineering*. 2010;44(2): 172-185.

[21] Shanin SA, Knyazeva AG, Kryukova ON. Evolution of the cover with deposition ti&n on the substrate of cylindrical shape. *Russian Physics Journal*. 2015;58(6/2): 311-316.

[22] Kryukova ON, Knyazeva AG. Critical phenomena in particle dissolution in the melt during electron-beam surfacing. *Journal of Applied Mechanics and Technical Physics*. 2007;48: 109-118.

[23] Bakinovskii AA, Knyazeva AG, Krinitcyn MG, Kryukova ON, Pobol IL, Fedorov VV, Rajczyk J. Electron Beam Assisted Deposition of Ni–Al Coating on to Steel Substrate. *Journal of Self-Propagating High-Temperature Synthesis*. 2019;28: 245-255.

[24] Knyazeva A, Kryukova O. Modeling Ti-Al-C-composite synthesis on a substrate under control of electron beam. *Journal of Crystal Growth*. 2020;531: 125349.

[25] Knyazeva AG, Kryukova ON. Modeling of controlled synthesis of intermetallic coatings. *IOP Conf. Series: Journal of Physics: Conf. Series*. 2017;899: 072001.

[26] Kryukova O, Knyazeva A. Coating combustion synthesis controlled by moving electron beam. *IOP Conf. Series: Journal of Physics: Conf. Series*. 2018;1115: 042028.

[27] Rykalin N, Zuev IV, Uglov AA. *Fundamentals of electron beam processing of materials*. Moscow: Mashinostroenie; 1978. (In Russian)

[28] Schultz H. *Electron Beam Welding*. Woodhead Publishing,Cambridge; 1993;93.

[29] Kryukova ON, Knyazeva AG. The effect of the dynamics of particle inclusion into melt on the phase structure and properties of the coating formed by electron-beam cladding. *Physical mesomechanics*. 2004;7(2): 205-208. (In Russian)

[30] Kryukova ON, Knyazeva AG. Modelling the structure of composition of the coating formed by electron-beam cladding. *Physical mesomechanics*. 2004;7(2): 81-89. (In Russian)

[31] Grigoriev IS, Meilikhov EZ. *Handbook of physical quantities*. CRC Press Inc; 1997.

[32] Valencia JJ, Quested PN. Thermophysical Properties. In: *ASM Handbook. Casting.* ASM International; 2008. p.468-481.

[33] Stolovich NN, Minitskaya NS. *Temperature Dependence of Thermophysical Properties of Some Metals*. Minsk; 1975. (In Russian)

[34] Samsonov GV. *Handbook of the Physicochemical Properties of the Elements*. Springer; 1968.

[35] Tikhonov AN, Samarskiy AA. *Equations of mathematical physics*. Moscow: Nauka; 1972. (In Russian)

INFLUENCE OF THE SIZE OF TURMERIC MICROPARTICLES REINFORCING AGENT ON MECHANICAL AND BIODEGRADATION PROPERTIES OF CORNSTARCH-BASED BIOPLASTIC MATERIAL: CURRENT STUDIES, EXPERIMENTAL RESULTS, AND PROPOSAL MATERIAL CRACK PHENOMENA DURING MECHANICAL TESTING

A.B.D. Nandiyanto[1*], F. Triawan[2], M. Fiandini[1], I.O. Suryani[2], G.K. Sunnardianto[3]

[1]Departemen Kimia, Universitas Pendidikan Indonesia, Jl. Dr. Setiabudhi No. 229, Bandung, Indonesia

[2]Department of Mechanical Engineering, Faculty of Engineering and Technology, Sampoerna University,

Jl. Raya Pasar Minggu No. 16, Jakarta, Indonesia

[3]Research Center for Physics, Indonesian Institute of Sciences (LIPI), Kawasan Puspiptek Serpong, Tangerang

Selatan, 15314, Indonesia

*e-mail: nandiyanto@upi.edu

Abstract. The purpose of this study was to investigate the effect of sizes of turmeric microparticles (as a reinforcing agent) on the mechanical and biodegradation properties of cornstarch-based bioplastic material. The following fabrication procedures were performed: (1) diluting cornstarch in water; (2) making homogeneous mixture of cornstarch, glycerol and acetic acid by heating at less than 100ºC, (3) additional turmeric with a specific size (i.e. 250, 125, 100, 74 μm); (4) molding process; and (5) drying process to obtain solid bioplastic materials. This study shows the importance of reinforcing agent size for improving the mechanical properties of bioplastic materials. The smaller turmeric size brings better mechanical properties than the larger turmeric size that has more void space. To support the analysis, the present study also was completed with a literature review regarding bioplastic production and proposal bioplastics material crack phenomena during mechanical testing.
Keywords: bioplastics, cornstarch, particle size, mechanical properties, turmeric

1. Introduction
The synthesis of bioplastics based on biodegradable materials has been attracted tremendous attention. One of the attractive materials is starch-based bioplastics. However, starch-based bioplastics have disadvantages such as poor performance, hydrophilicity, and resistance to moisture [1].

To solve problems regarding the limitation of starch-based bioplastics, several strategies have been implemented. Bioplastics were usually formed from a combination of several materials, one of which acts as the main material and the other as reinforcing agents. In addition to the additional reinforcing agents, several parameters must be considered [2,3], including size [4-6], composition [7-9], shape [10], and surface structure [11,12].

Based on our previous studies [13,14] regarding the use of micrometer-sized starch particles and their composition impacts on the bioplastic performance, the present study aims

to examine the effect of turmeric microparticles' size on the mechanical and biodegradation properties of cornstarch-based bioplastic material. Turmeric was selected since it is enriched with natural antimicrobial, accessible material at relatively low cost, and having high biodegradability. Different from other studies that mostly focused on composition, the present study considered the use of micrometer-sized raw material. While other reports did not concern about the particle size, the present study focused on the effect of particle size of raw materials, which this study brings excellent insight for the development of bioplastic material. To support the analysis, the present study also was completed with a literature review regarding bioplastic production and proposal bioplastics material crack phenomena during mechanical testing.

2. Materials and Method

Preparation of Cornstarch-based Bioplastic Material. This study used micron-sized cornstarch particles (purchased from PT Egafood, Jakarta, Indonesia), turmeric (*Curcuma Longa*; collected from Bandung, Indonesia), acetic acid (25%; purchased from Sakura Medical Stores, Bandung, Indonesia), glycerol (95%; purchased from Sakura Medical Stores, Bandung, Indonesia), and distilled water (purchased from Sakura Medical Stores, Bandung, Indonesia). The experimental procedure is explained in Fig. 1.

Turmeric was washed, sliced into small pieces, and dried to remove the existence of water using an electrical furnace under atmospheric conditions. Dried turmeric was ground and mashed using a saw-milling process with a rotating speed of 18,000 rpm to obtain homogenous milling. Detailed information about the saw-milling process is explained in previous literature [15]. To obtain a specific size the milled turmeric was put into sieve test measurement with (PT Rumah Publication Indonesia, Indonesia with various holes of 2000, 1000, 530, 250, 125, 99, 74, 58, and 48 μm).
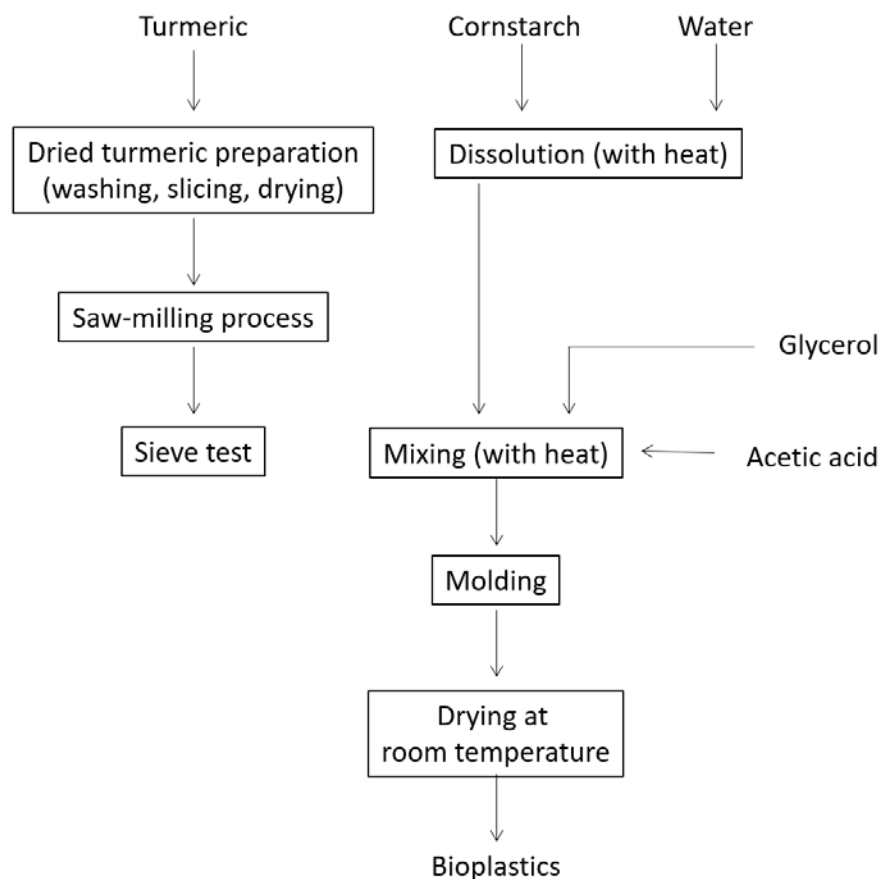
Fig. 1. Experimental procedure for the preparation of bioplastic

In the experimental procedure, to produce bioplastics, the following steps were carried out. The starch solution was prepared by dissolving cornstarch in distilled water and heating the mixture. Then, we added 95% of glycerol, 25% of acetic acid, and turmeric powder with various sizes of 250, 125, 100, and 74 µm, and the mixture was stirred until it gets homogeneous. At the same time with the gelatinization and manual mixing process, the mixture was heated at 60°C for 30 minutes using an electrical heater to obtain a viscous product. The viscous product was molded and dried at room temperature for more than 24 hours until it formed a solid yellow film.

Physicochemical properties. The morphology of the prepared samples was analyzed using a Digital Microscope (BXAW-AX-BC, China). To support the analysis, we conducted characterizations using a Fourier Transform infrared (FTIR-4600, Jasco Corp., Japan).

Mechanical properties. The observation of the bioplastic turmeric mechanical properties was observed using a compression test. The compression test was performed using 313 Family test machines at a scan rate of 1 mm/s at a temperature of 24°C and humidity of 10%, respectively. The compression test preparation was done by measuring the dimension of the sample using Vernier caliper and coat the compression plate using the lubricant. In this case, the lubricant is Vaseline that aims to reduce the friction effect.

Table 1 shows the mesh variation of the sample and its corresponding dimension. Data collected from compression tests such as Load vs Displacement, Stress vs Strain, and Young's modulus were evaluated for each sample to analyze its mechanical properties.

Table 1. Sample dimension

Sample, mesh	Particle size, µm	Dimension (length × width × thickness), cm
60	250	$2.00 \times 2.00 \times 0.50$
120	125	$2.00 \times 2.00 \times 0.70$
150	100	$2.00 \times 1.70 \times 0.70$
200	74	$2.00 \times 2.00 \times 0.50$

The following formula can be used to process the raw data from the compression test for further analysis:

(1) *Ultimate compression strength* (MPa) is defined as the maximum force that can be held in the sample when being compressed before the material is broken. The ultimate compression strength can be calculated by dividing maximum stress (F_M; N) with the cross-section area of the specimen (A; mm^2) as shown in Eq. (1).

$$\text{Compression strength} = \frac{F_M}{A}. \tag{1}$$

(2) *Young's modulus* (MPa) is a mechanical property that measures the stiffness of elastic deformation of specimens under a given load. Young's modulus can be obtained from the slope of the stress-strain since defines the relationship between stress (σ) and strain (ε) of material deformation in the linear elasticity regime. Young's modulus can be determined using Eq. (2).

$$\text{Young's Modulus} = \frac{\sigma_2 - \sigma_1}{\varepsilon_2 - \varepsilon_1}, \tag{2}$$

where ε_1 and ε_2 are the conditions of relative elongation and σ_1 and σ_2 are the stress that occurs at ε_1 and ε_2, respectively. The method of observing the slope-strain of the sample for defining Young's modulus is adopted since the slope of the sample can be directly observed as a function of the material deformation (strain)[16].

Biodegradability. The biodegradability tests were conducted by slicing the prepared bioplastics with sizes of about $5 \times 5 \times 5$ mm and then immersing them into ultrapure water. The weight losses of the sample were measured at the interval time of two days. In line with this test, during the immersing process, it was also visually observed the change of color. Detailed information about the biodegradability test is explained in our previous report[13].

3. Results and Discussion

Current reports on the preparation of bioplastics. To form a better bioplastic performance, the bioplastic raw materials were usually a combination of several materials, one of which acts as the main material and the other as reinforcing agents. The most recent reports on the synthesis of bioplastic materials with reinforcing agents are presented in Table 2.

Production of cornstarch-based bioplastics with varying turmeric microparticles. The production of cornstarch-based bioplastics with the addition of turmeric microparticles size variations is shown in Fig. 2. Visually, the bioplastic is yellow with the addition of turmeric to the cornstarch-based bioplastic. Figures 2(a-d) is a bioplastic appearance with variations in the size of turmeric: (a) 250, (b) 125, (c) 100, and (d) 74 μm. The large particle size of turmeric causes the bioplastic to crack more easily than the smaller particle size of turmeric.

The microscope analysis of bioplastic with the addition of turmeric size variations is shown in Fig. 2(e-j). Figures 2(e) and (f) are materials for the fabrication of bioplastics, namely micron-sized corn and variations size of turmeric powder, respectively. Micrometer-sized cornstarch particles were white crystals, solid, and dense. Turmeric powder has a yellow color, heterogeneous surface, and agglomerated. Figures 2(g-h) are the bioplastic surface appearance with variations in the size of turmeric of 250, 125, 100, and 74 μm, respectively. The bioplastic surface with the smallest turmeric size has a more homogeneous surface and is less brittle compared to the large turmeric size because of the size of the starch, which is almost the same as the size of turmeric that has a rigid structure. Figure 2(k) is the appearance of the bioplastic after being immersed for 6 days in water. The color of the bioplastic starts to change from yellow to brownish-yellow. It can be observed that after 6 days of immersion, cracks were found due to the swelling phenomenon. Figure 2(l) is the appearance of the bioplastic after being immersed for 4 weeks. The bioplastic surface with immersion for 4 weeks experienced a bad brittle phenomenon and a black fungus appears on the bioplastic surface.

Figure 3 shows the proposal formation mechanism of bioplastics prepared from the combination of cornstarch and turmeric with glycerol. The mechanism has used the assumption of two-particle interaction (i.e. Particle A and B) and they attach each other with glycerol (red molecule). Particles A and B have chemical structures of CR1 and CR2, respectively. CR1 and CR2 can be from starch (shown as green molecule) or turmeric (presented as blue molecule). In short, the polymerization was started from the interaction between Particle A and glycerol (see route R1). Then, additional heat treatment and catalyst (such as acetic acid), the interaction continues to the formation of glycerol-Particle A bonding (by releasing OH group). When there are other movements of Particle B (see route R2) to the surface of the glycerol-Particle A component (see route R3), another polymerization happens. This makes the final component contained a packed balls-like structure[13].

Table 2. Current reports on the synthesis of bioplastic with an additional reinforcing agent

Type of carbohydrate	Reinforcing agent	Raw material	Results	Ref.
Cassava starch	Zinc oxide/clay	Cassava starch, glycerol, distilled water, zinc oxide/organoclay	Additional zinc oxide/clay improve mechanical properties. The best ratio with the addition of 0.3:0.7 of zinc oxide/clay has a tensile strength of 20.87 MPa	[17]
	Oil palm	Cassava starch, oil palm, glycerol, and distilled water	Additional oil palm has not increased mechanical properties. However, it accelerated biodegradation	[18]
	Chitosan and Kraft fiber	Cassava starch, distilled water, Kraft fiber, chitosan, acetic acid, and glycerol	The best bioplastic with the addition of 30% of Kraft fiber and 4% of chitosan had properties similar to polystyrene foam	[19]
	Pumpkin residues and oregano essential oil	Cassava starch, pumpkin residues (skin), oregano essential oil, glycerol, 2,2-diphenyl-1-picrylhydrazyl radical (DPPH), thiobarbituric acid (TBA), trichloroacetic acid (TCA), butyl hydroxyl toluene (BHT), 1,1,3,3-tetraethoxypropane (TEP)	Compared with pumpkin residues (skin), bioplastic with oregano essential oil increased antimicrobial activity	[20]
	Cornstarch	Cassava starch, cornstarch, glycerol, distilled water	Starch-based bioplastics (40 g/kg) had mechanical properties comparable to LDPE-based films	[21]
	Polycaprolactone (PLC)	Cassava starch, Polycaprolactone (PLC), glycerol, and ethanol (99.8% v/v absolute ethyl alcohol	Bioplastic made from a mixture of PCL/cassava starch does not improve the mechanical properties	[22]

Table 2 (continue). Current reports on the synthesis of bioplastic materials

Type of carbohydrate	Reinforcing agent	Raw material	Results	Ref.
Cornstarch	Taro starch nanoparticles (TSNPs)	Cornstarch, taro starch,	Bioplastic with the addition of taro starch increased tensile strength from 1.11 to 2.87 MPa. However, increased concentration of taro starch decreases water vapor permeability (WVP) of bioplastic	[23]
	Palm fibers	Cornstarch, palm fibers, NaOH, acetic acid, glycerin, and distilled water	The additions of the reinforcement (palm fibers) improve the tensile strength, biodegradation, Young's modulus, and water uptake.	[24]
	Cornhusk fiber	Cornstarch, corn husk fiber, fructose, and distilled water	Bioplastics with the addition of husk fibers improve mechanical properties and thermal stability. However, it decreases biodegradation	[25]
	Barley straw (*Hordeum vulgare L.*)	Cornstarch (CS), glycerol, distilled water, and Barley straw (*Hordeum vulgare L.*)	Bioplastic with the addition of 15% of barley straw increased tensile strength, Young's modulus, and thermal stability	[26]
	Sisal fibers	Cornstarch, sisal fiber, and glycerol	Sisal fibers increase tensile strength and Young's modulus. It also improved chemical modification in matrix	[27]
Sugar palm starch	Sugar palms Nano fibrillated cellulose (SPNFCs)	Sugar palms fiber, sugar palm starch, Sodium hydroxide, sodium chlorite (80% purity), acetic acid, sorbitol, and glycerol	It increased water barrier properties sugar palm-based bioplastic	[28]
Jack fruit seed starch	Banana fruit skin powder (BSP)	Jack fruit starch, banana fruit skin powder, distilled water, and glycerol	The best bioplastic with the addition of 1% of banana skin powder had maximum tensile strength of 10.90 MPa and good biodegradability	[29]

Table 2 (continue). Current reports on the synthesis of bioplastic materials

Type of carbohydrate	Reinforcing agent	Raw material	Results	Ref.
Potato starch	Corn fibers and poly (vinyl alcohol) (PVA)	Potato starch, corn fibers, distilled water, and glycerol	The addition of corn fiber decreases mechanical properties and improved water resistance.	[30]
	Wood fiber	Potato starch, wood fiber, guar gum, and magnesium stearate	40% of wood fiber has the highest tensile strength of 128 MPa and Young's modulus of 3200 MPa	[31]
	Titanium oxide nanoparticles (TiO$_2$ NPs)	Potato starch, titanium oxide nanoparticles (TiO$_2$-NPs), distilled water, and glycerol	The addition of TiO$_2$-NPs at low concentrations improved the mechanical properties and moisture barrier of the bioplastic.	[32]
Pea starch	Waxy maize starch nanocrystals	Pea starch (about 40% amylose), Waxy maize starch (98% amylopectin), glycerol, sulfuric acid, potassium carbonate.	Bioplastics with the addition of waxy maize nanocrystals increase tensile strength. The highest tensile strength values contain 5% of waxy maize nanocrystals	[33]
Wheat gluten	Coconut fiber	Wheat gluten, (3-triethoxysilylpropyl)-tbutylcarbamate (carbamate silane) sodium hydroxide, and coconut fiber	Bioplastics with the addition of coconut fiber increase the tensile strength by 80%	[34]
	Flax fiber	Wheat gluten powder, glycerol, ethanol, and flax fiber	19% of flax fiber improved the quality crack resistance and stress maximum from 2 to 29 MPa. The bioplastic surface is homogeneous	[35]
	Lignin nanoparticles (LNP)	Wheat gluten, lignin nanoparticles, distilled water, glycerol, and hydrochloric acid	Bioplastic with the addition of LNP increased mechanical properties, thermal stability, and water sensitivity. However, the transparency of bioplastic decreases	[36]

Table 2 (continue). Current reports on the synthesis of bioplastic materials

Tamarin seed	Banana fiber	Tamarin seed, banana fiber, distilled water, and glycerol	The temperature condition of tamarind seeds 130°C has the highest tensile strength of 3.97 MPa	[37]
Banana peel	Cornstarch	Banana peel, cornstarch, hydrochloric acid, glycerol, and sodium hydroxide	4% of cornstarch has the highest tensile strength of 34.72 N/m^2	[38]
	Zinc oxide (ZnO)	Banana peel, glycerol, chitosan flakes, NaOH, glacial acetic acid, distilled water, and zinc oxide	Bioplastic composition with 4-30% of chitosan, starch, glycerol, 5% of ZnO shows the bioplastic with the best microbial activity	[39]
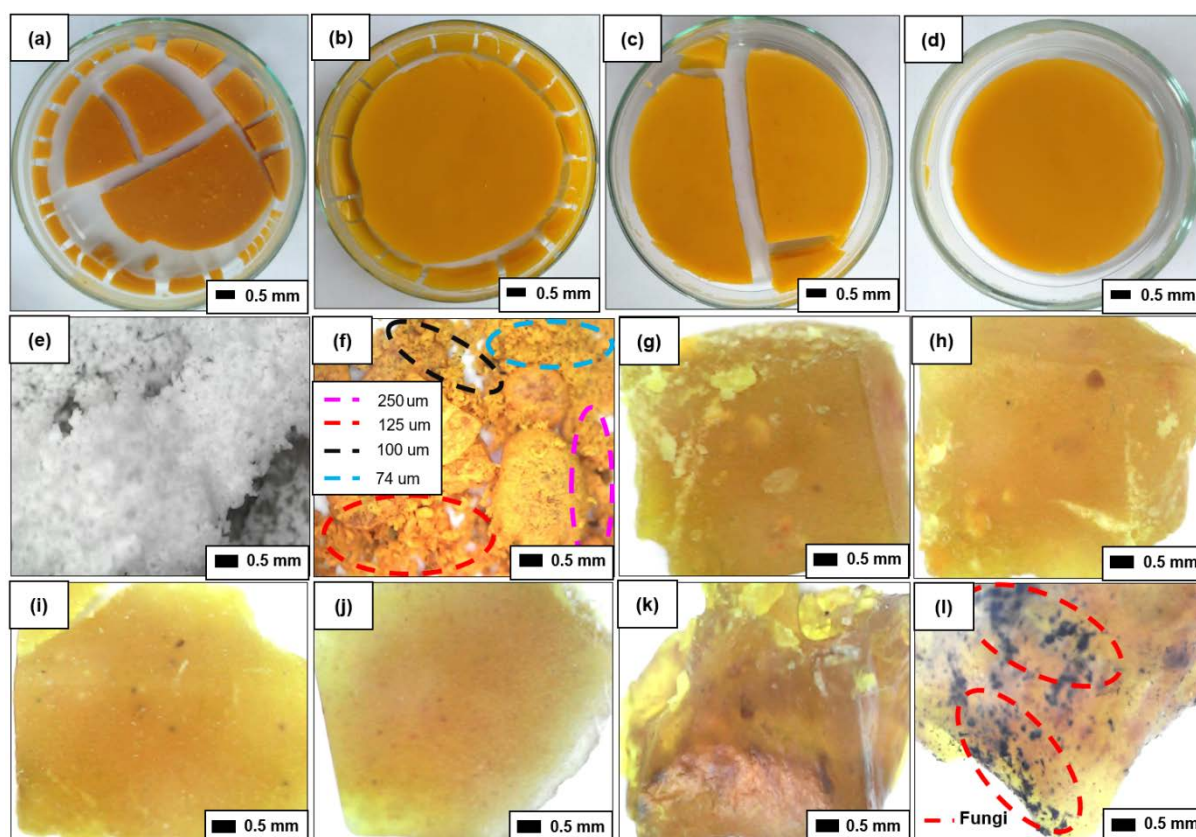
Fig. 2. Photograph image of cornstarch-based bioplastics with the addition various size turmeric (a) 250, (b) 125, (c) 100 and (d) 74 μm. Microscope images of (e) micro-sized cornstarch, (f) turmeric powder, (g-j) bioplastic prepared using turmeric with sizes of 250, 125, 100, 74 μm, respectively, (k) bioplastics after 6 days immersed in water and (l) fungi bioplastic after 4 weeks immersed in water
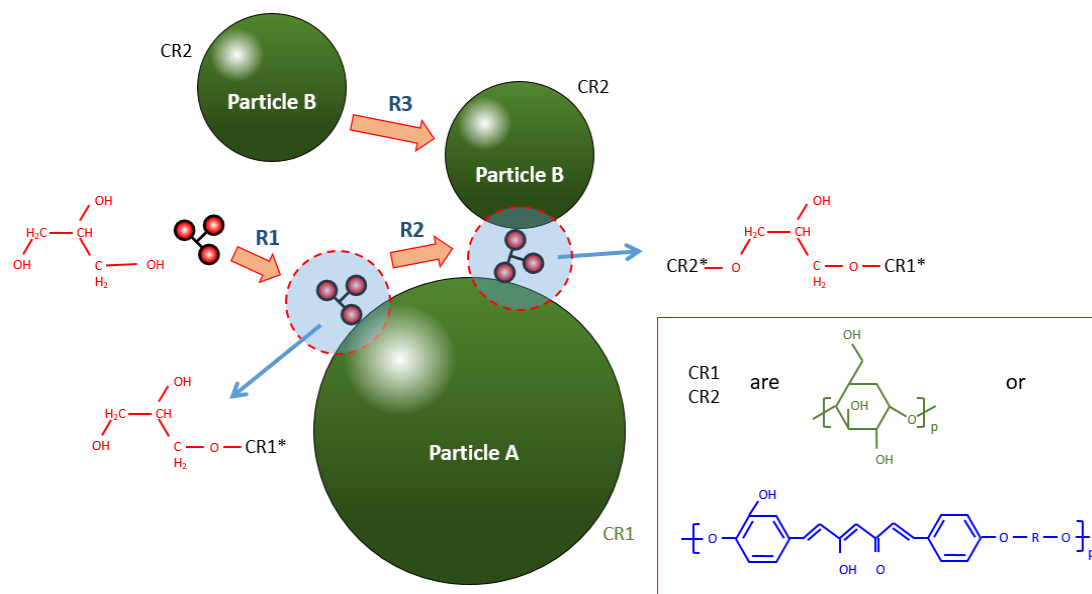
Fig. 3. Proposal reactions during the polymerization in the formation of bioplastic. Particles A and B have the chemical structure of CR1 and CR2 respectively. CR1 and CR2 can be from starch or turmeric

Biodegradability of cornstarch-based bioplastics with varying turmeric microparticles. To confirm the phenomenon during the immersion process as shown in Figs. 2(k) and (l), Fig. 4 shows the results of the FTIR analysis results of as-prepared bioplastics, bioplastics immersed for 2 weeks in water, and the surface of the bioplastic samples immersed for 4 weeks. The as-prepared bioplastic content results were identified at wavelengths of 1014, 1723, and 3300 cm^{-1} [40]. The comparison of the FTIR peaks for bioplastics before and after 2-week immersion in water confirms that the biodegradability in water was only the dilution of the outer component on the bioplastics. The reaction between water and bioplastics involves a dilution process and did not interfere with complicated reactions.

We also found that immersion for 4 weeks caused the appearance of fungi on the bioplastic surface. The bioplastic surface analysis shows that the fungus degrades the bioplastics, converting the bioplastic chemical structure to the fungal structure (see the green dashed area in Fig. 4) [41].

To confirm the weight losses during the immersion process, we analyzed the mass of bioplastic as a function of the day (see Table 3). Table 3 shows the results of bioplastic weight loss carried out for a week. The results showed that bioplastics' weight decreased for 4 days of immersion in water. The possible weight loss during 2-week immersion is because the bioplastics' outer surfaces were diluted in water, confirmed by the identical FTIR patterns. This result is different for 4-week immersion bioplastic, in which the mass loss was followed by the appearance of fungus (see Fig. 2 (l)) and fungus chemical structure (see Fig. 3). The present bioplastics were made from cornstarch, making microorganisms more easily break the polymer chain inside the bioplastics themselves [41]. In addition, compared to the bioplastic prepared from cornstarch only [13], the decomposition of the present bioplastic is slower. The existence of turmeric deters the growth of microorganisms since turmeric has an antiseptic effect.
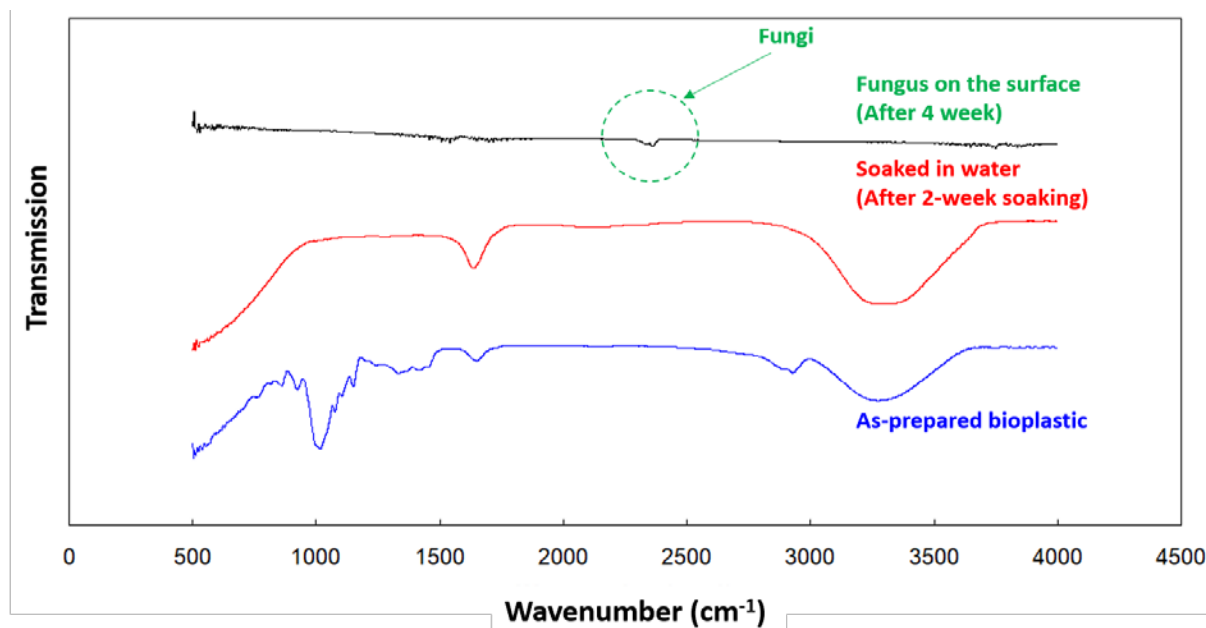
Fig. 4. FTIR analysis results of as-prepared bioplastic, 2-week immersed bioplastic in water, and fungus on the 4-week immerged sample

Mechanical properties of cornstarch-based bioplastics with varying turmeric microparticles. The mechanical properties of samples were determined by applying load gradually to the samples and measuring their deformation [42]. The load and deformation data is then used to obtain the stress and strain curve [43]. The stress-strain curve of bioplastic samples with variation of micrometer size is presented in Fig. 5. Based on the stress-strain curve, the ultimate strength is determined from the first peak of the stress-strain curve (see Fig. 6). Table 4 summarizes the ultimate strength of all samples. The curve shows a random trend where the highest ultimate strength achieved by the sample of 74 μm and the lowest ultimate strength obtained from sample of 125 μm while sample of 250 μm is in between.

The ultimate strength values of samples prepared using turmeric particles size of 74, 100, and 125 μm are 2563, 1618, and 1164 kPa respectively (Table 4). It shows the decreasing value of ultimate strength with the increasing particle size of the sample. Smaller particles have a higher total surface area of the filler particles, allowing more efficient stress transfer mechanisms and resulting in the higher ultimate strength of the sample [44]. Smaller particles also affect the adhesive factor that increases intermolecular bonding, hence resulting in higher material strength. However, the larger particles (sample of 250 μm) did not show the same characteristics. This could be caused by the microstructural mechanism, thus further observation on sample morphology needs to be performed to observe this phenomenon.

A.B.D. Nandiyanto, F. Triawan, M. Fiandini, I.O. Suryani, G.K. Sunnardianto

Table 3. Weight loss bioplastics with addition of size turmeric during immersion process

Size (um)	Days	Initial Dimension, cm^2	Initial mass, g	Mass after Immersion, g	Mass loss, wt%	Decay dimension, g/cm^2
250	1	1.084	0.133	0.080	40	0.050
	2	1.161	0.113	0.053	53	0.051
	4	1.216	0.143	0.063	56	0.067
	6	1.128	0.100	0.040	60	0.055
	8	0.972	0.137	0.047	66	0.102
	10	1.115	0.143	0.043	70	0.095
	14	1.117	0.140	0.037	74	0.104
125	1	1.090	0.123	0.077	38	0.043
	2	1.249	0.117	0.057	51	0.047
	4	1.165	0.190	0.083	56	0.092
	6	1.262	0.137	0.043	68	0.074
	8	1.268	0.137	0.040	71	0.077
	10	1.220	0.147	0.037	75	0.092
	14	1.242	0.133	0.030	77	0.084
100	1	1.013	0.127	0.073	43	0.053
	2	1.127	0.110	0.063	45	0.043
	4	1.044	0.130	0.050	62	0.077
	6	0.894	0.117	0.037	68	0.094
	8	1.188	0.137	0.037	73	0.090
	10	1.290	0.143	0.033	77	0.087
	14	1.274	0.143	0.030	79	0.093
74	1	0.895	0.150	0.110	28	0.045
	2	1.080	0.133	0.053	60	0.075
	4	0.960	0.137	0.047	66	0.096
	6	1.124	0.147	0.043	70	0.092
	8	1.020	0.133	0.033	75	0.099
	10	0.870	0.140	0.027	81	0.135
	14	1.010	0.133	0.020	85	0.114
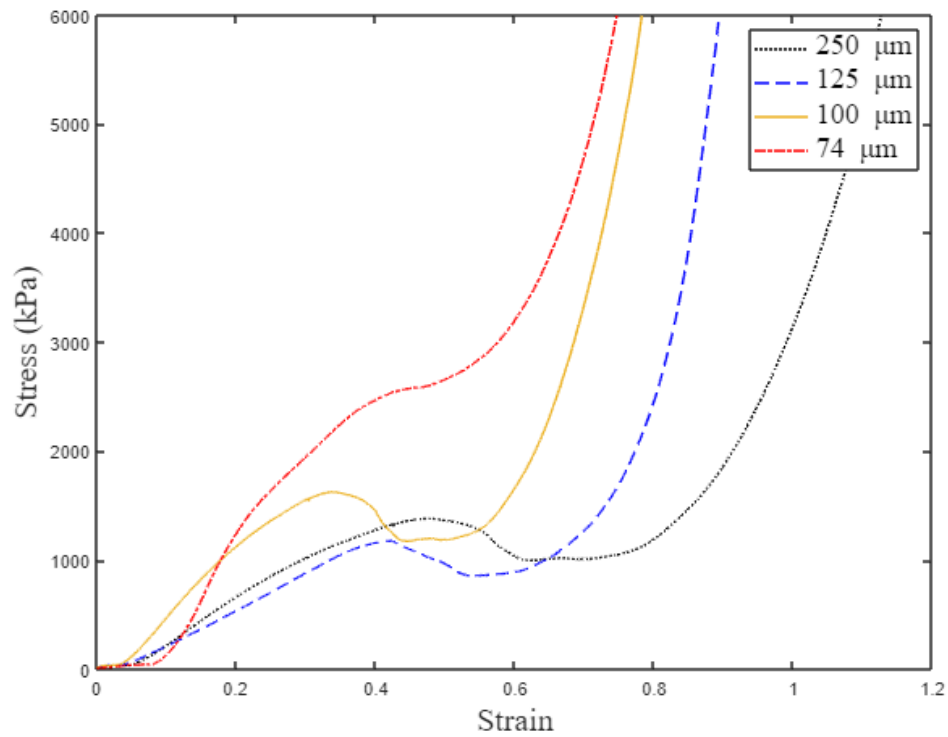
Fig. 5. Stress vs Strain of bioplastic samples
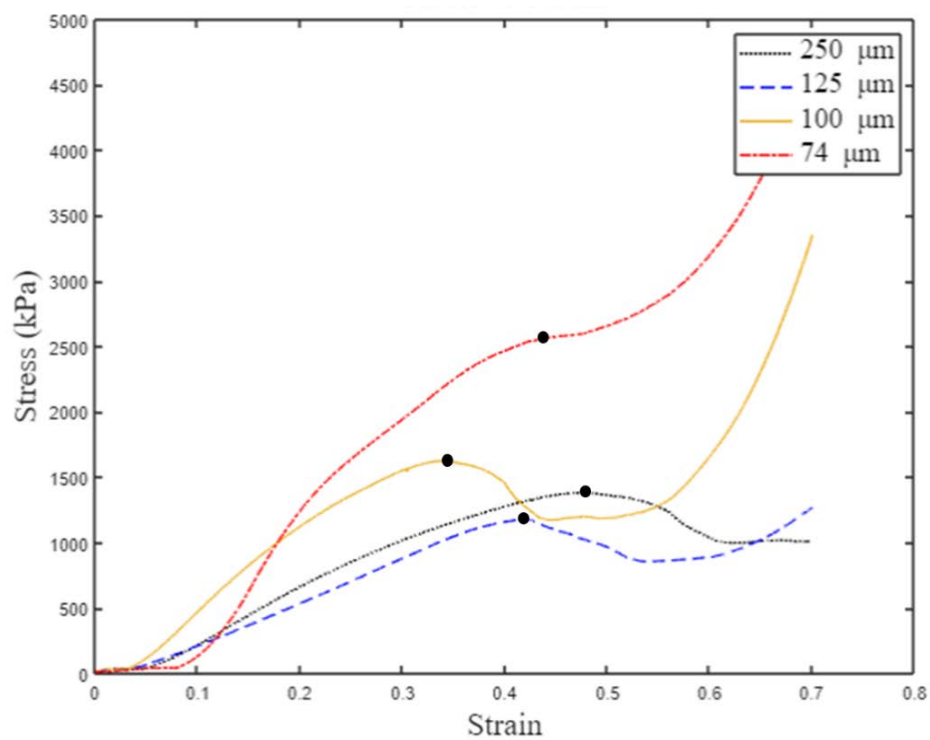
Fig. 6. Stress vs Strain of bioplastic samples limited at strain of 0.70 and stress of 4500 kPa

Table 4. The ultimate strength of bioplastic samples

Sample, μm	Ultimate strength, kPa
250	1379
125	1164
100	1618
74	2563

Variation of particle size affecting the Young's modulus (stiffness) of the sample. As the particle size increases, the stiffness of the sample tends to decrease as shown in Fig. 7. The highest slope of stress-strain curve shown in Fig. 7 indicates the Young's modulus value of each sample, in which the sample with particle sizes of 74, 100, and 125 μm are 14780, 7724, and 2626 kPa, respectively (Table 5). The addition of small microparticles to the polymatrix result in higher Young's modulus as they have higher intermolecular bonding in the larger area, making the material difficult to deform as a load is applied. Different trends for the sample with particle sizes of 250 μm that has Young's modulus of 5116 kPa need to be observed in terms of its microstructure, as previously reported that microstructure (due to particle size distribution) affects the material stiffness.
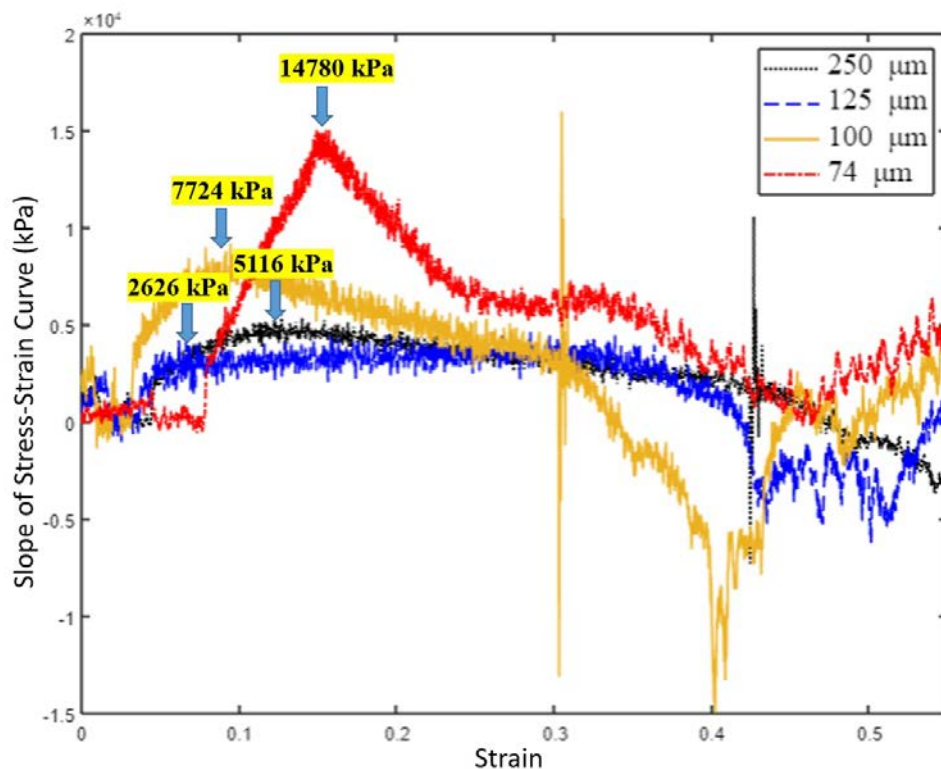
Fig. 7. Young's modulus vs Strain of bioplastic samples

Table 5. The Young's moduli of bioplastic samples

Sample, μm	Young's modulus, kPa
250	5116
125	2626
100	7724
74	14780

Proposal cornstarch-based bioplastics crack. To get deeper insights into the bonds, area having a minimum and maximum stress concentration, and the bond-breaking initiation, an illustrative model is qualitatively shown in Fig. 8. The figure shows a particle stress distribution evolution, a bond breaking, crack nucleation, and growth scenario of the system during the applied compression test. The concept was derived from the existence of particle-particle interaction based on Fig. 3. The polymerization happens on the surface of the particle, and there is no change in the chemical composition inside the particle.

Figure 8(a) shows stress distribution before bond breaking. Prior to the applied stress, the particle arrangement was in the perfect lattice site. At the initial stage of loading, the particle position of chains started to shift from the perfect position. As shown in Fig. 8(b), as the loading increased, more particles deviated from their original perfect position. These deviated particles increased the interaction with their neighboring causing the lattice re-arrangement [43]. This particle arrangement basically has a vital role to create small defects, which is indicated by changing particle stress color from light green to other colors (blue and red), mostly particles at loading points and center of the cell. Here, the force due to the compression is gradually localized into two chains with the formed symmetrical region, resulting in the agglomeration of deformation due to particles having the highest stress. In Figure 8(c), further loading leads to the highest stress distribution at the loading point initially, and reconstruction of the geometry of the chain propagated towards the loading direction and accumulate at the center of the cell. Thus, it initiates the bond-breaking simultaneously at the loading point and along the chain propagates vertically in the direction of loading. This bond-breaking leads to the small destruction of small clustering deformation in the center of the particle. With agglomerate deformation, the degree of force and stress increased at the center. Then, subsequent breaking bonds leading to the formation of initiated crack, which grows along the y-direction. The crack was initiated at the center of the cell, indicated by the highest stress (red-colored) where the established bonds are still in an unstable bonding, propagated in y-direction toward its loading platens. In the end, with the further increases in the applied loading, the region having the highest stress experienced more bond breaking, resulting in successive de-bonding along the y-direction. Then, it causes damaging the bond connection and ends up with the fracture of the system. After the bond breaking, the highest stress changes to the lower stress. This compressive loading induced alternating local and the whole binding configurations and its subsequent impact on the initiation of failure of the system. As a result, it breaks the polymer chain until complete rupture (See Fig. 8(d)).
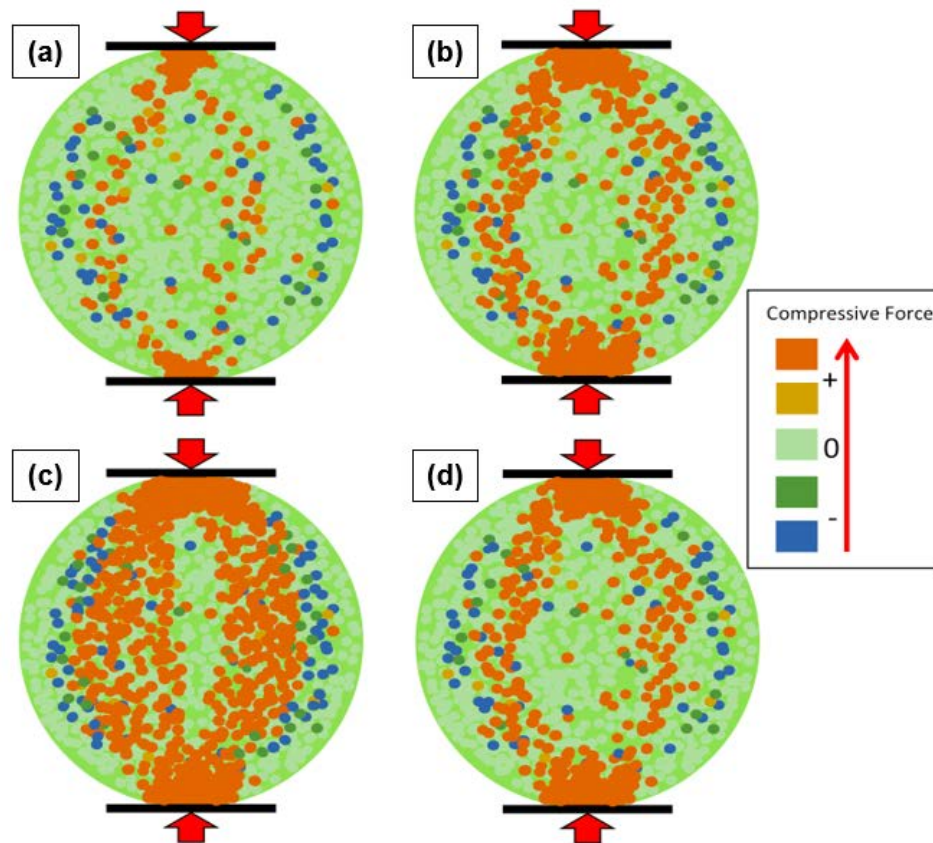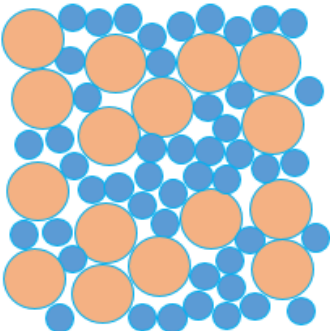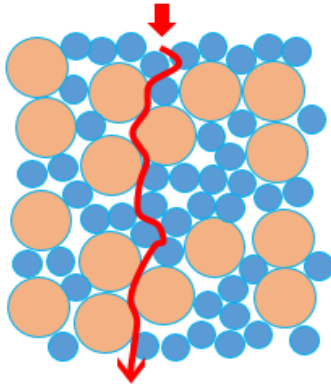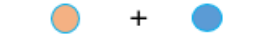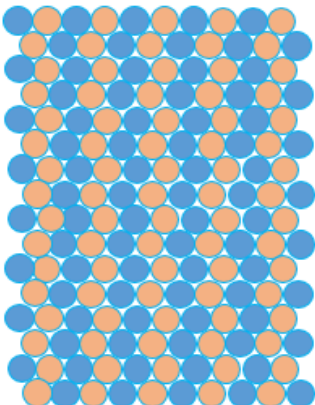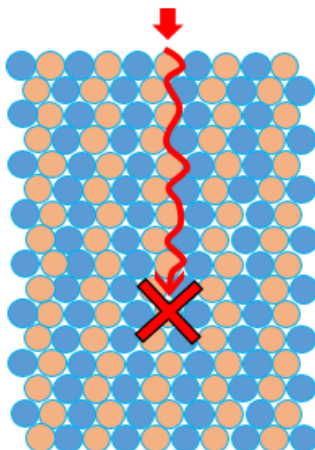
Fig. 8. The model of particle stress distribution in the bioplastic during the loading. Particles are colored cording to the corresponding particle stresses. Light green represents a perfect structure, blue or green showing for low stress, and red color for high stress. The system to be investigated is represented by a visualization cell, in which all particles are enclosed and interacted. The top and bottom surface is subjected to a compression force in y-direction

Table 6 shows a 2-dimensional model of the crack propagation path of the sample under the compression load. When a load is applied to the material, the cracks will propagate to a region with less bonding energy in the particle structure. As the region with lower interfacial energy, the interface between particles plays an important role in the crack propagation mechanism. When there are two types of particles (i.e. Particles A and B), the packing particles depend on the initial sizes of particles A and B. The red arrow is the position of the crack due to the applied load during the compression test, and the red line is the crack path in the sample.

As illustrated in Table 6, the surface area to volume ratio increases for material with smaller particle size. It introduces a larger proportion of particles to be found in the material. Those small particles induce small volume voids inside the material that makes the material to be more compact and stronger. The small volume voids prevent the crack propagation movement in the material. Under the applied load, the material with larger particles is likely to experience a severe disturbance of opening matrix angle that eventually results in bigger cracking compared to material with smaller particles. Larger particles also result in a material with larger voids inside it, allowing the crack easily propagate in the material since the material is less rigid.

Table 6. Illustration cracking progression

Type	Model	Crack Model
2 particles with different sizes		
2 particles with almost the same sizes		

5. Conclusion

The mechanical and biodegradation properties of bioplastics from turmeric with various sizes were evaluated. The results showed that particle size affects the mechanical properties of the material. Turmeric particles with a small size tend to have a larger surface area, allowing for a stronger bonding area between particulates, and resulting in a higher stiffness and strength of the material. In contrast, larger particles have a lower interfacial strength, which makes a crack easier to propagate even at lower loads. However, there is a nonlinear trend found in this study where up to 250 μm has a higher strength than that of 125 μm. This is probably due to the non-uniform distribution of particles, which affects the strength of the material. Bioplastic biodegradability is also influenced by particle size. The smaller the size of the turmeric, the greater solubility it will be. Apart from the solubility parameters, a larger weight loss is also observed in a sample with smaller size, indicating good biodegradation.

References

[1] Santana RF, Bonomo RCF, Gandolfi ORR, Rodrigues LB, Santos LS, dos Santos Pires AC, de Oliveira CP, Fontan RdCI, Veloso CM. Characterization of starch-based bioplastics

from jackfruit seed plasticized with glycerol. *Journal of Food Science and Technology*. 2018;55(1): 278-286.

[2] Sagnelli D, Hooshmand K, Kemmer GC, Kirkensgaard JJK, Mortensen K, Giosafatto CVL, Holse M, Hebelstrup KH, Bao J, Stelte W. Cross-linked amylose bio-plastic: A transgenic-based compostable plastic alternative. *International Journal of Molecular Sciences*. 2017;18(10): 2075.

[3] Salahin N, Begum RA, Hossian S, Ullah MM, Alam MK. Degradation of soil properties under ginger, turmeric, aroid, and jhum rice cultivation in hilly areas of Bangladesh. *Bangladesh Journal of Agricultural Research*. 2013;38(2): 363-371.

[4] Baek CS, Cho KH, Ahn JW. Effect of Grain Size and Replacement Ratio on the Plastic Properties of Precipitated Calcium Carbonate Using Limestone as Raw Material. *Journal of the Korean Ceramic Society*. 2014;51(2): 127-131.

[5] Codou A, Misra M, Mohanty AK. Sustainable biocarbon reinforced nylon 6/polypropylene compatibilized blends: Effect of particle size and morphology on performance of the biocomposites. *Composites Part A: Applied Science and Manufacturing*. 2018;112: 1-10.

[6] Farley R, Valentin FHH. Effect of particle size upon the strength of powders. *Powder Technology*. 1968;1(6): 344-354.

[7] Abdullah AHD, Pudjiraharti S, Karina M, Putri OD, Fauziyyah RH. Fabrication and characterization of sweet potato starch-based bioplastics plasticized with glycerol. *Journal of Biological Science*. 2019;19(1): 57-64.

[8] Lubis M, Harahap MB, Ginting MHS, Maysarah S, Gana A. The effect of ethylene glycol as plasticizer against mechanical properties of bioplastic originated from jackfruit seed starch and cocoa pod husk. *Nusantara Bioscience*. 2018;10(2): 76-80.

[9] Sumarni W, Prasetya AT, Rahayu EF. Effect of glycerol on physical properties of biofilms gembili starch (dioscorea esculenta)-chitosan. *Proceeding of Chemistry Conference*. 2017;2: 56-65.

[10] Oleyaei SA, Almasi H, Ghanbarzadeh B, Moayedi AA. Synergistic reinforcing effect of TiO_2 and montmorillonite on potato starch nanocomposite films: Thermal, mechanical and barrier properties. *CarbohydratePolymers*. 2016;152: 253-262.

[11] Borchani KE, Carrot C, Jaziri M. Biocomposites of Alfa fibers dispersed in the Mater-Bi® type bioplastic: Morphology, mechanical and thermal properties. *Composites Part A: Applied Science and Manufacturing*. 2015;78: 371-379.

[12] Vadori R, Mohanty AK, Misra M. The effect of mold temperature on the performance of injection molded poly (lactic acid)-based bioplastic. *Macromolecular Materials and Engineering*. 2013;298(9): 981-990.

[13] Nandiyanto ABD, Fiandini M, Ragadhita R, Sukmafitri A, Salam H, Triawan F. Mechanical and biodegradation properties of cornstarch-based bioplastic material. *Materials Physics and Mechanics*. 2020;44(3): 380-391.

[14] Triawan F, Nandiyanto ABD, Suryani IO, Fiandini M, Budiman BA. The influence of turmeric microparticles amount on the mechanical and biodegradation properties of cornstarch-based bioplastic material: From bioplastic literature review to experiments. *Materials Physics and Mechanics*. 2020;46(1): 99-114.

[15] Nandiyanto ABD, Andika R, Aziz M, Riza LS. Working volume and milling time on the product size/morphology, product yield, and electricity consumption in the ball-milling process of organic material. *Indonesian Journal of Science and Technology*. 2018;3(2): 82-94.

[16] Triawan F, Nakagawa R, Inaba K, Budiman BA, Kishimoto K. Experimental investigation of shear stress effect on the flexural behavior of aluminum foam beam. *Journal of Mechanical Science and Technology*. 2020;34: 1831-1836.

[17] Yunus M, Fauzan R. Effect of clove essential oil addition on characteristics of cassava starch bioplastic film incorporated zinc oxide-organoclay as reinforcement. *IOP Conference Series: Materials Science and Engineering*. 2019;536(1): 012138.

[18] Abdullah AHD, Fikriyyah AK, Dewantoro R. Fabrication and characterization of starch based bioplastics with palm oil addition. *Jurnal Sains Materi Indonesia*. 2019;20(3): 126.

[19] Kaisangsri N, Kerdchoechuen O, Laohakunjit N. Biodegradable foam tray from cassava starch blended with natural fiber and chitosan. *Industrial Crops and Products*. 2012;37(1): 542-546.

[20] Dos Santos Caetano K, Lopes NA, Costa TMH, Brandelli A, Rodrigues E, Flôres SH, Cladera-Olivera F. Characterization of active biodegradable films based on cassava starch and natural compounds. *Food Packaging and Shelf Life*. 2018;16: 138-147.

[21] Luchese CL, Spada JC, Tessaro IC. Starch content affects physicochemical properties of corn and cassava starch-based films. *Industrial Crops and Products*. 2017;109: 619-626.

[22] Petnamsin C, Termvejsayanon N, Sriroth K. Effect of particle size on physical properties and biodegradability of cassava starch/polymer blend. *Agriculture and Natural Resources*. 2000;34(2): 254-261.

[23] Dai L, Qiu C, Xiong L, Sun Q. Characterisation of corn starch-based films reinforced with taro starch nanoparticles. *Food Chemistry*. 2015;174: 82-88.

[24] Ibrahim H, Farag M, Megahed H, Mehanny S. Characteristics of starch-based biodegradable composites reinforced with date palm and flax fibers. *Carbohydrate Polymers*. 2014;101: 11-19.

[25] Ibrahim MIJ, Sapuan SM, Zainudin ES, Zuhri MYM. Potential of using multiscale corn husk fiber as reinforcing filler in cornstarch-based biocomposites. *International Journal of Biological Macromolecules*. 2019;139: 596-604.

[26] Silva-Guzmán JA, Anda RR, Fuentes-Talavera FJ, Manríquez-González R, Lomelí-Ramírez MG. Properties of thermoplastic corn starch based green composites reinforced with barley (Hordeum vulgare L.) straw particles obtained by thermal compression. *Fibers and Polymers*. 2018;19(9): 1970-1979.

[27] Campos A, Marconcini JM, Imam SH, Klamczynski A, Ortis WJ, Wood DH, Williams TG, Martins-Franchetti SM, Mattoso LHC. Morphological, mechanical properties and biodegradability of biocomposite thermoplastic starch and polycaprolactone reinforced with sisal fibers. *Journal of Reinforced Plastics and Composites*. 2012;31(8): 573-581.

[28] Ilyas RA, Sapuan SM, Ishak MR, Zainudin ES. Water transport properties of bio-nanocomposites reinforced by sugar palm (Arenga Pinnata) nanofibrillated cellulose. *Journal of Advanced Research in Fluid Mechanics and Thermal Sciences*. 2018;51(2): 234-246.

[29] Shahrim NA, Rani NNSA, Sarifuddin N, Zaki HHM, Azhar AZA. Effects of banana skin powder on properties of jackfruit seed starch/poly (vinyl alcohol) PVA film. In: *Proc. of AMCT 2017*. 2017. p.571.

[30] Cinelli P, Chiellini E, Lawton JW, Imam SH. Foamed articles based on potato starch, corn fibers and poly (vinyl alcohol). *Polymer Degradation and Stability*. 2006;91(5): 1147-1155.

[31] Duanmu J, Gamstedt EK, Pranovich A, Rosling A. Studies on mechanical properties of wood fiber reinforced cross-linked starch composites made from enzymatically degraded allylglycidyl ether-modified starch. *Composites Part A: Applied Science and Manufacturing*. 2010;41(10): 1409-1418.

[32] Dash KK, Ali NA, Das D, Mohanta D. Thorough evaluation of sweet potato starch and lemon-waste pectin based-edible films with nano-titania inclusions for food packaging applications. *International Journal of Biological Macromolecules*. 2019;139: 449-458.

[33] Li X, Qiu C, Ji N, Sun C, Xiong L, Sun Q. Mechanical, barrier and morphological properties of starch nanocrystals-reinforced pea starch films. *Carbohydrate Polymers*. 2015;121: 155-162.

[34] Hemsri S, Grieco K, Asandei AD, Parnas RS. Wheat gluten composites reinforced with coconut fiber. *Composites Part A: Applied Science and Manufacturing*. 2012;43(7): 1160-1168.

[35] Wu Q, Rabu J, Goulin K, Sainlaud C, Chen F, Johansson E, Olsson RT, Hedenqvist MS. Flexible strength-improved and crack-resistant biocomposites based on plasticised wheat gluten reinforced with a flax-fibre-weave. *Composites Part A: Applied Science and Manufacturing*. 2017;94: 61-69.

[36] Yang W, Kenny JM, Puglia D. Structure and properties of biodegradable wheat gluten bionanocomposites containing lignin nanoparticles. *Industrial Crops and Products*. 2015;74: 348-356.

[37] Kiruthika AV, Priyadarzini TRK, Veluraja K. Preparation, properties and application of tamarind seed gum reinforced banana fibre composite materials. *Fibers and Polymers*. 2012;13(1): 51-56.

[38] Sultan NFK, Johari WLW. The development of banana peel/corn starch bioplastic film: A preliminary study. *Bioremediation Science and Technology Research*. 2017;5(1): 12-17.

[39] Agustin YE, Padmawijaya KS. Effect of glycerol and zinc oxide addition on antibacterial activity of biodegradable bioplastics from chitosan-kepok banana peel starch. *IOP Conference Series: Materials Science and Engineering*. 2017;223(1): 012046.

[40] Nandiyanto ABD, Oktiani R, Ragadhita R. How to read and interpret FTIR spectroscope of organic material. *Indonesian Journal of Science and Technology*. 2019;4(1): 97-118.

[41] Valdés A, Fenollar O, Beltrán A, Balart R, Fortunati E, Kenny JM, Garrigós MC. Characterization and enzymatic degradation study of poly (ε-caprolactone)-based biocomposites from almond agricultural by-products. *Polymer Degradation and Stability*. 2016;132: 181-190.

[42] Sukrawan Y, Hamdani A, Mardani SA. Effect of bamboo weight faction on mechanical properties in non-asbestos composite of motorcycle brake pad. *Materials Physics and Mechanics*. 2019;42(3): 367-372.

[43] Nandiyanto ABD, Triawan F, Firly R, Abdullah AG, Aono Y, Inaba K, Kishimoto K. Identification of micro-mechanical characteristics of monoclinic tungsten trioxide microparticles by nanoindentation technique. *Materials Physics and Mechanics*. 2019;42(3): 323-329.

[44] Wu J, Feng M, Chen Z, Mao X, Han G, Wang Y. Particle size distribution effects on the strength characteristic of cemented paste backfill. *Minerals*. 2018;8(8): 322.

RESULTS OF MEASUREMENTS OF SUBSTRATE DEFORMATION AND DETERMINATION BY BENDING OF INTERNAL STRESSES IN Ti-TiC-DLC COATING OBTAINED BY USING HiPIMS TECHNOLOGY

A.V. Ryzhenkov, A.V. Volkov, A.F. Mednikov, A.B. Tkhabisimov[*], O.S. Zilova,

S.V. Sidorov

National Research University "Moscow Power Engineering Institute", 14 Krasnokazarmennaya st., Moscow,

Russia

*e-mail: abt-bkt@mail.ru

Abstract. The paper presents the results of studies of internal stresses in ion-plasma coating Ti-TiC-DLC. A method based on measuring the deformation of the substrate was used to carry out this research. Plates of 08kp steel were used as a substrate, the geometry of which was chosen based on their further application for droplet erosion testing and determination of stresses arising in the coating under high-speed drop impact. A technique is presented for conducting research on substrates with a geometry that is changed in comparison with the classical configuration used to determine the internal stresses in the coating by the bending method. Bending values were obtained from the surface profiles obtained before and after coating, which were used to calculate stresses by using the Stoney formula. Application of the selected coating leads to the appearance of compressive stresses ranging from 3 to 9 GPa.
Keywords: stress measurement, diamond-like carbon coatings, high power impulse magnetron sputtering, droplet erosion

1. Introduction
Diamond-like carbon (DLC) coatings had a number of valuable properties that gave rise to interest in the application of such coatings in various fields of science and technology (automotive and mechanical engineering, medicine, electronics, etc.) [1]. They are quite easy to adapt to different substrates, have low resistance, high mechanical hardness, high wear resistance, chemical inertia and resistance to aggressive media, biological compatibility, good dielectric properties, and high heat conductivity [2-5]. However, in the manufacture of diamond-like coatings, it was practically impossible to avoid the appearance of residual internal mechanical stresses, which limited their use.

Internal stresses have a significant effect on the strength, adhesion, and other performance of the coatings. They arise in the coating at the forming stage, as well as in the operation of the articles due to various influencing factors, one of which is the water droplet impact, leading to erosion wear of the protected substrate material.

There are a number of methods used to investigate stresses in the material [6-9]. A widely used method for determining stresses in thin films is the bending method based on measuring the substrate deformation resulting from stresses in the coating [10-21].

The study of changes in internal stresses in the coating after water droplet impact is possible when using substrates with geometry that meets the requirements for substrates for erosion tests at the set of research and development equipment of Unique Research Installation (URI) «Hydroshock rig «Erosion-M» NRU «MPEI».

The purpose of this work was to study the internal stresses exerted during the formation of the Ti-TiC-DLC coating using the HiPIMS technology (High Power Impulse Magnetron Sputtering) based on the developed method for measuring the deformation of a substrate with geometry changed in comparison with the classical configuration.

2. Materials and methods of research

To study internal stresses using the bending method, 08KP sheet steel substrates in the form of plates with a size of $10 \times 20 \times 1$ mm were selected. The plates had holes for their attachment in the tooling during coating and in the holders for subsequent erosion tests on the URI «Hydroshock rig «Erosion-M» NRU «MPEI» (see Fig. 1).

The initial surface of the plates (hereinafter referred to as substrates) was subjected to pre-abrasive treatment, after which the primary surface profiles were measured. Profiles were measured on a Dektak 150 mechanical profilometer in two mutually perpendicular directions in accordance with the diagram (see Fig. 2). The scheme for measuring the curvature of the substrate is due to its geometry and the intended location of the erosion "trace", which is formed on the surface due to the high-speed water drop impact of the mono-dispersed flow.
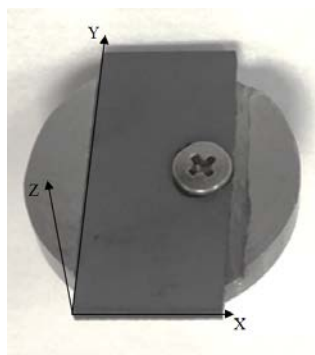
Fig. 1. Attachment of substrate in erosion test holder
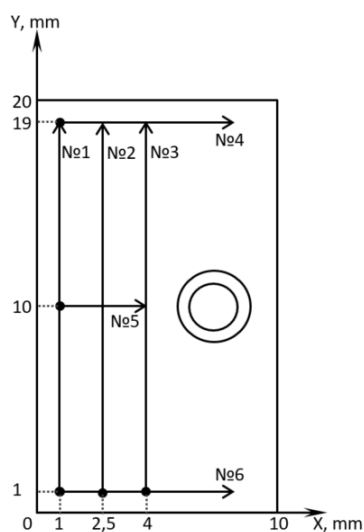
Fig. 2. Diagram of substrate surface profile measurement

The length of the profiles, when measured along the long side of the substrates (along the Y-axis) was 18 mm, when measured along the short side (along the X-axis) – from 8 to 4 mm (the length of the profiles is reduced due to the presence of a fastening hole). Note here that said cross-profiles are auxiliary to assess substrate outlier unevenness (Z-axis) due to its fixation in tooling at the subsequent application of cover and at fixation in the holder at erosion test with due account being taken of a relatively large area of fasteners relative to the width. Longitudinal profiles are intended for subsequent assessment of the effect of water drop impact action on substrate bending. Their location was determined based on the fact that the expected width of the erosion "trace" arising from the water droplet impact, the composition is 2÷3 mm, and in the future, the profiles will pass in the area of the water drops impact and near it.

After obtaining the primary (preliminary) surface profiles, a coating of the type Ti-TiC-DLC was formed on the substrates by a magnetron method on the specialized ion-plasma equipment «Gefest-HiPIMS». The coating mode was based on the study results of the main mode parameters influence the coating properties. The selected mode provides a good combination of hardness, adhesion, and tribological characteristics. For the synthesis of coatings, target-cathodes from titanium VT1.0 were used. The substrates were degreased and wiped prior to installation in the vacuum chamber. Then they were installed in a vacuum chamber, providing planetary rotation inside the plant. After that, the vacuum chamber was closed and pumped out to a high vacuum to a pressure of 10^4 Pa. Simultaneously with the pumping out of the vacuum chamber, it was heated to 200 °C to intensify degassing processes. After reaching the pressure in the vacuum chamber 10^{-4} Pa, the heating was turned off, the vacuum gate was throttled for half and plasma-forming gas was supplied to a pressure of 0.3 Pa. High purity argon was used as plasma-forming gas. On the substrates moving inside the vacuum chamber planetary, supply negative voltage (bias voltage) of the order of 1000 V and anomalous discharge was burned, ion cleaning (IC) was carried out. To intensify the IC process, 2 magnetrons for low power (up to 1 kW) were included on the surfaces of the substrates. After IC, an adhesive layer of pure carbide-forming metal – titanium – was applied to the surface of the substrates. At the same time, magnetrons worked in dual-mode at a power of up to 5 kW. The negative voltage applied to the substrates was 110-120 V. An intermediate layer of titanium carbide was applied after the adhesive layer was formed. For this purpose, reaction gas of high purity methane with a flow rate of up to 1.8 l/h was additionally supplied to the chamber through the gas inlet system. After the intermediate layer was formed, the final coating layer, DLC, was applied. For this, the flow rate of the reaction gas – methane smoothly increased in the range from 1.8 l/h to 9 l/h, while the negative bias voltage was up to 180 V.

After the coating formation, the surface profiles were re-measured in the same areas and the same length as the preliminary profiles. The determination of stresses in the coating was carried out by using the well-known Stoney formula [17-21]:

$$\sigma = \frac{1}{6}\left(\frac{1}{R_{post}} - \frac{1}{R_{pre}}\right)\frac{E}{(1-v)}\frac{t_s^2}{t_f}, \qquad (1)$$

where σ – stress in the film, after deposition, R_{pre} – substrate radius of curvature, before deposition, R_{post} – substrate radius of curvature, after deposition; E – Young's modulus substrate material, v – Poisson's ratio substrate material, t_s – substrate thickness, t_f – film thickness. For 08KP steel, Young's modulus was assumed to be 203 GPa, the Poisson coefficient was 0.28.

To define the radius of curvature of the substrate surface before and after coating formation (Pre-, Post-deposition) using profilometer software for the obtained primary profiles (Raw curves), the roughness component was excluded (see Fig. 3). After eliminating

the roughness of the profile (Pre-, Post-deposition Data Curves), the bend of the substrate was evaluated, then it determined the radius of curvature of the surface and the amount of internal stresses.
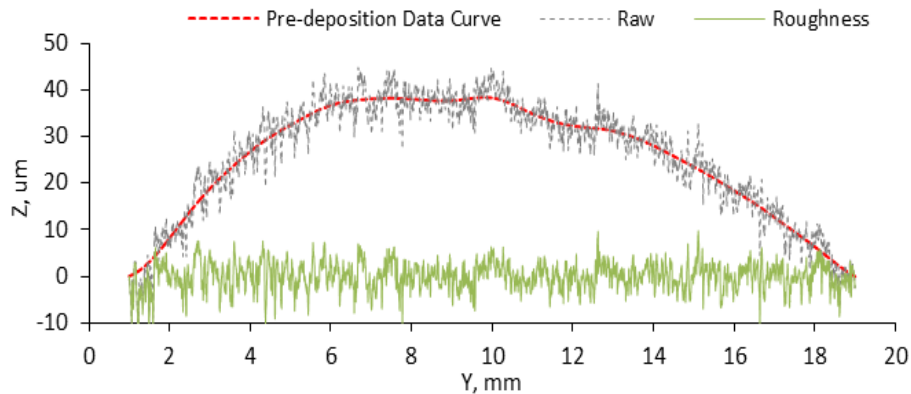

Fig. 3. Characteristic view of the division of the primary surface profile into a roughness profile and a waviness profile with macro-deviation

The surface curvature radius was estimated according to the formula:

$$R = \frac{l^2/4 + d^2}{2d},$$ (2)

where R is the radius of curvature of a substrate, l is profile length (or the analyzed site of a profile), d is a vertical (in the Z-axis direction) bend of a substrate on l length. The thickness of a coating demanded calculation of internal stresses for formula (1) was defined on the metallographic cross-section slips made after measurement of profiles of a surface.

At the production of cross-sections slips the cutting of substrates on the abrasive detachable machine with a linearly mobile system of a cut PowerMet of 3000 (Buehler GmbH) was carried out. Then substrates were pressed with the use of an automatic press for a hot press-fitting of Simplimet of 1000 (Buehler GmbH) in an electroconductive compound with the high content of graphite for providing further researches of a substrate on the scanning electron microscope. Grinding and polishing of the pressed substrates were carried out on the grinding and polishing BETA/1 (Buehler GmbH) machine with an automatic nozzle of VECTOR.

The made metallographic cross-section slips were investigated on the scanning electron microscope of TESCAN MIRA 3 LMU with the cathode Schottky with field emission issue in the mode of the return reflected electrons (BSE).

3. Results and discussion
The characteristic appearance of coated and uncoated substrates is shown in Fig. 1. The initial substrates are characterized by the presence of a curvature prior to coating due to fabrication and pre-abrasion of the surface. The characteristic view of the longitudinal and transverse profiles (after eliminating the roughness profile) before and after coating formation is represented by Figs. 4-5.

The amount of vertical bending in the Z-axis direction of the substrates on cross profiles having a length of 4 to 8 mm taken in the X direction (see Fig. 2) is 3.5 to 10 μm. Defined on longitudinal, taken in the Y direction (see Fig. 2), profiles having a long length (18 mm), the total vertical bend of the images in the Z-axis direction is from 9 to 60 microns. If there are sections with a reverse bend (in-bent parts), the sign of the vertical bend and the radius of curvature determined by it was considered negative. The radius of curvature of the initial substrates varies in the range of 0.29÷0.40 m when determining the central transverse profiles No. 5 from the shortest and closest to the fastening hole. from 0.80 to 1.86 m – when

determined by edge cross profiles No. 4 and 6, from 0.66 to 1.26 m – along with the profile No. 3 closest to the fastening hole, from 0.77 to 0.88 m – according to longitudinal profiles No. 1 and No. 2.
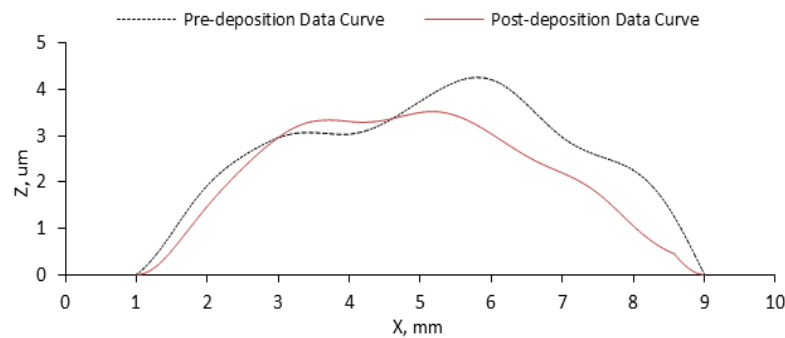

Fig. 4. Characteristic view of transverse profiles (after exclusion of roughness profile) before and after coating formation
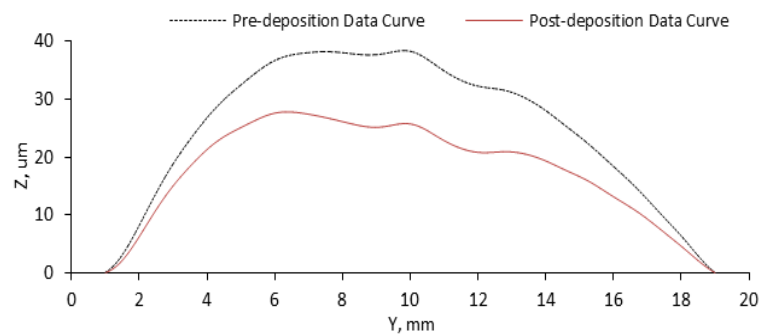

Fig. 5. Characteristic view of longitudinal profiles (after elimination of roughness profile) before and after coating formation

The ion-plasma diamond-like coating of type Ti-TiC-DLC, formed using the HiPIMS technology, according to the results of a micro-microscopic study, has a thickness that varies from 1.2 to 1.9 μm for the test batch of substrates. A characteristic view of the coating structure is given in Fig. 6.
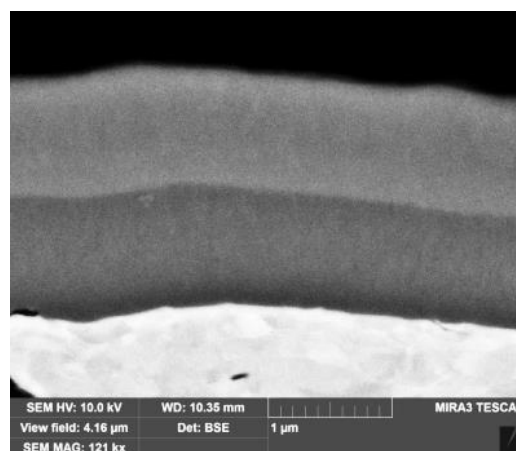
Fig. 6. A characteristic view of the Ti-TiC-DLC coating

The coating reduces vertical bending and increases the radius of curvature of the substrate. Vertical bending on transverse profiles having a length from 4 to 8 mm after application of the coating on different substrates is from 1.5 to 8 mcm. The bend defined on the longitudinal profiles having a length of 18 mm is 7 to 57 μm. The radius of curvature of coated specimens Ti-TiC-DLC ranges from 0.31÷0.44 m when deter-mining the central transverse profiles No. 5 from the shortest and closest to the fastening hole, from 1.0 to 3.0 m – at determination by edge cross profiles No.4 and No. 6, from 0.7 to 2.47 m – along with the closest of the longitudinal profile No. 3 to the fastening hole, from 0.79 to 1.1 m – according to longitudinal profiles No. 1 and No. 2.

The surfaces of the value of average internal tension calculated by a formula Stoney (1) for various substrates on various profiles in a covering of Ti-TiC-DLC fluctuate in the range from 1 to 10 GPa. The average (for the entire batch of samples examined) stress values obtained from longitudinal and transverse surface profiles in different substrate regions for erosion testing are shown in Figs. 7-8. At the same time the dispersion of values of internal tension if to compare various substrates in similar areas, is from 1.5÷3 of GPa for longitudinal profiles and up to 3÷5 of GPa for the cross.

When using the considered geometry of the samples to further follow the change in stresses during erosion tests, it was proposed to exclude from the assessment the pros closest to the fastening hole (longitudinal profile No. 3 and transverse profile No. 5) due to the greatest dispersion of the values obtained. In case of exclusion from the calculation of these profiles, the average value of stresses in the considered coating Ti-TiC-DLC in the longitudinal direction will be 3.0 GPa, in the transverse direction will be 9.0 GPa.
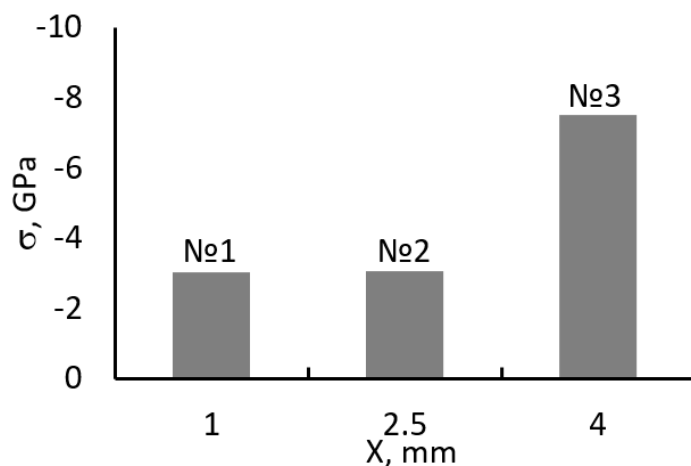
Fig. 7. Mean stress values obtained for different substrate regions for erosion testing on longitudinal surface profiles
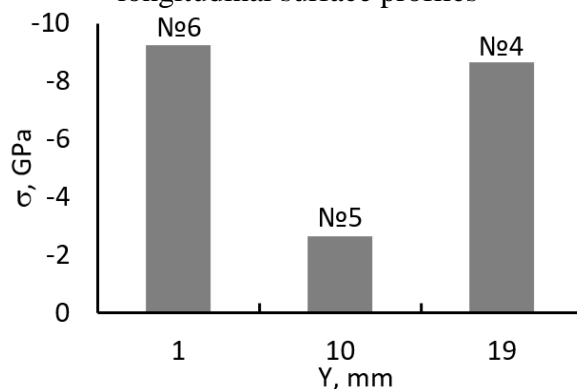
Fig. 8. Mean stress values obtained for different areas of substrates for erosion tests on transverse surface profiles

4. Conclusion

In the work, studies of internal stresses in the Ti-TiC-DLC coating obtained by using the HiPIMS technology were carried out. Pressure studies were carried out by using a developed technique for substrates with geometrics other than the classical configuration used in determining internal stresses in the coating by bending. According to the profiles on the top of the substrates obtained before and after the coating in the longitudinal and transverse directions, bending values were obtained, which were used to calculate curvature and stresses according to the Stoney formula. As a result of conducting studies of a batch of samples, it was revealed that the application using the HiPIMS technology of the selected ion-plasma diamond-like carbon coating of the Ti-TiC-DLC type leads to compressive stresses from 3 (in the longitudinal direction) to 9 GPa (in the transverse direction).

The obtained high values of stresses in the coating can be associated with a non-excluded contribution to the determined bending of temperature deformations in the material of the substrates themselves, which occur during heating due to the process of coating formation. To take this into account, it is further planned to evaluate the bending of the substrates after the technological process, carried out with a protective shield installed for a number of samples, preventing the application of the coating, but preserving the remaining influencing factors. Nevertheless, to assess the effect of the water drop impact on the deformation of coated samples, only the surface condition preceding it is important, so overstatement of the stress value in the coating will not affect it.

References

[1] Boghe M. DLC Coatings. In: *MTZ Worldw*. 2007. p.12-14.

[2] Grigoriev S, Volosova M, Fyodorov S. DLC-coating Application to Improve the Durability of Ceramic Tool*s. Journal of Materials Engineering and Performance.* 2019;28: 4415-4426.

[3] Liskiewicz T, Patnaik A. DLC Coatings in Oil and Gas Production. *Journal of Coating Science and Technology.* 2014;1(1): 59-68.

[4] Hadinata SS, Lee MT, Pan SJ, Tsai WT, Tai CY, Shih CF. Electrochemical performances of diamond-like carbon coatings on carbon steel, stainless steel, and brass. *Thin Solid Films.* 2013;529: 412-416.

[5] Depner-Miller U, Ellermeier J, Scheerer H, Oechsner M, Bobzin K, Bagcivan N, Brögelmann T, Weiss R, Durst K, Schmid C. Influence of application technology on the erosion resistance of DLC coatings. *Surface and Coatings Technology.* 2013;237: 284-291.

[6] Glang R, Holmwood R, Rosenfeld R. Determination of stress in films on single crystalline silicon substrates. *Review of Scientific Instruments.* 1965; 36(1): 7-10.

[7] Singer P. Film Stress and How to Measure it. *Semiconductor International.* 1992;10: 54-58.

[8] Zayonchkovsky V, Zhuo A, Milyaev I, Perov N, Prokhorov I, Klimov A, Andreev A. Thin metal films with precipitation-hardening magnetic layers of Fe – Cr – Co alloy. *Condensed Media and Interphase Boundaries.* 2019;21(4): 505-518.

[9] Prokhorov I, Zakharov B. X-ray diffraction studies of the features of relaxation and distribution of macrostresses in epitaxial structures. *J. Surf. Invest.: X-Ray, Synchrotron Neutron Tech.* 1999;2: 106-109. (In Russian)

[10] Astashenkova O, Korlyakov A. Mechanisms of the formation of mechanical stresses in films of silicon carbide and aluminum nitride obtained by the magnetron method. *Modern science. Research, Ideas, Results, Technologies.* 2014;15(2): 57-61. (In-Russian)

[11] Petrova A, Mukhametov R, Akhmadieva K. Internal stresses in hardened polyester binders for PCM. *Works of VIAM.* 2019;77(5): 12-21. (In Russian)

[12] Ayvazyan G. On the determination of internal stresses in the film-substrate system. *Izv. NAS RA and SEUA.* 2000;53(1): 63-67. (In Russian)

[13] Danilaev M, Theologian E, Polsky Y, Yanilkin I, Vakhitov I, Gumarov A, Tagirov L. Internal stresses in polymer film coatings obtained by plasma deposition. *Physics and Chemistry of Materials.* 2018;3: 21-26.

[14] Novak A, Novak V, Dedkova A, Gusev E. Dependence of mechanical stress in silicon nitride films on conditions of plasma-enhanced chemical vapor deposition. *Izvestiya vuzov. Electronics.* 2017;22(2): 138-146.

[15] Naragino H, Egiza M, Tominaga A, Yoshitake T. Obtaining a superhard nanocomposite film by coaxial plasma deposition. *Laboratory and Production.* 2019;6(2): 156-160.

[16] Gainutdinov I, Azamatov M, Mikhailov A, Galiev A, Nurullin I, Shusharin S. Hybrid AR coating with a diamond-like layer. *Optical Magazine.* 2015;82(1): 70-73.

[17] Karasev P, Podsvirov O, Titov A, Karabeshkin K, Vinogradov A, Belyakov V, Arkhipov A, Nikulina L, Shakhmin A, Shubina E, Karasev N. Effect of ion bom-bardment on the phase composition and mechanical properties of diamond-like films. *J. Surf. Invest.: X-Ray, Synchrotron Neutron Tech.* 2014;8: 49-53. (In Russian)

[18] Stoney G. The tension of metallic films deposited by electrolysis. In: *Proceedings of the Royal Society of London. Series A, Containing Papers of a Mathematical and Physical Character. Royal Society.* 1909. p.172-175.

[19] Lindroos V, Tilli M, Lehto A, Motooka T. *Handbook of silicon based mems materials and technologies.* Burlington: Elsevier; 2010.

[20] Dyuzhev N, Dedkova A, Gusev E, Novak A. A technique for measuring mechanical stresses in thin films on a wafer using an optical profilometer. *Izvestiya vuzov. Electronics.* 2016;21(4): 367-372. (In Russian)

[21] Kvashennikov D, Vainer Y, Zuev S, Polkovnikov V. Internal stresses in Mo/Y multi-layer mirrors. *J. Surf. Invest.: X-Ray, Synchrotron Neutron Tech.* 2019;3: 14-18. (In Russian)

STUDY OF THE INFLUENCE OF TECHNOLOGICAL FEATURES OF LASER STEREOLITHOGRAPHY PROCESS ON FUNCTIONAL CHARACTERISTICS OF PARTS

V.V. Vnuk[1], E.V. Ippolitov[1*], S.V. Kamaev[1], M.A. Markov[1], A.A. Nikulenko[2], M.M. Novikov[1], S.A. Cherebylo[1]

[1]Institute on Laser and Information Technologies Branch of the Federal Scientific Research Centre

"Crystallography and Photonics" of the Russian Academy of Sciences, Svyatoozerskaya 1,140700, Shatura,

Moscow Region, Russia

[2]Central Aerohydrodynamic Institute "TsAGI", Zhukovsky St. 1, 140180, Zhukovsky, Moscow Region, Russia

*e-mail: ippevg@yandex.ru

Abstract. The article reports on the effect the building orientation of the part, produced by laser stereolithography technology, has on achieving its best functional characteristics. Based on the example of IPLIT-3 and IPLIT-4 resins, the study shows that in contrast to the literature data on other commercial photocurable resins (PCRs), there is no definite advantage of the vertical orientation of the test samples compared to their horizontal orientation for obtaining the best values of the manufactured part functional characteristics.

Keywords: additive technologies, laser stereolithography, photopolymerization, three-dimensional modeling, photocurable resin

1. Introduction

The additive technologies, which include laser stereolithography [1-3], are nowadays able to produce not only prototypes but also fully functional parts. The functionality of the parts is defined by both the properties of the photocurable resin (PCR) used and the parts building technology [4-8]. For structural materials, strength characteristics, such as tensile and bending strength, tensile modulus, hardness, etc., are usually specified. However, the technological features of manufacturing the tested samples are not specified. All materials intended for use in additive technologies allow obtaining parts in a simpler way – by filling the molding tooling with this material, followed by hardening, sintering, or fusion of the material. Although the samples obtained in this way will be made of the same material, their mechanical properties may differ from the parts obtained additively. It can be assumed that differences in the objects' properties made of the same material can also arise if changes are made to the additive building technology of the parts or their post-processing. Parts manufacturing parameters at laser stereolithography technology, which can potentially influence mechanical characteristics, include hatch type and pitch, layer thickness, product building orientation, as well as UV radiation dose received during the part post-processing in the additional polymerization chamber [1,3,9-11].

UV post-curing is a stage of the manufacturing process and its parameters are set by the developer of the PCR in order to achieve the best strength characteristics of the given PCR. Therefore, the user has only to follow the manufacturer's recommendations for UV curing of the parts. Layer hatching parameters (hatching pattern and pitch) are the most important

technological characteristics and are determined by the resin developer in order to achieve the best part accuracy. In addition, these parameters are also tightly linked to the laser type and the optical system parameters of the machine used. Changing these parameters manually will result in a low-quality product. The thickness of the working layer will determine the distribution of absorbed laser energy along with the depth of the layer of liquid PCR, and, consequently, the parameters of the three-dimensional polymer mesh being formed, which will inevitably affect the strength characteristics of the final part. The same reason causes the effect of improvement of physical and mechanical properties after UV post-curing of the fabricated sample, the so-called "green part".

The effect the part orientation during building has on its mechanical characteristics is discussed in the literature both at the level of theoretical description [1,9] and experimental observation of this effect [10-11]. The authors of these articles consider the dependence of the mechanical properties of the part on the above-mentioned parameters of fabrication and post-processing. In the studies mentioned, a conclusion is made that the improvement of strength characteristics when decreasing the thickness of the working layer and at the vertical orientation of the part is a consequence of the fact that under these conditions the part is formed of a larger number of layers. Namely, according to the literature data, a zone with the best mechanical properties for this material is formed at the interface "lower layer – upper layer". Consequently, the more layers a part is formed of, the more such zones it will include and the stronger it will be.

Thus, in order to achieve the best mechanical properties without changing the PCR, the user has little choice but to decide in favour of a smaller layer thickness and/or the part building orientation on the platform to allow for the number of layers being as large as possible. Although modern PCRs allow fabricating parts with layer thickness ranging from tens to several hundred microns, there is a narrower range of layer thicknesses for each PCR that is optimal in the balance of the "precision – production time". Decreasing the layer thickness leads to an increase in the building time and, consequently, in the cost of the part fabrication. Changing the part orientation on the platform can also lead to an increase of the processing time, but to a lesser degree, because if the number of layers becomes larger in the Z coordinate, for example, then the size of each layer in the XY plane decrease.

It is worth noting that in each case the authors of the studies mentioned provide experimental data for one polymer material, reporting that by changing the part orientation during its fabrication they achieved a certain increase in the mechanical strength characteristics. The present article constitutes an attempt to test what effect the change of the platform orientation has when fabricating the part from different resins produced at ILIT RAS. The article further studies whether it is possible to achieve improvement of the part mechanical characteristics, resorting neither to modification of the PCR itself, nor to the significant correction of the manufacturing technology; resorting neither to making changes in the part for subsequent reinforcement, nor to other methods that complicate the technological chain and raise the cost of the parts.

2. Materials and equipment

In order to investigate the mechanical properties of cured PCR, 3D computer models of two types were manufactured. These represented standard samples for testing polymer materials according to the requirements of GOST 11262-80 (for tension) and GOST 4648-71 (for static bending). Figure 1 shows the respective sketches.

PCRs IPLIT-3 [12] and IPLIT-4 [13] were used for the fabrication of test samples. All fabrication processes were performed at ILIT RAS on stereolithographic machines SLA-250 (3D Systems) and LS-400e (ILIT RAS). Fabrication accuracy was 0.1 mm in each of the coordinates regardless of the part orientation, which is considered acceptable according to the

requirements of the above-mentioned GOSTs for the study of such samples. The HeCd-laser with a wavelength of 325 nm was used as a UV beam source in the machines. Strength tests of the fabricated samples were carried out on the rupture machine I1185M-100-01-1 (100kN) at Prof. N.E. Zhukovsky Institute "TsAGI". Modeling of the samples was performed in SOLIDWORKS CAD.
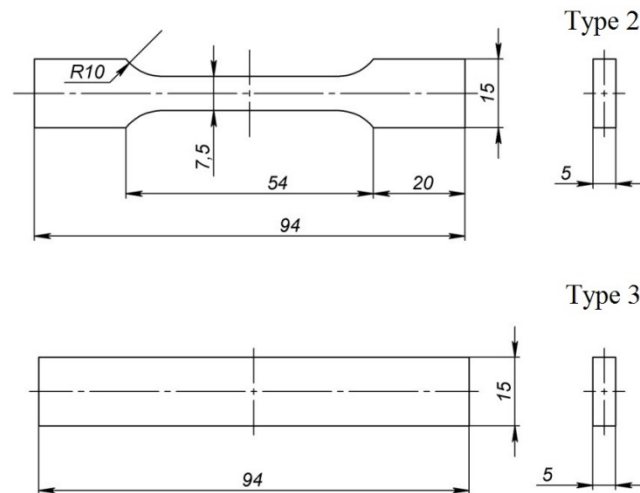

Fig. 1. Sketches of standard samples for testing polymer materials

The computer models were then converted to the STL format. During the transformation, the surface of the original model is approximated with a given accuracy by the faceted surface, formed by a set of flat triangular facets. The approximation accuracy, in this case, was 0.005 mm – linear and 1 degree – angular.

Magics software by Materialise was used to work with the STL files. Models converted to the STL format by means of Magics were placed on the building platform of the stereolithographic machines. Two-part building orientations were selected for fabrication. For each orientation, the necessary technological supports were formed. Figure 2 shows screenshots of the software interface with two-part orientations on the building platform.
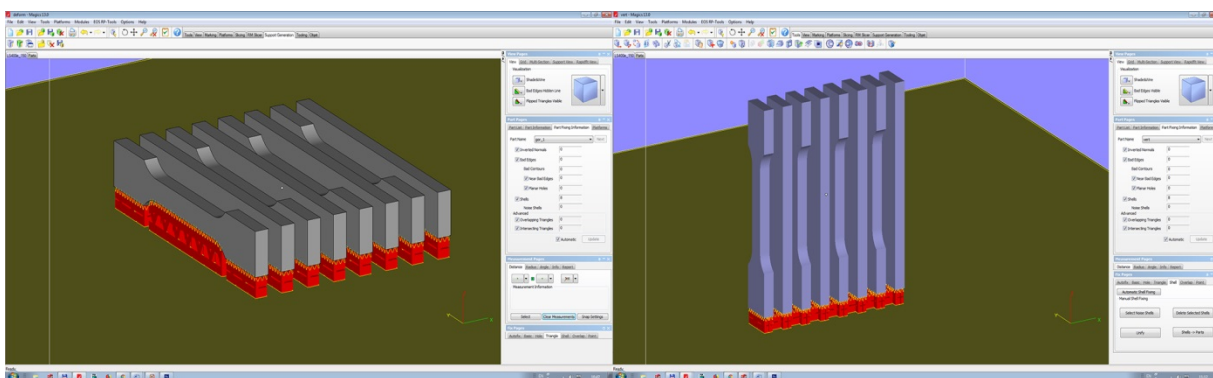
Fig. 2. Interface Magics with two variants of part orientation on a building platform

After the test samples were built and washed, they were placed in the UV post-curing chamber. Ultraviolet treatment of the parts helps to achieve the maximum degree of the polymer network cross-linking to reduce the content of methacrylic groups to the lowest possible values. The post-curing of the parts was performed in the UV post-curing chamber and lasted 0.5 hours. This is enough to achieve the minimum of a 95% conversion of

unreacted methacrylic groups in the polymer. The Philips TLK 40W/05 lamps, used in the chamber, have a spectrum of the 315-460 nm range, with a maximum of 365 nm. Power consumption is 40W, UV-A power is 5W. During the post-curing process, the parts were rotated in order to achieve their uniform illumination.

Studies of the post-curing process of IPLIT-3 and IPLIT-4 resins were not carried out in this study. Earlier experiments using first versions of PCR developed at ILIT RAS, both multi-component and single-component in composition, as well as acrylic resins supplied by 3D Systems showed that the content of unreacted methacrylic groups in all examined samples after curing did not exceed 50 %, falling to the level of 5-10 % of the initial amount in the liquid resin after UV post-curing. The content of such groups was monitored using an FTIR spectrometer by the intensity of the absorption peak of the C=C bond in the acrylic group in the region of 1610-1650 cm^{-1} [14]. The post-curing process lasted for 30 minutes, as mentioned above. Longer irradiation resulted in the subsequent rapid aging of such parts. According to these studies, we developed technological recommendations for the post-curing process for acrylic oligomers and PCRs based on them, used in the LS series stereolithography machines. Our experimental data which have not been previously published but made available as technological recommendations to buyers of stereolithography machines and PCRs produced by ILIT RAS correlate well with the existing literature data [9-11].

The rupture machine (Fig. 3) was equipped with two screw drives and an AC digital frequency servo drive with encoder speed feedback. The machine was operated via PC. The limits of the permissible relative error of load measurement within the confidence range were not more than 1%.
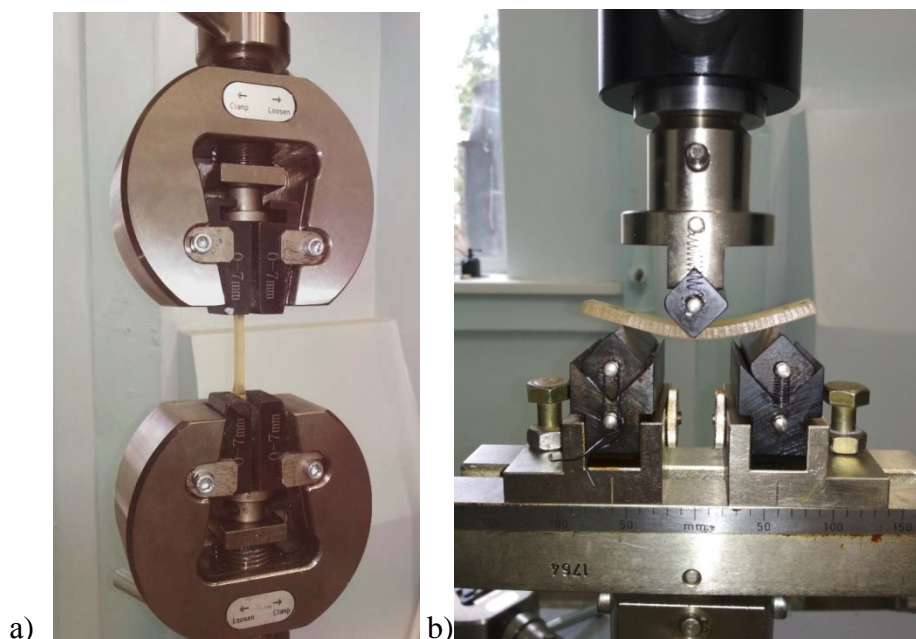
Fig. 3. Central Aerohydrodynamic Institute "TsAGI" experimental installations: a) tensile testing of samples; b) three-point bending tests

3. Experimental results

Below you can find the experimental data on mechanical testing of the test samples.

Table 1. Results of tensile testing of a series of the IPLIT-3 samples, vertical orientation

№ exp.	Max. load P_{max}, N	Elongation at break ε_{M}, %	Breaking load P_p, N	Breaking strength σ_p, MPa	Elastic modulus E, MPa	Line color in the figure (Fig. 4)
1	300	0.737	300	8	526.7	
2	401	-	401	10.69	493.3	
3	589	0.118	538	14.35	413.3	
average value	430	0.427	413	11.01	477.8	
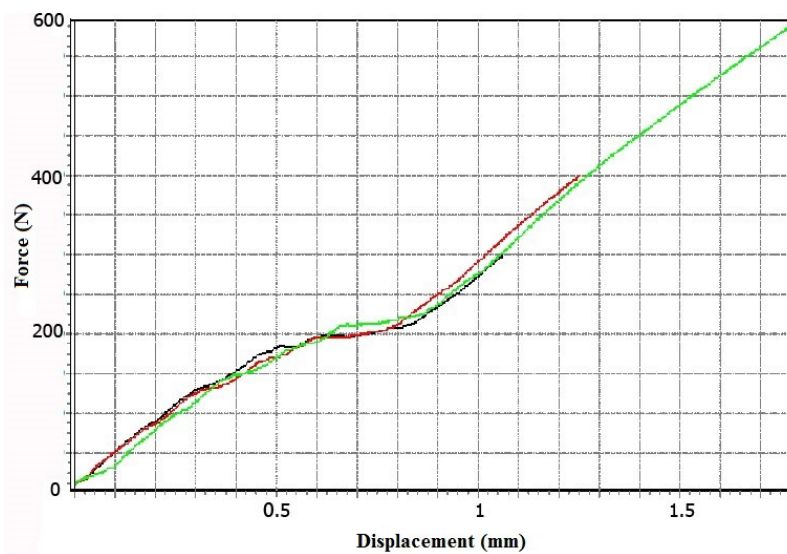
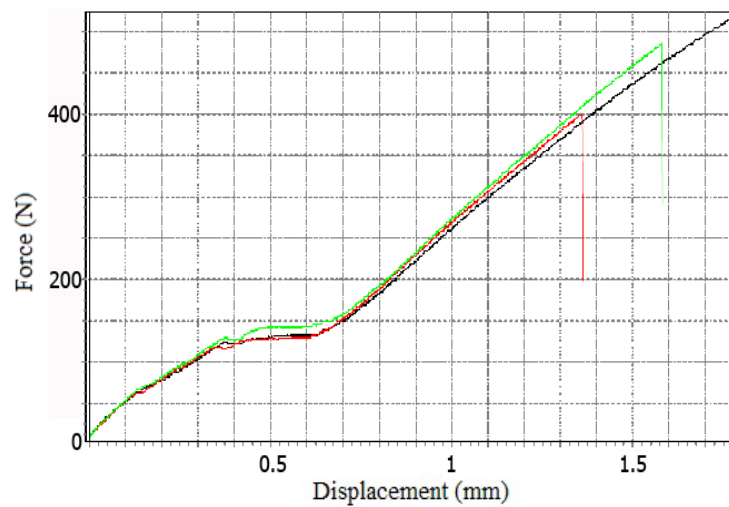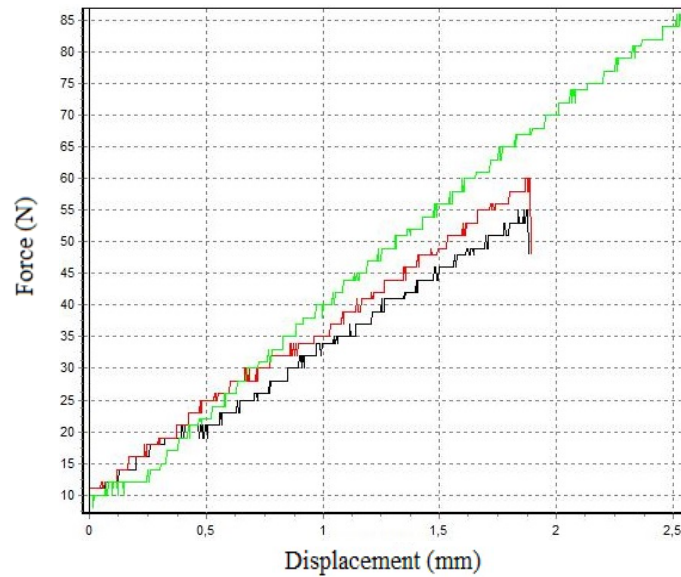**Fig. 4.** Dependence of force (N) on the displacement of the crosshead of the unit during tensile testing of the IPLIT-3 samples manufactured with vertical orientation

Table 2. Results of tensile testing of the IPLIT-3 samples, horizontal orientation

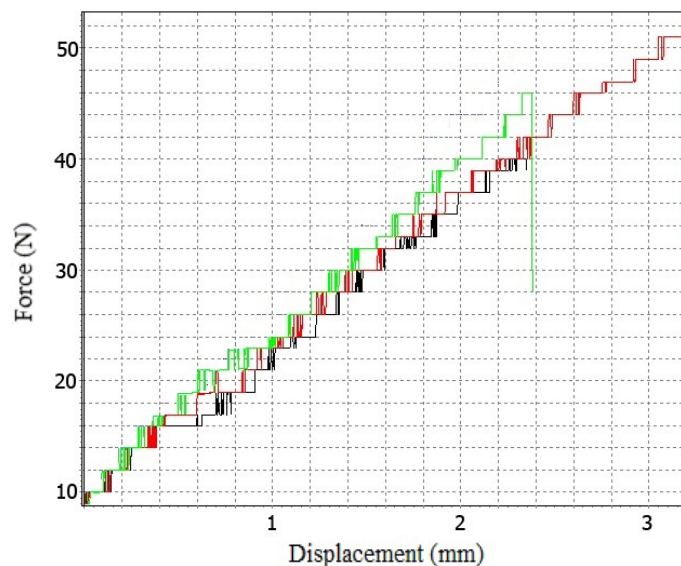| № exp.	Max. load P_{max}, N	Tensile strength σ_{max}, MPa	Elongation at break ε_{M}, %	Breaking load P_p, N	Breaking strength σ_p, MPa	Elastic modulus E, MPa	Line color in the figure (Fig. 5)
1	308	8.213	0.017	222	5.92	426.7	
2	349	9.307	0.071	321	8.56	400	
3	255	6.8	0.012	224	5.973	360	
average value	304	8.107	0.033	256	6.818	395.6	
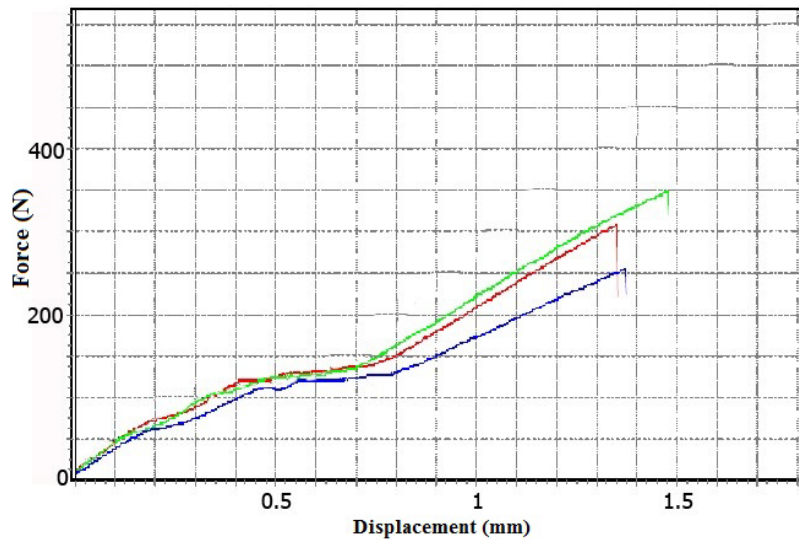
Fig. 5. Dependence of force (N) on the displacement of the crosshead of the machine during tensile testing of the IPLIT-3 samples manufactured with horizontal orientation

Table 3. Results of tensile testing of a series of the IPLIT-4 samples, vertical orientation

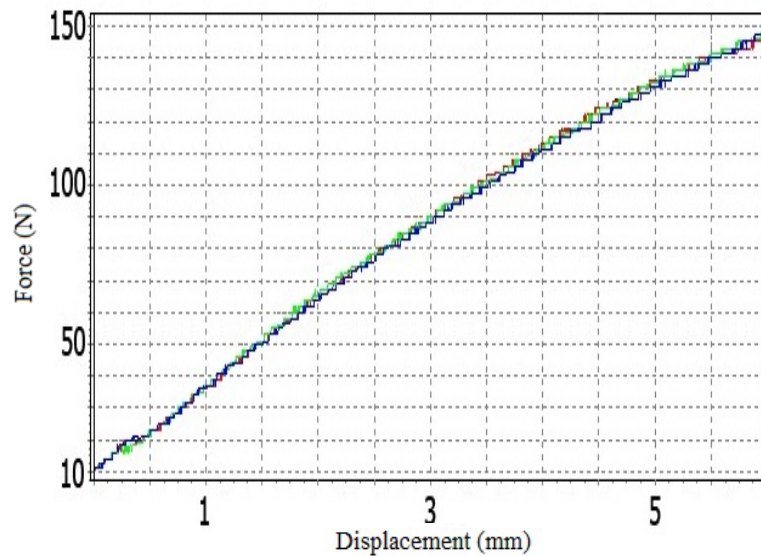| № exp.	Max. load P_{max}, N	Tensile strength σ_{max}, MPa	Breaking load, P_p, N	Breaking strength σ_p, MPa	Elastic modulus E, MPa	Line color in the figure (Fig. 6)
1	672	19.44	649	18.78	528.1	
2	603	16.75	538	14.94	347.2	
3	744	20.67	619	17.19	569.4	
average value	673	18.95	602	16.97	481.6	
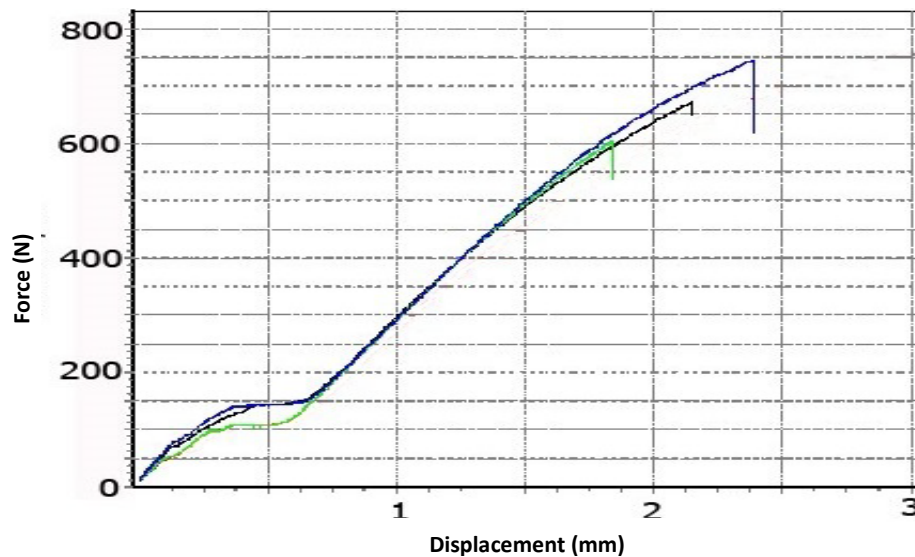
Fig. 6. Dependence of force (N) on the displacement of the crosshead of the machine during tensile testing of the IPLIT-4 samples manufactured with vertical orientation

Table 4. Results of tensile testing of the IPLIT-4 samples, horizontal orientation

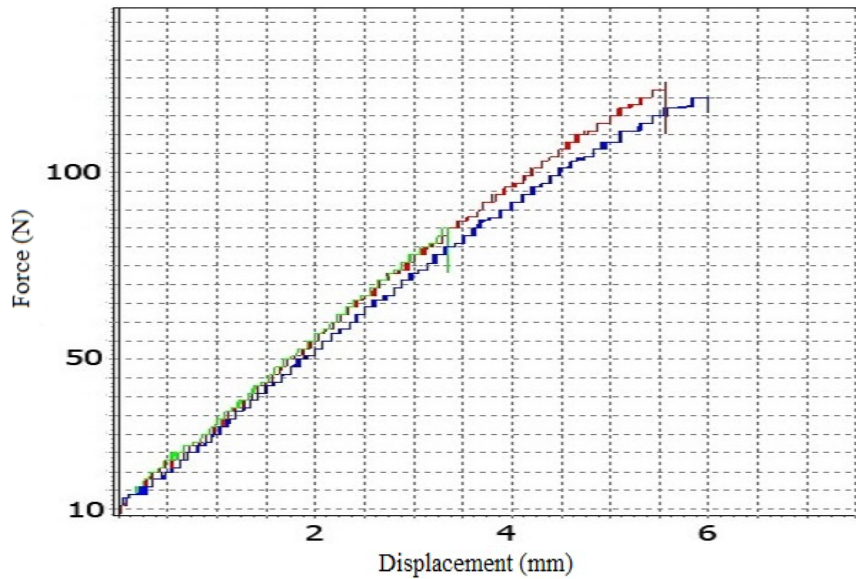| № exp.	Max. load P_{max}, N	Tensile strength σ_{max}, MPa	Convent. yield strength σ_y, MPa	Breaking load P_p, N	Breaking strength σ_p, MPa	Elastic modulus E, MPa	Line color in the figure (Fig. 7)
1	517	13.81	10.33	353	9.428	454.1	▬
2	400	10.68	6.43	199	5.315	454.1	▮
3	484	12.93	8.78	291	7.772	480.8	▬
average value	467	12.47	8.512	281	7.505	463	

Fig. 7. Dependence of force (N) on the displacement of the crosshead of the unit (mm) during tensile testing of the IPLIT-4 samples manufactured with horizontal orientation

Table 5. Test results on bending of the IPLIT-3 samples, vertical orientation

№ exp.	Maximum load for cross-bending P_{max}, N	Transverse stress at max. load σ_{max}, MPa	Elastic modulus E, MPa	Line color in the figure (Fig. 8)
1	55	13.2	720	▬
2	60	14.4	600	▬
3	86	19.84	576.7	▬
average value	67	15.81	632.2	

Fig. 8. Dependence of force (N) on the displacement of the crosshead of the unit (mm) during bend testing of the IPLIT-3 samples manufactured with vertical orientation

Table 6. Test results on bending of the IPLIT-3 samples, horizontal orientation

№ exp.	Maximum load for cross-bending P_{max}, N	Transverse stress at max. load σ_{max}, MPa	Elastic modulus E, MPa	Line color in the figure (Fig. 9)
1	40	9.166	458.3	
2	53	12.72	480	
3	46	10.97	476.8	
average value	46.3	10.95	571.7	

Fig. 9. Dependence of force (N) on the displacement of the crosshead of the unit (mm) during bend testing of the IPLIT-3 samples manufactured with horizontal orientation

Table 7. Test results on bending of the IPLIT-4 samples, vertical orientation

№ exp.	Maximum load for cross-bending P_{max}, N	Transverse stress at max. load σ_{max}, MPa	Elastic modulus E, MPa	Line color in the figure (Fig. 10)
2	147	35.28	720	🟥
3	148	36	486.5	🟩
4	147	35.52	845.6	🟦
average value	147.3	35.6	684	

Fig. 10. Dependence of force (N) on the displacement of the crosshead of the unit (mm) in bend testing of the IPLIT-4 samples manufactured with vertical orientation

Table 8. Results of bend testing of the IPLIT-4 samples, horizontal orientation

№ exp.	Maximum load for cross-bending P_{max}, N	Transverse stress at max. load σ_{max}, MPa	Elastic modulus E, MPa	Line color in the figure (Fig. 11)
1	124	31.66	893.6	🟥
2	85	21.7	765.9	🟩
3	120	30.24	504	🟦
average value	109	27.9	721	

Fig. 11. Dependence of force (N) on the displacement of the crosshead of the unit (mm) during bend testing of the IPLIT-4 samples manufactured with horizontal orientation

The results of tensile and flexural testing of the samples made of IPLIT-3 and IPLIT-4 materials with different orientations on the platform (vertical and horizontal) are presented in table 9. As would be expected, the PCR IPLIT-4, as a more modern development, has better tensile strength characteristics and is more flexible to bending than the PCR IPLIT-3.

Table 9. Consolidated results of tensile and bending tests (mean values)

Parameter	IPLIT-3, vertically	IPLIT-3, horizontally	IPLIT-4, vertically	IPLIT-4, horizontally
Tensile Strength σ_{max}, MPa	11	8.107	18.95	12.47
Max.load (tensile) P_{max},N	430	304	673	467
Tensile modulus E, MPa	477.8	395.6	481.6	463
Voltage at max. load (bending) σ_p, MPa	15.81	10.95	35.6	27.9
Max. bending load, P_{max},N	67	46.3	147.3	109
Elastic modulus (bending) E, MPa	632.2	471.7	684	721

The measurement results indicate that having used both studied resins we obtained the parts whose mechanical properties depend on the part orientation in the process of layer-by-layer manufacturing. As mentioned earlier all the parts were subjected to UV post-curing, after which no presence of microzones with a weak degree of three-dimensional cross-linking was detected. Both the PCRs and the respective technologies have much in common: curing by radiation of 325 nm, the same photoinitiator, both consisting of methacrylic oligomers.

The main similarity though remains the fact that both PCRs present a mixture of oligomers, with none of its components being basic in percentage.

4. Discussion of results

Polymeric materials are characterized by the results of strength test experiments [15] and, if possible, it is recommended to use statistical processing of such data. Samples may contain inhomogeneities and microdefects, which will affect the experimental results. We excluded the least reliable series that significantly differ from the rest of the results.

The 2018 study [16], examining some technological features of the use of multicomponent PCR, describes situations when during the formation of supports or layers containing small area sections, the cured polymer contained the original oligomers in a ratio different from that of the original PCR. This was due to the different reactivity of the oligomers and monomers that made up the PCR. Each of the oligomers or monomers is characterized by its own rate constant of chain growth, the rate constant of oxygen addition, which inhibits polymerization, and the rate constant of radical recombination [5]. The "slowest" components are pushed out of the polymerization zone by the "faster" components. So the initially formed polymer network contains the PCR components in a ratio that is different from the original resin. As mentioned above, the 2018 study [16] proposed a mechanism for the separation of this PCR during the curing of thin layers by displacing the "slow" components in the horizontal direction. Due to this, in the usual mode of curing the IPLIT-4 PCR layer, thin-walled elements and auxiliary supporting structures are formed mainly from the urethane component of this PCR. If the area of the hardened layer is large, the displacement of the "slow" components of the composition occurs vertically, with movement into the depth of the layer. The result of this phenomenon is the "quasi-layering" of the obtained part when horizontal layers differing in the composition are independently formed inside the apparatus-formed layer due to the separation of fast and slow polymerization zones.

PCR IPLIT-3 [12] contains three oligomers, two of which, according to their weight fraction (40% each) in the composition, can be considered as a principle. These components are very different in molecular weight, and the formation of a three-dimensional network from the "fastest" component saves enough space for the "slower" component with a smaller molecule size. Thus, IPLIT-3 polymerizes more uniformly, without vertical or horizontal delamination. As a result, when the orientation of the samples changes during building, we see the effect arising from an increase in the number of layers only, similar to the literature data [9-11]. In PCR IPLIT-4 [13], there are four such oligomers and monomers, and there is no significant difference in the mass or size of the molecules. The multicomponent nature of this PCR is attributed to a combination of technological and economic requirements for modern stereolithographic materials.

The performance of samples made from IPLIT-4 is somewhat unconventional for all the cases described in the literature. The tensile and breaking strength has improved, as for other resins described in the literature. But bending tests show that parts grown from this material will have more elasticity when oriented vertically. This can also be considered to be a confirmation of the assumption of "quasi-layering" of vertically oriented parts due to the formation of horizontal zones with different stoichiometric ratios of the original PCR components.

5. Conclusion

The experimental data obtained by us allow us to conclude that there is no unambiguous improvement in the mechanical characteristics of parts manufactured using laser stereolithography technology with the vertical orientation for the two investigated materials.

While the tensile and breaking strength does increase for vertically oriented parts, elastic characteristics of the parts can demonstrate both increasing and decreasing elasticity. Unlike other studies on this topic, according to our results, the final choice of the part orientation depends on the specific PCR used and on the parameters that the user deems most important when using the part. Technological recommendations provided by the developers and/or manufacturers of the used PCR, based on the results of similar studies, should constitute the basis for such a choice.

References
[1] Jacobs PF. *Rapid prototyping & manufacturing: fundamentals of stereolithography.* Dearborn MI: Society of Manufacturing Engineers; 1992.
[2] Kablov EN. New generation materials are the basis for innovation, technological leadership and national security in Russia. *Intellect and technology.* 2016;2(14): 16-21. (In Russian)
[3] Evseev AV, Kamaev CV, Kotcuba EV, Markov MA, Novikov MM, Panchenko VY, Semeshin NM, Yakinin VP. *Laser technology for rapid prototyping and direct fabrication of three-dimensional objects. Laser technologies of materials processing: modern problems of fundamental research and applied developments.* Moscow: Fizmatlit; 2009. p.333-397. (In Russian)
[4] Begishev VP, Guseva LR. *Theory and practice of photopolymerization processes.* Ekaterinburg: Ural Branch of the Russian Academy of Sciences; 1998. (In Russian)
[5] Berlin AA, Korolev GV, Kefeli TY, Sivergin YM. *Acrylic oligomers and materials based on them.* Moscow: Chemistry; 1983. (In Russian)
[6] Tsybin AI, Tkachuka AI, Grebeneva TA, Samatadzea AI, Novikov MM. A Study of the Performance Properties of Oligoetheracrylate Binder Cured by Coherent UV Radiation. *Polymer Science, Series D.* 2017;1: 13-18.
[7] Szykiedans K, Credo W. Mechanical properties of FDM and SLA low-cost 3-D prints. *Procedia Engineering.* 2016;136: 257-262.
[8] Mikitaev AK, Kozlov GV. Structural Model of Strength of Nanocomposites Pimethylmetacrylate/Functionalized Carbon Nanotubes. *Materials Physics and Mechanics.* 2015;24(2): 187-193. (In Russian)
[9] Kazemi M, Rahimi A. Stereolitography process optimization for tensile strength improvement of products. *Rapid Prototyping Journal.* 2018;24(4): 688-697.
[10] Watters MP, Bernhardt ML. Curing parameters to improve the mechanical properties of stereolithographic printed specimens. *Rapid Prototyping Journal*, 2018;24(1): 46-51.
[11] Chockalingam K, Jawahar N, Ramanathan KN, Banerjee PS. Optimization of stereolithography process parameters for part strength using design of experiments. *International Journal of Advanced Manufacturing Technology.* 2006;29: 79-88.
[12] Patent RF № 2395827. *Liquid photocuring resin for laser stereolithography.*
[13] Patent RF № 2685211. *Liquid photocuring resin for laser stereolithography.*
[14] Sureshbabu C, Vasubabu M, Jeevan Kumar R. FTIR Investigation on the Structure of Acrylic Resin Based Dental Biomaterial. *Research Journal of Pharmaceutical, Biological and Chemical Sciences.* 2016;7(4): 1157-1159.
[15] Gul VE. *Strength of polymers.* Moscow: Chemistry; 1964. (In Russian)

[16] Vnuk VV, Kamaev SV, Markov MA, Cherebylo SA. Features of the manufacture of models from multicomponent photopolymers by laser stereolithography. *Aviation materials and technologies*. 2018;4: 31-34. (In Russian)

STRUCTURAL AND MAGNETIC PROPERTIES OF ZINC DOPED COPPER FERRITE SYNTHESIZED BY SOL-GEL AND HYDROTHERMAL ROUTE

Naveen Kumar, Deepak Singh, Abhishek Nigam[*]**, Omprakash Rajpoot, Mayank Kumar, Yadav, Yogendra Pratap Singh, P. Shakti Prakash, Samarjit Singh**

Applied Mechanics Department, Motilal Nehru National Institute of Technology Allahabad, Prayagraj-211004,

India

*e-mail: abhishek.bmi5@gmail.com

Abstract. In this work, Cu-Zn spinel ferrites having chemical formula $Cu_{(1-x)}Zn_xFe_2O_4$ for x ranging from 0.2 to 0.8 were synthesized by sol-gel auto-combustion method and hydrothermal method with a step size of 0.2. The effect of Zn doping on structural properties, crystallite size, and magnetic properties synthesized by both methods are reported. Rietveld refinement of the XRD patterns was analyzed using Maud for the determination of crystallite size. The X-ray diffraction pattern shows that single phase Cu-Zn spinel ferrite was formed, and it has a cubic structure. Additionally, the lattice parameter size increases with Zn doping and then decreases after x=0.6. A vibrating sample magnetometer (VSM) was done to determine magnetic properties like saturation magnetization (Ms), remanence (Mr), and coercivity (Hc). The scanning electron microscopy (SEM) shows the morphology and confirms the average particle size.
Keywords: copper, hydrothermal, sol-gel, spinel ferrite, zinc

1. Introduction

Ferrites are ceramic materials possessing properties like very high electrical resistivity, low power loss at high frequencies, suitable for temporary and permanent magnetic applications due to their spontaneous magnetization and conductivity behavior like those of semiconductors [1,2]. Ferrites with narrow hysteresis loop form softs magnets, which are used for audio transformers, television transformers, gyrators, inductance cores. Ferrite nanoparticles have high electrical resistivity because they have a better response at high frequencies [3,4]. Ferrites are the outstanding core material choice for frequencies from 10 kHz to a few MHz, when we require low cost, high stability, and lowest volume [5,6]. Ferrites are widely studied due to their applications in protecting living bodies from microwaves, anechoic chamber, satellite communication, microwave darkroom, and microwave industries as radar absorbing material. Ferrites having chemical formula MFe_2O_4 with the spinel structure have face-centered cubic (FCC) lattice of the oxygen ions. Every spinel unit cell comprises eight formula units. In every unit cell, there exists 64 tetrahedral sites and 32 octahedral sites. Therefore, their composition depends on the structural, chemical, and electromagnetic properties of ferrites, dependent on the preparation methodologies [7,8]. Zn doped Cu ferrites have a significant temperature-dependent magnetic moment near body temperature, therefore successfully used in temperature sensor in MRI properties [9-11]. Various cations can be placed at these tetrahedral sites and octahedral sites to get interesting

chemical and physical [12,13]. It is reported that Ni–Cu–Zn ferrites with less content of Zn could obtain high Curie temperature, but the initial permeability of Ni–Cu–Zn ferrites reached only up to 2000 [14-16]. This paper will distinguish two well-known methods of preparation ferrite nano powders to synthesize Cu-Zn spinel ferrites. The study's objective was to investigate the effect of Zn substitution on magnetic (saturation magnetization, remanence, and coercivity) and structural properties (lattice parameter, grain size, and crystallite size). The prepared ferrite nano powders are characterized by using X-ray diffraction (XRD), vibrating-sample magnetometer (VSM), and scanning electron microscopy (SEM).

2. Experimentation

Methodology. Cu-Zn spinel was synthesized by using the sol-gel auto combustion method and hydrothermal method. A balanced equation for synthesis by each method is mentioned below:

$$(1 - x)Cu(NO_3)_2.3H_2O + x(CH_3COO)_2Zn.2H_2O + 2Fe(NO_3)_2.9H_2O + 3C_6H_8O_7.H_2O = Cu_{(1-x)}Zn_xFe_2O_4. \tag{1}$$
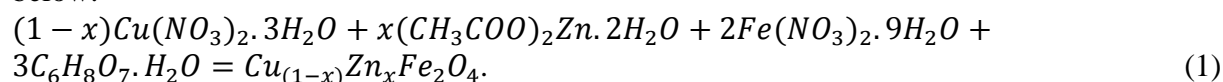
Synthesis by Sol-gel Route. Stoichiometric calculations were done for the synthesis of $Cu_{(1-x)}Zn_xFe_2O_4$. Copper nitrate ($Cu(NO_3)_2.3H_2O$), Zinc acetate (($CH_3COO)_2Zn.2H_2O$), Iron nitrate ($Fe(NO_3)_3.9H_2O$), and citric acid were used as precursors. All nitrates and citric acid were dissolved insufficient amount of distilled water to form a clear solution to obtain metal ions solution in separate beakers. All the nitrates were mixed in a beaker and were kept for continuous stirring for 15 minutes, as shown in Fig. 1. Citric acid was added to the solution as a chelating agent, and then ammonia solution was slowly added to maintain the pH of the solution at 7 with continuous stirring. Citric acid to metal ion ratio was taken as 1:1 [4]. The temperature of the hotplate was gradually increased to 60ºC. Then the solution was heated and stirred for about 4 hours. The gel was formed after 4 hours, and it was heated at the same temperature for about 25 minutes. Auto combustion took place, and a homogenous powder was formed. Various gases were evolved during this process. After complete combustion of the sample, the hotplate temperature was decreased slowly. The product of auto combustion was grounded into a fine powder with the help of agate mortar. The powder formed was calcinated at 750 ºC for 8 hours to form crystalline spinel ferrite. The phase identification of the calcined powder was performed by X-ray diffraction (XRD) using Cu-Kα radiation. Magnetic properties of the spinel ferrite like saturation magnetic flux, remnant magnetic flux, and coercive force were determined using VSM.
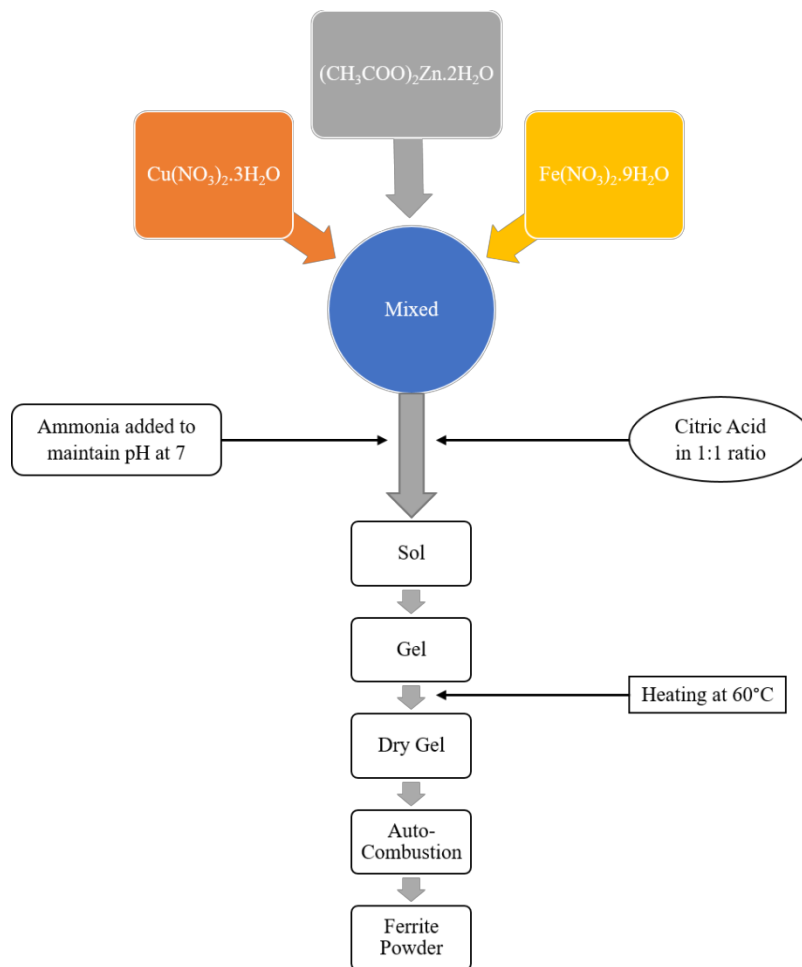
Fig. 1. Typical flow chart of Sol-Gel method for synthesizing Cu-Zn spinel ferrite

Synthesis by Hydrothermal Route. Stoichiometric calculations were done for the synthesis of $Cu_{(1-x)}Zn_xFe_2O_4$. Copper nitrate ($Cu(NO_3)_2.3H_2O$), Zinc acetate (($CH_3COO)_2Zn.2H_2O$), and Iron nitrate ($Fe(NO_3)_3.9H_2O$) were used as precursors. All nitrates dissolved an insufficient amount of distilled water to form a clear solution to obtain metal ions solution in separate beakers, as shown in Fig. 2. The 2M NaOH solution was prepared by adding 16 gm NaOH in 200 mL of distilled water to maintain the pH of 12.5. A beaker with iron nitrate solution was placed on the hotplate, and a magnetic capsule (stirrer) was put in the solution. Copper nitrate and zinc acetate solution were added to it under continuous stirring. 2M NaOH solution was slowly added to the solution to maintain the pH of the solution at 12.5 with continuous stirring. The temperature of the hotplate was kept at room temperature. Then the solution was stirred for about 2 hours for complete mixing of the metal ions. The solution was poured into a Teflon tube and kept at 220 ℃ for 8 hours in the oven. The precipitate was formed after 8 hours of heating; this precipitate was filtered using filter paper and distilled water. After filtering the precipitate, it was again kept in the oven for 24 hours at 60℃ for drying along with filter paper. With the help of a spatula, powder formed after drying was collected from filter paper and grounded to a fine powder using agate mortar.
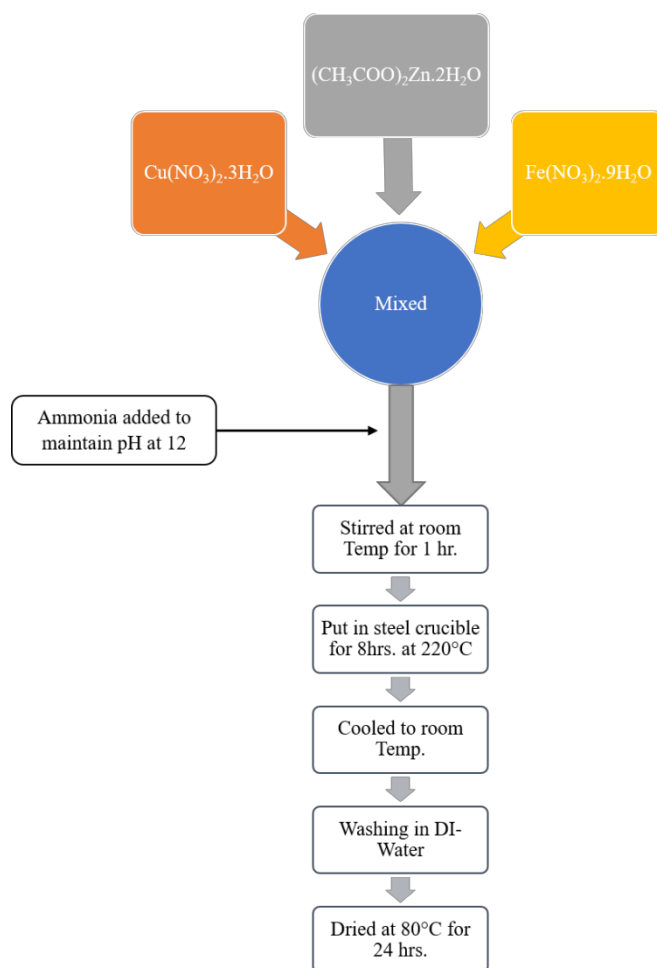
Fig. 2. Flow chart for preparation of Cu-Zn spinel ferrite through hydrothermal route

Characterization. Phase identification and structural characterization were performed using X-ray diffraction technique (Target: Cu-Kα, 10°-90°, step size – 0.02°, holding time: 0.2 seconds) which confirms the existence of a well-defined single-phase spinel ferrite structure. The SEM image for ferrite powder synthesized by each method was obtained using SEM machine. VSM was done to determine magnetic properties like saturation magnetization, remanence, and coercivity.

3. Results and Discussion

Structural Properties. The general formula for spinel ferrite synthesized is $Cu_{(1-x)}Zn_xFe_2O_4$. Spectra from XRD for x = 0.2-0.8 are shown in Fig. 3 and Fig. 4 were matched with the standard XRD pattern of Cu-Zn spinel ferrite, and it confirmed that single phase Cu-Zn spinel ferrite is formed for both methods. The most intense peaks in all specimens are (220), (311), (222), (400), (422), (333), and (440) are found to be well-matched with single-phase cubic spinel. The average crystallite size for all the samples was calculated using Debye Scherrer's formula with respect to the high-intensity peak plane (311). Debye Scherrer's formula can be expressed to calculate the crystallite size [17-18].

$$t = \frac{0.9\lambda}{BCos\theta_B},\tag{2}$$

where t – crystallite size (Å), λ – wavelength of incident X-rays (Å), θ_B – Bragg's angle (degree), B – width of major peak at FWHM (radian).
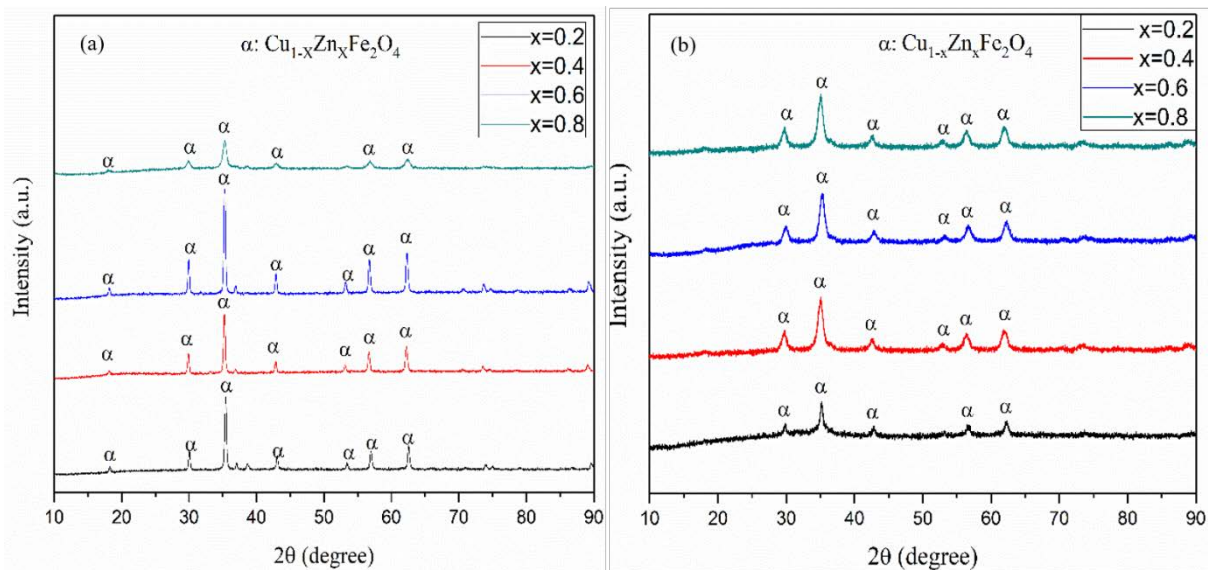
Fig. 3. XRD pattern for Cu-Zn spinel ferrite synthesized by (a) sol-gel auto-combustion method and (b) hydrothermal method
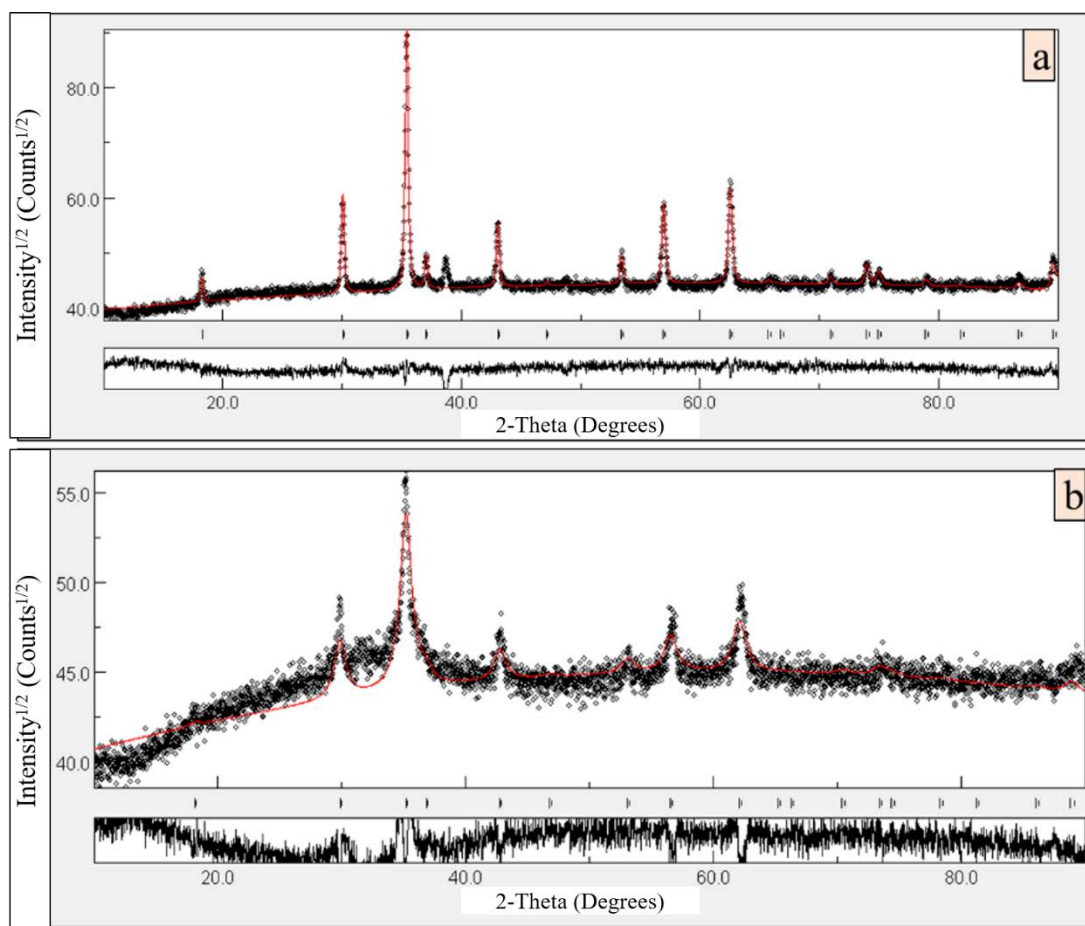
Fig. 4. Maud analysis of $Cu_{(1-x)}Zn_xFe_2O_4$ ferrite (a) Sol-gel (b) Hydrothermal

From Table 1 and Table 2, it can be noticed that the lattice parameter of Cu-Zn spinel ferrite increases with an increase in Zn substitution for both methods for x = 0.2–0.6. This can be explained as the size of the Zn ion is larger than the size of the Cu ion, so as we increase the concentration of Zn in the Cu-Zn spinel ferrite lattice parameter. But the value of the

lattice parameter decreases for x = 0.6–0.8, which can be explained as the further addition of Zn in the Cu-Zn spinel ferrite has led to a distortion of the lattice [19].

Table 1. Lattice parameter (a) and crystallite size (t) $Cu_{(1-x)}Zn_xFe_2O_4$ (x=0.2–0.8) ferrite nanopowders for sol-gel method

Sol-gel auto-combustion method		
x	t (Å)	a (Å)
0.2	764.098	8.3905
0.4	844.64	8.3974
0.6	657.11	8.4248
0.8	296.877	8.418

Table 2. Lattice parameter (a) and crystallite size (t) $Cu_{(1-x)}Zn_xFe_2O_4$ (x=0.2–0.8) ferrite nanopowders for hydrothermal method

Hydrothermal method		
x	t (Å)	a (Å)
0.2	296.877	8.418
0.4	302.687	8.423
0.6	205.465	8.472
0.8	175.317	8.4665

SEM. The SEM of Zinc doped copper ferrite is shown in Fig. 5. The image gives the impression that the product of the auto combustion reaction was very spongy and feathery, and it also confirms that the sub-micrometer-sized primary particles were agglomerated into the larger secondary particles. SEM has done for x=0.6 in $Cu_{(1-x)}Zn_xFe_2O_4$.
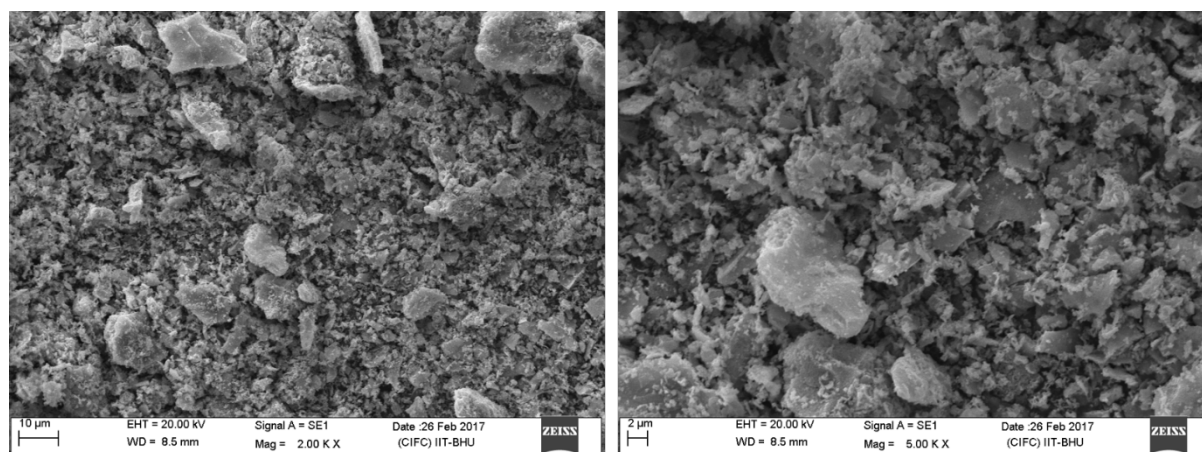
Fig. 5. SEM images of $Cu_{(1-X)}Zn_XFe_2O_4$ for x=0.6

Magnetic property. The saturation magnetization (Ms) and coercivity (Hc) of nanopowders synthesized by the sol-gel method as a function of Zn substitution (x) are shown in Fig. 6. It is observed that Ms gradually increases with an increase in Zn concentration for x=0.2–0.4 as the packing of magnetic material in a specified volume increases and then decreases with an increase in Zn concentration for x=0.6–0.8.
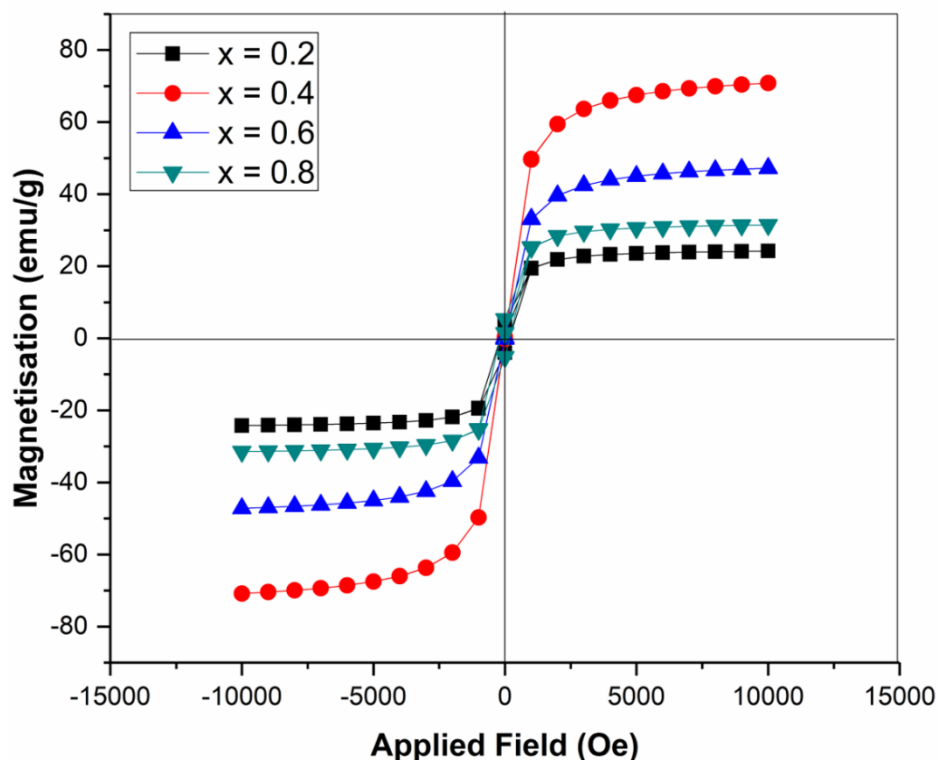
Fig. 6. Hysteresis loop for Cu-Zn spinel ferrite synthesized by sol-gel auto combustion method for varying composition of Zn (x)

Table 3. Values of Saturation magnetization (MS), Coercivity (H_C), and Remanence Magnetization (Mr)

Zn content	Ms (emu/g)	Mr (emu/g)	Hc (Oe)
x=0.2	24.21	6.14	184.47
x=0.4	70.82	5.33	174.46
x=0.6	47.21	3.22	116.26
x=0.8	31.17	2.33	102.26

The hysteresis plot of all synthesized samples shown in Fig. 6 and Table 3 enlists the effect of Zn doping on saturation magnetization (Ms), coercivity (Hc), and remenance (Mr). In the case of Zn Ferrite, the magnetic [20-22] properties can be explained by Neel's two sublattice models. According to this model, a spinel having a AB_2O_4 structure has two types of sublattices, octahedral (B) and tetrahedral (A) sites. Owing to exchange energy, the ions occupying A and B sites have their magnetic moments arranged in an anti-parallel fashion. Here, the Fe^{3+} ions are equally distributed amongst the A and B sites, while the Cu^{2+} ions have a strong preference for B sites. The net magnetic moment is determined by Cu^{2+} ($\mu B=1$) ions as the same due to Fe^{3+} ($\mu B=5$) ions present at A and B sites cancel out. Thus, the overall magnetization of the material is the difference in magnetization present at these two sites.

Site B dominates as it contains a more significant number of ions. However, on substituting Cu^{2+} with nonmagnetic ions Zn^{2+}. Zn^{2+} having a strong preference for A sites, they are disposed of there. This results in the dislocation of some of the Fe^{3+} ions from A to B sites. Unlike in the case of Cu ferrite, the compensation in the magnetic moment of Fe^{3+} will not occur, and they contribute with large magnetic moments to B sites. This results in an increase in magnetization. Mr and Hc present a decreasing nature with Zn doping. As seen, the minimum value of coercivity is obtained for x=0.8, with a general decreasing trend for

increasing x value. It is possibly due to the alternation of particle and grain size of Cu ferrite before and after Zn doping. Zn doped Cu ferrite, having a larger particle size, may have more magnetic domain and domain walls, resulting in demagnetization with ease. Also, the anisotropic constant value of Cu ferrite is more than that of Zn ferrite.

4. Conclusions

Cu-Zn spinel ferrite having chemical formula $Cu_{(1-x)}Zn_xFe_2O_4$ was synthesized for x ranging from 0.2 to 0.8 by sol-gel auto-combustion method and hydrothermal method, and its single phase was verified by XRD results. An increasing trend in lattice parameter was observed for x=0.2-0.6 for both methods as the size of Zn ion is more than the size of Cu ion, and then it decreases for x=0.8 due to lattice distortion. From VSM results, it was observed that saturation magnetization increases as Zn doping increases from 0.2 to 0.4, i.e., 24.21 to 70.82 emu/g then Ms decreases with an increase in Zn doping from 47.21 to 31.17 for x= 0.6–0.8 as initially, Zn occupies A sites initially but with further increases in Zn doping causes saturation of Zn ions at A site and hence Zn ions to occupy B site. This causes a decrease in Ms with an increase in Zn doping. Mr and Hc decrease with an increase in Zn doping.

References

[1] Li LZ, Peng L, Zhong XX, Wang R, Tu XQ. Structural, magnetic and electrical properties of Cu-Zn ferrite nanopowders. *Journal of Magnetism and Magnetic Materials*. 2016;419:407-411.

[2] Gao JM, Cheng F. Study on the preparation of spinel ferrites with enhanced magnetic properties using limonite laterite ore as raw materials. *Journal of Magnetism and Magnetic Materials*. 2018;460: 213-222.

[3] Mahmoud MH, Hassan AM, Said AE-AA, Hamdeh HH. Structural; magnetic and Catalytic properties of nanocrystalline $Cu_{0.5}Zn_{0.5}Fe_2O_4$ synthesized by microwave combustion and ball milling methods. *Journal of Molecular Structure*. 2016;1114: 1-6.

[4] Maria KH, Choudhury S, Hakim MA. Structural phase transformation and hysteresis behavior of Cu-Zn ferrites. *International Nano Letters*. 2013;3.

[5] Kavas H, Baykal A, Demir A, Toprak MS, Aktas B. $Zn_xCu_{(12x)}Fe_2O_4$ Nanoferrites by Sol–Gel Auto Combustion Route: Cation Distribution and Microwave Absorption Properties. *J. Inorg. Organomet. Polym.* 2014;24: 963-970.

[6] Wu W, Cai J, Wu X, Wang K, Hu Y, Wang Q. Nanocrystalline $Cu_{0.5}Zn_{0.5}Fe_2O_4$: Preparation and Kinetics of Thermal Decomposition of Precursor. *J. Supercond. Nov. Magn.* 2013;26: 3523-3528.

[7] Tatarchuk T, Bououdina M, Macyk W, Shyichuk O, Paliychuk N, Yaremiy I, Al-Najar B, Pacia M. Structural, Optical, and Magnetic Properties of Zn-Doped $CoFe_2O_4$ Nanoparticles. *Nanoscale Research Letters*. 2017;12.

[8] Yadav RS, Kuritka I, Havlica J, Hnatko M, Alexander C, Masilko J, Kalina L, Hajduchova M, Rusnak J, Enev V. Structural, Magnetic, Elastic, Dielectric and Electrical Properties of Hot-Press Sintered $Co_{1-x}Zn_xFe_2O_4$ (x=0.0, 0.5) Spinel Ferrite Nanoparticles. *Journal of Magnetism and Magnetic Materials*. 2017;447: 48-57.

[9] Parashar J, Saxena VK, Jyoti, Bhatnagar D, B.Sharma K. Dielectric behaviour of Zn substituted Cu nano-ferrites. *Journal of Magnetismand Magnetic Materials*. 2015;394: 105-110.

[10] Yadav RS, Havlica J, Hnatko M, Šajgalík P, Alexander C, Palou M, Bartonickova E, Bohac M, Frajkorova F, Masilko J, Zmrzly M, Kalina L, Hajdúchova M , Enev V. Magnetic properties of $Co_{1-x}Zn_xFe_2O_4$ spinel ferrite nanoparticles synthesized by starch-assisted sol–gel

autocombustion method and its ball milling. *Journal of Magnetism and Magnetic Materials*. 2015;378: 190-199.

[11] Baykal A, Esir S, Demir A, Güner S. Magnetic and optical Properties of $Cu_{1-x}Zn_xFe_2O_4$ Nanoparticles Dispersed in a silica matrix by a solgel auto-combustion method. *Ceramics International*. 2014;41(1): 231-239.

[12] Rana MU, Abbas T. The effect of Zn substitution on microstructure and magnetic properties of $Cu_{1-x}Zn_xFe_2O_4$ ferrite. *Journal of Magnetism and Magnetic Materials*. 2002;246(1-2): 110-114.

[13] Ajmal M, Maqsood A. Structural, electrical and magnetic properties of $Cu_{1-x}Zn_xFe_2O_4$ ferrites ($0{\leq}x{\leq}1$). *Journal of Alloys and Compounds*. 2008;460(1-2): 54-59.

[14] Hu J, Ma Y, Kan X, Liu C, Zhang X, Rao R, Wang M, Zheng G. Investigations of Co substitution on the structural and magnetic properties of Ni-Zn spinel ferrite. *Journal of Magnetism and Magnetic Materials*. 2020;513: 167200.

[15] Agarwal N, Narang SB. Magnetic characterization of Nickel-Zinc spinel ferrites along with their microwave characterization in Ku band. *Journal of Magnetism and Magnetic Materials*. 2020;513: 167052.

[16] Tangcharoen T, Ruangphanit A, Pecharapa W. Structural and magnetic properties of nanocrystalline zinc-doped metal ferrites (metal¼Ni; Mn;Cu) prepared by sol–gel combustion method. *Ceramics International*. 2013;39(S1): S239-S243.

[17] Nigam A, Pawar SJ. Structural, magnetic, and antimicrobial properties of zinc doped magnesium ferrite for drug delivery applications, *Ceramics International*. 2020;46: 4058-4064.

[18] Nigam A, Pawar SJ. Synthesis and characterization of ZnO nanoparticles to optimize drug loading and release profile for drug delivery applications. *Materials Today: Proceedings*. 2020;26(2): 2625-2628.

[19] Kumar N, Bharti A, Kumar A, Nigam A. Effect of process parameters on the crystal-parameters of Cu-Zn spinel-ferrites. *Materials Physics and Mechanics*. 2021;47: 65-73.

[20] Khudyakov A, Mazur A, Pleshakov I, Bibik E, Fofanov Y, Kuzmin Y, Shlyagin M. Transverse Relaxation of a Nuclear Spin System in Bulk and Nanostructured Magnetically Ordered Materials. In: *Proceedings of the 2020 IEEE International Conference on Electrical Engineering and Photonics*. EExPolytech; 2020. p.201-203.

[21] Esarev IV, Gurzhiy VV, Selyutin AA, Laptenkova AV, Poddel'skyc AI, Medvedskiy NL, Ponyaev AI, Trifonov RE, Eremin AV. First example of a click-reaction on the aminate copper complexes: effect of reaction parameters. *Mendeleev Communications*. 2018;28(6): 606-608.

[22] Singh S, Goswami G, Kumar A. Influence of Ph and Calcination Temperature on Magnetic Properties of Nanosized Zn-Ferrite Synthesized by Sol–Gel Citrate Method. *International Journal of Research in Engineering and Technology*. 2017;06(01): 23-29.

NUCLEATION AND GROWTH OF FULLERENES AND NANOTUBES HAVING FOUR-FOLD SYMMETRY

Alexander I. Melker[1*], **Maria A. Krupina**[2], **Aleksandra N. Matvienko**[3]

[1]St. Petersburg Academy of Sciences on Strength Problems, [2]Department of Physics

[3]Department of Mechanics and Control Processes, Peter the Great St. Petersburg Polytechnic University

Polytekhnicheskaya 29, 195251, St. Petersburg, Russian Federation

*e-mail: ndtcs@inbox.ru

Abstract. We have studied possible ways of generating and growing the fullerenes having four-fold symmetry. Beginning with cyclobutane C_4H_8 and clusters C_8, we obtained elementary fullerenes C_8 and mini-fullerenes C_{16}, which produce the following fullerenes from C_{24} to C_{64}, perfect (basic) and imperfect, as well as nanotubes. The imperfection is connected either with extra 'interstitial' or 'vacancy' carbon dimers, both types of dimers playing the role of defects. Only the basic fullerenes C_{24}, C_{32}, C_{40}, C_{48}, $C_{56,}$ and C_{64} have the ordinary four-fold symmetry in the corresponding column of the periodic system of fullerenes, the intermediate fullerenes having no such symmetry. Considering the latter as imperfect due to defects, one can define them as the fullerenes conserving topological four-fold symmetry. We have calculated their energies and discussed possible reasons for their dependence on a fullerene size and shape.
Keywords: carbon, embedding, energy, fullerene, fusion reaction, graph representation, growth, nanotube, periodic system, single and double bonds, topological symmetry

1. Introduction
Any calculations of fullerene properties need input data, first of all, the thorough knowledge of fullerene structure. However, up to now, there is no clear and unique theory of fullerene growth, and therefore there is no standard way of obtaining fullerene structures. "The problem here is not the lack of imagination, because quite numerous models have been proposed. What is rather lacking is a model using quantities that might be evaluated and measured. Moreover, a theoretical model, in order to deserve its name, should lead to numerical predictions. In order to represent something more than a set of circular arguments, a model should predict more numerical values, parameters or functional relations than the number of input parameters" [1]. That was written more than a quarter of the century ago. Although there has been considerable activity from both the experimental and theoretical sides [2,3] to gain a detailed understanding of fullerene formation, since then almost nothing has changed [4]. The first effort to make a prediction was done in Ref [5]. Succeeding modeling the fullerene growth allowed classifying the fullerenes, known and predicted, on the base of the periodic system of fullerenes formulated [6].

Classification is the most important and most difficult question for any science. The periodic system suggested is based on symmetry principles; it can be said that any fullerene is inspected for elements of symmetry. The system consists of horizontal series and vertical columns (groups). The horizontal series form the Δn periodicities, where the fullerene structure changes from threefold symmetry to sevenfold through four, five, and sixfold ones.

The vertical columns include the fullerenes of one and the same symmetry, the mass difference Δm for each column being equal to a double degree of symmetry. It was assumed that both Δm and Δn periodicities can be taken as a basis for rigorous fullerene classification.

The Δn periodicities studied make up the following series: $\Delta n = 6, 8, 10, 12, 14,$ and 16; they include basic perfect fullerenes from C_{14} to C_{96}. The structure, energy, and formation mechanism for these series are discussed elsewhere [6-10]. The system leaves room for incorporating into its other fullerene columns.

Up to this point, it has been desirable to work entirely with the Δn series in order to discover general features of the transition from one symmetry to another. Now that we have found the corresponding regularity, we need to focus upon particulars of one and the same column (group). Since in the periodic system of fullerenes, the vertical columns (groups) incorporate the fullerenes of one and the same symmetry, we suppose that the fullerenes of one and the same group have similar properties. In addition to the classification of fullerenes, the crucial point, which should be given more attention to, is the nucleation and growth of fullerenes relating to one and the same column.

In this contribution, we have studied the nucleation of fullerenes and nanotubes referring to the column of four-fold symmetry.

2. Generation of clusters having four-fold symmetry

We assume that the embryo of fullerenes of four-fold symmetry is a cluster having just the same symmetry. The question arises: Are there in nature similar molecules, from which it is possible to obtain such cluster? To our mind cyclobutane C_4H_8 with D_{4h} symmetry [11] could be such a molecule.

Suppose that we have removed eight hydrogen atoms and added four carbon atoms instead. In doing so we obtain carbon cluster C_4C_4 with several types of carbon atoms. They are shown, together with cyclobutane C_4H_8, in Fig. 1. We have calculated their optimized structures and energy of these compounds as well as of the succeeding ones through the use of Avogadro package [12].
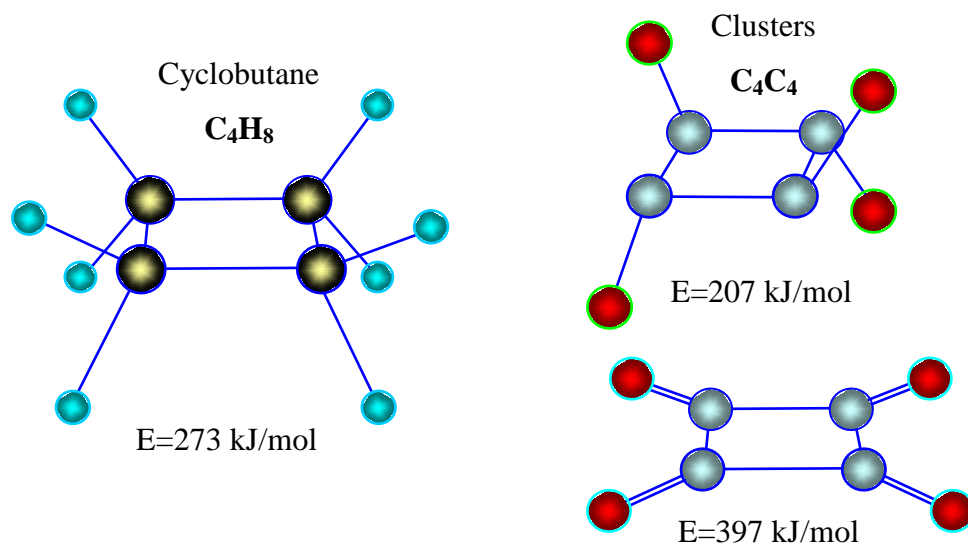
Fig. 1. Cyclobutane and two eight-atom carbon clusters of four-fold symmetry

The carbon atoms of cyclobutane remain in the initial electronic state; they are considered, as is customary, being sp^2 hybridized atoms. The newly added ones are reactive carbon atoms, which are connected with the initial carbon atoms by single or double bonds, being ionized to a different degree. One way of looking at the gradual evolution of the

clusters shown is folding the clusters and fusion the structures obtained with the following growth.

3. Generation of fullerenes and nanotubes

Cluster folding. The elementary fullerene of four-fold symmetry is a cube. It can be obtained as a result of folding the carbon clusters shown above. Two extreme electronic structures are presented in Fig. 2. In addition to the structures, the graphs of cubes are shown. Here and below we use area-colored graphs because they gain a better understanding of the structures obtained. In our case all the areas, in spite of their shapes, are tetragons and they are grey painted.

E=1076   E=2612
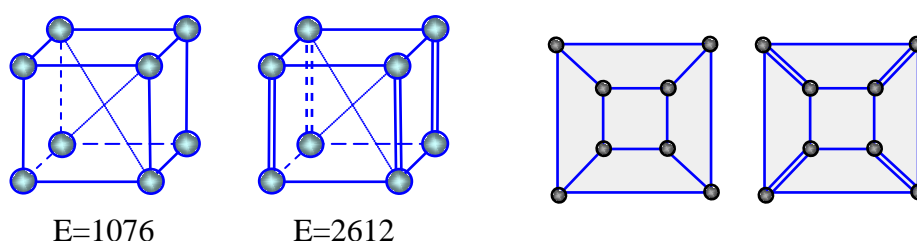
Fig. 2. Two electronic isomers of a carbon cube, energy in kJ/mol

Fusion of cubes. The elementary fullerenes can grow, conserving its symmetry, by the mechanism known as "fusion of fullerenes having compatible symmetry" [13]. The final configuration produced by the fusion of two cubes is shown in Fig. 3. The shape of the mini-fullerene resembles a square barrel. In its turn this fullerene can continue growing, which conserves the symmetry, through the use of the above-mentioned mechanism, i.e. joining another cube (Fig. 4). The reaction is possible since the reacting structures have four-fold symmetry and therefore they are compatible with each other.

C_{16}

E=671   E=2070

C_{24}

E=853   E=2452
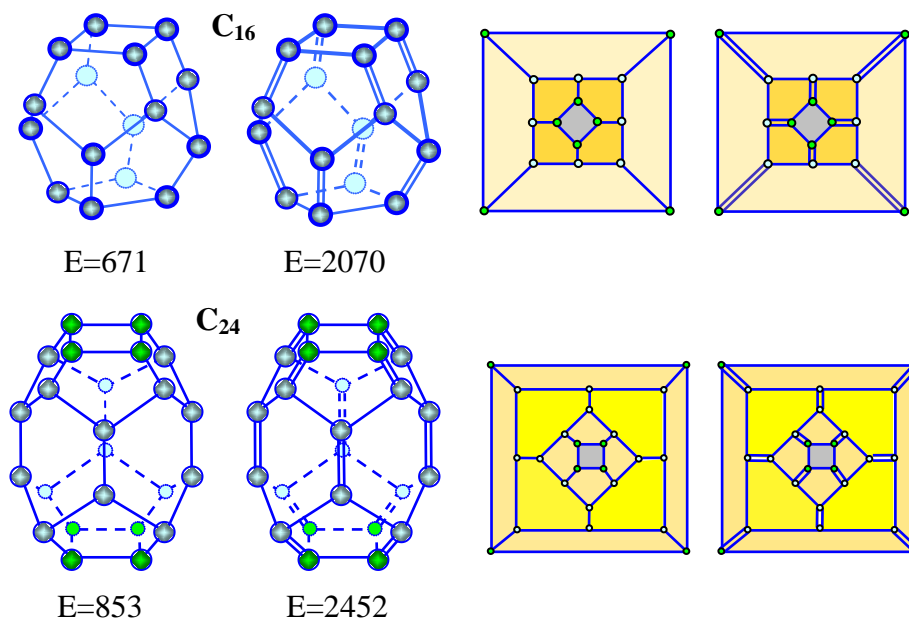
Fig. 4. Fusion of two fullerenes C_8 and C_{16}: structure and graphs; energy in kJ/mol

It must be emphasized that the faces of fullerenes now contain not only tetragons but pentagons and hexagons too. To gain a better understanding of the fullerene structure, the

graph areas are painted in different colors: tetragons in grey as before, pentagons in goldish, and hexagons in yellow.

One can consider the structure obtained both as fullerene and as an embryo of the nanotube. Really, if to continue the fusion of cubes, there appears a narrow nanotube of four-fold symmetry (Fig. 5). It is worth noting that at first extremely narrow nanotubes were considered only as a new type of nanotubes being of academic interest [14]. Recently it has been discovered that small diameter single-walled carbon nanotubes were mimics of ion channels found in natural systems [15]. These properties make them a promising material for developing membrane separation technologies [16].
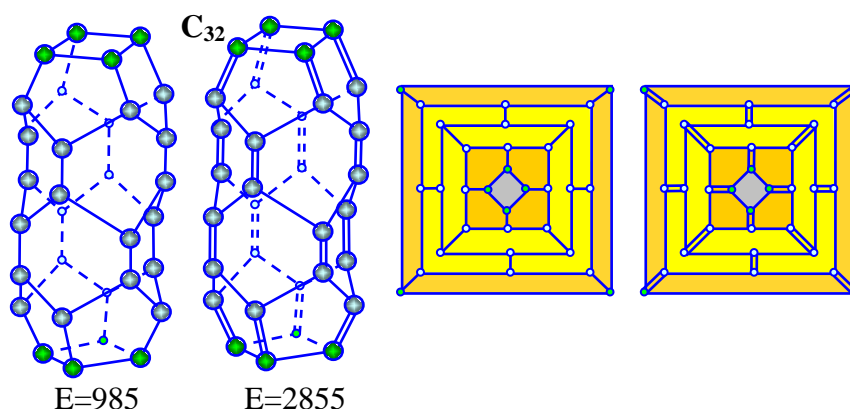
Fig. 5. Joining two mini-fullerenes C_{16} through the use of the rotation-reflection symmetry: structure and graphs; energy in kJ/mol

Growth of fullerene C_{24}. The polyhedron shown in Fig. 4 can be thought over as a primary fullerene having the possibility to use for growing the mechanism known as "embedding carbon dimers" which was suggested by M. Endo and the Nobel Prize winner H.W. Kroto in 1992 [17]. According to it, a carbon dimer embeds into a hexagon of an initial fullerene. This leads to stretching and breaking the covalent bonds which are normal to the dimer and to creating new bonds with the dimer (Fig. 6). As a result, there arises a new atomic configuration and there is a mass increase of two carbon atoms. The fullerenes designed through the use of the Endo-Kroto mechanism are illustrated in Figs. 6-10.
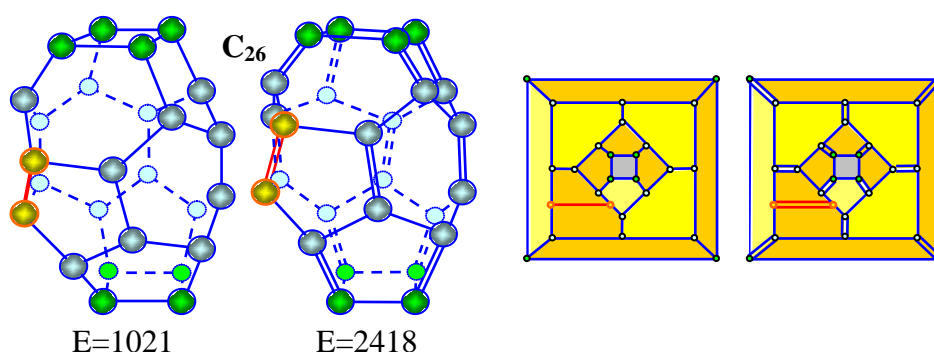
Fig. 6. Imperfect fullerene C_{26} as a result of embedding a carbon dimer (yellow atoms) into fullerene C_{24}: structure and graphs; energy in kJ/mol

C_{28} a

E=1082   E=2358
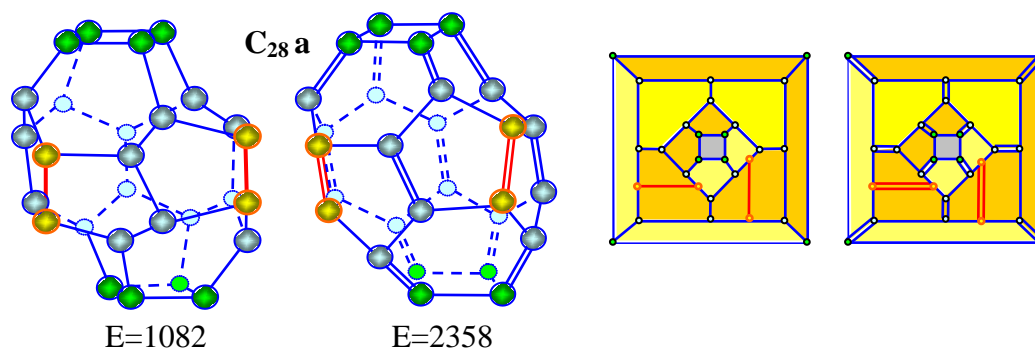
Fig. 7. Asymmetric imperfect fullerene C_{28} as a result of embedding a carbon dimer into fullerene C_{26}: structure and graphs; energy in kJ/mol

C_{28} s

E=1104   E=2382
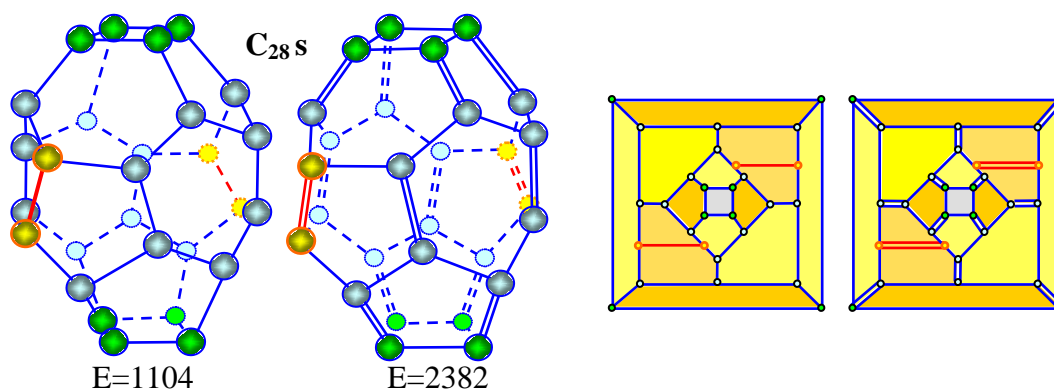
Fig. 8. Symmetric semi-perfect fullerene C_{28} as a result of embedding a carbon dimer into fullerene C_{26}: structure and graphs; energy in kJ/mol

C_{30}

E=1142   E=2318
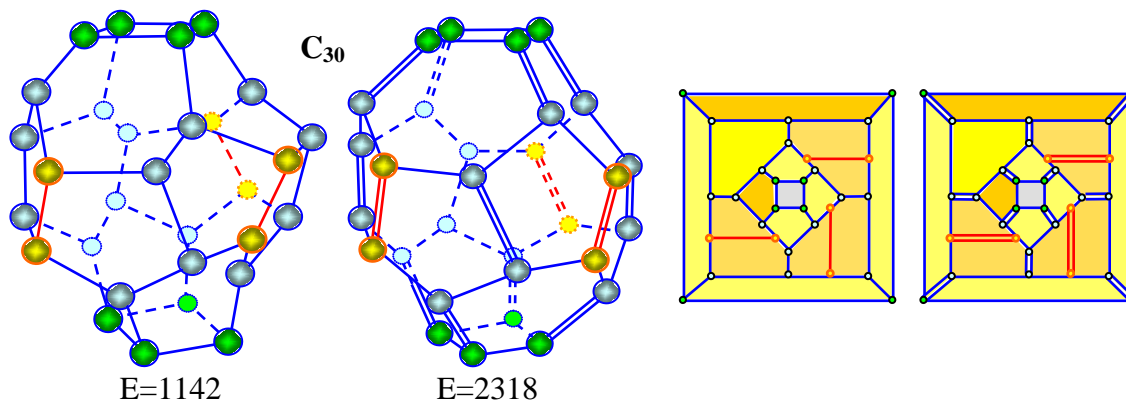
Fig. 9. Asymmetric imperfect fullerene C_{30} as a result of embedding a carbon dimer into fullerene C_{28}: structure and graphs; energy in kJ/mol

E=1306   E=2853
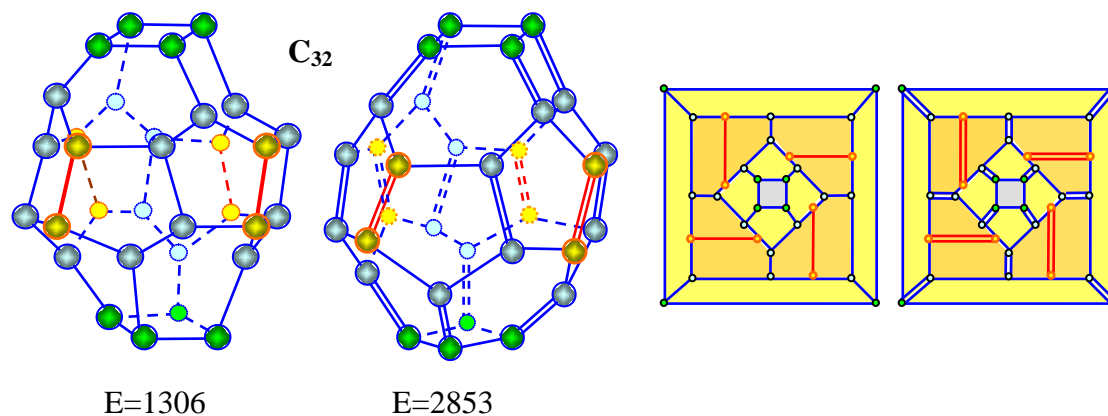
Fig. 10. Perfect fullerene C_{32} as a result of embedding a carbon dimer into fullerene C_{30}: structure and graphs; energy in kJ/mol

From the figures, of special note, are the graphs, we notice that only the initial C_{24} and final C_{32} fullerenes and have ordinary four-fold symmetry. They are perfect fullerenes. The intermediate fullerenes C_{26}, C_{28} and C_{30}, as was analyzed in Ref [6], have topological four-fold symmetry. As follows from its graph, fullerene C_{32} can't grow any further by means of the Endo-Kroto mechanism. It is a dead-end fullerene.

4. Cupolas and their fusion

There is a second way for the generation of fullerenes to have the four-fold symmetry. It consists of the growth of the initial clusters which then transform into half-fullerenes (cupolas) conserving the four-fold symmetry (Fig. 11). From the figures we notice that all the cupolas have one and the same base of eighteen atoms; therefore they can combine with each other creating new fullerenes as well as nanotubes. Let us investigate this process in detail.

E=335   E=652

E=576   E=1112

C_{32}

E=732   E=1163

C_{40}

E=790   E=1350
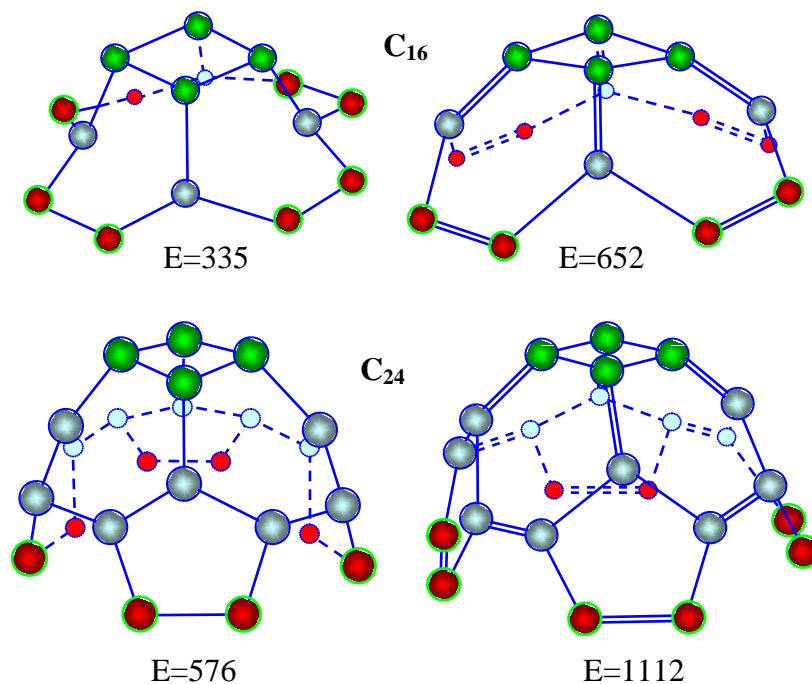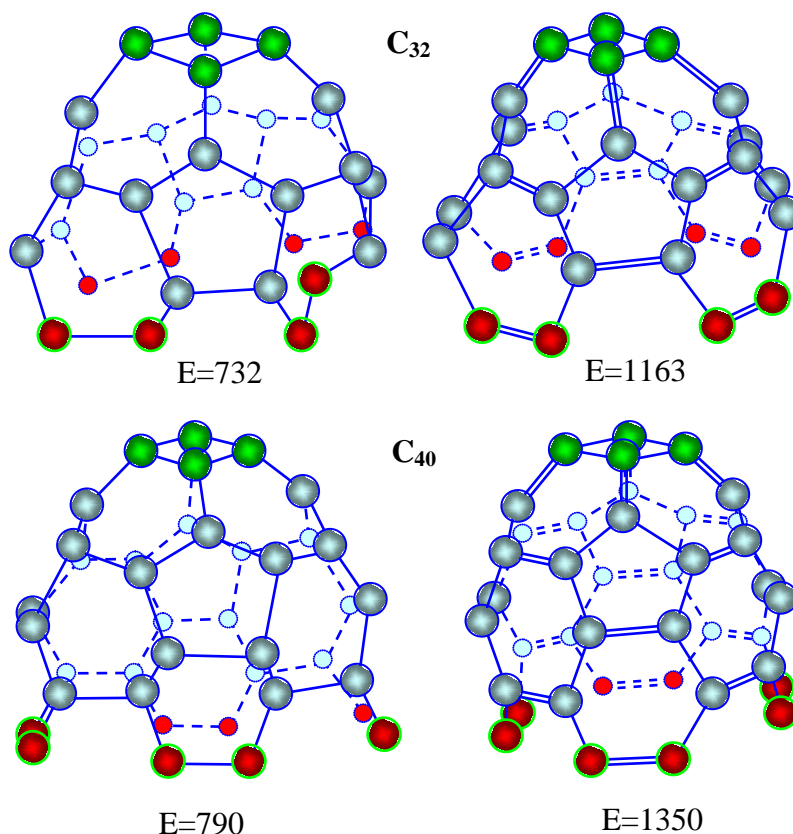
Fig. 11. Growth of cupolas of four-fold symmetry: structure and graphs; energy in kJ/mol

Fusion of cluster C_8 with cupola C_{16}. The fullerene obtained contains six squares and eight hexagons (Fig. 12). Its shape is a truncated octahedron (cuboctahedron) having four-fold symmetry. The fullerene is an isomer of the bifurcation fullerene C_{24} shown in Fig. 4. It should be emphasized that the cuboctahedron can't grow through the use of the Endo-Kroto's mechanism conserving the four-fold symmetry. It is a dead-end fullerene.

C_{24}

E=2067   E=3046
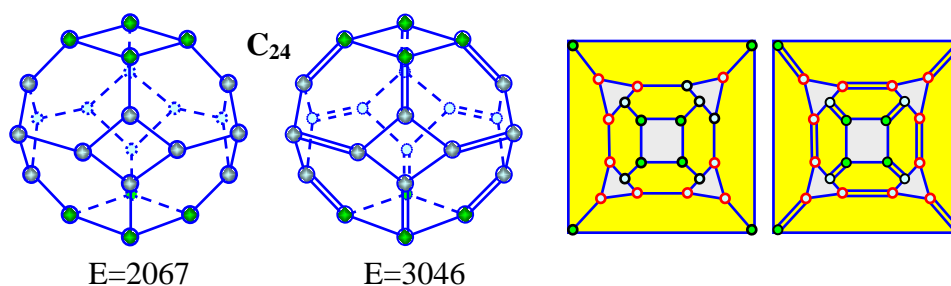
Fig. 12. Joining plane cluster C_8 with cupola C_{16}; structure and graphs; energy in kJ/mol

Fusion of two cupolas C_{16}. There are two ways of joining: mirror symmetry and rotation-reflection one. In the first case (Fig. 13) the lower cupola is a mirror copy of the upper one. The fullerene obtained consists of six squares and twelve hexagons; it is a tetra$_6$-hexa$_{12}$ polyhedron.
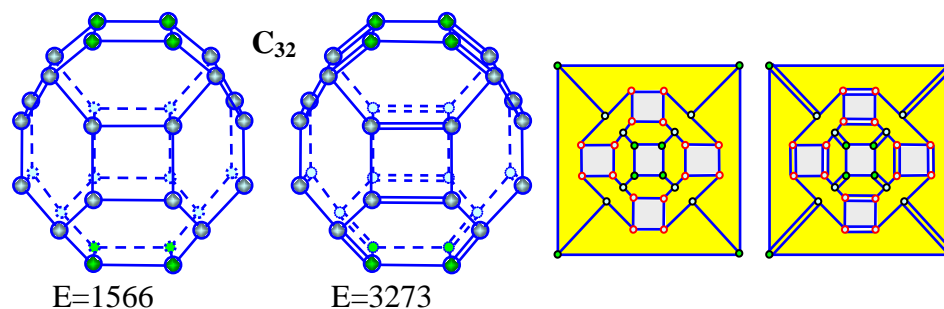
Fig. 13. Joining two half fullerenes C_{16} of four-fold symmetry; the mirror symmetry fusion; structure and graphs; energy in kJ/mol

In the second case (Fig. 14) the lower cupola is a rotatory reflection of the upper one. The fullerene contains two squares, eight pentagons, and eight hexagons; it is a tetra$_2$-(penta-hexa)$_8$ polyhedron. The pentagons form a ring at the equator. It should be emphasized that this fullerene is a dead-end one.
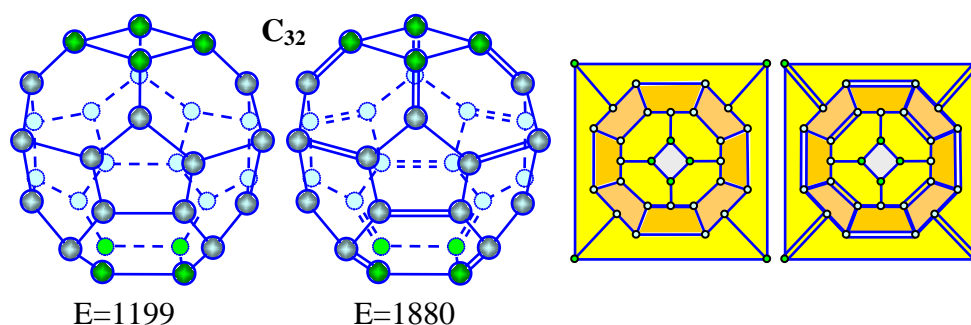
Fig. 14. Joining two half fullerenes C_{16} of four-fold symmetry; the rotation-reflection symmetry; structure and graphs; energy in kJ/mol

Fusion of two cupolas: C_{16} and C_{24} (Fig. 15).
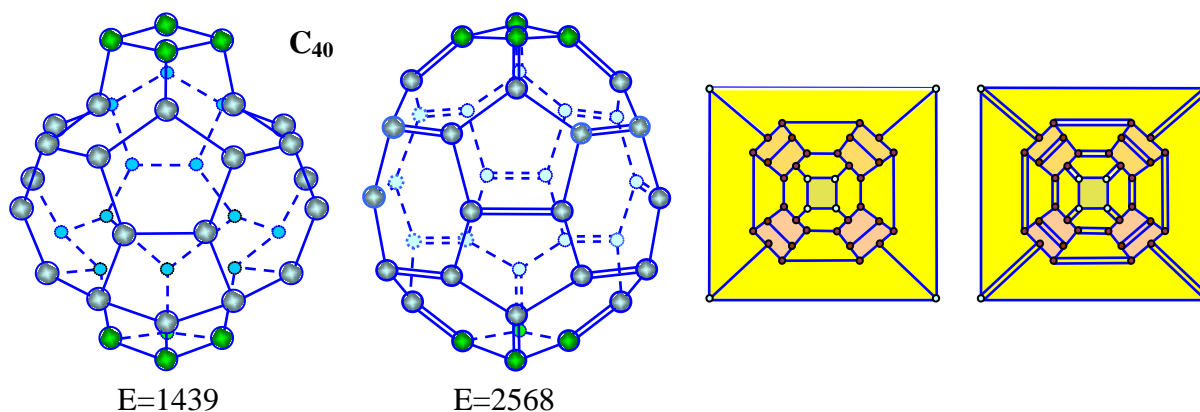
Fig. 15. Mirror symmetry fusion of two cupolas (half-fullerenes) C_{16} and C_{24} having four-fold symmetry; structure and graphs; energy in kJ/mol

Fusion of two cupolas C$_{24}$ (Fig.16).

E=1442   E=2500
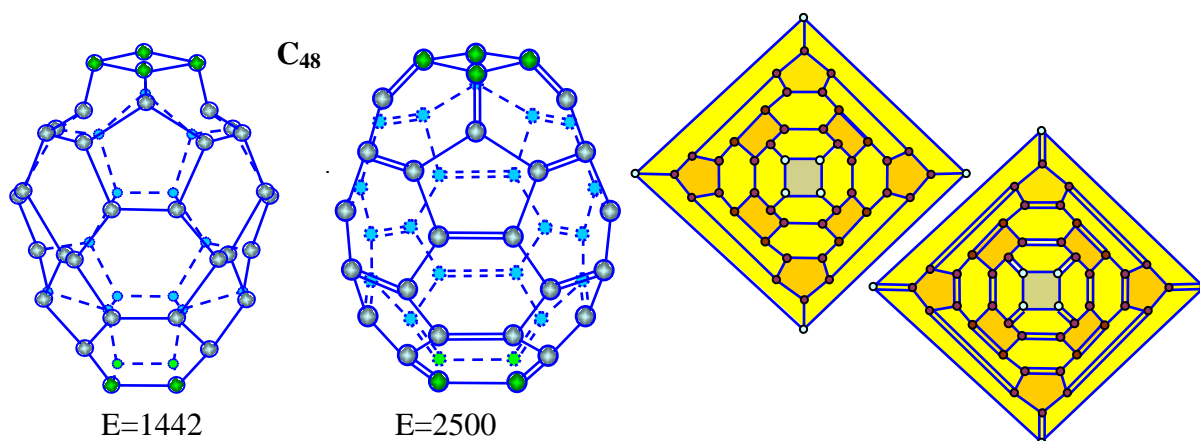
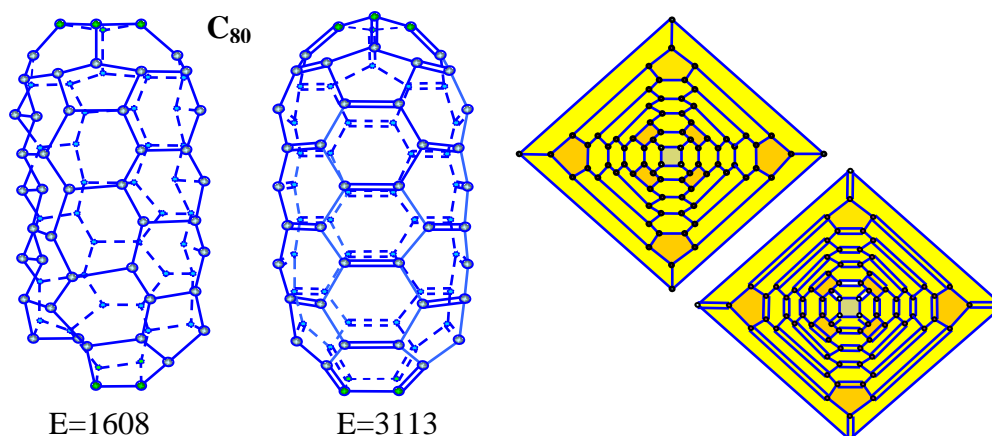**Fig. 16.** Rotation-reflection symmetry fusion of two cupolas (half-fullerenes) C$_{24}$ having four-fold symmetry; structure and graphs; energy in kJ/mol

Fusion of two cupolas: C$_{24}$ and C$_{32}$ (Fig. 17).

E=1580   E=2643
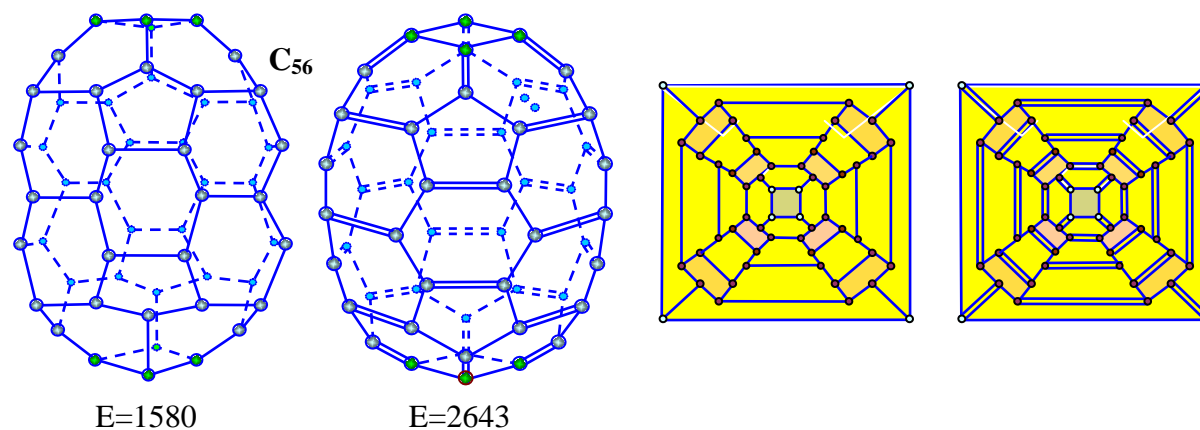
Fig. 17. Mirror symmetry fusion of two cupolas (half-fullerenes) C$_{24}$ and C$_{32}$ having four-fold symmetry; structure and graphs; energy in kJ/mol

Fusion of two cupolas C$_{32}$ (Fig. 18).

E=1544   E=2802
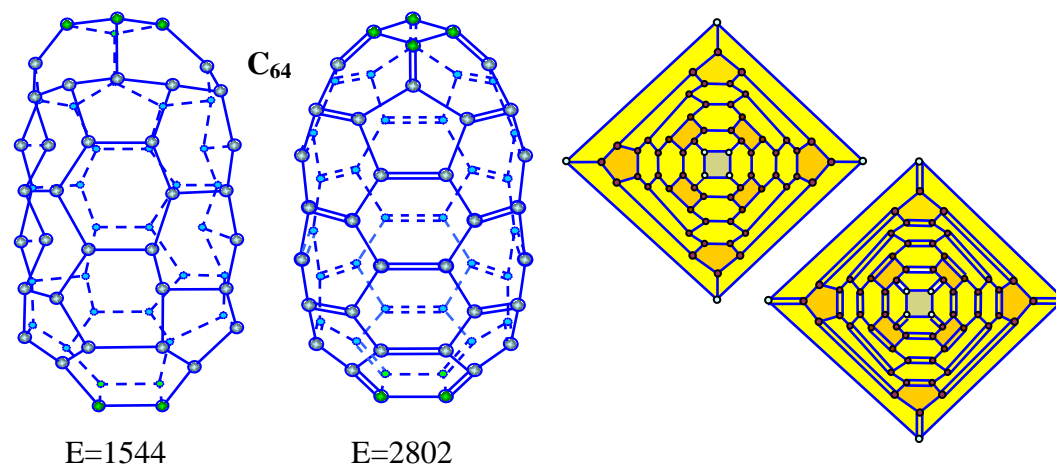
Fig. 18. Rotation-reflection symmetry fusion of two cupolas (half-fullerenes) C$_{32}$ having four-fold symmetry; structure and graphs; energy in kJ/mol

Fusion of two cupolas: C₃₂ and C₄₀ (Fig. 19).

E=1729   E=2958
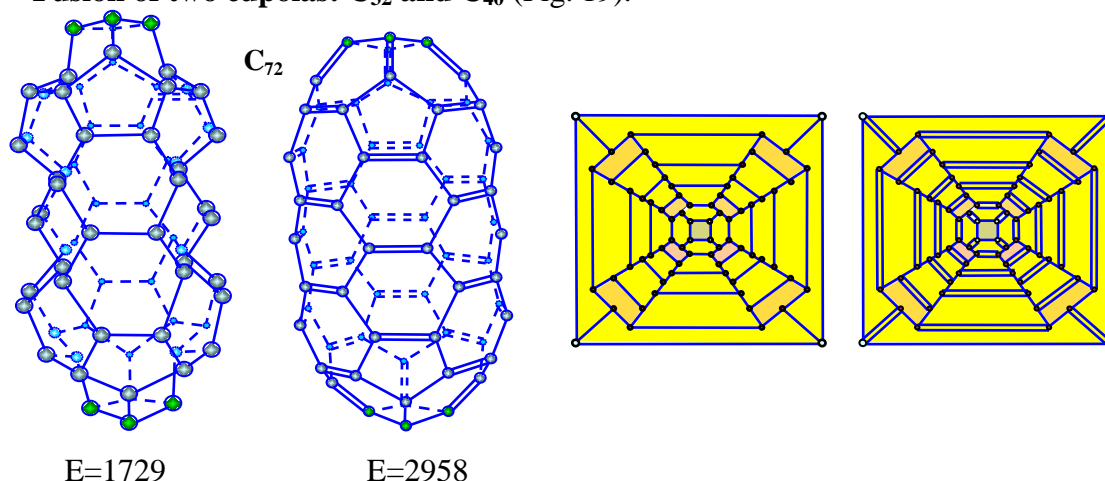
Fig. 19. Mirror symmetry fusion of two cupolas (half-fullerenes) C_{32} and C_{40} having four-fold symmetry; structure and graphs; energy in kJ/mol

Fusion of two cupolas C₄₀ (Fig. 20).

E=1608   E=3113

Fig. 20. Rotation-reflection symmetry fusion of two cupolas (half-fullerenes) C_{40} having four-fold symmetry; structure and graphs; energy in kJ/mol

A fullerene or a nanotube? Let's analyze Figures 15-20. The question arises: What have we obtained, fullerenes or nanotubes? As indicated earlier, one can consider the structure C_{24} shown in Fig. 4 as fullerene and as an embryo of the nanotube. This is a bifurcation structure. During its growth, it can transform either into a fullerene or into a nanotube. The situation is not uncommon in nature. The situation is not uncommon in nature. For example, in radiation solid-state physics it is well known that one and the same small vacancy cluster (embryo) during its growth can transform either into a void (volume configuration) or into a dislocation loop (plane configuration) [18,19]. In our case, this brings up the question: Where the boundary between fullerenes and nanotubes is?

In Ref [4] we have considered forming fullerenes and nanotubes in the context of one and the same graph approach. In this study, we have obtained the fullerenes which geometrically resemble more the nanotubes (Figs. 18-20). The question arises where the boundary between fullerenes and nanotubes is. An intuitive idea says: a fullerene is a spheroid; a nanotube with open ends is a cylinder; a nanotube with closed ends is a cylinder with two hemispheres. However, we need an exact quantitative criterion. Under these circumstances, we should look at the electron theory for clues.

Electronic aspects of fullerene structure are briefly considered in Ref [3]. In C_{60}–I_h there are two different types of bonds according to the atomic field microscopy (AFM) image. The measured bond lengths are r_{hh} = 1.38 Å and r_{hp} = 1.4654 Å. This fullerene is considered as an ideal one, having only equal isolated pentagons and forming a perfect sphere. The larger bonds are singular, the lesser bonds are double ones. Therefore in an ideal fullerene, each hexagon has three single and three double bonds. In contrast to this, in an ideal nanotube with open ends, there are only hexagons with four single and two double bonds. Each spheroid can be divided into three parts; two hemispheres with hexagons having three single and three double bonds and one cylinder with four single and two double bonds. If the height of the cylinder is less than the height of two hemispheres, we assume that it is a fullerene. On the contrary, we have a nanotube.

In its turn, the cylinder height is defined by the number of adjacent hexagons with four single and two double bonds. To form a cylinder one needs to have along with its height at least two such hexagons. Referring to the graphs shown, we admit that the nanotubes begin with the structure C_{72}.

5. Alive and dead fullerenes

From the results obtained, of special note are the graphs, it follows that there are two ways of joining the cupolas: mirror symmetry fusion and rotation-reflection one. However, it is necessary to take into account also the nearest circumference of a hexagon. In the first case, we notice in the fullerene structure the mutually penetrating configurations consisting of a hexagon with two or four *symmetry* adjacent pentagons, C_{24}, $C_{40,}$ and C_{56}. (For fullerene C_{32} there are two *symmetry* adjacent *tetragons*). In the second case, the mutually penetrating configurations contain a hexagon with three *symmetry* adjacent pentagons, C_{48}, or only one adjacent pentagon, C_{64} and C_{64}. The fullerenes of the first subgroup can grow further by the use of the Endo-Kroto's mechanism producing new fullerenes; they are alive. The fullerenes of the second subgroup are the dead-end ones (Fig. 21). It should be emphasized that all these fullerenes are basic perfect ones. It is worth noting that they have one and the same number of pentagons, namely eight, being equal to a double degree of symmetry.
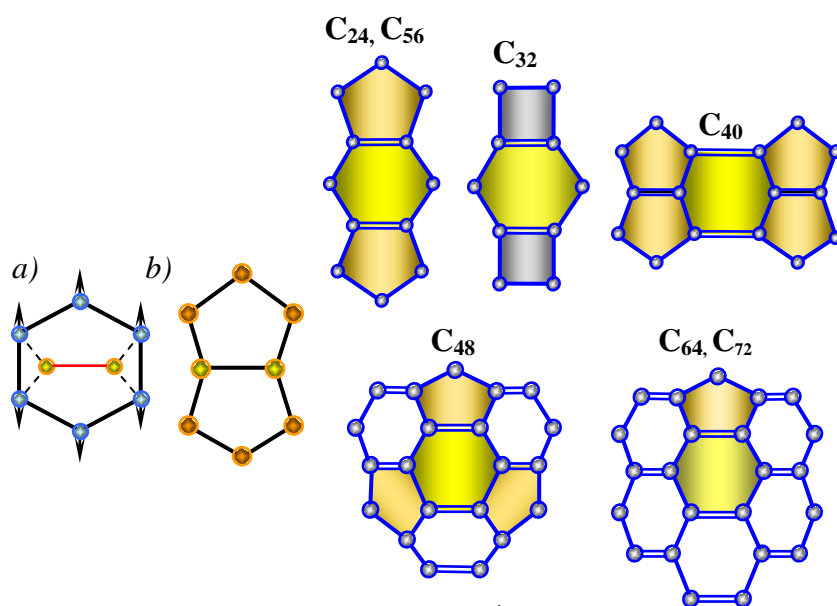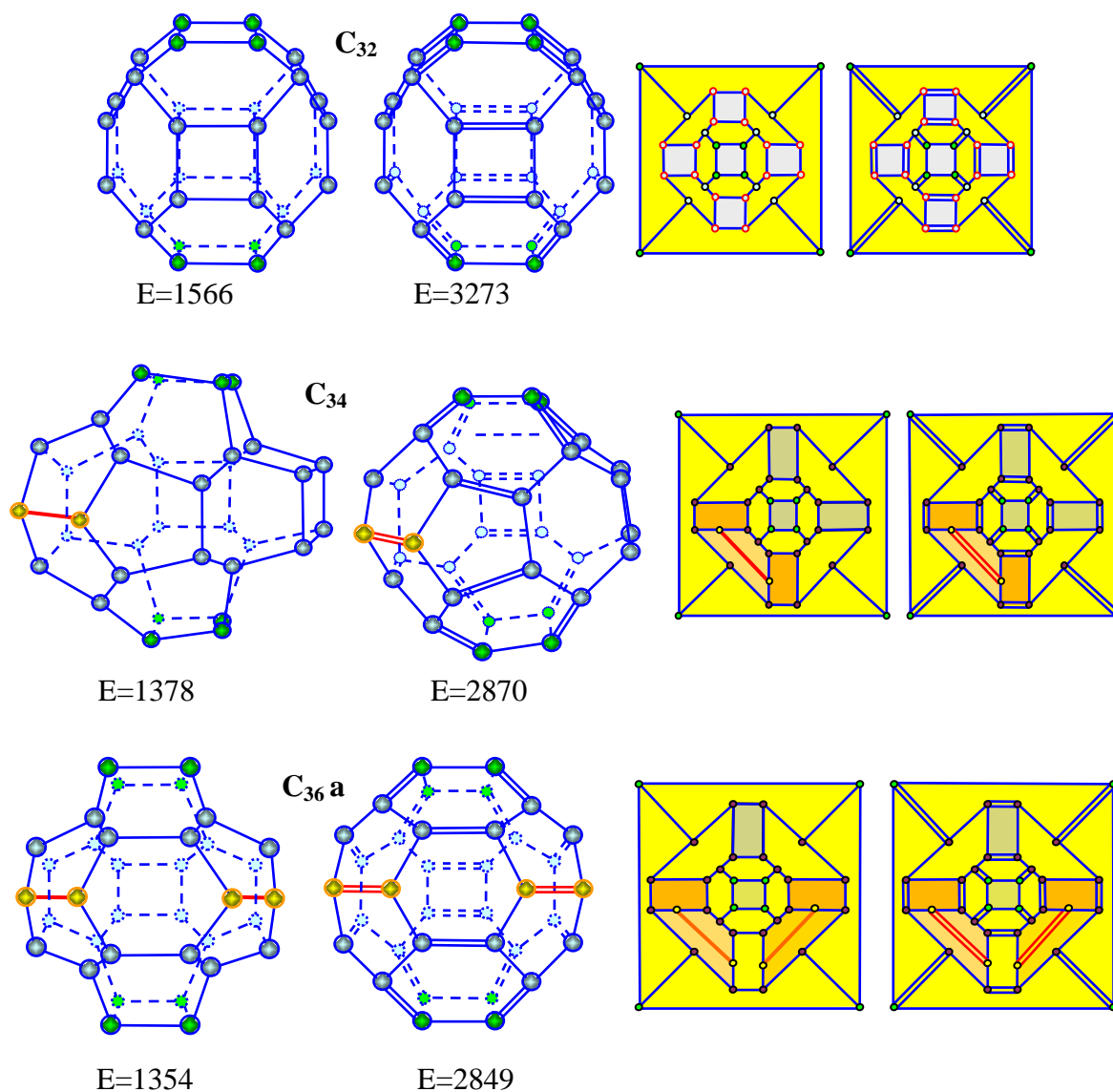

Fig. 21. Endo-Kroto's mechanism of fullerene growth (*a, b*); hexagon nearest circumference in different fullerenes

6. Growth of fullerene C$_{32}$

Contrary to the dead-end fullerene C$_{32}$ shown in Fig. 14 which can't increase in size any further through the use of the Endo-Kroto's classical mechanism of growing, the tetra$_6$-hexa$_{12}$ fullerene C$_{32}$ (Fig. 13) is able to be a base for further growth. The fullerenes designed by this mechanism are illustrated in Fig. 22. From the figures, it follows that only the initial and final fullerenes C$_{32}$ and C$_{40}$ have ordinary four-fold symmetry. They are perfect fullerenes. The intermediate fullerenes C$_{34}$, C$_{36,}$ and C$_{38}$ have topological four-fold symmetry. To gain a better understanding of the mechanism of dimer embedding, its main features are given in the form of schematic representation in Fig. 23.

C$_{32}$

E=1566   E=3273

C$_{34}$

E=1378   E=2870

C$_{36}$ a

E=1354   E=2849

C$_{36}$ s

E=1096   E=2496

C$_{38}$

E=1253   E=2452

C$_{40}$

E=1439   E=2426
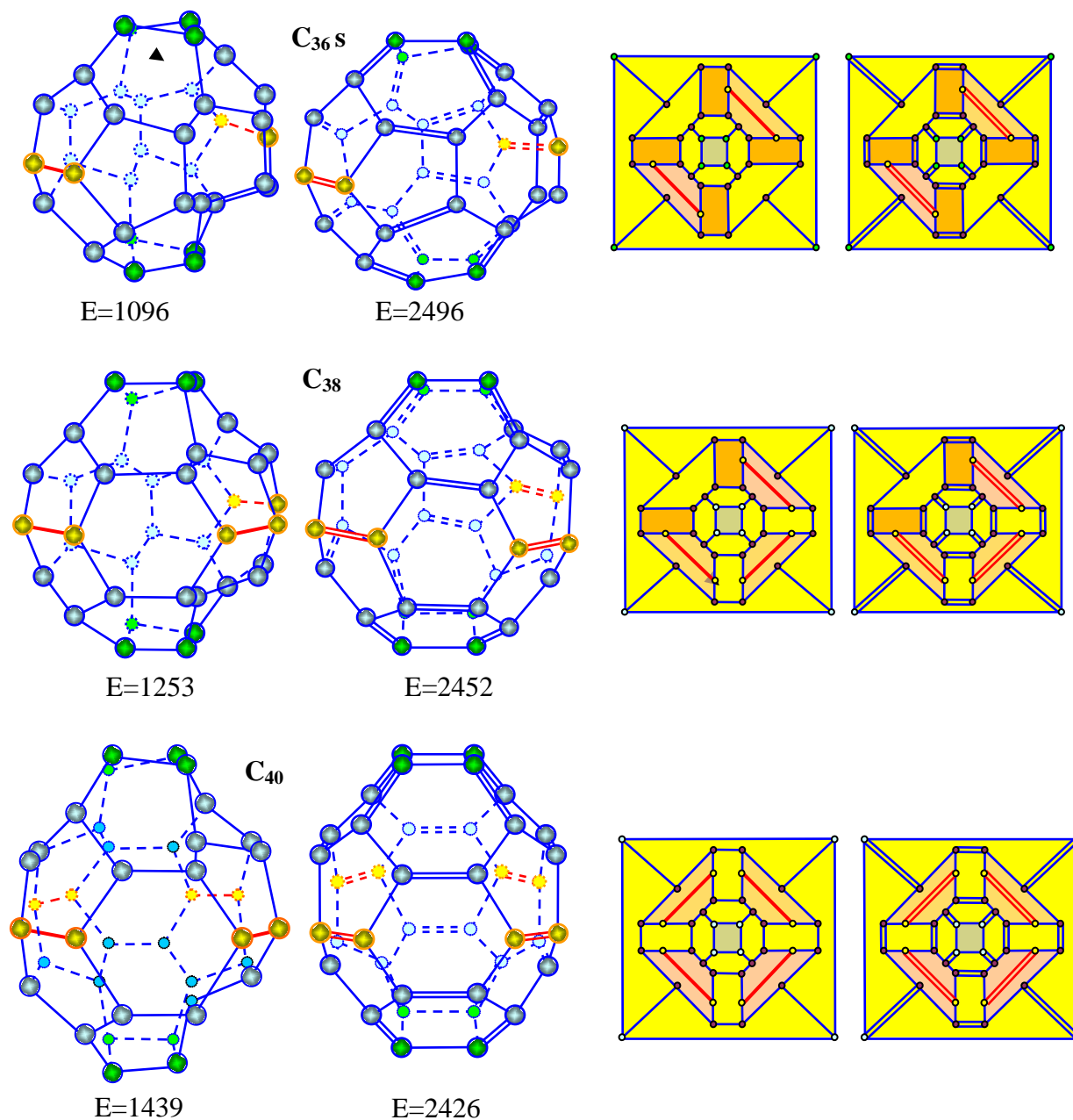
Fig. 22. Fullerenes C$_{34}$, C$_{36}$, C$_{38,}$ and C$_{40}$ as a result of embedding one after another carbon dimer into fullerene C$_{30}$: structure and graphs; energy in kJ/mol
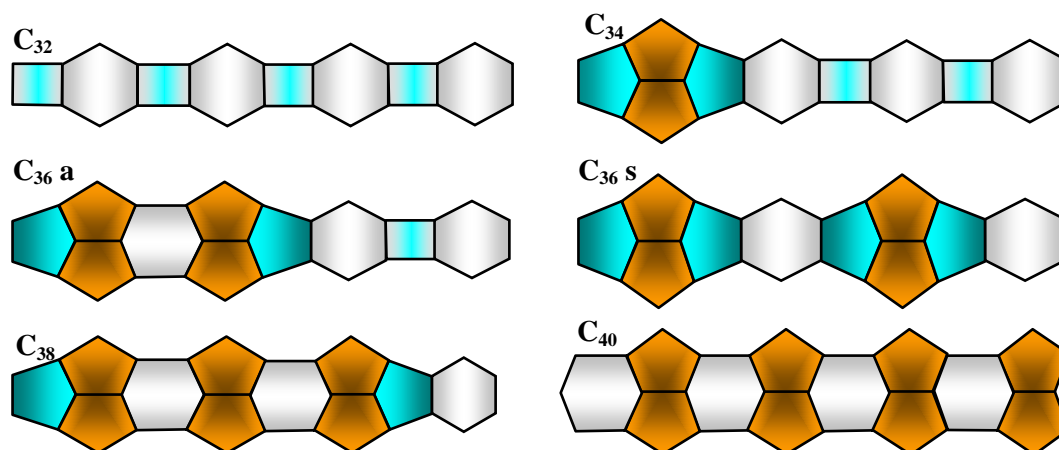
Fig. 23. Scheme of the main structural changes during the growth from C_{32} to C_{40}

From the configurations shown it follows that the first embedding, which transforms fullerene C_{32} into fullerene C_{34}, influences deeply only on one of the hexagons and two of its square neighbours. This hexagon transforms into two adjacent pentagons and its square neighbors become pentagons; the fullerene C_{34} losing four-fold symmetry. It becomes an imperfect fullerene with the ordinary D_{1h} symmetry, however conserving topological four-fold symmetry. At that in the fullerene, there appears a cell that contains four pentagons. The second embedding transforms fullerene C_{34} into fullerene C_{36}. There are two possible ways of embedding, asymmetric and symmetric. In the first case, the nearest to the cell hexagon transforms into two adjacent pentagons, its square neighbor into a pentagon and its pentagon neighbor into a hexagon. In the second case, two cells of four pentagons are separated from each other and one obtains the semi-perfect fullerene C_{36} having two-fold symmetry. It belongs to the ordinary D_{2h} symmetry and its energy is less than that of the asymmetric isomer.

The third embedding leads to the transition from fullerene C_{36} to fullerene C_{38}. It transforms one more hexagon and two of its neighbors into two adjacent pentagons with abut hexagons of another local orientation. Again the fullerene becomes less symmetric, it belongs to D_{1h} symmetry. At last, the fourth embedding restores D_{4h} symmetry. The perfect fullerene C_{40} obtained could be named a tetra$_2$-penta$_8$-hexa$_{12}$ polyhedron where every two adjacent pentagons have the form of a bow tie.

7. Growth of fullerene C_{40}

Classical fullerenes. The growth can continue producing imperfect fullerenes C_{42}, C_{44}, C_{46}, and perfect fullerene C_{48} (Fig. 24). The fullerenes are obtained as a result of embedding one after another carbon dimer into fullerene C_{40} at an angle to the four-fold axis. From the figures, of special note, are the graphs, we notice again that only the initial and final fullerenes C_{40} and C_{48} have ordinary four-fold symmetry. They are perfect fullerenes. The intermediate fullerenes C_{42}, C_{44} and C_{46}, as was analyzed in Ref [1], have topological four-fold symmetry. To gain a better understanding of the mechanism of dimer embedding into fullerene C_{40}, its main features are given in the form of schematic representation (Fig. 25).
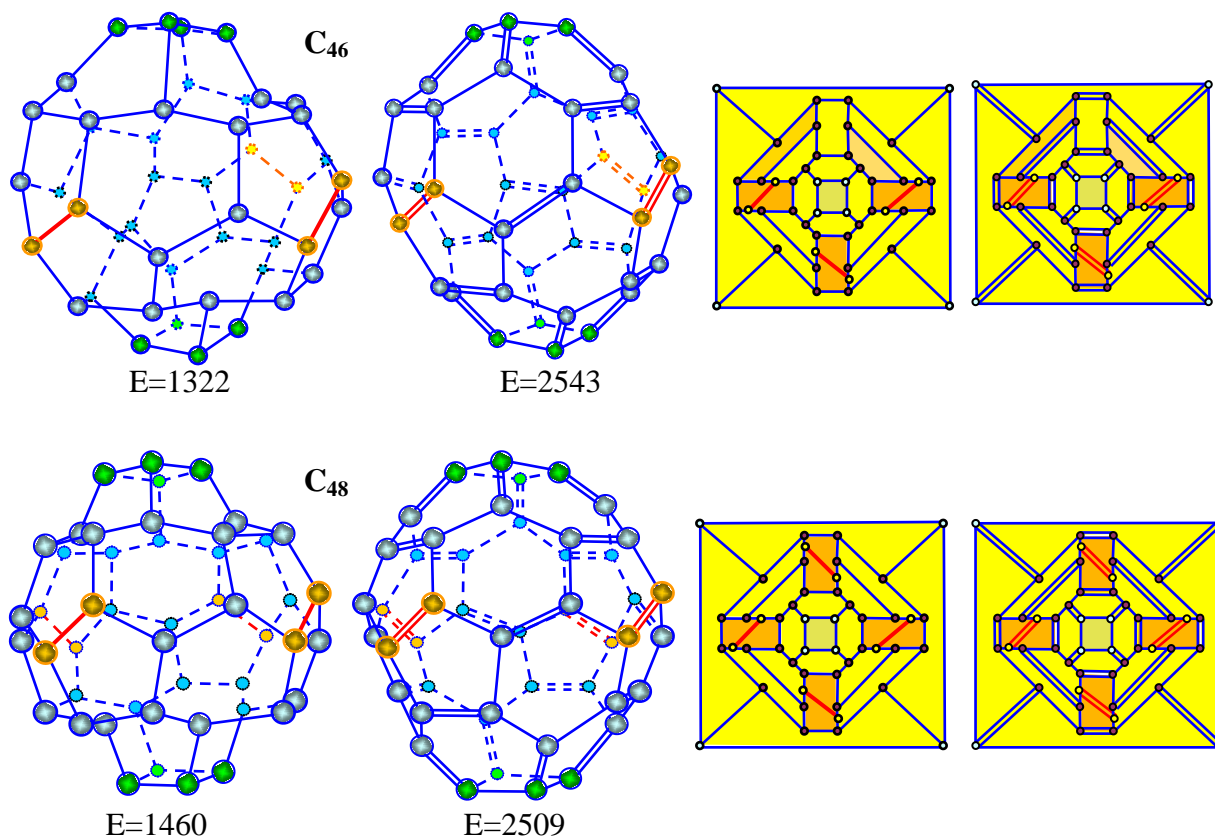
C₄₀

E=1439   E=2426

C₄₂

E=1323   E=2519

C₄₄ a

E=1323   E=2533

C₄₄ s

E=1343   E=2586
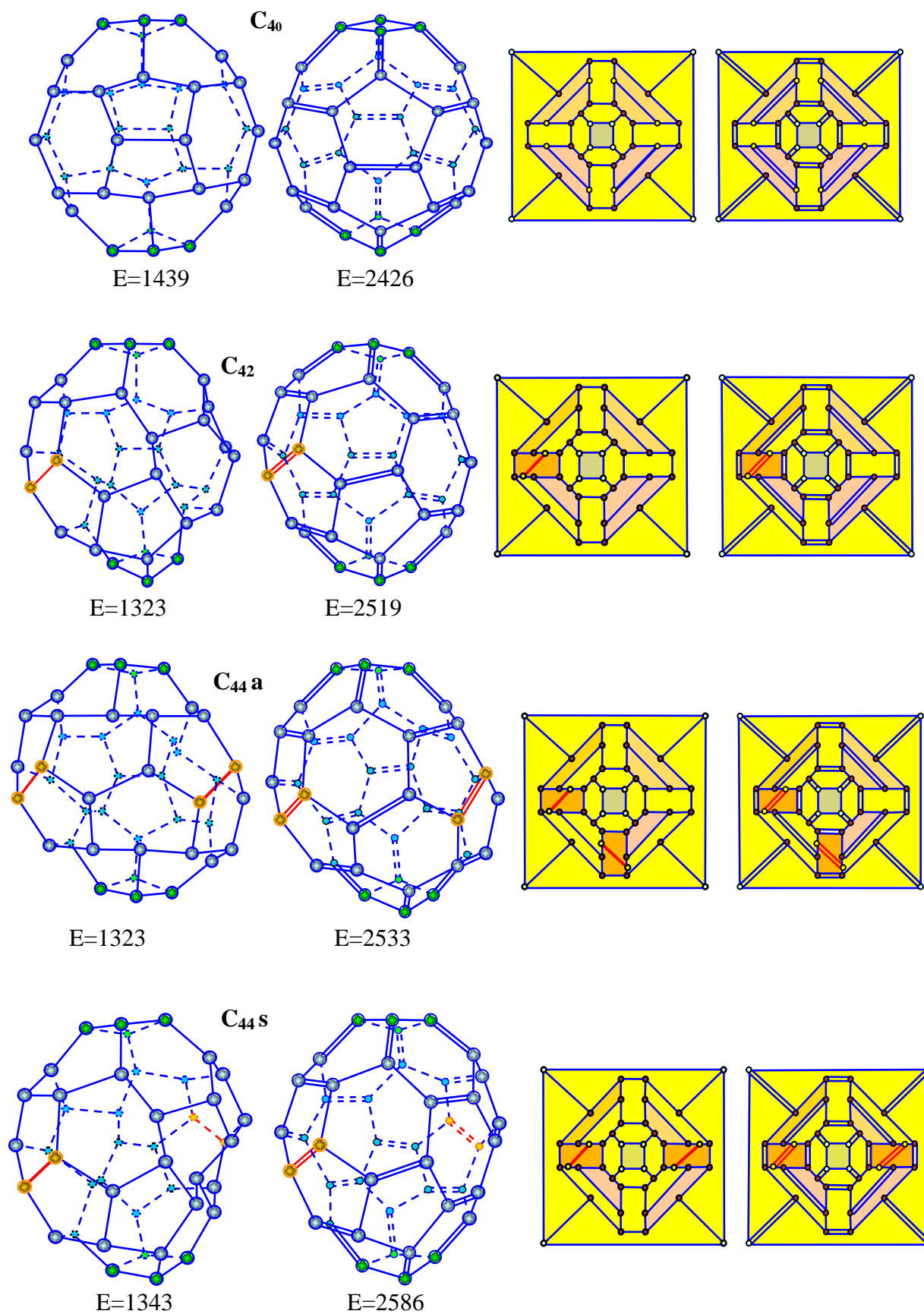
Fig. 24. Fullerenes C_{42}, C_{44}, $C_{46,}$ and C_{48} as a result of embedding carbon dimers into fullerene C_{40} at an angle to the four-fold axis: structure and graphs; energy in kJ/mol
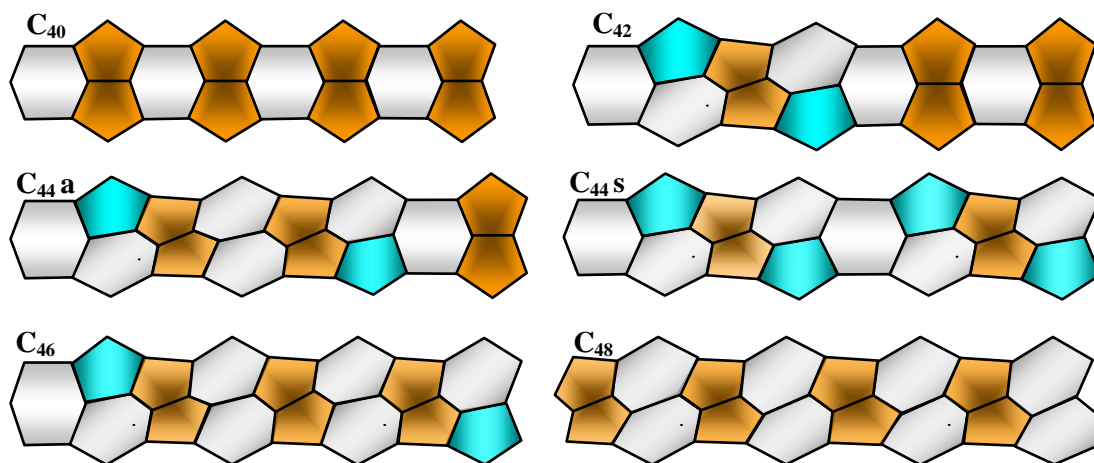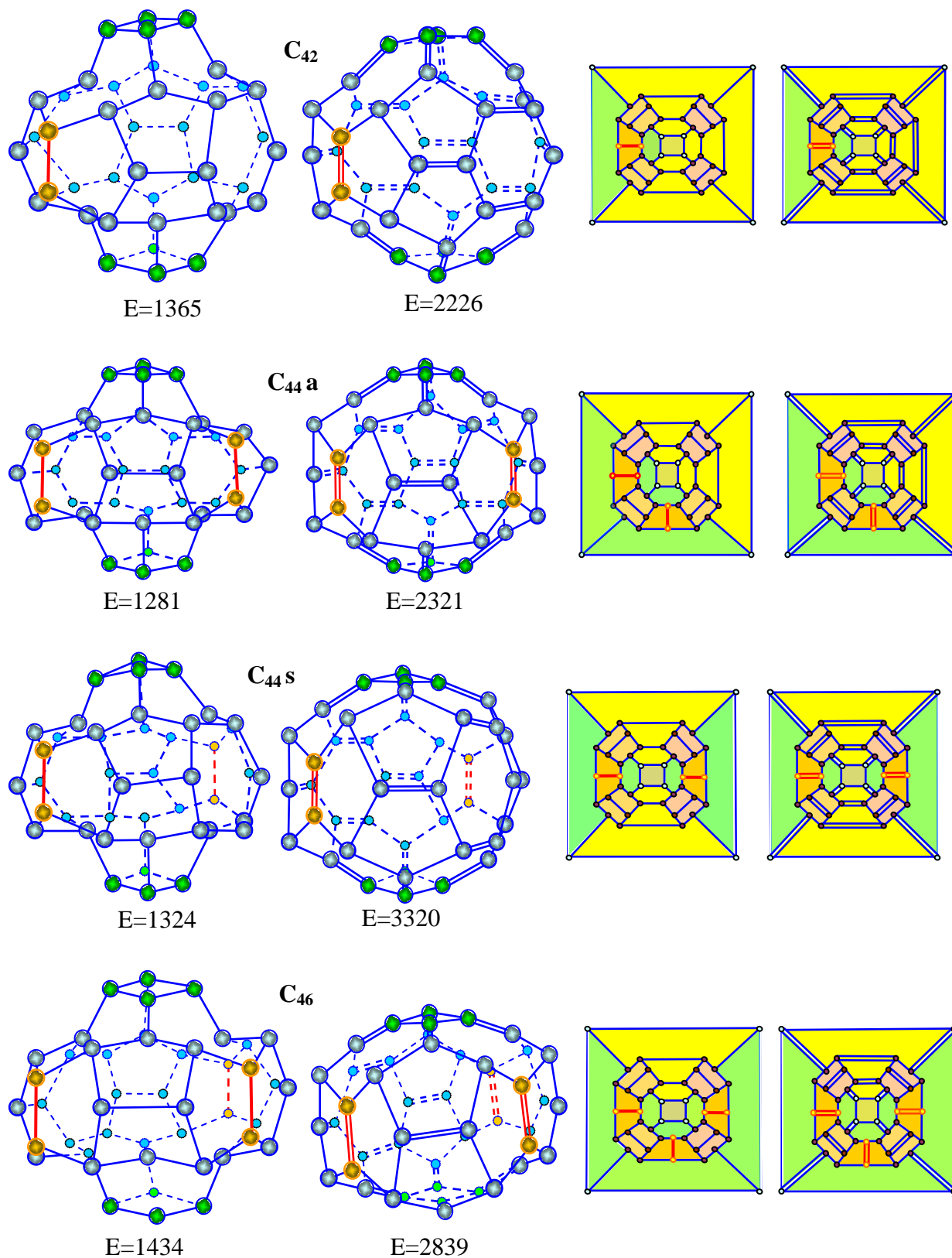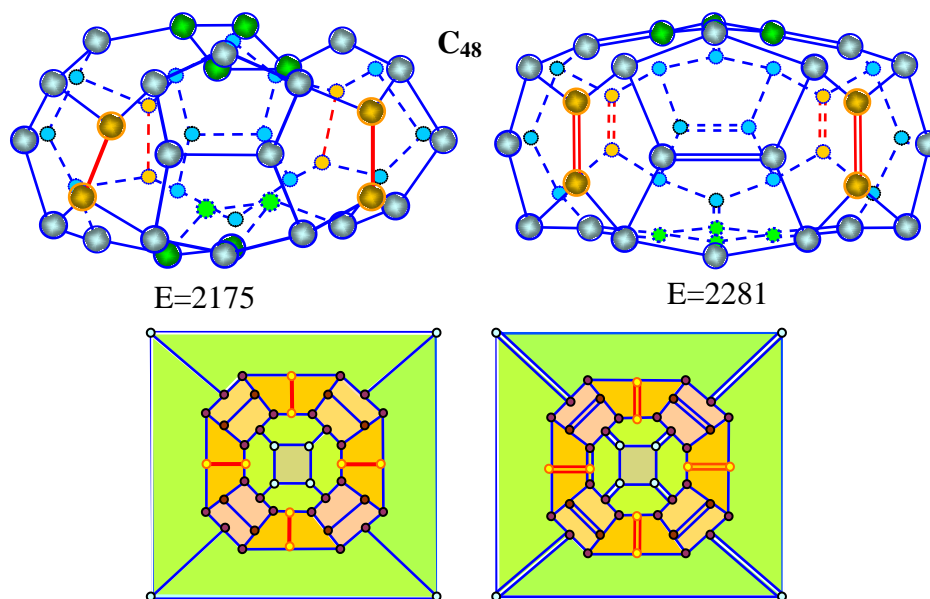

Fig. 25. Scheme of the main structural changes during the growth of fullerene C_{40}

Non-classical fullerenes. The growth of fullerene C_{40} can continue by another way producing also imperfect fullerenes C_{42}, C_{44}, $C_{46,}$ and perfect fullerene C_{48} (Fig. 26). The fullerenes are obtained as a result of embedding one-after-another carbon dimer into fullerene C_{40} parallel to the four-fold axis. From the figures, of special note, are the graphs, we notice again that only the initial and final fullerenes C_{40} and C_{48} have ordinary four-fold symmetry. They are perfect fullerenes. The intermediate fullerenes C_{42}, C_{44} and C_{46}, as was analyzed in Ref [1], have topological four-fold symmetry.

C$_{42}$

E=1365   E=2226

C$_{44}$ a

E=1281   E=2321

C$_{44}$ s

E=1324   E=3320

C$_{46}$

E=1434   E=2839

C₄₈

E=2175   E=2281

Fig. 26. Fullerenes C_{42}, C_{44}, $C_{46,}$ and C_{48} as a result of embedding carbon dimers into fullerene C_{40} parallel to the four-fold axis: structure and graphs; energy in kJ/mol

These results deserve further comment. For a detailed discussion of this subject see Ref [3]. According to the authors, "In general, classical fullerenes are cage-like, hollow molecules of pseudospherical symmetry consisting of pentagons and hexagons *only*, resulting in a trivalent (and in the most ideal case) convex polyhedron with exactly three edges (bonds) joining every vertex occupied by carbon, idealized as sp^2 hybridized atoms. What happens if we relax the rules a little bit, and allow for other types of three-valent (sp^2) carbon framework? There are many generalizations that lead to structures of beautiful shapes that have both elegant mathematical theory and physical realizations: allowing for polygons with faces different form pentagons and hexagons. What kinds of fulleroids, which are fullerene-like structure, are allowed? Can we tile a sphere or a torus with heptagons only, or with only pentagons and heptagons?"

Figure 26 gives an example of such structures and answers the questions. From the configurations shown it follows that the first embedding, which transforms fullerene C_{40} into fullerene C_{42}, influences deeply only on one of the hexagons and two of its hexagon neighbors. This hexagon transforms into two adjacent pentagons and its hexagon neighbors become heptagons; the fullerene C_{42} losing ordinary four-fold symmetry. It becomes an imperfect fullerene with the ordinary D_{1h} symmetry, however conserving topological four-fold symmetry. At that in the fullerene, there appears a cell that contains four pentagons. The second embedding transforms fullerene C_{42} into fullerene C_{44}. There are two possible ways of embedding, asymmetric and symmetric. Notice that in the first case we obtain the fullerene which consists of two halves; one contains only pentagons and heptagons and the other only pentagons and hexagons. It should be emphasized that the energy of such a structure with single and double bonds is significantly less. The third embedding leads to the transition from fullerene C_{44} to fullerene C_{46}. It transforms one more hexagon and two of its neighbors into two adjacent pentagons with abut heptagons. Again the fullerene becomes less symmetric. At last, the fourth embedding restores D_{4h} symmetry. The perfect fullerene C_{48} obtained contains two tetragons, eight pairs of adjacent pentagons, eight heptagons, and no hexagons. It is a tetra₂-(penta₂)₈-hepta₄ polyhedron; its shape resembles more a disk than a spheroid.

8. Growth of fullerene C_{48}

Input fullerenes. In principle, any hexagon of fullerene C_{48}, having two neighboring mutually antithetic pentagons, is able to incorporate a dimer C_2 and to form fullerene C_{50}. There are eight such hexagons in the equatorial part of the fullerene. One of the realizations is shown in Fig. 27. All the other realizations are identical from the symmetry standpoint.
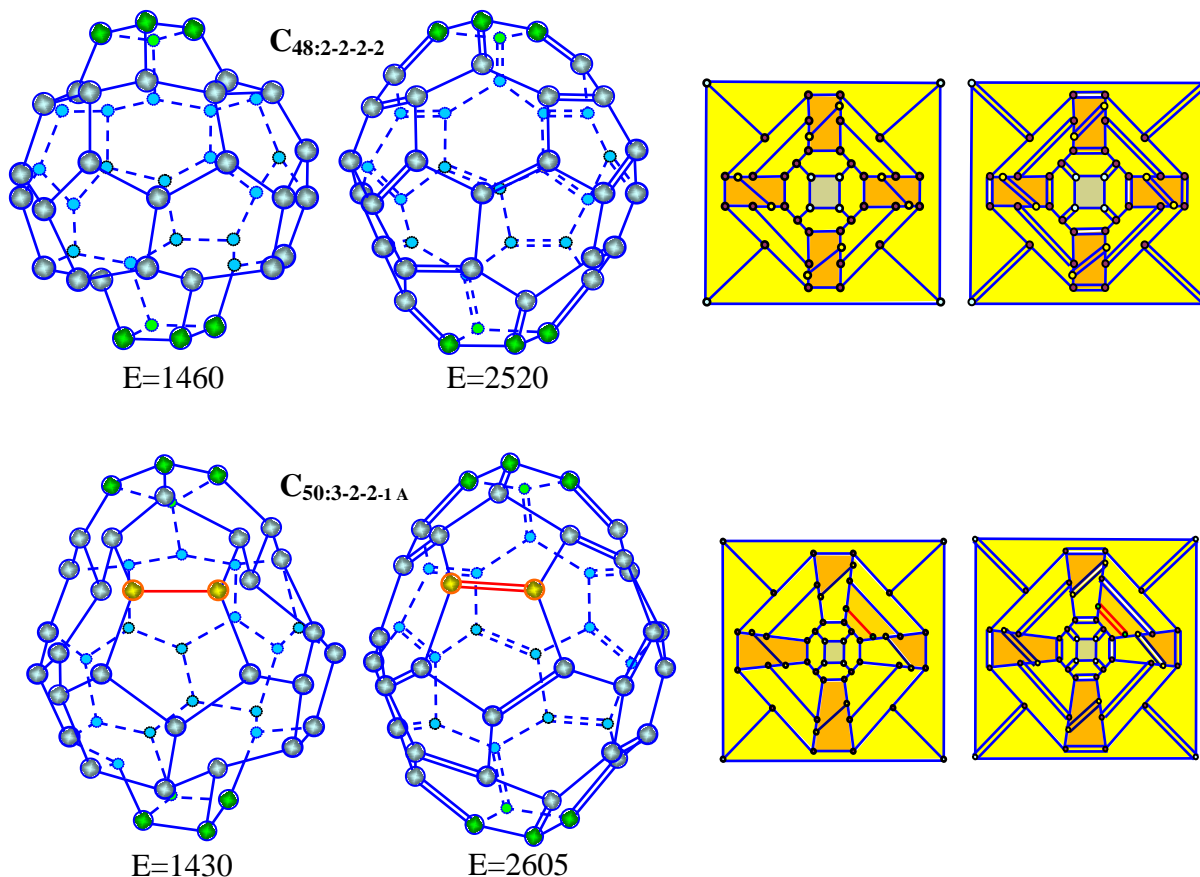

$C_{48:2\text{-}2\text{-}2\text{-}2}$

E=1460   E=2520

$C_{50:3\text{-}2\text{-}2\text{-}1\,A}$

E=1430   E=2605

Fig. 27. Input fullerenes C_{48} and C_{50}; the latter is obtained after embedding a carbon dimer: structure and graphs; energy in kJ/mol

Isomers of fullerene C_{52}. There are several possibilities for incorporating a carbon dimer into fullerene C_{50}. Such a situation leads to production of isomers. To gain a better understanding of these variants of dimer embedding, consider all the possible graphs corresponding to the process (Fig. 27). The graph analysis simplifies not only the understanding of the ways of fullerene forming but guarantees that all the variants are taken into consideration.

$C_{50:3-2-2-1}$ A $C_{52: 4-2-2}$ AA $C_{52: 2-2-1-2-1}$ AB

$C_{52:3-1-3-1}$ AC1 $C_{52:3-3-1-1}$ AC2 $C_{52:3-2-3}$ AD
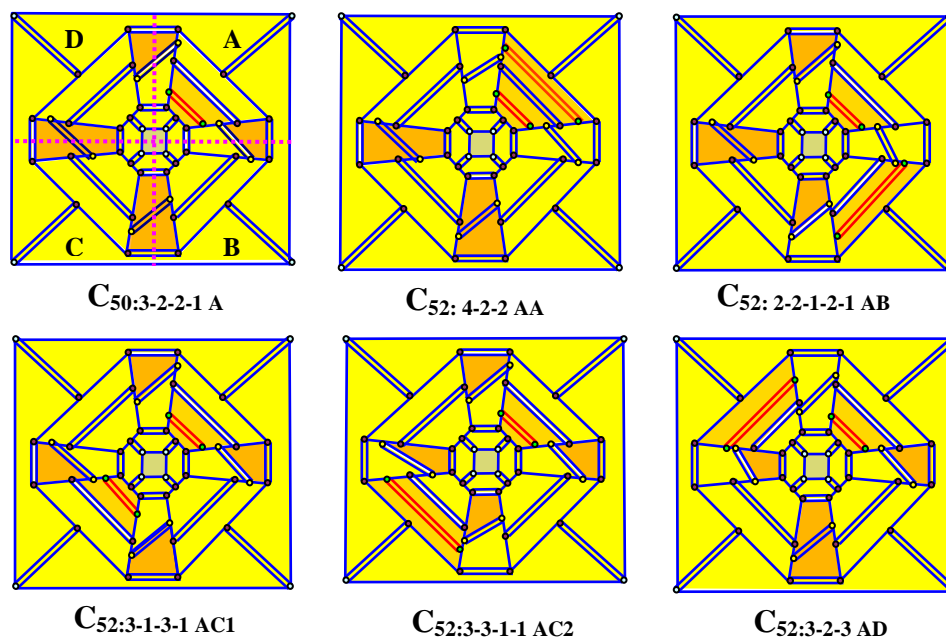
Fig. 27. Graphs of initial fullerene C_{50}: and the isomers of fullerene C_{52}

$C_{52: 4-2-2}$ AA

E = 1703   E = 2928

$C_{52: 2-2-1-2-1}$ AB

E = 1378   E = 2472
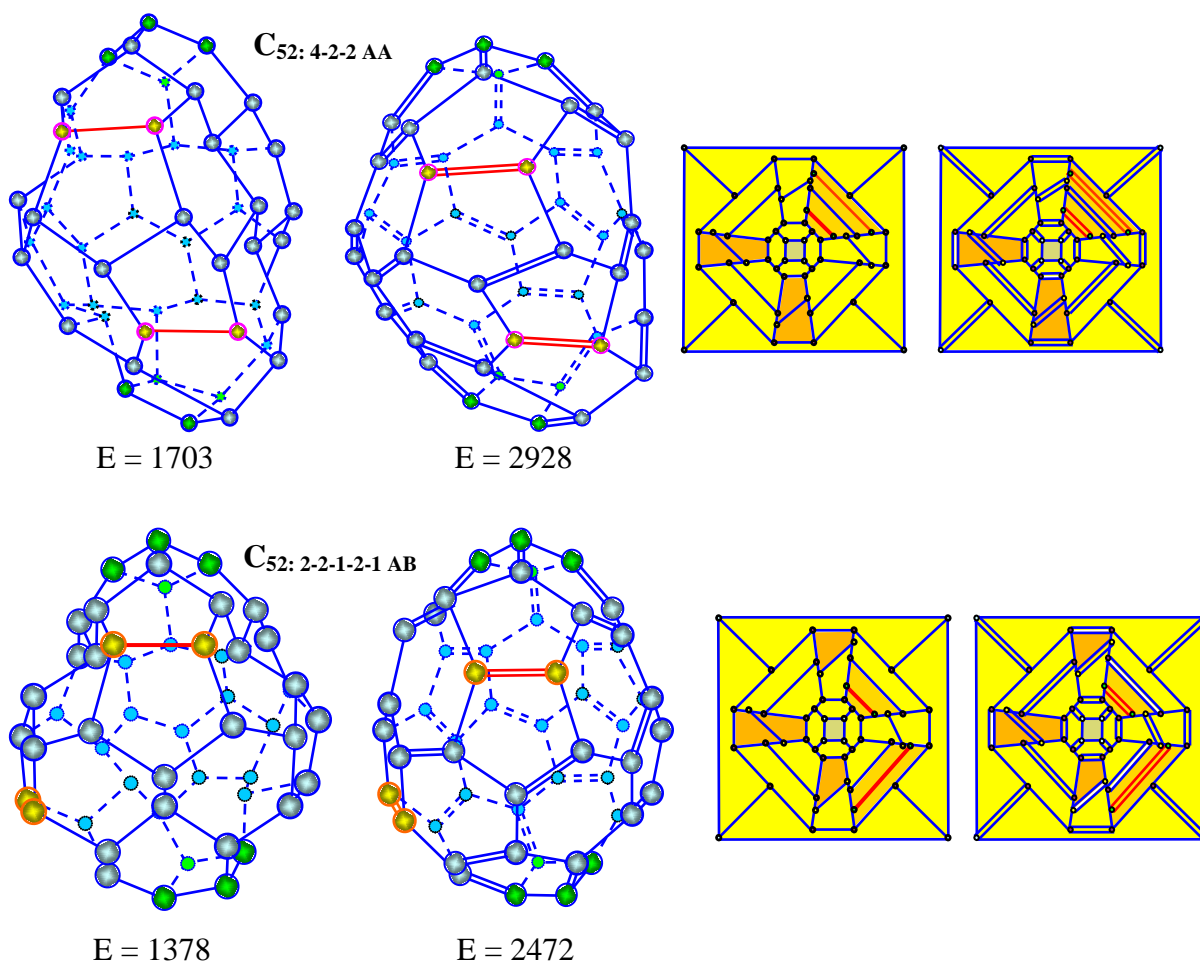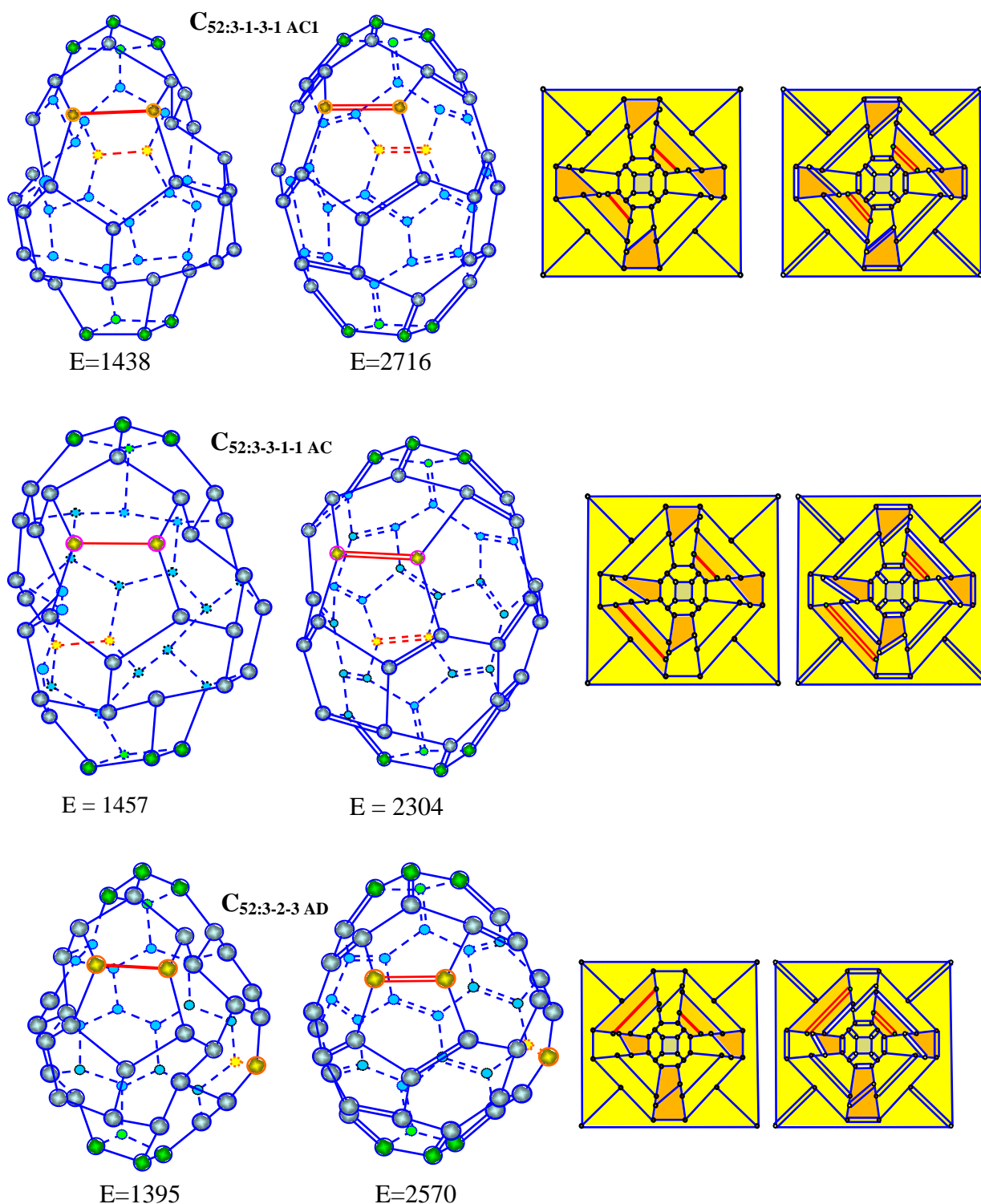
Fig. 28. Isomers of fullerene C_{52}: structure and graphs; energy in kJ/mol

These results deserve further comment. From the figure, it follows that there are *only five natural* isomers of fullerene C_{50}. It is necessary to stress that we are dealing with the isomers which can be obtained during the *natural growth* in the framework of the Endo-Kroto C_2 insertion mechanism [17]. Why have we used the term *natural isomers*? The reason is that we would be separated from the investigators producing a countless number of *mathematically possible isomers* [20].

According to their views [20], "a perennial problem in the chemistry and physics of fullerenes is the question how these organized cage structures emerge from chaotic low-nuclearity carbon vapor. Various mechanisms for carbon ingestion/extrusion and summarization/annealing have been proposed and assessed by comparison with experimental data and quantum mechanical calculations. *A parallel line* of investigation involves the use of graph theoretical techniques to catalogue the mathematically possible fullerene structures and their interconversions based on assumed sets of rules for construction and transformations. The present study extends this approach, exploring the ways that fullerenes can be formally generated from 'seed' polyhedra, using either a predefined set of graph transformations or a set that is restricted by a cost function intended to mimic the energetics of bond rearrangement and carbon insertion."

In Ref [20] the two mechanisms for interconversion of fullerene polyhedra are considered: the Stone-Wales summarization patch and the Endo-Kroto C_2 insertion patch. By the latter is meant in fact two different configurations: a hexagon with its two neighboring mutually antithetic pentagons (before growth) and a pair of adjacent pentagons with its two neighboring mutually antithetic hexagons (after growth). The following is noteworthy: applying any mathematical model to a physical problem, it is important to keep in mind that except for the mathematical rules there are *physical restrictions* [4].

Why have we cited the authors [20] at great length? The reason is that the physical restrictions were not even discussed by them. As a consequence, one deals here with two forms of *scientific despotism* which can depress the creative work of a scientist [21 p. 83]. One of them is *mathematical despotism*. Mathematics has penetrated into the multitude of sciences. If a scientist has no good mathematical qualification, such mathematical papers suggest his inferiority complex. It takes much time before he begins to understand that the majority of such papers are not worthy of reading. The second form is *programming despotism.* This type was generated after the appearance of neo-programmers, the scientists who are not programmers, but being able to write programs. Such scientist substitutes thought process by doing programs, not putting the question whether the methods are so good what they need to be programmed.

As a result, the authors [20] came to the conclusion that the number of isomers increases with an increasing number of atoms, and "a family of transformations based on the Endo-Kroto C_2 insertion mechanism gives access to *all* isomers of *all* fullerenes up to C_{200} from a C_{24} seed". In reality, it is not the case. For example, the appearance of the first EK patch in fullerene C_{50} excludes from eight possible sites not only this patch but also two neighboring sites (Look carefully at Fig. 26). Therefore for the second insertion, there left only five possibilities but not seven. So instead of increasing isomers during the growth we have decreasing. The next sections make it clearer.

Isomers of fullerene C_{54}. Five isomers of fullerene C_{52} can be classified into two subgroups of intermediate fullerenes. The isomer of the first subgroup $C_{52:3-3-1-1\ AC}$ is a dead-end fullerene since its hexagons have no diametrically opposite pentagons. The other isomers can grow further by using the Endo-Kroto's mechanism and producing new fullerenes; they are alive. It is interesting to note that fullerenes $C_{52:3-1-3-1\ AC1}$ and $C_{52:3-2-3\ AD}$ produce one and the same direct descendant $C_{54:\ 3-1-2-2\ AC1D}$. At first glance, it seems that there are *three natural* isomers of fullerene C_{54}. They are shown in Fig. 29. However, on close examination of these graphs, it becomes evident that graphs $C_{54:\ 2-2-3-1\ ABC1}$ and $C_{54:\ 3-1-2-2\ AC1D}$ reflect also one and the same structure. It follows algebraically from the fact that their symbolic designations: 2-2-3-1 and 3-1-2-2 form a circular permutation, as well as geometrically: one needs to rotate any of them through 180 deg and to obtain its antipode. So fullerenes $C_{52:\ 2-2-1-2-1\ AB}$ and $C_{52:3-2-3\ AD}$ produce one and the same descendant and we have only *two natural* isomers of fullerene C_{54}.
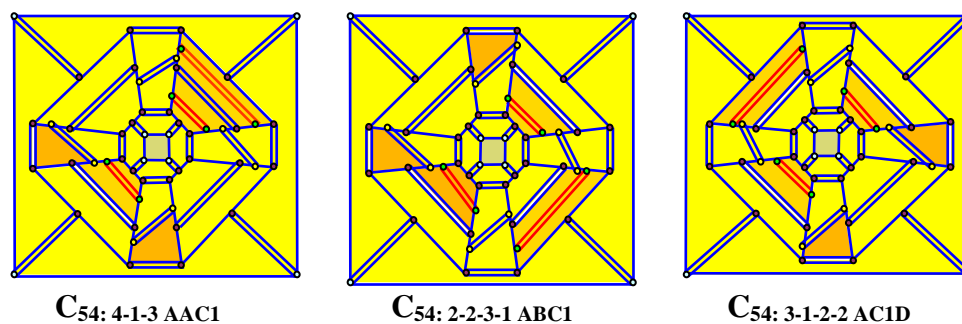
C$_{54:}$ 4-1-3 AAC1   **C$_{54:}$ 2-2-3-1 ABC1**   **C$_{54:}$ 3-1-2-2 AC1D**

Fig. 29. Graphs of the isomers of fullerene C$_{54}$

C$_{54:}$ 4-1-3 AAC1

E = 1380   E = 2579

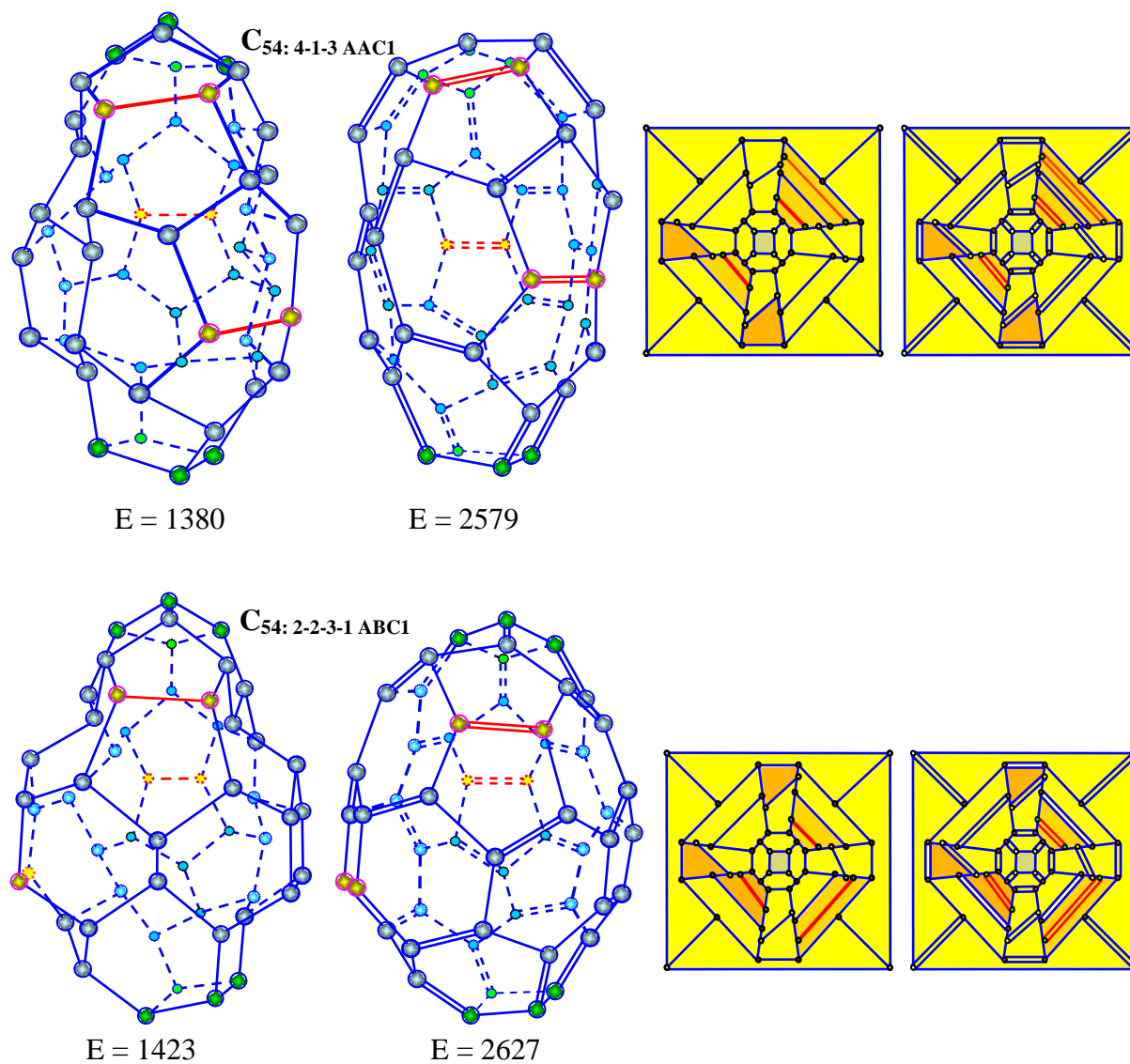**C$_{54:}$ 2-2-3-1 ABC1**

E = 1423   E = 2627

Fig. 30. Isomers of fullerene C$_{54}$: structure and graphs; energy in kJ/mol

Isomers of fullerene C$_{56}$. Each of the two isomers of fullerene C$_{54}$ produces only one descendant. They are shown in Fig. 31. The scheme of all isomer generations is presented in Fig. 32.

C₅₆: 2-2-2-2 ABC1D

E = 1563   E = 2674

C₅₆: 4-4 AACC

E = 1453   E = 3170
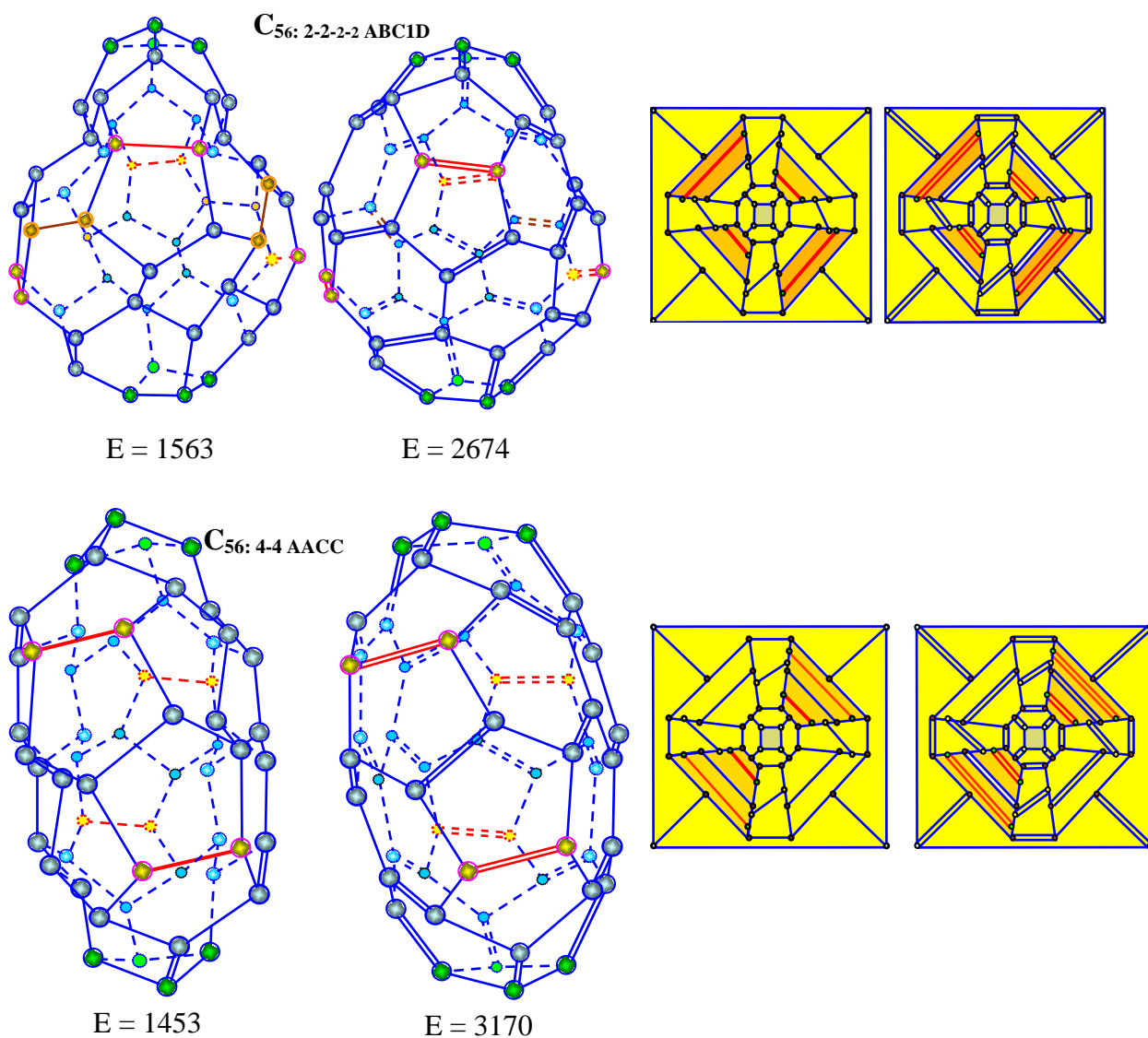
Fig. 31. Isomers of fullerene C₅₆: structure and graphs; energy in kJ/mol
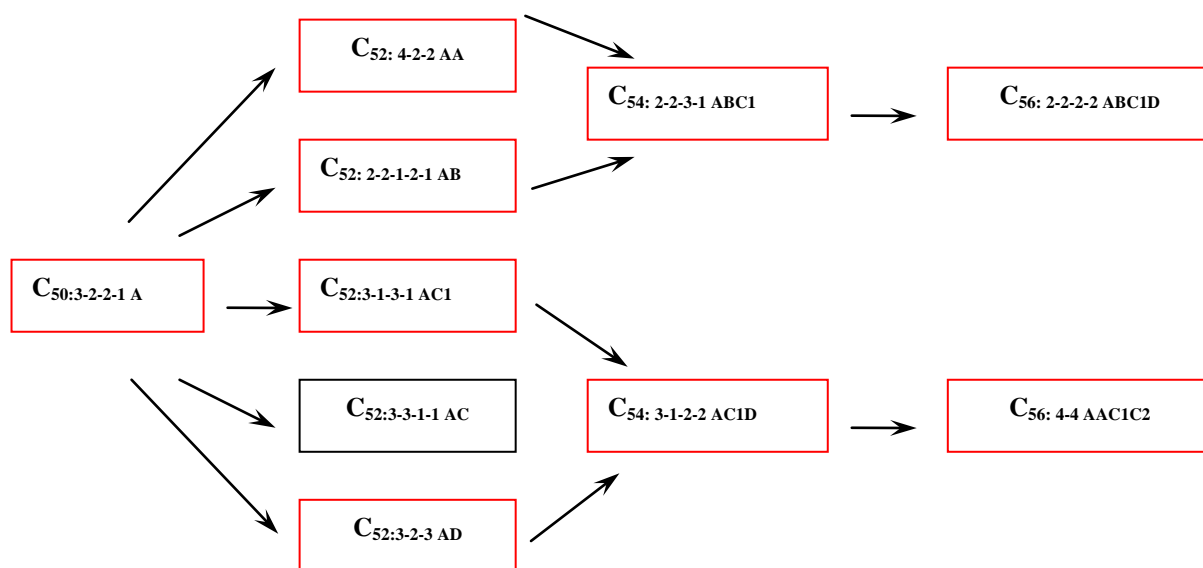
Fig. 32. Generation of isomers of fullerene C₅₀ and their descendants

We have to turn back to the *physical restrictions* to clear up the fullerene-isomer problem. The transition from individual atoms to the patches contains implicitly *two-scale averaging*. The *first averaging* is the transition from electrons and nuclei to atoms. After such averaging one forgets the constituents of the atom (electrons and nucleus) and operates with the atoms investigating their interactions. The *second averaging* is the transition from the atoms to polygons and even to the patches. After that one forgets the atoms and operates with these atomic agglomerates in studies of fullerenes. The averaging puts physical restrictions both on the interaction and the agglomeration. Moreover any averaging includes assumptions, but the more assumptions, the more mistakes.

Experimentally [3], "In C_{60}–I_h there are two different types of bonds according to atomic field microscopy (AFM) image. The measured bond lengths are $r_{hh} = 1.38$ Å and $r_{hp} = 1.4654$ Å. The larger bonds are singular, the lesser bonds are double ones". Therefore in the ground state, each carbon atom takes part in the formation of one double bond and two single ones. It also means that although all carbon atoms are equal, the bonds are nonequivalent [22,23], and that fact puts restrictions on their agglomeration.

Mathematicians design their theories on the *basis of definitions*. In doing so they replace the assumptions with definitions; the latter taking a role of *axioms*. Consider two typical examples. Ref [20]: "The classical definition of a fullerene as a carbon cage whose skeleton is a trivalent polyhedron with hexagonal and pentagonal faces will be used". Ref [3]: "Classical fullerenes are cage-like, hollow molecules of pseudospherical symmetry consisting of pentagons and hexagons only, resulting in a trivalent (and in the most ideal case) convex polyhedron with exactly three edges (bonds) joining every vertex occupied by carbon, idealized as sp^2 hybridized atoms".
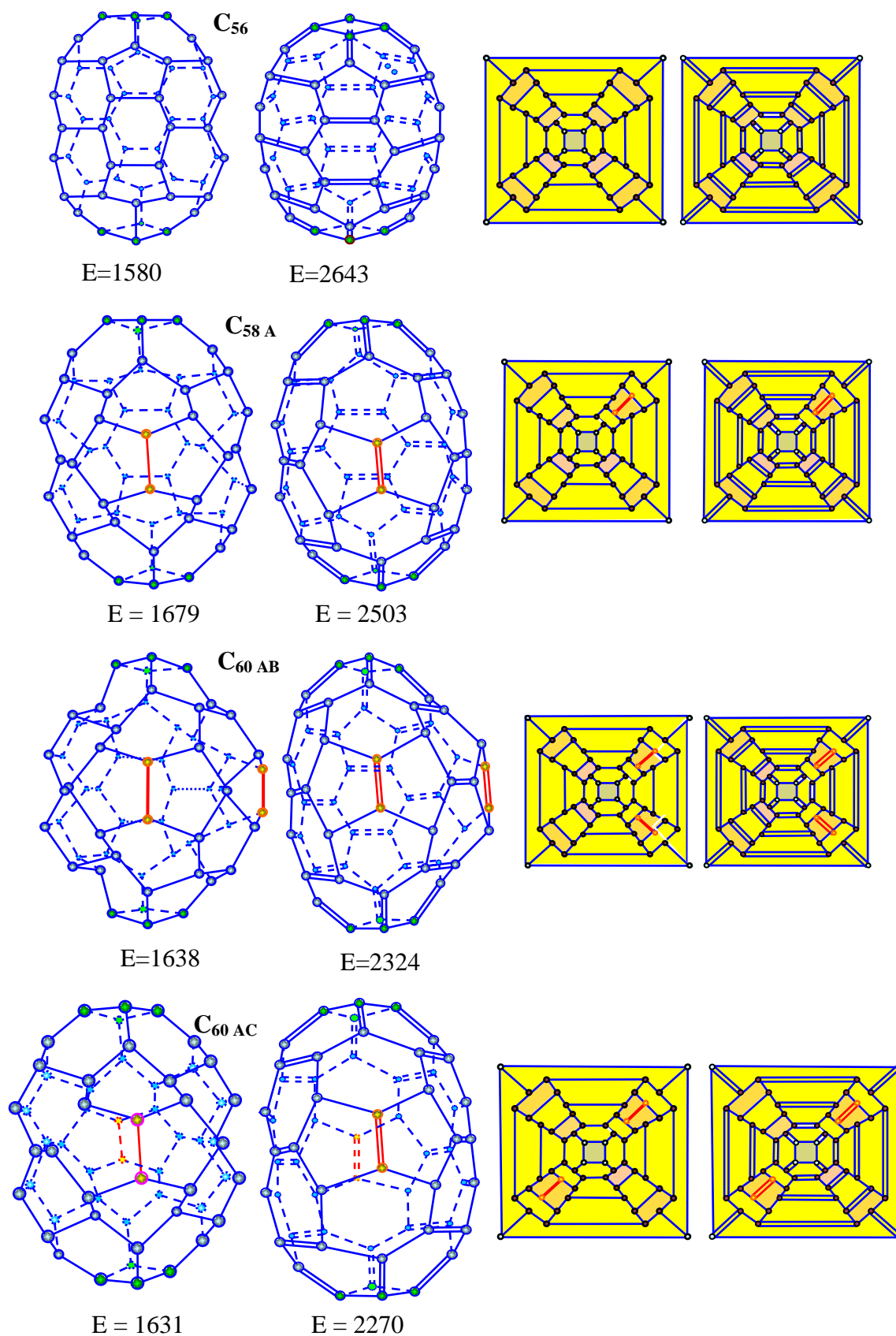
We agree with the authors [3] that "a number of chemical properties of a fullerene can be derived from its graph structure". But we don't understand the word-combination "mathematical properties of fullerenes". Nobody says about the mathematical properties of metals or semiconductors. To our mind, there is a logic bifurcation after which there appear two different branches of fullerene study: the natural fullerenes as carbon molecules and the mathematical fullerenes as polyhedrons. If one writes "many mathematical properties of fullerenes have found simple and beautiful solutions", one must emphasize that this affirmation refers only to the mathematical fullerenes. On contrary, one misjudges the problem propagating mathematical despotism.

The papers cited are written by the groups of three [3] and four [20] authors; among them are physicists, chemists, and mathematicians. These papers were chosen as a typical example of the new style of investigations when physicists and chemists get sidetracked leaving the key role to mathematicians. However, one must bear in mind [21]: "At a distance well removed from an empirical source, mathematics is threatened with degeneracy. Super-mathematization of an empirical field where there are no constant hypotheses is a disaster" (John von Neumann). We would like to add also the words which were said many years ago by R.B. Hamming. Having a wealth of experience in the field of computational mathematics (he was the President of American Association on Computers and the Head of the Mathematical Service of Bell Telephone Laboratories), Hamming wrote in his book "Numerical Methods for Scientists and Engineers" [24] the following. "Two theses are at the basis of this book. Before solving a problem think what you are going to do with its solution. The aim of calculations is understanding, but not the numbers."

Conclusion: the number of natural fullerene isomers is less than the millions of isomers produced by unskilled using algebraic geometry.

9. Growth of fullerene C$_{56}$

The fullerene belongs to the column of basic perfect fullerenes having four-fold symmetry. It can produce the natural isomers shown in Fig. 33
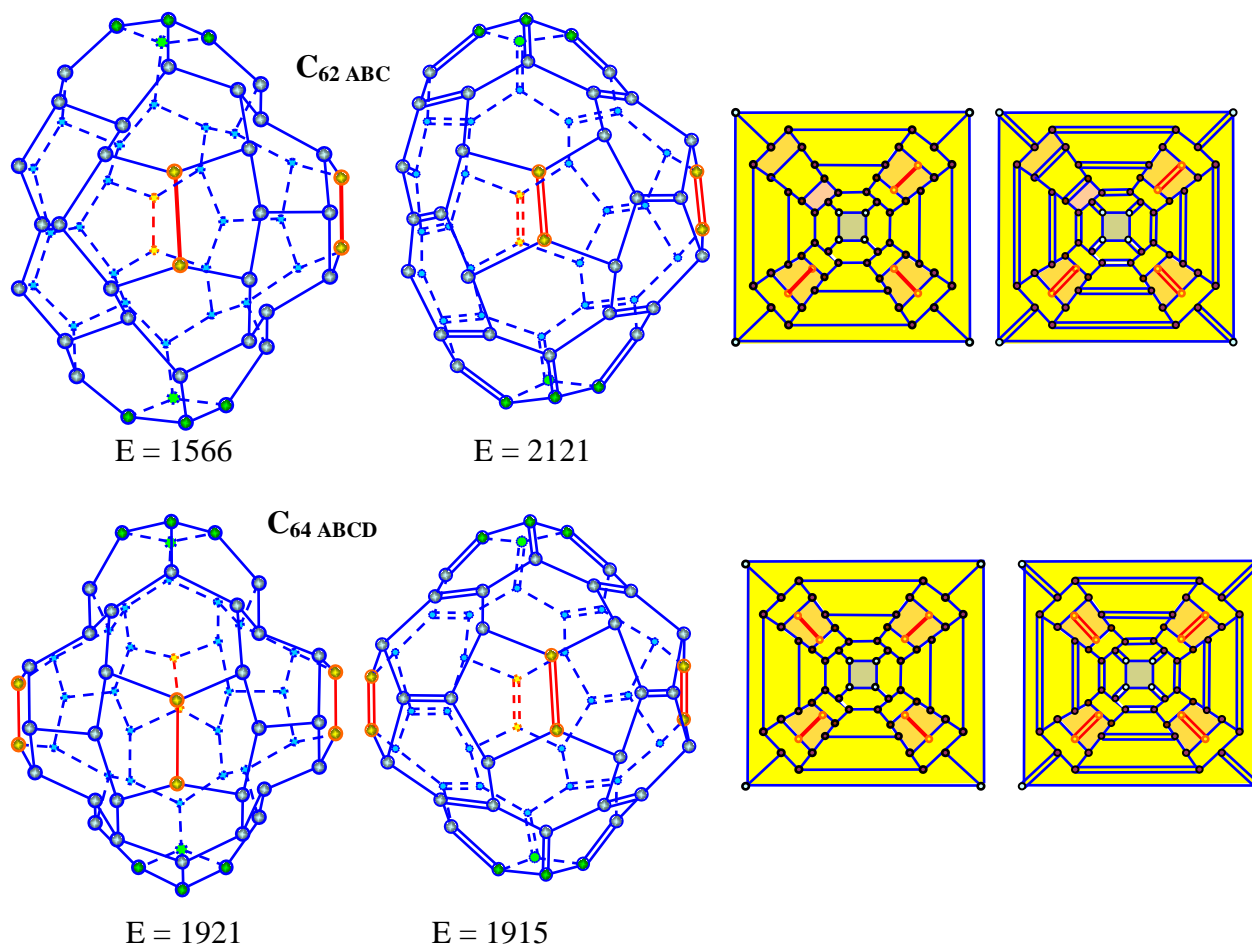

C$_{56}$

E=1580   E=2643

C$_{58\ A}$

E = 1679   E = 2503

C$_{60\ AB}$

E=1638   E=2324

C$_{60\ AC}$

E = 1631   E = 2270

$C_{62\ ABC}$

E = 1566   E = 2121

$C_{64\ ABCD}$

E = 1921   E = 1915

Fig. 33. Fullerenes C_{58}, C_{60}, C_{62}, and C_{64} as a result of embedding one after another carbon dimer into fullerene C_{56}: structure and graphs; energy in kJ/mol

10. Conclusion

We have studied possible ways of generating and growing the fullerenes and nanotubes having four-fold symmetry. We assumed that cyclobutane C_4H_8 can be transformed into different electronic isomers of clusters C_4-C_4. In its turn, the clusters can initiate the generation of elementary fullerenes C_8, mini-fullerenes C_{16}, and cupolas from C_{16} to C_{40}. These aggregates produce the fullerenes from C_{24} to C_{64}, perfect and imperfect, as well as nanotubes. There are three the most natural mechanisms of obtaining new fullerenes: 1) Fusion of carbon cupolas having one and the same symmetry; in our case, fourth-fold symmetry; 2) Fusion of fullerenes having compatible symmetry; 3) Embedding carbon dimers into initial fullerenes (the Endo-Kroto's mechanism).

The first mechanism is the most promising. It leads to generating basic perfect fullerenes. The second mechanism produces, as a rule, nanotubes. The third mechanism creates imperfect fullerenes. The imperfection is connected either with extra 'interstitial' or 'vacancy' carbon dimers, both types of dimers playing the role of defects. Only the basic fullerenes C_{24}, C_{32}, C_{40}, C_{48}, C_{56}, and C_{64} have the ordinary four-fold symmetry in the corresponding column of the periodic system of fullerenes, the intermediate fullerenes having no such symmetry. Considering the latter as imperfect due to defects, one can define them as the fullerenes conserving *topological* four-fold symmetry.

We have given a quantitative criterion that allows distinguishing fullerenes and nanotubes, and have calculated their energies. We have found that among the perfect fullerenes there are alive and dead. The fullerenes of the first subgroup can grow further by

the use of the Endo-Kroto's mechanism producing new fullerenes. The fullerenes of the second subgroup have no such possibility. The reason is connected with a hexagon-nearest circumference in different fullerenes.

We carefully examined the problem of fullerene isomerism and showed that it is necessary to differentiate natural and mathematical isomers. The first ones can be obtained during the natural growth in the framework of the Endo-Kroto C_2 insertion mechanism. The second ones are the mathematically possible fullerene structures and their interconversion is based on assumed sets of rules for construction and transformations without physical restrictions.

References
[1] Kerner R. Nucleation and growth of fullerenes. *Computational Materials Science.* 1994;2: 500-508.
[2] Irle S, Page AJ, Saha B, Wang Y, Chandrakumar KRS, Nishimoto Y, Qian HJ, Morokuma K. Atomistic mechanisms of carbon nanostructure self-assembly as predicted by nonequilibrium QM/MD simulations. In: Leszczynski J, Shukla MK. (Eds.) *Practical Aspects of Computational Chemistry II: An Overview of the Last Two Decades and Current Trends.* Springer; 2012.
[3] Schwerdtfeger P, Wirz LN, Avery J. The topology of fullerenes. *WIREs Comput. Mol. Sci.* 2015;5(1): 96-145.
[4] Melker AI, Krupina MA. Unified approach to forming fullerenes and nanotubes. *Materials Physics and Mechanics.* 2017;34(1): 1-17.
[5] Melker AI, Krupina MA. Geometric modeling of midi-fullerenes growth from C_{32} to C_{60}. *St. Petersburg State Polytechnical University Journal: Physics and Mathematics.* 2017;10(1): 47-54.
[6] Melker AI, Krupina MA. Modeling growth of midi-fullerenes from C_{48} to C_{72}. *Materials Physics and Mechanics.* 2017;34(1): 29-36.
[7] Melker AI, Vorobyeva TV. Fusion reactions of cupola half-fullerenes. *St. Petersburg State Polytechnical University Journal: Physics and Mathematics.* 2016;3(248): 59-67.
[8] Melker AI, Vorobyeva TV, Zarafutdinov RM. Fullerenes of the Δn=6 series. *J. Appl. Theor. Phys. Res.* 2018;2(1): 1-4.
[9] Melker AI, Vorobyeva TV. Structure and energy of the Δn=14 series fullerenes. *Int. J. Atom. & Nucl. Phys.* 2018;3: 008.
[10] Melker AI, Vorobyeva TV, Zarafutdinov RM. Modeling fullerene growth by fusion reactions of cupola half fullerenes: Δn=16 series. *Materials Physics and Mechanics.* 2019;41(1): 36-41.
[11] Sverdlov LM, Kovner MA, Krainov EP. *Vibration Spectra of Many-Atomic Molecules.* Moscow: Nauka; 1970. (In Russian)
[12] Hanwell MD, Curtis DE, Lonie DC, Vandermeersch T, Zurek E, Hutchison GR. Avogadro: an advanced semantic chemical editor, visualization, and analysis platform. *Journal of Cheminformatics.* 2012;4: 17.
[13] Melker AI, Matvienko AN. Periodic system of fullerenes: isomers from C_{20} to C_{28}. In: *Proc. 18th Int. Workshop: Nano-Design, Technology, Computer Simulations.* 2019. p.72-78.
[14] Slanina Z, Zhao X, Uhlik F. Model narrow nanotubes related to C36, C32 and C20: initial computational structural sampling. *Materials Science and Engineering.* 2002;B96: 164-168.
[15] Amiri H, Nickolis KL, Hernandez Sanchez R. Single-walled carbon nanotubes: mimics of biological channels. *Nano Letters.* 2017;17(2): 1204-1211.

[16] Tunuguntla RH, Henley RY, Yao YC, Anh T. Enhanced water permeability and tunable ion selectivity in subnanometer carbon nanotube porins. *Science.* 2017;357: 792-796.

[17] Endo M, Kroto HW. Formation of carbon nanofibers. *J. Phys. Chem.* 1992;96: 6941-6944.

[18] Melker AI. On the nature of void swelling. *Proc. SPIE.* 2008;7377: 737710.

[19] Melker AI. *Dynamics of Condensed Matter, Vol. 2, Collisions and Branchings.* St. Petersburg Academy of Sciences on Strength Problems; 2010.

[20] Brinkmann G, Franceus D, Fowler PW, Graver JE. Growing transformations of fullerene polyhedral. *Chemical Physics Letters.* 2006;428: 386-393.

[21] Melker AI. *Dynamics of Condensed Matter, Vol. 3, Noophysics (Science and Scientists).* St. Petersburg Academy of Sciences on Strength Problems; 2006.

[22] Gray HB. *Electrons and Chemical Bonding.* NY: W.A. Benjamin; 1965.

[23] Spice JE. *Chemical Binding and Structure.* Oxford: Pergamon Press; 1965.

[24] Hamming RW. *Numerical Methods for Scientists and Engineers.* NY: McGraw-Hill Book Co; 1962.

THE NATURE OF DC CONDUCTIVITY AND STRUCTURAL FEATURES OF GLASSES OF THE Ag – As – Se SYSTEM AS MATERIALS FOR PHOTONICS AND INTEGRAL OPTICS

E.V. Bochagina[1], V.A. Klinkov[1*], V.A. Markov[1,2], V.V. Polyakova[1], I.A. Sokolov[1,2]

[1]Peter the Great St.Petersburg Polytechnic University, (SPbPU), Polytechnicheskaya 29, St. Petersburg, Russia.

[2]Institute of Silicate Chemistry, Russian Academy of Sciences (ISC RAS), Makarov embankment 2,

St. Petersburg, Russia 199034

*e-mail: klinkovvictor@yandex.ru

Abstract. The physical and chemical properties (density, microhardness, thermal effects, elastic modulus, dc conductivity, and the transfer number of silver ions) of glasses of the As – Se – Ag system along the AsSe – Ag and AsSe$_{1.5}$ – Ag sections were investigated. The transfer numbers of Ag$^+$ ions were determined by a direct method; from their changes, it was found that the glasses of the investigated sections have mixed ion-electronic conductivity. The threshold concentration of silver at which the ionic component of the conductivity becomes dominant over the electron was determined. The volume fraction of the fluctuation free volume was calculated using elastic modulus, microhardness, and glass-transition temperatures values. It was shown that Ag$^+$ ions do not experience serious steric hindrances during the process of migration.
Keywords: chalcogenide glass, dc conductivity, ionic conductivity, femtosecond laser, glass microhardness, transfer number

1. Introduction
The advent of femtosecond lasers has led to an increasing number of studies on laser recording of gradient 3D structures in optically transparent materials. The use of femtosecond pulses markedly expands the possibilities of modifying glassy materials by implementing multi-photon absorption in the microvolume of material around the focal point. With the precision focus of the laser beam, it is possible to carry out a local change in the structure of the optical media, and consequently, modify their physical and chemical properties with high resolution. The femtosecond laser is able to obtain a significant local change in the refractive index in glass and to form a waveguide (including in the volume of glass) [1,2], to create crystallized tracks and metal threads in the volume of glass [3-5], micro- and nano-cavities [6], which is undoubtedly of interest for the development of photonics and integrated optics technologies. It should be noted that existing studies are carried out mainly with oxide glasses, transparent in the visible region. the number of such researches for glasses based on oxygen analogs – sulfur, selenium, and tellurium, is just a few.

The unique optical properties of chalcogenide glasses are well known for a long time. Nevertheless, interest in chalcogenide glasses does not fade away and there are works devoted to the study of them as optical elements in photonics, as well as a new generation of information storage devices, which is also implemented using laser radiation, including femtosecond. There is no doubt that when obtaining gradient structures, it is necessary to take

into account various diffusion processes. In this regard, the study of the migration characteristics of glasses is of fundamental importance.

This work is devoted to the study of the physical and chemical properties of the As – Se – Ag glass system enriched with silver. The research aimed to determine the influence of the features of the glass structure on the migration characteristics of the Ag^+ ion. Ag^+ ions determine both the nature and the conductivity of glasses under the influence of various factors – applied voltage, temperature, concentration, thermal history, and temperature gradient.

The research is aimed at obtaining information on the migration processes of monovalent ions in chalcogenide glasses under the influence of femtosecond laser radiation. According to [7], laser radiation in the glass leads to the appearance of an induced potential difference between the high-temperature region at the focal point of the laser beam and the cold boundaries of the affected region. This is the reason for the noticeable migration of monovalent ions from the focal point to the edges of the laser action area, which causes a local change in some physical and chemical properties of the glass. Processes of this kind are not only of theoretical but also practical interest since laser processing can form a gradient optical structure in a single technological stage.

However, this migration of monovalent ions under the influence of the induced potential is hindered by a counter process – the migration of the same ions from the "cold" region to the "hot" one (closer to the focal point of the laser beam). This is a manifestation of the Soret effect, well known for gases and liquids.

A relatively small number of works [8] are devoted to the study of thermal diffusion processes in solid oxide glasses, which is mainly determined by methodological difficulties when working with such a fragile material as glass (exclusively oxide) when creating a high-temperature gradient over the sample. To understand the physical essence of the processes occurring under the action of laser radiation, the study of the migration characteristics of the Ag + ion in model and relatively simple in composition and structure chalcogenide glasses of the Ag – As – Se system is of great importance.

2. Experimental technique (Methods)

Chalcogenide glasses were synthesized in an electric furnace from elementary substances of semiconductor purity in evacuated quartz ampoules with stirring at a maximum temperature of 950°C for 4-6 hours. The sample weight was 5-8 grams. Elemental selenium was preliminarily distilled in a vacuum to remove impurities of hydrocarbons (carbon) and water. The glasses were tempered in the air or ice water, depending on the composition; the subsequent annealing to remove residual stresses was carried out at a temperature ~ 15°C below T_g for 4-5 hours. As a result, homogeneous monolithic samples were obtained without signs of crystallization.

Electrical conductivity was measured at direct current using a Wheatstone bridge (P4060) in heating and cooling mode. Silver amalgam (anode) and mercury (cathode) were used as electrodes. In all cases, the temperature dependence of the specific electrical conductivity (σ) was a straight line, no hysteresis was observed ($-log\sigma = f(1/T)$). The measurement error did not exceed ± 5%.

The activation energy of electrical conductivity (E_σ) was calculated using the Arrhenius equation:

$$\sigma = \sigma_0 exp\left(-E\sigma / 2kT\right), \tag{1}$$

where σ_0 is the preexponential factor, k is the Boltzmann's constant, and T is the temperature.

Keysight N5769A stabilized power supplies, X603 electrolytic integrator, and an Instek GDM-8145 multimeter were used to conduct electrolysis and determine the transfer numbers of silver ions.

The density of the samples was determined by the method of hydrostatic weighing in CCl_4 with an accuracy of $\pm 5 \times 10^{-4}$ g using a Vibra HT-224RCE analytical balance, the microhardness by the method of indentation of a diamond pyramid (according to Vickers) was determined by PMT-3M (LOMO) device with an accuracy $\pm 5\%$.

The speed of propagation of longitudinal and transverse ultrasonic waves was measured using a UD 2-12 flaw detector. Thermal effects were determined on derivatographs Q-1500 (Hungary, "MOM") and "Termoscan-2M" (Analitpribor) in heating mode; fused quartz and Al_2O_3 powders were used as standards; the weighed portion of the studied glass was 0.5 g, the heating rate was 5-15 deg/min. Measurements accuracy was $\pm 5°C$.

3. Results and discussion

Physical and chemical properties. The area of glass formation of arsenic-selenium-silver glasses has been studied systematically for a relatively long time (for more details see [9,10]). Different authors obtained two noticeably different regions of glass formation, separated by regions of compositions in the crystalline and glass-crystalline states. The region in which glassy samples can be obtained under not very severe conditions consists of two parts (Fig. 1). Thus, according to the sections $AsSe_{0.8}$, $AsSe$, $AsSe_{1.5}$ – Ag, it is possible to obtain homogeneous glasses, and from the sections, $AsSe_{2.5}$, $AsSe_4$ – Ag with a high selenium content, inhomogeneous glasses [9,10] are obtained.
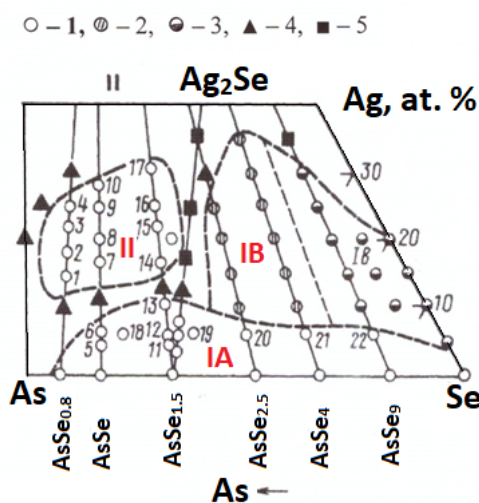
Fig. 1. The region of glass formation in the Ag – As – Se system according to [9 and 10]. 1 – homogeneous glasses, 2 – heterogeneous glasses, 3 – liquidating glasses, 4 – crystals, 5 – glass crystals

The regions of homogeneous and inhomogeneous glasses are separated by crystalline and glass-crystalline compositions along the As_2Se_3 – Ag_2Se section. This section contains several ternary compounds ($AgAsSe_2$, Ag_7AsSe_6, Ag_3AsSe_3), which have not been obtained in glassy form; along with the binary compound Ag_2Se, they are not glass-forming agents in the Ag – As – Se system. However, the ability of all three components to interact and form complex structural chemical units (s.c.u.) contributes to glass formation in this system.

Region **IA** mainly corresponds to the field of crystalline selenium and As_2Se_3 crystallization. Silver in these glasses plays the role of an impurity, as the content of which increases in the glass structure, the accumulation of s.c.u. $AgAsSe_2$ occurs, which leads to a

significant increase in its crystallization ability. Compositions with a predominant content of AgAsSe$_2$ do not form glasses at all. Region **IB** corresponds to the area of liquation.

The region of homogeneous glasses (Fig. 1, II) is in the field of arsenic evolution. For glass formation in this region, the ability of arsenic to easily pass into an amorphous state is of great importance. Glass formation in this area is also facilitated by the complex structural and chemical composition of alloys, in which the formation and interaction of at least four types of spatially different structural chemical units (s.c.u.) complicate the separation of crystalline phases from the glass melt [9,10]. This region of compositions, which easily forms homogeneous glasses, was chosen in this study.

Glasses of the following sections were selected as objects of study: AsSe – Ag and AsSe$_{1.5}$ – Ag. Some properties of the synthesized glasses are presented in Table 1. It should be noted that the data of this work are in satisfactory agreement with the literature data (Table 1).

Table 1. Some physical and chemical properties of glasses from sections AsSe – Ag and AsSe$_{1.5}$ – Ag

Section	Ag, at. %	$d,$ g/cm^3	$H,$ kgf/mm^2	$d,$* g/cm^3	$T_g,$ $^\circ$C	H*, kgf/mm^2	T_g*, $^\circ$C
AsSe	-	4.55	136	4.48	171	130	164
AsSe – Ag	5.0	4.68	110	4.71	155	95	148
	6.0	-	-	4.76	-	90	140
	10.0	4.93	107	-	158	-	-
	15.0	5.16	118	-	167	-	-
	16.7	-	-	5.30	-	99	150
	20.0	5.43	138	5.50	171	112	160
	25.0	5.69	155	5.86	178	147	172
	28.0	-	-	6.04	-	161	176
AsSe$_{1.5}$	-	4.550	150	4.59	172	150	169
AsSe$_{1.5}$ – Ag	1.0	4.550	150	-	170	-	-
	3.4	4.800	153	-	-	-	-
	5.0	4.862	142	4.85	155	150	152
	10	5.105	155	5.09	147	138	146
	15	5.309	127	5.62	150	146	150
	20.0	5.581	134	-	150	-	147
	25.0	5.776	115	5.76	155	150	149
	30.0	6.015	110	6.04	170	155	158

(d – density, H – Vickers microhardness, T_g – glass-transition temperature. * – data from [9,10])

The character of the H and T_g changes with an increase in the silver content depends both on the arsenic/selenium ratio and on the position in the region of glass formation. For example, for glasses from the AsSe$_{1.5}$ – Ag section, the first silver additions exhibit a sequential decrease in microhardness, while the T_g values, after a slight decrease, practically do not change at a silver content from 5 to 25 at.%.

Determination of the nature of conductivity. Until the mid-seventies of the last century, it was believed that all chalcogenide glasses are *p*-type semiconductors, and only by the eighties the first works appeared, indicating the presence of ionic conductivity in certain silver-containing compositions of some chalcogenide systems [9-10]. It should be noted that the presence of ionic conductivity and the determination of the transport numbers of current carrier ions for a number of silver-containing chalcogenide glasses was carried out using a highly simplified electromotive force (emf) method [10,11], and the values of the transport

numbers of Ag^+ ions obtained using this method, in our opinion, cannot be considered indisputable.

The essence of the emf method is to create a concentration element of the following type:

$C, Ag \mid CG_{Ag} \mid Ag_2S \mid S, C,$
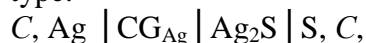
where CG_{Ag} is the investigated silver-containing chalcogenide glass, C is graphite contact. Upon contact of the studied glass with metallic silver on the one hand and elemental sulfur on the other, according to [10,11], a redox reaction begins in the element, the emf of which is fixed and compared with the emf of the reaction:

$$2Ag_m + S_m = (Ag_2S)_m, \tag{2}$$

which occurs in this system.

The cell emf values obtained experimentally (E_{exp}), as a rule, are lower than the theoretical value (E_{theor}): the mean transfer numbers of silver ions (t_{Ag+}) are determined from the ratio of the experimentally obtained emf of the indicated reaction and its theoretical value:

$$t_{Ag+} = E_{exp} / E_{theor}. \tag{3}$$

Thus, for the $AsSe_{1.5} - Ag_x$ glass system with a silver content from 10.7 to 30.6 at.% (in the temperature range from 30 to 800°C), the values of the transfer numbers of Ag^+ ions lie in the range 0.70-0.75 [10,11].

It should be noted that the emf method itself does not have any theoretical justification, and, most importantly, the reaction that may occur in the element used is postulated and has no real experimental confirmation. Some time ago, we studied the nature of conductivity and determined the transport numbers of current carrier ions in a number of glassy systems, including chalcogenide ones, using the direct method - the weight modification of the Hittorff method - the modernized Tubandt method, which has shown its validity for the noted problem [12].

The classical Hittorff technique, developed for solutions, involves the determination of the transfer numbers of current carrier ions through the analytical determination of the concentration change in the near-electrode regions of the electrolyte after passing a known amount of electricity. Nevertheless, the real values of the transport numbers of current carrier ions cannot be determined by this method (or it is extremely difficult), since the change in the concentration of carriers in the near-electrode spaces involves ions surrounded by a hydration shell. In other words, during migration, ions carry with them attracted solvent molecules, which affects the change in the concentration of the electrolyte and affects the result obtained.

The Tubandt method was developed for solids and is devoid of this drawback, since migration in a solid of any associate is unlikely, and the result obtained by this technique allows one to obtain the true transfer numbers of charge carrier ions. So, in the case of the transfer of electricity by ions of the same sign (a cation or anion, or an ion and an electron, i.e., when migration processes are accompanied by a transfer of mass in one direction), the transfer numbers of these ions can be determined by the change in the mass of the electrodes between which the investigated sample after electrolysis. In the classical version, the same solid electrolyte was used as these electrodes (cathode and anode), which was the subject of research [13].

If a known amount of electricity is passed through the electrolyte, then the transport numbers of carrier ions can be determined from the ratio of the decrease in the weight of the anode (and the increase in the weight of the cathode) and the amount of carrier released as a result of electrolysis (according to Faraday's law). In this case, the condition for the correct conduct of the experiment is the constancy of the weight of the test sample before and after electrolysis should not change. In this work, a PTFE thermocell was used to determine the transfer numbers of silver ions (shown in Fig. 2). A silver wire dipped into a silver amalgam

was used as an active anode, and pure mercury was used as a cathode. The cell is detachable, allows quantitative weighing of electrodes before and after electrolysis.
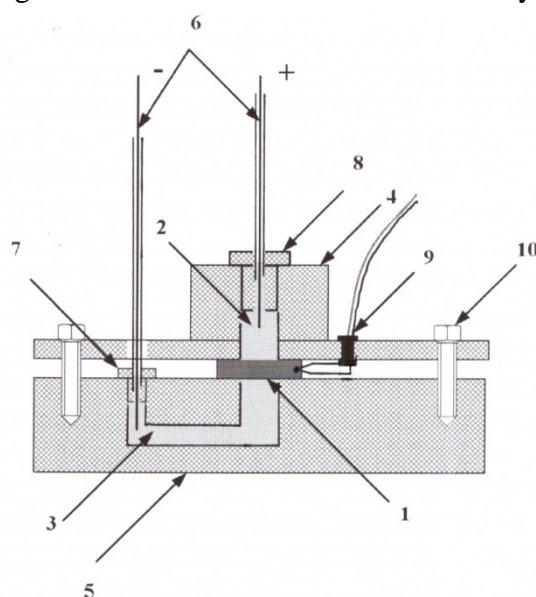

Fig. 2. Thermocell with active electrodes for determination of the transfer numbers of glassy solid electrolytes.
1 – glass sample, 2 – amalgam anode with a silver wire (+), 3 – mercury cathode (-),
4 – upper part of the cell, 5 – lower part of the cell, 6 – electrodes in metal tubes, 7, 8 – plugs,
9 – thermocouple, 10 – connecting screws

Electricity is supplied through silver wires passing through thin nickel tubes. The mercury electrodes and sample are weighed before and after the experiment. The transport numbers of Ag + ions are determined from the ratio of the amount of silver obtained as a result of a known amount of electricity passed through the sample and theoretically calculated according to Faraday's law. The experimental conditions and some of the results obtained within the framework of this study are presented in Table 2. It should be noted that the presented results are consistent with the literature data [9,10,12].

Table 2. Experimental conditions and the values of the transfer numbers of silver ions, obtained by the Hittorff method

Composition	x	Ag, at.%	t, °C	Q, C	$\Delta m_{average} \cdot 10^5$, g	t_{Ag+}
	0.064	2.5	100	1.01	40	0.3_5 *
	0.13	5.0	80	1.1	70	0.5_8 *
	0.28	10.0	80	0.8	70	0.7_9 *
	0.44	15.0	60	1.4	130	0.8_3 *
	0.63	20	60	3.1	304	0.8_8 *
AsSe$_{1.5}$ – Ag$_x$	0.83	25	80	2.8	277	0.8_8 *
	0.28	10	110	2.5	215	0.7_7
	0.44	15	110	1.95	175	0.8_1
	0.63	20	100	2.13	205	0.8_5
	0.83	25	100	1.66	165	0.8_9

(Here: t is the temperature of the experiment, Q is the amount of passed electricity, $\Delta m_{average}$ is the average change in the mass of electrodes after electrolysis, t_{Ag+} is the transfer numbers of silver ions, (*) – data obtained earlier, see [12]).

The electrical conductivity of glasses in the arsenic-selenium-silver system varies widely depending on the ratio of all three components, but silver has a decisive influence. When the first 10 at. % silver is introduced into glassy $AsSe_{1.5}$, the conductivity increases by more than five orders of magnitude. Glasses of sections $AsSe - Ag$ and $As_2Se_3 - Ag_2Se$ behave similarly.

For the glasses with a constant Ag (for example, ~ 6 at.%), a conductivity decrease was observed with an increase in the As/Se ratio. The complex structural and chemical composition complicates the process of electrical transfer in glasses of this system (almost all glasses of the As – Se – Ag system have underestimated $log\sigma o$ values), with the exception of glasses of the $As_2Se_3 - Ag_2Se$ and $As_2Se_3 - Ag$ sections, which have the simplest structure, the conductivity of which approaches the through [9,10] (for more details see Table 3).

In addition, for glasses of the As-Se-Ag system, with an increase in the silver content, not only the magnitude but also the conduction mechanism changes: the values of the silver transfer numbers become more than 0.5. With an increase in the silver content to 5-10 at. %, The type of current carriers changes: the purely electronic conductivity, characteristic of the initial arsenic selenides, is replaced mainly by the ionic one [9,10,12].

Table 3. Electrical properties of glasses in sections $AsSe - Ag$ and $AsSe_{1.5} - Ag$

Section	Ag, at. %	$-lg_\sigma$, ohm^{-1}·cm^{-1}	E_σ, eV	$-lg\sigma_0$	$*-lg_\sigma$, ohm^{-1}·cm^{-1}	$* E_\sigma$,eV	$*-lg\sigma_0$
AsSe – Ag	5.0	5.8	1.15	1.7	12.2	1.45	-0.3
	6.0	-	-	-	8.8	1.07	-1.0
	10.0	4.0	0.93	2.2	-	-	-
	15.0 (17*)	4.1	0.67	2.4	4.8	0.72	1.6
	20.0	3.9	0.63	2.4	4.6	0.68	1.5
	25.0	3.9	0.63	3.0	4.4	0.65	1.4
	30.0 (28.6*)	-	-	-	3.9	0.56	1.4
AsSe$_{1.5}$ – Ag	1.0	12.9	1.81	2.4	12.8	1.80	2.2
	3.4	11.2	1.77	2.3	-	-	-
	5.0	9.7	1.30	2.7	9.8	1.36	2.0
	10 (11*)	6.9	0.83	3.3	7.6-7.8	1.10	1.0
	15 (17*)	6.4	0.85	3.3	6.3	0.90	2.2
	20.0 (22*)	5.3	0.80	2.3	5.6	0.81	1.2
	25.0 (24*)	4.9	0.65	1.7	5.5	0.78	1.3
	30.0	4.2	0.63	1.8	4.6	0.70	2.0

($-lg_\sigma$ is electrical conductivity at room temperature, E_σ is the activation energy of electrical conductivity, $log\sigma_0$ – preexponential factor. (*) – generalized literature data according to [9,10] and the closest compositions to those investigated in this work)

To determine the ratio between the ionic and electronic components of conductivity in glasses enriched with a silver (with content from 10 to 30 at.%) in [9,10] in the temperature range from 30 to 80°C, the transfer numbers of Ag^+ ions were determined using the emf method. The obtained values of the average transfer numbers of Ag^+ ions lie in the range from 0.75 to 0.70. Moreover, with an increase in the silver content, the values of the transfer numbers slightly decrease. Nevertheless, despite the relatively low reliability of the indicated emf method, it is noted that in glasses of the As – Se – Ag system with a silver content of more than 15 at%, the main type of charge carrier changes: predominantly electronic

conductivity is replaced mainly by ionic conductivity [9,10]. This conclusion is partially confirmed by a joint study of the diffusion of silver ions and the electrical conductivity of glasses of this system, described in [11]. It should be noted that in chalcogenide glasses in general, and the As – Se – Ag system in particular, diffusion processes have practically not been studied and we have not found other works on this topic. In [11], a rather narrow concentration interval was studied along the AsSe – Ag and $(AsSe_{1-x})_{0.8} – Ag_{0.2}$ sections (with a constant silver content). The calculated diffusion coefficients of Ag^+ ions (at 100°C) for the studied glasses are in the range $(2.5-7.9)\cdot 10^{-9}$ and $(5.0-0.8)\cdot 10^{-9}$ cm^2/s, respectively. In this case, the activation energy of diffusion for glasses from the AsSe – Ag section is constant. While in glasses $(AsSe_{1-x})_{0.8} – Ag_{0.2}$ the activation energy of diffusion decreases from 0.74 to 0.57 eV and correlates with a decrease in the selenium content.

For all studied glasses, the activation energy of electrical conductivity (E_σ) and the activation energy of diffusion practically coincide in magnitude, which allowed the authors to conclude the identity of the nature of electrical and mass transfer [11].

In the study of diffusion, the question of the migration mechanism is of particular interest. To elucidate the mechanism of migration of Ag^+ ions in the studied chalcogenide glasses, we analyzed the value of the correlation factor (*f*) in the Nernst-Einstein equation: for all glasses, with an increase in the silver content, there is a slight decrease in *f* values (from 0.8 to 0.5), and for glasses with a constant silver content – with a decrease in selenium content. The obtained values do not allow an unambiguous answer to the question of the mechanism of silver migration in these glasses, since according to [14], these values can be attributed to both relay and vacancy mechanisms and direct interstitial mechanisms.

Structural features of ionic conductivity. The electrical properties of glasses of the As-Se-Ag system are satisfactorily described from the point of view of the model of the micro-inhomogeneous structure of glass, which, from a unified standpoint, describes the physical and chemical properties of both oxide and chalcogenide glasses. According to this model, at high temperatures in the melt, a selective interaction of the components of the initial charge occurs, during which structural and chemical groups are formed.

These groups in multicomponent glasses determine the physical and chemical properties of future solid glasses. In this case, all structural fragments (s.c.u.) can be divided into two groups: polar and non-polar. Non-polar s.c.u. (which do not dissociate and block both possible processes of dissociation of current carrier ions and their subsequent migration in their environment) include fragments linked by a non-polar or weakly polar covalent bond. These s.c.u. are mainly involved in the formation of a three-dimensional glass network: these include $BO_{3/2}$, $SiO_{4/2}$, $PO_{4/2}$, $AsS_{3/2}$, $AsAs_{3/3}$, selenium chains, etc. In a medium formed mainly by these fragments (with low dielectric constant), dissociation of ionogenic chemical units and subsequent migration of current carrier ions is hindered.

Polar (ionogenic) fragments have in their composition a bond with a significant ionic component: these are fragments of the type $Na^+[BO_{4/2}]^-$, $Li^+O^-SiO_{3/2}$, $Ag^+Se^-AsSe_{2/2}$, etc. Consequently, the environment formed by them has a relatively high dielectric constant and to some extent, they behave like electrolyte solutions. That is, in glass, these fragments, on the one hand, dissociate with the formation of current carrier ions, on the other hand, the medium formed by similar chemical units contributes not only to dissociation processes (in contrast to nonpolar chemical units) but also facilitates the subsequent migration of these ions with lower energy costs. It is clear that the concentration of polar agricultural units is proportional to the number of components with increased bond ionicity introduced into the glass composition, i.e. those that contain potential current carrier ions (both cations and anions).

At low concentrations of components with increased bond ionicity, the regions formed by polar s.c.u. are isolated from each other by the medium of nonpolar chemical units. Glasses with such a structure have no ionic conductivity. The reduced electrical conductivity

of these glasses is limited both by the small number of free current carriers and by the need for their migration in the main nonpolar medium, which requires overcoming high activation barriers. The ionic conductivity in glasses appears when isolated regions of polar s.c.u coalesce with each other and form continuous areas that permeate the entire volume of the glass. At the same time, not only the number of current carriers increases (due to the dissociation of polar chemical units) but also the activation energy of electrical conductivity decreases due to their migration in a polar medium.

To determine the critical concentration of polar chemical units, at which they merge into continuous channels, penetrating the glass throughout the entire volume, thereby violating the blockade of through migration of ions and the appearance of ionic conductivity, the parameter "degree of blocking" (γ) was adopted. γ is determined by the ratio of the concentration of non-polar and polar s.c.u. by the following equation:

$$\gamma = \frac{polar\_s.c.u.}{non-polar\_s.c.u.}. \tag{4}$$

For a number of oxides and halogen-containing glasses, the blockade of ion migration by a medium from nonpolar chemical elements is observed at values of $\gamma \sim 6$: in this case, a nonpolar fragment ceases to fit between two polar fragments. In other words, when $\gamma > 6$, polar s.c.u. are isolated by non-polar s.c.u. and ionic conductivity is practically absent. At values $\gamma \leq 6$, polar s.c.u. are combined into a continuous sublattice, their degree of dissociation increases, and the dissociated ions acquire the ability to migrate throughout the glass volume with lower energy consumption in the medium formed by them. With an increase in the concentration of the ionogenic component and the degree of its dissociation, ionic conductivity appears. Therefore, knowing the probable structural-chemical composition of multicomponent glasses, one can calculate the degree of blocking and judge both the presence of ionic conductivity in them and the boundary compositions in which this conductivity appears. (A more detailed model of the microheterogeneous structure of glass and its application for a wide range of glasses is described in [15]). However, in contrast to the description of the unit cell of a crystal, for which there are direct experimental methods, there are no such direct methods for the structural-chemical unit of multicomponent glass. Complex s.c.u. in glasses are the model that reflects some approximation to real structural units in the glass.

As mentioned above, in the As – Se – Ag system, the compositions along the sections AsSe – Ag and $AsSe_{1.5}$ – Ag with a silver content of up to 30 at. % lie in the crystallization field of the ternary compound $AgAsSe_2$, with a congruent melting point of 410°C, and As_2Se_3 [9,10]. We chose these sections because, despite a certain deficiency of selenium, it is possible to introduce up to ~ 30 at. % of silver into these glass compositions. In addition, at Ag concentration less than 30 at. % the only polar fragments are s.c.u. type $Ag^+Se^-AsSe_{2/2}$, corresponding to the compound $AgAsSe_2$, in which the Se – Ag bond has an approximately (6-8)% higher degree of ionicity than, for example, the As – Se bond. Assuming that all silver introduced into the glass composition of the investigated sections binds to polar s.c.u. type $Ag^+Se^-AsSe_{2/2}$, and all other fragments – As_2Se_3, AsSe, and $AsAs_{3/3}$ – are non-polar and blocking, we calculated the degree of blocking γ. For glasses of the $AsSe_{1.5}$ – Ag section, the results of such calculations are presented in Table 4 and Fig. 3.

Figure 3 shows that with an increase in the silver content, all electrical parameters change rather smoothly, while near the compositions with 4.5-5.0 at. % of silver, a sharp change in the slope of the concentration dependence of γ is observed. The last one can be explained by the actual violation of the blockade of ion migration Ag^+. This is confirmed by the values of the transfer numbers of these ions: in glasses containing more than 4-5 at. % of Ag ($\gamma \approx 4.5$-5), the values of the transfer numbers of silver ions exceed 0.5; the nature of the conductivity changes from predominantly electronic to predominantly ionic.

Table 4. Probable structural-chemical composition and magnitude of the degree of blocking (γ) for glasses from the $AsSe_{1.5}$ – Ag section

Glass composition	Ag, at. %	Probable structural and chemical composition	γ
$AsSe_{1.5} Ag_{0.026}$	1.04	$0.05 AgAsSe_2 \cdot 0.9As_2Se_3 \cdot 0.05AsSe$	19.0
$AsSe_{1.5} Ag_{0.21}$	7.9	$0.3 AgAsSe_2 \cdot 0.4As_2Se_3 \cdot 0.3AsSe$	2.33
$AsSe_{1.5} Ag_{0.33}$	11.8	$0.4 AgAsSe_2 \cdot 0.2As_2Se_3 \cdot 0.4AsSe$	1.5
$AsSe_{1.5} Ag_{0.5}$	16.7	$0.5 AgAsSe_2 \cdot 0.5AsSe$	1.0
$AsSe_{1.5}Ag_{0.61}$	19.6	$0.55 AgAsSe_2 \cdot 0.25AsSe \cdot 0.05AsAs_{3/3}$	0.55
$AsSe_{1.5}Ag_{0.75}$	23.1	$0.86 AgAsSe_2 \cdot 0.14AsAs_{3/3}$	0.16
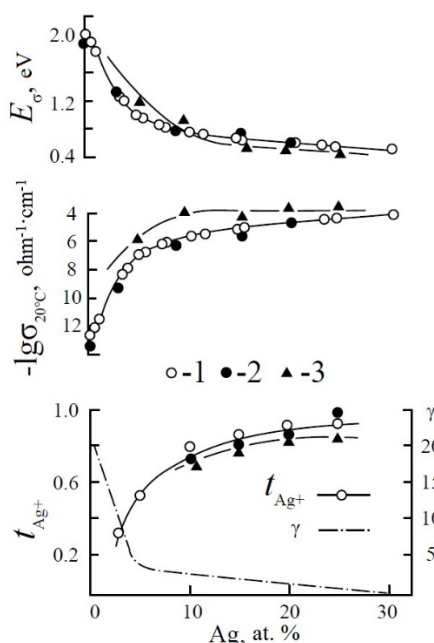
Fig. 3. Concentration dependences on the electrical conductivity parameters (lg_σ), the transfer numbers of Ag^+ ions (t_{Ag^+}), and the degree of blocking (γ) for glasses $AsSe_{1.5}$ – Ag (2) and AsSe – Ag (3). (1) – literature data [9,10]

In this concentration range, isolated nonpolar s.c.u. areas of polar s.c.u. type $Ag^+Se^-AsSe_{2/2}$ for the first time merge into fragments penetrating the entire glass fragments. This is probably due to the dipole-dipole interaction with the formation of quadrupoles of the following type:

$$\begin{bmatrix} Se_{2/2}As - Se^-Ag^+ \\ Ag^+Se^- - AsSe_{2/2} \end{bmatrix}$$
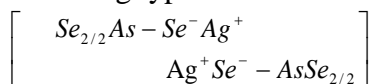
Their formation causes a change in the main type of current carrier. At a higher silver concentration, there are more and more such quadrupoles, the conductivity of glasses increases, and the transfer numbers reach their maximum values of 0.86-0.88 for compositions at the boundary of the glass formation region, which, as expected, is limited by the release of crystalline arsenic. For glasses of the section AsSe – Ag, depleted in silver, the study of the electrical properties and determination of the transfer numbers of silver ions were not carried out. The electrical properties and transfer numbers for silver-enriched glasses from this section are also shown in Fig. 3.

Estimation of the conductivity value from the concentration of current carriers. Since the electrical conductivity of metal-containing chalcogenide glasses noticeably exceeds

the electrical conductivity of other classes of glasses – silicate, borate, and phosphate, it is of interest to evaluate the conduction mechanism depending on the concentration of current carriers and their structural and chemical features and compare the results with similar data for other types of glasses [22]. For this, it is advisable to determine the activation volume of migration of the silver cation in chalcogenide glasses with conductivity with their participation. The activation volume of migration is a certain effective parameter that includes not only the thermodynamic characteristics of the migration process, the geometric dimensions of the ion migrating in a solid but also the geometric dimensions of structural defects along which this migration is carried out. This approach was theoretically developed for crystals [16] but has been successfully applied to a number of oxide glasses. However, such studies are extremely few, since they require unique installations that allow one to measure the electrical conductivity of samples when high pressure is applied (tens of thousands of atmospheres). Under the action of high pressure, the electrical conductivity of ion-conducting materials decreases, while in the case of conductors with electronic conductivity, its growth is observed [17,18]. It should be noted that, as applied to glasses, it is possible to use other parameters instead of the activation volumes of migration - the volumes of fluctuation microcavities, which are much easier to determine, but for several classes of oxide glasses these parameters practically coincide (for more details, see, for example, [12,19]). In accordance with Eyring's theory [20], the electrical conductivity of solutions is given by:

$$\sigma = \sigma_o exp\left(-\Delta G^{\#} / RT\right),\tag{5}$$

where σ is the specific electrical conductivity, $\Delta G^{\#} = \Delta H^{\#} + P\Delta V^{\#}$ – ($\Delta G^{\#}$ is the original notation, according to [20]) is the activation free energy of the process – a value identical to the activation energy of electrical conductivity (E_σ).

The multiplier in the exponent determines the probability of the activated complex existence. The activated complex in this case is some effective value characterizing the migration process, i.e. the number of particles with the energy required for the process of dissociation of an ionogenic structural fragment and subsequent migration of the dissociated ion.

Parameters $\Delta H^{\#}$ and $\Delta V^{\#}$ are the minimum values of molar enthalpy and molar activation volume required for the formation of this activated complex [20], which can be determined from the following thermodynamic equalities:

$$\Delta H^{\#} = \left[\frac{\partial(\Delta G^{\#} / T)}{\partial(1/T)}\right]_P = -R\left[\frac{\partial \ln \sigma}{\partial(1/T)}\right]_P,\tag{6}$$

$$\Delta V^{\#} = \left[\frac{\partial(\Delta G^{\#})}{\partial P}\right]_T = -RT\left[\frac{\partial \ln \sigma}{\partial P}\right]_T,\tag{7}$$

where R and T are gas constant and temperature. The numerical values of $\Delta H^{\#}$ can be determined from the temperature dependences of electrical conductivity at constant pressure, and the values of $\Delta V^{\#}$, respectively, from the data on the effect of high pressure (uniform compression) on electrical conductivity under isothermal conditions.

The free activation energy of electrical conductivity $\Delta G^{\#}$ (in this work, E_σ) can be divided into two components and presented in the following form:

$$\Delta G^{\#} = \frac{1}{2}\Delta G_d + \Delta G_a,\tag{8}$$

where ΔG_d is the free energy of dissociation, and ΔG_a is the free activation energy of ion displacement.

Then the expression for the temperature dependence of the electrical conductivity can be written in the following form:

$$\sigma \; = \; \sigma_o exp\left[-\frac{1}{RT}\left(\frac{\Delta G_d}{2}+\Delta G_a\right)\right]. \tag{9}$$

Taking into account the ratio

$$\Delta V^{\#}=\left(\frac{\partial \Delta G^{\#}}{\partial P}\right)_T, \tag{10}$$

total activation volume will be equal to

$$\Delta V^{\#}=\frac{1}{2}\Delta V_d + \Delta V_a, \tag{11}$$

where ΔV_d is the partial activation volume of the formation of a dissociated ion (vacancy), and ΔV_a is the partial activation volume of the movement of this ion.

There is a correlation between $\Delta H^{\#}$ and $\Delta V^{\#}$ of the form $\Delta V^{\#} = \text{const}\cdot\Delta H^{\#}$ [16] and this constant has the dimension of compressibility, therefore, the expression for $\Delta V^{\#}$ can be written in the following form:

$$\Delta V^{\#}=\xi \cdot \vartheta \cdot \Delta H^{\#}, \tag{12}$$

where ϑ is the compressibility (in the first approximation, χ_s is the adiabatic compressibility), ξ is a dimensionless constant, the value of which can be determined from the following relation:

$$\xi \; =\frac{2}{3}\left(\frac{1+\mu}{1-2\mu}\right). \tag{13}$$

Then the theoretical value of the volume of the activated complex ($\Delta V_{th}^{\#}$) can be calculated through the elastic modulus from a ratio:

$$\Delta V_{th}^{\#}=\frac{2(1+\mu)}{E}\cdot\Delta H^{\#}, \tag{14}$$

where E is Young's modulus, μ is Poisson's ratio.

Earlier, we investigated the electrical conductivity of several chalcogenide glassy compositions under the influence of high (up to 6000 atm) pressure [12,19]: it was shown that glass of the $AgAsS_2$ composition, with purely cationic conductivity for silver ($t_{Ag+} = 0.999$), the electrical conductivity under high pressure decreases, while the conductivity of the compositions $Ag_{0.8}Tl_{0.2}AsS_2$ ($t_{Ag_+} = 0.86$) and $Ag_{0.63}AsSe_{1.5}$ ($t_{Ag_+} = 0.88$) increases. It is impossible to calculate the activation volume for mixed ion-electronic conductors, but for the $AgAsS_2$ composition, the calculated activation volume is $\Delta V^{\#} = 4.0 \pm 1.0$ cm^3/mole.

It was of interest to compare the values of activation volumes obtained from data on the effect of high hydrostatic pressure on electrical conductivity with values calculated through elastic modulus. It is known from the literature that these values are close for different classes of glasses, for example, silicate or phosphate glasses [17]. Previously, we measured the propagation velocity of longitudinal and transverse ultrasonic waves and calculated elastic modulus, including for $AgAsS_2$ glass [12]. It is known that the process of compaction of the structure of a solid (including glass) under the influence of all-round (hydrostatic) compression is by its nature identical to compaction in a small volume under the influence of an indenter when determining the Vickers microhardness by the indentation method [21]. This process of structure compaction can be considered as the process of liquidation of fluctuating microcavities in glass, which can ultimately be described within the framework of the free volume theory. Within the framework of this theory, it is possible to satisfactorily describe and explain the various properties of glasses and their melts.

It is known that the volume of solid glass is always greater than the volume of a crystal of the same composition. The reason for the increase in the volume fraction of the fluctuation free volume (f_g) in the glass is the freezing of the structure of the glass-forming melt during the glass transition, and the presence of bridging atoms with distorted bond angles in the glass

is precisely the main reason for this phenomenon. The fluctuation volume of amorphous (glassy) substances is caused by freezing in the process of glass transition, the displacement of structural fragments from equilibrium positions [22]. Therefore, f_g is a floating parameter and directly depends on the thermal history of a particular sample.

In general, the free volume can be used to judge the degree of loosening of the glass structure, which partially determines steric hindrances in the process of ion migration in solid glass and to some extent explains the fact that the conductivity of glass is usually higher than the conductivity of a crystal of the same composition.

The volume of fluctuation microcavity in glass (V_h) can be calculated in terms of elastic modulus, Vickers microhardness, and softening temperature by the following expressions:

$$V_h = \frac{3(1-2\mu)}{f_g} \cdot \frac{kT_g}{E}, \tag{15}$$

$$V_h = ln\left(\frac{1}{f_g}\right) \cdot \frac{kT_g}{H}, \tag{16}$$

where H is the microhardness and f_g is the volume fraction of the fluctuation free volume "frozen" below the glass-transition temperature.

The value of f_g can be determined through the elastic modulus (E, μ) from the following relationship:

$$f_g \cdot ln\left(\frac{1}{f_g}\right) = \frac{(1-2\mu)^2}{2(1+\mu)}. \tag{17}$$

Based on the presented expressions, we determined the values of these parameters. The f_g values obtained for chalcogenide glasses are approximately 2-3 times lower than for oxide glasses (f_g values, for example, for silicate glasses, are in the range 0.027-0.030) [23,24]. It is known that with an increase in the degree of connectivity of the glass network, an increase in Young's modulus and Poisson's ratio is observed, i.e. low values of μ correspond to increased elasticity of the material. In this case, it can be concluded that the degree of cohesion of chalcogenide glasses decreases in comparison, for example, with silicate glasses. From the values of elastic constants (Table 5), the volume fraction of the fluctuation free volume and microcavity volumes were calculated.

Table 5. Elastic constants, Young's modulus (E), Poisson's ratio (μ), *the* volume fraction of the fluctuation free volume (f_g), microcavity volume (V_h), the molar volume of glasses (V_{mol}), and equilibrium distance between the particles (r_n) of glasses from the $AsSe_{1.5} - Ag$ section

Ag, at. %	$\upsilon_l \cdot 10^{-3}$, m/s	$\upsilon_t \cdot 10^{-3}$, m/s	μ	$E \cdot 10^{-8}$, H/m^2	f_g	V_h, Å^3	V_h, cm^3/mole	V_{mol}, cm^3/mole	r_n, Å
5	2.80	1.40	0.330	280	0.008	6.7	4.0	42.6	1.17
10	2.65	1.30	0.334	240	0.006	8.0	4.8	44.2	1.24
15	2.45	1.20	0.338	200	0.007	9.0	5.4	45.5	1.29
20	2.25	1.10	0.347	190	0.008	8.3	5.0	46.7	1.25
25	2.15	1.05	0.350	180	0.008	8.5	5.1	49.0	1.25

(Note: the molar volume of glass is $V_{mol} = M/d$ (M is the molecular weight of glass, d is the density), $r_n \approx (V_h)^{1/3}$).

According to [25], the formation of an activated complex for inorganic network structures occurs without breaking valence bonds but is realized by switching them. It is with the switching of bridging bonds that the jump of an ion into microcavities in the case of silicate glasses is associated. Probably, in the case of ion-conducting chalcogenide glasses, including the aforementioned $AgAsS_2$ and the compositions of the sections AsSe – Ag and $AsSe_{1.5}$ – Ag with a high ionic component, a similar phenomenon is observed. Comparison of the activation volumes $\Delta V^{\#}$, calculated from the dependence of electrical conductivity on pressure, for $AgAsS_2$ glass ($\Delta V^{\#} = 4.0 \pm 1.0$ cm^3/mole) with the volumes of fluctuation microcavities ($V_h = 5.0 \pm 1.0$ cm^3/mole) indicates their proximity, not only for the series oxide glasses but also for chalcogenide glasses [17,19].

Taking into account the volume of the migrating silver cation ($V_{Ag+} = 3.7$ cm^3/mole), it can be concluded that the migration of these ions in the structure of chalcogenide glasses does not experience serious steric hindrances and rather resembles the mechanism of ion migration in liquids [17,19], than in crystals for which $\Delta V\# \approx V_{Me+}$.

The values of the activation volumes for silver-containing chalcogenide glass and, for example, silicate glass with a volume of migrating silver cation, allows one to clearly explain the higher electrical conductivity of chalcogenide glasses with ionic conductivity compared to other classes.

4. Conclusions

Based on a comprehensive study of the electrical and structural properties of chalcogenide glasses with different silver content, it was found that glasses of the As – Se – Ag system along the AsSe – Ag and $AsSe_{1.5}$ – Ag sections have mixed ion-electronic conductivity, the magnitude, and the main carrier of which change in depending on the silver content. The study showed that at a silver concentration of more than 5 at.%, The main current carrier changes: predominantly electronic conductivity is replaced by predominantly ionic. In chalcogenide glasses, the activation volumes of the migration of silver ions are close in magnitude to the volumes of fluctuation microcavities and noticeably exceed the volume of the migrating Ag^+ ion, which allows us to conclude that there are no serious steric hindrances during their migration and the high electrical conductivity of glasses in the AsSe – Ag and $AsSe_{1.5}$ – Ag sections.

References
[1] Dubov M, Mezentsev V, Manshina AA, Sokolov IA, Povolotskiy AV, Petrov YV. Waveguide fabrication in lithium-niobo-phosphate glasses by high repetition rate femtosecond laser: route to non-equilibrium material's states. *Optical materials express.* 2014;4(6): 1197-1206.
[2] Man'Shina AA, Povolotskiĭ AV, Sokolov IA, Kurushkin MV. The formation of optical phase structures in the volume of phosphate glasses by means of thermal diffusion caused by the action of femtosecond laser radiation. *Journal of Optical Technology.* 2015;82(2): 120-126.
[3] He X, Fan C, Poumellec B, Liu Q, Zeng H, Brisset F, Chen G, Zhao X, Lancry M. Size-controlled oriented crystallization in SiO 2-based glasses by femtosecond laser irradiation. *JOSA B.* 2014;31(2): 376-381.
[4] Vasileva AA, Nazarov IA, Olshin PK, Povolotskiy AV, Sokolov IA, Manshina AA. Structural features of silver-doped phosphate glasses in zone of femtosecond laser-induced modification. *Journal of Solid State Chemistry.* 2015;230: 56-60.

[5] Ha S. *Advancing single-molecule instrumentation through nanoscale optics, fabrication, and surface functionalization (Doctoral dissertation).* Delft University of Technology; 2018.

[6] Glezer EN, Milosavljevic M, Huang L, Finlay RJ, Her TH, Callan JP, Mazur E. Three-dimensional optical storage inside transparent materials. *Optics letters*. 1996;21(24): 2023-2025.

[7] Povolotsky AV. *Processes due to laser-induced excitation of electrons and their migration in systems with discrete and band energy spectrum. (Doctoral dissertation)*. St. Petersburg state university; 2017.

[8] Markov VA, Sokolov I, Bozhko M, Kovalenko E. Ionic Seebeck Effect in Alkali Niobophosphate Glasses. *InKey Engineering Materials*. 2019;822: 818-823.

[9] Borisova Z. *Glassy semiconductors*. Springer; 2013.

[10] Borisova ZU, Rykova TS. Some features of glass-forming in the Silver-Arsenic-Selenium system. *The Soviet Journal of Glass Physics and Chemistry*. 1977;3(6): 537. (In Russian)

[11] Zhabrev VA, Kazakova EYu. Study of electrical conductivity and diffusion in chalcogenide glasses containing silver. *The Soviet Journal of Glass Physics and Chemistry*. 1982;8(1): 51-55. (In Russian)

[12] Sokolov IA. *Glassy solid electrolytes. Structure and nature of conductivity.* Publishing house of the St. Petersburg State Polytechnic University; 2010. (In Russian)

[13] Gurevich YY, Kharkats YI. Features of the thermodynamics of superionic conductors. *Soviet Physics Uspekhi*. 1982;25(4): 257. (In Russian)

[14] Evstropiev KK. *Diffusion processes in glass*. Leningrad; 1970. (In Russian)

[15] Pronkin AA, Murin IV, Sokolov IA. Development of the RL Muller model of the microheterogeneous structure of glass and its application for various glass types. *Glass Physics and Chemistry*. 2015;41(1): 35-41. (In Russian)

[16] Nachtrieb NH, Lawson AW. Effect of Pressure on Self-Diffusion in White Phosphorus. *The Journal of Chemical Physics*. 1955;23(7): 1193-1195.

[17] Pronkin AA, Evstrop'ev KK, Murin IV, Veksler GI. Conduction mechanism in alkaline aluminofluorophosphate glasses. *The Soviet Journal of Glass Physics and Chemistry*. 1978;4(2): 202. (In Russian)

[18] Kolomiets BT, Raspopova EM. Effect of pressure on the electrical and photoelectric properties of amorphous and single-crystal As2Se3. *Phys*. 1970;4(1): 157-161. (In Russian)

[19] Sokolov IA, Glumov OV. On the influence of hydrostatic pressure on the electrical conductivity of metal-containing chalcogenide glasses. *The Soviet Journal of Glass Physics and Chemistry*. 1986;12(4): 406-11. (In Russian)

[20] Glasston S, Leidler K, Eyring G. *The theory of Rate Processes*. McGraw-Hill; 1941.

[21] Sanditov DS, Bartenev GM, Razumovskaya IV. On the mechanism of compaction of inorganic glasses under high pressure. In: *Glass and glassy coatings*. Riga; 1970. p.70-79.

[22] Sanditov DS, Mashanov AA. Fluctuation volume of amorphous materials in the model of delocalized atoms. *Technical Physics*. 2017;62(11): 1660-1666.

[23] Sanditov DS. Method of calculating the the volume of fluctuation microcavities in silicate glasses. *The Soviet Journal of Glass Physics and Chemistry*. 1977;3(6): 533. (In Russian)

[24] Sanditov DS, Damdinov DG. Volume of fluctuation microcavities, activation volume of viscous flow, and the molar volume of alkali silicate glasses. *The Soviet Journal of Glass Physics and Chemistry*. 1980;3: 208-214. (In Russian)

[25] Felz A .*Amorphous and glassy inorganic materials*. Moscow: Mir; 1986. (In Russian)

DEFORMATION OF A RECTANGULAR PLATE MEDIUM THICKNESS FROM ORTHOTROPIC DIFFERENTLY RESISTANT MATERIAL

A.A. Treschev, E.A. Zhurin[*]

Tula State University, Tula, Lenin Ave., 92, Russia

*e-mail: eazhurin@mail.ru

Abstract. The construction of a physically nonlinear model of deformation of a rectangular orthotropic plate of average thickness loaded with a transverse uniform distributed load is considered. This model is limited by the scope of small deflections. In the formulation and solution, not only the orthotropy of the plate material was taken into account, but also the nonlinear differential resistance, which was described using the equations of state, constructed using the normalized stress space. The plate fastening is presented in two versions: hinged support and rigid fastening along the contour. An algorithm for solving this class of problems was developed and implemented. A practical solution was made using the MATLAB software package.

Keywords: rectangular plate, rigid clamping, hinged support, orthotropic material, nonlinear resistance to resistance

1. Introduction

The development of science and technology has given impetus to the design of more complex, improved, and unique buildings, structures, machine parts, and apparatus. An example of this is modern research centers, sports stadiums, military equipment, and the aviation industry. In all these industries, materials are used whose properties don't obey the linear laws of mechanics. All these objects require careful calculation since the slightest error at the initial design stage can lead to serious accidents and death of people later.

For the error-free design of such structures, various calculation theories are developed and simplified models of objects are proposed. Also, more and more technologically advanced materials are used, for the calculation of which conventional (classical) models aren't enough, for example, a structural material, a composite of carbon fiber AVCO Mod 3a [35]. The desire to reduce the weight of the structure while improving its quality makes it necessary to use modern calculation methods in the design process. That is why the development of new and modernization of old models is an urgent task of modern structural mechanics and mechanics of a deformable solid.

The issue of calculating material with different resistance, and specifically plates made of them, was dealt with by many researchers: S.A. Ambartsumyan [1-5], R.M. Jones [6-9], C.W. Bert [10-13], A.A. Zolochevsky [14-21], Lomakin E.V. [22-23], A.V. Berezin [24], N.M. Matchenko [26] and A.A. Treschev [25,27-32].

So S.A. Ambartsumyan in his works [1-3] proposed simple constitutive relations in the form of equations of state with tangential-linear dependencies between the principal stresses and deformations, and the question of the relations between shear stresses and shears wasn't

discussed. In his model, the field, the principal stresses are divided into regions of the first and second kind [4-5]. This model is similar in shape to the classical generalized Hooke's law of orthotropic material, but the elastic moduli and transverse strain coefficients in the directions of the principal axes are determined separately from the experiments on axial tension (E_k^+, ν_{km}^+) and compression (E_k^-, ν_{km}^-). Direct application of the proposed relations is possible only in those cases when the distribution of the principal stresses by their signs at different points of the body is known in advance, as well as subject to model constraints on the constants arising from the symmetry condition of the compliance tensor.

In the model of R.M. Jones [6-9] featured symmetric weighted compliance matrices. Their symmetry was achieved by different signs of the principal stresses due to the introduction of weight coefficients into the off-diagonal components. They were pairwise ratios of the modules of principal stresses ($k_1 = |\sigma_1| / (|\sigma_1| + |\sigma_2|)$, $k_2 = |\sigma_2| / (|\sigma_1| + |\sigma_2|)$).

One of the simplest models of equations of state for materials with different resistance was proposed by K.V. Bert (C.W. Bert) [10-13]. This model is applicable to fibrous materials, where the components of the compliance matrix depend on the sign of the normal stresses arising in the direction of the fibers. When equal to 0 along the fibers of normal stresses, this theory ceases to be valid.

The most complex and controversial model was proposed by A.A. Zolochevsky [14-21]. He introduced equivalent stress, the second degree of which determines the deformation potential. The potential constants are "hidden" in the expressions that make up the equivalent stress. Equivalent stress is determined by the sum of linear and quadratic joint stress invariants. Due to the presence of irrationality in the equations for the relationship between stresses and strains, it isn't possible to single out the compliance matrix in a general form. The complexity of this model lies in the experimental determination of a many numbers of constants (which can't always be isolated from experiments in sufficient quantities). In particular, for an orthotropic material in the quasi-linear approximation, it is necessary to determine thirty-two constants, and from the simplest reference experiments (uniaxial tension and compression in the direction of the main orthotropic axes and at an angle of 45 ° to them) only eighteen can be established.

2. Methods

It is obvious that even a detailed analysis of the most well-known models of constitutive relations for anisotropic materials with different resistances indicates that these models aren't free from serious shortcomings and are based on individual hypotheses, often unfounded by experimental facts. In particular, E.V. Lomakin in [22-23] formulates the strain potential for anisotropic materials in the form of an energy function of the ratio of average stress to stress intensity $\xi = \sigma / \sigma_i$ (where $\sigma = \sigma_{ij} \cdot \delta_{ij} / 3$ – average stresses, $\sigma_i = \sqrt{1,5 S_{ij} S_{ij}}$ – average stresses; $S_{ij} = \sigma_{ij} - \delta_{ij} \sigma$ – components of the stress deviator; δ_{ij} – Kronecker symbol), multiplied by the convolution of the fourth rank compliance tensor with second rank stress tensors in the principal axes of material anisotropy. A serious drawback of the introduced relations is the emergence of uncertainties for the functional parameter of the ξ level $\pm\infty$, which was repeatedly pointed out in [24-26].

In the works of N.M. Matchenko and A.A. Trescheva [25-27] deformation potentials are constructed for anisotropic multi-resistive materials admitting quasi-linear approximation in nine-dimensional normalized stress space. In these works, equations of state of two levels of accuracy were obtained. Despite the rationality of this approach, the relations obtained are also not free from significant drawbacks, which for equations of the first level of accuracy are complex functional dependencies between uncorrelated constants of materials, and for

equations of the second level, there is an excessively large number of constants subject to experimental determination, which requires the involvement of experiments on complex stress conditions.

In subsequent works [28,31-32], a correcting formulation of the equations of state was carried out for a different class of anisotropic materials, both in quasilinear and nonlinear formulations. In the nonlinear model [29-30], equations of state are used, represented by the type of generalized Hooke's law for anisotropic materials by the type:

$$e_{km} = H_{kmpq}\left(\sigma_i, \alpha_{st}\right) \cdot \sigma_{pq}; \qquad H_{kmpq} = H_{pqkm}; \qquad k, m, q, p, s, t, = 1, 2, 3. \tag{1}$$

In particular, for an orthotropic material, these dependencies are presented as follows:

$$e_{11} = \left(A_{1111} + B_{1111} \cdot \alpha_{11}\right) \cdot \sigma_{11} + \left[A_{1122} + B_{1122} \cdot \left(\alpha_{11} + \alpha_{22}\right)\right] \cdot \sigma_{22} + \tag{2}$$

$$+ \left[A_{1133} + B_{1133} \cdot \left(\alpha_{11} + \alpha_{33}\right)\right] \cdot \sigma_{33};$$

$$e_{22} = \left[A_{1122} + B_{1122} \cdot \left(\alpha_{11} + \alpha_{22}\right)\right] \cdot \sigma_{11} + \left(A_{2222} + B_{2222} \cdot \alpha_{22}\right) \cdot \sigma_{22} + \tag{3}$$

$$+ \left[A_{2233} + B_{2233} \cdot \left(\alpha_{22} + \alpha_{33}\right)\right] \cdot \sigma_{33};$$

$$e_{33} = \left[A_{1133} + B_{1133} \cdot \left(\alpha_{11} + \alpha_{33}\right)\right] \cdot \sigma_{11} + \left[A_{2233} + B_{2233} \cdot \left(\alpha_{22} + \alpha_{33}\right)\right] \cdot \sigma_{22} + \tag{4}$$

$$+ \left(A_{3333} + B_{3333} \cdot \alpha_{33}\right) \cdot \sigma_{33};$$

$$2e_{12} = C_{1212}\left(\sigma_i\right) \cdot \tau_{12}; \tag{5}$$

$$2e_{23} = C_{2323}\left(\sigma_i\right) \cdot \tau_{23}; \tag{6}$$

$$2e_{13} = C_{1313}\left(\sigma_i\right) \cdot \tau_{13}; \tag{7}$$

where $a_{ij} = \sigma_{ij} / S$; – normalized stresses in the principal axes of material anisotropy;

$S = \left(\sigma_{ij} \cdot \sigma_{ij}\right)^{0.5} = \sqrt{\sigma_{11}^2 + \sigma_{22}^2 + \sigma_{33}^2 + 2\left(\tau_{12}^2 + \tau_{23}^2 + \tau_{31}^2\right)}$ – total stress modulus (stress space norm);

$A_{ijkm}, B_{ijkm}, C_{ijkm}$, – nonlinear functions that determine the mechanical properties of the material.

For orthotropic bodies, the number of independent material functions reaches fifteen [31-32]. The representation of these functions that determine the properties of the material is carried out by approximating the experimental deformation diagrams under uniaxial tension and compression along the principal anisotropy axes and diagrams obtained for shear in three principal orthotropic planes by processing them in the Microcal Origin Pro 8.0 program (Microcal Software Inc.). In this case, for a structural orthotropic nonlinearly resistive composite material AVCO Mod 3a [35] are represented as follows:

$$A_{kkkk}\left(\sigma_i\right) = 0.5 \cdot \left[1 / E_k^+\left(\sigma_i\right) + 1 / E_k^-\left(\sigma_i\right)\right]; \tag{8}$$

$$B_{kkkk}\left(\sigma_i\right) = 0.5 \cdot \left[1 / E_k^+\left(\sigma_i\right) - 1 / E_k^-\left(\sigma_i\right)\right]; \tag{9}$$

$$A_{kkmm}\left(\sigma_i\right) = -0.5 \cdot \left[\frac{v_{km}^+\left(\sigma_i\right)}{E_m^+\left(\sigma_i\right)} + \frac{v_{km}^-\left(\sigma_i\right)}{E_m^-\left(\sigma_i\right)}\right]; \tag{10}$$

$$B_{kkmm}\left(\sigma_i\right) = -0.5 \cdot \left[\frac{v_{km}^+\left(\sigma_i\right)}{E_m^+\left(\sigma_i\right)} - \frac{v_{km}^-\left(\sigma_i\right)}{E_m^-\left(\sigma_i\right)}\right]; \tag{11}$$

$$C_{kmkm}\left(\sigma_i\right) = 1 / G_{km}\left(\sigma_i\right); \tag{12}$$

$$E_k^\pm\left(\sigma_i\right) = a_k^\pm + m_k^\pm \cdot \sigma_i + n_k^\pm \cdot \sigma_i^2; \tag{13}$$

$$v_{km}^{\pm}\left(\sigma_i\right) = \lambda_{km}^{\pm} + \beta_{km}^{\pm} \cdot \sigma_i + \mu_{km}^{\pm} \cdot \sigma_i^2; \tag{14}$$

$$G_{km}\left(\sigma_i\right) = g_{km} + p_{km} \cdot \sigma_i + q_{km} \cdot \sigma_i^2; \tag{15}$$

where $a_k^{\pm}$, $m_k^{\pm}$, $n_k^{\pm}$, $\lambda_{km}^{\pm}$, $\beta_{km}^{\pm}$, $\mu_{km}^{\pm}$, g_{km}, p_{km}, q_{km} – constants of nonlinear material functions, determined by processing experimental deformation diagrams by the least-squares method and presented in Table 1.

This model of a nonlinear orthotropic resistive material [28,31] is currently the least controversial, gives the results as close as possible to the experimental data, and therefore is used here as the basis for constructing a method for calculating plates.

The nonlinear properties of such materials manifest themselves already at the elastic stage of deformation, and this significantly affects the stress distribution with a further increase in the load. It isn't possible to describe the process of deformation of a plate made of similar materials by ordinary linear functions with the required degree of accuracy, and especially in a complex stress state, which is realized within the framework of transverse bending.

We consider the elastic equilibrium of a rectangular single-layer plate, referred to the Cartesian coordinate system (the X_1 axis is along the long side of the plate, the X_2 axis is along the short side of the plate, and the X_3 axis is along the plate thickness). At an arbitrary point on the plate, one of the symmetry planes is parallel to the median surface, and the other two are perpendicular to the coordinate lines: $x_1 = const$, $x_2 = const$.

Two options for supporting the plate along the contour are considered:
- plate with rigidly clamped contours in accordance with Figure 1a;
- the plate is hingedly supported along the contours in accordance with Fig. 1b.
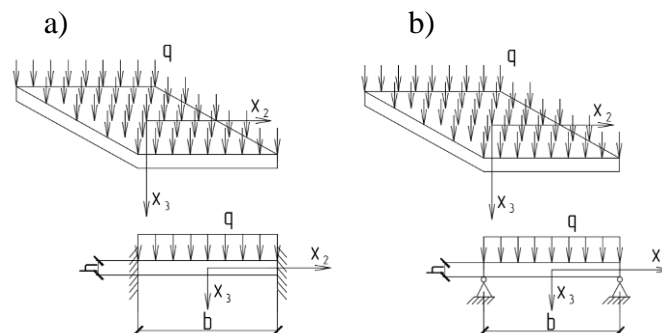
Fig. 1. Design diagram of a rectangular plate with two types of support:
a) with rigidly clamped contours; b) with hingedly supported contours

Table 1. Constants of composite material AVCO Mod 3a [35]

Sample test type	Technical parameter	1st element of nonlinear function	2nd element of nonlinear function	3rd element of nonlinear function
Uniaxial tension along the principal axes of orthotropy	$E_k^+\left(\sigma_i\right)$, Pa	α_1^+	m_1^+	n_1^+
		$1.058\cdot10^{-10}$	62.829	$1.535\cdot10^{-6}$
		α_2^+	m_2^+	n_2^+
		$2.864\cdot10^{-10}$	-105.476	$5.893\cdot10^{-7}$
		α_3^+	m_3^+	n_3^+
		$2.301\cdot10^{-10}$	88.349	$3.711\cdot10^{-6}$
	$v_{km}^+\left(\sigma_i\right)$	λ_{12}^+	β_{12}^+	μ_{12}^+

Sample test type	Technical parameter	1st element of nonlinear function	2nd element of nonlinear function	3rd element of nonlinear function
		0.158	$-3.106\cdot10^{-9}$	$2.192\cdot10^{-17}$
		λ_{21}^{+}	β_{21}^{+}	μ_{21}^{+}
		0.103	$-1.79\cdot10^{-9}$	$9.106\cdot10^{-18}$
		λ_{13}^{+}	β_{13}^{+}	μ_{13}^{+}
		0.203	$2.15\cdot10^{-9}$	$6.148\cdot10^{-17}$
		λ_{23}^{+}	β_{23}^{+}	μ_{23}^{+}
		0.104	$0.87\cdot10^{-10}$	$6.741\cdot10^{-17}$
		λ_{31}^{+}	β_{31}^{+}	μ_{31}^{+}
		0.146	$-0.146\cdot10^{-10}$	$6.971\cdot10^{-17}$
Uniaxial compression along the main axes of orthotropy	$E_k^{-}(\sigma_i)$, Pa	α_1^{-}	m_1^{-}	n_1^{-}
		$9.988\cdot10^{9}$	-12.943	$6.71\cdot10^{-7}$
		α_2^{-}	m_2^{-}	n_2^{-}
		$2.326\cdot10^{10}$	-436.81	$-6.077\cdot10^{-7}$
		α_3^{-}	m_3^{-}	n_3^{-}
		$5.14\cdot10^{9}$	-129.15	$-78.31\cdot10^{-6}$
	$\nu_{km}^{-}(\sigma_i)$	λ_{12}^{-}	β_{12}^{-}	μ_{12}^{-}
		0.118	$-1.457\cdot10^{-9}$	$2.136\cdot10^{-17}$
		λ_{21}^{-}	β_{21}^{-}	μ_{21}^{-}
		0.06	$1.77\cdot10^{-9}$	$2.947\cdot10^{-17}$
		λ_{13}^{-}	β_{13}^{-}	μ_{13}^{-}
		0.264	$-1.118\cdot10^{-9}$	$3.01\cdot10^{-17}$
		λ_{23}^{-}	β_{23}^{-}	μ_{23}^{-}
		0.189	$2.156\cdot10^{-9}$	$2.104\cdot10^{-17}$
		λ_{31}^{-}	β_{31}^{-}	μ_{31}^{-}
		0.134	$-0.457\cdot10^{-10}$	$5.819\cdot10^{-17}$
Offset in principal orthotropy planes	$G_{km}(\sigma_i)$, Pa	g_{12}	p_{12}	q_{12}
		$4.07\cdot10^{9}$	$-1{,}6$	$-8.38\cdot10^{-6}$
		g_{23}	p_{23}	q_{23}
		$1.723\cdot10^{9}$	16.899	$-1.1\cdot10^{-5}$
		g_{31}	p_{31}	q_{31}
		$2.43\cdot10^{9}$	-54.455	$-1.97\cdot10^{-5}$

For the posed problem, model assumptions, traditional for this class of problems, were introduced over the entire plate thickness [12,19,31] in the following formulation:

1) the normal to the median plane after deformation is rotated by an angle ψ_1 relative to the axis x_1 and by $-\psi_2$ relative to the axis x_2;

2) when determining the parameters of the stress state, the influence of normal stresses σ_3 due to their smallness, is neglected.

Based on the above assumptions, for the displacements of the plate points we have:

$$u_1(x_1, x_2, x_3) = u_1(x_1, x_2) + x_3 \cdot \psi_2(x_1, x_2); \qquad (16)$$

$$u_2(x_1, x_2, x_3) = u_1(x_1, x_2) + x_3 \cdot \psi_2(x_1, x_2); \tag{17}$$

$$u_3(x_1, x_2, x_3) = w(x_1, x_2); \tag{18}$$

where u_1, u_2, u_3 – mid-surface displacement; ψ_1, ψ_2 – angles of rotation of the plate sections relative to the axes; w – deflection.

In this case, the constitutive relations for a nonlinearly resistive orthotropic material (2-7), according to the adopted model, are represented as:

$$e_{11} = \left(A_{1111}(\sigma_i) + B_{1111}(\sigma_i) \cdot \alpha_{11}\right) \cdot \sigma_{11} + \left[A_{1122}(\sigma_i) + B_{1122}(\sigma_i) \cdot (\alpha_{11} + \alpha_{22})\right] \cdot \sigma_{22}; \tag{19}$$

$$e_{22} = \left[A_{1122}(\sigma_i) + B_{1122}(\sigma_i) \cdot (\alpha_{11} + \alpha_{22})\right] \cdot \sigma_{11} + \left(A_{2222}(\sigma_i) + B_{2222}(\sigma_i) \cdot \alpha_{22}\right) \cdot \sigma_{22}; \tag{20}$$

$$e_{33} = \left[A_{1133}(\sigma_i) + B_{1133}(\sigma_i) \cdot \alpha_{11}\right] \cdot \sigma_{11} + \left[A_{2233}(\sigma_i) + B_{2233}(\sigma_i) \cdot \alpha_{22}\right] \cdot \sigma_{22}; \tag{21}$$

$$2e_{12} = C_{1212}(\sigma_i) \cdot \tau_{12}; \tag{22}$$

$$2e_{13} = C_{1313}(\sigma_i) \cdot \tau_{13}; \tag{23}$$

$$2e_{23} = C_{2323}(\sigma_i) \cdot \tau_{23}; \tag{24}$$

where:

$$S = \sqrt{\sigma_{11}^2 + \sigma_{22}^2 + 2(\tau_{12}^2 + \tau_{23}^2 + \tau_{31}^2)} \; ; \tag{25}$$

$$\sigma_i = \sqrt{\sigma_{11}^2 - \sigma_{11}\sigma_{22} + \sigma_{22}^2 + 3(\tau_{12}^2 + \tau_{23}^2 + \tau_{31}^2)}; \tag{26}$$

$$C_{1111} = A_{1111}(\sigma_i) + B_{1111}(\sigma_i) \cdot \alpha_{11}; \tag{27}$$

$$C_{1122} = A_{1122}(\sigma_i) + B_{1122}(\sigma_i) \cdot (\alpha_{11} + \alpha_{22}); \tag{28}$$

$$C_{1133} = A_{1133}(\sigma_i) + B_{1133}(\sigma_i) \cdot \alpha_{11}; \tag{29}$$

$$C_{2222} = A_{2222}(\sigma_i) + B_{2222}(\sigma_i) \cdot \alpha_{22}; \tag{30}$$

$$C_{2233} = A_{2233}(\sigma_i) + B_{2233}(\sigma_i) \cdot \alpha_{22}; \tag{31}$$

$$D_{1212} = C_{1212}(\sigma_i); \quad D_{2323} = C_{2323}(\sigma_i); \quad D_{3131} = C_{3131}(\sigma_i). \tag{32}$$

Expressing stresses through deformations, taking into account the simplifying equations (8-15, 19-24, 27-32), after simple mathematical manipulations, we come to the following dependencies:

$$\sigma_{11} = D_{1111}\left(u_{1,1} - x_3 \cdot \psi_{2,1}\right) + D_{1122}\left(u_{2,2} - x_3 \cdot \psi_{1,2}\right); \tag{33}$$

$$\sigma_{22} = D_{1122}\left(u_{1,1} - x_3 \cdot \psi_{2,1}\right) + D_{2222}\left(u_{2,2} - x_3 \cdot \psi_{1,2}\right); \tag{34}$$

$$\tau_{12} = \frac{u_{1,2} + u_{2,1} - x_3 \cdot \left(\psi_{1,1} + \psi_{2,2}\right)}{D_{1212}}; \tag{35}$$

$$\tau_{23} = \frac{\left(\psi_2 + w_{,1}\right)}{D_{2323}}; \tag{36}$$

$$\tau_{31} = \frac{\left(\psi_1 + w_{,2}\right)}{D_{3131}}; \tag{37}$$

where:

$$D_{1111} = \frac{C_{2222}}{C_{1111} \cdot C_{2222} - C_{1122} \cdot C_{1122}}; \tag{38}$$

$$D_{1122} = \frac{C_{1122}}{C_{1111} \cdot C_{2222} - C_{1122} \cdot C_{1122}}; \tag{39}$$

$$D_{2222} = \frac{C_{1111}}{C_{1122} \cdot C_{1122} - C_{2222} \cdot C_{1111}}. \tag{40}$$

Deformations aren't explicitly included here, but they are easily calculated from the third equation of the system (19-24).

Taking into account that taking the new physical equations as a basis, we thus don't make changes in the dependences of the static-geometric nature, we represent the static conditions for a rectangular plate in a Cartesian coordinate system in the traditional form [12,19,31]:

$$N_{ij,j} = 0; \qquad Q_{k,k} = -q; \qquad M_{ij,j} - Q_i = 0. \tag{41}$$

Forces and moments are determined by integrating stresses (31-35) over the plate thickness:

$$N_{ij} = \int_{-h/2}^{h/2} \sigma_{ij} dx_3, \qquad (i,j = 1,2); \tag{42}$$

$$Q_k = \int_{-h/2}^{h/2} \tau_{k3} dx_3, \qquad (k = 1,2); \tag{43}$$

$$M_{ij} = \int_{-h/2}^{h/2} \sigma_{ij} \cdot x_3 dx_3, \qquad (i,j = 1,2). \tag{44}$$

Considering dependences (31-44) together, after some transformations, we obtain the resolving equations for bending of rectangular orthotropic plates of average thickness from a nonlinear material with different resistance:

$$\psi_{2,11} \cdot B_{1111} + \psi_{2,1} \cdot B_{1111,1} + \psi_{1,21} \cdot B_{1122} + \psi_{1,2} \cdot B_{1122,1} + u_{2,21} \cdot B_{1122} + u_{2,2} \cdot B_{1122,1} +$$
$$+u_{1,1} \cdot B_{1111,1} + u_{1,11} \cdot B_{1111} + 0,5 \cdot \psi_{1,12} \cdot B_{1212} +$$
$$+0,5 \cdot \psi_{1,1} \cdot B_{1212,2} + 0,5 \cdot \psi_{2,22} \cdot B_{1212} + 0,5 \cdot \psi_{2,2} \cdot B_{1212,2} + \tag{45}$$
$$+0,5 \cdot u_{1,12} \cdot D_{1212} + 0,5 \cdot u_{1,2} \cdot D_{1212,2} + 0,5 \cdot u_{2,12} \cdot D_{1212} + 0,5 \cdot u_{2,1} \cdot D_{1212,2} = 0;$$

$$\psi_{1,2} \cdot B_{2222,2} + \psi_{1,22} \cdot B_{2222} + \psi_{2,1} \cdot B_{1122,2} + \psi_{2,12} \cdot B_{1122} + u_{2,2} \cdot B_{2222,2} + u_{2,22} \cdot B_{2222} +$$
$$+u_{1,12} \cdot B_{1122} + u_{1,1} \cdot B_{1122,2} + 0,5 \cdot \psi_{1,1} \cdot B_{1212,1} +$$
$$+0,5 \cdot \psi_{1,11} \cdot B_{1212} + 0,5 \cdot \psi_{2,2} \cdot B_{1212,1} + 0,5 \cdot \psi_{2,21} \cdot B_{1212} + \tag{46}$$
$$+0,5 \cdot u_{1,2} \cdot D_{1212,1} + 0,5 \cdot u_{1,21} \cdot D_{1212} + 0,5 \cdot u_{2,1} \cdot D_{1212,1} + 0,5 \cdot u_{2,11} \cdot D_{1212} = 0;$$

$$0,5 \cdot \psi_2 \cdot D_{1313,1} + 0,5 \cdot \psi_{2,1} \cdot D_{1313} + 0,5 \cdot w_3 \cdot D_{1313,1} + 0,5 \cdot w_{,11} \cdot D_{1313} +$$
$$+0,5 \cdot w_1 \cdot D_{2323,2} + 0,5 \cdot w_{,2} \cdot D_{2323} + 0,5 \cdot w_{,22} \cdot D_{2323} + 0,5 \cdot w_{,2} \cdot D_{2323,2} = -q; \tag{47}$$

$$\psi_{2,11} \cdot K_{1111} + \psi_{2,1} \cdot K_{1111,1} + \psi_{1,21} \cdot K_{1122} + \psi_{1,2} \cdot K_{1122,1} + u_{2,21} \cdot B_{1122} +$$
$$+u_{2,2} \cdot B_{1122,1} + u_{1,11} \cdot B_{1111} + u_{1,1} \cdot B_{1111,1} +$$
$$+0,5 \cdot \psi_{1,1} \cdot K_{1212,2} + 0,5 \cdot \psi_{1,12} \cdot K_{1212} + 0,5 \cdot \psi_{2,22} \cdot K_{1212} + \tag{48}$$
$$+0,5 \cdot \psi_{2,2} \cdot K_{1212,2} + 0,5 \cdot u_{1,22} \cdot B_{1212} + 0,5 \cdot u_{1,2} \cdot B_{1212,2} +$$
$$+0,5 \cdot u_{2,1} \cdot B_{1212} + 0,5 \cdot u_{2,12} \cdot B_{1212,2} - 0,5 \cdot \psi_2 \cdot D_{1313} - 0,5 \cdot w_{,1} \cdot D_{1313} = 0;$$

$$\psi_{1,22} \cdot K_{2222} + \psi_{1,2} \cdot K_{2222,2} + \psi_{2,12} \cdot K_{1122} + \psi_{2,1} \cdot K_{1122,2} + u_{2,22} \cdot B_{2222} +$$

$+u_{2,2} \cdot B_{2222,2} + u_{1,12} \cdot B_{1122} + u_{1,1} \cdot B_{1122,2} +$

$+0,5 \cdot \psi_{1,11} \cdot K_{1212} + 0,5 \cdot \psi_{1,1} \cdot K_{1212,1} + 0,5 \cdot \psi_{2,21} \cdot K_{1212} +$ (49)

$+0,5 \cdot \psi_{2,2} \cdot K_{1212,1} + 0,5 \cdot u_{1,21} \cdot B_{1212} + 0,5 \cdot u_{1,2} \cdot B_{1212,1} +$

$+0,5 \cdot u_{2,11} \cdot B_{1212} + 0,5 \cdot u_{2,1} \cdot B_{1212,1} - 0,5 \cdot \psi_1 \cdot D_{2323} - 0,5 \cdot w_{,2} \cdot D_{2323} = 0.$

To solve the obtained equations (45-49), we use the finite-difference method with the approximation of the second order of accuracy [33-34]. This procedure is implemented in the MATLAB environment.

3. Results and discussion

The main calculation results are given for a plate with dimensions of 1.0×0.75×0.075 (a×b×h) m, under the action of a uniformly distributed load q=1.45 MPa. As a result of solving the problem posed for the transverse bending of a rigidly fixed (Figs. 2-19) and hingedly supported (Figs. 20-34) rectangular plate made of orthotropic nonlinear multi-resistive composite material AVCO Mod 3a [35], distributions of the main characteristics of the stress-strain state were obtained. Additionally, the effect of the load value on deflections and maximum moments in the plate was analyzed to demonstrate nonlinearity for various fixing options.

Rigidly clamped plate made of graphite AVCO Mod3a [35]
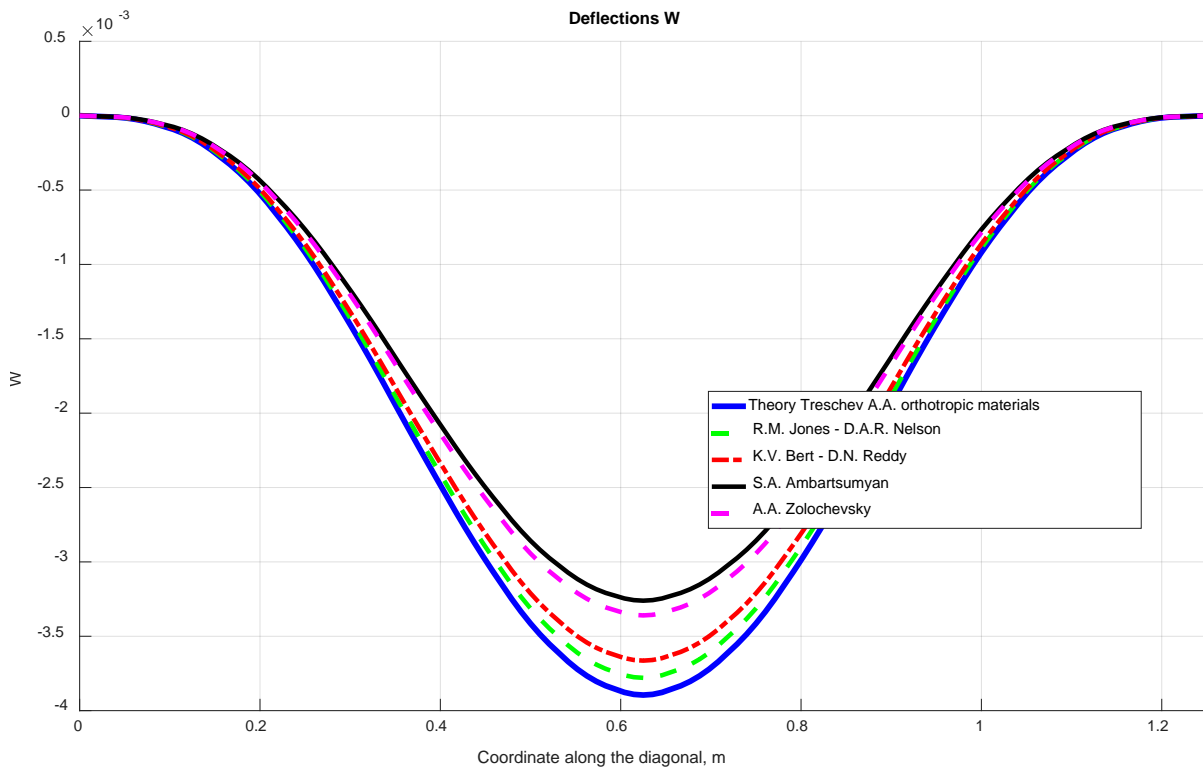
Fig. 2. Deflections W along the diagonal of the plate
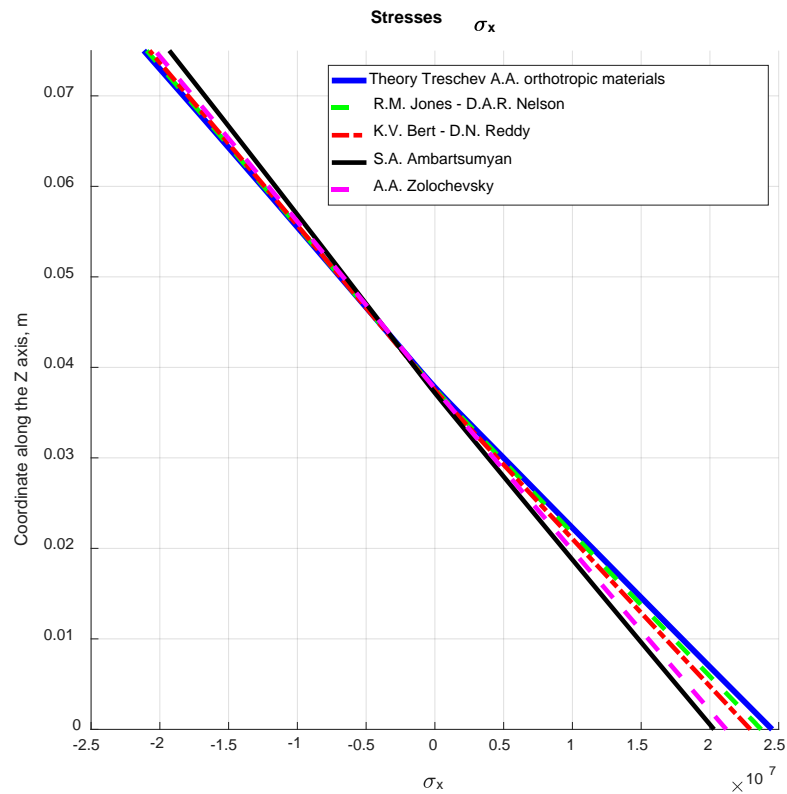
Fig. 3. Distribution of σ_x stresses over the plate thickness at point 0.5a 0.5b
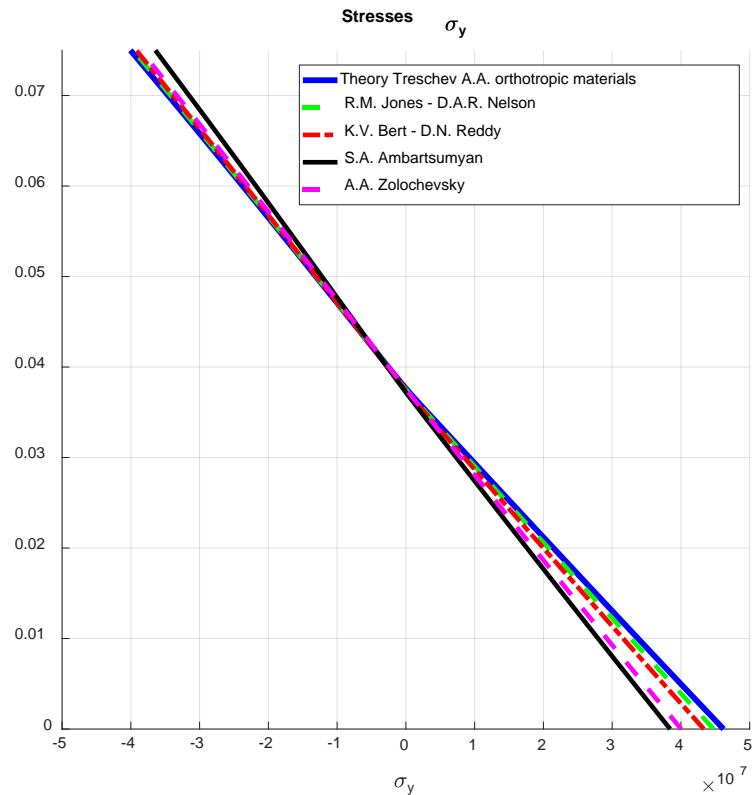
Fig. 4. Distribution of σ_y stresses over the plate thickness at point 0.5a 0.5b
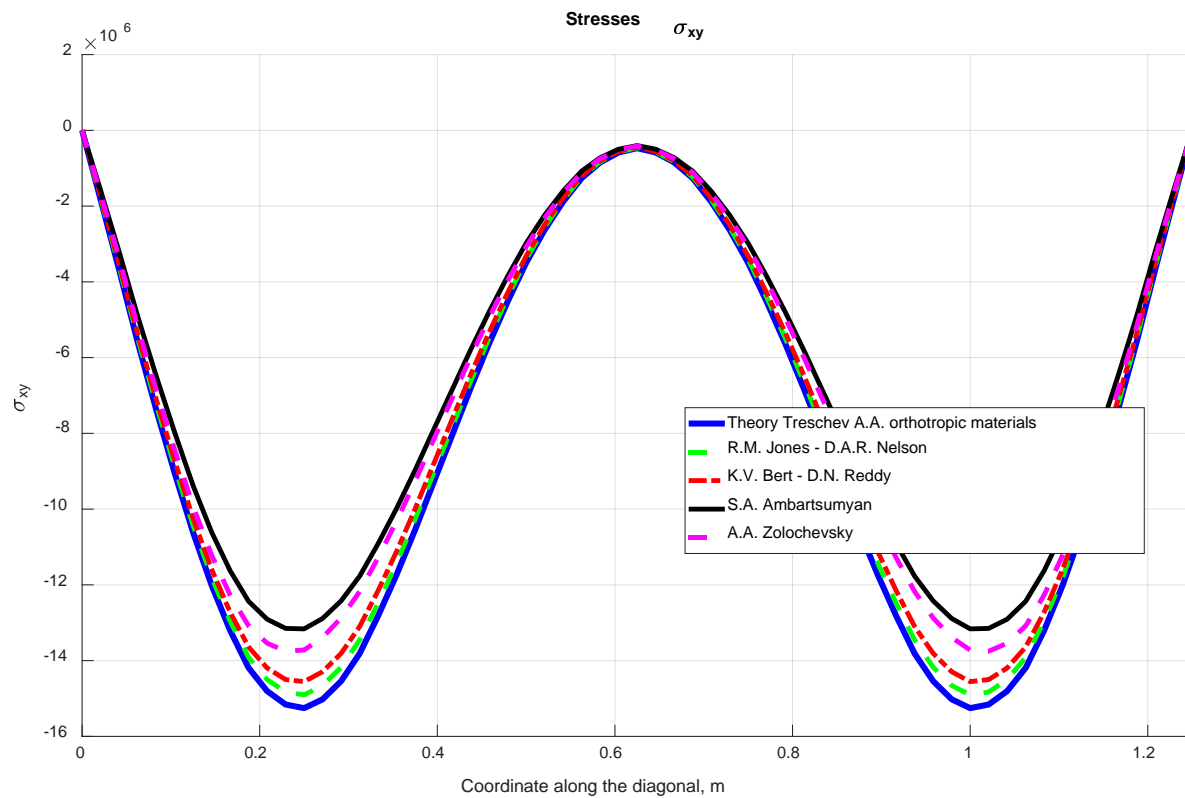
Fig. 5. Distribution of shear stresses σ_{xy} along the platinum diagonal in the lower section
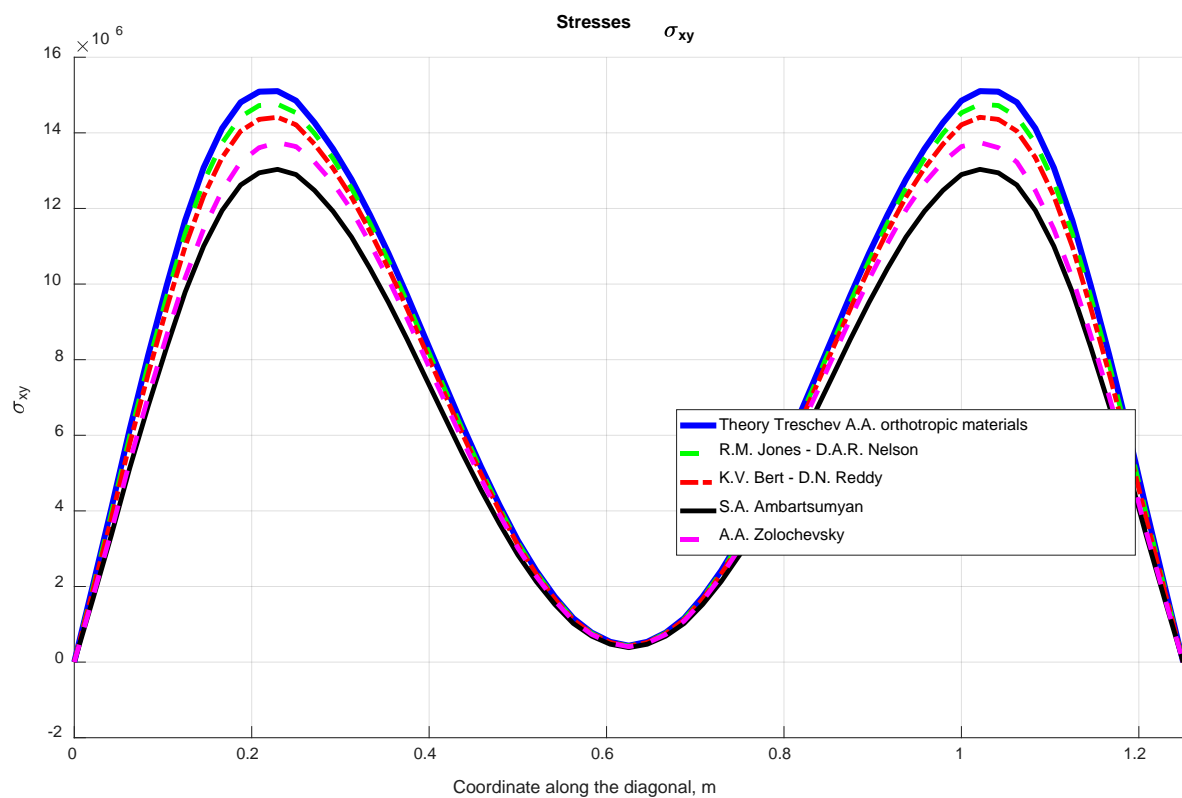
Fig. 6. Distribution of shear stresses σ_{xy} along the diagonal of platinum in the upper section
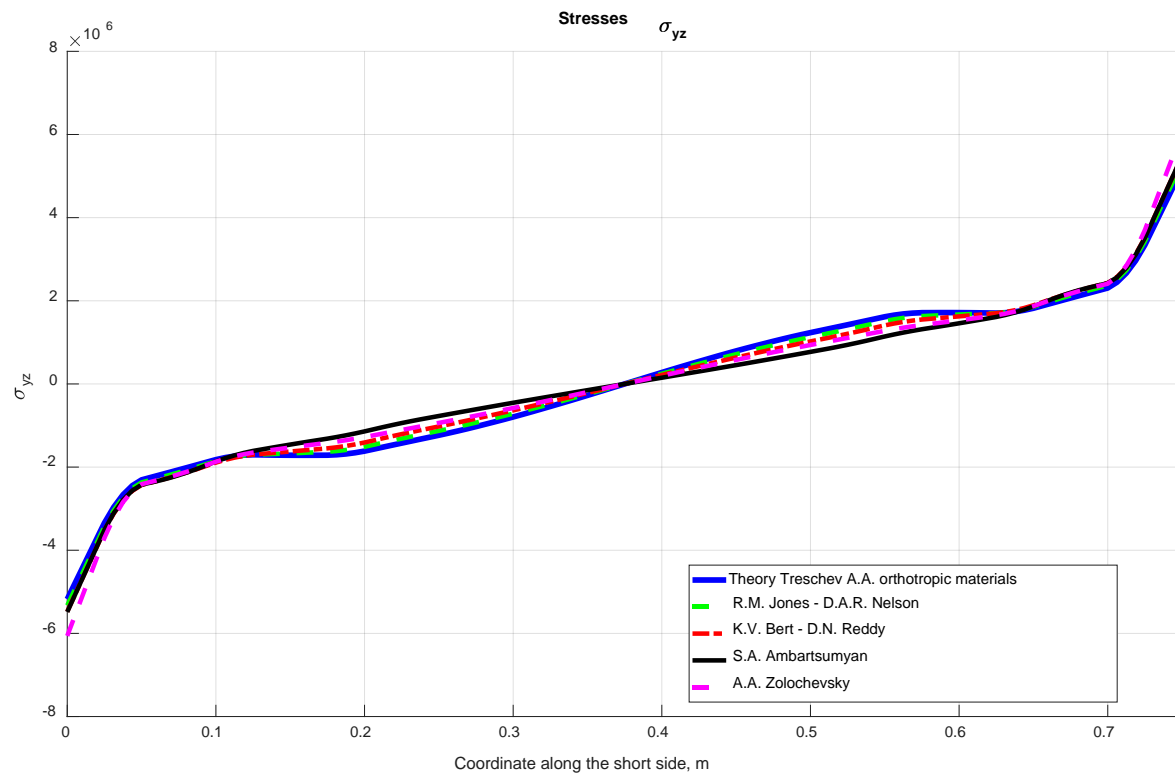
Fig. 7. Distribution of shear stresses σ_{yz} along the X_2 axis in the lower section
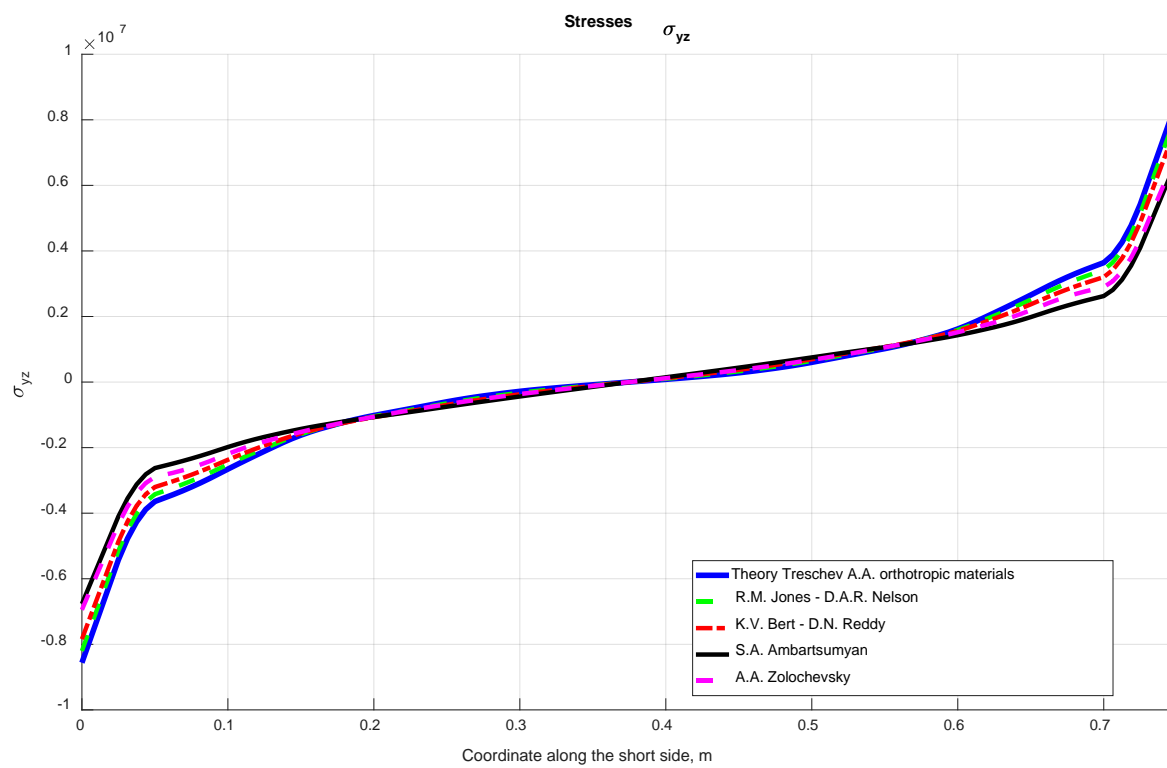
Fig. 8. Distribution of shear stresses σ_{yz} along the X_2 axis in the upper section
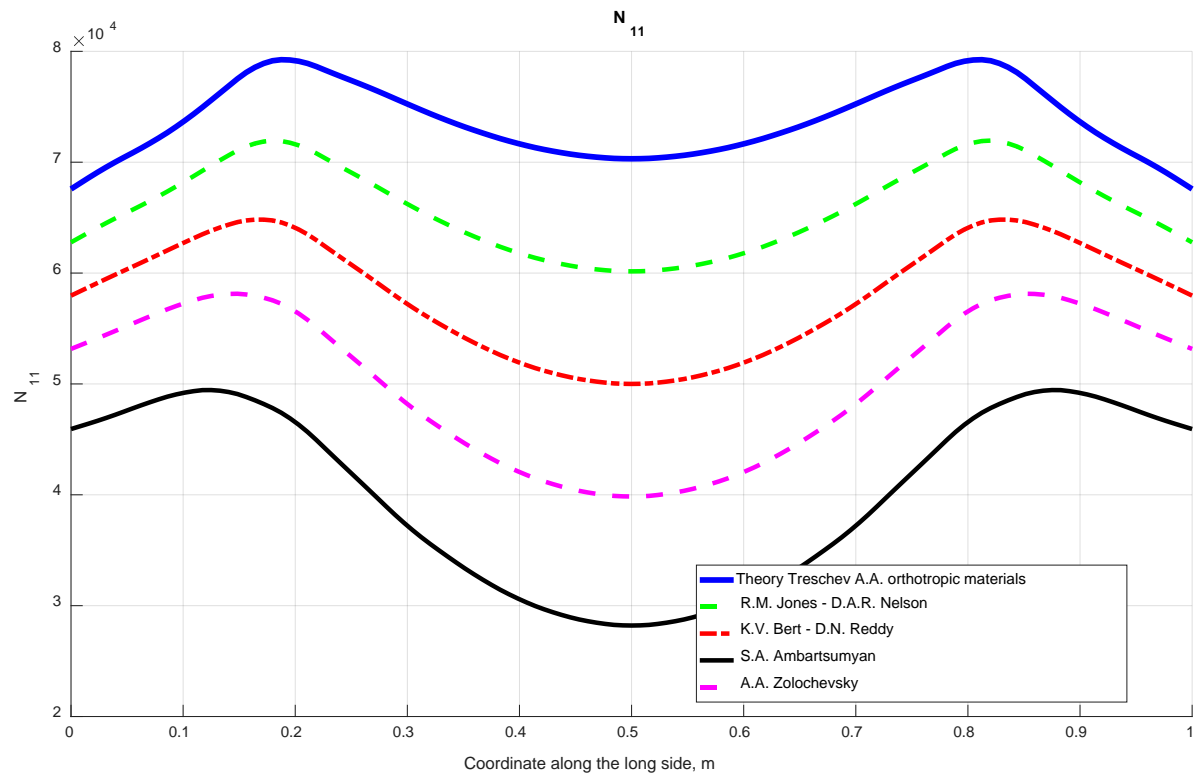
Fig. 9. Efforts N_{11} along the X_1 axis
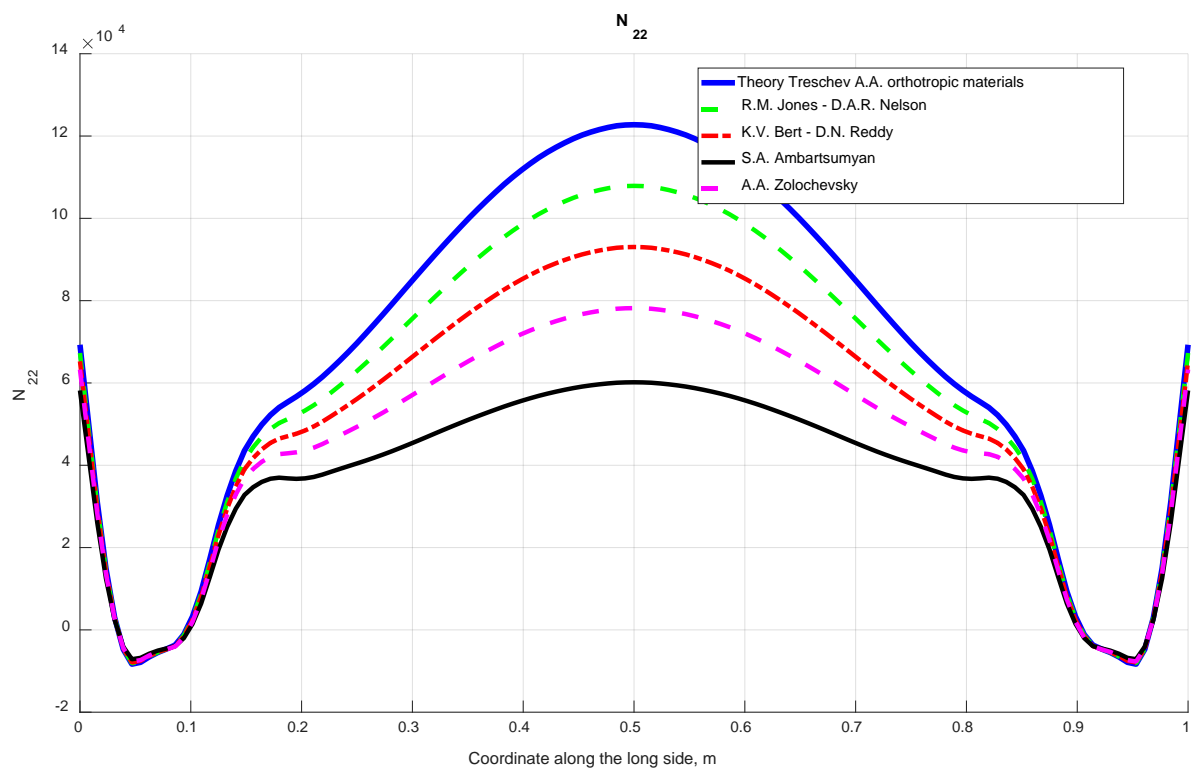
Fig. 10. Efforts N_{22} along the X_1 axis
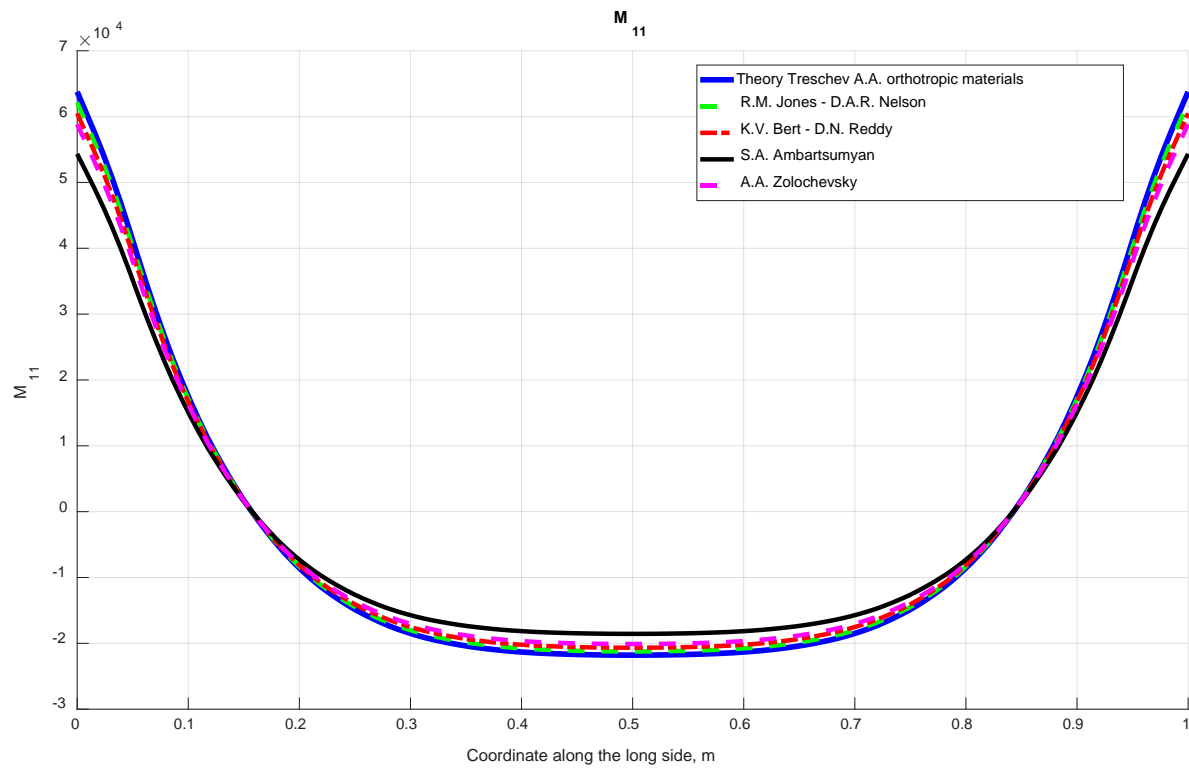
Fig. 11. Bending moment M_{11} along the X_1 axis
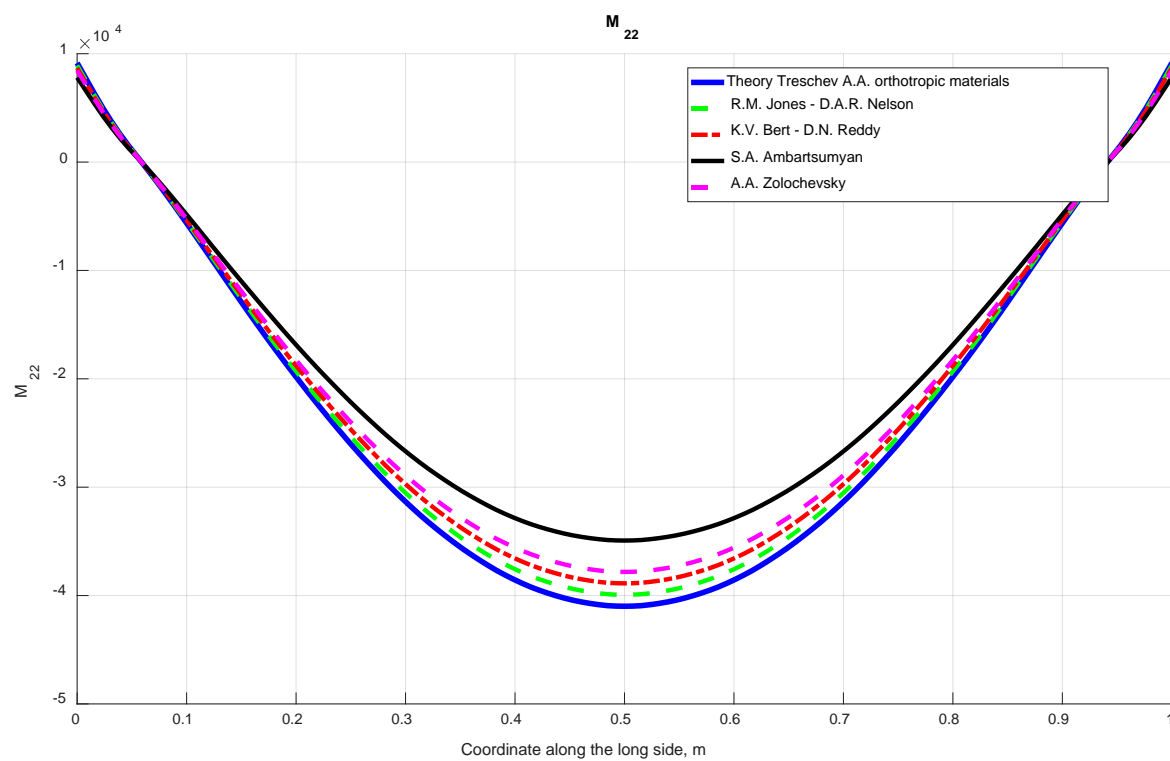
Fig. 12. Bending moment M_{22} along the X_1 axis
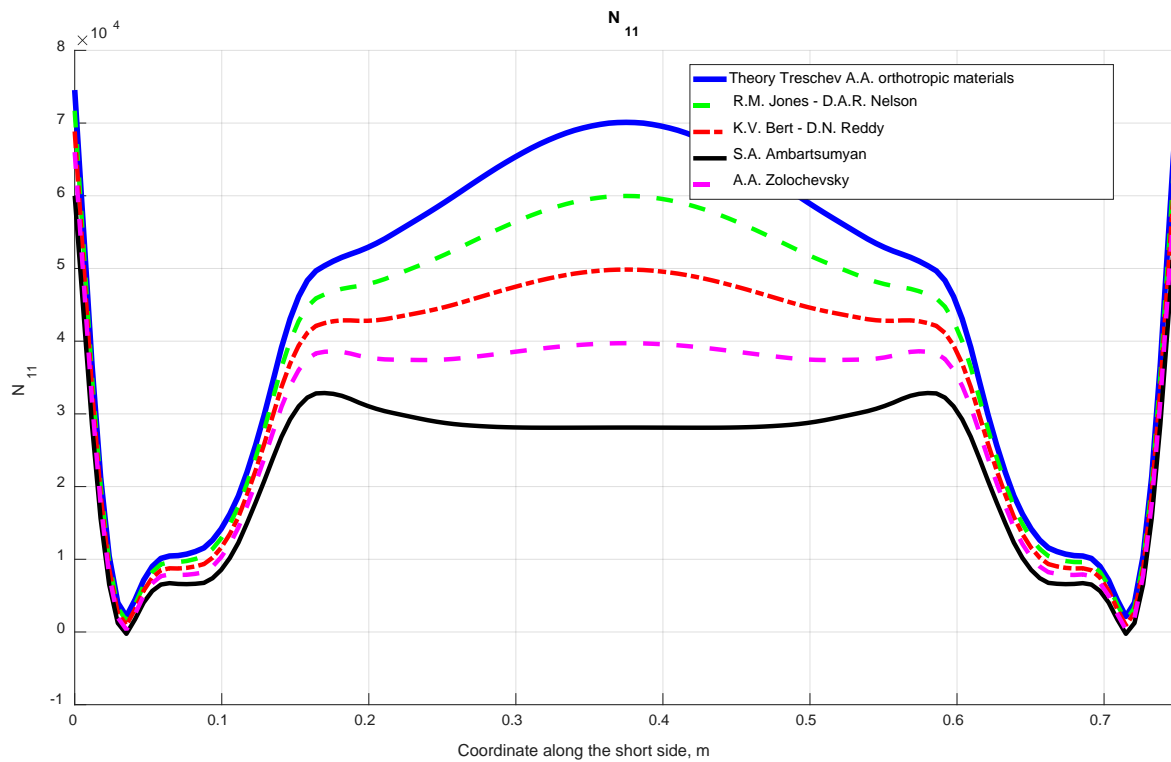
Fig. 13. Efforts N_{11} along the X_2 axis
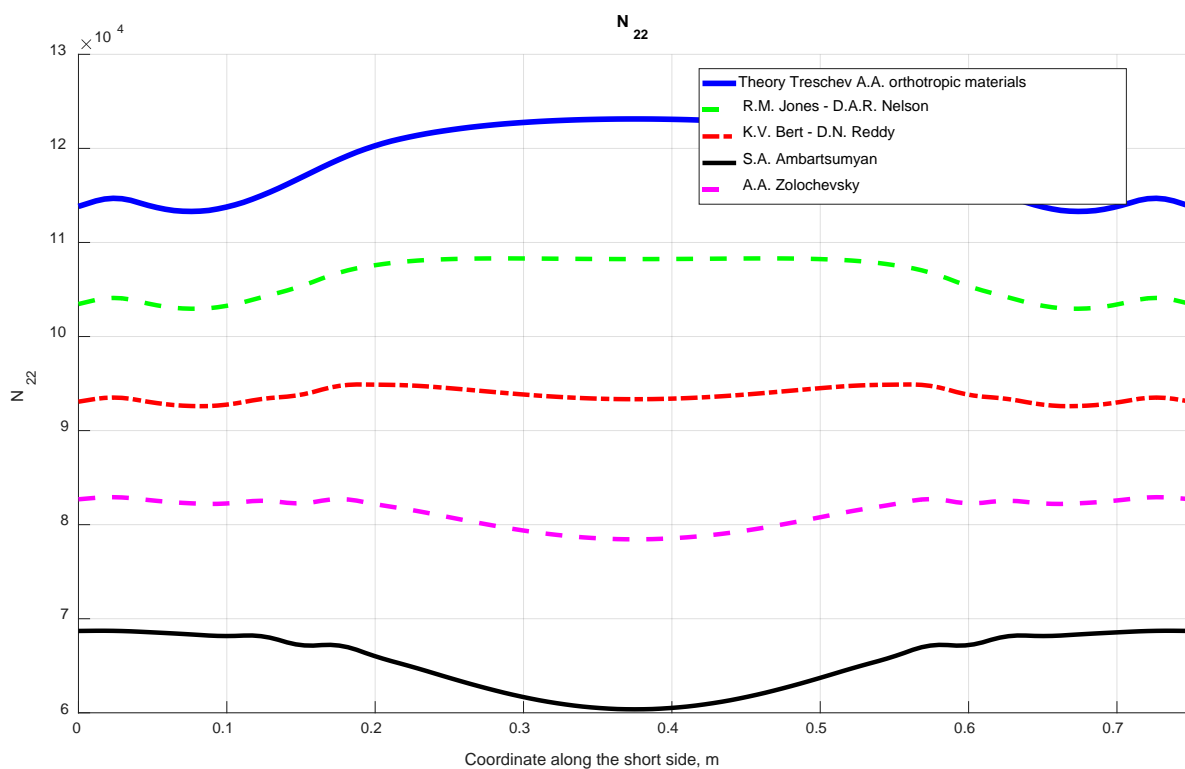
Fig. 14. Efforts N_{22} along the X_2 axis
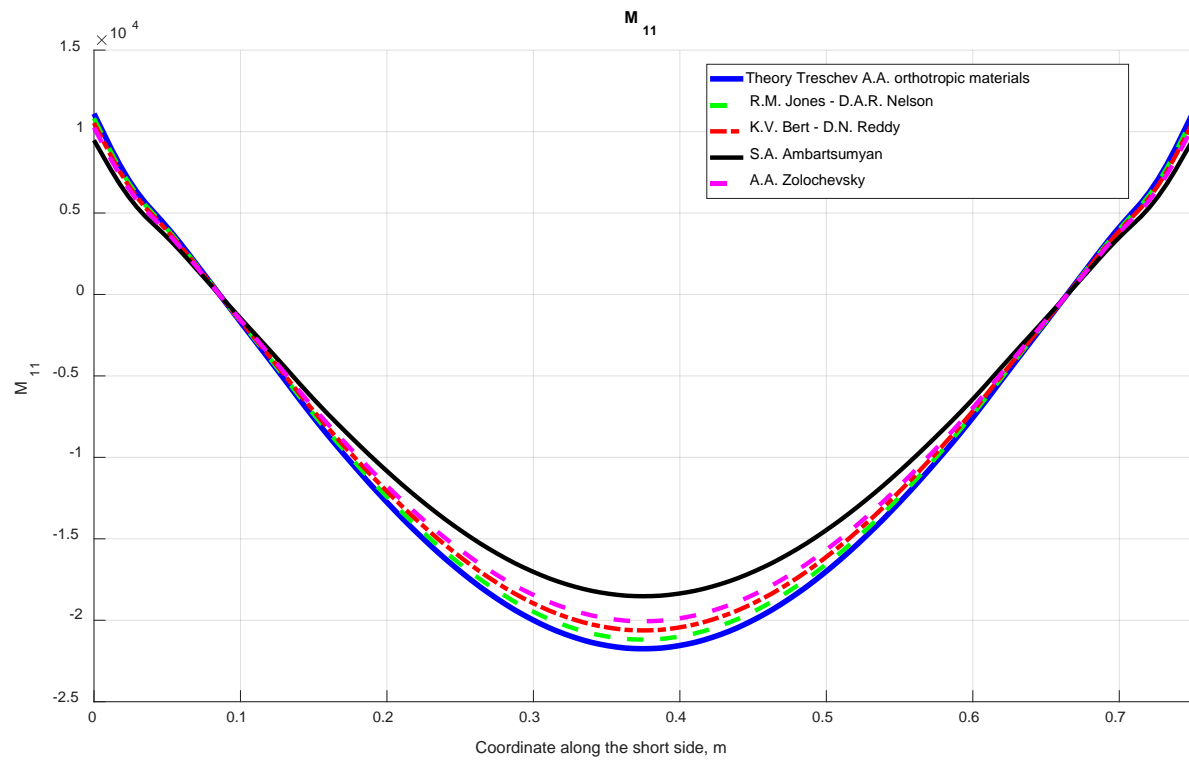
Fig. 15. Bending moment M_{11} along the X_2 axis
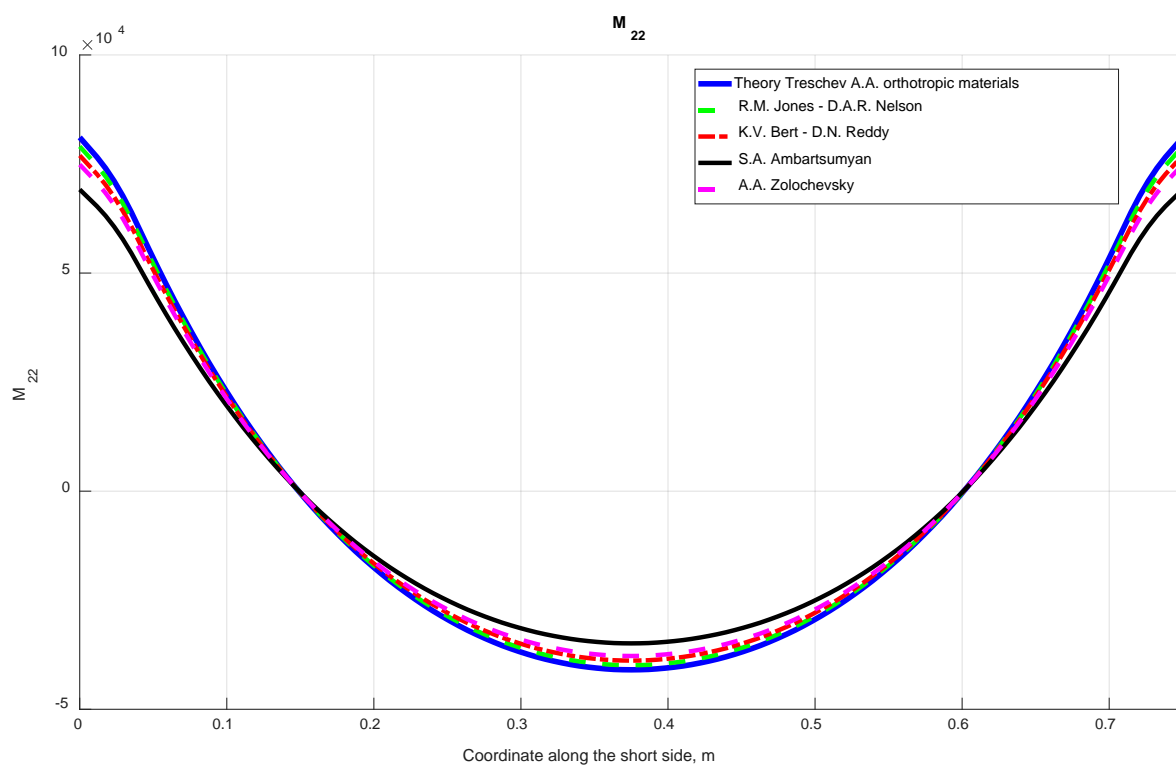
Fig. 16. Bending moment M_{22} along the X_2 axis
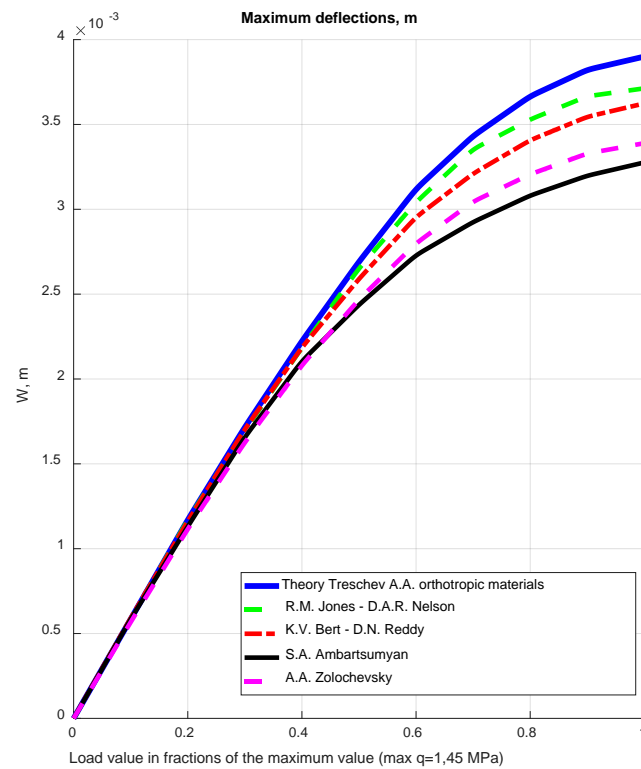
Fig. 17. Effect of load value on deflections
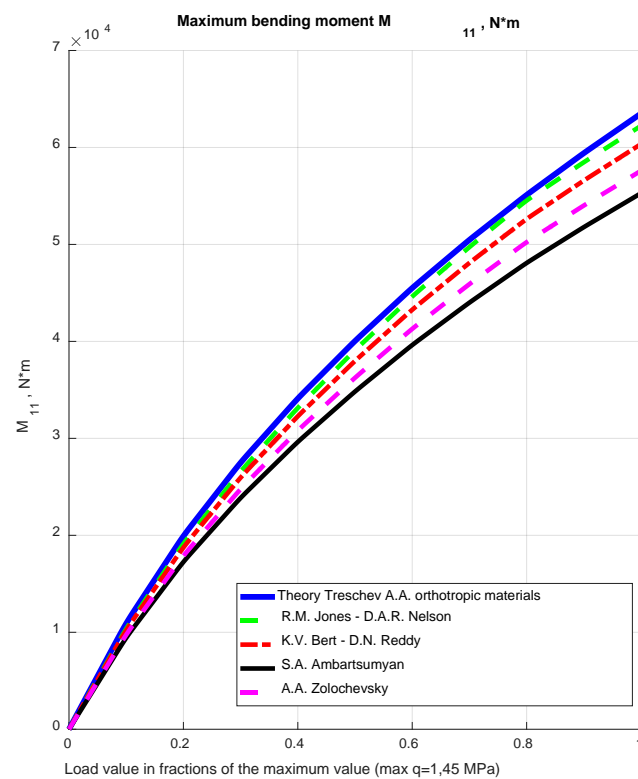
Fig. 18. Influence of the magnitude of the load on the maximum bending moment M_{11}
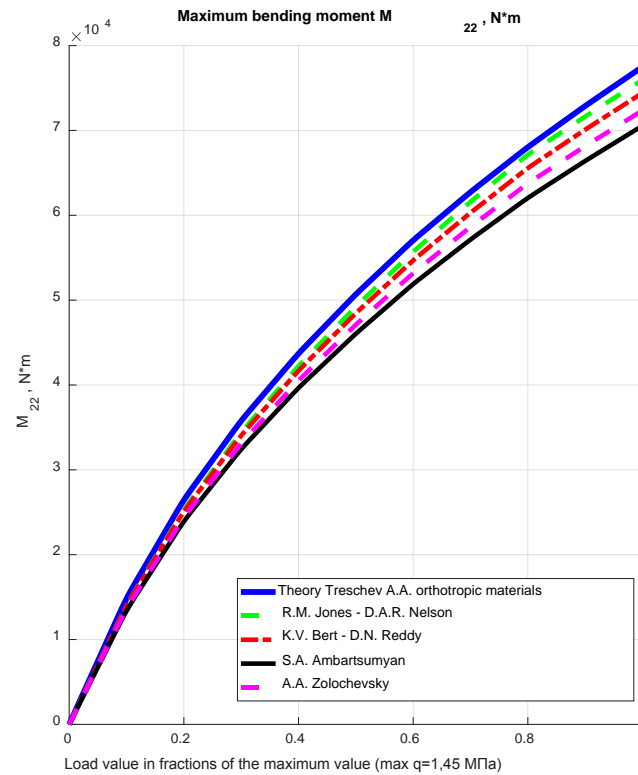
Fig. 19. Influence of the magnitude of the load on the maximum bending moment M_{22}

Freely supported plate made of graphite AVCO Mod3a
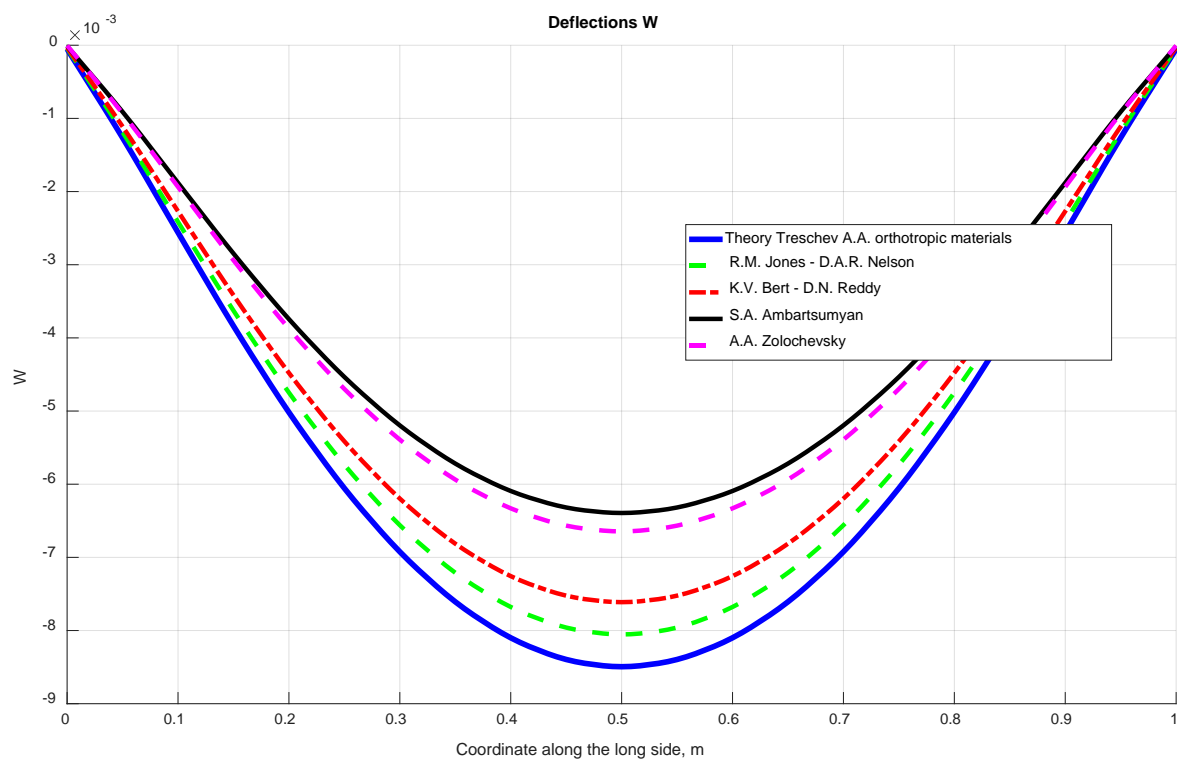
Fig. 20. Deflections W along the X_1 axis
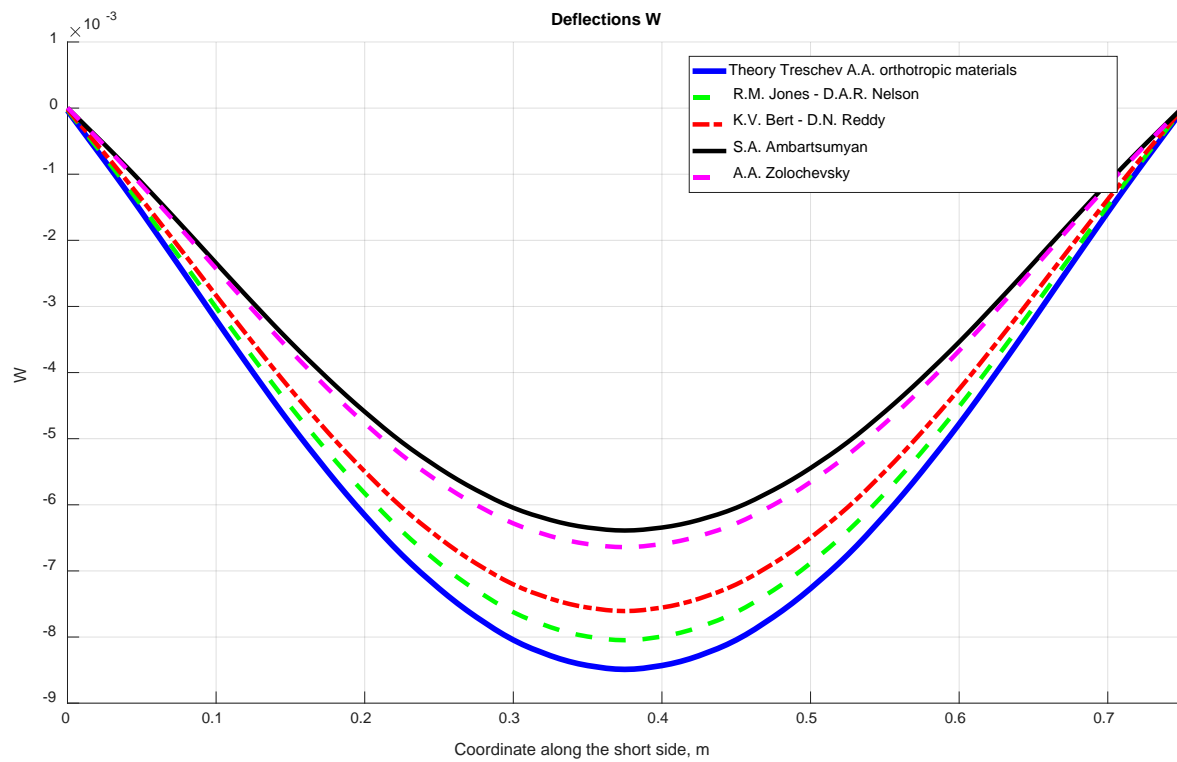
Fig. 21. Deflections W along the X_2 axis
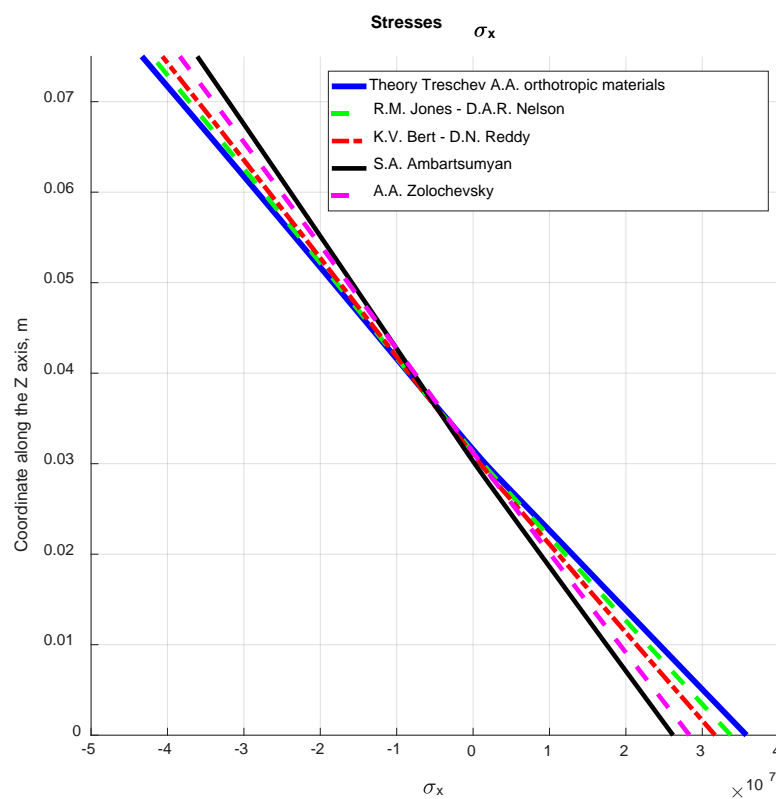
Fig. 22. Distribution of σ_x stresses over the plate thickness at point 0,5a 0,5b
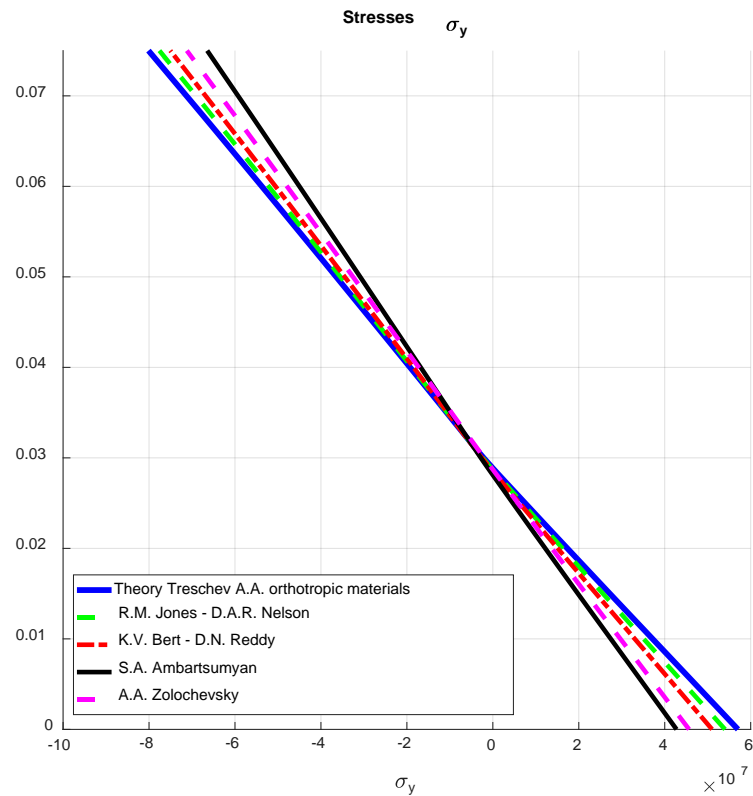
Fig. 23. Distribution of σ_y stresses over the plate thickness at point 0,5a 0,5b
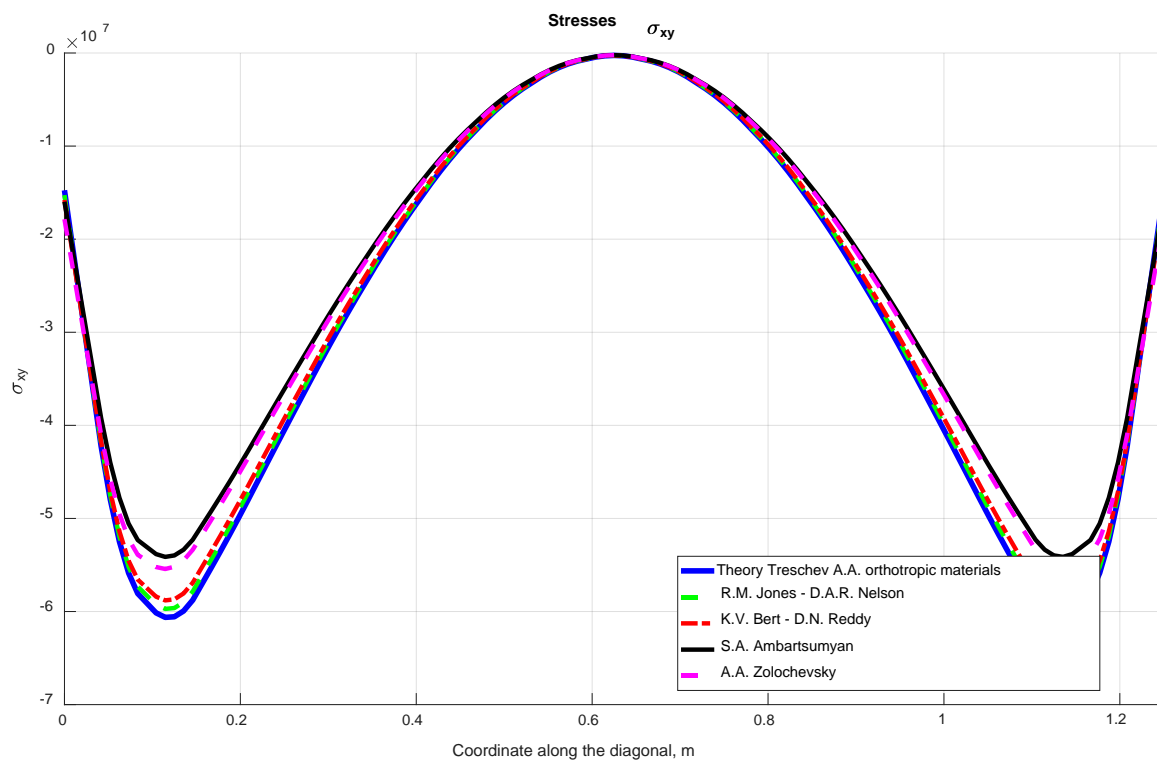
Fig. 24. Distribution of shear stresses σ_{xy} along the diagonal of platinum in the lower section
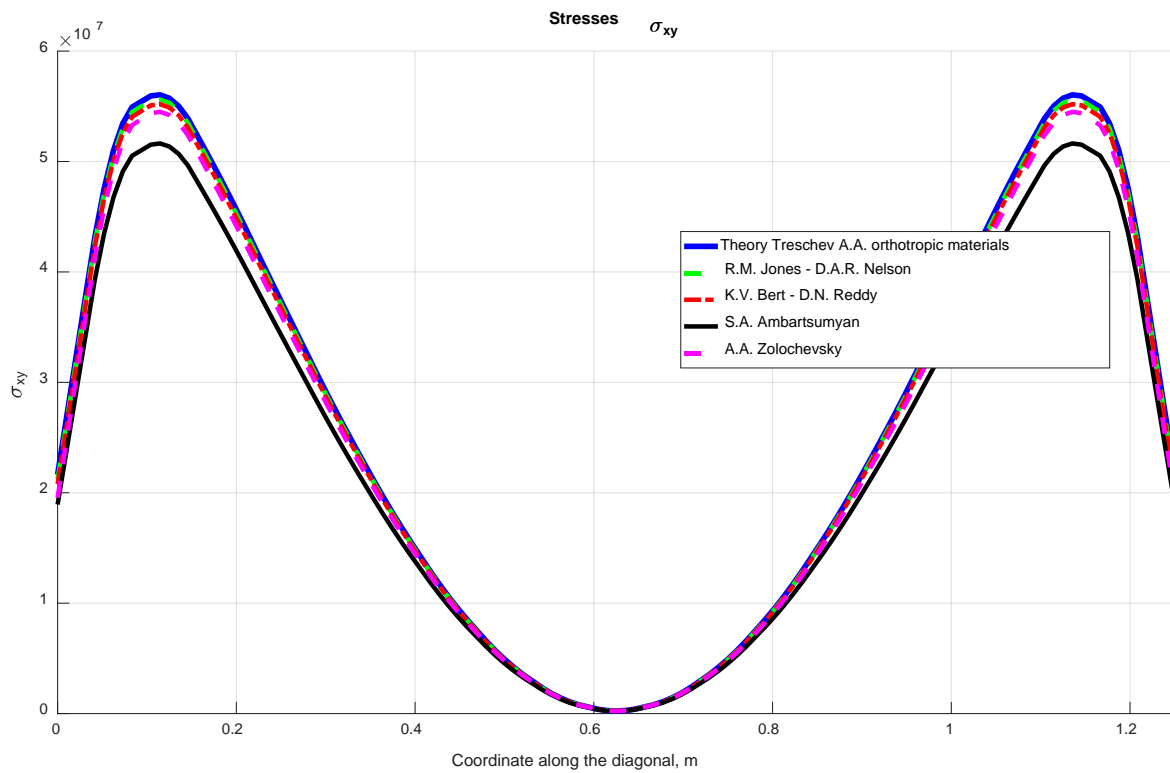
Fig. 25. Distribution of shear stresses σ_{xy} along the diagonal of platinum in the upper section
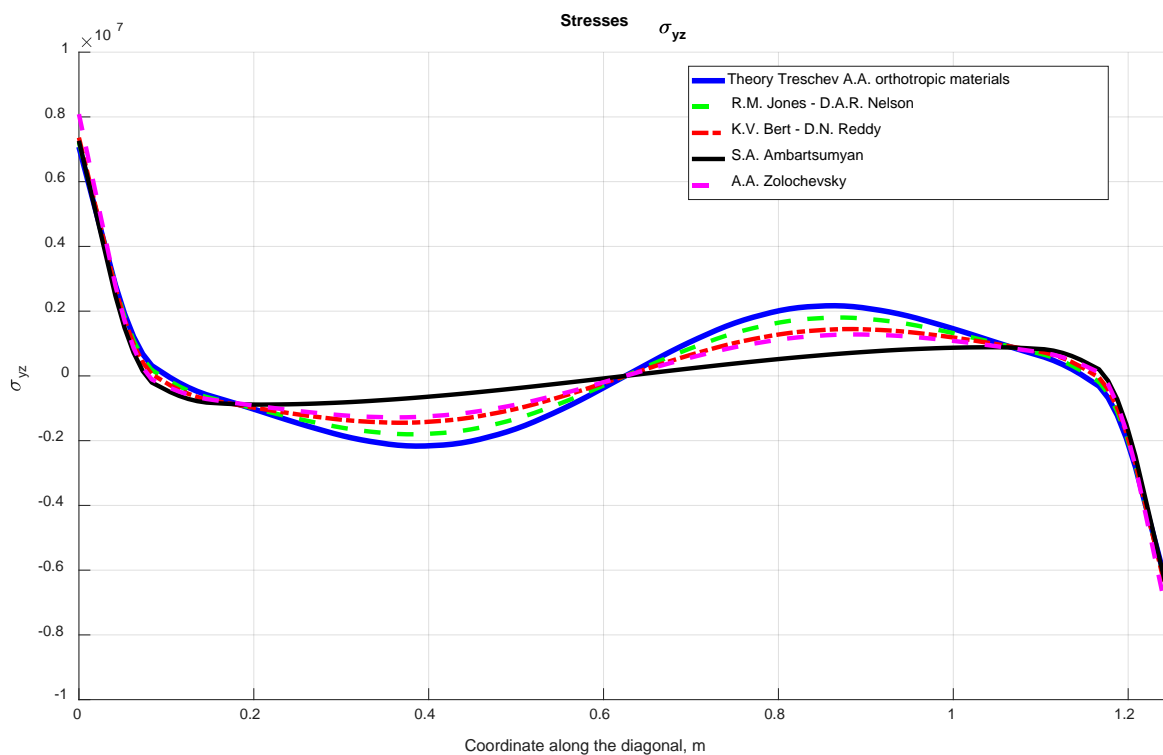
Fig. 26. Distribution of shear stresses σ_{yz} along the diagonal of the slab in the upper section
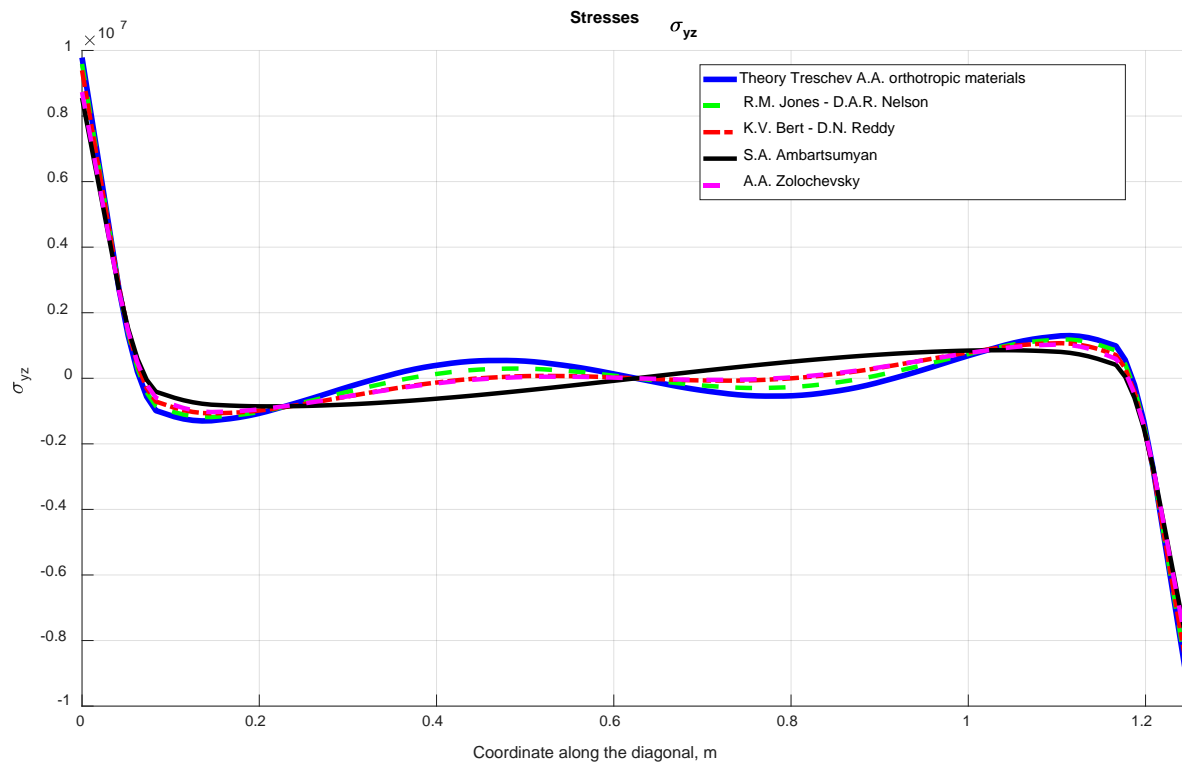
Fig. 27. Distribution of shear stresses σ_{yz} along the diagonal of the slab in the upper section
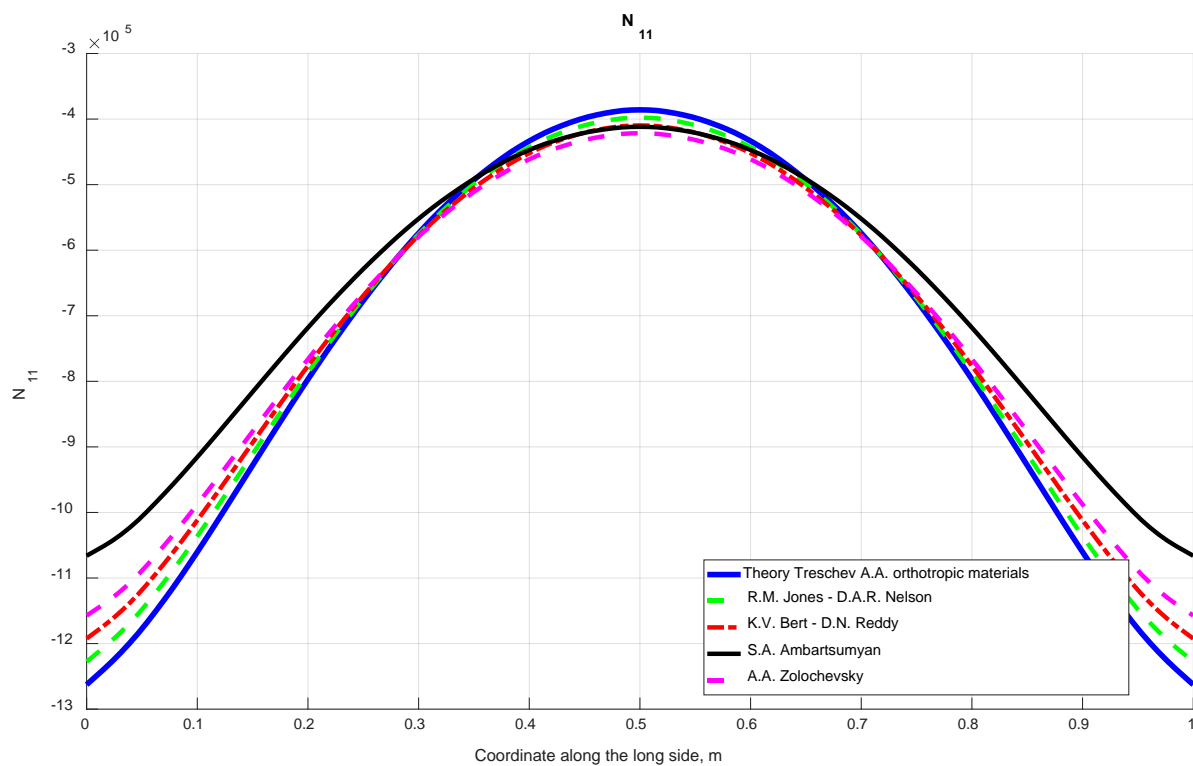
Fig. 28. Efforts N_{11} along the X_1 axis
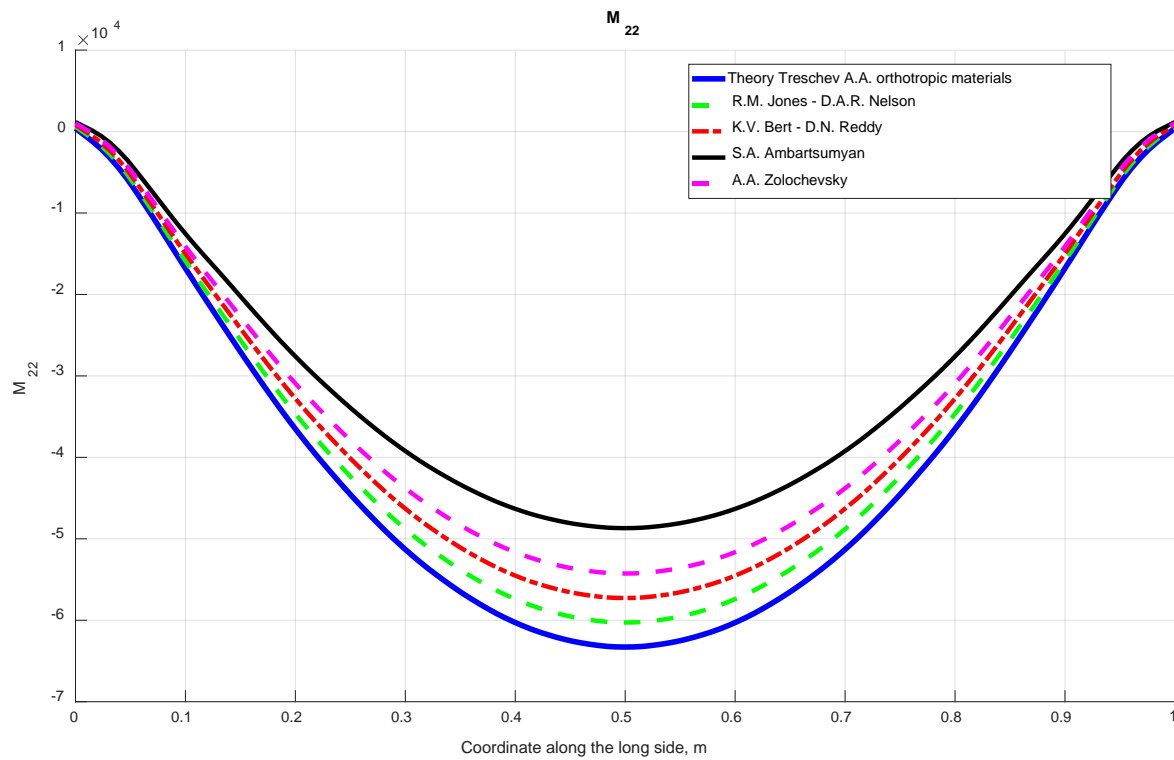
Fig. 29. Bending moment M_{22} along the X_1 axis
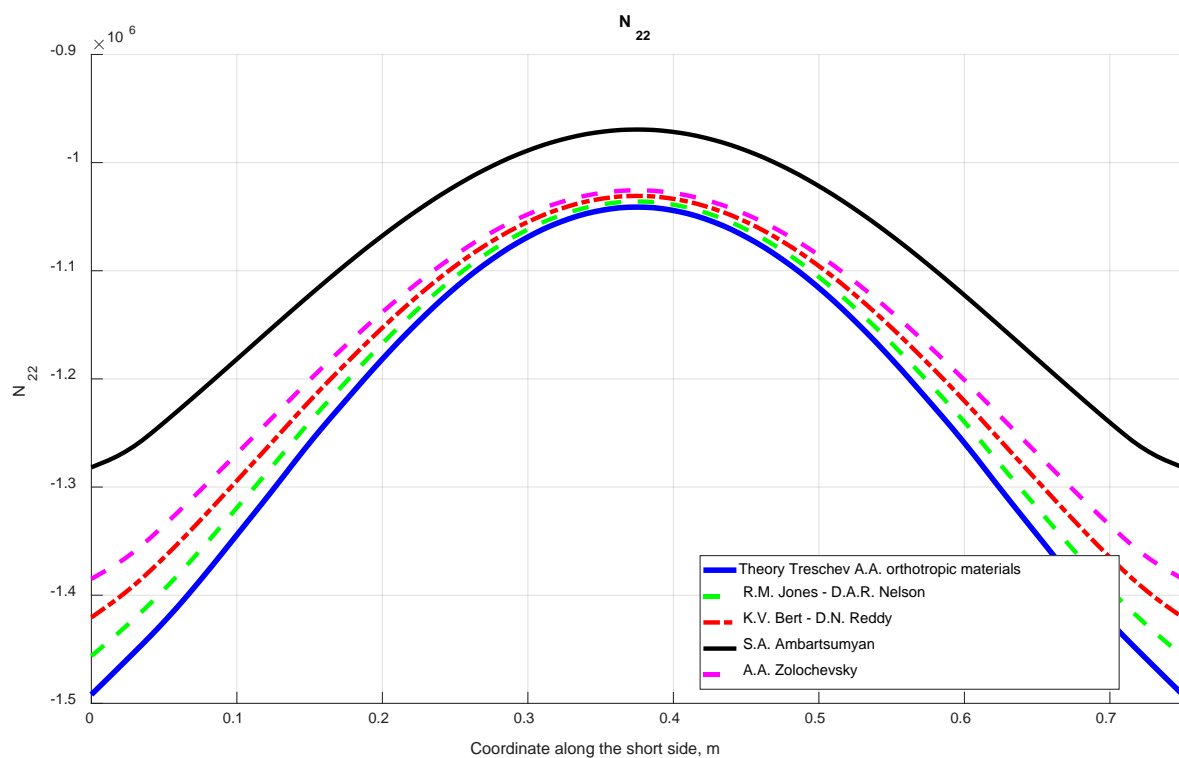
Fig. 30. Efforts N_{22} along the X_2 axis
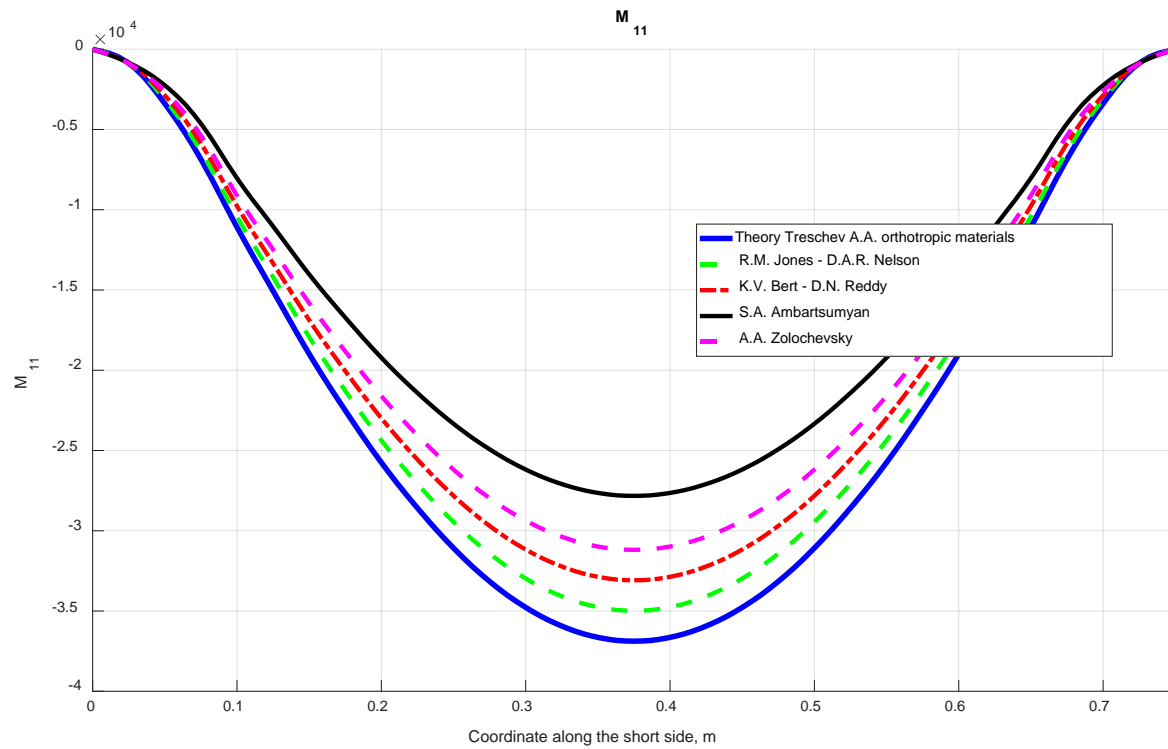
Fig. 31. Bending moment M_{11} along the X_2 axis
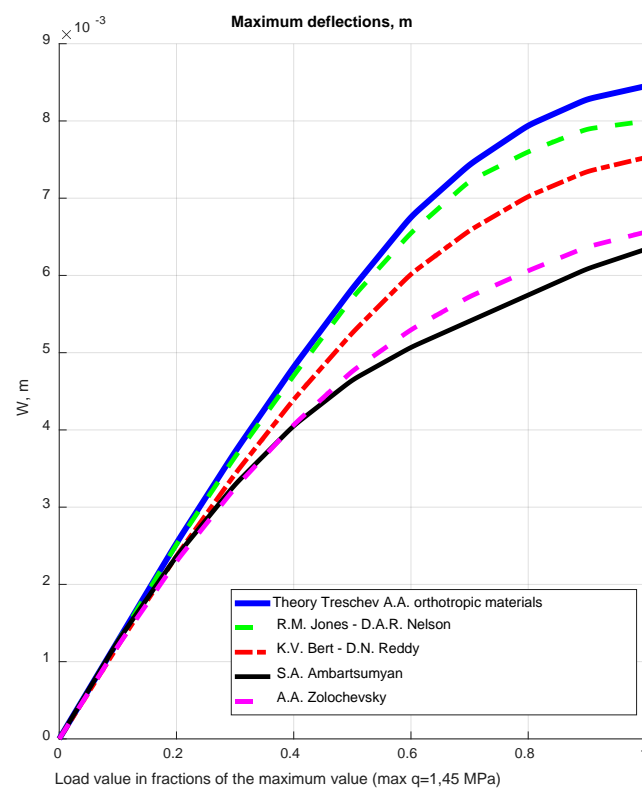
Fig. 32. Effect of load value on deflections
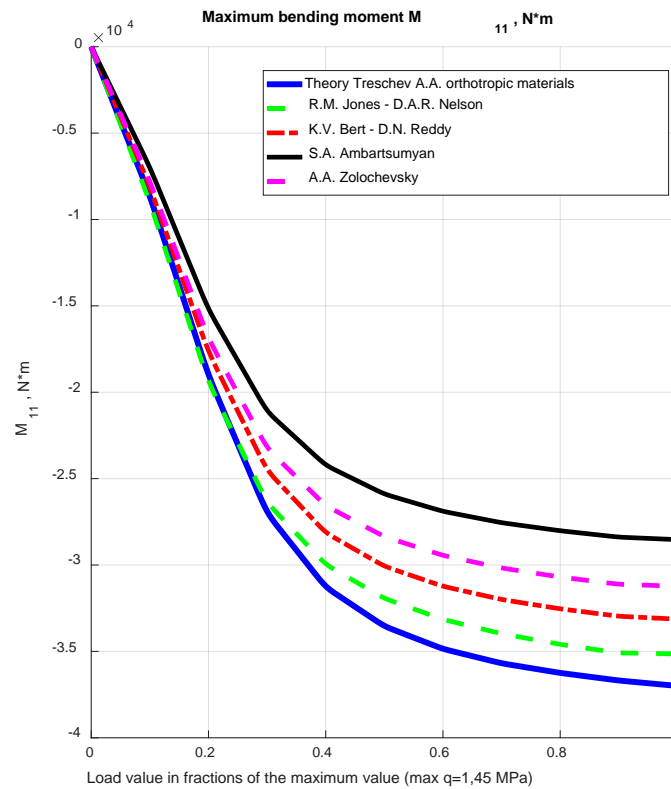
Fig. 33. Influence of the magnitude of the load on the maximum bending moment M_{11}
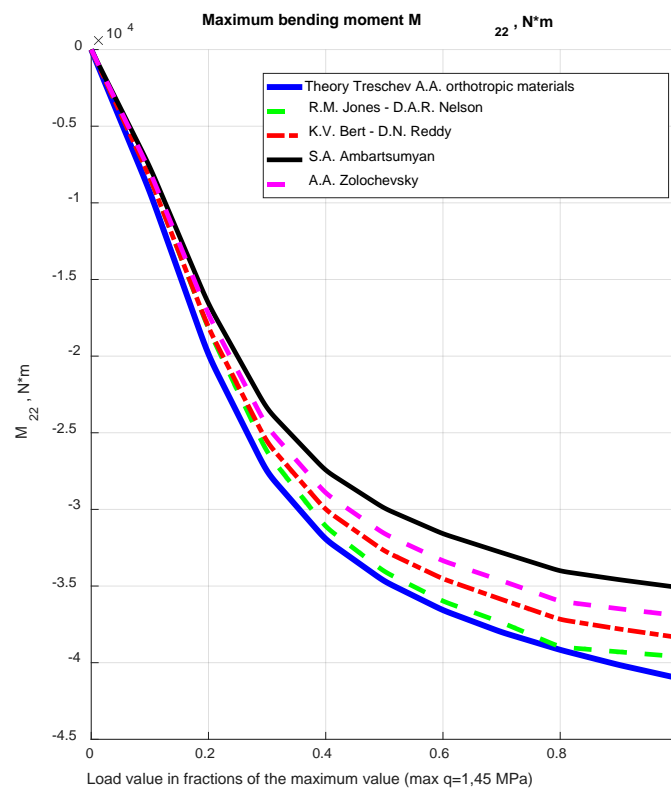
Fig. 34. Influence of the magnitude of the load on the maximum bending moment M_{22}

4. Summary

Analyzing the above graphical dependencies, it should be noted that the disregard for nonlinearity leads to a very significant error in the results. It should be said that when using materials in which the nonlinearity is more pronounced than that of the carbon fiber – carbon AVCO Mod 3a composite, and considering structures in large displacements and in a more complex stress-strain state, the stress-strain state will change even more significantly.

Based on the above, it can be concluded that this work is relevant and will serve as the first step towards a more accurate calculation of building structures within the framework of the proposed theory [32].

In a similar vein, the problem of axisymmetric transverse bending of an annular plate made of an orthotropic nonlinear material with different resistance was considered in [36]. During the deformation of the plate under consideration, there are no tangential stresses in the middle plane σ_{xy} and in the cross-section along the second coordinate σ_{yz}, and only tangential stresses in the cross-section along the radial coordinate σ_{rz} are taken into account. The presence of tangential stresses σ_{xy} and σ_{yz} (Figs. 5-8 and Figs. 24-27) significantly complicate the picture of the stress-strain state of rectangular plates due to the redistribution of stresses. Taking these stresses into account gives a more complete picture of the process of plate deformation during transverse bending, expanding the understanding of the picture of the stress-strain state of bent plates (especially the moment of the onset of the limiting state).

5. Conclusions

The main results and conclusions of the work are as follows:

1. A number of theories of deformation of nonlinear anisotropic materials with different resistances are considered, it is concluded that the constitutive relations used by the authors describe the process of deformation of plates made of these materials most fully.

2. The governing equations for the bending of rectangular plates of average thickness made of an orthotropic physically nonlinear material sensitive to the type of stress state are obtained in a geometrically linear formulation.

3. For a comparative analysis of the calculations of the proposed variant of deformation, the calculation of a rectangular plate of average thickness was carried out. The analysis of the results is demonstrated by the example of a rectangular plate with characteristic dimensions of 1.0×0.5×0.075 (a×b×h) m.

4. An algorithm for solving the resulting resolving equations based on the method of variable parameters of elasticity and finite-difference approximation of the second order of accuracy has been developed. Developed special software which implements the algorithm using MATLAB computing system to calculate the stress-strain state of the plates.

5. The results of the calculation of the plates showed that taking into account the phenomenon of nonlinear differential resistance allows obtaining more precise results, in comparison with the "linear theory of elasticity" and theories: S.A. Ambartsumyan, A.A. Zolochevsky, R.M. Jones – D.A.R. Nelson, C.W. Bert – J.N. Reddy up to 26.8% for maximum displacements, up to 38% for maximum stresses, and in some cases the difference for force factors can reach 60%;

6. The analysis of the results obtained allows us to conclude that it is necessary to take into account the phenomenon of nonlinear resistance of the material when carrying out strength calculations, due to the fact that this phenomenon has a significant effect on the qualitative and quantitative characteristics of the stress-strain state of structures (in particular, for a rectangular plate of average thickness).

References

[1] Ambartsumyan SA. *Theory of anisotropic plates: strength, stability, vibrations*. Moscow: Nauka; 1967. (In Russian)

[2] Ambartsumyan SA. Basic equations and ratios of the multi-modular theory of elasticity of an anisotropic body. *Izv. Academy of Sciences of the USSR. MTT*. 1969;3: 51-61.

[3] Ambartsumyan SA. *Multi-modular theory of elasticity*. Moscow: Nauka; 1982. (In Russian)

[4] Ambartsumyan SA, Khachatryan AA. The basic equations of the theory of elasticity for materials of different resistance to tension and compression. *Inzh. journals MTT*. 1966;2: 44-53.

[5] Ambartsumyan SA, Khachatryan AA. Towards a multimodular theory of elasticity. *Ing. journals MTT*. 1966;6: 64-67.

[6] Jones RM. A Nonsystemmetric Compliance Matrix Approach to Nonlinear Multimoduls Ortotropic Materials. *AIAA Journa*. 1977;15(10): 1436-1443.

[7] Jones RM, Nelson DAR. Material for nonlinear Deformation. *AIAA Journal*. 1976;14(6): 709-716.

[8] Jones RM. Modeling Nonlinear Deformation of the Carbon-Carbon Composite Materials. *AIAA Journal*. 1980;18(8): 995-1001.

[9] Jones RM. Stress-Strain Relations for Materials with Moduli in Tension and Compression. *AIAA Journal*. 1977;15(1): 16-25.

[10] Bert CW. Models for fibrous composites with different properties in tension and compression. *J. Eng. Matls. and Tech., Trans. ASME*. 1977;99HD(4): 344-349.

[11] Bert CW. Micromechanics of the different elastic behavior of filamentary composites in tension and compression. In: Bert CW. (ed.) *Mechanics of Bimodulus Materials*. 1979. p.17-28.

[12] Bert CW. Gordaninejad F. Multi-modular Materials. *International Journal for Numerical Methods in Engineering*. 1984;20: 479-503.

[13] Bert CW, Reddy JN, Chao WC. Bending of Thick Rectanqular Plates Laminated of Bimodulus Composite Materials. *AIAA Journal*. 1981;19(10): 1342-1349.

[14] Zolochevsky AA. To tensor coupling in the theories of elasticity and plasticity of anisotropic composite materials that are differently opposed to tension and compression. *Mechanics of Composite Materials*. 1985;1: 53-58.

[15] Zolochevsky AA. Determining equations and some problems of the multimodular theory of elasticity of anisotropic materials. *PMTF*. 1985;4: 131-138.

[16] Zolochevsky A.A. On the theory of plasticity of materials differently resisting tension and compression. *Izv. universities. Engineering*; 1986;6: 13-16.

[17] Zolochevsky AA. On the relations of the theory of elasticity of anisotropic multi-modular materials. *Dynamics and durability of machines*. 1981;34: 3-8.

[18] Zolochevsky AA. Ratios of the multimodular theory of elasticity of anisotropic materials based on three mixed invariants. *Dynamics and Strength of Machines*. 1987;46: 85-89.

[19] Zolochevsky AA, Morachkovsky OK. The directions of development of models and methods for calculating the nonlinear deformation of bodies and elements of engineering structures. *Dynamics and strength of machines*. 1989;50: 3-9.

[20] Zolochevsky AA, Sklepus SN. On the theory of plasticity with three invariants of the stress state. *Izv. universities. Engineering*. 1987;5: 7-10.

[21] Zolochevsky AA. Concerning consideration of the multiresistance in the theory of creep of isotropic and anisotropic materials. *PMTF*. 1982;4: 140-144.

[22] Lomakin EV. Multi-modularity of composite materials. *Mechanics of composite materials*. 1981;1: 23-29.

[23] Lomakin EV. Relations of the theory of elasticity for an anisotropic body, the deformation characteristics of which depend on the type of stress state. *Izv. Academy of Sciences of the USSR. MTT.* 1983;3: 63-69.

[24] Berezin IS, Zhidkov NP. *Computing methods vol. 1.* Moscow: State publishing house physical. lit-ry; 1959. (In Russian)

[25] Treschev AA. *The theory of deformation and strength of materials sensitive to the type of stress state. Defining relations.* Moscow: RAASN; 2008. (In Russian)

[26] Matchenko NM, Treschev AA. *Theory of deformation of materials with different resistance. Determining relations.* Tula: TSU; 2000. (In Russian)

[27] Treschev AA. To bending of thick rectangular orthotropic slabs made of nonlinear materials sensitive to the type of stress state. In: *Proceedings of the 7th International Conference «Actual Problems of Construction and Building Industry».* Tula: TulSU; 2006. (In Russian)

[28] Treschev AA. *The theory of deformation and strength of materials with initial and induced sensitivity to the type of stress state. Defining relations: monograph.* Moscow: RAASN; 2016. (In Russian)

[29] Treschev AA. Description of deformation of nonlinear anisotropic materials. *Architectural and construction materials science at the turn of the century: materials of reports of the International conference.* Belgorod: BelGTASM; 2002. (In Russian)

[30] Treschev AA. Description of nonlinear deformation of anisotropic materials *Problems and achievements of construction materials science.* Belgorod: BSTU; 2005. p. 233-234. (In Russian)

[31] Treschev AA. *Anisotropic plates and shells of materials with different resistance: monograph.* Moscow: RAACS; 2007. (In Russian)

[32] Treschev AA, Romashin DA. Defining relations for nonlinear anisotropic materials sensitive to the type of stress state. *Bulletin of Nizhny Novgorod University. N.I. Lobachevsky.* 2011;4(4): 1740-1742.

[33] Birger IA, Mavlyutov RR. *Resistance materials: Tutorial.* Moscow: Science. Ch. ed. Phys. Mat. lit.; 1986. (In Russian)

[34] Pisarenko GS, Mozharovsky NS. *Equations and boundary value problems of the theory of plasticity and creep. Reference book.* Kiev: Science; 1981. (In Russian)

[35] Jones RM, Nelson DAR. Theoretical-experimental correlation of material models for nonlinear deformation of graphite. *AIAA Journal.* 1976;14(10): 1427-1435.

[36] Zhurin EA, Treschev AA. Bending of ring plates, performed from an orthotropic nonlinear differently resistant material. *International Journal for Computational Civil and Structural Engineering.* 2020;16(1): 130-146.

ОПРЕДЕЛЕНИЕ НАПРАВЛЕНИЯ ГЛАВНЫХ НАПРЯЖЕНИЙ В ЭЛЕМЕНТАХ МЕТАЛЛОКОНСТРУКЦИЙ ПО ЗНАЧЕНИЯМ КОЭРЦИТИВНОЙ СИЛЫ

Д.П. Мохнаткин*, Г.М.Завьялова

Военно-космическая академия имени А.Ф.Можайского, Санкт-Петербург, ул.Ждановская, 13, Россия

*e-mail: t9119420944@yandex.ru

Аннотация. Изучено изменение значений круговой диаграммы зависимости коэрцитивной силы от угла намагничивания при переходе схемы нагружения двутавровой балки из стали 10 (P1.1.Z.AN) от симметричного изгиба к изгибу со стеснённым кручением при упругих деформациях в зоне сжатия. Обоснована необходимость построения круговой диаграммы коэрцитивной силы от угла намагничивания в зоне контроля для получения информации о направлении главных напряжений при определении напряженно-деформированного состояния металлоконструкции.
Ключевые слова: направление главных напряжений, упругое деформирование, угол намагничивания, коэрцитивная сила

1. Введение

В настоящее время магнитный метод неразрушающего контроля является одним из перспективных методов для определения напряженно-деформированного состояния (НДС) металлоконструкций. По данной тематике опубликовано немало работ [1-29]. Результаты исследований по изучению влияния разной степени упругих и пластических деформаций на магнитные характеристики металлов описаны в работах [2,8,10,15,19,24,25,29], в частности, подобное влияние для образцов с наведенной магнитной анизотропией описано в работе [17]. Закономерностям изменения от внешних силовых воздействий такого наиболее перспективного и часто применяемого параметра магнитного контроля, как коэрцитивная сила адресованы работы [3,9,11,12,18]. Целый ряд работ посвящен учету особенностей и погрешностей, связанных с применением прикладных преобразователей [1,4,5,6,7], именно они чаще всего применяются при магнитном контроле массивных объектов. В работе [16] получены зависимости магнитных характеристик стали при упругом одноосном растяжении на образцах из высокопрочной трубной стали с предварительной пластической деформацией. Если в большинстве работ по этой тематике уделено внимание поведению магнитных характеристик металла при нормальных напряжениях, то в работе [14] показана такая зависимость и от касательных напряжений в том числе. Успешно используются полученные зависимости в практически реализованных методах для определения НДС и остаточного ресурса металлоконструкций, такие примеры описаны в работах [21,22]. Все научные результаты в этой области основываются на теории, объясняющей механизмы влияния внешних напряжений на магнитные характеристики ферромагнетиков (в частности, коэрцитивную силу), и описаны в работах [9,20,23].

Во всех способах реализации данного метода фигурируют значения коэрцитивных сил, измеренных вдоль и поперек линии «действия» напряжений, но мало внимания уделено тому, как определить направление главных напряжений. Особенно актуальна данная проблема на практике, где сложнонапряженное состояние является нормой эксплуатации металлоконструкций. Так, металлоконструкции пусковых столов стартовых комплексов ракет космического назначения испытывают нагрузки с большим процентом случайности параметров вектора воздействия и по направлению, и по значению, что исключает симметричное и сбалансированное силовое воздействие на них. Сложнонапряженное состояние, возникающее при одновременном действии гидростатического напора, растяжения и кручения, также характерно при эксплуатации трубных систем.

Настоящая работа посвящена изучению изменяющихся значений коэрцитивной силы, измеренной в одной точке, но в разных направлениях, от условий нагрузки с целью обоснования необходимости учета угла намагничивания при определении направления и значения главных напряжений.

2. Методика проведения исследований

При решении указанной задачи были проведены экспериментальные исследования. Объектом исследования служила двутавровая балка из стали 10 десятого профиля длиной 1100 мм. Для формирования желаемых схем нагружения применялась установка для механических испытаний Р-30, позволяющая обеспечить изгиб балки с требуемым усилием в упругой зоне деформации, и набор опор для реализации схем действия, как только нормальных напряжений в зоне контроля (Рис. 1а), так и в сочетании с касательными (Рис. 1б).
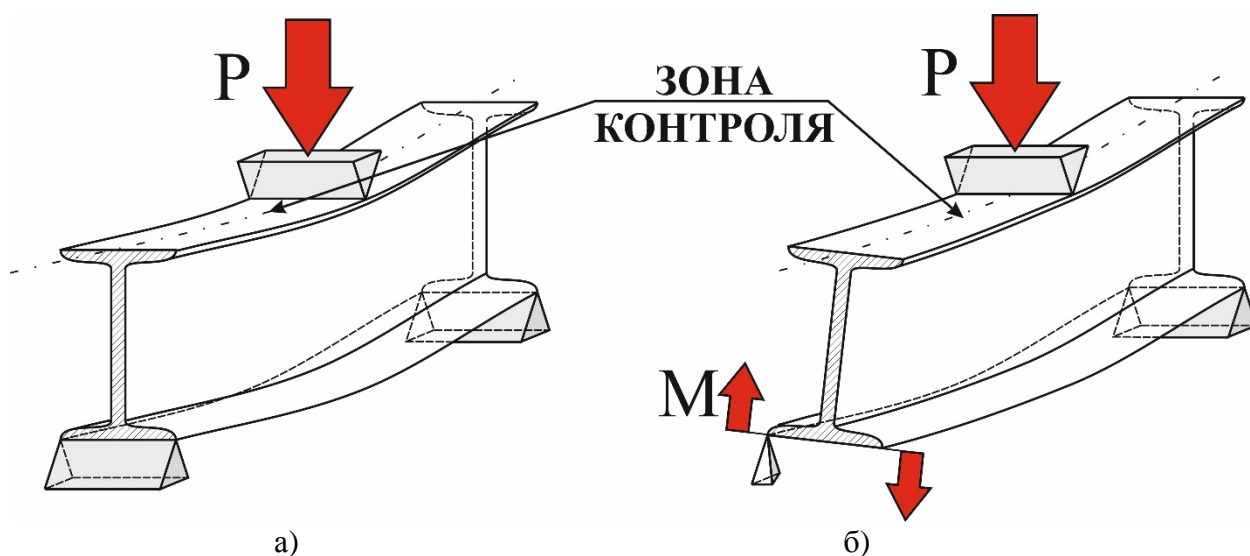
Рис. 1. Схемы нагружения двутавровой балки: а – симметричная; б – асимметричная с кручением

Для реализации указанных схем нагрузка прилагалась в верхней части по центру балки. При этом, обеспечивая наличие только нормальных напряжений в сечении, изгибающему усилию подвергалась балка, установленная краями на широкие роликовые опоры (Рис. 1а). При реализации второй схемы нагружения одна из роликовых опор была заменена на точечную, установленную с краю балки. Под действием нагрузки по центру балки в районе точечной опоры создавался крутящий момент, который и обеспечивал наличие касательных напряжений в сечении в

дополнение к нормальным от изгибающего усилия в вертикальной плоскости. Так же в условиях стесненного кручения, добавились нормальные напряжения от растяжения в горизонтальной плоскости по верхнему краю балки в районе ролика нагружения со стороны противоположной точечной опоре. Таким образом, при реализации второй схемы нагружения создавалось сложнонапряженное состояние двутавровой балки (Рис. 1б).

Для магнитных измерений использовали два прибора – КИМ-2М и КРМ-Ц. Выбор указанных приборов обуславливался тем, что приставные электромагнитные устройства (ПЭМУ) удобно использовать при локальном намагничивании участков контролируемых конструкций, дополнительно они дают возможность изменять направление намагничивания относительно направления действующих нагрузок. Площадь поперечного сечения полюсов приставных электромагнитов составляла $S_{\text{пол}} = 5 \times 15$ мм для КИМ-2М и $S_{\text{пол}} = 15 \times 30$ мм для КРМ-Ц. Расстояние между полюсами $L_{\text{пол}} = 15$ мм и $L_{\text{пол}} = 35$ мм соответственно. Размеры ПЭМУ указанных приборов позволяли разворачивать их вокруг своей оси на поверхности балки в зоне контроля (Рис. 2).
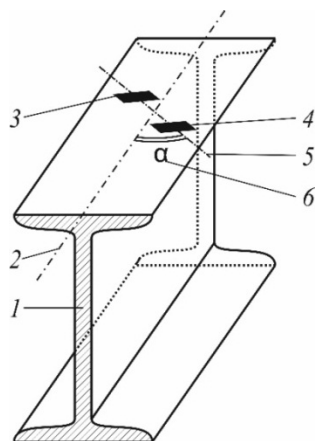
Рис. 2. Схема контроля двутавровой балки: 1 – сечение; 2, 5 – оси балки и ПЭМУ соответственно; 3, 4 – места приложения полюсов ПЭМУ;
6 – угол намагничивания

Исследования проводились в три этапа. На первом этапе снимались показания указанными приборами на балке без нагрузки в четырех направлениях, при этом угол намагничивания α составлял 0, 45, 90 и 135°. На втором этапе измерения в тех же направлениях проводили на балке под нагрузкой в соответствии со схемой, показанной на Рис. 1а. Прилагаемое усилие обеспечило максимальное нормальное напряжение сжатия в зоне контроля в 166 МПа – это 80% от предела текучести используемой стали. На третьем этапе показания приборов снимались в указанных направлениях в той же точке и с таким же усилием в 2,5 тонны только при реализации второй схемы нагружения (Рис. 1б). На всех трех этапах исследования зона контроля не менялась.

3. Результаты исследований и их обсуждение

На Рисунках 3 и 4 в виде круговых диаграмм $H_C = f(\alpha)$ приведены результаты измерений коэрцитивной силы на двутавровой балке из стали 10, полученные с помощью серийных приборов КИМ-2М (Рис. 3) и КРМ-Ц (Рис. 4).
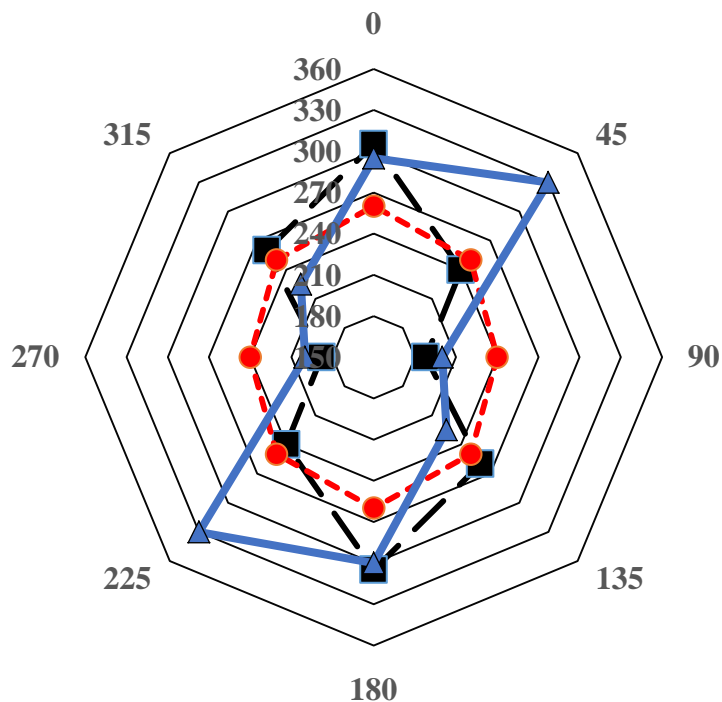
Рис. 3. Круговая диаграмма значений коэрцитивной силы [А/м], измеренной прибором КИМ-2М, от угла намагничивания $H_{C1} = f(\alpha)$:
● – состояние без нагрузки; ■ – с симметричной нагрузкой; ▲ – в сложнонапряженном состоянии
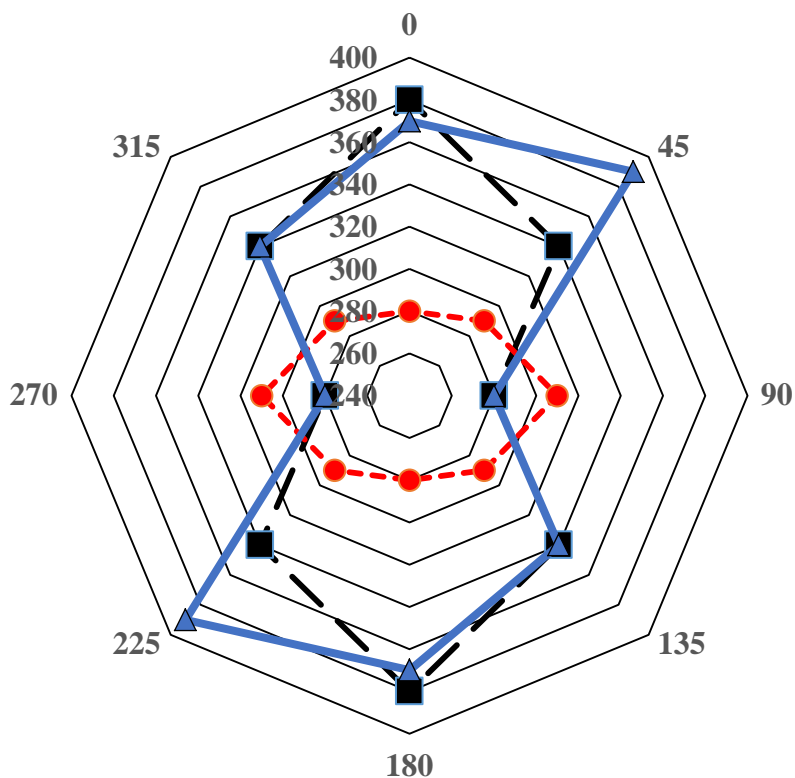
Рис. 4. Круговая диаграмма значений коэрцитивной силы [А/м], измеренной прибором КРМ-Ц, от угла намагничивания $H_{C2} = f(\alpha)$:
● – состояние без нагрузки; ■ – с симметричной нагрузкой; ▲ – в сложнонапряженном состоянии

Предыстория механических нагружений балки неизвестна, однако уровень коэрцитивной силы свидетельствует о том, что незначительная пластическая деформация имеет место. Этот вывод можно сделать по степени отдаленности формы круговой диаграммы $H_C = f(\alpha)$, построенной по результатам измерения ненагруженной балки, от окружности. Из диаграммы, построенной по результатам измерения прибором КИМ-2М (Рис. 3), видно, что $H_{C1}(0°) = 1{,}083 H_{C1}(90°)$.

Так как численный коэффициент превышает значения относительной погрешности прибора, которая составляет около 8% в измеряемом диапазоне, то по нему можно судить о наличии пластической деформации сжатия в направлении $\alpha=0°$, однако ее уровень не помешает дальнейшим исследованиям. При рассмотрении круговой диаграммы, построенной по данным с КРМ-Ц (Рис. 4), на балке без нагрузки видно, что $H_{C2}(0°) = 0{,}9 H_{C2}(90°)$ (отношение этих значений тоже больше относительной погрешности прибора, которая составляет около 4% для рассматриваемого диапазона), то есть форма диаграммы вытянута больше в поперечном направлении. Происходит это по причине того, что расстояние между внешними границами полюсов ПЭМУ КРМ-Ц совпадает с шириной балки, а значит, на показания прибора оказывает влияние так называемый *краевой эффект*, когда физический размер ферромагнетика ограничивает пространство для магнитного потока от приставного электромагнита.

При рассмотрении круговых диаграмм, полученных при симметричном нагружении балки, видно, что $H_C(0°)$ значительно увеличивает, а $H_C(90°)$ заметно уменьшает свое значение. Диаграммы принимают вид своеобразной «восьмерки», которая направлением своих максимальных значений указывает на линию главных напряжений сжатия. В зоне растяжения изменение этих параметров обратное [26].

Для расчета главных (эквивалентных) напряжений, напряженно-деформированного состояния двутавровой балки использовался программный комплекс ANSYS Mechanical 15.0 (Рис. 5).
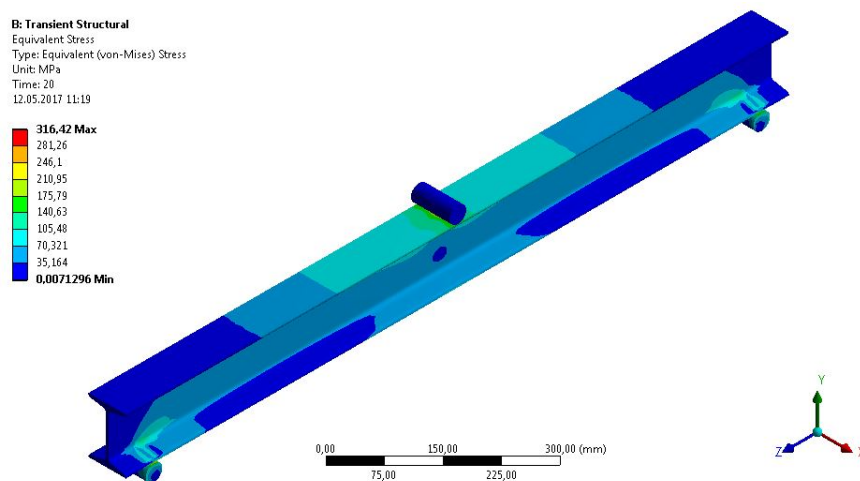
Рис. 5. Определение главных напряжений при симметричной нагрузке двутавровой балки

Необходимо отметить, что показания разных приборов имеют некоторые различия при одинаковых условиях получения значений коэрцитивной силы. Это связано с различными характеристиками ПЭМУ, в частности, площади поперечного сечения магнитопровода. У прибора КРМ-Ц она в 6 раз больше, чем у КИМ-2М, и именно эта характеристика определяет глубину промагничивания металла по выводам работы [1]. Характерно, что в нашем случае $H_{C1}= (0{,}7 – 0{,}78) H_{C2}$ абсолютно по всем измеряемым направлениям. Это дает возможность применять поправочный

коэффициент при использовании всего одной зависимости $H_C= f(\sigma)$, полученной любым из этих приборов.

В случае применения такого диагностического признака, как анизотропия коэрцитивной силы (ΔH_C), а по сути, разницы между $H_C(90°)$ и $H_C(0°)$, отметим, что значения ΔH_C для двух разных приборов одинаковы при одинаковой нагрузке и составят (105 ± 5)А/м. Этот факт дает преимущество в выборе диагностического признака нормальных напряжений именно ΔH_C, как величине, не зависящей от типа прибора и его датчика. Зависимость $\Delta H_C= f(\sigma)$ для этой балки показана в работе [27].

В сложнонапряженном состоянии балки (в нашем случае изгиб со стеснённым кручением) круговая диаграмма меняет значение своего максимума, его новое направление $\alpha=45°$ регистрируют оба прибора. Приращение значений в этом направлении существенное $H_{C1}(45°) = =1{,}12H_{C1}(0°)$ для КИМ-2М и $H_{C2}(45°) = 1{,}06H_{C2}(0°)$ для КРМ-Ц. Существенной может оказаться и ошибка, если при наличии касательных напряжений измерения производить вдоль оси симметрии балки. Анизотропия коэрцитивной силы, судя по показаниям КИМ-2М, вдоль направления $\alpha=45°$ также на 10% больше, чем анизотропия в направлении, соосном балке ($\alpha=0°$), что соответствует расчетной схеме при сложнонапряженном состоянии (Рис. 6). При рассмотрении расчетной схемы проясняется причина снижения значений показателей $H_{C1}(0°)$ и $H_{C2}(0°)$, один из полюсов ПЭМУ (ближний к линии нагружения) попадает в зону меньших напряжений, обозначенной цифрой 1 на Рис. 6. Однако КРМ-Ц не показал прироста $\Delta H_{C2}(45°)$ по сравнению $\Delta H_{C2}(0°)$, это связано с тем, что при измерении $H_{C2}(135°)$ полюс ближний к линии нагружения попадает в зону повышенных напряжений, обозначенной цифрой 2 на Рис. 6. В этой зоне складываются напряжения сжатия от изгибов в двух плоскостях. Дополнительным фактором искажений показаний КРМ-Ц является масштабный фактор. Влияние толщины металла объекта контроля на показания коэрцитиметра описаны в работе [28].
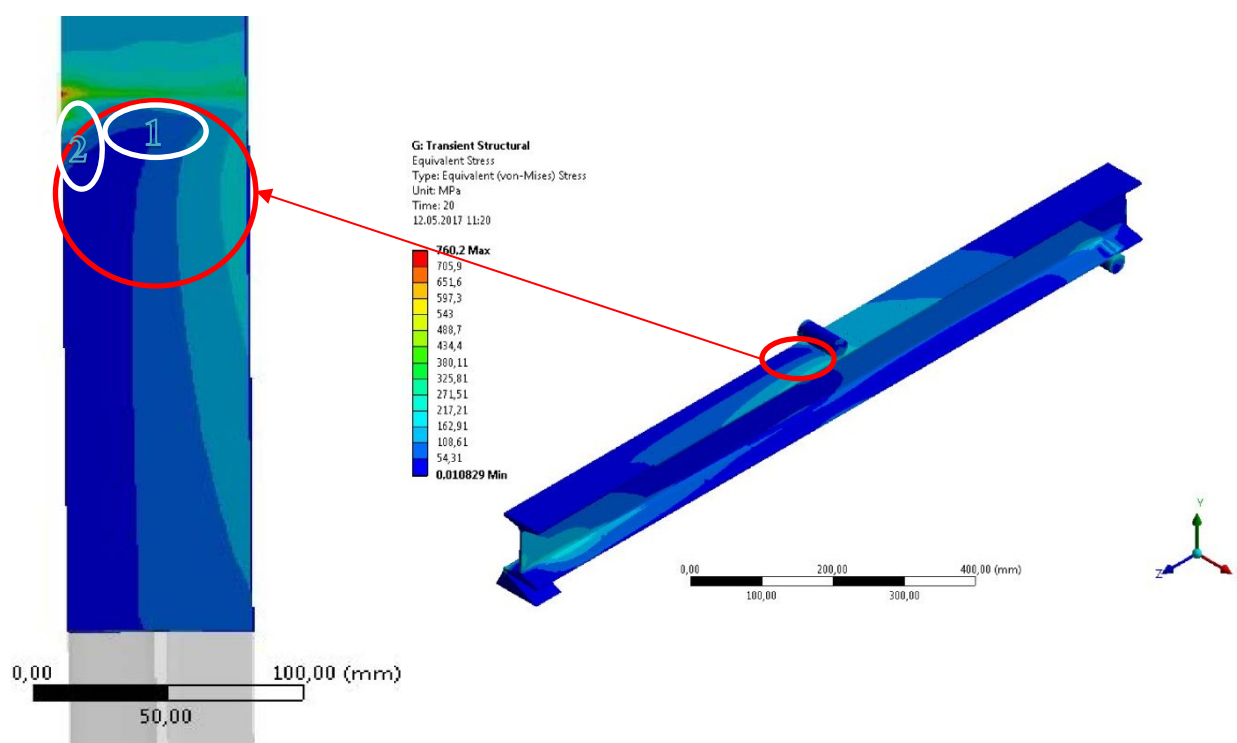
Рис. 6. Определение главных напряжений при реализации изгиба со стеснённым кручением двутавровой балки

Схема нагружения двутавровой балки, показанная на Рис. 6, характерна тем, что при стеснённом кручении в зоне контроля нормальные напряжения сжатия от изгиба в вертикальной плоскости частично компенсируются нормальными напряжениями растяжения на одной из кромок балки при изгибе в горизонтальной плоскости (зона 1 на Рис. 6). Таким образом, линии главных напряжений описывают дуги с бóльшим отклонением от оси симметрии балки со стороны линии соприкосновения с роликом нагружения, что и фиксируют используемые в эксперименте коэрцитиметры. Подобные, сложные конструкции полей напряжения не поддаются точному анализу при эксплуатации, даже с исчерпывающими исходными данными. Однако при оценивании НДС элементов металлоконструкции необходимо учитывать направление действия главных напряжений, таким образом определять их максимальное значение в зоне контроля.

4. Выводы

Проведенный эксперимент показал, что с помощью коэрцитиметрического метода магнитного контроля возможно определение направления главных напряжений в точке контроля элемента металлоконструкции. Сделать это можно по экстремальным значениям коэрцитивной силы на круговой диаграмме в зоне контроля. Кроме того, показано, что при одинаковом усилии в частном случае сложнонапряженного состояния на балке регистрируется уменьшение значений коэрцитивной силы в соосном с ней направлении по сравнению со схемой симметричной нагрузки. Поэтому учет показаний прибора только в направлениях $\alpha=0°$ и $\alpha=90°$ может привести к существенной ошибке в определении напряженно-деформированного состояния объекта контроля. Однако при построении круговой диаграммы необходимо учитывать и масштабный фактор, и параметры используемого прибора.

Использование приборов с разными характеристиками ПЭМУ показали, что бóльшую корреляцию с расчетными данными дает прибор с меньшим расстоянием между полюсами магнитопровода своего датчика.

Показано, что при выборе диагностического параметра НДС металлоконструкции магнитным методом контроля рядом преимуществ обладает анизотропия коэрцитивной силы.

Литература

[1] Бида ГВ. О глубине намагничивания массивных изделий приставным электромагнитом и глубине контроля эксплуатационных свойств. *Дефектоскопия*. 1999;9: 70-81.

[2] Горкунов ЭС, Царькова ТП, Смирнов СВ, Вичужанин ДИ, Емельянов ИГ, Кузнецов ВЮ. Влияние отклонений от соосности между направлениями намагничивания и наложения механической нагрузки на результаты магнитного контроля упругих деформаций в сталях. *Дефектоскопия*. 2004;5: 40-52.

[3] Захаров ВА, Ульянов АИ, Горкунов ЭС. Коэрцитивная сила ферромагнитных сталей при двухосном симметричном растяжении материала. *Дефектоскопия*. 2011;6: 3-15.

[4] Гусев АП. Гистерезис магнитного поля поверхностных дефектов различных сталей при намагничивании приставным электромагнитом. *Дефектоскопия*. 2015;10: 24-32.

[5] Валиев ММ. Расчет магнитного сопротивления неплоскопараллельного воздушного зазора магнитной системы. *Дефектоскопия*. 2004;5: 24-31.

[6] Бида ГВ. Влияние зазора между полюсами приставного электромагнита и

контролируемой деталью на показания коэрцитиметра и способы его уменьшения. Обзор. *Дефектоскопия*. 2010;11: 62-81.

[7] Ничипурук АП, Бида ГВ, Царькова ТП, Гобов ЮЛ, Сташков АН, Поволоцкая АМ. О снижении влияния зазора на результат коэрцитиметрии при учете свойств приставного преобразователя. *Дефектоскопия*. 2010;8: 45-53.

[8] Горкунов ЭС, Федотов ВП, Бухвалов АБ, Веселов ИН. Моделирование диаграммы деформирования на основе измерения ее магнитных характеристик. *Дефектоскопия*. 1997;4: 87-95.

[9] Кулеев ВГ, Горкунов ЭС. Механизмы влияния внутренних и внешних напряжений на коэрцитивную силу ферромагнитных сталей. *Физика и химия обработки материалов*. 1997;5: 3-18.

[10] Бида ГВ, Кулеев ВГ. Влияние упругой деформации на магнитные свойства сталей с различной структурой. *Дефектоскопия*. 1998;11: 12-26.

[11] Захаров ВА, Боровикова МА, Комаров ВА, Мужицкий ВФ. Влияние внешних напряжений на коэрцитивную силу углеродистых сталей. *Дефектоскопия*. 1992;1: 41-46.

[12] Новиков ВФ, Яценко ТА, Бахарев МС. Зависимость коэрцитивной силы малоуглеродистых сталей от одноосных напряжений (часть 1). *Дефектоскопия*. 2001;11: 51-57.

[13] Горкунов ЭС, Захаров ВА, Мужицкий ВФ, Ульянов АИ, Чулкина АА. Влияние упругой и пластической деформаций на коэрцитивную силу пористых ферромагнитных материалов. *Дефектоскопия*. 2005;10: 5-12.

[14] Горкунов ЭС, Поволоцкая АМ, Соловьев КЕ, Задворкин СМ. Влияние магнитоупругого эффекта на гистерезисные свойства среднеуглеродистой стали при одноосном нагружении. *Дефектоскопия*. 2010;9: 17-25.

[15] Бида ГВ. Магнитный метод оценки одноосновных упругих напряжений растяжения и сжатия. *Дефектоскопия*. 2011;8: 64-75.

[16] Горкунов ЭС, Субачев ЮВ, Поволоцкая АМ, Задворкин СМ. Влияние предварительной пластической деформации на поведение магнитных характеристик высокопрочной трубной стали контролируемой прокатки при упругом одноосном растяжении (сжатии). *Дефектоскопия*. 2015;9: 49-60.

[17] Ничипурук АП, Сташков АН, Огнева МС, Королев АВ, Осипов А.А. Наведенная магнитная анизотропия в пластически деформированных растяжением пластинах из низкоуглеродистой стали. *Дефектоскопия*. 2015;10: 19-23.

[18] Мусихин СА, Новиков ВФ, Барсенко ВН. Об использовании коэрцитивной силы в качестве индикаторного параметра при неразрушающем контроле механических напряжений. *Дефектоскопия*. 1987;9: 57-59.

[19] Михеев МН, Кулеев ВГ, Нестеренко ВВ, Ригмант МБ, Михайловская ГИ, Немков ВЛ, Лобанова ЛВ. Новый способ неразрушающего контроля механических свойств изделий из среднеуглеродистых сталей. *Дефектоскопия*. 1987;7: 3-7.

[20] Кондорский ЕИ. К вопросу о природе коэрцитивной силы и необратимых изменениях при намагничивании. *Журнал экспериментальной и теоретической физики*. 1937;9/10: 1117-1131.

[21] Безлюдько ГЯ, Мужицкий ВФ, Попов БЕ. Магнитный контроль напряженно-деформированного состояния и остаточного ресурса стальных металлоконструкций подъемных сооружений и сосудов, работающих под давлением. *Дефектоскопия*. 2001;1: 38-46.

[22] Горкунов ЭС, Задворкин СМ, Весслов ИН, Митропольская СЮ, Ничужанин ДИ. Влияние одноосного растяжения на магнитные характеристики трубной стали 12ГБ, подвергнутой воздействию сероводорода. *Дефектоскопия*. 2008;8: 67-76.

[23] Ничипурук АП, Розенфальд ЕВ, Огнева МС, Сташков АН, Королев АВ. Экспериментальный метод оценки критических полей смещающихся доменных границ в пластически деформированных растяжением проволоках из низкоуглеродистой стали. *Дефектоскопия*. 2014;10: 18-26.

[24] Федотов ВП, Бида ГВ, Ничипурук АП. Построение упругопластических диаграмм нагружения конструкционных сталей по магнитным свойствам. *Дефектоскопия*. 2011;9: 17-24.

[25] Костин ВН, Царьков ТП, Ничипурук АП, Лоскутов ВЕ, Лопатин ВВ, Костин КВ. Необратимые изменения намагниченности как индикаторы напряженно-деформированного состояния ферромагнитных объектов. *Дефектоскопия*. 2009;11: 54-66.

[26] Алексеев КВ, Мохнаткин ДП, Лебедев ЕЛ. Определение направления напряжений в упругой зоне деформации стальных конструкций при их магнитном контроле. *Фундаментальные исследования*. 2015;12: 9-12.

[27] Лебедев ЕЛ, Алексеев КВ, Мохнаткин ДП. Коэрцитивная сила как определяющий показатель напряженности металла при его упругих деформациях. *Труды Военно-космической академии имени А.Ф. Можайского*. 2015;648: 157-160.

[28] Лебедев ЕЛ, Мохнаткин ДП, Смуров СА. Анализ влияния масштабного фактора на оценивание напряженного состояния металлоконструкций магнитным методом контроля. *Труды Военно-космической академии имени А.Ф. Можайского*. 2016;652: 187-193.

[29] Горкунов ЭС, Субочев ЮВ, Поволоцкая АМ, Задворкин СМ. Влияние упругой деформации на гистерезисные свойства двуслойного ферромагнетика, составленного из компонентов, обладающих магнитострикцией разных знаков. *Дефектоскопия*. 2014;8: 42-56.

DETERMINATION OF THE DIRECTION OF THE PRINCIPAL STRESSES IN THE ELEMENTS OF STEEL STRUCTURES BY THE VALUES OF THE COERCIVE FORCE

D.P. Mokhnatkin*, G.M. Zav'yalova

A.F. Mozhaisky Military Space Engineering Academy, Saint Petersburg, Russia

*e-mail: t9119420944@yandex.ru

Abstract. The change of values of circular diagram of the coercive force on the magnetization angle at the transition of loading scheme of I-beam made of steel 10 (P1.1.Z.AN) from symmetric bending to bending with constrained torsion at elastic deformations in the compression zone was studied. The necessity of constructing a circular diagram of the coercive force from the magnetization angle in the control zone to obtain information about the direction of the principal stresses when determining the stress-strain state of steel structure is substantiated.

Keywords: principal stress, elastic deformation, magnetization angle, coercive force, steel structure

References

[1] Bida GV. About the depth of magnetization of massive products with an auxiliary electromagnet and the depth of monitoring of operational properties. *Defektoskopiya*. 1999; 9: 70-81. (In Russian)

[2] Gorkunov ES, Tsar'kova TP, Smirnov SV, Vichuzhanin DI, Emel'yanov IG, Kuznetsov VY. Effect of deviation from coaxiality between the directions of magnetization and mechanical strain on the results of magnetic testing of elastic strain in steels. *Russian Journal of Nondestructive Testing*. 2004;40(5): 317-325.

[3] Zakharov VA, Ul'yanov AI, Gorkunov ES. Coercive force of ferromagnetic steels under the biaxial symmetrical tension of a material *Russian Journal of Nondestructive Testing*. 2011;47(6): 359-368.

[4] Gusev AP. Hysteresis of the magnetic field of surface flaws in different steels during magnetization with an attachable electromagnet. *Russian Journal of Nondestructive Testing*. 2015;51(10): 616-623.

[5] Valiev MM. Calculation of the magnetic resistance of a non-plane-parallel air gap of a magnetic system. *Defektoskopiya*. 2004;5: 24-31. (In Russian)

[6] Bida GV. The effect of a gap between the poles of an attachable electromagnet and a tested component on coercimeter readings and methods for decreasing it (review). *Russian Journal of Nondestructive Testing*. 2010;46(11): 836-853.

[7] Nichipuruk AP, Bida GV, Tsar'kova TP, Gobov YL, Stashkov AN, Povolotskaya AM. Decrease in the effect of a gap on coercimetry results when taking the properties of an attachable transducer into account. *Russian Journal of Nondestructive Testing*. 2010;46(8): 580-586.

[8] Gorkunov ÉS, Fedotov VP, Bukhvalov AB, Veselov IN. Simulating a strain diagram from magnetic-characteristics measurements. *Russian Journal of Nondestructive Testing*. 1997;33(4): 272-278.

[9] Kuleev VG, Gorkunov ÉS. Influence of inside and outside stresses upon coercive force of ferromagnetic steels. *Fizika i khimiya obrabotki materialov*. 1997;5: 3-18. (In Russian)

[10] Bida GV, Kuleev VG. Effect of elastic deformation on the magnetic properties of steels having different structures. *Russian Journal of Nondestructive Testing*. 1998;34(11): 783-794.

[11] Zakharov VA, Borovkova MA, Komarov VA, Muzhitskij VF. Influence of external tensiles upon coercivity of carbon steels. *Defektoskopiya*. 1992;1: 41-46. (In Russian)

[12] Novikov VF, Yatsenko TA, Basharev MS. Coercive force of low-carbon steels as a function of uniaxial stress. Part I. *Russian Journal of Nondestructive Testing*. 2001;37(11): 799-804.

[13] Gorkunov ES, Zakharov VA, Muzhitskii VF, Ul'yanov AI, Chulkina AA. Effect of elastic and plastic deformations on the coercive force of porous ferromagnetic materials. *Russian Journal of Nondestructive Testing*. 2005;41(10): 627-631.

[14] Gorkunov ES, Solov'ev KE, Povolotskaya AM, Zadvorkin SM. Effect of the magnetoelastic effect on the hysteresis properties of medium-carbon steel under uniaxial loading. *Defektoskopiya*. 2010;9: 17-25. (In Russian)

[15] Bida GV. Magnetic method for estimating uniaxial compressive and tensile elastic stresses. *Russian Journal of Nondestructive Testing*. 2011;47(8): 551-560.

[16] Gorkunov ES, Subachev YV, Povolotskaya AM, Zadvorkin SM. The influence of a preliminary plastic deformation on the behavior of the magnetic characteristics of high-strength controllably rolled pipe steel under an elastic uniaxial tension (compression). *Russian Journal of Nondestructive Testing*. 2015;51(9): 563-572.

[17] Nichipuruk AP, Stashkov AN, Ogneva MS, Korolev AV, Osipov AA. Induced magnetic anisotropy in low-carbon steel plates subjected to plastic deformation by stretching *Russian Journal of Nondestructive Testing*. 2015;51(10): 610-615.

[18] Musikhin SA, Novikov VF, Barsenko VN. On the use of coercive force as an indicator parameter for non-destructive testing of mechanical stresses. *Defektoskopiya*. 1987;9: 57-59. (In Russian)

[19] Mikheev MN, Kuleev VG, Nesterenko VV, Rigmant MB, Mikhailovskaya GI, Nemov VL, Lobsnova LV. A new method of non-destructive testing of mechanical properties of products made of medium-carbon steels. *Defektoskopiya*. 1987;7: 3-7. (In Russian)

[20] Kondorskiy EI. On the nature of the coercive force and irreversible changes in magnetization. *Journal of Experimental and Theoretical Physics*. 1937;9/10: 1117-1131. (In Russian)

[21] Muzhitskii VF, Popov BE, Bezlyud'ko GY. Magnetic measurements of stressed-strained states and remaining service lives of steel structures in hoisting machines and pressurized vessels. *Russian Journal of Nondestructive Testing*. 2001;37(1): 29-36.

[22] Gorkunov ES, Zadvorkin SM, Veselov IN, Mitropol'skaya SY, Vichuzhanin DI. Influence of uniaxial tension on magnetic characteristics of the 12γcyrillic capital letter be pipe steel exposed to hydrogen sulfide. *Russian Journal of Nondestructive Testing*. 2008; 44(8): 566-573.

[23] Nichipuruk AP, Rozenfel'd EV, Ogneva MS, Stashkov AN, Korolev AV. An experimental method for evaluating the critical fields of moving domain boundaries in plastically tension-deformed low-carbon wires. *Russian Journal of Nondestructive Testing*. 2014;50(10): 566-573.

[24] Fedotov VP, Bida GV, Nichipuruk AP. Construction of elastic-plastic diagrams of structural steel loading by magnetic properties. *Defektoskopiya*. 2011;9: 17-24. (In Russian)

[25] Kostin VN, Tsar'kova TP, Loskutov VE, Kostin KV, Nichipuruk AP, Lopatin VV. Irreversible changes in the magnetization as indicators of stressed-strained state of ferromagnetic objects. *Russian Journal of Nondestructive Testing*. 2009;45(11): 786-796.

[26] Alekseev KV, Mokhnatkin DP, Lebedev EL. Determination of the direction of stresses in the elastic zone of deformation of steel structures during their magnetic control. *Basic research.* 2015;12: 9-12. (In Russian)

[27] Alekseev KV, Mokhnatkin DP, Lebedev EL. Coercive force as a determining indicator of the strength of a metal under its elastic deformations. *Proceedings of the Military Space academy named after A.F. Mozhaisky.*2015;648, 157-160. (In Russian)

[28] Lebedev EL, Mokhnatkin DP, Smurov SA. Analysis of the influence of the scale factor on the assessment of the stress state of metal structures by the magnetic control method. *Proceedings of the Military Space academy named after A.F. Mozhaisky.* 2016;652: 187-193. (In Russian)

[29] Gorkunov ES, Subachev YV, Povolotskaya AM, Zadvorkin SM. The influence of elastic deformations on the hysteresis properties of a two-layer ferromagnet composed of components with magnetostrictions of opposite signs. *Russian Journal of Nondestructive Testing*. 2014;50(8): 469-480.

Submission of papers:
Manuscript should be submitted (**both MS Word and PDF**) by e-mail to: **mpmjournal@spbstu.ru**
After a confirmation of the paper acceptation, the authors should send the signed hard copy of the "Transfer of Copyright Agreement" form (available at http://www.mpm.spbstu.ru section "Authors") by regular post to "Materials Physics and Mechanics" editorial office:
Periodicals Editorial Office, Institute of Advanced Manufacturing Technologies, Peter the Great St.Petersburg Polytechnic University, Polytechnicheskaya, 29, St.Petersburg 195251, Russia.
The scanned copy of the signed "Transfer of Copyright Agreement" should be send by e-mail to: mpmjournal@spbstu.ru.

Filetype:
Authors are invited to send their manuscripts **as MS Word file with PDF format copy.**
MS Word file should be prepared according to the general instructions bellow; we are kindly asking the authors to look through the detail instruction at: http://www.mpm.spbstu.ru.

Length:
Papers should be limited to 30 typewritten pages (including Tables and Figures placed in the proper positions in the text).

Structure of the manuscript:

PAPER TITLE: CENTERED,

TIMES NEW ROMAN 14 BOLD, CAPITAL LETTERS

A.B. Firstauthor[1], C.D. Secondauthor[2*] – Times New Roman 12, bold, centered

[1]Affiliation, address, country - Times New Roman 10, centered

*e-mail: e-mail of the corresponding author - Times New Roman 10, centered

Abstract. Times New Roman 12 font, single line spacing. Abstract should not exceed 12 lines.
Keywords: please, specify paper keywords right after the abstract.

Paper organization. Use Times New Roman 12 font with single line spacing. Use *Italic* font in order to stress something; if possible, please, use **bold** for headlines only.

Page numbering. Please, do not use page numbering.

Tables, Figures, Equations. Please, see the sample file at http://www.mpm.spbstu.ru for more details.

References
References should be subsequently numbered by Arabic numerals in square brackets, e.g. [1,3,5-9], following the sample style below:
[1] Koch CC, Ovid'ko IA, Seal S, Veprek S. *Structural Nanocrystalline Materials: Fundamentals and Applications*. Cambridge: Cambridge University Press; 2007.
[2] Hull D, Bacon DJ. *Introduction to Dislocations*. 5nd ed. Amsterdam: Butterworth-Heinemann; 2011 Available from: https://www.sciencedirect.com/science/book// 9780080966724?via%3Dihub [Accessed 19th June 2018].
[3] Romanov AE, Vladimirov VI. Disclinations in crystalline solids. In: Nabarro FRN (ed.) *Dislocations in Solids*. Amsterdam: North Holland; 1992;9. p.191-402.
[4] Mukherjee AK. An examination of the constitutive equation for elevated temperature plasticity. *Materials Science and Engineering: A*. 2002;322(1-2): 1-22.

[5] Soer WA, De Hosson JTM, Minor AM, Morris JW, Stach EA. Effects of solute Mg on grain boundary and dislocation dynamics during nanoindentation of Al–Mg thin films. *Acta Materialia*. 2004;52(20): 5783-5790.

[6] Matzen ME, Bischoff M. A weighted point-based formulation for isogeometric contact. *Computer Methods in Applied Mechanics and Engineering*. 2016;308: 73-95. Available from: doi.org/10.1016/j.cma.2016.04.010.

[7] Joseph S, Lindley TC, Dye D. Dislocation interactions and crack nucleation in a fatigued near-alpha titanium alloy. To be published in *International Journal of Plasticity. Arxiv.* [Preprint] 2018. Available from: https://arxiv.org/abs/1806.06367 [Accessed 19th June 2018].

[8] Pollak W, Blecha M, Specht G. *Process for the production of molded bodies from silicon-infiltrated, reaction-bonded silicon carbide*. US4572848A (Patent) 1983.

[9] Brogan C. *Experts build pulsed air rig to test 3D printed parts for low carbon engines*. Available from: http://www.imperial.ac.uk/news/186572/experts-build-pulsed-test-3d-printed/ [Accessed 19th June 2018].

НАЗВАНИЕ СТАТЬИ: ВЫРОВНЯТЬ ПО ЦЕНТРУ, ШРИФТ, TIMES NEW ROMAN 14 BOLD, ЗАГЛАВНЫЕ БУКВЫ

Автор(ы): **А.Б. Первыйавтор[1], В.Г. Автор[2*]** - шрифт Times New Roman 12, bold, по центру

[1]Наименование организации, адрес, страна - шрифт Times New Roman 10, по центру

* e-mail автора, представившего статью - шрифт Times New Roman 10, по центру

Аннотация. Аннотация статьи составляет не более 12 строк. Используйте шрифт Times New Roman 12, одинарный межстрочный интервал.

Ключевые слова: укажите ключевые слова после аннотации.

Как организовать текст статьи. Используйте шрифт Times New Roman 12, одинарный межстрочный интервал. При необходимости выделить какую-либо информацию используйте *курсив*. Используйте **полужирный** шрифт только для заголовков и подзаголовков.

Номера страниц. Пожалуйста, не используйте нумерацию страниц

Таблицы, Рисунки, Уравнения. Подробные правила оформления данных элементов статьи приведены в инструкции на сайте журнала http://www.mpm.spbstu.ru

Литература

Ссылки приводятся в тексте в квадратных скобках [1,3,5-9]. Стиль оформления ссылок:

[1] Koch CC, Ovid'ko IA, Seal S, Veprek S. *Structural Nanocrystalline Materials: Fundamentals and Applications*. Cambridge: Cambridge University Press; 2007.

[2] Hull D, Bacon DJ. *Introduction to Dislocations*. 5nd ed. Amsterdam: Butterworth-Heinemann; 2011 Available from: https://www.sciencedirect.com/science/book// 9780080966724?via%3Dihub [Accessed 19th June 2018].

[3] Romanov AE, Vladimirov VI. Disclinations in crystalline solids. In: Nabarro FRN (ed.) *Dislocations in Solids*. Amsterdam: North Holland; 1992;9. p.191-402.

[4] Mukherjee AK. An examination of the constitutive equation for elevated temperature plasticity. *Materials Science and Engineering: A*. 2002;322(1-2): 1-22.

[5] Soer WA, De Hosson JTM, Minor AM, Morris JW, Stach EA. Effects of solute Mg on grain boundary and dislocation dynamics during nanoindentation of Al–Mg thin films. *Acta Materialia*. 2004;52(20): 5783-5790.

[6] Matzen ME, Bischoff M. A weighted point-based formulation for isogeometric contact. *Computer Methods in Applied Mechanics and Engineering*. 2016;308: 73-95. Available from: doi.org/10.1016/j.cma.2016.04.010.

[7] Joseph S, Lindley TC, Dye D. Dislocation interactions and crack nucleation in a fatigued near-alpha titanium alloy. To be published in *International Journal of Plasticity. Arxiv.* [Preprint] 2018. Available from: https://arxiv.org/abs/1806.06367 [Accessed 19th June 2018].

[8] Pollak W, Blecha M, Specht G. *Process for the production of molded bodies from silicon-infiltrated, reaction-bonded silicon carbide*. US4572848A (Patent) 1983.

[9] Brogan C. *Experts build pulsed air rig to test 3D printed parts for low carbon engines*. Available from: http://www.imperial.ac.uk/news/186572/experts-build-pulsed-test-3d-printed/ [Accessed 19th June 2018].